Mechanics and Physics of Creep, Shrinkage, and Durability of Concrete

A Tribute to Zdeněk P. Bažant

ASCE

Edited by Franz-Josef Ulm; Hamlin M. Jennings; and Roland Pellenq

EMI 1687 ASCE ENGINEERING MECHANICS INSTITUTE

MECHANICS AND PHYSICS OF CREEP, SHRINKAGE, AND DURABILITY OF CONCRETE

A Tribute to Zdeněk P. Bažant

PROCEEDINGS OF THE NINTH INTERNATIONAL CONFERENCE ON CREEP, SHRINKAGE, AND DURABILITY MECHANICS (CONCREEP-9)

September 22–25, 2013
Cambridge, Massachusetts

SPONSORED BY
IA-CONCREEP
Engineering Mechanics Institute of ASCE
American Concrete Institute
Concrete Sustainability Hub at MIT
Groupement de Recherche International "Multi-scale Materials Under the Nanoscope" of CNRS

EDITED BY
Franz-Josef Ulm
Hamlin M. Jennings
Roland Pellenq

Published by the American Society of Civil Engineers

Library of Congress Cataloging-in-Publication Data

International Conference on Creep, Shrinkage, and Durability Mechanics (9th : 2013 : Cambridge, Mass.)
Mechanics and physics of creep, shrinkage, and durability of concrete : a tribute to Zdenek P. Bažant : proceedings of the Ninth International Conference on Creep, Shrinkage, and Durability Mechanics (CONCREEP-9), September 22-25, 2013 Cambridge, Massachusetts / sponsored by IA-CONCREEP, Engineering Mechanics Institute of ASCE, American Concrete Institute, Concrete Sustainability Hub at MIT, Groupement de recherche international "multi-scale materials, under the nanoscope" of CNRS ; edited by Franz-Josef Ulm, Hamlin M. Jennings, Roland Pellenq.
pages cm
Includes bibliographical references.
ISBN 978-0-7844-1311-1 (print : alk. paper) -- ISBN 978-0-7844-7796-0 (ebook) 1. Concrete--Creep--Congresses. 2. Concrete--Expansion and contraction--Congresses. I. Bažant, Z. P. II. Ulm, F.-J. (Franz-Josef) III. Jennings, Hamlin. IV. Pellenq, Roland. V. Engineering Mechanics Institute. VI. Title.
TA440.I5225 2013
624.1'834--dc23
2013030292

American Society of Civil Engineers
1801 Alexander Bell Drive
Reston, Virginia, 20191-4400

www.pubs.asce.org

Any statements expressed in these materials are those of the individual authors and do not necessarily represent the views of ASCE, which takes no responsibility for any statement made herein. No reference made in this publication to any specific method, product, process, or service constitutes or implies an endorsement, recommendation, or warranty thereof by ASCE. The materials are for general information only and do not represent a standard of ASCE, nor are they intended as a reference in purchase specifications, contracts, regulations, statutes, or any other legal document. ASCE makes no representation or warranty of any kind, whether express or implied, concerning the accuracy, completeness, suitability, or utility of any information, apparatus, product, or process discussed in this publication, and assumes no liability therefore. This information should not be used without first securing competent advice with respect to its suitability for any general or specific application. Anyone utilizing this information assumes all liability arising from such use, including but not limited to infringement of any patent or patents.

ASCE and American Society of Civil Engineers—Registered in U.S. Patent and Trademark Office.

Photocopies and permissions. Permission to photocopy or reproduce material from ASCE publications can be obtained by sending an e-mail to permissions@asce.org or by locating a title in ASCE's online database (http://cedb.asce.org) and using the "Permission to Reuse" link. *Bulk reprints.* Information regarding reprints of 100 or more copies is available at http://www.asce.org/reprints.

Copyright © 2013 by the American Society of Civil Engineers.
All Rights Reserved.
ISBN 978-0-7844-1311-1
Manufactured in the United States of America.

Preface

Concrete, the solid that forms at room temperature from mixing Portland cement with water, sand, and aggregates, is the backbone material of our society's legitimate need for housing, shelter, hospitals, energy, and transport. But concrete suffers from time-dependent deformation under load. This creep occurs at a rate that deteriorates the durability and truncates the lifespan of concrete structures. However, the fundamental causes of concrete creep are still an enigma and have deceived many decoding attempts from both experimental and theoretical sides. In the United States alone, concrete creep is partly responsible for an estimated 78.8 billion dollars required annually for highway and bridge maintenance. In some applications, concrete creep and shrinkage is considered a serious threat to longevity and safety of our built concrete infrastructure, including bridges, containment structures, oil and gas well cement seals, and so on.

The contributions assembled in this book all aim at contributing to dissecting the very physical origin of creep and shrinkage of concrete, and to propel this knowledge from the scale of a few atoms to the scale of day-to-day engineering applications. They comprise both the invited and contributed papers presented at the Ninth International Conference on Creep, Shrinkage, and Durability Mechanics (ConCreep-9@MIT), held at the Massachusetts Institute of Technology, Cambridge, MA, U.S.A., from September 22–25, 2013. Now in its 9th edition, ConCreep-9@MIT continues a highly successful conference series on Creep, Shrinkage, and Durability Mechanics of Concrete and other Quasi-Brittle Materials, that started more than a half a century ago in Munich (1958,1968), Leeds (1978), Evanston (1986), Barcelona (1993), Cambridge (2001), Nantes (2005), and Ise-Shima (2008).

Hosted by the Concrete Sustainability Hub at MIT (http://web.mit.edu/cshub/), ConCreep-9@MIT brings together scientists and engineers at the leading edge of research and implementation of innovation related to creep, shrinkage, and durability mechanics of concrete and concrete structures. While the main objective of Concreep-9@MIT remains true to the original objectives of this conference series, to review and discuss novel efforts in both research and engineering practice on physical origin, prediction, and structural effects of time-dependent deformation, we recognize that the development of the next generation of science-enabled engineering solutions requires an outreach to fields that have classically not been associated with the ConCreep community. Specifically, through the co-sponsorship of this conference by the Groupement de Recherche International Multi-scale Materials Under the Nanoscope (GDRI, M2UN), we extend the outreach to the community of soft matter scientists, glasses physicists, and computational materials scientists. The results of this synergy can be traced throughout this book, from molecular and mesoscale scale

simulations and measurements to loss of prestress assessment due to creep and shrinkage using the latest advances in engineering design creep models.

We dedicate this collective work of the state-of-the-art of the science and engineering of creep and shrinkage of concrete to Zdeněk P. Bažant, the McCormick Institute Professor, Walter P. Murphy Professor of Civil and Environmental Engineering, Mechanical Engineering and Material Science and Engineering at Northwestern University, Evanston, Illinois, at the occasion of his 75th birthday. Zdeněk P. Bažant epitomizes like no other the theme of this conference series at the cross-road of fundamental physics and engineering. A native of Prague, Zdeněk P. Bažant's first encounter with creep and shrinkage was during his early practice as a Structural Bridge Engineer in the early 1960s in the former communist Czechoslovakia, which culminated in his 1963 doctoral dissertation on creep effects in concrete structures (subsequently published as a book). His postdoctoral studies in Paris and Toronto, during the short-lived period of liberalization in communist Czechoslovakia that preceded the Prague Spring in 1968, brought him to the West and to the forefront of research on creep and shrinkage of concrete. It culminated in his early fundamental contribution to the surface thermodynamics of volume change, hindered adsorbed water and disjoining pressure, which laid the foundation for the modern theory of creep and shrinkage mechanisms and its application in constitutive modeling and engineering design codes. After more than 45 years, this topic continues to be focus of cutting edge research. In the fall of 1969, he joined the faculty at Northwestern University. For more than four decades, Zdeněk P. Bažant continues to shape and redefine the engineering sciences in civil and mechanical engineering in general and of creep, shrinkage, and fracture of concrete and other quasi-brittle materials in particular. He is member of the National Academy of Engineers and the National Academy of Sciences of the United States of America and the founding president of IA-Concreep, the international association organizing the ConCreep conference series.

As the future of sustainable concrete engineering solutions is at stake, we trust that the conference papers in the ConCreep-9@MIT Proceedings will significantly contribute to Concrete Science and Engineering in the 21st Century and be a permanent tribute to the groundbreaking work of a scientist and engineer, educator, mentor, and friend, Zdeněk P. Bažant.

Franz-Josef Ulm
Hamlin M. Jennings
Roland Pellenq

Cambridge, MA, June 2013

Dedicated to
Zdeněk P. Bažant
on the occasion of his 75th birthday.

This page intentionally left blank

Contents

Keynote Lectures

Progress in Creep and Shrinkage Prediction Engendered by Alarming Bridge Observations and Expansion of Laboratory Database 1
Z. P. Bažant, M. H. Hubler, R. Wendner, and Q. Yu

Structure and Small Angle Scattering of Polydisperse Granular Porous Materials: A Fingerprint for Cement Paste 18
P. Levitz and S. Brisard

Nanoscale Numerical Study of C-S-H Precipitation and Gelation 30
Emanuela Del Gado and Katerina Ioannidou

The Counteracting Effects of Capillary Porosity and of Unhydrated Clinker Grains on the Macroscopic Strength of Hydrating Cement Paste: A Multiscale Model 40
Bernhard Pichler, Christian Hellmich, Josef Eberhardsteiner, Jaromír Wasserbauer, Pipat Termkhajornkit, Rémi Barbarulo, and Gilles Chanvillard

Creep Properties of Cementitious Materials from Indentation Testing: Significance, Influence of Relative Humidity, and Analogy Between C-S-H and Soils 48
M. Vandamme, Q. Zhang, F.-J. Ulm, R. Le Roy, B. Zuber, E. Gartner, and P. Termkhajornkit

A Depinning Model for Creep and Plasticity of Disordered Materials 62
David Bouttes and Damien Vandembroucq

Molecular and Meso-Scale Simulations and Characterization

NANO-CREEP of Synthetic CSH Produced using 1.5 and 0.7 CAO/SIO_2 Mixture Ratios 70
Michelle L. Begaye, Sherif H. Aboubakr, Jung J. Kim, and Mahmoud M. Reda Taha

Applying Tools from Glass Science to Study Calcium-Silicate- Hydrates 78
MJ. Abdolhosseini Qomi, M. Bauchy, R. J-M. Pellenq, and F-J. Ulm

Mechanical Behaviour of Ordered and Disordered Calcium Silicate Hydrates under Shear Strain Studied by Atomic Scale Simulations 86
H. Manzano, E. Masoero, I. Lopez-Arbeloa, and H. M. Jennings

Hydrothermal and Mechanical Stability of Metal-Organic Frameworks 98
François-Xavier Coudert, Aurélie Ortiz, Marta De Toni, Anne Boutin, and Alain H. Fuchs

NMR Investigations of Water Retention Mechanism by Cellulose Ethers in Cement-Based Materials 102
J.-P. Korb, L. Patural, A. Govin, and Ph. Grosseau

Water Sorption Hysteresis in Cement Nano Slits **110**
Wen Hui Duan, Shu Jian Chen, and Mija Hubler

Interpretation of Full Sorption-Desorption Isotherms as a Tool for Understanding Concrete Pore Structure **118**
Matthew B. Pinson, Hamlin M. Jennings, and Martin Z. Bazant

Multi-scale Hydric Transport in Hardened Cement Pastes and Reference Porous Silicate Materials **126**
H. Chemmi, V. Tariel, D. Petit, J-P. Korb, R. Denoyel, and P. Levitz

Water Isotherms, Shrinkage and Creep of Cement Paste: Hypotheses, Models and Experiments **134**
Hamlin M. Jennings, Enrico Masoero, Matthew B. Pinson, Elena G. Strekalova, Patrick A. Bonnaud, Hegoi Manzano, Q. Ji, Jeffrey J. Thomas, Roland J.-M. Pellenq, Franz-Josef Ulm, Martin Z. Bazant, and Krystyn J. Van Vliet

Diffusion Properties of Sodium and Lithium Silicates through Cement Pastes and its Mitigating Effect on Alkali-silica Reaction **142**
Irfan Prasetia, Soyo Asano, and Kazuyuki Torii

New Experimental Approach to Study Creep and Shrinkage Mechanisms of Concrete on the Nano-scale Level **150**
Harald S. Müller, Joerg-Detlef Eckhardt, and Michael Haist

Infinitesimal Shrinkage as Determined by Inverse Analysis Based on Drying and Shrinkage Tests **158**
B. Villmann, V. Slowik, P. Wang, and F. H. Wittmann

Kinetic Simulation of the Logarithmic Creep of Cement **166**
E. Masoero, H. Manzano, E. Del Gado, R. J.-M. Pellenq, F.-J. Ulm, and S. Yip

Recent Developments in Durability Mesomechanics of Concrete, Including Cracking via Interface Elements **174**
Joaquin Liaudat, Mariana Rodriguez, Carlos Lopez, and Ignacio Carol

Finite Element Based Characterization of the Creep Properties of the Cement Paste Phases by Coupling Nanoindentation Technique and SEM-EDS **182**
L. Sorelli, D.-T. Pham, D. Vallée, J. Chen, and M. Fafard

In-situ Chemo-Mechanical Characterization of Cementitious Microstructures with Coupled X-Ray Microanalysis and Indentation Technique **190**
Konrad J. Krakowiak, William Wilson, Simon James, and Franz.-J. Ulm

Micromechanics of Creep and Shrinkage

Efficient Homogenization of Ageing Creep of Random Media: Application to Solidifying Cementitious Materials **201**
J. Sanahuja

Multi-scales Characterization of the Early-age Creep of Concrete **211**
M. Farah, F. Grondin, M. Matallah, A. Loukili, and J. Saliba

Coupled Damage and Multiscale Creep Model Applied to Cementitious Materials **219**
B. Bary, Q.-C. He, and M.-Q. Thai

Micromechanical Model of Concrete Creep 227
Lev Khazanovich and Kairat Tuleubekov

Experimental Analysis of Drying Shrinkage Cracking in Coating Mortars by Digital Image Correlation 235
F. Benboudjema, T. Mauroux, P. Turcry, A. Ait-Mokthar, and O. Deves

Numerical Analysis of Cracking Induced by Drying Shrinkage in Concrete using a Mesoscopic Approach: Influence of Aggregates Restraint and Skin Effect 243
M. Briffaut and F. Benboudjema

Delayed Strains of Cementitious Materials – Impact of Heterogeneities and Creep on Cracking Induced by Drying 251
C. De Sa, C. Benboudjema, and A. Michou

Influence of the Initial Water Saturation of Aggregates on Concrete Shrinkage 261
E. Roziere, R. Cortas, A. Loukili, A. Hamami, and S. Staquet

Multiscale Creep, Shrinkage, Fracture and Durability Properties

Freeze-Thaw Resistance of Fiber Reinforced Composites with Superhydrophobic Admixtures 269
Scott Muzenski, Ismael Flores-Vivian, and Konstantin Sobolev

Experimental Study on Effect of Internal Cracking on Corrosion Rate of Reinforcement in Concrete 277
Isao Ujike, Shinichiro Okazaki, and Ryoichi Sato

Mechanical Properties of Deteriorated Hardened Cement Paste 285
K. Kurumisawa, H. Owada, and M. Shibata

Microstructure Improvement of Cementitious Systems using Nanomaterials: A Key for Enhancing the Durability of Concrete 293
L.P. Singh, S.K. Bhattacharyya, U. Sharma, G. Mishra, and S. Ahalawat

The use of Superabsorbent Polymers to Mitigate Shrinkage of Concrete 301
A. Assmann and H.W. Reinhardt

Measuring the Chemical Shrinkage of Alkali-Activated Slag Cements Using the Buoyancy Method 308
Christopher P. Cartwright, Farshad Rajabipour, and Aleksandra Radlińska

An Apparatus for Dissecting Volumetric Changes in Hydrating Cement Paste 316
M. Abuhaikal, S. Musso, J. Thomas, and F.-J. Ulm

Effectiveness of Various Superabsorbent Polymers (SAP) in Mitigating Autogenous Shrinkage of Cement-based Materials 324
V. Mechtcherine, C. Schroefl, and M. Gorges

Macrocrack Propagation in a Concrete Specimen Subjected to a Sustained Loading: Influence of Tensile Creep 332
Pierre Rossi and Jean-Louis Tailhan

Experimental Research and Numerical Simulation of Post-Crack Creep Behavior of SFRC Loaded in Tension 340
Guanyu Zhao, Marco di Prisco, and Lucie Vandewalle

Analysis of Concrete Creep in Compression, Tension and Bending: Numerical Modeling **348**
A. Hilaire, F. Benboudjema, A. Darquennes, Y. Berthaud, and G. Nahas

Improvement of Crack Resistance of Slag Concrete by Utilizing High Alite Cement **356**
Huynh Phuong Nam and Akira Hosoda

Experimental Determination of Early Age Fracture Toughness and Fracture Process Zone Size in Cement Pastes **364**
C. Hoover

The Significance of Nanosilica on Degradation of Oil Well Cement in Carbonated Brine Environments **372**
Andrew S. Griffin, Muhammad K. Rahman, Jung J. Kim, and Mahmoud Reda Taha

Optimization of Anti-creep Admixtures for Plasterboards **380**
J. Colombani and M. Bellotto

Role of Recycled Concrete Aggregates on the Long-term Behavior of Structural Concrete **388**
C. Mazzotti, S. Manzi, and M.C. Bignozzi

Effects of Poly Vinyl Alcohol Fibers in Fracture Energy of Concrete **396**
H. R. Ahmadian and M. Ganji

From Material Creep and Shrinkage to Structural Design

Desiccation Shrinkage of Large Structures: Is there a Size Effect? **404**
J. M. Torrenti and F. Benboudjema

Development of Comprehensive Platform for the Estimation of Volume Change and Damage in Cementitious Material **412**
T. Tanabe, S. Ono, H. Morimoto, H. Nakamura, and Y. Ishikawa

Simulation of Time-dependent Tensile Behavior of Concrete under Various Loading and Drying Path **421**
T. Shimomura, Y. Aoki, and H. Obata

The B4 Model for Multi-decade Creep and Shrinkage Prediction **429**
R. Wendner, M. H. Hubler, and Z. P. Bažant

Improved Estimation of Long-Term Relaxation Function of Aging Concrete from Its Compliance Function **437**
Z. P. Bažant, M. H. Hubler, and M. Jirásek

Overall Stiffness Reduction of Cracked Reinforced Concrete Beams Due to Long Term Effects **443**
Arnaud Castel, Raymond Ian Gilbert, and Gianluca Ranzi

An Effective Flexural Stiffness Equation for Long Term Deflection of Prestressed Concrete with and without Cracks **451**
R. Sato, K. Nakarai, Y. Ogawa, and K. Kawai

Viscoplastic Constitutive Relation for Relaxation of Prestressing Steel at Varying Strain and Temperature..... 459
Qiang Yu and Zdeněk P. Bažant

Material Law on the Time-dependent Stress-strain Behavior of Young Concretes 467
Isabel Anders and Harald S. Müller

Inverse Estimation of Thermal Properties of Concrete During Hydrating Process 475
Osvaldo D. Quintana, Antonio Aquino, Rubén López, Jean Marie Désir, and Eduardo M. B. Campello

Effect of Heat Elimination by Pipe Cooling System for Temperature Rise with Heat of Cement Hydration in Beam Using High Strength Engineered Cementitious Composites 483
T. Mizobuchi, T. Kanda, and M. Kunieda

Development of FEM Thermal Analysis for Concrete Structures with Pipe Cooling System 491
Yasuaki Ishikawa, Toshiaki Mizobuchi, and Tada-aki Tanabe

This page intentionally left blank

Author List

Abdolhosseini Qomi, MJ., 78
Aboubakr, Sherif H., 70
Abuhaikal, M., 316
Ahalawat, S., 293
Ahmadian, H. R., 396
Ait-Mokthar, A., 235
Anders, Isabel, 467
Aoki, Y., 421
Aquino, Antonio, 475
Asano, Soyo, 142
Assmann, A., 301
Barbarulo, Rémi, 40
Bary, B., 219
Bauchy, M., 78
Bazant, Martin Z., 118, 134
Bažant, Z. P., 1, 429, 437
Bažant, Zdeněk P., 459
Begaye, Michelle L., 70
Bellotto, M., 380
Benboudjema, C., 251
Benboudjema, F., 235, 243, 348, 404
Berthaud, Y., 348
Bhattacharyya, S.K., 293
Bignozzi, M.C., 388
Bonnaud, Patrick A., 134
Boutin, Anne, 98
Bouttes, David, 62
Briffaut, M., 243
Brisard, S., 18
Campello, Eduardo M. B., 475
Carol, Ignacio, 174
Cartwright, Christopher P., 308
Castel, Arnaud, 443
Chanvillard, Gilles, 40
Chemmi, H., 126
Chen, J., 182
Chen, Shu Jian, 110
Colombani, J., 380
Cortas, R., 261
Coudert, François-Xavier, 98
Darquennes, A., 348
Del Gado, E., 166
Del Gado, Emanuela, 30
Denoyel, R., 126
Désir, Jean Marie, 475
Deves, O., 235
Duan, Wen Hui, 110
Eberhardsteiner, Josef, 40
Eckhardt, Joerg-Detlef, 150
Fafard, M., 182
Farah, M., 211
Flores-Vivian, Ismael, 269
Fuchs, Alain H., 98
Ganji, M., 396
Gartner, E., 48
Gilbert, Raymond Ian, 443
Gorges, M., 324
Govin, A., 102
Griffin, Andrew S., 372
Grondin, F., 211
Grosseau, Ph., 102
Haist, Michael, 150
Hamami, A., 261
He, Q.-C., 219
Hellmich, Christian, 40
Hilaire, A., 348
Hoover, C., 364
Hosoda, Akira, 356
Hubler, M. H., 1, 429, 437
Hubler, Mija, 110
Ioannidou, Katerina, 30
Ishikawa, Y., 412
Ishikawa, Yasuaki, 491
James, Simon, 190
Jennings, Hamlin M., 118, 134
Ji, Q., 134
Jirásek, M., 437
Kanda, T., 483
Kawai, K., 451
Khazanovich, Lev, 227
Kim, Jung J., 70, 372
Korb, J.-P., 102

Korb, J-P., 126
Krakowiak, Konrad J., 190
Kunieda, M., 483
Kurumisawa, K., 285
Le Roy, R. , 48
Levitz, P., 18, 126
Liaudat, Joaquin, 174
Lopez, Carlos, 174
López, Rubén, 475
Lopez-Arbeloa, I., 86
Loukili, A., 211, 261
M. Jennings, H., 86
Manzano, H., 86, 166
Manzano, Hegoi, 134
Manzi, S., 388
Masoero, E., 86, 166
Masoero, Enrico, 134
Matallah, M., 211
Mauroux, T., 235
Mazzotti, C., 388
Mechtcherine, V., 324
Michou, A., 251
Mishra, G., 293
Mizobuchi, T., 483
Mizobuchi, Toshiaki, 491
Morimoto, H., 412
Müller, Harald S., 150, 467
Musso, S., 316
Muzenski, Scott, 269
Nahas, G., 348
Nakamura, H., 412
Nakarai, K., 451
Nam, Huynh Phuong, 356
Obata, H., 421
Ogawa, Y., 451
Okazaki, Shinichiro, 277
Ono, S., 412
Ortiz, Aurélie, 98
Owada, H., 285
Patural, L., 102
Pellenq, R. J.-M., 166
Pellenq, R. J-M., 78
Pellenq, Roland J.-M., 134
Petit, D., 126
Pham, D.-T., 182
Pichler, Bernhard, 40
Pinson, Matthew B., 118, 134
Prasetia, Irfan, 142
Prisco, Marco di, 340
Quintana, Osvaldo D., 475
Radlińska, Aleksandra, 308
Rahman, Muhammad K., 372
Rajabipour, Farshad, 308
Ranzi, Gianluca, 443
Reda Taha, Mahmoud, 372
Reda Taha, Mahmoud M., 70
Reinhardt, H.W., 301
Rodriguez, Mariana, 174
Rossi, Pierre, 332
Roziere, E., 261
Sa, C. De, 251
Saliba, J., 211
Sanahuja, J., 201
Sato, R., 451
Sato, Ryoichi, 277
Schroefl, C., 324
Sharma, U., 293
Shibata, M., 285
Shimomura, T., 421
Singh, L.P., 293
Slowik, V., 158
Sobolev, Konstantin, 269
Sorelli, L., 182
Staquet, S., 261
Strekalova, Elena G., 134
Tailhan, Jean-Louis, 332
Tanabe, T., 412
Tanabe, Tada-aki, 491
Tariel, V., 126
Termkhajornkit, P., 48
Termkhajornkit, Pipat, 40
Thai, M.-Q., 219
Thomas, J., 316
Thomas, Jeffrey J., 134
Toni, Marta De, 98
Torii, Kazuyuki, 142
Torrenti, J. M., 404
Tuleubekov, Kairat, 227
Turcry, P., 235
Ujike, Isao, 277

Ulm, F.-J., 48, 166, 316
Ulm, F-J., 78
Ulm, Franz.-J., 190
Ulm, Franz-Josef, 134
Vallée, D., 182
Van Vliet, Krystyn J., 134
Vandamme, M., 48
Vandembroucq, Damien, 62
Vandewalle, Lucie, 340
Villmann, B., 158
Wang, P., 158
Wasserbauer, Jaromír, 40
Wendner, R., 1, 429
Wilson, William, 190
Wittmann, F. H., 158
Yip, S., 166
Yu, Q., 1
Yu, Qiang, 459
Zhang, Q., 48
Zhao, Guanyu, 340
Zuber, B., 48

This page intentionally left blank

Progress in Creep and Shrinkage Prediction Engendered by Alarming Bridge Observations and Expansion of Laboratory Database

Z. P. Bažant[1], M. H. Hubler[2], R. Wendner[3], and Q. Yu[4]

[1] Northwestern University, Department of Civil and Environmental Engineering, Tech 2145 Sheridan Rd. A135, Evanston, IL 60208-3109; PH (847) 491-4025; email: z-bazant@northwestern.edu
[2] Northwestern University, Department of Civil and Environmental Engineering, Tech 2145 Sheridan Rd. A236, Evanston, IL 60208-3109; email: m-hubler@u.northwestern.edu
[3] University of Natural Resources and Life Sciences Vienna, Institute of Structural Engineering, Peter Jordanstr. 82, Vienna, Austria; email: roman.wendner@boku.ac.at
[4] University of Pittsburgh, Department of Civil and Environmental Engineering, 3700 O'Hara Street 730 Benedum Hall, Pittsburgh, PA 15261; PH (412) 624-9899; email: qiy15@pitt.edu

ABSTRACT

This keynote lecture presents a broad yet concise overview of the advances at Northwestern University since ConCreep-8, triggered by the success in 2008 in enforcing the release of the (legally sealed) data on the tragic 1996 collapse and the preceding, grossly excessive, deflections of the record-span segmental box-girder bridge in Palau. Subsequent analysis put the main blame for the excessive deflections on wrong design codes or recommendations. This revelation stimulated an extensive effort, generously funded by DoT and NSF, to advance the knowledge of concrete creep. First, several advances, presented in detail in other papers at ConCreep-9, are briefly reviewed; they include: 1) assembly of a greatly enlarged database of laboratory creep and shrinkage data for various concretes without and with admixtures; 2) collection of a database on deflections of 69 segmental bridges, mostly excessive; 3) development of an improved creep and shrinkage prediction model, labeled B4, and its joint statistical calibration by both databases; 4) improved rate-type algorithm for creep analysis in which the inverse Laplace transform is used in each time step to obtain the current retardation spectrum; 5) a realistic viscoplastic constitutive law for prestressing steel, applicable to time-varying strain and temperature; and 6) an improved algebraic formula for converting the aging compliance function to the relaxation function. Development of new formula for cyclic creep is described next, in detail. The formula is derived from Paris' law for the growth of micrometer size cracks. Its consequences for segmental bridges of various spans are discussed. The final discussion outlines new theoretical results showing that one mechanism causing the hysteresis of nanopore water sorption-

desorption isotherms consists of snap-through instabilities of water content, and of molecular coalescence. The nanopore water content matters for the disjoining pressure and the corresponding microprestress which destabilizes the bonds whose ruptures and restorations cause creep.

INTRODUCTION

Concrete creep, shrinkage, moisture sorption, diffusion, chemical hydration, cracking and evolution of self-equilibrated micro-stresses in the nano-structure are complex phenomena, all of which are important for predicting the long-time serviceability and sustainability of structures. Although the shrinkage of concrete was discovered by Le Chatelier already in 1887 and creep by Hatt in 1907, these phenomena are not yet sufficiently understood, despite many important advances achieved during more than a century of research (see, e.g., the literature review in Bažant,1987, and Jirásek and Bažant, 2003).

This lecture reviews several advances since ConCreep-8, triggered in 1998 by the success in enforcing the release of the (legally sealed) data from the tragic 1996 collapse of the record-span prestressed segmental bridge in Palau. These advances include: 1) a great enlargement of the database of laboratory creep and shrinkage tests; 2) a new database on excessive multi-decade bridge deflections; 3) an improved algorithm for step-by-step creep structural analysis; 4) a model for prestressing steel relaxation at variable strain and temperature; 5) a new model for sorption of water in the nanopores of concrete; and 6) a model for concrete creep under cyclic loading based on the growth rate of micrometer scale cracks. Only the excessive deflections and the cyclic creep model are described here in some detail, while the others are reviewed only cursorily since their details are presented separately.

EXCESSIVE MULTI-DECADE BRIDGE DEFLECTIONS—AN AWAKENING

Impetus: The initial impetus for revisiting the problem of creep effects (Bažant, Yu et al. 2010, 2012) came from Koror-Babeldaob (KB) Bridge in Palau. Built in 1977, this prestressed segmentally erected box girder had the world-record span of 241 m. Within 18 years, it deflected by 1.61 m, compared to the design camber (Fig. 1), and the average prestress loss in the tendons (bonded bars) was measured as 49%. Remedial prestressing undertaken in 1996 led, after a 3-month delay, to a sudden collapse, with fatalities.

This triggered attention to the multi-decade creep deflections of segmental bridges in general. A resolution of the 3rd Structural Engineers' World Congress in November 2007, proposed by Bažant, declared an engineer's consent to the sealing of technical data from legal litigation of structural collapses and damages to be a violation of engineering ethics (Bažant, Yu et al. 2010). In January 2008, the previously sealed technical data from the collapse investigation and litigation were released to Northwestern University (by Gary J. Klein of WJE, Highland Park, Illinois).

Analysis of Palau Data and Results: The data have been subjected to three-dimensional (3D) finite-element step-by-step creep analysis, taking into account the effects of cracking, segmental erection, sequential prestressing, concrete aging, age differences, viscoplasticity of prestressing steel at variable strain and temperature, shear lags in slabs and walls, non-uniform shrinkage and nonuniform drying creep properties.

The results have shown that the excessive deflections and prestress loss can be explained and closely matched if the theoretically based model B3 (Bažant and Baweja 1995, 2000), which became a 1995 RILEM Recommendation (Bažant and Baweja 1995), is used to characterize the creep and shrinkage properties. The B3 parameters giving a close fit of the deflection history were found to agree with the 30-year laboratory creep tests of Brooks (Brooks 2005); see the Set 2 curves in Fig. 1.

The same 3D finite element program was also run for model RILEM-B3 as originally calibrated by a worldwide laboratory database (see Set 1 curves in Fig. 1), and for other models which included the creep and shrinkage models of the current ACI-209, JSCE, GL and CEB-*fib* Model Code 2010 draft (ACI 209 1972, 2008, CEB-FIB 1990, fib 2010, FIB 1999, Gardner and Lockman 2001, JSCE 1996, JRA 2002); see Fig. 1. These other models have a form that does not allow recalibration by observed data since their only input is the concrete strength, which is given. The 18-year mid-span deflections computed from the CEB-fib, ACI-209, and GL models and the non-recalibrated model RILEM-B3 (Set 1) were, respectively, 34%, 31%, 43% and 57% of the measured deflection, and the computed 18-year prestress losses were 48%, 44%, 54% and 80% of the mean measured loss. Through the courtesy of Yasumitsu Watanabe, chief engineer of Shimizu Co., Tokyo, additional detailed data have subsequently been received on four of the excessively deflecting segmental bridges of that company.

Conclusions from Analysis: They are essentially two (Bažant, Yu et al. 2010, Bažant and Yu 2012):

a) The main cause of error lies in the creep and shrinkage model. All of the aforementioned models are unsatisfactory. Nonetheless, model RILEM-B3 gives significantly better predictions than the others and, if adjusted to fit the recently released 30-year laboratory data of Brooks (Brooks 2005), fits the measurements in Palau closely (Bažant, Yu et al. 2010, Bažant and Yu 2012); note, model B4, about to be released at Northwestern University, gives superior predictions. Hence, the creep specifications of fib (CEB-FIP 1990, *fib* Model Code 2010), as well as ACI-209 (ACI 209 1972, 2008) need to be revised (a 2012 revision of *fib* Model Code gives better prediction but still worse than B3 and B4).

b) Secondary contributing causes consist of the use of obsolete commercial beam-type creep analysis programs, neglect of differences in shrinkage and drying creep rates in slabs of different thicknesses and different thermal exposures, disregard of nonlinear response due to cracking, gross underestimation of prestress losses, and poor representations of segmental erection, sequential prestressing and concrete age differences (Bažant and Yu 2012) (the effect of cyclic creep is discussed later).

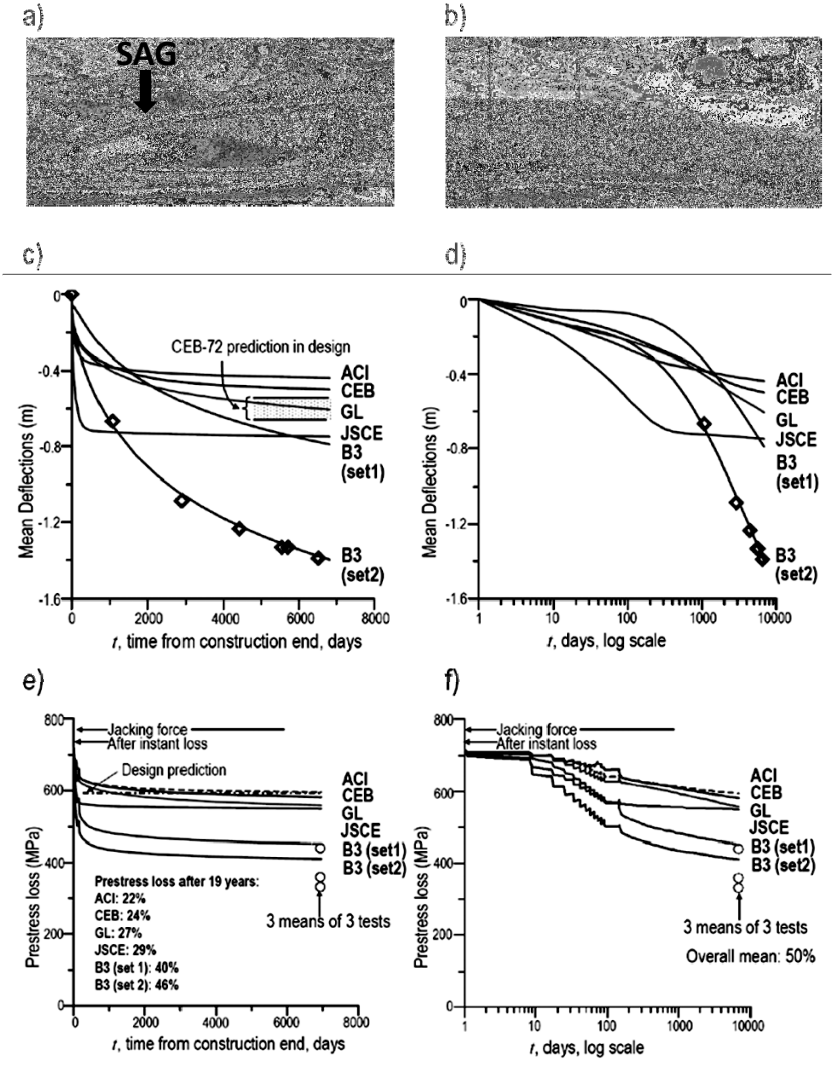

Figure 1. a,b) Creep sag of 1.61 m at mid-span of KB Bridge in Palau in 1996; b) ACI authorized reprint of photo from the cover of ACI SP-194 (2000) taken by Adam Neville before retrofit. c,d) Deflections calculated by 3D finite elements using models of CEB-fib, ACI-209, GL, JSCE and RILEM-B3 in linear (c) and logarithmic (d) time scales, compared to measurements (data points); d,e) Similar comparisons for prestress loss.

Excessive Deflections of Other Bridges: Are they rare? They are not. A subsequent search of various papers, company reports and society reports under the auspices of RILEM Committee TC-MDC was an awakening—excessive deflection histories of 69 large-span prestressed bridges from 9 countries have been obtained and 56 of them are fitted into Fig. 2 (Vítek 1997, Burdet and Muttoni 2006, Fernie and Leslie 1975, Pfeil 1981, Manjure 2001-2002). Most of them are excessive or will become excessive (all of them are segmental box girders except for one arch, and the horizontal dashed lines show the maximum acceptable deflection, 1/800 of the span). Hard to obtain though such examples are, hundreds more probably exist.

Of course, segmental bridges that have not deflected excessively (such as the Pine Valley Creek Bridge in California built in 1975) exist, too, but appear to be a minority. Even if a poor creep model is used, the deflections can be low if one adopts various precautionary measures listed at the end of (Bažant, Yu et al. 2010, Bažant and Yu 2012). Some of them, though, may be costly or span-limiting and may prevent daring slenderness.

It is particularly noteworthy that the logarithmic time plots in Fig. 2 give no hint of an approach to an asymptotic bound, a feature incorrectly implied by all the society recommendations, except model RILEM-B3 (and its predecessors since 1978) and the 2012 revision of *fib* Model Code 2010. The bridge observations document that the long-term creep is a logarithmic curve (as noticed on the basis of laboratory data already in Bažant, Carreira, and Walser (1975)).

Inferences from Collection of Deflection Histories: Why have the standard society recommendations on creep been misleading, for decades? Aside from disregard of the theoretical basis and wishful thinking in interpreting laboratory data, the problem has also been the inevitable statistical bias of the world-wide laboratory database (Bažant and Li 2008a, 2008b). In the latest and largest database, assembled at Northwestern in 2011, only 6% of creep test curves exceed 6 years, and only 4% 12 years. Also, there is a bias due to crowding of the data readings at short times and ages. Even if the statistical bias is removed by proper weighting (Bažant and Li 2008b), the laboratory database does not reveal the multi-decade trend.

In this light, inverse interpretation of the bridge deflection histories in Fig. 2 appears to be essential. Ideally, one should conduct statistical inverse 3D finite element creep analysis of these bridges. But it has appeared impossible to obtain data that would suffice for finite element analysis of the collected 69 bridge deflection histories, except for 6 of them.

Nonetheless, examination of the accurate solutions of the bridge in Palau and a few others showed that, for times $t > t_m$ (where $t_m = t_c + 1000$ days, $t_c =$ span closing time), the complex effects of nonuniform drying, segmental erection, sequential prestressing, concrete age differences and changes of structural system nearly die out. By comparisons with the accurate 3D solutions for the KB Bridge it was thus shown that the subsequent deflection $w(t)$ can be extrapolated from the measured 1000-day deflection w_{1000} with a surprisingly good accuracy by means of the simple formula:

$$w = w_{1000}\,[J(t, t_a) - J(t_c, t_a)] \,/\, [J(t_m, t_a) - J(t_c, t_a)] \qquad (1)$$

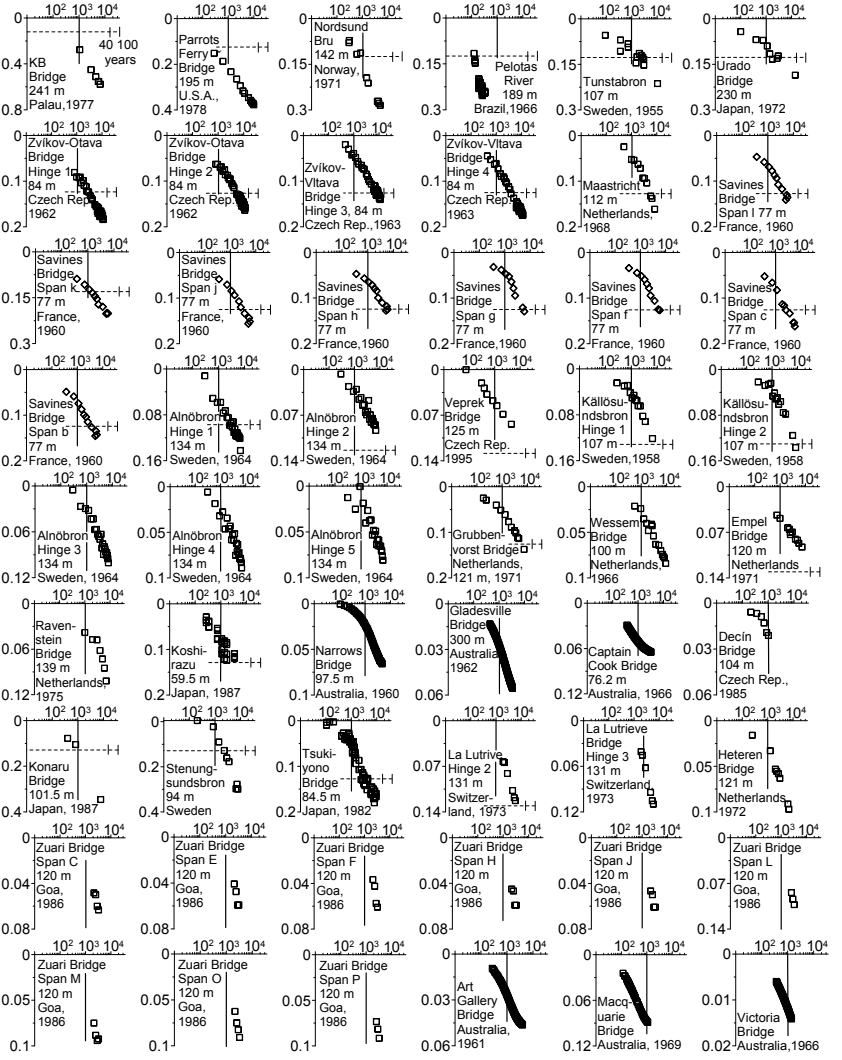

Figure 2. Deflection/span in % versus log-time in days of 56 (among 69) prestressed segmentally built box girder bridges (as a function of time t_c, in days, after span closing, in logarithmic scale). The horizontal lines shows allowable deflection (span / 800).

derived in 2010 by Bažant and verified in (Bažant, Hubler and Yu 2010); $t_a =$ average age of concrete at permanent load application; $t_m = t_c + 1000$ days, $t_c =$ time at span closing. However, the deflection w_{1000} at 1000 days after span closing cannot be predicted without detailed three-dimensional finite element creep analysis.

Although it turned out to be impossible to obtain the concrete strength and composition data for the 69 bridges (except 6) in Fig. 2, the average concrete properties for 36 of them (Fig. 3) could be estimated and statistical analysis conducted (Bažant, Hubler and Yu 2010). As a result, it was concluded that the long-time creep parameters q_3 and q_4 determined from concrete composition by the empirical formulas of model RILEM-B3 should be multiplied by correction factor 1.6. With this factor, the prediction of model RILEM-B3 for the terminal slopes becomes correct in the mean (Fig. 3) and the coefficient of variation of errors in the terminal slope gets greatly reduced (Bažant, Hubler and Yu 2010).

A problem related to creep is that the steel relaxation in prestressing tendons is generally defined only for a constant strain in steel. Analysis of the KB Bridge in Palau showed that the strain in steel can change by as much as 30% during lifetime, which (aside from temperature) has a significant effect on the stress relaxation in steel thus on prestress losses. An incremental viscoplastic model for prestressing steel, which is easy to use in time steps of rate-type finite element creep analysis, has been developed (Bažant and Yu 2012b) and should be introduced into the codes.

CYCLIC CREEP AND MICROMETER-SCALE CRACK GROWTH

In the discussions of KB Bridge deflections at ConCreep-8 and generally of creep damage papers at conferences during the last few decades, someone would typically ask: “And what about the effect of cyclic creep?" A hesitant intuitive answer would then follow since a realistic, experimentally verified, mathematical model of cyclic creep has been unavailable in the literature.

The phenomenon of cyclic creep of concrete, also called the fatigue creep or vibro-creep, was experimentally detected by Féret in 1906. Many researchers then studied it experimentally. The tests of Kern and Mehmel (1962) and of Gaede (1962) led to the first approximate estimates of the cyclic creep effects on prestressed segmental bridges (Bažant 1968a, b). The most important test data with a sufficient range were obtained by (Whaley and Neville 1973, Hirst and Neville 1977, Neville and Hirst 1978). In a recent report, Bažant and Hubler (2012) used these data to calibrate their new theory of cyclic creep based on the Paris law for the growth of micrometer-scale cracks. Development of this theory will now be briefly reviewed (for full detail, see (Bažant and Hubler 2013)).

Strain Due to Microcrack Growth: For various reasons, the cyclic creep must be attributed to the subcritical growth of microcracks. Since the compressive cyclic creep in the service stress range causes no significant degradation of strength, the size of these microcracks is probably in the micrometer range. Consider a generic three-dimensional planar macrocrack of size a (denoting, e.g., the radius of a penny-shaped crack); Fig. 4a. Although, in the case of compression loading, a shear crack with a combination of modes II and III seems to be most relevant, the analysis of a

tensile mode I crack is expected to be similar. The energy release rate due to three-dimensional self-similar growth of the crack may be expressed as

$$\mathcal{G} = \frac{\gamma_1}{a}\left[\frac{\Pi^*}{\partial a}\right]_\sigma \tag{1}$$

where Π^* is the complementary energy (or Gibbs' free energy) per microcrack, σ = applied remote stress, and γ_1 = dimensionless geometry factor (which, e.g., would be equal to $1/\pi$ in the case of a penny-shaped crack in mode I). The effective stress intensity factor at the crack edge may be defined on the basis of the average energy release rate, $K = \sqrt{E\mathcal{G}}$.where, in general, $\mathcal{G} = \gamma_2 a\sigma^2/E$. Here E = Young's elastic modulus and γ_2 = dimensionless geometry factor. For a mode I penny-shaped crack, $K = K_I = 2\sigma\sqrt{a/\pi}$, which gives $\gamma_2 = 4/\pi$.

According to Eq. (1), the total energy release rate of the crack is:

$$\left[\frac{\partial\Pi^*}{\partial\alpha}\right]_\sigma = \frac{\gamma_2\sigma^2}{3\gamma_1 E}a^2 \tag{2}$$

Integrating at constant σ, one gets

$$\Pi^* = \frac{\gamma_2\sigma^2}{3\gamma_1 E}a^3 \tag{3}$$

Let the volume per microcrack be l_c^3 and consider, for the sake of simplicity, that all the microcracks are normal to the direction of applied stress σ. According to Castigliano's first theorem, the displacement, u, per crack is:

$$u = \left[\frac{\partial\pi^*}{\partial P}\right]_a = \frac{1}{l_c^2}\left[\frac{\partial\Pi^*}{\partial\sigma}\right]_a = \frac{\gamma_0}{El_c^2}\sigma a^3 \tag{4}$$

where $P = \sigma l_c^2$, the applied force per crack, and $\gamma_0 = 2\gamma_2/3\gamma_1$= dimensionless constant characterizing the geometry. Since $u = l_c\epsilon$, the macroscopic strain caused by the formation of microcracks of size a under remotely applied stress σ is $\epsilon = u/l_c$ or

$$\epsilon = \frac{\gamma_0}{El_c^3}\sigma a^3 \tag{5}$$

The total increment of microcrack size over N cycles is $\Delta a_N = a_N - a_0$ where a_N is the crack size after N cycles and a_0 is the initial crack size before cyclic loading. According to Eq. (5), the strain increment due to cyclic loading is

$$\Delta\epsilon_N = \frac{\gamma_0}{El_c^3}\left(a_N^3 - a_0^3\right) = \frac{\gamma_0}{El_c^3}\sigma a_0^3\left[\left(1 + \frac{\Delta a_N}{a_0}\right)^3 - 1\right] \tag{6}$$

Since the creep strains in service are always small, we may assume that $\Delta a_N/a_0 \ll 1$. According to the binominal theorem, $(1+x)^3 \approx 1 + 3x$ when $x \ll 1$. Eq. (6) may thus be linearized as follows:

$$\Delta\epsilon_N = 3\gamma_0\ \frac{\sigma}{E}\left(\frac{a_0}{l_c}\right)^3\frac{\Delta a_N}{a_0} \tag{7}$$

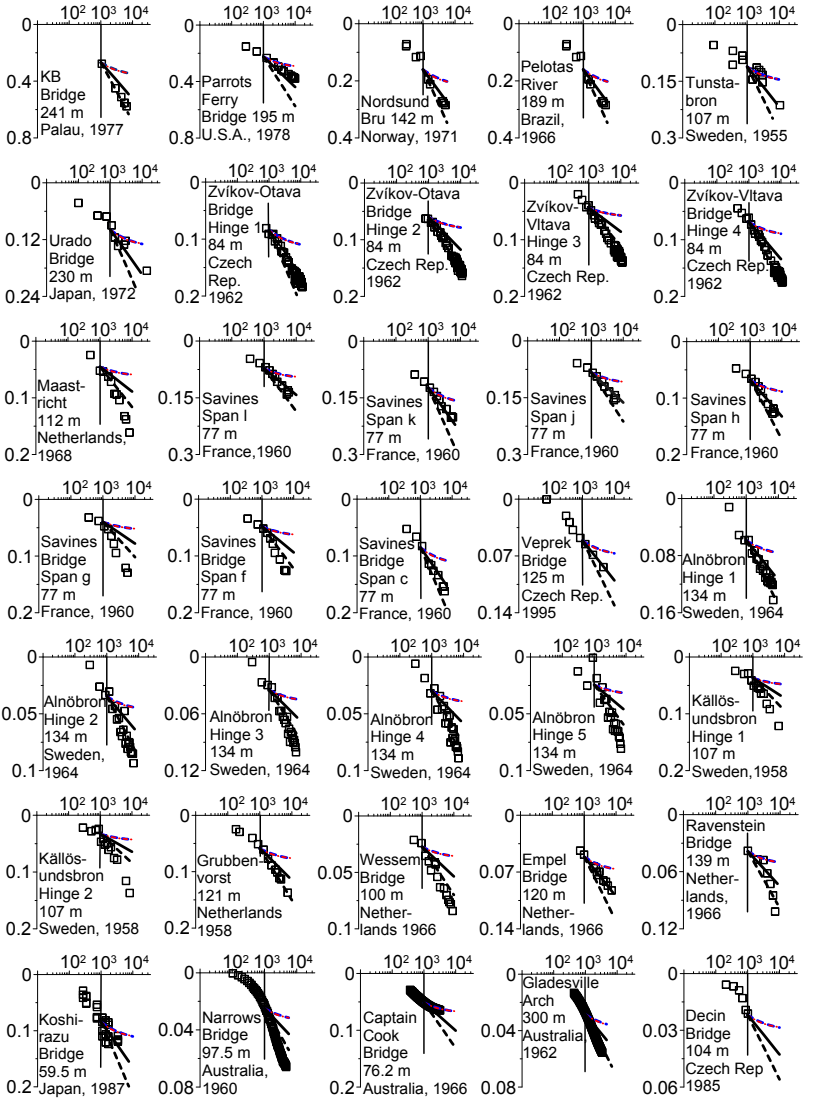

Fig. 3 Extrapolations by Eq. (1) from measured 1000-day deflection w_{1000} for 36 sets of bridge deflection records and for average concrete properties; calculated for models CEB-*fib* (— · —), ACI-209 (— —), RILEM-B3 (——), and RILEM-B3 model (— –) with terminal slope adjusted by $r = 1.6$.

Consequence of Paris Law: Consider now cyclic loading of amplitude $\Delta\sigma = \sigma_{max} - \sigma_{min}$ (Fig. 4b). Paris (with Erdogan) (Paris and Erdogan 1963) showed that (except for very small and very large ΔK) the subcritical fatigue growth of a crack depends almost only on the amplitude ΔK but not on the maximum or minimum of *K* individually. So the Paris law reads:

$$\frac{\Delta a}{\Delta N} = \lambda \left(\frac{\Delta K}{K_c}\right)^m \tag{8}$$

where K is the stress intensity factor, K_c is the critical value of K for monotonic loading (or fracture toughness), and λ and *m* are empirical constants. For mode I microcracks, $K = K_I =$ mode I stress intensity factor, while for shear cracks and compressive loading, *K* is a certain effective value for a combination of modes II and mode III and may better be interpreted as a characteristic derived from the average of the energy release rate $\mathcal{G} = K^2/E$ along the crack edge.

For the macrocracks in concrete, $m \approx 10$ (Le and Bažant 2011), while for embrittled polycrystalline metals, for which the fracture process zone (FPZ) size is of the micrometer scale, exponent m is known to be around 4. This difference is probably explained by the recent finding that the exponent of Paris law must roughly double when moving one scale up through the scales of material microstructure (Le Bažant 2011). The amplitude ΔK is proportional to the remotely applied stress amplitude $\Delta\sigma$, i.e.,

$$\Delta K = c\sqrt{a}\Delta\sigma \tag{9}$$

where c is a dimensionless geometry constant. E.g., for mode I penny shaped cracks, $c = 2/\sqrt{\pi}$. Substituting Eq. (9) into (8), we would get variable a on both sides of the equation. Although the resulting differential equation could easily be integrated by parts, we may consider that, in the case of creep under service loads, $\Delta a \ll a_0$. So, $\Delta K = c\sqrt{a_0}\Delta\sigma$. Integration at constant $\Delta\sigma$ then furnishes, for small crack extensions:

$$a_N - a_0 = \lambda \left(\frac{c\Delta\sigma\sqrt{a_0}}{K_c}\right)^m N \tag{10}$$

Cyclic Creep Law and Compliance: Substituting this into (7) and rearranging, we obtain for the strain increment due to cyclic creep after N cycles the formula:

$$\epsilon_N = C_1\, \sigma \left(\frac{\Delta\sigma}{f'_c}\right)^m N \tag{11}$$

$$\text{where} \qquad C_1 = \frac{3\gamma_0}{E}\,\frac{\lambda}{a_0}\left(\frac{ca_0}{l_c}\right)^3 \left(\frac{f'_c\sqrt{a_0}}{K_c}\right)^m \tag{12}$$

Here $f'_c =$ standard compression strength of concrete, introduced merely for convenience of dimensionality. Note that ϵ_N is predicted to depend on both σ and N

linearly. This agrees with the available cyclic creep measurements and is convenient for structural analysis.

Because σ appears in Eq. (11) linearly, it is possible to define the cyclic creep compliance $\Delta J_N = \Delta\epsilon_N/\sigma$, i.e.

$$\Delta J_N = C_1 \left(\frac{\Delta\sigma}{f_c'}\right)^m N \tag{13}$$

The total material compliance in presence of a cyclic loading component is $J_{tot} = J(t,t') + \Delta J_N$ where $J(t,t') =$ compliance for static creep (including elastic response).

While the foregoing analysis was exemplified by a tensile crack, it can be shown by dimensional analysis and similitude arguments that this analysis can be transplanted to cyclic creep due to micrometer size cracks under compressive or compression-shear loading, with a similar result (Bažant and Hubler 2013).

Test Data and Quantitative Estimates: Let us now use Eq. (7) to estimate the magnitude of $\Delta a_N/a_N$. This can be done easily for mode I penny-shaped cracks. According to the aforementioned values of γ_1 and γ_2, we have $\gamma_0 = 2\gamma_2/3\gamma_1 = 2(4/\pi)/(3\pi) = 8$. The ratio $\epsilon_{el} = \sigma/E$ represents the elastic strain under the static stress component. The ratio $\Delta\epsilon_N/\epsilon_{el}$ is roughly equal to the ratio of the cyclic creep deflection to the elastic deflection. According to estimates for typical prestressed box girder bridges and typical traffic loads, this ratio can reach up to 0.07 under service conditions.

To estimate the macro-strain, one may assume that the microcracks are very dense. In that case, following the classical philosophy of Eschelby, one microcrack may be assumed to be embedded in a homogeneous elastic continuum in which E represents the effective or average macroscopic properties of the microcracked material. Considering that, e.g., $l_c \approx a_0$, it can be estimated that $\Delta a_N/a_0 = 0.05/(8/3) \approx 0.019$. This means that the linearization in Eq. (6) is acceptable. At the same time, it agrees with the test data.

The data set of Whaley and Neville (1973) seems to be the only set comprehensive enough for calibration. It has been found that the present theory can fit these data closely. These experiments show that the cyclic creep exponent $m \approx 4$. According to the activation energy based probabilistic theory of quasibrittle fracture (Bažant and Le 2009, Le and Bažant 2011), exponent m of the Paris law should be equal to 2 on the nano-scale. Moving up through the scales causes the exponent m of the crack growth law to increase by approximately 2 for each scale order of magnitude. It is noteworthy that this value matches the fact that for metals and fine-grained ceramics, in which the RVE is of micrometer size, m is also approximately 4. For cyclic growth of macrocracks in concrete, the exponent is about 10, which is not surprising since several more scales must be crossed to get from the nano- to the macro-scale.

An indicator of the relative importance of cyclic creep in structures is the ratio of the cyclic (or residual) creep stress $E\epsilon_r$ to the tensile strength f_t', i.e.

$$\rho = \frac{E\epsilon_r}{f'_t} \tag{15}$$

where E is the Young's modulus. The values of this ratio calculated for typical segmental prestressed box girder bridges under various cyclic-to-dead load ratios and for various spans are shown in Fig. 4(e,f).

Because the cyclic creep is proportional to the mean stress and to the fourth power of the ratio of the load amplitude to the mean load, the cyclic creep is entirely negligible when the dead load is a high portion of the live load, more than 0.9. It can be significant when this portion is about 0.5 and is again negligible when the portion is very small. It is thus not unexpected that for bridges of large spans >150 m, the cyclic creep deflection is absolutely negligible. For medium spans between 60 m and 150 m, contrary to what has been often suspected, the effect is only minor, though not negligible. It should be taken into account in accurate analysis. For smaller spans such as 60 m the cyclic creep strain becomes larger, but is not important for deflections since the static creep deflections are small. In medium-span statically indeterminate girders, the cyclic creep can cause non-negligible redistributions of bending moments.

A much more important effect of cyclic creep is the development of tensile strains due to cyclic bending on the top and bottom faces of girders. Calculations show that it can significantly enhance surface cracking and thus contribute to the ingress of various ions and corrosion of reinforcement (for details, see Bažant and Hubler 2013). It remains to be checked whether the tensile strain due to cyclic bending could be important for surface cracking in concrete frames supporting heavy rotating machinery such turbines or electricity generators, or for wind-induced oscillations of tall slender towers or masts. The cyclic creep effects would be major for many-times repeated overloads well above the maximum allowable stress. But safety against such overloads are not a part of the usual design procedures.

OTHER ADVANCES

Extensive Lab/Bridge Databases and Model B4 Optimization: To develop a better model for creep and shrinkage prediction, the existing RILEM database of laboratory creep and shrinkage tests of RILEM and its subsequent extension at Northwestern has further been improved in a major way. The number of test histories in the database has been approximately tripled, to about 4000, and numerous data on modern high performance concretes with various admixtures have been included. Joint optimization of the simultaneous fit of the laboratory database and of the bridge deflection data, along with Bayesian updating, has been used to obtain an improved prediction model labeled B4. This effort is described in another paper at this conference (Wendner, Hubler, and Bažant 2013).

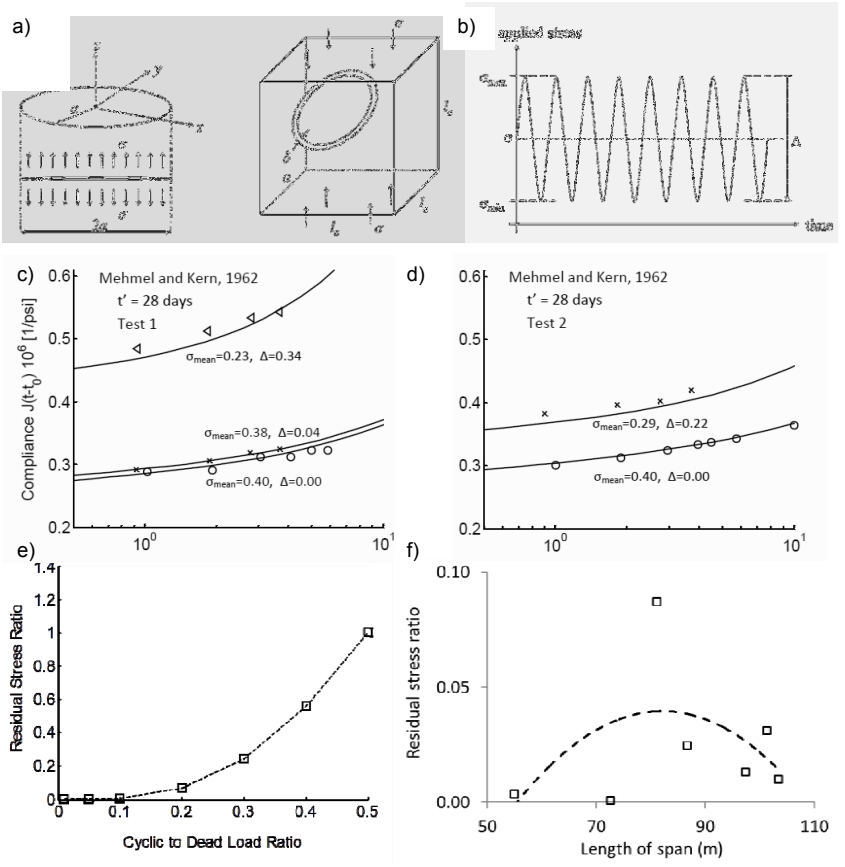

Fig. 4 a) Generic microcrack in three dimensions, and a mode I penny-shaped crack; b) typical cyclic stress history; c, d) optimal fitting of test data by Kern and Mehmel, 1962; e) the calculated residual stress ratio for a selection of cyclic to dead load moments, the dashed line representing an optimal parabolic curve fit; f) the residual stress ratio, calculated at the pier for a selection of typical section geometries and typical high traffic loads, designed to allowable limits, as a function of prestressed bridge span.

Improved Rate-Type Algorithm: To benefit from a refined creep prediction model such as B3 or B4, as well as its enhancement by cyclic creep, a rate-type algorithm for step-by-step 3D finite element analysis of structures is necessary. The treatment of the aging aspect in this algorithm has recently been facilitated by determining the current retardation spectrum by means of Widder's formula for the Laplace transform inversion. The Laplace transform is, of course, applicable only if there is no aging, but the absence of aging can be assumed for the duration of short time steps. Because of aging from one time step to the next, the spectrum must be recalculated in each time step in each integration point of each finite element.

Prestressing Steel Relaxation: Another refinement to be used in a rate-type algorithm is the development of a viscoplastic constitutive law for prestressing steel at variable strain and variable temperature. It is described in a separate paper at this conference (Yu and Bažant 2013).

Approximate Relaxation Function: Another paper at this conference presents an improved approximate formula for determining the relaxation function $R(t,t')$ from the compliance function $J(t,t')$. Compared to the previous formula, it gives better predictions for multi-decade relaxation for compliance functions such as those of B3 or B4 which terminate with a logarithmic curve (Bažant, Hubler, and Jirásek 2013).

Water Sorption in Nanopores as Creep Influencing Factor: Finally, the conference presentation includes brief information on new theoretical results showing that the hysteresis of sorption-desorption isotherms of nanopore water is caused not by pore collapse but by snap-through instabilities of water content, as well as by molecular coalescence of surface diffusion along nanopores. The sorption behavior controls the disjoining pressure in the nanopores and thus the corresponding microprestress which destabilizes the bonds whose ruptures cause creep in the solid nano-skeleton of hydrated cement. Thus it is important for a fundamental non-mechanics based theory of creep.

CLOSING REMARKS ON SOCIETAL IMPLICATIONS

Sadly, a tragic collapse of a big structure was necessary to trigger the present advances and obtain the necessary funding. But that is how the past advances in structural engineering have often happened. Sadly, too, the initial sealing of the data on the KB Bridge at the close of legal litigation delayed this trigger by about a dozen years, and it was only the public pressure of an ethics resolution of the Structural Engineers World Congress that eventually forced the lawyers' hand.

It appears, and is quite revealing, that the main cause of the KB Bridge deflection (and thus also the consequent collapse) turned out to be the obsoleteness of the design codes or recommendations of engineering societies. Interestingly, the correct explanation of the deflections is different from what the lawyers and court experts decided. This disaster, and the consequent revelation of the pervasiveness of excessive deflections of segmental bridges, underscores how important it is for engineering societies to introduce into their extensive ethics codes a clause declaring it to be unethical for an engineer to agree to a legal sealing of technical data from

major disasters. Regrettably, except for an inconsequentially watered down resolution to this effect passed by the civil engineering section of the U.S. National Academy of Engineering, proposals to the American civil engineering societies to institute such a clause have met with apathy. It is, unfortunately, in the interest of the litigating parties that their blame would not get revealed, and in the interest of court experts that their technically wrong testimony could not get reexamined by others.

Finally, note the difference from commercial aviation. In that field, the withholding of data from any disaster, or even a potential disaster, is not only unethical but actually a criminal act. Why the difference? Doubtless the societal pressure.

Acknowledgment: Generous support by the US National Science Foundation under grant CMMI-1129449 to Northwestern University, and by the US Department of Transportation for a grant 27740 under the auspices of the Infrastructure Technology Institute of Northwestern University, is gratefully acknowledged. Financial support for the development of the improved multi-decade prediction model B4 through the Austrian Science Fund (FWF) in the form of the Erwin-Schrödinger Scholarship J3619-N13 is greatly appreciated.

REFERENCES

ACI Committee 209 (1972, 2008) “Prediction of creep, shrinkage and temperature effects in concrete structures” *ACI-SP27, Designing for Effects of Creep, Shrinkage and Temperature*, Detroit, pp. 51—93 (reapproved 2008).

ACI Committee 209 (2008). “Guide for Modeling and Calculating Shrinkage and Creep in Hardened Concrete.” *ACI Report* 209.2R-08, Farmington Hills.

Bažant, Z. and Yu, Q. (2013). "Relaxation of Prestressing Steel at Varying Strain and Temperature: Viscoplastic Constitutive Relation." *J. Eng. Mech.ASCE*, July.

Bažant, Z. P. (1968). “On causes of excessive long- time deflections of prestressed concrete bridges. Creep under repeated live load” (in Czech), *Inženýrské Stavby*, 16, 317–320.

Bažant, Z. P., & Le, J. L. (2009). “Nano-mechanics based modeling of lifetime distribution of quasibrittle structures.” *Engineering Failure Analysis*, 16(8), 2521-2529.

Bažant, Z. P., and Hubler, M. H. (2013). “Theory of Cyclic Creep of Concrete Based on Paris Law for Fatigue Growth of Subcritical Microcracks.” to be submitted.

Bažant, Z., Hubler, M. H., and Jirásek, Z. P. (2013). “Improved Estimation of Long-Term Relaxation Function of Aging Concrete from Its Compliance Function.” CONCREEP-9, MIT.

Bažant, Z.P. and Baweja, S. (1995). “Creep and shrinkage prediction model for analysis and design of concrete structures: Model B3” (RILEM Recommendation), *Materials and Structures* 28, pp. 357--367 (Errata, Vol. 29, p. 126).

Bažant, Z.P. and Baweja, S. (2000). "Creep and shrinkage prediction model for analysis and design of concrete structures: Model B3." *Adam Neville Symposium: Creep and Shrinkage---Structural Design Effects*, ACI SP--194, A. Al-Manaseer, ed., pp. 1--83 (update of 1995 RILEM Recommendation).

Bažant, Z.P. and Li, G.-H. (2008). "Unbiased Statistical Comparison of Creep and Shrinkage Prediction Models." *ACI Materials Journal*. 105 (6), 610-621.

Bažant, Z.P., and Li, Guang-Hua (2008). "Comprehensive database on concrete creep and shrinkage." *ACI Materials Journal*. 106 (6, Nov.-Dec.), 635-638.

Bažant, Z.P., Carreira, D., and Walser, A. (1975). "Creep and shrinkage in reactor containment shells." *Jour. of Struct. Div*., Am. Soc. Civil Engrs., 101, 2117-2131.

Bažant, Z.P., Hubler, M.H., Yu, Q. (2010) "Pervasiveness of Excessive Deflections of Segmental Bridges: Wake-Up Cal for Creep" *Structural Egrg. Report*, Northwestern University; also *ACI Structural Journal*. 2011;108(6), 766-774.

Bažant, Z.P., Yu, Q., Li, G.-H., Klein, G.J., and Křístek, V. (2010), "Excessive deflections of record-span prestressed box girder: Lessons learned from the collapse of the Koror-Babeldaob Bridge in Palau." *ACI Concrete International* 32 (6), June, 44-52.

Bažant, Z.P., Yu, Qiang, and Li, Guang-Hua (2012). "Excessive long-time deflections of prestressed box girders: I. Record-span bridge in Palau and other paradigms, II. Numerical analysis and lessons learned." *ASCE J. of Structural Engrg.* 138 (6), 676—686 and 687--696.

Bažant. Z. P. (1968). "Langzeitige Durchbiegun- gen von Spannbetonbrücken infolge des Schwingkriechens unter Verkehrslasten" (Long-time deflections of pre-stressed concrete bridges due to cyclic creep under traffic loads), *Beton und Stahlbetonbau*, 63, 282–285.

Brooks, J.J., (2005) "30-year creep and shrinkage of concrete," *Magazine of concrete research* 57, pg. 545-556.

Burdet, O., Muttoni, A., (2006) "Evaluation of existing measurement systems for the long-term monitoring of bridge deflections," *Confederation Suisse*, Dec.

CEB-FIP Model Code 1990. *Model Code for Concrete Structures*. Thomas Telford Services Ltd., London, Great Britain; also published by Committee euro-international du béton (CEB), *Bulletin d'Information* No. 213 and 214, Lausanne, Switzerland.

Draft of *fib Model Code* 2010. Fédération internationale de béton (fib). Lausanne.

Fernie, G. N., Leslie, J. A., (1975) "Vertical and Longitudinal Deflections of Major Prestressed Concrete Bridges," Proc., *Institution of Engineers*, Australia no. 7516, *Symposium of Serv. of Concrete*, Melbourne, August.

FIB (1999). "Structural Concrete: Textbook on Behaviour, Design and Performance, Updated Knowledge of the CEB/FIP Model Code 1990." *Bulletin* No. 2, Fédération internationale du béton (FIB), Lausanne, Vol. 1, pp. 35--52.

Gaede, K. (1962). "Versuche uber die Festigkeit und die Verformungen von Beton bei Druck-Schwellbeansruchung." *Deutscher Ausschuß für Stahlbeton*, Heft 144, W. Ernst & Sohn, Berlin.

Gardner, N.J., and Lockman, M.J. (2001) "Design provisions for drying and creep of normal-strength concrete." *ACI Materials Journal*, 98 (2): 159-167.

Hatt, W.K. (1907). "Notes on the effect of time element in loading reinforced concrete beams." *Proc. ASTM* 7, 421-423.

Hirst, G.A., and Neville, A.M. (1977). "Activation energy of concrete under short-term static and cyclic stresses." *Mag. Concr. Res*., 29 (98), 13–18.

Jirásek, M., & Bažant, Z. P. (2002). *Inelastic analysis of structures*. Wiley.

JRA (2002). "Specifications for Highway Bridges with Commentary. Part III. Concrete." Japan Road Association, (in Japanese).

JSCE (1996). *Standard Specifications for Design and Construction of Concrete Structures*. Part I, Design. Japan Soc. of Civil Engrs. (in Japanese).

Kern, E., and Mehmel, A. (1962). "Elastische und plastische Stauchungen von Beton infolge Druckschwell- und Standbelastung". *Deutscher Ausschuß für Stahlbeton*, Heft 153, W. Ernst & Sohn, Berlin.

Le Chatelier, M. H. (1887). *Recherches experimentales sur la constitution des mortier hydrauliques*, Paris.

Le, J.-L., and Bažant, Z. P. (2011). "Unified nano-mechanics based probabilistic theory of quasibrittle and brittle structures: II. Fatigue crack growth, lifetime and scaling." *J. of the Mechanics and Physics of Solids*, 59, 1322–1337.

Manjure, P. Y., (2001-2002) "Rehabilitation/Strengthening of Zuari Bridge on NH-15 in Goa," Paper No.490, *Indian Roads Congress*, pp. 471.

Neville, A. M., and Hirst, G. A. (1978). "Mechanism of Cyclic Creep of Concrete." Douglas McHenry International Symposium on Concrete and Concrete Structures, ACI SP-55, 83–101.

Paris, P. C., and Erdogan, F. (1963). "Critical analysis of propagation laws." *J. Basic Eng*., 85, 528–534.

Pfeil, W., (1981) "Twelve Years Monitoring of Long Span Prestressed Concrete Bridge," *Concrete International*. Vol . 3 No. 8, pg. 79-84, Aug. 1.

RILEM Committee TC-69 (1988). (Z.P. Bažant, Chairman and princ. author), "State of the art in mathematical modeling of creep and shrinkage of concrete," in *Mathematical Modeling of Creep and Shrinkage of Concrete*, ed. by Z.P. Bažant, J. Wiley, Chichester and New York, 57–215.

Vítek, J.L., (1997) "Long-Term Deflections of Large Prestressed Concrete Bridges," *CEB Bulletin d'Information* No. 235, "Serviceability Models" Behaviour and Modeling of Serviceability Limit States Including Repeated and Sustained Load, CEB, Lausanne, pp. 215-227 and 245-265.

Wendner, R., Hubler, M. H., and Bažant, Z. (2013). "The B4 model for multi-decade creep and shrinkage prediction." CONCREEP-9, MIT.

Whaley, C. P., and Neville A. M. (1973). "Non-elastic deformation of concrete under cyclic compression." *Mag. Concr. Res*., 25 (84), 145–154.

Yu, Q. and Bažant, Z. P. (2013). "Viscoplastic Constitutive Relation for Relaxation of Prestressing Steel at Varying Strain and Temperature," CONCREEP-9, MIT.

Structure and small angle scattering of polydisperse granular porous materials: a fingerprint for cement paste.

P. Levitz[1] and S. Brisard[2]

[1] Université Pierre et Marie Curie, CNRS, Laboratoire PECSA, 75252 Paris Cedex 5, France. pierre.levitz@upmc.fr
[2] Université Paris-Est, Laboratoire Navier, IFSTTAR, 6-8 av. Blaise Pascal, Marne-la-Vallée F-77455, France

ABSTRACT

Small-angle X-ray and neutrons scattering (SAXS or SANS) is a widespread experimental tool for the investigation of the microstructure of random heterogeneous materials such as granular porous media. Such experiments allow operating on macroscopic samples and providing quantitative 3D information at length-scales between 1 and 500 nm, while keeping sample preparation to a minimum. SANS or SAXS can also be considered as a fingerprint of the morphology, allowing to test and to discard some microstructure hypothesizes. In this presentation, an analysis of various reconstructed polydisperse granular porous media is proposed. The evolution of the computed small angle scattering with the level and the nature of the polydispersity (ranging from monodisperse to very large polydispersity) are presented. Finally, our results are critically analyzed and reviewed in the perspective of hardened cement pastes.

INTRODUCTION

Numerous geomaterials, manufactured porous materials or concentrated colloidal suspensions are made of an intricate clustering of polydisperse grains. The particle organization on a length-scale ranging from a few tens of nanometers to some micrometers is a cornerstone to properly understand transport properties (diffusion-permeation) and mechanical strength. In this context, small angle X ray and neutron scattering (SAXS and SANS) are attractive and no destructive tools for the investigation of the microstructure of these strongly disordered systems. These experiments have the ability to probe a hierarchical organization on a large length scale ranging from nm to few hundred nanometers.
The case of cementitious materials is particularly challenging and investigation of cement pastes by SAXS or SANS started in the mid-eighties (Allen-1982, Allen-1987). Regardless of the precise composition or the age of the hardened cement paste, the scattering intensity I(q) invariably behaves as a fractional power of q in a low and very low q range ($I(q)\alpha\ q^{-\beta}$ with $\beta \sim 3\text{-}3.2$). Recently (Brisard-2012) using both

Transmission X ray Microscopy (TXM) (see Fig 1) and SAXS experiments (see fig 2), we have confirmed such an I(q) evolution on aged hardened cement paste (1.5 year old CEM-1). Figure 2 is a typical example of the intensity scattered by a cement paste. In the present case, the specimen was made from CEM-I cement, cast in a cylindrical mold where it stayed for a year; the water-to-cement ratio was w/c=0.35 and the final porosity is certainly lower than 0.25. The mold was then unsealed, and the specimen was wrapped in two layers of aluminum foil and stored at room temperature for six months; this sample preparation is routinely invoked at IFSTTAR in order to maintain endogenous conditions. This sample, previously cut in 0.1 mm thick slices, and stored in water was then submitted to small-angle X-ray scattering at the synchrotron Soleil-France (beamline SWING).

The resulting spectrum (see figure 2) clearly shows the existence of two power-law regimes, with a transition around q=0.2 nm^{-1} such as:

$$I(q) \propto q^{-(3+\gamma_1)}$$

for q<0.2 nm^{-1} with γ_1 around 0.2 and

$$I(q) \propto q^{-(2+\gamma_2)}$$

for q>0.2 nm^{-1} with γ_2 slightly above 0.

These results are in good agreement with many other published results (Allen-1987, Allen-1991, Allen-1998, Bedoe-1994, Heineman-2000, Winslow-1984 and Winslow-1995)

Various organization have been proposed to explain such a result ranging from a dense aggregation of strongly polydisperse particles to the popular globular model where an assembly of near-spherical colloids are densely packed (Jenning-2000,Jenning-2004,Jenning-2008). However, the microstructure of calcium--silicate hydrates C--S--H, one of the main hydration products of cement pastes, is still a matter of debate.

In this presentation, we propose an analysis of various reconstructed polydisperse granular porous media. The evolution of the computed small angle scattering with the level and the nature of the polydispersity (ranging from monodisperse to very large polydispersity) are presented. For a set of densely packed particles, the possibility to observe or not a correlation peak is analyzed (Brisard-2013). Some conditions allowing generating an algebraic evolution of I(q) are discussed. The possible appearance of a plateau at very small q (statistical homogeneity) is commented.

Figure 1: TXM image of two years-old Portland cement paste under vacuum. The image size is 554*851 pixels with a pixel size of 15.6 nm

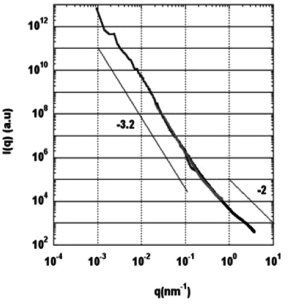

Figure 2: Small angle scattering curves of the hydration products shown in Fig 2a. Full line: computation using the TXM projection image. Full squares: SAXS experiments conducted on the same sample.

I/ SMALL ANGLE SCATTERING OF WEAKLY POLYDISPERSE GRANULAR MEDIA

We first present the case of well know random close packing (RCP) of monodisperse spheres of diameter D. A configuration of this medium is shown in Fig 3 (see for the way to generate it (Levitz-1003, Brisard-2013 and Donev-2005). The porosity is 0.27. The main feature of the computed small angle scattering shown in the rigth part of Fig 3 is a strong peak localized slightly above $2\pi/D$. This peak indicated the

emergence of strong positional correlation between proximal monodisperse spheres when the compactness is high (or the porosity is weak). Above this peak, one observes a series of oscillations with a global envelop evolving as q^{-4} (not shown in Fig 3). This is typical of the Porod regime of monodisperse spheres and is associated to the so-called form factor. Finally, one observe a strong I(q) depression in the left side of the correlation peak. This is remarkable feature associated to the zero compressibility of the random closed packing of hard spheres. In fact, when the size effect of the simulation box is corrected (see Brisard-2013 and Donev-2005), I(q)=0 as q=0. To sum up, a correlation peak and the q^{-4} are not observed in the case of CSH. Moreover, the low q CSH algebraic regime is not reproduced in the small angle scattering of a random close packing of spheres.

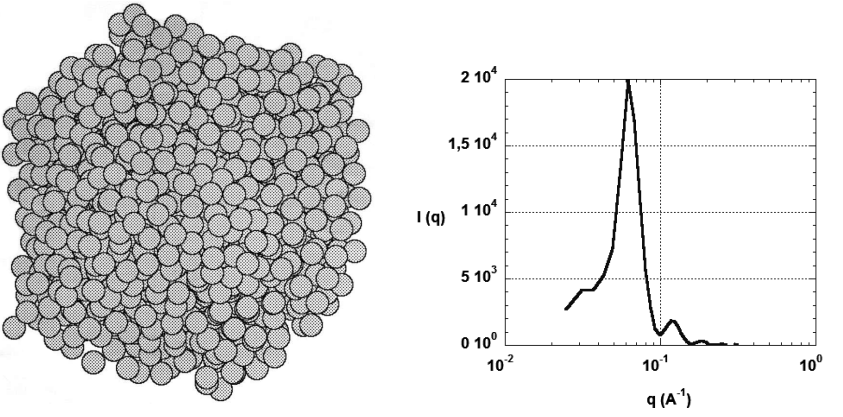

Figure 3: Computation of the small angle scattering of a random close packing of monodisperse spheres interacting with a hard core potential. The sphere diameter is 10 nm. On the left part: a snapshot of the simulation. On the right part: the small angle scattering not corrected from the finite size effect (see Brisard-2013).

The q^{-2} regime observed in Fig 2 could be the fingerprint of anisotropic flat particles. In the following we have generated a loosely packing of monodisperse discotic particles having a thickness of 3 nm and a diameter of 30 nm. A configuration with porosity of 0.47 is shown in the left part of Fig 4. As expected, close inspection of this configuration shows a local orientational order. A similar observation was performed for dense packing of oblates spheroids (Brisard-2013). The small angle scattering curve shown in the right part of Fig 4 is essentially dominated by the form factor of isolated particle (an extended q^{-2} regime between 0.02 and 0.2 A^{-1}). A plateau is observed at low q, meaning that at the corresponding correlation length, the packing looks homogeneous. Again for this type of granular medium, we did not succeed to generate the low q algebraic evolution observed in CSH.

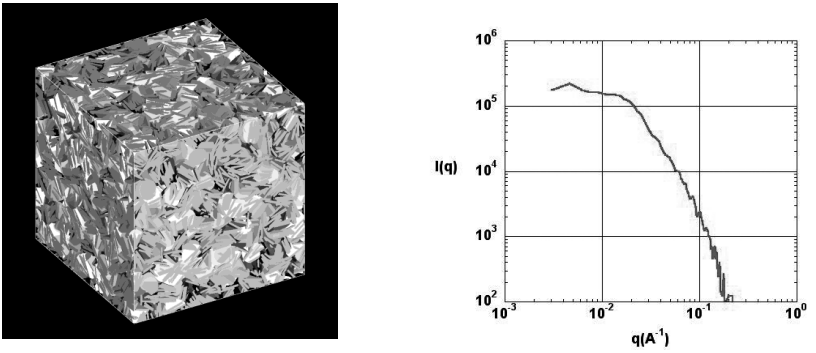

Figure 4: Computation of the small angle scattering of a random packing of monodisperse flat disks interacting with a hard core potential. The disk diameter is 30 nm and its thickness 3 nm. On the left part: a snapshot of the simulation. On the right part: the small angle scattering.

In order to generate more realistic situations, we now turn to the polydisperse dense configuration of spheres. The compacity is set at 0.64. The polydispersity is characterized by a log normal distribution with a characteristic polydispersity index α ranging from zero (monodisperse case) to 1. Similarly to the monodisperse case, each spectrum is strongly peaked around a rather small value. This again indicates pseudo-periodicity in the real space, which is due to the high compacity of the systems we generated. We note that the location of this peak shifts towards the origin (q=0) as the polydispersity index α increases. We were not able, however, to relate the location of the peak to the average radius of the particles <a>, through a simple law such as q_{peak}<a>=Const. Therefore, the physical interpretation of the characteristic length-scale to which q_{peak} relates remains unclear. We also note that this peak tends to widen as the polydispersity index α increases; this suggests that it would ultimately vanish for very high polydispersity. Finally, after finite size correction (Brisard-2013), no diverging algebraic regime is observed at very small q but a I(q) depression appearing in the left side of the correlation peak. This depression is less and less important as the polydispersity index increases, evolving toward a pseudo plateau.

A/

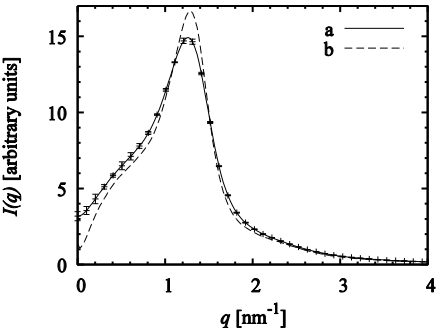

B/

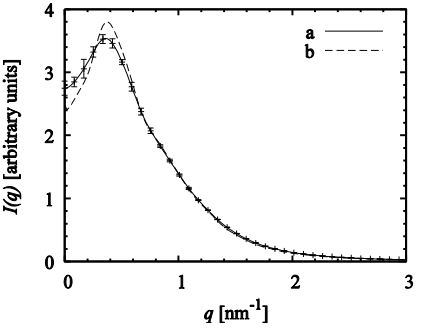

C/

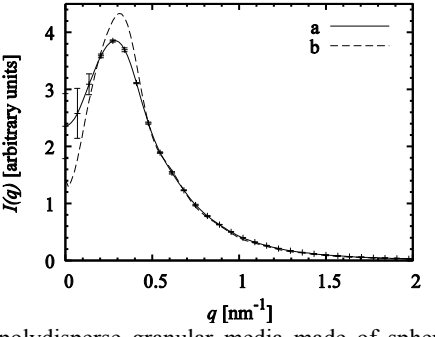

Figure 5. Generation of polydisperse granular media made of spheres with a log normal distribution of diameters and evolution of the small angle scattering. The compacity is set at 0.64. The polydispersity increases from A to C. Polydispersity index = 0.2 for A, 0.51 for B and 0.78 for C. The dotted lines (b) are the small angle scattering spectra corrected from finite size effects (See for details Brisard-2013)

II/ SMALL ANGLE SCATTERING OF STRONGLY POLYDISPERSE GRANULAR MEDIA

Small angle scattering spectra of gentle or weak polydispersed granular media presented in the former section share no common feature with the experimental cement scattering curves. The experimental algebraic divergence observed at small q in Fig 2 is probably associated to the existence of a set of multiscale features spreading on one or perhaps two orders of magnitude in size. One simple possibility to introduce such a multiscale character is to consider the random association of strongly polydisperse spheres characterized by a particle radius distribution N(r):

$$N(r) \propto \frac{1}{r^{\beta}} \qquad \text{Eq(1)}$$

where the algebraic evolution is obeyed in the window:

$$r_{\min} \leq r \leq \xi$$

One seminal example of such a dense and strongly polydisperse granular medium is the Apollonius packing where β=3.47 (Borkovec-1994). We have generated this Apollonian packing and computed its scattering intensity (Brisard-2013). A 3D view of this system is shown in Fig 6.

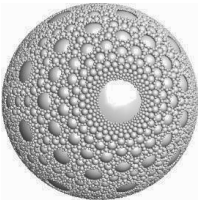

Figure 6: Three-dimensional view of an apollonian packing of spheres

Fig 7 shows that the scattering intensity curve comprises two power-law branches with a transition at $q=\pi/r_{min}$. At high-q, the Porod regime evolving as q^{-4} is retrieved, while at low q, the fractional power-law $q^{-2.47}$ is observed until $q=\pi/\xi$. This latter regime is consistent with the fractal dimension $d_p=2.47$ of the apollonian packing, which is a "mass" fractal characterizing the scale invariance of the pore space left between the spheres (Borkovec-1994). The organized hierarchy of the Apollonius packing allows reaching very low porosity (here 0.05).
As shown in Fig 7, the computed small angle scattering spectrum can be closely approximated by the following expression (Levitz-1992):

$$I(q) \propto -\frac{1}{q}\frac{d}{dq}\left[g(q)\right] \qquad \text{Eq. (2)}$$

With

$$g(q) = \frac{1}{q^2} \mathrm{Re}\, al\left(\frac{(1-\hat{f}_m(q)).(1-\hat{f}_p(q))}{1-\hat{f}_m(q).\hat{f}_p(q)}\right)$$

Eq. (3)

$\hat{f}_m(q)$ and $\hat{f}_p(q)$ are the Fourier transform of the probability density functions of the μ chords measured in the solid and the pore space respectively. We have checked on numerous other granular materials that Eqs. (2) and (3) represent a good approximation of the small angle scattering spectra of highly polydisperse systems.

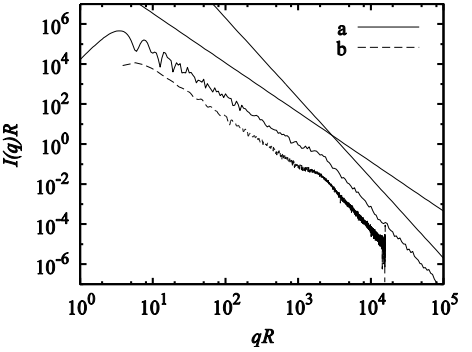

Figure 7: Scattered intensity pattern of the Apollonius packing shown in figure 6. computed with the method proposed in (Brisard-2013) (a), or using Eq. 3 (b). The two curves are in excellent agreement, and match perfectly without rescaling; for the sake of readability, curve (b) has been translated vertically. In order to allow for the direct comparison of the two methods, both q and I(q) have been made dimensionless through multiplication by the external radius R of the packing.

Interestingly enough, the use of eqs 2 and 3 and the knowledge of the chord distribution functions $f_m(r)$ and $f_p(r)$ allow separating the contribution of the so-called "form factor" linked to the size distribution of the spheres considered in infinite dilute situation and the part due to the mass correlation in this compact granular medium. As shown in Fig 8 and in good agreement with analytical properties of Eq.3, the form factor exhibits two power-law branches with a transition at $q=\pi/r_{min}$. At high-q, the Porod regime evolving as q^{-4} is retrieved, while at low q, the fractional power-law $1/q^{(7-\beta)}$ is observed until $q=\pi/\xi$. This last regime differs greatly from that of the global scattering evolving as $1/q^{(\beta-1)}$.

The present calculation is encouraging, as it suggests that the scattering intensity of packing with carefully chosen power-law size distributions might exhibit the two features: absence of correlation peak, existence of power-law branches (other than the classical Porod regime), which are required to provide a convincing model of cement pastes scattering curves.

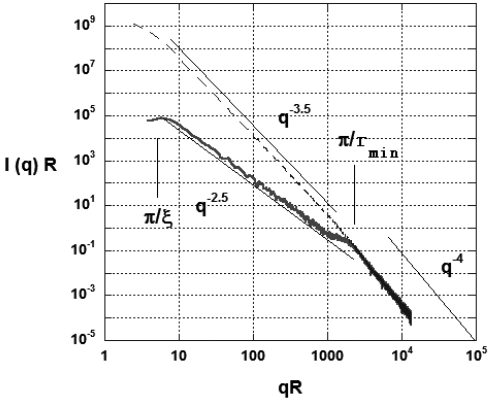

Figure 8. Small angle scattering spectra of the Apollonius computed with Eqs 2 and 3. In continuous line: the full spectra in good agreement with the direct computation using the configuration shown in Fig 6. Dotted line: computation of the"form factor".

These results might suggest that the sizes of the CSH globules in hardened cement pastes are distributed according to some very large size distributions. Such distribution would also lead to very large CSH colloidal particles.
Owing to Babinet's principle, a dual hypothesis is to assume that the sizes of the pores are distributed according to a power-law and they are the main contribution of the small angle scattering experiments at small q. In a recent NMR relaxation experiments (Plassais-2005), it was shown that the microstructure of cement evolves during and after completion of hydration in a range of length scales between 2 and 500 nm. In particular, the pore size distribution in volume of the cement paste reaches progressively an algebraic law running as $V_p(r) \sim 1/r^{\delta}$ with a characteristic exponent δ around 0.6-0.7. If the pore size distribution in number follows Eq. 1, we can easily get the relationship $\delta=\beta-3$ and a value of $\beta \sim 3.6\text{-}3.7$.

On the other hand, let us assume that the pore network has a low porosity (which is the case for the cement paste) and that it is made of random association of polydisperse spheres characterized by the pore radius distribution N(r) given by Eq 1. Using some analytical properties of Eqs 2 and 3 (Levitz-2013), it is possible to shown that on a large part of the q domain ranging from $q=\pi/\xi$ to $q=\pi/r_{min}$, g(q) evolves as

$$g(q) \propto \frac{1}{C_1 q + C_2 q^{5-\beta}}$$

From Eq 2, we see that in this q range, I(q) runs in between two power laws, q^{-3} and $q^{-(7-\beta)}$. For β=3.7 or δ=0.7, we can get in the large part of the q domain ranging from $q=\pi/\xi$ to $q=\pi/r_{min}$, a small angle scattering evolving as a pseudo power law with a exponent between 3 and 3.3.

III/ PERPECTIVES AND CONCLUSION

Concerning the structure of cement paste, our work shows that I(q) can be considered as a fingerprint of the structure, allowing to test and to discard some microstructure hypothesizes. More precisely, the analysis of our computations shows that if the particle size distribution is too narrow, the small-angle scattering spectrum of densely packed particles exhibits a sharp correlation peak, and no power-law regime (other than the Porod regime). By contrast, the correlation peak vanishes as the particle size distribution widens. This might suggest that the sizes of the CSH globules in hardened cement pastes are distributed according to some very large size distributions. We find this conclusion questionable, since such distribution would also lead to very large CSH colloidal particles. Owing to Babinet's principle, a dual hypothesis is to assume that the sizes of the pores are distributed according to a power-law and they are the main contribution of the small angle scattering experiments at small q. This hypothesis was outlined in this presentation with some support of recent experimental data published in the literature. A more comprehensible analysis of these topics will be published soon (Levitz-2013).

REFERENCES

Allen, A. J. and Windsor, C. G. and Rainey, V. and Pearson, D. and Double, D. D. and Alford, N. A (1982) small-angle neutron scattering study of cement porosities. *Journal of Physics D: Applied Physics*, 15, 1817--1833

Allen A.J., Oberthur R.C., Pearson D., Schofield P., and Wilding C R (1987), Development of the fine porosity and gel structure of hydrating cement systems *Philosophical Magazine Part B* 56, 263-288

Allen, A. J.(1991). Time-resolved phenomena in cements, clays and porous rocks. *Journal of Applied Crystallography*, 24, 624-634

Allen, A. J.(1991). Relationship between differences in silica fume additives and fine-scale microstructural evolution in cement based materials. *Advanced Cement Based Materials*, 8, 118-131.

Beddoe, R. E. and Lang, K.(1994) Effect of moisture on fractal dimension and specific surface of hardened cement paste by small-angle {X}-ray scattering. *Cement and Concrete Research*, 24, 605-612

Borkovec, M., De Paris, W. and Peikert, R. (1994). The fractal dimension of the apollonian sphere packing. *Fractals*. 2, 521—526.

Brisard, S; Chae, RS; Bihannic, I; Michot, L; Guttmann, P; Thieme, J; Schneider, G ; Monteiro, PJM ; Levitz, P (2012). Morphological quantification of hierarchical geomaterials by X-ray nano-CT bridges the gap from nano to micro length scales. *American Mineralogist*, Vol: 97 Issue: 2-3 Pages: 480-483.

Brisard S. and Levitz P (2013). Small-angle scattering of dense, polydisperse granular porous media: computation free of size effects, *Phys. Rev. E* 87, 1 013305.

Donev, A., Stillinger, F. H. and Torquato S (2005) Unexpected Density Fluctuations in Jammed Disordered Sphere Packings. *Physical Review Letters.* 95. 090604

Heinemann A. and Hermann H. and Haussler F. (2000). SANS analysis of fractal microstructures in hydrating cement paste. *Physica B: Condensed Matter*, 276—278, 892-893

Jennings, H-M. (2000) A model for the microstructure of calcium silicate hydrate in cement paste. *Cement and Concrete Research* 30, 101-116

Jennings, H. M.(2004). Colloid model of C-S-H and implications to the problem of creep and shrinkage. *Materials and Structures*. 37, 59-70

Jennings, H. M.(2008). Refinements to colloid model of {C--S--H} in cement:CMII. *Cement and Concrete Research*. 38, 275-289

Levitz, P. and Tchoubar (1992), D. Disordered porous solids : from chord distributions to small angle scattering. *Journal de Physique I*. 2, 771-790.

Levitz P (1993) Knudsen diffusion and excitation transfer in random porous media. *The Journal of Physical Chemistry* 97, 3813-3818

Levitz P. et al (2013) *submitted.*

Plassais A., Pomiès M.P., Lequeux N., Korb J-P, Petit D., Barberon F., and Bresson B.(2005 Microstructure evolution of hydrated cement pastes. *Phys. Rev. E* 72, 041401

D. N. Winslow (1985), The fractal nature of the surface of cement paste. *Cement and Concrete Research* 15, 817-824.

Winslow, D. N. and Bukowski, J. M. and Young, J. F(1994). The early evolution of the surface of hydrating cement, *Cement and Concrete Research*, 24, 1025--1032

Nanoscale numerical study of C-S-H precipitation and gelation

Emanuela Del Gado[1] and Katerina Ioannidou[1]
[1]Department of Civil, Environmental and Geomatic Engineering, ETH Zurich, Schafmattstrasse 6, 8093 Zurich (Switzerland); email: delgadoe@ethz.ch

ABSTRACT

Mechanical and viscoelastic behavior of cement crucially depends on the Calcium-Silicate-Hydrate (C-S-H) gels, the "glue" of cement, and on the slow evolution (aging) of its local composition and morphology. Hence, design of high performance and more environmentally friendly cement demands a deeper understanding of physical processes underlying the precipitation process, when the C-S-H gel develops, and cement sets. C-S-H gel forms and become denser by precipitation of colloidal particles of few nanometers within a couple of hours. To access the relevant length and time scale for the development of the microstructure and of the mechanical strength of C-S-H gel, we developed a coarse-grained colloidal model for precipitation of C-S-H nano-particles using a combination of Monte Carlo and Molecular Dynamics numerical simulations. The microstructure of C-S-H gel is determined by the chemical conditions and the continuous particle precipitation that drives the system out of equilibrium. In our simulations, we control the chemical conditions by the effective interaction of the C-S-H particles and the particle precipitation rate. Here, we compare results on the evolution of C-S-H microstructure for two different effective interactions that comply with experimental and theoretical finding on C-S-H, and different precipitation rates. In particular, we can monitor the development and the evolution of the microstructure and mechanical properties of C-S-H during the precipitation. Combining this information we aim at rationalizing how the precipitation process can be tuned to control the microstructure formation and hence, the mechanical performance of C-S-H.

INTRODUCTION

The development of C-S-H (calcium-silicate-hydrate) gels during cement hydration is crucial to the mechanical performance of cement and concrete, but is still poorly rationalized, with several fundamental issues under debate. In particular, the forefront of industrial and academic research is now on chemical modification of cement, aimed at reducing its environmental impact (5-8% of man-made CO_2 comes from cement processing for concrete). It is increasingly clear that no progress is really possible without understanding how such chemical modifications may affect structure, cohesion and mechanics of C-S-H gels. During dissolution in water of the clinker grains that contain calcium silicates, C-S-H hydrates precipitate in the supersaturated ionic solution in the capillary pores of the paste. These nano-scale colloidal clusters form the gel, an interconnected, cohesive soft solid that has structural complexity on multiple length-scales and it is the main responsible for cement strength [Allen, Bullard, Muller, Nicoleau, Pellenq 2010, Taylor, Vandamme 2009]. Whereas recent studies have systematically investigated the chemical evolution, from the dissolution of the clinker to the precipitation of C-S-H [Bullard, Nonat], the development of the physical properties of the gel is mainly unexplored. Modeling and computational studies have been mostly focused on sub-nanometer scales or otherwise on the micron-scale structure [Manzano, Bishnoi] leaving aside

the range of length scales from several tens to hundreds of nanometers. This is instead particularly crucial because the structural heterogeneity and lack of long-range order, that clearly arise over these length scales, ultimately determine their mechanics [Constantinidis, Masoero 2012, Masoero 2013, Vandamme 2009, Vandamme 2010]. Hence investigating and rationalizing the complex development of the gels between nano-meters and microns during hydration could enable completely new ways of designing cement performance and green formulations.
Only very recently new approaches have been developed to address the physical properties of C-S-H in the critical range of length-scales between nano-meters and microns [Masoero 2012]. Here, with an approach quite unusual for cement research, we study the formation of C-S-H gels during cement hydration in terms of a colloidal *open* system, where nano-particles can precipitate. Within this framework, we have developed a combination of Grand Canonical Monte Carlo (GCMC) and Molecular Dynamics (MD) numerical simulations that allows us to investigate the development of the gel microstructure and mechanics during hydration [Ioannidou].

HYDRATION KINETICS AND GEL STRUCTURE

In our model, C-S-H hydrates are represented by colloidal particles that progressively *precipitate* in the simulation box, ideally representing a small volume in a capillary pore. Structural and mechanical properties of colloidal gels are typically the results of a complex interplay between the kinetics of the gel formation, controlled by the external conditions, and the local interactions. We want to investigate how the structure and the mechanical properties of the C-S-H gel emerge during precipitation as the results of the interplay between the precipitation kinetics, controlled by the evolution of the chemical composition and the dissolution of the clinker, and the effective interactions between the hydrates. Most crucially, these properties will depend on how fast precipitation takes place with respect to the time scale associated to structural relaxation in the gel that is progressively formed.
We mimic the precipitation with a Grand-Canonical Monte Carlo, where a particle can be inserted or deleted with a probability given by a Metropolis Monte Carlo (MC) scheme [Frenkel] and determined by the related total cost in free energy. This is obtained as the difference, at a fixed temperature T, between the change in the internal energy (due to inter-particle interactions) and the free energy gain corresponding to the formation of a C-S-H hydrate. The latter is expressed by the chemical potential whose value corresponds to the nucleation barrier for a C-S-H hydrate (the nano-scale unit of our gel) in the initial solution and sets the equilibrium density of C-S-H that can be reached in the pore. During cement hydration and C-S-H precipitation, the pore solution is always supersaturated. To reproduce these conditions we choose values of the chemical potential that favor insertion and drive the system towards progressive densification.
Starting from this, we have designed a hybrid scheme in which we couple the MC insertion/deletion events to a Molecular Dynamics (MD) simulation. MD allows us to follow the microscopic dynamics and the formation of the microstructure as the density increases [Ioannidou]. The number of MC attempts over the number of MD

steps defines the precipitation rate R, a parameter that characterizes the kinetics of dissolution/precipitation in the experimental system. Overall, the amount of precipitated particles in the simulation box is the results of the effective interactions between particles, the chemical potential and the imposed precipitation rate. This conceptually simple approach allows us to rationalize the role of the rate (and therefore of the parameters that control it) on the development of the physical properties of the system and its interplay with emerging cooperative processes due to the densification of the microstructure.

We use effective interactions between the colloidal nano-particles that mimic different chemical conditions (e.g., lime concentration) as obtained in experiments [Plassard, Lesko]: AFM measurements confirm the presence of strong non contact attractive forces, whose strength increases with the ion coupling in the pore solution [Jönsson, Pellenq 2004]. The inter-particle force displays a strong attractive minimum and a secondary maximum (due to the crossover from anionic to cationic concentration profiles). The position of minimum, secondary maximum and strength of the related interaction potential are chosen within the range of the experimental values. For the potential we use a simple form based on a generalized Lennard-Jones (LJ) attraction and Yukawa repulsion, as often used for colloidal systems [De Candia, Toledano]:

$$V(r) = 4\varepsilon\left[\left(\frac{\sigma}{r}\right)^{2\gamma} - \left(\frac{\sigma}{r}\right)^{\gamma}\right] + A\frac{e^{-kr}}{r}$$

where r is the distance between two particles. In the following we consider two sets of values for the parameters (**ε, γ,** A, k) which correspond respectively to high (S1) and low (S2) lime concentration in the experiments.

Kinetics and densification. In Figure 1, we show the evolution of the volume fraction φ(t) occupied by the C-S-H hydrates over time, obtained from our numerical simulations. The data refer to systems of 100-20000 particles and they have been averaged over 5 statistically independent samples. The time here is measured in the natural time unit of the MD simulations $(m\sigma^2/\varepsilon)^{1/2}$, where m is the mass of the colloidal hydrates, σ is their diameter and ε is the unit energy that gives the interaction strength [Frenkel]. For C-S-H hydrates we consider that σ ≈1- 20 nm, and we set the unit energy ε to the strength of the attraction measured in AFM experiments. The simulations are performed at a fixed temperature T=0.15 in reduced units, corresponding to the room temperature in the experiments. The volume fraction φ(t) is estimated as

$$\varphi(t) \approx \frac{\pi}{6}\sigma^3\frac{N(t)}{V}$$

where V is the fixed volume of the simulation box and N(t) is the number of particles in the simulation box over time. Hence φ(t) is the fraction of the total volume available in the simulations (i.e., a small volume within a capillary pore) that is

occupied by C-S-H hydrates as the hydration proceeds. Although this is not a quantity easily accessible in experiments on C-S-H, it allows us to immediately connect the stages of the densification process to the filling of the physical volume available. Moreover we can compare the values to the ones typically attained for interacting colloidal suspensions (e.g., random close packing for hard repulsive spherical particles, where jamming occurs, can be located around 64%) [Zaccone].

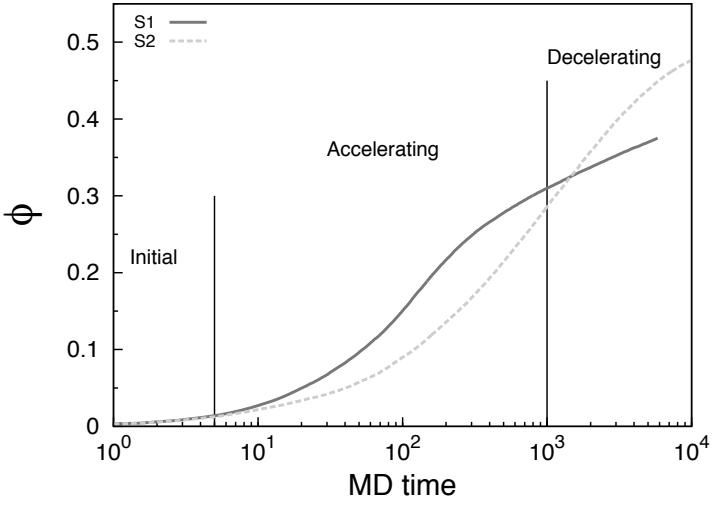

Figure 1. Hydration kinetics as obtained from numerical simulations in terms of the volume fraction occupied by C-S-H hydrates in the pore solution as a function of simulation time for S1 (continuum line) and S2 (dashed line). The vertical lines for the onset of acceleration and deceleration regimes refer to S1.

On the other hand, the volume fraction occupied by the hydrates over time is in good approximation directly proportional to the amount of hydrates produced as hydration proceeds and hence to the degree of hydration that can be measured in experiments [Garrault, Ioannidou]. The two curves in the Figure refer to different effective interactions potentials (S1 and S2) that correspond to different lime concentrations (respectively low and high) considered in the experiments [Lesko, Plassard].

The simulations in this case were performed using a precipitation rate R=1, that is roughly in the middle of the range of values explored in our numerical study. The data display a sigmoidal shape of the same kind of the one typically measured in experiments by monitoring the degree of hydration over time. In particular, the acceleration and deceleration regimes found in the simulations appear also in the experimental data and have been indeed extensively discussed in the literature, where they are typically interpreted in terms of the evolution of the chemical compositions during the hydration process [Garrault, Nonat]. The data show that, although

precipitation is overall more effective in S2 (where higher volume fractions are reached at earlier times), the acceleration takes place earlier in S1, with a stronger dependence on the precipitation rate. The deceleration regime takes place more abruptly in S1, where ultimately the rate of the hydrate volume fraction seems to reach a steady state (small but finite) value over the simulation time window. S2 displays instead a slower transition into the deceleration regime that seems to correspond to a complete arrest of the precipitation process within the simulation time window. Overall the data indicate that the differences in the evolution of the degree of hydration reported in experimental studies for different lime concentrations could be ascribed to the differences of the effective physical interactions emerging under different chemical conditions. This points in general to the role of the evolution of physical properties in the system during the hydration for determining the features of C-S-H gels, an issue that has been hardly addressed so far.

Morphology of the gels and local packing. In Figure 2 we show snapshots of the gel obtained for S1 and S2 in simulations: the left and central snapshots refer to simulations performed for S1 and S2 respectively at a fixed volume fraction 20%, where the structure of the gel forms by spontaneous assembly of the particles in the simulations without precipitation.

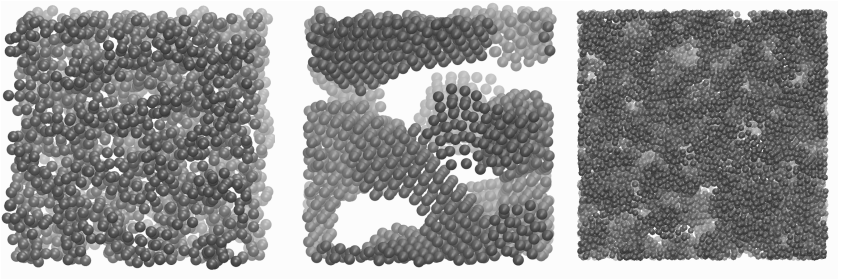

Figure 2. Snapshots of the gel formed in S1 (left) and S2 (center) in equilibrium (i.e., at a fixed volume fraction 20%). For S2 the structure of the gel depends strongly on R: on the right, the gel obtained with R=4 at the same φ.

The different interactions correspond to stable phases that are morphologically very different, hence the gels that form upon kinetic arrest of those phases also display significantly different morphologies [Ioannidou 2013]. The right-end snapshot has been obtained for S2 in the hybrid simulations MC-MD using a precipitation rate R=1 and the comparison with the central one well exemplifies how the kinetics of precipitation may dramatically change the gel morphology (e.g. pore sizes). Interestingly enough, this effect is clearly stronger for S2 than for S1, where the same variation of the precipitation rate produced much smaller changes of the gel morphology.

We can identify how these morphological changes in the gels takes place already at the level of the local packing. We quantify the local structure of aggregates and gels in the simulations by computing the pair correlation function g(r) that measures the probability of finding a particle at a distance r from another one [Frenkel]. In Figure 3 and 4 the pair correlation function g(r) is plotted as a function of r for S1 and S2 respectively at volume fraction 20%, without precipitation and with R=0.2 and R=4.0.

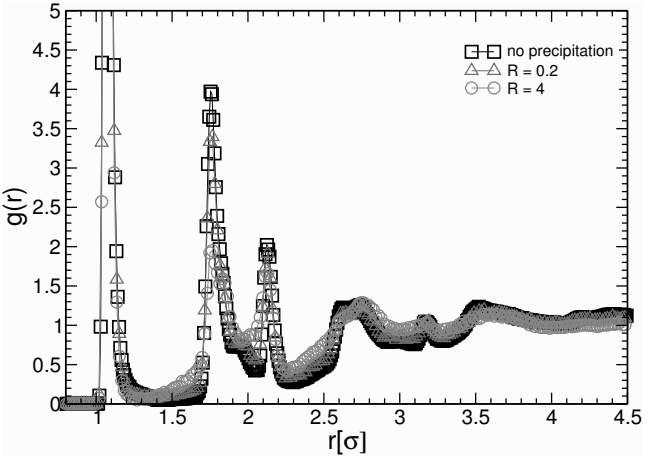

Figure 3. Pair correlation function g(r) for the gel formed in S1 formed at constant density (squares), and upon precipitation of the hydrates.

The peaks in the pair correlation function allow us to identify the local packing of colloidal particles in the gels obtained at various volume fractions. For S1, the gel obtained at volume fraction 20% without precipitation is a branched random network due to the assembly of elongated aggregates, within which particles are preferentially packed at the vertices of face-sharing tetrahedral, quite similar to Bernal spirals [Ioannidou 2013, De Candia, Toledano].

The gels formed upon precipitation at the same volume fraction display very similar patterns in the g(r), with deviations that increase upon increasing the precipitation rate. In S2 the gels obtained at 20% in volume fraction are formed instead from fairly large, compact and more isotropic clusters, whose internal structure closely resembles HCP crystalline order. Precipitation favors the formation of a disordered spanning network and this is achieved by a dramatically different development of the local structure. As shown in Figure 4, for the structures formed under precipitation the g(r) does not show the patterns typical of a HCP lattice anymore: the peaks indicate a significantly different local packing, and the differences increase with the precipitation rate.

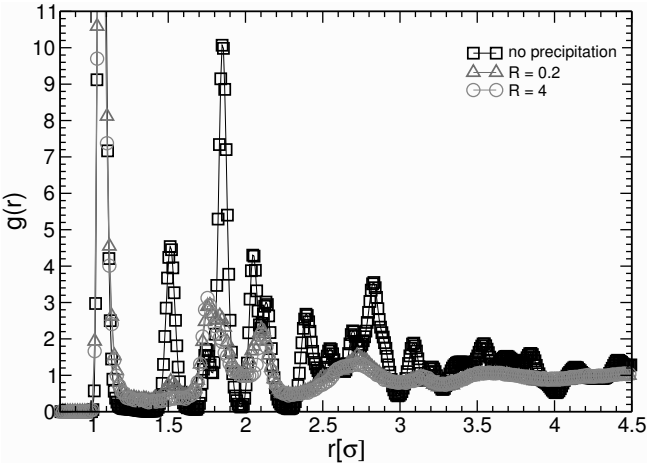

Figure 4. Local structure of the gel of volume fraction, formed in S2 at fixed volume fraction, and upon precipitation of the hydrates.

MECHANICAL TESTS AND GEL SHEAR MODULI

The morphological differences obtained in S1 and S2, as well as the changes observed upon varying the precipitation kinetics, correspond to a variation of the mechanical properties of the gels. We have quantified them in terms of the shear modulus, as measured in numerical mechanical tests.

We performed pure shear deformations on various microscopic configurations extracted from the rate dependent densification at a fixed volume fraction. This is done with non-equilibrium molecular dynamics simulations (NEMD) using SLLOD equations of motion coupled to a Nosé-Hoover thermostat as implemented on LAMMPS [Evans, Frenkel, Plimpton]. The tests have been performed over 5 different samples. In Figure 5 the shear modulus measured in the mechanical tests is plotted as a function of the volume fraction φ. The results of the numerical simulations show that the gel formed in S1 has a measurable mechanical modulus at much lower volume fractions. Moreover for S1 the precipitation kinetics does not apparently disrupt the local packing in the structure, leading to a gel whose building blocks are mechanically stronger. In S2, instead, we have seen that the precipitation kinetics can significantly modify the local packing, and produce, at high enough precipitation rates, gels whose local structure is far from optimizing local interactions and that are therefore mechanically weaker. On the other hand, we have also noticed that in S2 the high precipitation rate allows the system to develop a modulus at lower volume fractions with respect to the structures formed through aggregation at fixed density and to reach higher moduli at earlier times with respect to S1 because of the higher densities of the gels (see also Figure 1). Our findings mainly concern the early

stages of cement hydration and the question of how relevant they are for the mechanical properties of cement and ultimately concrete is still to be clarified. Nevertheless, they gain new insight into the mechanisms that may control the development of mechanical properties in C-S-H gels and give new indications on how to design it.

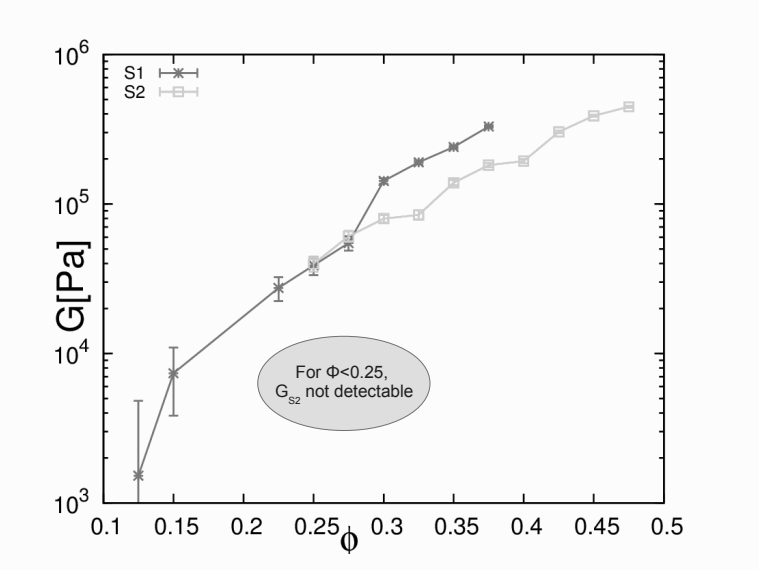

Figure 5. Shear modulus of the C-S-H gels obtained at high precipitation rate (R=4) for S1 and S2 as a function of the hydrates volume fraction.

CONCLUSIONS AND OUTLOOK

We have presented a new approach to investigate cement hydration at the level of the formation of C-S-H gels. The approach is based on a combination of Monte Carlo and Molecular Dynamics that allows us to mimic the precipitation kinetics of C-S-H in the capillary solution of the cement paste and to follow the evolution of the nano-scale gel morphology and mechanics. The approach is designed for the range of length scales between nano-meters and microns that is mainly still unexplored, in spite of being crucial for the development of the physical properties of C-S-H gels. Our results indicate that the differences observed in experiments in the hydration kinetics at low and high lime concentrations could be ascribed to different effective physical interactions emerging from the different chemical environment. Overall our study shows that different effective physical interactions possibly existing in C-S-H lead to the formation of gels that are morphologically very different and where the

precipitation kinetics also produces significantly different changes, by modifying the local packing *and* the meso-scale organization of the gel. We have shown, in particular, that this has an effect on the mechanical properties of the gels. Our investigations are useful to identify which combinations of chemical and physical mechanisms may control the development of the mechanical properties of C-S-H gels and which properties could be used to suitably design cement hydration.

Acknowledgments. This work was funded by SNSF (Grant No. PP002_126483/1).

REFERENCES

A.J. Allen, J. J. Thomas, H.M. Jennings, Nat. Mater. 6, 311-316 (2007).
S. Bishnoi and K. L. Scrivener, Cement and Concrete Research 39, 266 (2009).
J.W. Bullard, H.M. Jennings, R.A. Livingston, A. Nonat, G.W. Scherer, J.S. Schweitzer, K.L. Scrivener, J.J. Thomas, Cem. and Concr. Res., 41, 1208-1223(2010).
G. Constantinides and F.-J. Ulm, J. Mech. Phys. Solids (2007).
W.-S. Chiang, E. Fratini, P. Baglioni, D. Liu and S.-H. Chen, The Journal of Physical Chemistry C 116, 5055 (2012).
A. De Candia, E. Del Gado, A. Fierro, N. Sator, M. Tarzia and A. Coniglio, Phys. Rev. E 74, 010403 (2006).
D.J. Evans and G.P. Morris, Statistical Mechanics of Non-Equilibrium Liquids, Academic Press, London (1990).
D. Frenkel and B. Smit, Understanding Molecular Simulation: From Algorithms to Applications, Elsevier Science (2001).
S. Garrault, E. Finot, E. Lesniewska, A. Nonat, Materials and Structures 38, 435 (2005).
K. Ioannidou et al., in preparation (2013).
K. Ioannidou and E. Del Gado, preprint (2013).
B. Jönsson, A. Nonat, C. Labbez, B. Cabane and H. Wennerström, Langmuir 21, 9211 (2005).
S. Lesko, E. Lesniewska, A. Nonat, J. C. Mutin and J. P. Goudonnet, Ultramicroscopy 86, 11 (2001).
D. Lootens, P. Hébraud, E. Lécolier, H. Van Damme, Oil Gas Sci. Tech. 59, 31-40 (2004).
L. Nicoleau, T. Gädt, L. Chitu, G. Maier and O. Paris, Soft Matter, in press (2013).
H. Manzano, S. Moeini, F. Marinelli, A. C. Van Duin, F.-J. Ulm and R. J.- M. Pellenq, Journal of the American Chemical Society 134, 2208 (2012).
E. Masoero, E. Del Gado, R.J.-M. Pellenq, F.-J. Ulm, S. Yip, Phys. Rev. Lett. 109, 15 155503 (2012).
E. Masoero, E. Del Gado, R.J.-M. Pellenq, F.-J. Ulm, S. Yip, preprint (2013).
A. C. A. Muller, K.L. Scrivener, A.M. Gajewicz, and P. J. McDonald, J. Phys. Chem. C 117, 403 (2013).
A. Nonat, Cement and Concrete Research 34, 1521 (2004).
R.J.-M. Pellenq, H. Van Damme, MRS Bull 29, 319 (2004).

R. J.-M. Pellenq, A. Kushima, R. Shahsavari, K. J. Van Vliet, M. J. Buehler, S. Yip and F.-J. Ulm, Proceedings of the National Academy of Sciences 106, 16102 (2009).
C. Plassard, E. Lesniewska, I. Pochard, A. Nonat, Langmuir 21, 7263-7270 (2005).
S. Plimpton, Journal of Computational Physics 117, 1 (1995).
H. Taylor, Advanced cement based materials 1, 38 (1993).
J. C. F. Toledano, F. Sciortino and E. Zaccarelli, Soft Matter 5, 2390 (2009).
M. Vandamme and F.-J. Ulm, Proceedings of the National Academy of Sciences 106, 10552 (2009).
M. Vandamme, F.-J. Ulm and P. Fonollosa, Cement and Concrete Research 40, 14 (2010).

The counteracting effects of capillary porosity and of unhydrated clinker grains on the macroscopic strength of hydrating cement paste: a multiscale model

Bernhard Pichler[a], Christian Hellmich[a], Josef Eberhardsteiner[a], Jaromír Wasserbauer[a,b], Pipat Termkhajornkit[c], Rémi Barbarulo[c], Gilles Chanvillard[c]

[a] Institute for Mechanics of Materials and Structures; Vienna University of Technology (TU Wien); Karlsplatz 13/202, A-1040 Vienna, Austria; Bernhard.Pichler@tuwien.ac.at, Christian.Hellmich@tuwien.ac.at, Josef.Eberhardsteiner@tuwien.ac.at

[b] Centre for Material Research, Brno University of Technology, Purkyňova 118, CZ-61200 Brno, Czech Republic; jaromirw1@gmail.com

[c] Lafarge Centre des Recherches (LCR); 95, rue du Montmurier, BP 15; F-38291 Saint Quentin Fallavier, France; Pipat.Termkhajornkit@pole-technologique.lafarge.com, Remi.Barbarulo@pole-technologique.lafarge.com, Gilles.Chanvillard@pole-technologique.lafarge.com

ABSTRACT

Strength of cement pastes increases overlinearly with decreasing capillary porosity, such as suggested by the gel-space ratio model of Freyssinet (1933). This model, however, cannot explain that strength of mature sub-stoichiometric cement pastes increases with decreasing *w*/*c*-ratio, such as observed by Fagerlund (1972). The latter observation might well stem from a strengthening effect of unhydrated clinker grains, but until very recently an etiological model for quantification of this effect was out of reach. This provides the motivation for the present study, where we envision that the strength of microscopic cement hydrates is the limiting factor for the load carrying capacity of macroscopic cement paste samples. In more detail, we envision a stress-based strength criterion for microscopic hydrate needles, whereby the involved hydrate strength constant is determined from the results of nanoindentation experiments on low-density C-S-H, performed by Constantinides and Ulm (2006). Strength upscaling is performed within the framework of continuum micromechanics (Pichler et al., 2008-2013). Model-predicted macrostrength values of cement pastes (exhibiting different compositions and different maturities) agree very well with strength values measured at three different laboratories. The validated model confirms that strength of cement pastes is strongly influenced by capillary porosity, and that unhydrated clinker grains act as significantly strengthening reinforcements for mature substoichiometric pastes (Pichler et al. 2013).

INTRODUCTION

Since cement paste is the binder of cementitious materials, predictability of the strength evolution of hydrating cement paste is important for the construction business. To the best of our knowledge, Freyssinet (1933) introduced the nowadays widely used “gel-space ratio model”, stating that uniaxial

compressive strength of cement paste is proportional to the ratio of the volume of (gel-porous) hydration products and the sum of the volumes of these hydration products and the capillary pores. In other words, Freyssinet (1933) did not foresee any significant strengthening effect of unhydrated clinker grains. His model performs very well, particularly for super-stoichiometric cement pastes (i.e. pastes with an initial water-to-cement mass ratio $w/c > 0.42$), and hence, it still widely used in the international cement and concrete industry. Forty years later, Fagerlund (1972) observed that the strength of very mature sub-stoichiometric cement pastes (i.e. pastes with $w/c < 0.42$) increases with decreasing w/c-ratio. Since this could not be explained by Freyssinet's (1933) model, but microstructural properties of cement paste could not yet be linked to the macroscopic strength of cement pastes, Fagerlund (1972) proposed an empirical model. Another 40 years later, from a 2013's perspective, one could interpret that Fagerlund's (1972) observation stems from a strengthening effect of unhydrated clinker grains, but until very recently, no etiological model was available which could quantify this effect. This provides the motivation for the present study.

We here envision that the load carrying capacity of macroscopic cement paste samples is limited by the strength of the microscopic hydrates products, resulting from the chemical reaction between cement clinker and water. In more detail, we envision a stress-based strength criterion for microscopic hydrate needles, whereby the involved hydrate strength constant is determined from hardness results gained in nanoindentation experiments on low-density C-S-H, preformed by Constantinides and Ulm (2006) and reported in (Sarris and Constantinides, 2013). Strength upscaling is performed within the framework of continuum micromechanics (Pichler et al., 2008-2013), followed by model validation and use of the model for studying the counteracting effects of capillary porosity and of unhydrated clinker grains on the macroscopic strength of hydrating cement paste.

MULTISCALE STRENGTH MODEL FOR HYDRATING CEMENT PASTE

Cement paste is a hierarchically organized material which we here represent through a two-step homogenization scheme of Pichler and Hellmich (2011). Cement paste is considered to be a matrix-inclusion material, where a spherical clinker phase is embedded in a continuous hydrate foam matrix (Fig. 1b), and at the significantly smaller scale of a few microns, we envision the hydrate foam to be a polycrystal-type arrangement of capillary porosity (spherical water and air phases) and needle-shaped hydrate phases oriented isotropically in all space directions (Fig. 1a).

Modeling is performed within the framework of continuum micromechanics [see, e.g., Zaoui (2002) for a survey], following the lines of Kreher and Molinari (1993), as well as of Dormieux et al. (2002). In more detail, the multiscale representation of Fig.1 allows us to introduce a strength criterion for a *macro*scopic sample of cement paste, based on *micro*scopic hydrate stresses. We envision (i) that a representative sample of cement paste remains essentially intact as long as hydrate stress peaks are smaller than the hydrate strength, and (ii) that cement paste exhibits brittle failure, once hydrate stress peaks are equal to the hydrate strength (Pichler et. al., 2009). Notably, the hydrate strength represents a

material constant (and not a material parameter), i.e. the hydrate strength is considered to be independent of both material composition and maturity. The stress concentration, from loading imposed on a representative cement paste volume down to very small hydrate needles, in turn, depends on the microstructure of the material. This way, the model delivers strength estimates depending both on the material composition and on the maturity of cement paste. When it comes to the choice of a microscopic hydrate strength criterion, we consider the philosophy of engineering mechanics approaches, i.e. we introduce a strength criterion which is as simple as possible, and only as complex as necessary: a von Mises-type strength criterion for brittle failure of cement paste, including just one hydrate strength constant.

The hydrate strength is preferably identified from microscopic experiments at the length scale of individual hydrate needles. Strength properties of low-density C-S-H, for instance, are reported from nanoindentation experiments [e.g., Constantinides and Ulm (2006)]: the cohesion and the angle of internal friction amount to 50 MPa and to 12^o, respectively, reported by Sarris and Constantinides (2013). Considering the low-density C-S-H as weakest link in the overall material, we now derive, starting from the two nanoindentation-derived strength properties, the related von Mises-type hydrate strength. In this context, we note that the stress concentration into hydrate needles typically results in axial normal microstresses which are significantly larger than the normal microstresses in radial direction, such that the uniaxial compressive microstrength of hydrate needles is strongly related to hydrate failure. Feeding the standard Mohr-Coulomb criterion with the above-reported numerical values for cohesion and angle of internal friction, we determine the microscopic uniaxial compressive strength of a low-density C-S-H needle: it amounts to 123.5 MPa. The related von Mises

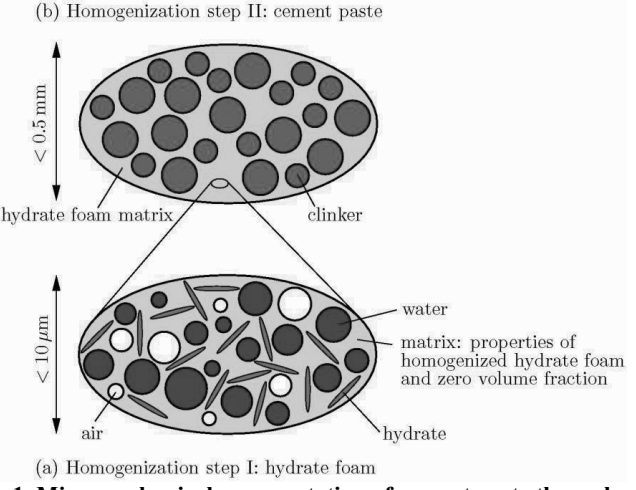

Figure 1. Micromechanical representation of cement paste through a two-step homogenization scheme, after (Pichler and Hellmich, 2011); both 2D sketches refer to 3D representative volume elements which are (i) significantly larger than the heterogeneities forming their microstructure, and (ii) significantly smaller than the structures built up by them

strength value is obtained as $(1/2\ \mathbf{s} : \mathbf{s})^{1/2} = 71.3$ MPa, where $\mathbf{s}$ denotes the stress deviator related to the uniaxial compressive stress state at hydrate failure. Next, we will upscale this von Mises-type (and, hence, "deviatoric") hydrate strength, from the scale of observation of individual hydrate needles up to the scale of observation of representative cement paste samples.

As for quantification of macroloading-induced stress peaks in microscopic hydrate needles, we compute quadratic stress averages over oriented hydrate needles, for related details, see (Pichler et al., 2008/2009). Such averages account for the hierarchical organization of cement paste (Fig. 1), for the elastic constants of clinker and hydrates, for their phase volume fractions of clinker, water, hydrates, and air [which are considered to evolve according to the hydration model of Powers and Brownyard (1948) and Acker (2001)], for their characteristic phase shapes, and for the interaction among the different phases (Fig. 1). Notably, the hydration model establishes analytical relations between phase volume fractions, on the one hand, and the initial water-to-cement mass ratio as well as the hydration degree, on the other hand. This way, material composition and maturity of cement paste represent input parameters for the described continuum micromechanics model.

MODEL VALIDATION

The above-described continuum micromechanics model of Pichler and Hellmich (2011) allows for upscaling the nanoindentation-derived hydrate strength value amounting to 71.3 MPa, up to the scale of representative cement paste samples, such as involved in classical macroscopic material testing. In the following, we specify the described continuum micromechanics model for different compositions and different maturities, and we compare resulting model-predicted macroscopic strength values of representative cement paste samples with available strength measurements, reported in the open literature.

In order to check the predictive capabilities of the described multiscale model at very early ages, we evaluate model predictions for young stoichiometric cement paste (w/c = 0.42), and we compare them with measurements from related strength tests carried out at Vienna University of Technology, documented in (Pichler et al., 2013). In these experiments, hydration degrees ranged from 9% to 49%. Model predictions agree very well with the strength measurements (Fig. 2), quantified through the quadratic correlation coefficient, amounting to very satisfactory 99.34%, and through the mean prediction error as well as the standard deviation, amounting to 2.1% and to 8.4%, respectively. Moreover, in order to check the predictive capabilities of the described multiscale model for more mature pastes, and for different compositions in terms of initial water-to-cement mass ratio, we specify the model for w/c-ratios amounting to 0.33, 0.50, and 0.508, respectively, and we compare model-predicted strength values with measurements from related strength tests carried out at Lafarge Centre de Recherche, documented in (Pichler et al., 2013). In these experiments, hydration degrees ranged from 47% to 87%. Model predictions agree very well with the strength measurements (Fig. 3), quantified through the quadratic correlation coefficient, amounting to very satisfactory 93.29%, and through the mean prediction error as well as the standard deviation, amounting to

–3.7% and to 13.7%, respectively. In order to further extend our model validation activities, particularly for sub-stoichiometric cement pastes, we specify our multiscale model for *w*/*c*-ratios being equal to 0.19, 0.24, 0.30, and 0.50, respectively, and we compare model predictions with measurements from related strength tests carried out by Lam et al. (2000). In these experiments, hydration degrees ranged from 41% to 75%. Again, model predictions agree very well with the strength measurements (Fig. 4), quantified through the quadratic correlation coefficient, amounting to 90.9%, and through the mean prediction error as well as the standard deviation, amounting to 1.9% and to 12.8%, respectively.

Summarizing, predictions of the used continuum micromechanics model agree very satisfactorily with measurements from three different experimental campaigns, carried out at three different laboratories, using different raw products, and involving samples with different compositions in terms of *w*/*c*-ratios ranging from 0.19 to 0.51, as well as different maturities in terms of hydrating degrees covering the interval from 9% to 87%. Therefore, we consider our model validations as (very) successfully.

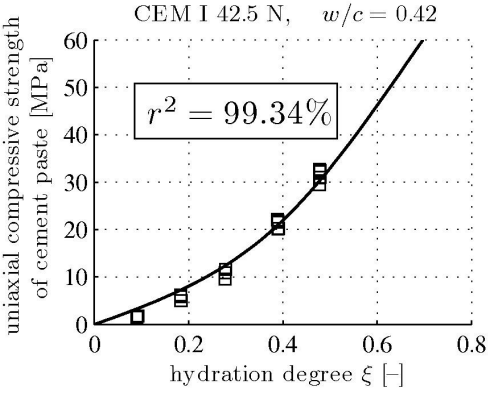

Figure 2. Strength values of stoichiometric cement paste tested at Vienna University of Technology (Pichler et. al., 2013) and corresponding model predictions (based on the nanoindentation-derived hydrate strength = 71.3 MPa)

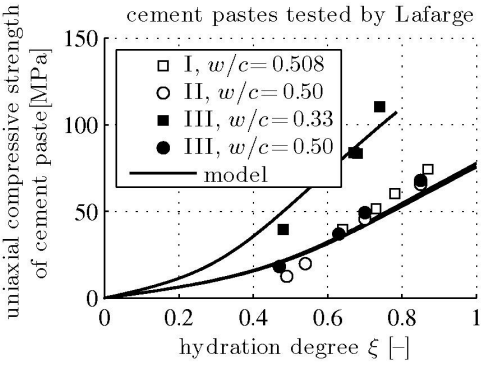

Figure 3. Strength values of cement pastes tested at Lafarge Centre de Recherche [see (Pichler et al., 2013)] and corresponding model predictions (based on the nanoindentation-derived hydrate strength = 71.3 MPa)

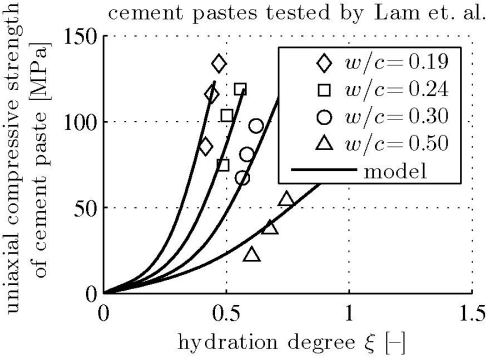

Figure 4. Strength values of cement pastes tested by Lam et al. (2006) and corresponding multiscale model predictions (based on the nanoindentation-derived hydrate strength = 71.3 MPa)

COUNTERACTING EFFECTS OF POROSITY AND CLINKER GRAINS

The satisfactory performance of our multiscale model motivates us to study the counteracting influences of capillary porosity and of unhydrated clinker grains on the strength of representative cement paste samples. This is done in the framework of Freyssinet's (1933) gel-space ratio which increases (i) with increasing hydration degree and (ii) with decreasing *w*/*c*-ratio. We specify our model for six different compositions in terms of initial water-to-cement mass ratio, ranging from 15.7% to 80%, such that both the sub-stoichiometric and the super-stoichiometric regime are well covered. When plotting model predictions as a function of gel-space ratio, a quite dense bundle of graphs is obtained (Fig. 5).

Our multiscale model allows us to study the relation between microstructural properties of cement pastes and the macroscopic strength of the materials:

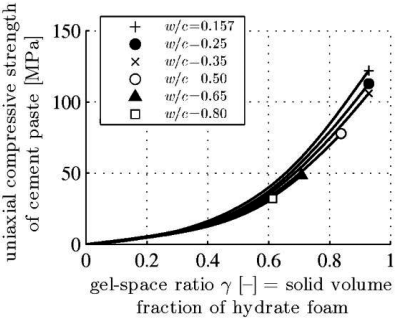

Figure 5. Model-predicted strength evolution of cement pastes as a function of Freyssinet's (1933) gel-space ratio

- Freyssinet's (1933) gel-space ratio parameter is identified to be equal to the solid volume fraction of the hydrate foam depicted in Fig. 1a (Pichler et al., 2013). The denser the hydrate foam, the larger the macroscopic strength of cement paste. This underlines the important role of porosity which needs to be reduced as much as possible, in order to optimize strength of cement paste.
- The validated model suggests that one "master curve" is able to explain – in very good approximation – the relationship between strength of super-stoichiometric cement pastes ($w/c > 0.42$) and gel-space ratio. In other words, the strengthening effect of unhydrated clinker grains is not significant in case of super-stoichiometric pastes, such as foreseen by Freyssinet (1933).
- As for sub-stoichiometric pastes ($w/c < 0.42$), however, the multiscale model indicates a significant strength-increasing effect of unhydrated clinker grains, in particular at large maturities; such as observed by Fagerlund (1972). As opposed to Fagerlund's empirical approach, the described multiscale model provides interesting insight into the load carrying behavior of the statically indeterminate microstructure of cement paste (Pichler et. al, 2013).

CONCLUSIONS

Herein, we upscaled nanoindentation-derived knowledge on strength of low density C-S-H from the level of observation of microscopic hydrate needles up to the scale of observation of representative cement paste samples. Predictions of the used continuum micromechanics model agree very satisfactorily with measurements from three different experimental campaigns, carried out at three different laboratories, using different raw products, and involving samples with different compositions in terms of w/c-ratios ranging from 0.19 to 0.51, as well as different maturities in terms of hydrating degrees covering the interval from 9% to 87%. In addition, model predictions are in perfect agreement with historical developments and observations, such as Freyssinet's (1933) gel-space ratio approach and Fagerlund's (1972) strength testing activities on mature sub-stoichiometric pastes.

Nowadays, great efforts are undertaken in order to achieve technological progress regarding the durability and strength of hydration products. As soon as related breakthroughs are made, we expect (i) nanoindentation to provide access to improved microstructural strength properties, and (ii) the continuum micromechanics model to represent the vehicle for upscaling microstructural strength properties to the macroscopic strength of representative samples of cementitious materials.

REFERENCES

Acker P. (2001). "Micromechanical analysis of creep and shrinkage mechanisms", in: Ulm F.-J., Bažant Z.P., and Wittmann F.H. (Eds.), "*Creep, Shrinkage and Durability Mechanics of Concrete and Other Quasi-brittle Materials*", 6th International Conference CONCREEP@MIT, Elsevier, Amsterdam, 15-26.

Constantinides G. and Ulm, F.-J. (2006) "The elastic properties of calcium leached cement pastes and mortars: a multiscale investigation" MIT CEE Report R02-01.

Dormieux L., Molinari A., and Kondo D. (2002). "Micromechanical approach to the behavior of poroelastic materials", *Journal of the Mechanics and Physics of Solids*, 50(10), 2203-2231.

Fagerlund G. (1972). "Samband mellan porositet och materials mekaniska egenskaper [Connections between porosity and mechanical properties of materials]." Technical Report 26, The Lund Institute of Technology, Division of Building Technology, Lund, Sweden. In Swedish.

Freyssinet, E. (1933). "Idées et voies nouvelles [Ideas and new ways]." *Science et Industrie, Edition mensuelle, Construction travaux publics,* 1,3-17. In French.

Kreher W. and Molinari A. (1993) "Residual stresses in polycrystals as influenced by grain shape and texture", *Journal of the Mechanics and Physics of Solids*, 41(12), 1955-1977.

Lam L., Wong Y.L., and Poon C.S. (2000). "Degree of hydration and gel/space ratio of high volume fly ash/cement systems", *Cement and Concrete Research* 30(5), 747–756.

Pichler B., Hellmich Ch., J. Eberhardsteiner (2009). "Spherical and acicular representation of hydrates in a micromechanical model for cement paste – prediction of early-age elasticity and strength", *Acta Mechanica*, 203(3-4), 137-162.

Pichler B., Scheiner S., Hellmich Ch. (2008). "From micron-sized needle-shaped hydrates to meter-sized shotcrete tunnel shells: micromechanical upscaling of stiffness and strength of hydrating shotcrete", *Acta Geotechnica*. 3(4), 273-294.

Pichler B. and Hellmich Ch. (2011). "Upscaling quasi-brittle strength of cement paste and mortar: a multi-scale engineering mechanics model." *Cement and Concrete Research*, 41(5), 467–476.

Pichler B., Hellmich Ch., Eberhardsteiner J., Wasserbauer J., Termkhajornkit P., Barbarulo R., and Chanvillard G. (2013). "Effect of gel-space ratio and microstructure on strength of hydrating cementitious materials: an engineering micromechanics approach." *Cement and Concrete Research*, 45(1), 55-68.

Powers T.C. and Brownyard T.L. (1948) "Studies of the physical properties of hardened Portland cement paste, Res. Lab. Portland Cem. Assoc. Bull. 22, 101-992.

Sarris E. and Constantinides G. (2013). "Finite element modeling of nanoindentation on C-S-H: Effect of pile-up and contact friction" *Cement and Concrete Composites*, 36, 78-84.

Zaoui A. (2002). "Continuum micromechanics: survey", Journal of Engineering Mechanics, ASCE, 128(8), 808-816.

Creep Properties of Cementitious Materials from Indentation Testing: Significance, Influence of Relative Humidity, and Analogy Between C-S-H and Soils

M. Vandamme[1], Q. Zhang[1,2], F.-J. Ulm[3], R. Le Roy[1], B. Zuber[2], E. Gartner[2], and P. Termkhajornkit[2]

[1]Université Paris-Est, Laboratoire Navier (UMR 8205), CNRS, ENPC, IFSTTAR, 6-8 Av. B. Pascal, F-77455 Marne-la-Vallée, France; PH (+33) 1-64-15-37-04; FAX (+33) 1-64-15-37-41; email: matthieu.vandamme@enpc.fr, robert.leroy@enpc.fr
[2]Lafarge Centre de Recherche, 95 rue du Montmurier, BP 15 38291 Saint Quentin Fallavier Cedex, France; PH (+33) 4-74-82-33-91; email: qing.zhang@pole-technologique.lafarge.com, bruno.zuber@lafarge.com, ellis.gartner@lafarge.com, pipat.termkhajornkit@lafarge.com
[3]MIT, Department of Civil and Environmental Engineering, 77 Massachusetts Avenue, Cambridge, Massachusetts 02139; PH (+1) 617-253-3544; email: ulm@mit.edu

ABSTRACT

Concrete creeps, and this creep must be well characterized and modeled to properly design civil engineering infrastructures. Here, we present some results on the creep properties of cementitious materials obtained by using the indentation technique. Firstly, we show that minutes-long microindentations on cement paste yield a quantitative measurement of their long-term logarithmic creep kinetics, which can be used to predict the rate of long-term creep of concrete. Then, by performing microindentations, we study the effect of relative humidity on the long-term creep properties of hydrated C_3S samples, compacted samples made of pure C-S-H, and compacted samples made of pure CH. The last part is dedicated to a study by nanoindentation of the creep properties of C-S-H phases directly within a hydrated cement paste. We identify scaling relations independent of mix proportion and heat treatment, which we can explain by drawing a thorough analogy between the mechanical behavior of C-S-H and that of clays.

INTRODUCTION

More concrete is manufactured than any other material on Earth. Given the availability of the raw materials necessary for its manufacture, this predominance is likely to last for many years to come. But concrete creeps, at a rate that can shorten the lifespan of civil engineering structures (Bažant et al., 2011). Therefore, in order to correctly design structures, the creep of concrete must be well modeled and

characterized. For large scale structures, such as large bridges, creep experiments are generally performed, but such experiments last many months and therefore have to be well planned, which is not always possible.

An alternative to macroscopic testing is small-scale testing such as the indentation technique, which provides bulk mechanical properties of cementitious materials through surface solicitation (Constantinides et al., 2003; Ulm et al., 2007; Zhu et al., 2007; Mondal et al., 2007; Němeček, 2009; Davydov et al., 2011). This technique is versatile, in the sense that, by playing with the loading conditions, the size of the probed volume can vary from several hundreds of micrometers down to below a micrometer. Therefore, with respect to the hierarchical microstructure of cementitious materials, the indentation technique can provide information at the scale of the cement paste (indentation at this scale is called microindentation) or at the scale of the individual phases (C-S-H, portlandite, etc.) of which the cement paste is made (indentation at this scale is called nanoindentation).

The analysis of sharp indentation testing has been extended to enable the measurement of viscous properties (Oyen and Cook, 2003; Vandamme and Ulm, 2006; Oyen, 2006; Cheng and Yang, 2009; Vandamme & al., 2012) and such properties of cementitious materials are therefore characterized by indentation (Vandamme and Ulm, 2009; Pichler and Lackner, 2009; Vandamme and Ulm, 2013). In this work, we provide an overview of indentation results on the creep properties of a variety of cementitious systems probed at a variety of scales. After introducing the technique, we first present microindentation results on cement pastes, the analysis of which enables us to discuss the significance of creep properties obtained by indentation with respect to creep properties obtained by macroscopic testing. Second, microindentation results on compacted samples are presented, which enable to characterize the influence of relative humidity on the creep properties of pure C-S-H, pure CH, and hydrated C_3S. In a last part, nanoindentations results on cement pastes are reported, from which we draw a mechanical analogy between the behavior of C-S-H phases and of clays.

MEASUREMENT OF CREEP PROPERTIES BY INDENTATION

Indentation technique. The indentation technique consists in applying a load to a probe of known geometry, perpendicular to the surface to be tested. The resulting depth is registered over time. Typically, in this study, nanoindentations were performed at a load of 2 mN and led to depths of a few hundreds of nanometers, while microindentations were performed at loads of a few N, leading to maximal depths of a few dozens of microns.

For each load-versus-depth curve resulting from an indentation test, the Oliver and Pharr method enabled us to obtain an indentation modulus M and an indentation hardness H (Oliver and Pharr, 1992). The indentation modulus $M = E/(1-\nu^2)$, where E is the Young's modulus and ν the Poisson's ratio, is an elastic property of the indented material. In contrast, the indentation hardness $H = P_{max}/A_c$ (where P_{max} is the load

applied to the indenter and A_c the projected area of contact between the indenter probe and the indented surface) involves the elastoplastic properties of the material, but also the loading conditions (i.e., type of probe, maximal load,...), and is not a material property *stricto sensu*.

Measurement of creep properties. By indentation, creep properties are measured by keeping the indentation load constant at a value P_{max} and monitoring the increase $\Delta h(t)$ of indentation depth over time. A typical indentation creep experiment lasts for about 3 minutes. The information is gathered in a creep compliance noted $L(t)$ and coined contact creep compliance. Below a sharp probe, plastic deformations cannot be avoided, even at the lowest load levels considered. In order to determine a contact creep compliance unbiased by time-independent plastic deformations, we used the formula (Vandamme & al., 2012):

$$L(t) = \frac{1}{M} + \frac{2a_u \Delta h(t)}{P_{max}},$$

where a_u is the radius of contact between the probe and the indented surface at the onset of unloading.

For all experiments performed in this study (at the scale of microindentations or of nanoindentations, on hydrated cement pastes or on compacted samples), the contact creep compliance was fitted by a logarithmic function of time $L(t) - 1/M = \ln(1+t/\tau)/C$. Such function proved to capture well the experimental data. The parameter τ is usually interpreted as being the characteristic time of the period during which creep is not logarithmic with respect to time. The parameter C is inversely proportional to the magnitude of this logarithmic creep and was coined the contact creep modulus.

SIGNIFICATION OF CREEP PROPERTIES OBTAINED BY INDENTATION

This section is dedicated to determining the significance of creep properties obtained by indentation. In order to do so, we compared microindentation creep experiments on cement pastes with macroscopic compression creep experiments on concrete (Le Roy, 1996).

Materials and methods. We used a CEM I 52.5 Portland cement from Saint-Vigor (France) and silica fume from Laudun. With this cement, cylindrical concrete samples were manufactured with a 20-cm diameter and a 100-cm height; their water-to-cement mass ratio w/c ranged from $w/c = 0.28$ to $w/c = 0.50$ and their silica-fume-to-cement mass ratio from 0% to 10%. The volume fractions of aggregates ranged from 67.3% to 73.1%. In addition, we also manufactured cylindrical cement paste samples with a 2-cm diameter and a 20-cm height. The mix composition of the latter samples was the same as the one of the cement paste in the manufactured concrete samples.

Concrete samples were subjected to uniaxial testing (for full experimental details, see Le Roy (1996)). Two specimens with identical mix designs were tested in parallel. The first specimen was dedicated to the characterization of autogenous shrinkage: its axial strain was measured over time in absence of any load. The second specimen was dedicated to creep testing: a load equal to 30% of its uniaxial strength at 28 days after casting was applied 28 days after casting and kept constant, and its axial strain was measured over time. The difference between the strain measured under load and the strain measured in the absence of any load yields the basic creep strain, from which the uniaxial creep function $J_u(t)$ of the concrete samples was obtained. On the various samples, experiments lasted up to 5 years. All tests were performed in sealed conditions at 20°C ± 2°C.

Cement paste samples were subjected to microindentation creep testing with a Vickers probe. First, from the cast cement paste samples, a 10-mm-thick disk was cut from the median part of the sample, ground, and polished with silicon carbide pads. On each specimen, 5 microindentations were performed with a 3-minutes-long creep phase during which the load was kept constant at 20 N. During testing, temperature was kept at 23.0°C ± 0.2°C and relative humidity was kept at 91% ± 2%.

Indentation testing as a measurement of long-term creep. Uniaxial creep functions of concrete samples were well captured by a function of the form $J_u(t) - 1/E = \ln(1+t/\tau_u)/C_u$ (Ulm et al. 1999). Fitting a function of this type to the experimental data yields, for each type of concrete, a characteristic time τ_u during which creep was not logarithmic with respect to time, and a uniaxial creep modulus C_u inversely proportional to the long-term logarithmic creep of the concrete.

As explained earlier, each microindentation yields the contact creep modulus C of the cement paste and the characteristic duration τ of the non-logarithmic creep kinetics. In order to compare microindentation results at the scale of cement paste with macroscopic compression results at the scale of concrete, we needed to perform some analytical homogenization. From the measured contact creep modulus C of the cement paste, the contact creep modulus C^{est} of the concrete made with this cement paste was estimated by using a Mori-Tanaka homogenization scheme (Mori and Tanaka, 1973), in which aggregates were introduced as non-creeping inclusions, and in which the creep of cement paste was considered as deviatoric. Analytical calculations provide (Vandamme and Ulm, 2013): $C^{est} = C\,(2 + 3\,f_{agg})/(2(1 - f_{agg}))$, where f_{agg} is the volume fraction of the aggregates in the concrete samples.

For all concrete specimens, Figure 1 displays their measured uniaxial creep modulus C_u and their contact creep modulus C^{est} estimated from microindentations of a cement paste identical to that of which the concrete was made. One observes a very good correlation between the two creep moduli: a linear regression forced to go through the origin yields $C_u = 0.967\ C^{est}$ with a coefficient of determination $R^2 = 0.913$. From this observation, we conclude that indentation testing provides a measurement of creep properties at the scale of the cement paste which, in combination with analytical homogenization, can provide a quantitative prediction of the rate of the long-term creep of concrete. Therefore, the logarithmic creep observed

in minutes-long microindentations is representative of the long-term creep kinetics of cementitious materials, although this long-term kinetics is usually reached after weeks or even years at the scale of macroscopic samples or of structures.

That is, the indentation technique could prove an invaluable tool for the engineer, if used in combination with macroscopic creep experiments: macroscopic creep tests allow characterizing the short-term creep of concrete, while indentation provides the rate of the long-term creep.

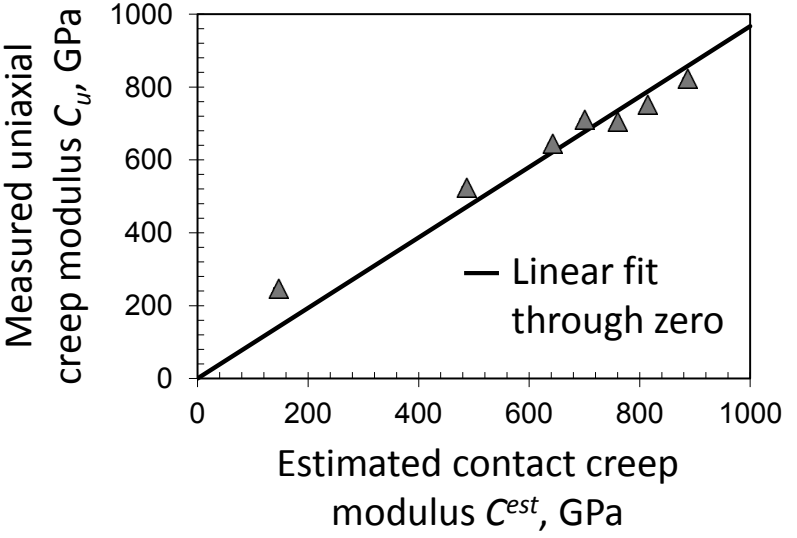

Figure 1. For all concrete samples, comparison of their uniaxial creep moduli measured by macroscopic compression with their contact creep moduli estimated from microindentations of the cement paste.

INFLUENCE OF RELATIVE HUMIDITY ON CREEP PROPERTIES

Hydrated cement pastes are always porous and, as a result, their mechanical properties are influenced by absorbed liquid water. The influence of liquid water on creep properties of the hardened paste can be assumed to depend on the overall porosity and pore size distribution of the paste plus its influence on the creep properties of the individual solid phases. In this section, we used pure tricalcium silicate (C_3S), the main active component of all Portland cements, as a model hydraulic cement. For comparison, we also determined the creep properties of the two hydrate phases, C-S-H and CH, which make up hydrated C_3S pastes. The C_3S paste was prepared by hydration, while the C-S-H and CH samples were prepared by compaction of powder. The mechanical properties of those compacted samples are

expected to be representative of those of the same hydration products found in regular cementitious materials obtained by hydration. Indeed, Soroka and Sereda (1968) showed that, at a given porosity, the hardness and elastic modulus of a cement paste are equal to those of the same cement paste ground and compacted.

Materials. The tricalcium silicate paste made with a water-to-C_3S mass ratio of 0.42 was cast in a cylindrical (Ø 20 mm × 160 mm) mold, removed from the mold after 24 hours, and then cured in pre-boiled deionized water. After 90 days of curing at 20°C, 3-mm-thick discs were cut from the middle of the cylinder, and one side of each disc was polished for indentation testing. The porosity of the discs was 18%.

Reagent-grade calcium hydroxide (portlandite) powder was dried in an oven at 120°C for 24 hours and transported to a glove box where it was cooled down and passed through a 50-μm sieve. Before compression, the powder was wetted with limewater at a water-to-powder mass ratio of about 0.5. The wet powder was placed into a cylindrical hollow mold and a load was applied to a piston that fitted into the mold, increased gradually up to 287 MPa, and held constant for 5 minutes. After the first load cycle, we flipped the mold and applied a second loading of 287 MPa for 5 minutes. During the compression cycle, some limewater was squeezed out of the sample. Compression yielded cylindrical samples with a diameter of 20.5 mm and a thickness of about 3.5 mm. The porosity of the sample dedicated to testing in saturated conditions was 23%, while that of the sample dedicated to testing at any lower relative humidity was 20%.

The preparation of C-S-H samples started with the preparation of precipitated C-S-H by double decomposition, following the procedure used by Chen et al (2004), except that the proportions used were as shown in the following equation:

$$3Ca(NO_3)_2(aq) + 2NaOH(aq) + 2Na_2SiO_3(aq) \Rightarrow 3CaO{\cdot}2SiO_2{\cdot}mH_2O\downarrow + 6NaNO_3(aq)$$

The extremely voluminous and gelatinous C-S-H precipitate was then dried under a pumped vacuum of about 1 Pa for 72 hours at room temperature. After drying, we determined the mean Ca/Si atomic ratio of the product to be 1.4. X-ray diffraction analysis of this product showed the presence of some portlandite, but no calcium carbonate was detected, so there was no evidence for carbonation during the preparation. The dried C-S-H was then moved to a glove box in which it was ground by hand to obtain a fine powder that passed a 50-μm sieve. Compacted samples with a porosity of 23% was then prepared by following the same procedure as for portlandite.

Conditioning and testing. All samples prepared for testing in relative humidities lower than 100% (i.e., hydrated C_3S, compacted CH and compacted C-S-H) were divided into fragments. One fragment of each sample was conditioned at each of the following relative humidities: 93%, 75%, 54%, 33%, and 11%. Conditioning was performed at 23°C and lasted for 3 months. The various relative humidities were provided by the appropriate saturated saline solutions. Additional samples were kept under water for testing in saturated conditions: for this latter case, the hydrated C_3S

sample was cured in water for 56 days prior to testing, while the C-S-H and CH samples were immersed in limewater for 7 days before testing.

After conditioning, each specimen was submitted to microindentation creep testing. During testing, the temperature was 23°C and the relative humidity was equal to that used for conditioning. Each specimen was subjected to 5 microindentation creep experiments with a 300-seconds-long holding phase. The maximum loads used for the each of the five microindentations were identical. From specimen to specimen, the maximum load varied from 8 N to 15 N in order to ensure that the maximum indentation depth was always around 35 μm.

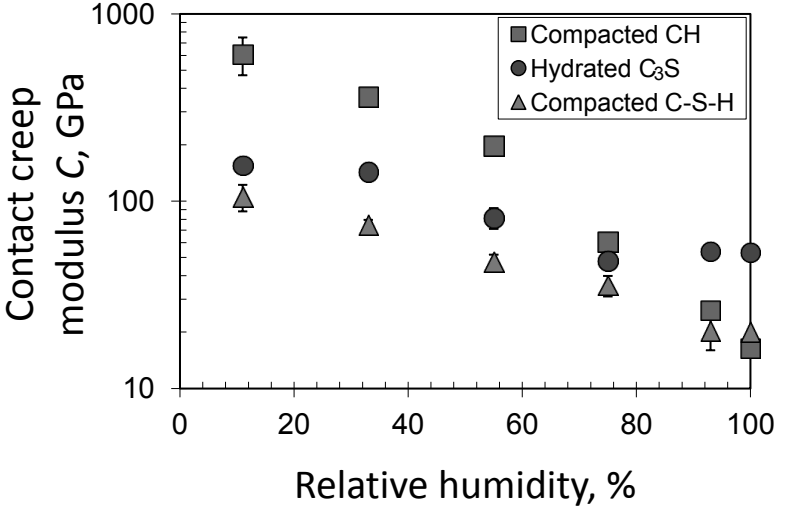

Figure 2. Influence of relative humidity on the contact creep modulus of hydrated C_3S, compacted CH, and compacted C-S-H. Data points at a relative humidity equal to 100% stand for data points acquired in saturated conditions.

Results. The results are displayed in Figure 2 on a logarithmic scale. For all tested specimens, the higher the relative humidity, the lower the contact creep modulus, i.e., the greater was the creep that the specimens exhibited. However, the effect of relative humidity on the creep properties was found to strongly depend on specimen type. The least sensitive to relative humidity was hydrated C_3S, for which decreasing the relative humidity from 100% (i.e., saturated conditions) to 11% increased the contact creep modulus by a factor of about 3. Compacted C-S-H was more sensitive, since decreasing the relative humidity over the same range increased its contact creep modulus by a factor of about 5. The most sensitive to relative humidity was, by far, CH: for this latter phase, the contact creep modulus was multiplied by about 35 when

the sample was dried at a relative humidity of 11%. Such high sensitivity, which is also observed in gypsum (Sattler, 1974), might be explained by creep that would occur by sliding at contact points between neighboring crystals rather than by creep of the crystals themselves.

For pure C-S-H and pure CH, the contact creep modulus decreased continuously with increasing relative humidity. In contrast, for hydrated C_3S pastes, relative humidity had no effect above 75%. Therefore, the manner in which long-term creep properties are affected by relative humidity appears to depend significantly on the composition and microstructure of the cementitious system considered.

As a consequence, new hydraulic binders should probably be screened with respect to their long-term creep properties over a representative range of relative humidities and temperatures. For this screening, the indentation technique could prove very useful, as it allows for a quick and handy way of characterizing creep behavior.

NANOSCALE CREEP PROPERTIES OF C-S-H: ANALOGY WITH CLAYS

It is generally admitted that the complex viscous behavior of regular Portland cement is due to the complex viscous behavior of its main hydration product, C-S-H. Therefore, C-S-H is the focus of this last section. In contrast to what was done in the previous section, in which C-S-H was studied by creating relatively large C-S-H samples by compaction of synthetic C-S-H, here we chose to study the creep properties of C-S-H *in vivo*, i.e., directly within a regular cement paste obtained by hydration. To do so, we performed nanoindentations.

Materials and methods. We tested sub-stoichiometric cement pastes with a variety of mix proportions and heat treatment. Their water-to-cement mass ratios w/c ranged from $w/c = 0.15$ to $w/c = 0.40$, their silica-fume-to-cement mass ratios ranged from 0% to 32% and their calcareous-filler-to-cement mass ratios ranged from 0% to 25%. Some pastes were not heat treated, some were heat treated 2 days after casting, and some were heat treated 5 days after casting. The heat treatment consisted in 2 days of curing at 90°C.

On each sample, 400 nanoindentation creep experiments were performed on a 20 by 20 grid with a 20-μm-wide spacing. Each nanoindentation creep experiment consisted in applying a load of 2 mN to the Berkovich indenter probe and keeping this load constant for 3 minutes. Such indentations yielded one indentation modulus M, one indentation hardness H, and one contact creep modulus C at the location of each indent. Only points that yielded $M < 63.5$ GPa and $H < 3$ GPa were attributed to hydration products and were considered next. For those nanoindentations performed on hydration products, in addition, the use of micromechanical relations enabled to estimate the local packing density η, i.e., the volume fraction occupied by solid phases (for more details, see Vandamme and Ulm (2013)).

The 20 by 20 grid of nanoindentations performed provided a variety of local mechanical properties, this variety being representative of the heterogeneity of the

cement paste at the probed scale. On each sample, the large amount of data was gathered into a few representative mechanical phases, a process known as deconvolution. For the indents performed on the hydration products of each sample, 3 representative phases were used: low-density C-S-H, high-density C-S-H, and a mixture of C-S-H with nanoscale CH. For each of those phases, the deconvolution of the grid of nanoindentations yielded the average mechanical properties (i.e., M, H, and C) of each phase, its average packing density η, and its volume fraction.

Results. The resulting data on all specimens are displayed in Figure 3. One observes that, independent of the mix proportions and of the heat treatment, the contact creep modulus scaled in a unique manner with the indentation modulus M, with the indentation hardness H, and with the packing density η (Vandamme and Ulm, 2009). Interestingly, a linear relation was found between contact creep modulus C and indentation hardness H:

$$C = 202.0H \,. \tag{1}$$

The rest of the section is devoted to showing that those unique scaling relations can be explained by a clay-like behavior of C-S-H. The proof is derived by considering a soil in an oedometric cell and interpreting an oedoemetric creep experiment with the formalism of indentation (Vandamme and Ulm, 2013).

In an oedometric cell, the behavior of soils is very peculiar (Lambe and Whitman, 1969). In terms of elasto-plastic behavior, the void ratio e of soils (defined as the volume of voids divided by the volume of solid) evolves in a bilinear manner with the logarithm $\log(\sigma)$ of the vertical stress: the slope of the $e(\log(\sigma))$ relationship is equal to the swell index C_s in the elastic range and to the compression index C_c in the plastic range. In terms of creep, after an initial period of consolidation, the amplitude of the logarithmic creep is governed by a so-called coefficient of secondary compression C_α through $de = C_\alpha\, d(\log(t))$.

***C*-versus-*H* scaling relation.** We consider a soil in an oedometric cell subjected to a constant vertical load σ. This oedometer creep experiment is interpreted as an indentation test performed with a flat probe as large as the top surface of the sample. In such a test, the indentation hardness is simply equal to the applied vertical stress. Making use of the definitions of the strain ε of the sample and of the void ratio e, one finds out that $\dot{\varepsilon} = \dot{e}\eta_0$, where η_0 is the packing density of the soil in the state of reference. Combining now this equation with the definition of the coefficient of secondary compression, one finds out that, over the oedometer creep test, the strain of the sample evolves as: $\dot{\varepsilon} = \sigma\eta_0 C_\alpha / tH$. Since $\dot{\varepsilon}/\sigma$ is the time derivative $\dot{L}(t)$ of the contact creep compliance, one eventually concludes that, for a soil, the contact creep

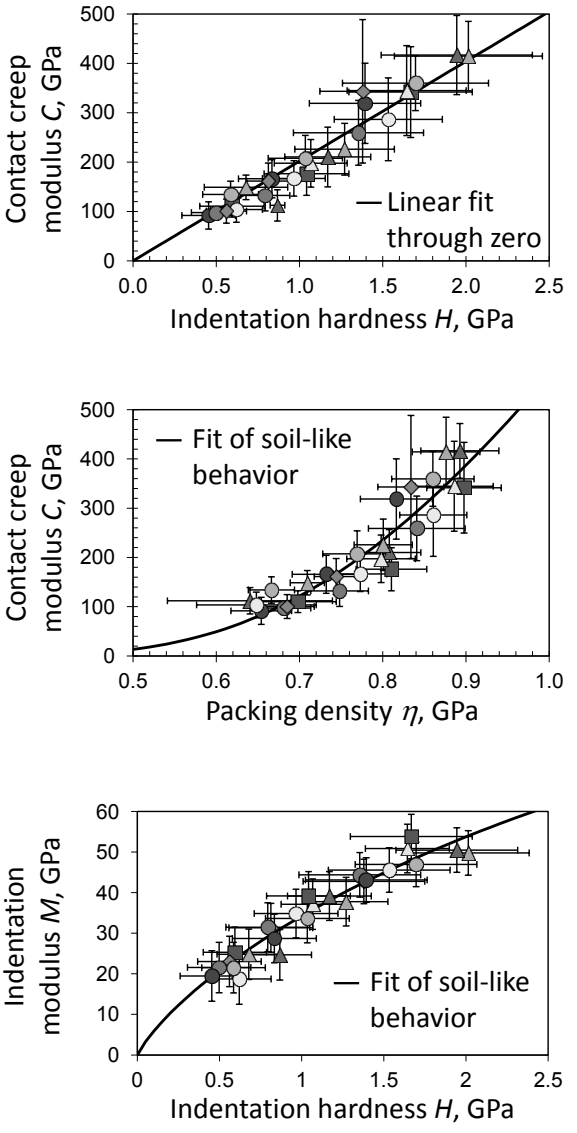

Figure 3. Scaling relations observed on sub-stoichiometric cement pastes and fitted relations for a soil-like behavior. Each symbol holds for a different sample.

modulus C should be related to the coefficient of secondary compression C_α and to the indentation hardness H through:

$$C = \frac{H}{\eta_0 C_\alpha}. \tag{2}$$

For a soil in the plastic regime, the coefficient of secondary compression is mostly independent of the stress (Lambe and Whitman, 1969). Making use of the above equation, this observation translates into a constant ratio C/H: such linear relation between contact creep modulus and indentation hardness is precisely what we observed with C-S-H (see Figure 3 and Equation (1)). In addition, Equation (1) translates, with the help of the above equation, into a coefficient of secondary compression for C-S-H of about $C_\alpha \sim 0.01$, which falls right in the range 0.005-0.02 observed for clays (Lambe and Whitman, 1969).

***C*-versus-η scaling relation.** For a soil in an oedometric cell, upon loading in the plastic range, the applied stress σ is related to the void ratio through $C_c d(\log(\sigma)) = -de$. Since $de = -d\eta / \eta^2$, and since the applied stress is equal to the hardness H, this relation translates into $C_c d(\log(H)) = d\eta / \eta^2$, which yields $H \propto 10^{-1/C_c \eta}$ after integration. Making use of Equation (2), this latter relation yields:

$$C \propto 10^{-1/C_c \eta}.$$

Thus, for a soil, close to a multiplying factor, the contact creep modulus is fully determined by the packing density, as was precisely observed with C-S-H (see Figure 3). A fit of the above relation is in excellent agreement with the experimental data on C-S-H for a compression index $C_c = 0.274$ (see Figure 3). Such a value, here fitted on C-S-H data, falls in the range 0.2-0.5 observed for clays (Lambe and Whitman, 1969).

***M*-versus-*H* relationship.** In a last step, aiming at bringing the analogy between clay and C-S-H one step further, we now set aside creep properties and focus on the unique relationship identified between indentation modulus and indentation hardness. By following the same kind of reasoning as before, one can show that, for a soil in an oedometric cell, those two parameters must be linked in a unique manner by the relationship:

$$M = \frac{\ln(10)}{C_s} H - \frac{C_c}{C_s} H \ln(H / \sigma_0),$$

where σ_0 is a reference stress. Fitting this relation to the experimental data on C-S-H yielded a very good fit for a ratio $C_c / C_s = 10.6$ (see Figure 3). In combination with the already identified compression index $C_c = 0.274$, this ratio yielded a swell index

C_s = 0.026 for C-S-H. Once again, this value falls in the range 0.02-0.1 observed for clays (Lambe and Whitman, 1969).

In conclusion, the various scaling relations observed for the C-S-H phases in Figure 3, which are independent of mix proportions and of heat treatment, could all be explained by considering a clay-like behavior of C-S-H. This striking mechanical analogy suggests that the reasons for the creep of C-S-H should be looked for into features that C-S-H bears in common with soils.

CONCLUSION

In this work, we reviewed recent experimental results on the creep properties of cementitious materials obtained by indentation.

We first discussed the significance of creep properties measured by indentation. We showed that indentation makes it possible to measure, in minutes, the long-term creep kinetics of cementitious materials. This result is of value for the engineer, since measuring such long term creep kinetics requires months or even years of testing at the macroscopic scale. As a counterpart, such a result means that the short-term creep kinetics of cementitious materials is not directly accessible to indentation testing. Consequently, the full characterization of the creep properties of a cementitious material could be performed by using a combination of macroscopic and indentation creep experiments: macroscopic experiments for the determination of the short-term creep properties, indentation for the rate of long-term creep.

In a second part, we presented a study by microindentation of the effect of relative humidity on the creep properties of hydrated C_3S, compacted C-S-H, and compacted CH samples. We showed that relative humidity had a very significant effect on those creep properties. The magnitude of this effect depended on the type of sample and was greatest for the most crystalline sample considered, i.e., compacted CH. Any potential new hydraulic binder should ideally be screened with respect to the sensitivity of its creep properties to relative humidity and temperature over a range relevant to its potential applications. To perform this screening, indentation could be of great value, since it is a quick and handy technique to measure creep properties.

In a last part, we presented a study by nanoindentation of the creep properties of C-S-H *in vivo*, i.e., directly in hydrated cement pastes. We identified unique scaling relations of the contact creep modulus with other mechanical properties (i.e., M or H) and with the packing density. We showed that those scaling relations could be explained by a mechanical analogy of C-S-H with clays. This analogy is of importance, since it suggests that the reasons for the creep of C-S-H should not be looked into what distinguishes C-S-H from soils, but into what C-S-H bears in common with soils.

REFERENCES

Bažant, Z. P., Hubler, M. H., and Yu, Q. (2011). "Pervasiveness of excessive segmental bridge deflections: Wake-up call for creep." *ACI Struct. J.*, 108(6), 767–774.

Chen, J. J., Thomas, J. J., Taylor, H. F. W., and Jennings, H. M. (2004). "Solubility and structure of calcium silicate hydrate." *Cement Concrete Res.*, 34(9), 1499–1519.

Cheng, Y. T., and Yang, F. Q. (2009). "Obtaining shear relaxation modulus and creep compliance of linear viscoelastic materials from instrumented indentation using axisymmetric indenters of power-law profiles." *J. Mater. Res.*, 24(10), 3013–3017.

Constantinides, G., Ulm, F.-J., and Van Vliet, K. J. (2003). "On the use of nanoindentation for cementitious materials." *Mater. Struct.*, 36(257), 191–196.

Davydov, D., Jirásek, M., and Kopecký, L. (2011). "Critical aspects of nano-indentation technique in application to hardened cement paste." *Cement Concrete Res.*, *41(*1), 20–29.

Lambe, T. W., and Whitman, R. W. (1969). *Soil mechanics*, Wiley, New York.

Le Roy R. (1996). *Déformations instantanées et différées des bétons à hautes performances*, Série ouvrages d'art, Laboratoire Central des Ponts et Chaussées, Paris.

Mondal, P., Shah, S. P., and Marks, L. (2007). "A reliable technique to determine the local mechanical properties at the nanoscale for cementitious materials." *Cement Concrete Res.*, 37(10), 1440–1444.

Mori, T., and Tanaka, K. (1973). "Average stress in matrix and average elastic energy of materials with misfitting inclusions." *Acta metallurgica*, *21(*5), 571–574.

Němeček, J. (2009). "Creep effects in nanoindentation of hydrated phases of cement pastes." *Mater. Charact.*, 60(9), 1028–1034.

Oliver, W. C., and Pharr, G. M. (1992). "An improved technique for determining hardness and elastic-modulus using load and displacement sensing indentation experiments." *J. Mater. Res.*, 7(6), 1564–1583.

Oyen, M. L., and Cook, R. F. (2003). "Load-displacement behavior during sharp indentation of viscous-elastic-plastic materials." *J. Mater. Res.*, 18(1), 139–150.

Oyen, M. L. (2006). "Analytical techniques for indentation of viscoelastic materials." *Philos. Mag.*, 86(33-35), 5625–5641.

Pichler, C., and Lackner, R. (2009). "Identification of logarithmic-type creep of Calcium-Silicate-Hydrates by means of nanoindentation." *Strain*, 45(1), 17–25.

Sattler, H. (1974). "Elastic and plastic deformations of plaster units under uniaxial compressive stress." *Mater Struct.*, 7(3), 159–168.

Soroka, I., and Sereda, P. J. (1968). "The structure of cement-stone and the use of compacts as structural models." *Proceedings of the Fifth International Symposium on the Chemistry of Cement*, Tokyo, Japan, 67–73.

Ulm, F.-J., Le Maou, F., and Boulay, C. (1999). "Creep and shrinkage coupling: new review of some evidence." *Revue Française de Génie Civil*, 3, 21–37.

Ulm, F.-J., Vandamme, M., Bobko, C. P., Ortega, J. A., Tai, K., and Ortiz, C. (2007). "Statistical indentation techniques for hydrated nanocomposites: Concrete, bone, and shale." *J. Am. Ceram. Soc.*, 90(9), 2677–2692.

Vandamme, M., Tweedie, C. A., Constantinides, G., Ulm, F.-J., and Van Vliet, K. J. (2012). "Quantifying plasticity-independent creep compliance and relaxation of viscoelastoplastic materials under contact loading." *J. Mater. Res.*, 27(1), 302–312.

Vandamme, M., and Ulm, F.-J. (2006). "Viscoelastic solutions for conical indentation." *Int. J. Solids Struct.*, 43(10), 3142–3165.

Vandamme, M., and Ulm, F.-J. (2009). "Nanogranular origin of concrete creep." *P. Natl. Acad. Sci. USA*, 106(26), 10552–10557.

Vandamme, M., and Ulm, F.-J. (2013). "Nanoindentation investigation of creep properties of calcium silicate hydrates." *Cement Concrete Res.*, accepted.

Zhu, W., Hughes, J. J., Bicanic, N., and Pearce, C. J. (2007). "Nanoindentation mapping of mechanical properties of cement paste and natural rocks." *Mater. Charact.*, 58(11-12), 1189–1198.

A depinning model for creep and plasticity of disordered materials

David Bouttes and Damien Vandembroucq

Laboratoire PMMH, UMR 7636 CNRS/ESPCI/Univ. Paris 6 UPMC/Univ. Paris 7 Diderot, 10 rue Vauquelin, 75231 PARIS cedex 05, FRANCE; email: damienvdb@pmmh.espci.fr

ABSTRACT

A mesoscopic model is introduced for shear plasticity of disordered materials. Plastic deformation is assumed to result from series of local reorganizations. The structural disorder is modeled by spatial fluctuations of plastic thresholds on a discretized lattice. The elastic interaction induced by local rearrangements are described by the far-field stress induced by an Eshelby inclusion. A complex phenomenology emerges from the interplay between disorder and elastic interactions. The macroscopic yield stress can be analyzed as the critical threshold of a depinning transition. This analogy with a dynamic phase transition naturally enables to predict finite size scaling. In the same way, creep behavior of disordered solids can be analyzed as the thermal rounding of the critical transition. A logarithmic creep behavior is recovered.

INTRODUCTION

From foams to pastes, glasses, granular materials or concrete, a large part of technological materials share a common characteristics : their structure is disordered. The nature of this disorder as well as its typical scale(s) are obviously material dependent. Still the mechanical behavior of these different materials present some common complex features: power-law or logarithmic creep, finite-size effects, crackling noise, localization and shear-banding... Here we would like to give an attempt of rationalization of these complex behaviors within a simple framework. We will develop a modeling at mesoscopic scale and try to clarify the common aspects of the mechanical behavior of disordered materials. More specifically, we will propose a simple depinning model relying on the interplay between the structural disorder and elastic interactions. This simple model will be shown to account for a large variety of the complex behaviors listed above.

LOCAL REARRANGEMENTS AND ELASTIC INTERACTIONS

In absence of underlying crystalline lattice, it is obviously difficult to invoke dislocations as a microscopic mechanism for the rheology of disordered materials. Instead, according to a growing consensus, the flow of disordered materials seems to results from a series of localized rearrangements of the structure (Argon 1979, Falk and Langer 1998, Vandamme and Ulm 2009). These stress driven rearrangements may occur at the atomic scale for glasses, at a nanometric scale in pastes or concrete, a micrometric or even millimetric scale for granular materials. In all cases, within a series, rearrangements will not be independent of each other. It is indeed necessary to account for the elastic reaction of the matrix that surrounds the rearranging zone. Most of the complex behavior discussed above will actually find its origin in the elastic coupling between the local random rearrangements events. Such ideas have been early used to develop numerical models of plasticity/rheology of disordered materials or complex fluids (Bulatov and Argon 1994a, 1994b, 1994c, Baret et al 2002, Homer and Schuh 2009, Picard et al 2004). Here we follow the same spirit and try to develop a minimal model for creep and amorphous plasticity.

As hinted above, a key ingredient consists of accounting for the elastic interactions between rearranging events. This question is not a simple one. Indeed, at small spatial scale, amorphous materials exhibit a significative non-affine elastic behavior (Tanguy 2002, Maloney 2006) : the convergence to the effective macroscopic behavior is much slower than for crystals. This also amounts to say that most disordered materials can be considered as elastically heterogeneous at small scale (Goldenberg 2007, Tsamados 2009). We choose here to perform a drastic simplification: we consider the disordered material as elastically homogeneous. In addition we only take into account the far-field contribution of the elastic field radiated by the rearranging zone. This simplification allows us to take advantage of the classical results obtained by Eshelby for the elastic field induced by a plastic inclusion (Eshelby 1957, Eshelby 1959). Far from the inclusion the dominant contribution of the elastic strain is given by the solution obtained for an equivalent sphere of radius a that experienced a typical plastic shear strain ε_p . We give here the result in polar coordinates (r,θ) centered on the inclusion for the case of plane strain:

$$\sigma_{xx} - \sigma_{yy} = A \frac{E}{1-\nu^2} \frac{a^2 \langle \varepsilon_p \rangle \cos(4\theta)}{r^2}$$

$$\sigma_{xy} = A \frac{E}{1-\nu^2} \frac{a^2 \langle \varepsilon_p \rangle \sin(4\theta)}{r^2}$$

$$\sigma_{xx} + \sigma_{yy} = A \frac{E}{1-\nu^2} \frac{a^2 \langle \varepsilon_p \rangle \cos(2\theta)}{r^2}$$

E and ν are the Young modulus and the Poisson coefficient respectively. A is a constant that depends on the Poisson coefficient. It is important to note here that this elastic response is long-ranged and anisotropic. The shear component is in particular characterized by a quadrupolar symmetry. Depending on the direction considered, the internal stress contribution will then increase or decrease the stress level experienced by other regions of the material and tend to favor or disfavor the onset of distant structural rearrangements.

.

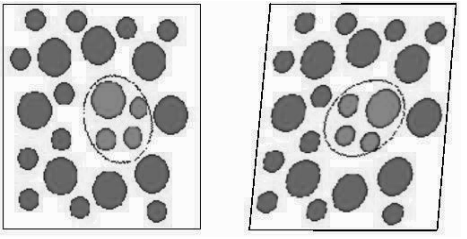

Fig. 1a: Sketch of a local plastic shear transformation. Under shear stress a local region of the disordered material experiences a structural reorganization.

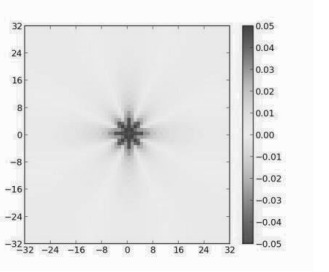

Fig. 1b: Elastic stress response to a unit plastic shear transformation. The color scale makes evident the quadrupolar symmetry.

DEPINNING MODEL

The knowledge of the elastic interaction allows us to build a simple depinning model for the plasticity of disordered materials. For the sake of simplicity, let us restrict to the two-dimensional case of plane strain. The material is discretized onto a square lattice at mesoscopic scale (typically a few times the size of a re-arranging zone). In order to make the model as simple as possible we consider a scalar criterion of plasticity. The implicit approximation being here that the symmetry of the local rearrangements are ruled by the symmetry of the externally applied stress Σ. We consider here a material submitted to a simple bi-axial stress : $\Sigma_{xx} = \Sigma_{ext}$; $\Sigma_{yy} = -\Sigma_{ext}$; $\Sigma_{xy} = 0$. Assuming a scalar plastic criterion based on the sole local shear component $\tau=|\sigma_{xx}- \sigma_{yy}|$ of the local stress σ, we can write a simple equation of evolution for the plastic strain ε_p (Talamali, 2012); in the framework of a quasi-static loading, an overdamped dynamics is considered:

$$\frac{\partial \varepsilon_p(r,t)}{\partial t} = \tau_{ext}(t) + \tau_{el}(r,t) - \tau_c\left[r, \varepsilon_p(r,t)\right]$$

where

$$\tau_{el}(r,t) = A\int \frac{\cos(4\theta_{rr'})}{(r-r')^2}\left[\varepsilon_p(r',t)-\varepsilon_p(r,t)\right]dr'$$

gives the elastic internal stress i.e. the sum of all elastic contributions induced by the past structural rearrangements. In the equation of evolution, the time scale is adjusted so that the effective viscosity is unity; τ_{ext} is the externally applied shear stress, τ_{el} is the elastic internal stress induced by the successive rearrangements and τ_c is the local yield stress that here depends on the the position r and on the state variable ε_p. The yield stress can thus be regarded as a quenched noise.

We recover here a typical depinning model. The competition between elasticity and disorder in that framework is known to induce a dynamic phase transition. Below some critical threshold, the elastic interface only advances a finite distance before arresting ; above threshold it can advance indefinitely and acquires a finite velocity. Close to threshold typical critical features are recovered: divergence of a correlation length, finite size effects, etc.

The direct numerical implementation of such a model is rather expensive from the computational point of view. We thus discuss two simpler versions : i) a cellular automaton based on extremal dynamics that is well suited to the athermal quasi-static limit (Talamali et al 2012) ii) a kinetic Monte Carlo algorithm that enables to model the creep regime at finite temperature (Bouttes and Vandembroucq 2013).

EXTREMAL DYNAMICS

Here the system is driven at a vanishing shear rate. In practice we consider a cellular automaton version of the above equation of evolution. A detailed description of the extremal dynamics algorithm briefly presented in the following can be found in (Talamali et al 2012). We first define a *local* criterion of plasticity: a site can experience plastic strain only if the local shear stress $\tau_{ij} = \tau^{ext} + \tau^{el}_{ij}$ (i.e. the addition of the externally applied stress and the internal stress due to other rearrangements) reaches the local yield stress τ^{c}_{ij} (chosen from a given random distribution). The system being discretized on a lattice of size NxN, it is possible to define for each of the N^2 sites an effective yield stress $\tau^{eff}_{ij} = \tau^{c}_{ij} - \tau^{el}_{ij}$. The choice of the current yield stress $\tau^{ext} = \tau^{y} = \min_{(i,j)} \{\tau^{eff}_{ij}\}$ enables to satisfies the plasticity criterion only at one site: the weakest one. An incremental slip (again chosen from a random distribution) is applied to that site and the associated quadrupolar elastic stress contribution is added to all sites of the lattice. Finally a new value of the local yield stress τ^{c}_{ij} is drawn from a random distribution and the sequence is iterated.

The extremal driving ensures that the systems always remains at the verge of stability. The maximum value $\tau^{Y} = \max\{\tau^{y}\}$ over the set of configurations visited by the system defines the macroscopic yield stress. The latter value can be interpreted as the

threshold of a dynamic phase transition. Whenever $\tau^{ext} < \tau^{y}$ the material only deforms over a finite extent and eventually arrests. Beyond τ^{Y} the material can flow indefinitely.

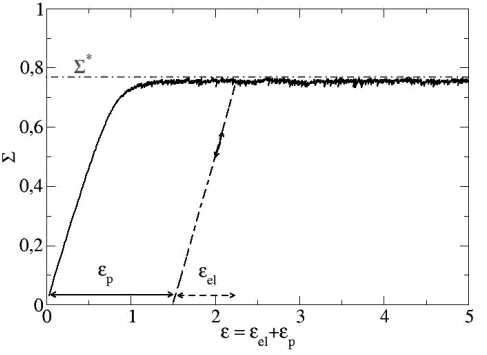

Fig. 2: Stress-strain curve obtained for a depinning model. The yield stress can be interpreted as the critical threshold of a dynamic phase transition

As usual, the approach of the critical point is accompanied by the divergence of a correlation length, series of plastic events appear to be highly correlated and power-law distributed. The anisotropic (quadrupolar) character of the elastic interaction has an interesting consequence: the plastic strain field gets localized. As shown in Fig. 3 when the external stress approaches the critical value, localized patterns obeying the very same quadrupolar symmetry as the elastic interaction develop over larger and larger scales. Let us mention here that once the correlation length has reached the size of the system, the localized patterns don not persist but rather diffuse throghout the system (Talamali et al 2013).

Another direct consequence of criticality is the existence of finite-size scaling. For systems of finite size L, the critical point is not uniquely defined but displays fluctuations within a distribution $p(\tau^{Y},L)$. the scaling form of the distribution $p(\tau^{Y},L)$ of the fluctuations for a system of size L as $p(\tau^{Y},L) = L^{\upsilon}\,\Psi[\tau^{*}-\tau^{Y})L^{\upsilon}]$ where τ^{*} is the critical threshold for a system of infinite size while τ^{Y} is a threshold obtained for a system of size L. A direct consequence of this finite size scaling is that we expect the following scaling for the mean yield stress τ^{Y} and its standard deviation $\delta\tau^{Y}$:

$$\tau^{*} - \tau^{Y} = C_1 L^{-\upsilon} \quad ; \quad \delta\tau^{Y} = C_2 L^{-\upsilon}$$

Numerically the finite size exponent υ was found to be close to unity (Talamali et al 12).

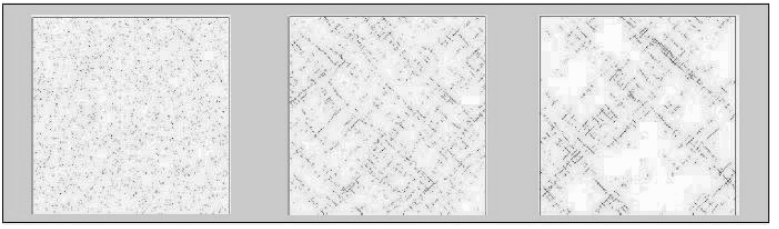

Fig. 3: Maps of plastic strain. From left to right, the plastic strain field gets more and more correlated as the external stress approaches the critical threshold (the macroscopic yield stress).

CREEP AT FINITE TEMPERATURE

At finite temperature, thermal noise may allow a rearrangement to take place even if the plastic criterion is not strictly satisfied. To account for this phenomenon it is convenient to develop an energetic approach. In the same spirit as the soft glassy rheology model developed in (Sollich et al 1997), we consider a trap model with a mechanical bias (Bouttes and Vandembroucq 2013). This model can also be viewed as a disorederd version of the early model developed by (Bulatov and Argon 1994a, 1994b, 1994c).

The probability that a site experiences plasticity writes:

$$p_{ij} \propto \exp\left(\frac{F_{ij} - \tau_{ij}\gamma_{ij}}{T}\right)$$

where F_{ij} is the energy trap, $\tau_{ij} = \tau^{ext} + \tau^{el}_{ij}$ is the local shear stress and γ_{ij} is the incremental plastic strain. A crucial difference with the SGR model is that we explicitly account for the elastic stress redistribution due to the successive plastic events. Another difference is that we do not assume the distribution of traps to be exponential, which is a key ingredient in the glassy behavior of the SGR model. A kinetic Monte Carlo algorithm (Vandembroucq et al 2004, Homer and Schuh 2009) is used to model the creep behavior at constant external stress.

As illustrated in Fig. 4 when submitted at finite temperature to a constant stress below yield stress, a power-law creep stage with an exponent close to unity is first observed. Then saturation takes place up to a stationary value. The lower the applied stress, the longer the creep stage. Logarithmic creep thus here appears as a transient (though long) stage before a stationary strain rate is obtained.

In Fig. 5 we reported the evolution of this stationary strain rate against external stress for different temperatures. One recovers a typical depinning scenario smeared by temperature: instead of obtaining an abrupt transition between a static phase and a mobile phase we get thermal rounding. Below yield stress, the material is able to flow but only at an exponentially low strain rate.

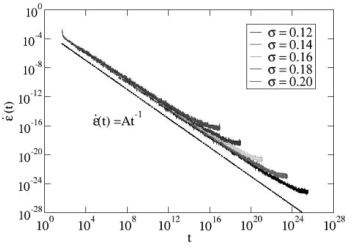

Fig. 5: Power-law creep

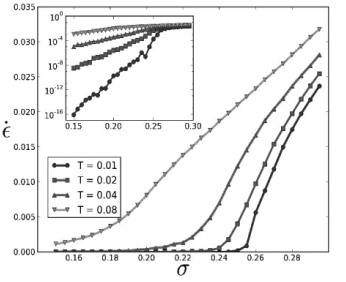

Fig. 4: Creep as a thermal rounded depinning transition

CONCLUSION

Creep and amorphous plasticity have been discussed in the framework of a very simple depinning model. The interplay between structural disorder and Eshelby-like elastic interactions allow one to obtain a complex phenomenology and to reproduce some of the most salient features of the mechanical behavior of disordered materials: localization, finite-size effects, logarithmic creep, etc.

ACKNOWLEDGEMENTS

We acknowledge enlightning discussion with S. Roux and M. Talamali.

REFERENCES

Argon, A.S. “Plastic deformation in metallic glasses” (1979) “Plastic deformation in metallic glasses”, *Acta Met.* 27, 47-58

Bouttes, D. and Vandembroucq, D. (2013) “Creep of amorphous materials: a mesoscopic model” *AIP Conf. Proc.* 1518, 481-486.

Bulatov, V.V. and Argon, A.S. (1994a) “A stochastic model for continuum elasto-plastic behavior I: Numerical approach and strain localization” *Modell. Simul. Mater. Sci. Eng.* 2, 167-184.

Bulatov, V.V. and Argon, A.S. (1994b) “A stochastic model for continuum elasto-plastic behavior II: a study of the glass transition and structural relaxation” *Modell. Simul. Mater. Sci. Eng.* 2, 185-202.

Bulatov, V.V. and Argon, A.S. (1994c) "A stochastic model for continuum elasto-plastic behavior III: Plasticity in ordered versus disordered solids" *Modell. Simul. Mater. Sci. Eng.* 2, 203.

Eshelby, J.D. (1957). "The determination of the elastic field of an ellipsoidal inclusion, and related problems" *Proc. Roy. Soc. A*, 241, 376-396.

Eshelby, J.D. (1959). "Elastic field of an ellipsoidal inclusion" *Proc. Roy. Soc. A* 252, 561-569.

Falk, M. and Langer, J.S. (1998) "Dynamics of viscoplastic deformation of amorphous solids" *Phys. Rev. E* 57, 7192.

Goldenberg, C., Tanguy, A. and Barrat, J.L. (2007). "Particle displacements in the elastic deformation of amorphous materials: Local fluctuations vs. non-affine field" *Europhys. Lett.* 80, 16003.

Herrmann, H.J. and Roux, S. (1990) *Statistical Models for the Fracture of Disordered Media*, North Holland, Amsterdam.

Homer, E.R. and Schuh, C.A. (2009) "Mesoscale modeling of amorphous metals by shear transformation zone dynamics" *Acta Mater.* 57, 2823-2833.

Maloney, C.E. and Lemaître, A. (2006) "Amorphous systems in athermal, quasistatic shear" *Phys. Rev. E* 74, 016118.

Sollich, P., Lequeux, F., Hébraud P. and Cates M.E. (1997) " Rheology of soft glassy materials" *Phys. Rev. Lett.* 78, 2020-2023.

Talamali, M., Petäjä, V., Vandembroucq, D. and Roux, S. (2012). "Strain Correlation and anisotropic correlation in a mesoscopic model of amorphous plasticity", *C.R. Mécanique* 340, 275-288.

Tanguy, A., Wittmer, J., Léonforte F. and Barrat J.L. (2002). "Continuum limit of amorphous elastic bodies: A finite-size study of low-frequency harmonic vibrations" *Phys. Rev. B* 66, 174205.

Tsamados, M., Tanguy, A., Goldenberg, C. and Barrat, J.L. (2009). "Local elasticity map and plasticity in a model Lennard-Jones glass" *Phys. Rev. E* 80, 026112.

Vandamme, M. and Ulm, F.J. (2009) "Nanogranular origin of concrete creep" (2009) *Proc. Nat. Acad. Sci.* 106, 10552-10557

Vandembroucq, D., Skoe, R. and Roux, S. (2004). "Universal fluctuations of depinning forces: application to finite temperature behavior" *Phys. Rev. E* 70, 051101.

NANO-CREEP OF SYNTHETIC CSH PRODUCED USING 1.5 AND 0.7 CAO/SIO_2 MIXTURE RATIOS

Michelle L. Begaye[1], Sherif H. Aboubakr[1], Jung J. Kim[2]
and Mahmoud M. Reda Taha[1]

[1]Department of Civil Engineering, University of New Mexico, MSC011070 1 University of New Mexico, Albuquerque, NM, 87131-0001 USA; PH: (505) 277-2722; mrtaha@unm.edu
[2]Department of Civil Engineering, Sejong University, Seoul, South Korea

ABSTRACT

Calcium Silicate Hydrate gel (C-S-H) is the main product of the cement hydration process responsible for strength and durability of concrete. While C-S-H can be obtained from Portland cement hydration, the process of hydrating cement produces other by-products such that make it difficult to characterize C-S-H solely. C-S-H is synthesized here by mixing calcium oxide (CaO) with fumed silica (SiO_2) and a large amount of deionized water (H_2O) making C-S-H slurry. Two Cao/SiO_2 mixture ratios of 1.5 and 0.7 were examined. The slurry was filtered to remove excess water for 24 hours and then dried at 11% relative humidity (RH) using Lithium Chloride for 5 weeks. The produced C-S-H powder was compacted under 400 MPa to produce C-S-H. Nano-creep of the composite C-S-H with the two calcium silica (C/S) mixture ratios was determined using nanoindentation. The experiments showed that C-S-H with 0.7 C/S has higher elastic modulus and lower creep compliance compared with C-S-H with 1.5 C/S. Microstructural investigations using ^{29}Si nuclear magnetic resonance (NMR), Transmission Electron Microscopes (TEM), Thermal Gravimetric Analysis (TGA) and X-ray diffraction (XRD) analysis were performed to explain the observations. Microstructural investigations showed a significant increase in silicate polymerization at 0.7 C/S ratio compared with 1.5 C/S. The high level of polymerization might be able to explain the reduced creep of C-S-H at low C/S ratios.

Keywords: Calcium Silicate Hydrate (CSH), Creep, Nanoindentation

INTRODUCTION

Calcium Silicate Hydrate (C-S-H) formulates almost two-thirds of hydrated Portland cement paste by volume (Neville, 2012). Notably, C-S-H partakes a vital role in the setting and hardening and thus strength and dimensional stability of concrete (Li and Roy 1988). In the hydrated cement system, C-S-H is the primary binding agent that causes controversies over its layered nature and the role of interlayer water on its physical and mechanical properties (Alizadeh and Beaudoin 2011). The dashes between the lettering of C-S-H signify that no specific stoichiometry is implied (Taylor 1997). This is because C-S-H formed from cement hydration has variable stoichiometry dependent upon the water to cement ratio, calcium oxide to silica ratio, curing condition, and usage of accompanying materials involved (Taylor 1997). A few definitions of the structure of C-S-H also exist.

Sugiyama (2008) defines C-S-H as an amorphous material with a poorly crystalline structure. A layered C-S-H gel with a structural role for the internal area of interlayer water was suggested by the Feldman and Sereda model. It was then suggested that C-S-H is formed in a globule like structure that enables C-S-H to exist in different packing densities such as low density (LD) C-S-H with packing density 0.63 and high density (HD) with packing density (0.76) (Jennings 2000). The LD and HD C-S-H format was attributed to losing the interlayer water in globule C-S-H formation (Jennings 2000, Alizadeh and Beaudoin 2011) as shown in Figure 1(a). CSH with varying levels of densities were observed under high temperature and pressure curing conditions (Kim et al. 2013). Chen et al. (2004) described C-S-H as a disarray material composed of short silicate chains clasped together by calcium oxide regions with water confined inside the structure. It has also been suggested that C-S-H has the atomic arrangement similar of 1.4 nm tobermorite and jennite (Taylor 1997). The crystal structure of 1.4 nm tobermorite, $Ca_5Si_6O_{16}(OH)_2{\cdot}8H_20$, has been resolved to have a layer of distorted central CaO sheet that is sandwiched between silicate tetrahedrals. Direct connection of silicate tetrahedron is called Paired tetrahedral and the silicate connecting to two pairs tetrahedral is called Bridging tetrahedral shown in Figure 1(b). C-S-H has similar structures to tobermorite but is lacking some bridging tetrahedral and is referred to as a defect tobermorite structure (Chen et al. 2004).

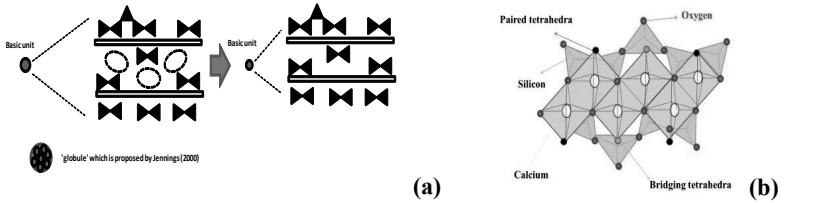

Figure 1. (a) Globule like CSH with significance of water on its density (Jennings 2000) (b) Schematic representation of tobermorite (Chen et al. 2004)

SYNTHESIS OF C-S-H

All C-S-H specimens were made by utilizing Reagent grade calcium carbonate ($CaCO_3$) from Mallinckrodt Chemicals to make lime (CaO). Fumed silica from Aldrich with 99.8% purity was used for the silicate percentage portion of the C-S-H, and deionized water was added for mixing an aqueous solution to form a gel-like structure. In each preparation batch for C-S-H with 0.7 and 1.5 calcium to silica (C/S) mixing ratios, 750 g of water were mixed with 30 g of SiO_2 and 21.1 g of CaO for 0.7 C/S mixing ratio and 44.9 g of CaO for 1.5 C/S mixing ratio. C-S-H was first synthesized by calcining $CaCO_3$ at 950 °C for 24 hours. Once pure lime was achieved through verification of weighing, it was placed in a dry box under nitrogen to prevent carbonation. CaO was dry-mixed with fumed silica and deionized water to produce aqueous concentrated slurry of C-S-H gel. The slurry was then transferred to a purged sealed mixing apparatus for continuous mixing for 7 days to allow complete reaction. The C-S-H gel was removed and transferred to a filtration system connected to a vacuum for removal of excess water for 24 hours under nitrogen to prevent carbonization. The filtration and drying systems are shown in Figure 2. The C-S-H

gel was then transferred for drying to 11% Relative Humidity (RH) using saturated lithium chloride (LiCl).

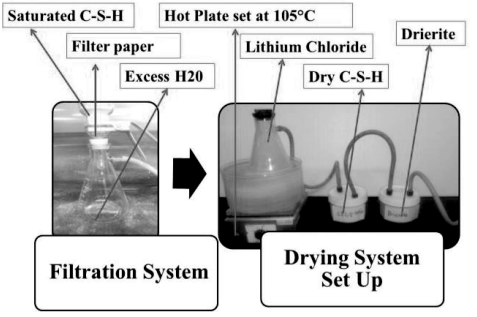

Figure 2. Filtration and drying systems for C-S-H synthesis.

All powder preparation was performed in a dry box filled with nitrogen to prevent any contamination. C-S-H was then compacted to form solid discs. For each compaction, a 6.0 g of dried C-S-H powder mixed with 3 ml of water for lubrication and was compacted in the cylinder apparatus. The load was applied at constant load rate of 1.6 kN/second and held at maximum load for 5 minutes before unloading. Five discs of each type of C-S-H were made under the pressure of 400 MPa.

NANO-CREEP OF C-S-H

All experiments were performed on powdered C-S-H except nanoindentation was performed on solid compacted C-S-H discs. Specimens were prepared for nanoindentation by casting thumbnails in a fast-set acrylic to keep the specimens in place for polishing. The specimens were polished on a Buehler Ecomet 3 auto-polisher with a Buehler 2 power head. Water was used to lubricate polishing. 125-micron, 70-micron, 30-micron, 9-micron, and 1-micron diamond pad were used on sequences for 10, 15, 15, 30, and 60 minutes respectively. Specimens were sonicated for 2 minutes in ethanol in between. After polishing, the C-S-H specimens had a mirror-like surface reflecting overhead light. Nanoindentation test was performed using NanoTest^{TM} 600 indenter system from Micro Materials, Inc., Wrexham, UK. Nanoindentation was performed using a Berkovich indenter tip with a loading and unloading rate of 0.0125 mN/sec, initial load of 0.05 mN and maximum load of 0.55 mN. The maximum load was held for dwell time of 60 seconds to observe nano-creep. 50 indentations were made on five gridlines spaced 200 μm apart with 10 indentations spaced at 200 μm on each gridline. Load-indentation data was analyzed using Oliver and Pharr (1992) method and the reduced modulus E_r was computed as:

$$E_r = \frac{\sqrt{\pi}}{2\beta}\left(\frac{\frac{dP}{dh}}{\sqrt{24.5\,h_c^2}}\right) \tag{1}$$

where β is a correction factor to account for the non-symmetrical shape of the indenter tip, which is equal to 1.034 for a 3-sided pyramidal (Berkovich) indenter. h_c

is the indenter contact depth. The slope of the indentation load-depth curve *dP/dh* was computed as the slope of a line tangent to (derivative of) the unloading curve. The creep compliance *J(t)* is defined as the change in the strain as a function of time under instantaneous applied constant initial load. The general mathematical formulation for viscoelastic constitutive models based on indentation via pyramid tip was developed by Giannakopoulos (2006).

$$h^2(t) = \frac{\pi(1-\upsilon)}{4\tan\alpha}\int_0^t J(t-\delta)\left[\frac{dP(\delta)}{d\delta}\right]d\delta \tag{2}$$

where *h(t)* is nanoindentation depth varying with time, υ is Poisson's ratio, α represents the indenter surface angle with the vertical axis and *J* represents creep compliance under nanoindentation. Equation (2) can thus be used to describe the integration to obtain the time-dependent indentation depth *h(t)* as a function of the applied load *P*. Lu et al. (2003) showed that the above integration can be solved by considering a constant loading rate $P(t) = \lambda_0 t\, H(t)$ where λ_0 is a constant and $H(t)$ is the step function, or under a step loading in the form of $P(t) = P_0\, H(t)$ where $H(t)$ is the step function and P_0 is a maximum load. We will consider the case of dwell period loading (t = 60 seconds) to be divided into a ramp loading occurring at time period t_1 within a very short rise time (t_1 = 1 second), then a constant load afterward for a time period t_2 = 59 seconds. Equation (2) can be re-written as

$$J(t) = \frac{4\,h^2(t)\tan\alpha}{\pi(1-\upsilon)P_0} \tag{3}$$

where P_0 represents the maximum applied indentation load at which the load was kept constant. Equation (3) was used to calculate creep compliance of C-S-H.

Nanoindentation data was analyzed using the above method. Figure 3 shows a comparison of the average reduced elastic modulus and creep compliance of the two types of C-S-H. It can be observed from Figure 3(a) that C-S-H made with low C/S mixture ratio of 0.7 has average elastic modulus 23% higher than that C-S-H made with high C/S mixture ratio of 1.5. Furthermore, the results in Figure 3(b) show that C-S-H made low C/S mixture ratio of 0.7 has average creep compliance 27% lower than that C-S-H made with high C/S mixture ratio of 1.5. Figure 4 shows a comparison of the statistical deconvolution analysis performed after Contantinedes and Ulm (2007). It shows that HD C-S-H phase indicated as HD* CSH in Figure 4(a) for 0.7 C/S mixture ratio has higher modulus of 35 MPa than the HD C-S-H modulus of 31 MPa for 1.5 C/S mixture ratio.

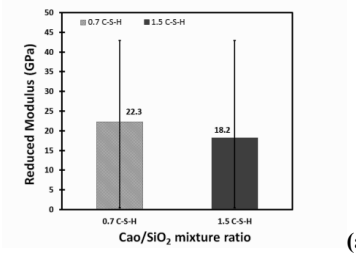

(a)

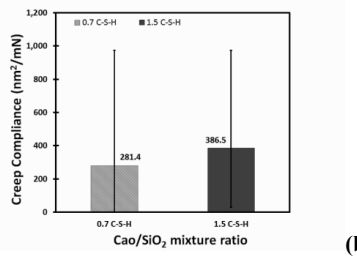

(b)

Figure 3: Nanoindentation of C-S-H (a) reduced modulus (b) creep compliance.

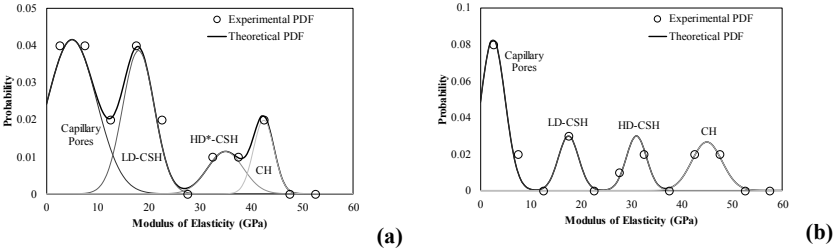

Figure 4: Deconvolution of C-S-H reduced modulus (a) 0.7 C/S (b) with 1.5 C/S.

MICROSTRUCTURAL CHARACTERIZATION OF C-S-H

All synthetic C-S-H where characterized using TGA, XRD, NMR and TEM. TGA tests were performed from 25 °C to 1000 °C, heated at 10 °C/min. The temperature range where water began to dissociate from the C-S-H between 125 °C and 150 °C was observed in this study. The mass losses at the temperature ranges from 145 °C to 400 °C, from 400 °C to 600 °C and from 600 °C to 825 °C are attributed to the dehydration of C-S-H, the dehydroxylation of calcium hydroxide and the decarbonation of calcite respectively. TGA curves for the synthetic C-S-H with C/S mixture ratio of 0.7 and 1.5 are shown in Figure 5 and the results are presented in Table 1. To exclude additional absorbing water prior to performing the TGA from the TGA results, the initial weight is taken at 145 °C (Foley et al. 2012). Using the mass loss results from TGA, the stoichiometric formula of synthetic C-S-H dried to 11% RH in this study are approximated as $C_{0.59}SH_{0.48}$ and $C_{1.08}SH_{0.77}$ for C/S mixture ratios 0.7 and 1.5 respectively. Detailed explanation of the method to identify the stoichiometric formula of synthetic C-S-H is provided elsewhere (Kim et al. 2013). TGA analysis shows that the synthetic C-S-H produced with 0.7 and 1.5 C/S mixture ratios resulted in C-S-H with 0.59 and 1.08 C/S ratios. The analysis also shows that for C-S-H made with 0.7 C/S ratio, incorporates almost 62% of the water in C-S-H made with 1.5 C/S ratio. Such significant reduction of C-S-H water content would definitely help in reducing creep. Finally, the mass loss from 400~600^{o}C in TGA in Table 1 is proportional to CH contents in both materials confirming that C-S-H made using 0.7 C/S ratio has 60% less CH crystals than that made using 1.5 C/S ratio.

The main crystalline phases detected from XRD analysis are Portlandite·$Ca(OH)_2$, Clinotobermorite·$Ca_5(Si_6O_{16})(OH)_2$ and tobermorite 9A·$Ca_5S_{16}O(_{16}(OH)_2$, indicating evidence regarding the formation of a 1.4-nm tobermorite type layer to be present in both ratios. XRD peaks for C/S mixture ratios of 0.7 and 1.5 are shown in Figure 6 confirming the formation of C-S-H. There is little difference between the two spectra with a tendency to enable CH formation at a high C/S mixture ratio of 1.5. The XRD spectra confirms that most of the higher stiffness phases observed in C-S-H made using 0.7 C/S mixture ratio compared with C-S-H produced using 1.5 C/S mixture ratio might not be attributed to high CH content but rather to either HD C-S-H or to the lower water content in the final C-S-H material as apparent from TGA analysis.

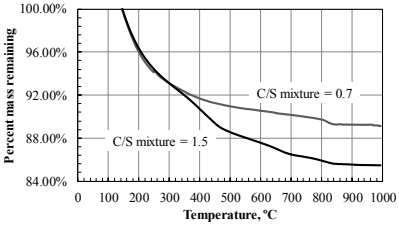

Figure 5. TGA plots of C-S-H with 0.7 and 1.5 mixture ratios.

Table 1. Mass Loss Resulting from TGA

C/S mixture	145 °C ~ 400 °C	400 °C ~ 600 °C	600 °C ~ 825 °C	Stoichiometric formula
0.7	7.691%	1.765%	1.138%	$C_{0.59}SH_{0.48}$
1.5	8.022%	4.417%	1.854%	$C_{1.08}SH_{0.77}$

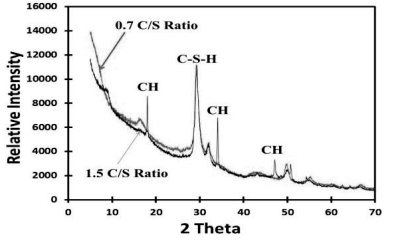

Figure 6. XRD comparison data for 0.7 C/S to 1.5 C/S of C-S-H.

^{29}Si MAS-NMR is a used for analyzing the silicate connectivity and polymerization of silica-based compounds. Figure 7 shows ^{29}Si MAS-NMR spectra of C-S-H for 0.7 and 1.5 C/S mixture. The silicate connectivity Q^n of Q^1, Q^2_b, Q^2 and Q^3 were observed near the corresponding peaks of -79.5 ppm, -82.7 ppm, -85.6 ppm and -92 ppm respectively. The Q^n intensities for 0.7 and 1.5 C/S mixture C-S-H are presented in Table 2. The average degree of silicate connectivity *n* can be calculated using the calculated Q^n intensities as $n = (Q^1+2Q^2+3Q^3) / (Q^1+Q^2+Q^3)$ (Saoût 2006). C-S-H with a 1.5 C/S mixture ratio shows near-equal Q^1 and Q^2 bonding at -79.5 and -85.6, respectively, while for 0.7C/S, mostly Q^2 is observed. Q^3 at -92 ppm, which indicates cross-linking between the chain layers, was also observed in 0.7 C/S mixture C-S-H. The average degree of silicate connectivity *n* for 0.7 and 1.5 C/S mixture ratio are calculated as 1.975 and 1.454 respectively. TEM specimens were made by producing a droplet including CSH and observing it under the TEM. TEM images shown in Figure 8 confirm NMR observation. While no particular feature can be observed in C-S-H produced using 1.5 mixture ratio, a very distinct rod-like structure is observed in C-S-H produced using 0.7 C/S mixture ratio. It is strongly believed that such rod-like connection represents silicate chain polymerization.

Table 2. Integration Results of Q^n Intensities from ^{29}Si MAS NMR

C/S mixture	Q^1	Q^2	Q^3	n
0.7	7.6%	87.2%	5.2%	1.975
1.5	54.6%	45.4%	-	1.454

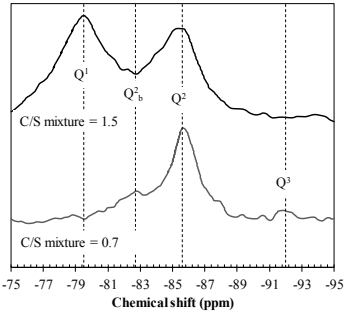

Figure 7. ^{29}Si MAS-NMR spectra of 0.7 and 1.5 C/S C-S-H.

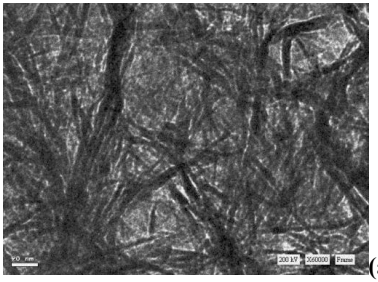
(a)
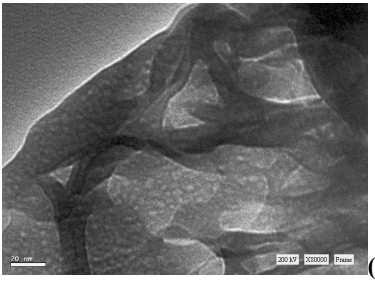
(b)

Figure 8. TEM images of C-S-H (a) 0.7 (b) 1.5 C/S mixture ratios.

CONCLUSIONS

Synthetic C-S-H was produced using two C/S mixture ratios of 1.5 and 0.7. The produced C-S-H was dried to standard levels and was then compacted to 400 MPa. Solid C-S-H was examined using nanoindentation while powder C-S-H was examined using TGA, XRD, NMR and TEM. Mechanical characterization of C-S-H using nanoindentation showed C-S-H produced using 0.7 C/S ratio to have a higher reduced elastic modulus and lower creep compliance compared with C-S-H produced using 1.5 C/S ratio. While the difference is statistically insignificant due to wide variation, statistical deconvolution analysis confirmed C-S-H produced with 0.7 C/S mixture ratio to have stiffer nanophases than C-S-H produced using 1.5 C/S ratio. TGA analysis confirmed that C-S-H produced with 0.7 mixture C/S to have much lower water content than C-S-H produced with 1.5 C/S mixture ratio. Furthermore, XRD and TGA analysis showed lower CH content in C-S-H produced with 0.7 C/S mixture ratio compared with C-S-H produced with 1.5 C/S mixture ratio. NMR and TEM observations confirmed that C-S-H produced with 0.7 C/S mixture ratio has a much higher silicate polymerization and a different microstructure than C-S-H

produced with 1.5 C/S mixture ratio. The increase in stiffness and reduction in creep compliance of C-S-H produced with 0.7 C/S mixture ratio might be attributed to such changes in water content, sub-microstructure and silicate polymerization.

ACKNOWLEDGEMENT

The authors like to acknowledge the support to the University of New Mexico team by US National Science Foundation (NSF) Award # 1131369. The financial support by the National Research Foundation of Korea (NRF) grant funded by the Korea government (MEST) (No. 2011-0030842) to the third author is greatly appreciated.

REFERENCES

Alizadeh, R. and Beaudoin, J. J. (2011) "Mechanical properties of calcium silicate hydrate." *Mat. and Structures*, 44, 13–28.

Chen, J. J., Thomas, J. J., Taylor, H. F. W, and Jennings, H. M. (2004) "Solubility and structure of calcium silicate hydrate." *Cem. & Conc. Res*, 34, 1499–1519.

Contantinedes, G., and Ulm, F. J. (2007) "The nanogranular nature of C-S-H." *J. Mech Phys. Solids*, 55, 64 –90

Foley, E. M., Kim, J. J., and Reda Taha, M. M. (2012) "Synthesis and nano-mechanical characterization of calcium silicate hydrate (C-S-H) made with 1.5 Ca/SiO2 mixture." *Cem. and Conc. Res.*, 42, 1225–1232

Giannakopoulos, A. (2006) "Elastic and viscoelastic indentation of flat surfaces by pyramid indenters." *J. of the Mech. and Phy. of Solids*, 54, 1305–1332.

Jennings, H. M. (2000) "A model for the microstructure of calcium silicate hydrate in cement paste." *Cem. and Conc. Res.*, 30, 101–116.

Kim, J. J., Foley, E. M., and Reda Taha, M. M. (2013) "Nano-mechanical characterization of synthetic calcium silicate hydrate (C-S-H) with varying Ca/SiO2 mixture." *Cem. and Conc. Comp.*, 36, 65–70.

Li, S. and Roy, D. M. (1988) "Preparation and characterization of high and low CaO/SiO2 ratio "pure" C-S-H for chemically bonded ceramics." *J. of Mat. Res.*, 3(2), 380–386.

Lu, H., et al. (2003) "Measurement of creep compliance of solid polymers by nanoindentation." *Mech. of Time-dependent Mater.*, 7, 189–207.

Neville, A. M. (2012) *Properties of concrete,* 5th ed., Prentice Hall, USA.

Oliver, W. C., and Pharr, G. M. (1992) "An improved technique for determining hardness and elastic modulus using load and displacement sensing indentation experiments." *J. of Mater. Res.*, 7(6), 1564–1583.

Saoût, G. L., Le´colier, E., Rivereau, A., and Zanni, H. (2006) "Chemical structure of cement aged at normal and elevated temperatures and pressures, Part I: Class G oilwell cement." *Cem. and Conc. Res.*, 36, 71–78.

Sugiyama, D. (2008) "Chemical Alteration of calcium silicate hydrate (C-H-S) in sodium solution." *Cem. and Conc. Res.*, 1270–1275.

Taylor, H. F. W. (1997) *Cement chemistry*, 2nd ed. Thomas Telford, London.

Applying Tools from Glass Science to Study Calcium-Silicate-Hydrates

MJ. Abdolhosseini Qomi[1], M. Bauchy[1], R. J-M. Pellenq[1,2] and F-J. Ulm[1]

[1] Department of Civil and Environmental Engineering, Massachusetts Institute of Technology, 77 Massachusetts avenue, 02139; Cambridge, United States; email: ulm@mit.edu
[2] Centre Interdisciplinaire des Nanosciences de Marseille, Centre National de la Recherche Scientifique and Marseille Universite´, Campus de Luminy, Marseille, 13288 Cedex 09, France; email: pellenq@mit.edu

Abstract:
To explain the similarities between a glass and amorphous C-S-H, a C-S-H molecular structure with stoichiometry of $(CaO)_{1.7}(SiO_2)_1(H_2O)_{1.9}$ is produced using a mixed reactive-nonreactive force field modeling. As the consequence of reactive modeling using REAXFF potential, part of water molecules in the interlayer spacing dissociate in to hydroxyl groups and proton, which produces Ca-OH bonds. In addition, it is shown that monomers condensate to produce dimmers. This reduces the monomer content and increases the mean silicate chain length. Comprehensive topological analysis is performed to identify the local environment of each atom, which is indicative of short range order in C-S-H. Specially, the topological analysis is shown to be essential to distinguish between oxygen atoms in water, hydroxyl groups, silica chain and calcium oxide sheets. The medium range order in C-S-H is shown to exist using first sharp diffraction pattern derived from structure factor calculations.

Introduction:

The main hydration phase of cementitious systems is calcium-silicate-hydrate (C-S-H). This phase is the binding phase responsible for concrete's strength, durability, viscoelastic and creep properties. Since all the physical properties of C-S-H originate from the nano-scale, a special attention is drawn to the molecular structure of C-S-H in the past few years. Specially, (Pellenq et al. 2009) proposed a realistic C-S-H model which exhibited many features of C-S-H nanostructure. Using the tools in statistical physics, the realistic C-S-H model were further analyzed in more details(Abdolhosseini Qomi et al. 2012; Ji et al. 2012; Youssef et al. 2011). Recently, the realistic C-S-H was further developed to include Ca-OH bonds (Manzano et al. 2012). This updated model confirmed again that realistic C-S-H models could reproduce both density and mechanical properties of C-S-H structures. The common point between all C-S-H structures are that they are composed of quasi-octahedral calcium-oxide layers with defective silica chains on the either sides. The calcium-silicate lamellar layer is negatively charged which is charge-balanced with Ca^{2+} cations in the interlayer spacing. The interlayer spacing separates stacks of calcium-silicate sheets.

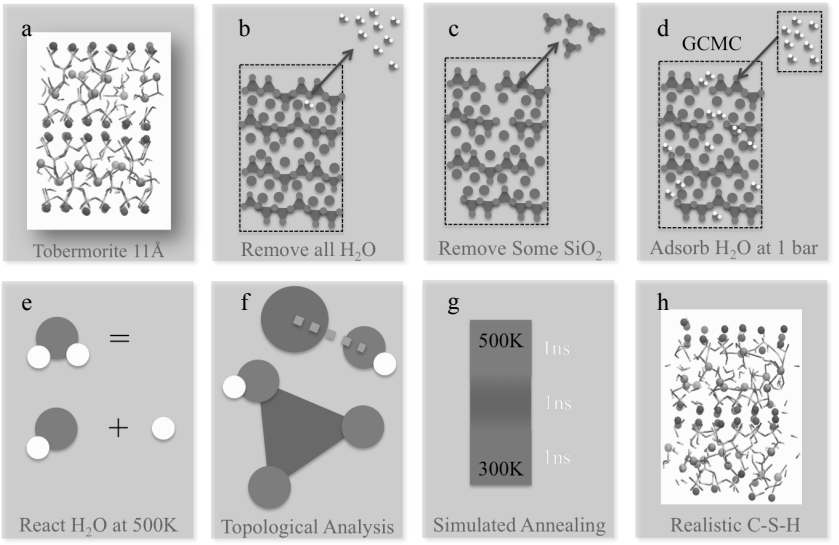

Figure 1: Different stages for the preparation of a realistic C-S-H model. a) Starting from a super-cell of Tobermorite 11Å. b) Removing water molecules from the structure. c) Removing SiO_2 bonds from the calcium-silicate backbone. d) Adsorbing water in the interlayer and defect sites. e) Reactive force field modeling at elevated temperature. f) Topological analysis to identify local environments. g) Simulated annealing using non-reactive potential. h) A snapshot of a realistic C-S-H model.

The molecular structures of C-S-H and glasses have many features in common. Given the recent advances in glass physics, it is of the general cement and concrete community to explore the molecular structure of C-S-H in terms of a glass. There are several prevalent tools such as topological analysis, first sharp diffraction patterns and constraint theory that can already be applied to the molecular structure of C-S-H. Using the tools in statistical physics, a C-S-H sample is created with Ca/Si=1.7. The topological analysis is performed to identify the short-range order in the syste. The medium range order is analyzed afterward to demonstrate that the order extends beyond the first coordination shell of atoms.

Realistic Modeling of C-S-H at Nano-Scale:

The methodology to produce a realistic C-S-H molecular structure is a combination of several atomistic-scale classical simulation techniques at different stages of the model preparation (see figure 1). The main statistical mechanics techniques employed are internal energy relaxation at constant volume or pressure, Grand Canonical Monte Carlo (GCMC) for water adsorption, NPT and NVT molecular dynamics using both reactive and non-reactive potentials at room and elevated temperatures. The interatomic interactions are described via REAXFF (Manzano, Pellenq, et al. 2012), CSHFF potential (Shahsavari et al. 2011) and a modified version of CSHFF potential to include the interactions with hydroxyl groups. The original CSHFF interatomic potential is a point-charge model designed to reproduce C-S-H's mechanical

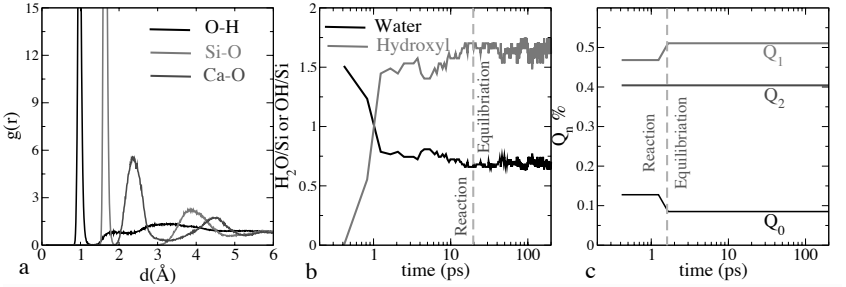

Figure 2: Reactive force field modeling in canonical ensemble. a) Radial distribution function for Si-O, Ca-O and O-H bonds. b) Dissociation of water molecules in C-S-H and production of hydroxyl groups. c) Condensation of silica groups in the silicate chain.

properties. The CSHFF potential has the ($E_{CSHFF}=E_{Coulomb}+E_{LJ}+E_{Radial}+E_{Angular}$) form. $E_{Coulomb}$, E_{LJ}, E_{Radial}, and $E_{Angular}$ are the electrostatic, short-range Van der Waals in the form of Lennard-Jones potential, bond stretching and bond bending contributions to the potential energy of the iono-covalent system. CSHFF is seen as an improved version of the generic ClayFF potential (Cygan et al. 2004). Despite all the advantages of using CSHFF potential, this force field is unable to describe chemical reactions.

REAXFF potential was subsequently developed and applied to C-S-H to study the state of water in the C-S-H's nano-porous medium (Manzano et al. 2012). REAXFF is a reactive force field originally based on the same ideas as bond order potentials (Tersoff 1988) with polarizable charge model. In this force field, the total potential energy reads ($E_{REAXFF}=E_{Coulomb}+E_{VdW}+E_{Radial}+E_{Angular}+E_{lp}+E_{OverCoord}+E_{UnderCoord}$). E_{lp} is lone pair energy, $E_{OverCoord}$ and $E_{UnderCoord}$ are over- and under-coordinated energy contributions, respectively. These three terms are added to this potential to make appropriately capture chemical reactions. REAXFF shows the ability to define each individual interaction between atoms depending on their environment. For more detailed discussion on the REAXFF potential, interested readers are referred to the work of (Russo Jr. and van Duin 2011).

To build a C-S-H model with Ca/Si=1.7, we started from a periodic simulation box containing 2*3*1 unit cells of Hamid's structure of 11Å Tobermorite (Hamid 1981). At this stage, we considered an anhydrous version of this structure, as we were only interested in creating the model itself. To produce the calcium-silicate backbone of the sample, a simple computer program was written that uses a random number generator to remove some SiO_2 groups with the constraint producing as much dimers, pentamers and octamers as possible. Since SiO_2 is a neutral group, the electro-neutrality is maintained. In fact, upon removal of all the bridging silica sites from the initial crystalline structure, the Ca/Si ratio is found to be 1.5. Therefore, some monomers inevitably exist in the initial solid skeleton of C-S-H samples.

We used the Grand Canonical Monte-Carlo (GCMC) simulation technique to adsorb water in the interlayer spacing and defect locations. GCMC is at constant volume V in contact with infinite fictitious reservoir of particles with chemical potential, μ, at temperature T. We did not calculate the entire water adsorption/desorption isotherm

but perform a single GCMC simulation with the water chemical potential fixed to a value that corresponds to the bulk liquid phase with a density of 1 gr/cm^3 at room temperature (μ=0 eV for the used flexible SPC water potential model). All the GCMC calculations are performed via GULP (Gale 1997).

All reactive simulations are performed using LAMMPS (Plimpton 1995), using velocity Verlet time integration scheme. In order to appropriately describe chemical reactions, the time step is set to 0.1fs. Additionally, to trigger and facilitate the reaction of water molecules, REAXFF simulations are carried out at 500K. This helps the water molecules to overcome the reaction energy barriers. Initially, all samples are relaxed in canonical ensemble (NVT) for at 200ps using Nose-Hoover thermostat. After relaxation in NVT ensemble, the samples are further relaxed in isothermal-isobaric ensemble (NPT) at the 500K and 1atm. The overall performance of a C-S-H sample with Ca/Si = 1.7 is presented in Figure 2.

Figure 2.a provides the radial distribution function, RDF or g(r), of Si-O, Ca-O and O-H bonds. Since the peaks in g(r) are intact, the slight elevated temperature has not affected the solid backbone of the C-S-H. It should be also noted that while Si-O and O-H RDFs have a very defined first sharp peaks, the Ca-O RDF exhibits a wider first peak. Ca-O bond has a much larger radial excursion meaning that Ca-O bond is not as stiff as Si-O and O-H. As it can be seen in figure 2.b, in the very first few picoseconds of the simulation, a large portion of water molecules dissociates to form OH^- and H^+ ionic pairs. While the hydroxyl groups coordinate with Ca^{2+} ions, the produced protons reacts with non-bridging oxygen atoms in silicate groups. No hydrogen atom was found coordinated to the bridging oxygen shared between adjacent silicate groups. The dissociation mechanism affects the large portion of interlayer water molecules in the C-S-H and the dissociation percentage depends on the Ca/Si ratio which is directly proportional to the number of non-bridging oxygen atoms in silicate chain. Reactive modeling also affects the solid skeleton of C-S-H. Figure 2.c shows the effect of reactivity on condensation of silicate groups. It is observed that silicate groups condensated in this C-S-H model. In the particular case, a pair of monomers has condensate to form a dimmer. This is in agreement with DFT calculation of isolated silicate groups (Manzano et al. 2011) showing that dimmers have high stability index. The observed condensation mechanism is triggered by two silicate tetrahedra pairing in which a dimmer is produced and an oxygen atom is released in the process. The free oxygen pairs with a H^+ atom and to complete the reaction path, the product hydroxyl group coordinates with Ca^{2+} atoms in the interlayer spacing. This signifies that due to random "cutting" of chains, some monomers have extremely unrealistic configuration. This unrealistic state is relaxed via polymerization of monomers producing energetically more stable dimers.

Topological Analysis:

REAXFF modeling is computationally expensive to undertake. In order to overcome the prohibiting computational cost of reactive modeling in extensive mechanical testing required to be performed on all of the C-S-H samples, all the samples are transferred to non-reactive modified C-S-H-FF environment after reaction. As the direct consequence of reactive modeling, the local environment of atoms undergoes drastic changes. This adds a level of complication and necessitates a precise

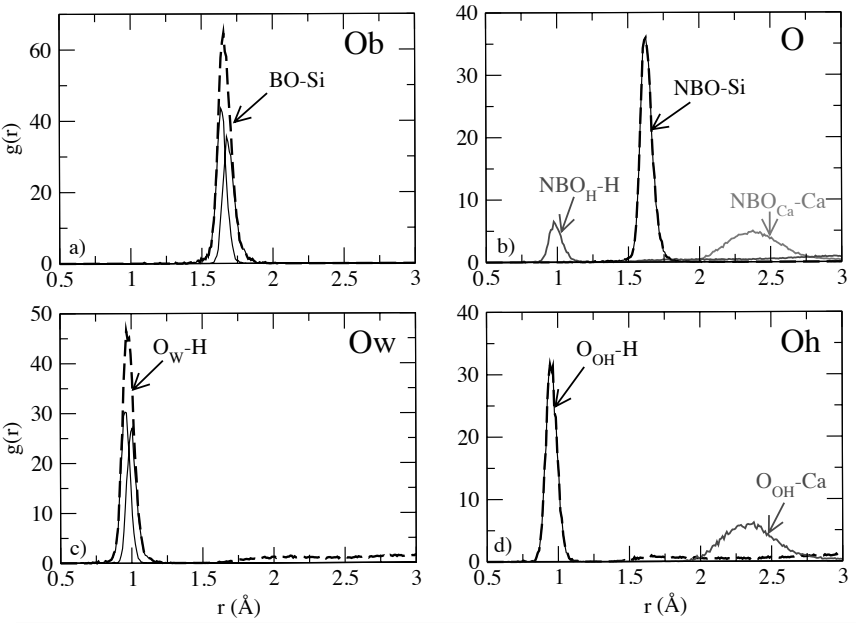

Figure 3: Radial distribution functions of Si, Ca, and H cations around Ob (a), O (b), Ow (c) and Oh (d). Figures a) and b) show the contributions of the two nearest Si neighbors and figures c) and d) the contributions of the two nearest H neighbors.

characterization of local environment of each single atom. Such a precise analysis can be performed using the fundamental ideas in topological constraint analysis(Bauchy and Micoulaut 2013). In C-S-H's molecular structure, Si, Ca and H cations are always connected to O atoms, the latters showing different local environment (see Figure 3). In order to differentiate these species, we performed a careful topological analysis of the coordination of each O atom. Bridging oxygen atoms (Ob) are thus defined as oxygen atoms showing exactly two Si neighbors in their O-Si first coordination shell (FCS), which limit has been fixed as the first minimum of the $g_{Si\text{-}O}$, typically 2.5Å. On the contrary, non-bridging oxygen atoms (O) show only one Si in their O-Si FCS. Those species arise from the depolymerization of the silicate network by Ca and H cations and can belong to hydroxyl groups O-H (Oh) if they show an H neighbor in their O-H FCS (minimum of the $g_{O\text{-}H}$ RDF, typically 1.3Å) or be connected to Ca atoms otherwise. Remaining O atoms that are not part of the silicate network have then been respectively differentiated into water oxygen atoms (Ow) and hydroxyl group oxygen atoms (Oh) when they respectively show two and one hydrogen atom in their O-H FCS. Following the topological analysis, the sample was relaxed for 1ns at 500k using modified C-S-H-FF potential in isobaric-isothermal ensemble with time steps as large as 1fs. All samples are subsequently quenched over 1ns to 300K and further relaxed in NPT ensemble for another 1ns at 300K to make sure that all the macroscopic observables have relaxed and converged to a proper value.

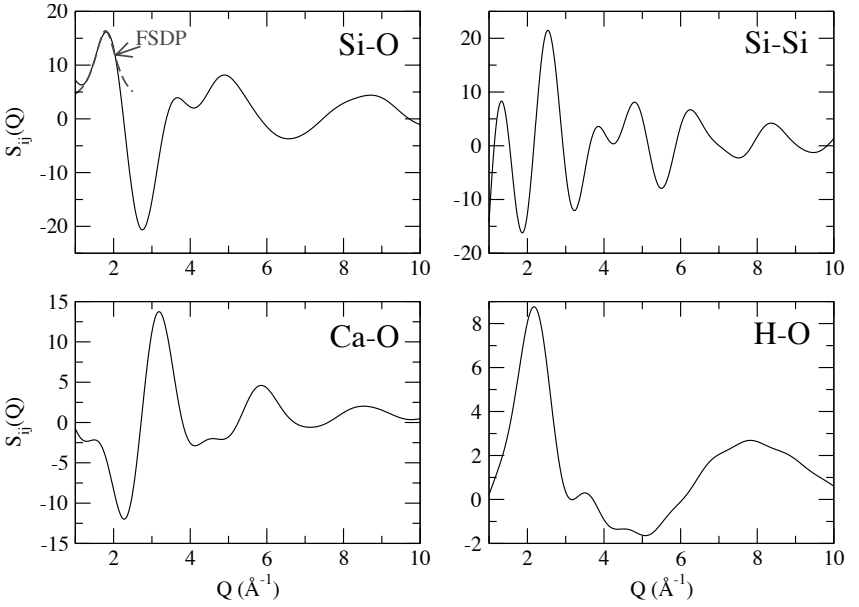

Figure 4: Computed a, Si-O, b, Si-Si, c, Ca-O and d, H-O structure factors at Ca/Si=1.7. The blue broken line shows a fit of the first sharp diffraction peak with a Lorentzian function.

Medium Range Order:

As presented before, RDFs give insights into the short-range order of the structure of the material, this length scale being mostly driven by coordination numbers and bond lengths. We analyzed the medium range order to understand the extent of order in C-S-H. To do so, we largely relied on tools introduced in glass science. The medium range order can be captured by the partial structure factors, which can be computed from the RDFs $g_{ij}(r)$:

$$S_{ij} = 1 + \rho_0 \int_0^R 4\pi r^2 \left(g_{ij} - 1\right) \frac{sin(Qr)}{Qr} F_L(r) dr$$

where $Q = 2\pi/r$ is the scattering vector, ρ_0 is the average atom number density and R is the maximum value of the integration in real space (here \$R = 6Å). The $sin\left(\frac{\pi r}{R}\right)/(\frac{\pi r}{R})$ term is a Lortch-type window function used to reduce the effect of the finite cutoff of r in the integration (Wright 1988). The use of this function reduces the ripples at low Q but can induce a broadening of the structure factor peaks. Figure 4 shows Si-O, Si-Si, Ca-O and H-O partial structure factors at Ca/Si=1.7, which are by all means similar to typical structure factors observed in silicate glasses.

Among the different features of structure factors, the so-called first sharp diffraction peak (FSDP) has received a lot of attention in glass science. Starting from the

principal peak, which position $Q_p = 2\pi/r_p$ is associated to the nearest-neighbor distance r_p, the FSDP is defined as the next peak located a lower $Q < Q_p$. It is thus related to the structural correlations in the medium range order at $r > r_p$. This feature has been observed both in covalent(Elliott 1991; Wilson and Madden 1994) and ionic (Wilson and Madden 1994) amorphous system. The FSDP origin is now usually explained by using a void-based model(Uhlherr and Elliott 1994; Zaug et al. 2008) in which ordering of interstitial voids occurs in the structure.

The FSDPs we obtained from simulations were further studied by fitting them with Lorentzian functions (example of fitted function can be seen on Figure 4). This choice is supported by the fact that the experimental results in neutron scattering factor of silica can be better fitted with a Lorentzian function than with a Gaussian one (Wright et al. 1991). It should be noted that the fit has been done on the low Q part of the FSDP to avoid the contribution of the following peaks. This allows us to track precisely the FSDP peak intensity, position and full-width at half maximum (FWHM) for each sample. Coming back to the real space structural correlations, the FSDP peak position Q_{FSDP} is usually related to a characteristic repetition distance $d = 2\pi/Q_{FSDP}$. The effect depolymerization of the network (a decrease of the atomic order) is associated to a decrease of the intensity of the FSDP and a decrease in the characteristic distance d (Bauchy 2012).

Conclusion:

In this paper, a C-S-H molecular structure with stoichiometry of $(CaO)_{1.7}(SiO_2)_1(H_2O)_{1.9}$ was produced using a mixed reactive-nonreactive force field modeling. Using REAXFF potential, part of water molecules in the interlayer spacing dissociates in to hydroxyl groups and proton. It was also shown that monomers condensate to produce dimmers. This reduces the monomer content and increases the mean silicate chain length. Comprehensive topological analysis is performed to identify the local environment of each atom, which is indicative of short-range order in C-S-H. Specially, the topological analysis is shown to be essential to distinguish between oxygen atoms in water, hydroxyl groups, silica chain and calcium oxide sheets. The medium range order in C-S-H is shown to exist using first sharp diffraction pattern derived from structure factor calculations.

References:

Abdolhosseini Qomi, M. J., Ulm, F.-J., and Pellenq, R. J.-M. (2012). "Evidence on the Dual Nature of Aluminum in the Calcium-Silicate-Hydrates Based on Atomistic Simulations." *Journal of the American Ceramic Society*, 95(3), 1128–1137.

Bauchy, M. (2012). "Structural, vibrational, and thermal properties of densified silicates: Insights from molecular dynamics." *The Journal of Chemical Physics*, 137(4), 044510–044510–12.

Bauchy, M., and Micoulaut, M. (2013). "Transport Anomalies and Adaptative Pressure-Dependent Topological Constraints in Tetrahedral Liquids: Evidence for a Reversibility Window Analogue." *Physical Review Letters*, 110(9), 095501.

Cygan, R. T., Liang, J.-J., and Kalinichev, A. G. (2004). "Molecular Models of Hydroxide, Oxyhydroxide, and Clay Phases and the Development of a General Force Field." *The Journal of Physical Chemistry B*, 108(4), 1255–1266.

Elliott, S. R. (1991). "Origin of the first sharp diffraction peak in the structure factor of covalent glasses." *Physical Review Letters*, 67(6), 711–714.

Gale, J. D. (1997). "GULP: A computer program for the symmetry-adapted simulation of solids." *Journal of the Chemical Society-Faraday Transactions*, 93(4), 629–637.

Hamid, S. (1981). "The Crystal-Structure of the 11-a Natural Tobermorite Ca2.25[si3o7.5(oh)1.5].1h2o." *Zeitschrift Fur Kristallographie*, 154(3-4), 189–198.

Ji, Q., Pellenq, R. J.-M., and Van Vliet, K. J. (2012). "Comparison of computational water models for simulation of calcium–silicate–hydrate." *Computational Materials Science*, 53(1), 234–240.

Manzano, H., Durgun, E., Abdolhosseine Qomi, M. J., Ulm, F.-J., Pellenq, R. J. M., and Grossman, J. C. (2011). "Impact of Chemical Impurities on the Crystalline Cement Clinker Phases Determined by Atomistic Simulations." *Crystal Growth & Design*, 11(7), 2964–2972.

Manzano, H., Moeini, S., Marinelli, F., van Duin, A. C. T., Ulm, F.-J., and Pellenq, R. J.-M. (2012). "Confined Water Dissociation in Microporous Defective Silicates: Mechanism, Dipole Distribution, and Impact on Substrate Properties." *Journal of the American Chemical Society*, 134(4), 2208–2215.

Manzano, H., Pellenq, R. J. M., Ulm, F.-J., Buehler, M. J., and van Duin, A. C. T. (2012). "Hydration of Calcium Oxide Surface Predicted by Reactive Force Field Molecular Dynamics." *Langmuir*, 28(9), 4187–4197.

Pellenq, R. J.-M., Kushima, A., Shahsavari, R., Vliet, K. J. V., Buehler, M. J., Yip, S., and Ulm, F.-J. (2009). "A realistic molecular model of cement hydrates." *Proceedings of the National Academy of Sciences*, 106(38), 16102–16107.

Plimpton, S. (1995). "FAST PARALLEL ALGORITHMS FOR SHORT-RANGE MOLECULAR DYNAMICS." *Journal of computational physics*, 117(1), 1–19.

Russo Jr., M. F., and van Duin, A. C. T. (2011). "Atomistic-scale simulations of chemical reactions: Bridging from quantum chemistry to engineering." *Nuclear Instruments and Methods in Physics Research Section B: Beam Interactions with Materials and Atoms*, 269(14), 1549–1554.

Shahsavari, R., Pellenq, R. J.-M., and Ulm, F.-J. (2011). "Empirical force fields for complex hydrated calcio-silicate layered materials." *Physical chemistry chemical physics: PCCP*, 13(3), 1002–1011.

Tersoff, J. (1988). "Empirical Interatomic Potential for Carbon, with Applications to Amorphous Carbon." *Physical Review Letters*, 61(25), 2879–2882.

Uhlherr, A., and Elliott, S. R. (1994). "Extended-range propagated order in amorphous solids." *Journal of Physics: Condensed Matter*, 6(8), L99.

Wilson, M., and Madden, P. A. (1994). "'"Prepeaks"' and '"first sharp diffraction peaks"' in computer simulations of strong and fragile ionic liquids." *Physical Review Letters*, 72(19), 3033–3036.

Wright, A. C. (1988). "Neutron and X-ray amorphography." *Journal of Non-Crystalline Solids*, 106(1–3), 1–16.

Wright, A. C., Hulme, R. A., Grimley, D. I., Sinclair, R. N., Martin, S. W., Price, D. L., and Galeener, F. L. (1991). "The structure of some simple amorphous network solids revisited." *Journal of Non-Crystalline Solids*, 129(1–3), 213–232.

Youssef, M., Pellenq, R. J.-M., and Yildiz, B. (2011). "Glassy Nature of Water in an Ultraconfining Disordered Material: The Case of Calcium–Silicate–Hydrate." *Journal of the American Chemical Society*, 133(8), 2499–2510.

Zaug, J. M., Soper, A. K., and Clark, S. M. (2008). "Pressure-dependent structures of amorphous red phosphorus and the origin of the first sharp diffraction peaks." *Nature materials*, 7(11), 890–899.

Mechanical behaviour of ordered and disordered calcium silicate hydrates under shear strain studied by atomic scale simulations

H. Manzano[1], E. Masoero[2], I. Lopez-Arbeloa[1], H. M. Jennings[2]

[1] Molecular Spectroscopy Laboratory, Department of Physical Chemistry, University of the Basque Country, UPV/EHU, Apartado 644, 48080-BILBAO, Spain; E-mail: hegoi.manzano@ehu.es
[2] Department of Civil and Environmental Engineering, Massachusetts Institute of Technology, 77 Massachusetts Avenue, 02139, Cambridge, (MA), U.S.A.

ABSTRACT

The C-S-H gel is the main constituent of cement, up to the 70% of the final material. It is the phase that gives cohesion to the material, and main responsible for cement's properties, including creep. Understand the intrinsic mechanical properties of the C-S-H gel and how it responds to applied load is therefore of vital importance for the design of the new generation of Portland Cement. However, the heterogeneous nature and characteristic length scale of the C-S-H gel makes very challenging an experimental determination of its properties. Therefore, atomic scale simulations are a valuable alternative to investigate the atomic scale forces and processes that govern creep and shrinkage. In this work, we study the mechanical processes that take place when the solid C-S-H is subject to a shear strain, using reactive force field molecular simulations. We have chosen two systems to model the C-S-H gel: the perfect mineral tobermorite and the glass-like C-S-H model developed by Pellenq et al (Pellenq et al., 2009). First, we have computed the elastic properties of both models. Second, we investigate the global and local stresses generated in the systems under large deformations, with the aim to understand the atomic forces that govern the mechanical response of the structures. The obtained results help to understand the changes that happen in the C-S-H gel under load.

INTRODUCTION

The Calcium Silicate Hydrate (C-S-H) gel is the main component of the cement paste, the binding phase that agglomerates other crystalline hydrate products and the unhydrated clinker grains. The properties of the cement paste are therefore defined to a high extend by those of the gel. Irreversible deformations such as creep and shrinkage are not an exception. For instance, long-term creep is attributed to an irreversible rearrangement of the solid C-S-H gel due to an external shear stress (Vandamme & Ulm, 2009). Understanding the creep origin is of great technological importance since it affects severely concrete durability, shortening the lifespan of structures. Consequently, studies on the mechanism of creep have been carried out for

a long time, pursuing a reliable predictions of concrete creep based on microstructural parameters and chemical compositions.

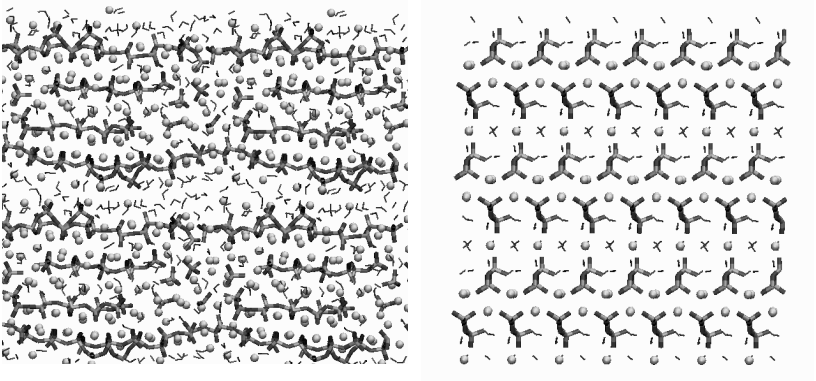

Figure 1. Representation of the atomic structure for the two models investigated in this work. On the left, the glass-like calcium silicate hydrate structure suggested by Pellenq et al. as a representative model of the C-S-H gels in cement. On the right side, the perfect crystal structure of the minetal Toberorite 14A. The order-disorder character of the structures can be easily noted. Calcium atoms are represented in yellow, the silicate chains as orange-blue sticks, and the water molecules as blue thin sticks.

In spite of the abundant research, the mechanism governing creep has not been fully elucidated. It has been suggested that creep is an aging process associated to the gradual crystallization of the C-S-H gel (Feldman & Sereda, 1970) or the growth of new C-S-H gel (Bazant & Prasannan, 1989). However, most theories associate creep to the water content of the C-S-H gel. Wittman proposed that water induces a disjoining pressure that weakens bonds between particles, facilitating creep (F. Wittmann, 1973). Comparably, interparticle water has been viewed as a lubricant layer that allows slipping between C-S-H gel particles (Tamtsia & Beaudoin, 2000). The irreversibility of creep was attributed to the reordering of certain zones of the solid, called “creep centres” into a new configuration of lower potential energy (F. H. Wittmann, 1980). Bazant developed the “microprestress model” which states that creep sites are overstressed areas that slip through the water layers more frequently than other zones due to the strain of the interparticle bonds (Bazant, Hauggaard, Baweja, & Ulm, 1997). Furthermore, nanoindentation studies have been determined that creep is originated at the nanoscale, due to the rearrangement of solid C-S-H regions (Vandamme & Ulm, 2009). All the previous models and experimental evidences indicate that atomic scale forces govern creep. Unfortunately, the heterogeneous nature, the characteristic length scale of the C-S-H gel, and the intricate porosity makes very challenging an experimental characterization of these atomic interactions. Molecular simulation is therefore a key technique to investigate

the atomic scale forces and processes that govern creep. As a matter of fact, shear deformations and creep has been previously studied using atomic scale simulations for metals, metallic glasses, and silicates (Lau, Kushima, & Yip, 2010; Rountree, Vandembroucq, Talamali, Bouchaud, & Roux, 2009; Shimizu, Ogata, & Li, 2007). Despite many properties of the C-S-H gel have been explored using atomistic simulation (Abdolhosseini Qomi, Ulm, & Pellenq, 2011; Bonnaud, Ji, Coasne, Pellenq, & Van Vliet, 2012; H. Manzano, Ayuela, & Dolado, 2007; H. Manzano, Dolado, & Ayuela, 2009; H. Manzano et al., 2012) there is no work dealing with creep of the C-S-H gel up to the author's knowledge.

In this work we aim to study the mechanical response of the solid C-S-H subjected to large shear deformations employing atomic scale simulation methods. We studied two different systems representative of the ordered and disordered regions of the solid C-S-H gel: the crystal tobermorite and the glass-like CSH model. We computed first the elastic properties of both systems. Then we applied larger deformations beyond elastic limit, and study the response of the systems. The localization of stress, strain, and stiffness at the atomic level is analyzed. Finally, we study the impact of different amounts of water on the properties of the solid gel, and relate our findings to the structure at the atomic and nanoscale of the C-S-H gel in cement.

COMPUTATIONAL DETAILS

The simulations have been done using the reactive force field ReaxFF. In ReaxFF short range interactions are based on bond order relationships, and the atomic charges are determined at each simulation step by a charge equilibration method (van Duin, Dasgupta, Lorant, & Goddard, 2001). This allows changes in molecular topologies, with bond braking and formation during the simulation. The set of parameters for the calcium silica hydrates has been tested in detail, and it reproduces accurately the structure, the water dynamics, and the elastic properties of porous calcium silicate hydrates and zeolite-clay interfaces (Hegoi Manzano, Sina Moeini, et al., 2012; Hegoi Manzano, Pellenq, Ulm, Buehler, & van Duin, 2012).

A 6x3x2 supercell of plombierite (14Å tobermorite) (Bonaccorsi, Merlino, & Kampf, 2005), and the equilibrated structure of the gCSH model from a previous work (Hegoi Manzano, Sina Moeini, et al., 2012) were taken as starting point. The simulations were done using the LAMMPS code. First, molecular dynamics simulation in the NPT ensemble were carried out for 1ns at 300 K and 1 atm. Second, the equilibrated structures were relaxed to an energy minimum with pressure tensor components close to zero using a conjugate gradient minimization algorithm, including the atomic position and the simulation box dimensions. The generated configurations are considered as the starting point of our mechanical test. A quasiestatic pure shear strain was applied in the xz direction in small steps of 0.1%, relaxing the atomic positions after each deformation and computing the energy, the total stress in all the crystallographic directions, and the stress per atom. In addition, the elastic tensor of the C-S-H model and tobermorite have been compute from strain – stress relationships, compressing and expanding the unit cell up to 3% in steps of 0.5%.

The local analysis of stress, strain, and stiffness is troublesome, since there are concepts that pertain to continuos theories, not to discrete atomic structures. Nevertheless, those concepts have been previously applied to study metals and glassy systems, and the results provide qualitative information of local quantities across the structure. We chose the atomic stresses per atom computed by LAMMPS, which follows the virial definition of stress using the forces on the atoms obtained during the minimization procedure. The atomic strain tensor was calculated following ref. 52 using a coarse graining approach (Tsamados, Tanguy, Goldenberg, & Barrat, 2009). We employed Gaussian coarse graining functions with width W = 5 Å, chosen after preliminary tests that indicated it as optimal to capture the heterogeneities of the strain field without introducing artifacts that emerge typically when W is of the order of the atom size. The local shear stiffness was estimated heuristically as the ratio between local shear stress and local shear strain between two successive load steps that are not accompanied by plastic events.

RESULTS AND DISCUSSION

1. Elastic deformations

In table one we present the elastic properties of tobermorite and the glassy CSH model derived from the elastic tensor. The bulk and shear moduli of elasticity are computed using the Voigt-Hill-Reuss approximation, and from them, the Young modulus, the Poisson's ratio, and the indentation modulus using the relationships for anisotropic materials. The layered structure of tobermorite is reflected on the anisotropy of the Young's moduli in the different crystallographic directions: the direction perpendicular to the layers (z) is sensibly smaller. The glassy CSH model also preserves such a difference between crystallographic directions, indicating that despite the disorder it conserves reminiscences from the layered structure. The obtained bulk modulus for tobermorite 14 Å (45.3 GPa) is in excellent agreement with the experimental of 47 ± 3 GPa 47, as well as with previous simulations using different methods (Al-Ostaz, Wu, Cheng, & Song, 2010; H. Manzano, Dolado, Guerrero, & Ayuela, 2007; Shahsavari, Buehler, Pellenq, & Ulm, 2009).

The moduli of the gCSH turn out to be about 12% higher than those of tobermorite. Such result is not surprising because, having excluded the effect of anisotropy and considering two systems with similar chemical interactions, the elastic properties are expected to increase simply with the density (Pellenq, Lequeux, & van Damme, 2008). Indeed, atomic scale simulations confirmed this dependence on the density is valid for calcium silicate hydrates in general, independently of their Ca/Si ratio, silicate chain length, and layered structure (H. Manzano, Gonzalez-Teresa, Dolado, & Ayuela, 2010).

Table 1. Structural paramenters and elastic properties of tobermorite and the glassy C-S-H model. K = bulk modulus, G = shear modulus, E = Young's modulus, v = Poissons ratio. The elastic properties are presented in GPa, except the Poissons ratio (*v*), which is dimensionless. The subscripts *xyz* represent the crystallographic direction, *VHR* values computed using the Voight-Hill-Reuss approximation, and *any* values computed assuming anisotropic media.

	Tobermorite		gCSH	
	This work	*Experimental*	*This work*	*Experimental*
a (Å)	*6.68*	*6.74 (Bonaccorsi et al., 2005)*		
b (Å)	*7.50*	*7.43 (Bonaccorsi et al., 2005)*		
c (Å)	*28.33*	*27.99 (Bonaccorsi et al., 2005)*		
α (°)	*91.08*	*90 (Bonaccorsi et al., 2005)*		
β (°)	*89.4*	*90 (Bonaccorsi et al., 2005)*		
γ (°)	*124.32*	*123.25 (Bonaccorsi et al., 2005)*		
ρ (g·cm^{-3})	*2.22*	*(2.2) (Bonaccorsi et al., 2005)*	*2.57*	*2.63 (Allen, Thomas, & Jennings, 2007)*
E_x	*51.1*		*72.9*	
E_y	*55.0*		*74.0*	
E_z	*36.4*		*59.3*	
G_{xy}	*23.1*		*21.3*	
G_{xz}	*19.9*		*21.0*	
G_{yz}	*19.9*		*21.0*	
K_{VHR}	*44.2*	*47 (Oh, Clark, Wenk, & Monteiro, 2012)*	*48.3*	
G_{VHR}	*21.8*		*24.8*	
E_{any}	*56.2*		*63.6*	
v_{any}	*0.29*		*0.28*	
M_{any}	*61.3*		*69.0*	*60 (Constantinides & Ulm, 2007)*

2. Large deformations

The shear stress-strain curves for tobermorite and for the glassy CSH model is shown in figure 2(a). At low strain, the glassy CSH exhibits small plastic events that are not present in tobermorite, and are due to small rearrangements enabled by the disorder. At about 15% strain, the glassy CSH reaches a plastic flow regime, with moderate stress drops in cascades of successive stress increase and relaxation. Tobermorite leaves the elastic regime at 25% strain when small stress drops start. Nevertheless, the stress keeps increasing up to 38% strain, at which the first large drop takes place. Subsequently, tobermorite enters a regime characterized by a series of stress drops. The more brittle nature of the crystal compared to the glassy CSH is reflected by the magnitude of the stress accumulation and drops. From the maximum stress, and applying the von Mises yield criterion for simple shear strain (von Mises, 1913), the computed yield strength of tobermorite and glassy CSH are 12 and 5.7 GPa respectively.

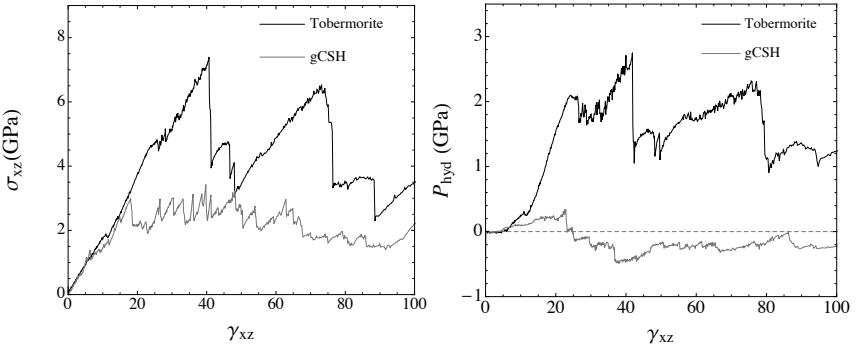

Figure 2. Left: Evolution of the shear stress with the shear strain for tobermorite and the gCSH model. Right: Evolution of the hydrostatic stress with the shear strain in the same simulations.

Figure 3(b) shows that the shear strain induces an accumulation of hydrostatic pressure, which indicates a coupling between volumetric and deviatoric strain components. There is a correspondence between shear stress and pressure drops, related to local rearrangements of the atoms aimed at reducing overall the strain energy. The built-up of pressure is qualitatively different for the tobermorite and for the gCSH. In the case of tobermorite, the pressure is always positive which means that the system would overall dilate if the simulation box were allowed to change its dimensions and maintain a constant pressure. Dilation is a known phenomenon at the atomic scale of crystals (Nedderman, 2005). It enables a temporary increase of the free volume of the atoms that "find space" to generate a slip plane. By contrast, the

gCSH experiences positive pressures only until the first drop of stress and then the pressure stays mostly negative, which indicates a tendency to compaction. Compaction under shear is a known effect in loosely packed disordered granular media and glasses (Nedderman, 2005).

3. Localization of stress, strain, and stiffness

The local stress plots reflect clearly the higher symmetry of the crystalline tobermorite, and the amorphous character of the glassy CSH model. A strong spatial correlation between local strain and local stiffness emerges for the glassy CSH, similarly to what was observed in ref (Tsamados et al., 2009) for a Lennard-Jones glass. The lower local stiffness zone corresponds to the water rich interlaminar space, where the water molecules screen the iono-covalent chemical interactions of the calcium silicates. The lubricant effect of water facilitates the triggering of plastic rearrangements in the interlaminar space, which constitutes an intrinsic shear band that only needs to be activated by a sufficiently high level of stress. Furthermore, one can notice that although there are two water-rich layers in the studied gCSH structures, only the thicker layer is activated and concentrates the plastic events. This points to the central role that water-rich defective regions in the molecular structure of the C-S-H can play in the development of irreversible deformations.

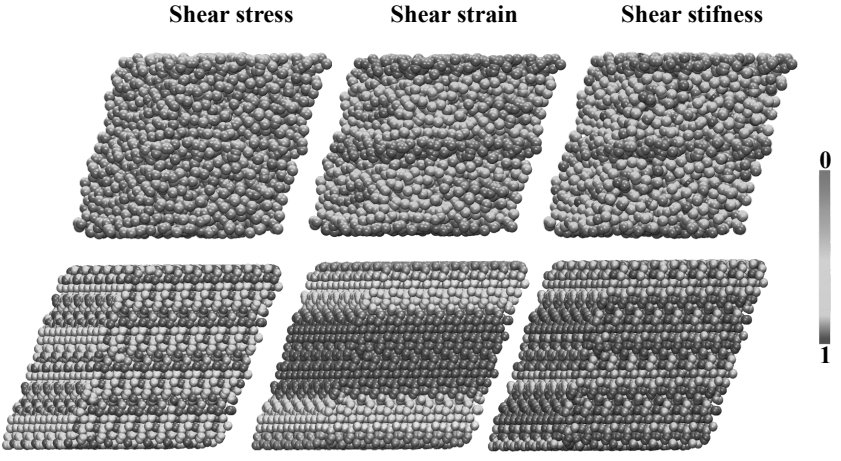

Figure 3. Spatial plots of the shear stress, shear strain, and shear stiffness of the gCSH (up) and tobermorite (down). The values are normalized to allow a comparison between the localization of the structures.

Also in the case of tobermorite the strain is strongly concentrated in one interlaminar space. Nonetheless, differently from the gCSH, there are no structural differences between water layers in the crystal structure, and therefore the activation

of one layer instead of another depends only on random fluctuations, probably in the hydrogen bond network. Consequently, the proportionality between stiffness and strain during a plastic event is lost. In fact, we also observe that different water layers can be mobilized in the tobermorite at different points during the same strain process.

4. Water content

We showed that, at the molecular scale, the irreversible deformations under shear develop preferentially in correspondence of water layers. This holds both for the ordered tobermorite crystal and for the glassy CSH model considered here. The strength of tobermorite compared to the gCSH is attributed to the structural character of the water molecules in the crystalline lattice. Furthermore, the irreversible deformations within the glassy CSH model develops preferentially in the thicker layer out of the two that are present.

The previous points indicate the pivotal role of water molecules on the mechanical response of the calcium silicate hydrates. In order to investigate deeper the effect of water, we have modified the water content in the interlaminar space of the glassy CSH model, and subject it to the same shear strain protocol. Water molecules were introduced randomly in the think interlaminar space, i.e. the one that developed the shear band. The modified structures have 25% more water molecules and 20% less water molecules than the original gCSH model. Then the atomic positions and the simulation box were relaxed to achieve a local minimum of energy.

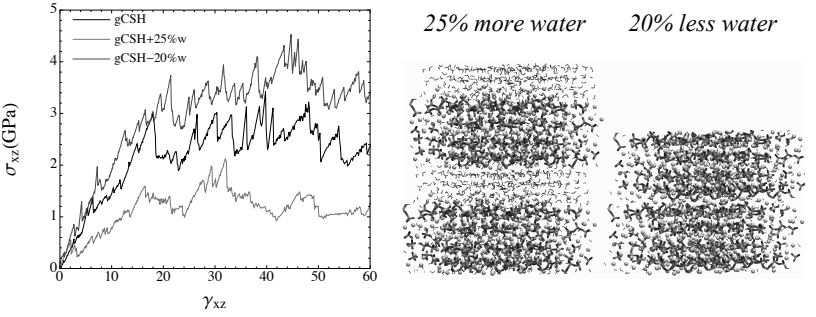

Figure 4. Evolution of the shear stress with the shear strain for the gCSH model with different water contents. Black line represents the original gCSH structure, the blue one the structure with 20% less water, and the red line the structure with 25% more water. The atomic representation of the modified gCSH models with more and less water molecules are presented. The code color is the same as in figure 1.

The result can be seen in figure 4, together with the atomic representations of the systems with extra amount of water and with less water in their structures. It can

be seen how water has a great influence on the mechanical response of the material under strain: as the water content decreases, the shear stress increases. The values of the yield strength, using von Misses yield criteria, are 7.1 and 3.6 GPa for the high and low water contents respectively, compared to the 5.7 GPa of the original structure. The trend agrees qualitatively with the result by Pellenq et al. (Pellenq et al., 2009), who found an increase of the shear yield strength in a fully dried structure compared to the gCSH model. These results confirm that water plays a key role in the shear behavior of the solid calcium silicate hydrates. Water acts as a lubricant that allows the sliding between adjacent layers, and higher water content increases the lubricity, decreasing the strength of the system.

CONCLUSIONS AND IMPLICATIONS

In this work we used atomic scale simulations to investigate the irreversible deformations of calcium silicate hydrates under shear strain. We have explored tobermorite and a glassy CSH model as representative of order and disorder regions in the C-S-H gel. Tobermorite is more brittle and has higher shear strength as a consequence of crystalline order, while the C-S-H model depicts the classical behavior of a glassy material. The local analysis of strain indicated that the water content in the interlayer space governs the mechanical response of both tobermorite and the gCSH. The water molecules screen iono-covalent interactions between calcium silicate sheets, creating areas with low local stiffness. In the tobermorite crystal the water molecules have structural character that provides a strong interlaminar bonding. By contrast, the thicker layers of the gC-S-H are filled with water in glassy state. This causes the higher strength of tobermorite compared to the gCSH.

These results have implications for the multi-scale description and mechanical behavior of cement. At the scale above the molecular one, between 1 and 100 nanometres, a number of structural and mechanical properties of the C-S-H gel can be captured modelling it as a colloidal aggregate of cohesive nanoparticles (Jennings, 2008; Masoero, Del Gado, Pellenq, Ulm, & Yip, 2012). Within the colloidal interpretation, one of the most compelling questions concerns the definition and characterization of the contact regions between particles that provide cohesion to the overall system. Our results suggest that such interface regions may have a structure akin to that of the interlaminar space: a water-rich region with calcium ions that counterbalance the surface charge. Within such picture, the distinction between interface regions and interlaminar water layers becomes blurred, and therefore also the distinction between discrete (colloidal) and continuum models of the C-S-H gel (Feldman & Sereda, 1970; Muller, Scrivener, Gajewicz, & McDonald, 2012). What can be still considered as a fuzzy criterion to differentiate between an interface region and an interlaminar water layer would be the thickness of the layer.

Our suggestion that thick layers of interlaminar water can be regarded effectively as interfaces between particles nanoparticles is consistent with a number of concepts that can be found in the literature on creep. Long-term creep of hardened cement pastes under low levels of external loads is a phenomenon of big technological importance that, in fact, relates with the accumulation of irreversible

deformations. “Creep sites” have been defined to indicate water-rich regions with low local stiffness, where slipping occurs preferentially. The reduced creep of dried cement samples can also be associated with the thinning of water layer and consequent lower predisposition to trigger irreversible deformations.

Finally, it must be noted that the macroscopic mechanical behaviour of cement is unlikely just a direct product of processes at the molecular scale. By contrast, other structural features that affect the macroscopic behaviour can rise at larger scales. For example, nanopores with size of 1-50 nm form the mesoporosity of the C-S-H gel that only larger scale models can capture using concepts like packing fraction, size polydipsersity, and number of contact points between C-S-H nanoparticles. Furthermore, at the even larger scale of microns, the heterogeneities in distribution of stresses and the cohexistence of different phases and interfaces between them are relevant to the overall picture. Achieving a comprehensive understanding of the multi-scale mechanics of cement still constitutes a great challenge. Our methodology and results regard some of the more fundamental mechanisms underlying irreversible deformations of C-S-H, and provides essential information for quantitative models at larger scales.

Acknowledgements
This work was supported by the Basque Government through the NANO-IKER project (ETORTEK program, grant IE11-304), and by the Concrete Sustainability Hub at MIT, with sponsorship provided by the Portland Cement Association (PCA) and the NRMCA Research & Education Foundation. H.M. acknowledges a postdoctoral fellowship from the Basque Country Department of Education, Research and Universities. The computing resources of the SGIker (UPV/EHU) and the i2Basque project are gratefully acknowledged.

REFERENCES

Abdolhosseini Qomi, M.J., Ulm, F.J., & Pellenq, R.J.M. (2011). Evidence on the Dual Nature of Aluminum in the Calcium-Silicate-Hydrates Based on Atomistic Simulations. *Journal of the American Ceramic Society*. 95 (3), 1128-1137

Al-Ostaz, A., Wu, W., Cheng, A. H. D., & Song, C. R. (2010). A molecular dynamics and microporomechanics study on the mechanical properties of major constituents of hydrated cement. *Composites Part B-Engineering, 41*(7), 543-549.

Allen, A. J., Thomas, J. J., & Jennings, H. M. (2007). Composition and density of nanoscale calcium-silicate-hydrate in cement. *Nature Materials, 6*(4), 311-316.

Bazant, Z.P., Hauggaard, A.B., Baweja, S., & Ulm, F.J. (1997). Microprestress-solidification theory for concrete creep. I: Aging and drying effects. *Journal of Engineering Mechanics, 123*(11), 1188-1194.

Bazant, Z.P., & Prasannan, S. (1989). Solidification theory for concrete creep. I: Formulation. *Journal of Engineering Mechanics, 115*(8), 1691-1703.

Bonaccorsi, E., Merlino, S., & Kampf, A. R. (2005). The crystal structure of tobermorite 14 Å (Plombierite), a C-S-H phase. *Journal of the American Ceramic Society, 88*(3), 505-512.

Bonnaud, P. A., Ji, Q., Coasne, B., Pellenq, R. J. M., & Van Vliet, K. J. (2012). Thermodynamics of Water Confined in Porous Calcium-Silicate-Hydrates. *Langmuir, 28*(31), 11422-11432. doi: 10.1021/la301738p

Constantinides, G., & Ulm, F. J. (2007). The nanogranular nature of C-S-H. *Journal of the Mechanics and Physics of Solids, 55*(1), 64-90.

Feldman, R. F., & Sereda, P. (1970). A new model for hydrated Portland cement and its practical implications. *Eng J Can, 53*(8-9), 53-59.

Jennings, H. M. (2008). Refinements to colloid model of C-S-H in cement: CM-II. *Cement and Concrete Research, 38*(3), 275-289.

Lau, T.T., Kushima, A., & Yip, S. (2010). Atomistic simulation of creep in a nanocrystal. *Physical Review Letters, 104*(17), 175501.

Manzano, H., Ayuela, A., & Dolado, J. S. (2007). On the formation of cementitious C-S-H nanoparticles. *Journal of Computer-Aided Materials Design, 14*(1), 45-51.

Manzano, H., Dolado, J. S., & Ayuela, A. (2009). Structural and Elastic Properties of the Main Species Present in the Cement Paste. *Acta Materialia, 57*(5), 1666-1674.

Manzano, H., Dolado, J. S., Guerrero, A., & Ayuela, A. (2007). Mechanical properties of crystalline calcium-silicate-hydrates: comparison with cementitious C-S-H gels. *Physica Status Solidi a-Applications and Materials Science, 204*(6), 1775-1780.

Manzano, H., Enyashin, A., Frenzel, J., Dolado, J. S., Ayuela, A., & Seifert, G. (2012). Do cement nanotubes exist? *Advanced Materials*.

Manzano, H., Gonzalez-Teresa, R., Dolado, J. S., & Ayuela, A. (2010). X-ray Spectra and Theoretical Elastic Properties of Crystalline Calcium Silicate Hydrates: Comparison with Cement Hydrated Gels. *Materiales de la Construcción, 60*(299), 7-19.

Manzano, Hegoi, Moeini, Sina, Marinelli, Francis, van Duin, Adri C. T., Ulm, Franz-Josef, & Pellenq, Roland J. M. (2012). Confined Water Dissociation in Microporous Defective Silicates: Mechanism, Dipole Distribution, and Impact on Substrate Properties. *Journal of the American Chemical Society, 134*(4), 2208-2215.

Manzano, Hegoi, Pellenq, Roland J. M., Ulm, Franz-Josef, Buehler, Markus J., & van Duin, Adri C. T. (2012). Hydration of Calcium Oxide Surface Predicted by Reactive Force Field Molecular Dynamics. *Langmuir, 28*(9), 4187-4197.

Masoero, E., Del Gado, E., Pellenq, R. J. M., Ulm, F. J., & Yip, S. (2012). Nanostructure and Nanomechanics of Cement: Polydisperse Colloidal Packing. *Physical Review Letters, 109*(15), 155503.

Muller, Arnaud C. A., Scrivener, Karen L., Gajewicz, Agata M., & McDonald, Peter J. (2012). Densification of C-S-H Measured by 1H NMR Relaxometry. *The Journal of Physical Chemistry C*.

Nedderman, Ronald Midgley. (2005). *Statics and kinematics of granular materials*: Cambridge University Press.

Oh, Jae Eun, Clark, Simon M., Wenk, Hans-Rudolf, & Monteiro, Paulo J. M. (2012). Experimental determination of bulk modulus of 14A tobermorite using high pressure synchrotron X-ray diffraction. *Cement and Concrete Research, 42*(2), 397-403.

Pellenq, R. J. M., Kushima, A., Shahsavari, R., Van Vliet, K. J., Buehler, M. J., Yip, S., & Ulm, F. J. (2009). A realistic molecular model of cement hydrates. *Proceedings of the National Academy of Sciences of the United States of America, 106*(38), 16102-16107

Pellenq, R. J. M., Lequeux, N., & van Damme, H. (2008). Engineering the bonding scheme in C-S-H: The iono-covalent framework. *Cement and Concrete Research, 38*, 159-174.

Rountree, C.L., Vandembroucq, D., Talamali, M., Bouchaud, E., & Roux, S. (2009). Plasticity-induced structural anisotropy of silica glass. *Physical Review Letters, 102*(19), 195501.

Shahsavari, R., Buehler, M. J., Pellenq, R. J. M., & Ulm, F. J. (2009). First-Principles Study of Elastic Constants and Interlayer Interactions of Complex Hydrated Oxides: Case of Study of Tobermorite and Jennite. *Journal of the American Ceramic Society, 92*(10), 2323-2330.

Shimizu, F., Ogata, S., & Li, J. (2007). Theory of shear banding in metallic glasses and molecular dynamics calculations. *Materials transactions, 48*(11), 2923-2927.

Tamtsia, Basile T., & Beaudoin, James J. (2000). Basic creep of hardened cement paste A re-examination of the role of water. *Cement and Concrete Research, 30*(9), 1465-1475.

Tsamados, Michel, Tanguy, Anne, Goldenberg, Chay, & Barrat, Jean-Louis. (2009). Local elasticity map and plasticity in a model Lennard-Jones glass. *Physical Review E, 80*(2), 026112.

van Duin, A. C. T., Dasgupta, S., Lorant, F., & Goddard, W. A. (2001). ReaxFF: A reactive force field for hydrocarbons. *Journal of Physical Chemistry A, 105*(41), 9396-9409.

Vandamme, M., & Ulm, F. J. (2009). Nanogranular origin of concrete creep. *Proceedings of the National Academy of Sciences of the United States of America, 106*(26), 10552-10557.

von Mises, R. (1913). Mechanik der festen Körper im plastisch deformablen Zustand. *G√∂ttin. Nachr. Math. Phys, 1*, 582-592.

Wittmann, F. H. (1980). *Properties of hardened cement paste.* Paper presented at the 7th International Conference on the Chemistry of Cement, Paris.

Wittmann, FH. (1973). Interaction of hardened cement paste and water. *Journal of the American Ceramic Society, 56*(8), 409-415.

Hydrothermal and Mechanical Stability of Metal–Organic Frameworks

François-Xavier Coudert,[1,*] Aurélie Ortiz,[1] Marta De Toni,[1]
Anne Boutin,[2] Alain H. Fuchs[1]

[1]CNRS & Chimie ParisTech, 11 rue Curie, 75005 Paris, France; email: fx.coudert@chimie-paristech
[2]ENS, Département de Chimie, 23 rue Lhomond, 75005 Paris, France

ABSTRACT

Metal–organic frameworks are a new class of microporous materials that garner a lot of attention for their potential applications in the fields of separation, strategic gas capture and storage, and catalysis. However, there is still little microscopic information available on their hydrothermal and mechanical stability, even though these properties are crucial for practical applications. In this paper, we detail our recent efforts to address these issues using a large gamut of molecular simulation methods: quantum chemistry calculations, first principles molecular dynamics and force field-based molecular dynamics.

INTRODUCTION

Much attention has recently been focused on metal–organic frameworks (MOFs), a recent class of microporous materials that garner a lot of attention for their potential applications in the fields of separation, strategic gas capture and storage, and catalysis. (Wright 2008) Soft Porous Crystals (SPCs) are a specific subclass of metal-organic frameworks that behave in remarkable stimuli-responsive fashion. These materials feature dynamic crystalline frameworks displaying reversible structural transformations of large amplitude in response of external physical constraints such as gas adsorption, temperature, or mechanical pressure. (Horike 2009) Previous studies have shown that the stress induced on the host framework by mechanical pressure or guest adsorption plays a big role in the structural transitions. (Triguero 2011) However, at a time where the first commercial MOFs are readily available from chemicals suppliers, the behavior of MOFs and SPCs under industrial application conditions (high temperature, high pressure, presence of water and other undesirable molecules) has not yet been thoroughly investigated.

We report here a three-pronged theoretical approach of this issue. First, we investigate the stability of IRMOF materials in presence of water using first principles molecular dynamics (FPMD). Secondly, we look at the mechanical stability of a Zeolitic Imidazolate Framework (ZIF) materials under pressure, using force field-based molecular dynamics (FFMD). Finally, we shed light into the mechanical

properties of Soft Porous Crystals by quantum chemistry calculations of their elastic stiffness tensor.

HYDROTHERMAL STABILITY

We used Car–Parrinello molecular dynamics to study of the behavior of the water-unstable IRMOF (Iso-Reticular MOF) family of materials, in order to better understand how hydration of the framework happens and the first steps towards the loss of crystallinity of the framework. This study (De Toni 2012) was performed by combining classical Monte Carlo simulations and first principles molecular dynamics, in order to obtain a broad view of the behavior of water in the IRMOF materials. GCMC studies allowed us to determine the thermodynamic and structural characteristics of water adsorption in IRMOFs. Then, we studied the mechanism of hydration as different water loadings by direct Car-Parrinello molecular dynamics. This study confirmed the influence of water loading on the material's stability, and showed that it is due to a collective mechanism involving at least 4 water molecules stabilizing the reaction intermediate. We fully characterized the kinetics of this attack, and showed that the reason for this stabilization is water-water polarization and the formation of short hydrogen-bonded water chains. After hydration, the second step of the mechanism (summarized in Figure 1) is the displacement of an organic linker by water.

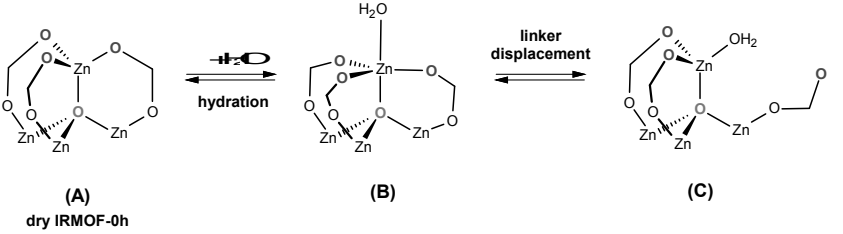

Figure 1. Mechanism of the hydration and linker displacement of IRMOF-0h, as established by ab initio molecular dynamics. Reprinted with permission from (De Toni 2012). Copyright 2012 Wiley-VCH Verlag GmbH & Co. KGaA, Weinheim.

MECHANICAL STABILITY

We have studied recently studied the behavior of Zeolitic Imidazolate Framework ZIF-8 under hydrostatic compression. ZIF-8 is known to undergo pressure-induced amorphization at moderate pressure (0.34 GPa), the microscopic nature of which had not previously been investigated in the literature. We have used force field-based molecular dynamics to calculate the elastic constants of the cubic ZIF-8 material for various values of hydrostatic pressure. (Ortiz 2013b) The results, depicted in Figure 2, show that while elastic constants C_{11} and C_{12} are almost not

impacted by the compression of the framework, the shear modulus C_{44} diminishes as pressure increases. This phenomenon, a pressure-induced shear softening of the material, leads to mechanical shear instability at pressure of 0.4 GPa, where the elastic constant C_{44} goes down to zero and the framework collapses into a denser phase. This shear softening is thus the root of the pressure-induced amorphization of ZIF-8. Further studies are ongoing to determine whether this is specific to ZIF-8 or generic to the whole family of Zeolitic Imidazolate Frameworks.

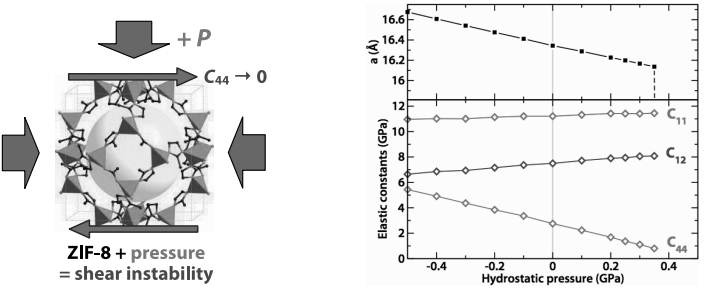

Figure 2. Left panel: representation of ZIF-8 frameworks; right panel: evolution of ZIF-8 lattice parameter (top) and elastic constants (bottom) as a function of hydrostatic pressure. Reprinted with permission from (Ortiz 2013b). Copyright 2013 American Chemical Society.

In order to link the local elastic behavior of these materials and the structural flexibility, we studied the mechanical properties of five different flexible MOFs. We performed quantum chemical calculations of the elastic constants of MIL-53(Al), MIL-53(Ga), MIL-47, DMOF-1 (both its lozenge and its square structure). From a full tensorial analysis of the stiffness matrix, we characterized the mechanical behavior of the material by calculating the Young's modulus, the linear compressibility, the shear modulus and the Poisson's ratio. This study allows us to highlight the highly anisotropic nature of the elastic properties of SPCs. For example, the MIL-47 Young's modulus anisotropy ratio is nearly 100:1 between the most rigid and the weakest directions (Figure 3). This is in stark contrast with the relatively isotropic mechanical properties of non-flexible MOFs such as MOF-5 and ZIF-8. We also showed that the flexible MOFs can present a high negative linear compressibility, one order of magnitude over the current "record holder" for inorganic materials. These results shed light onto the microscopic origin of stimuli-induced structural transitions in flexible MOFs. (Ortiz 2012, Ortiz 2013a)

CONCLUSION

We have shown that molecular simulation methods allow us to gain valuable insight into the microscopic details of hydrothermal and mechanical instabilities. This improved understanding is the first step toward the design of more hydrothermally

and mechanically stable materials, a necessity for practical applications at the industrial level.

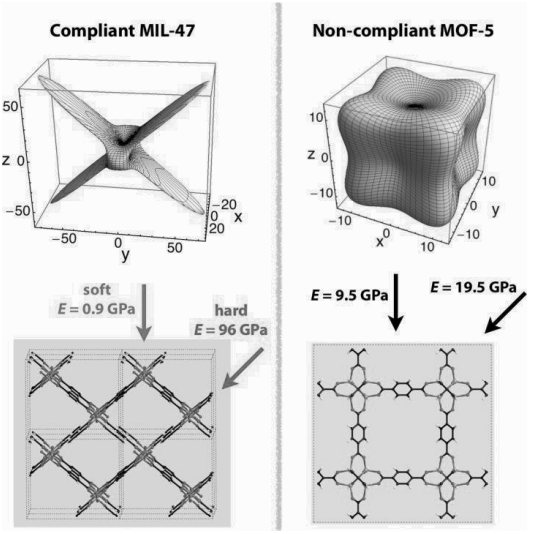

Figure 3. Comparison of the directional Young's modulus (3D representation, upper panel) for compliant MOF MIL-47 and noncompliant MOF-5. Lower panel: representation of the materials' unit cell featuring the stiffest and softest directions.

REFERENCES

De Toni, M., Jonchiere, R., Pullumbi, P., Coudert, F.-X., and Fuchs, A. H. (2012). "How Can a Hydrophobic MOF be Water-Unstable? Insight into the Hydration Mechanism of IRMOFs", *ChemPhysChem*, 13(15), 3497-3503.

Horike, S., Shimomura, S., and Kitagawa, S. (2009). "Soft porous crystals", *Nature Chem.*, 1, 695.

Ortiz, A. U., Boutin, A., Fuchs, A. H., and Coudert, F.-X. (2012). "Anisotropic Elastic Properties of Flexible Metal-Organic Frameworks: How Soft are Soft Porous Crystals?", *Phys. Rev. Lett.* 109(19), 195502.

Ortiz, A. U., Boutin, A., Fuchs, A. H., and Coudert, F.-X. (2013a). "Metal-Organic Frameworks With Wine-Rack Motif: What Determines Their Flexibility And Elastic Properties", *J. Chem. Phys.* 138, 174703.

Ortiz, A. U., Boutin, A., Fuchs, A. H., and Coudert, F.-X. (2013b). "Investigating the Pressure-Induced Amorphization of Zeolitic Imidazolate Framework ZIF-8: Mechanical Instability Due to Shear Mode Softening", *J. Phys. Chem. Lett.*, 4, 1861-1865.

Triguero, C., Coudert, F.-X., Boutin, A., Fuchs, A. H., and Neimark, A. V., (2011). "Mechanism of Breathing Transitions in Metal-Organic Frameworks", *J. Phys. Chem. Lett.*, 2(16), 2033-2037

Wright, P. A. (2008). *Microporous Framework Solids*, Royal Society of Chemistry.

NMR investigations of water retention mechanism by cellulose ethers in cement-based materials

J.-P. Korb[(1)*], L. Patural[(2)], A. Govin[(2)], Ph.Grosseau[(2)]

[(1)] Physique de la Matière Condensée, Ecole Polytechnique-CNRS, Route de Saclay, 91128 Palaiseau Cedex, France; email: jean-pierre.korb@polytechnique.fr .

[(2)] École Nationale Supérieure des Mines de Saint-Étienne ; Centre SPIN, LPMG FRE 3312, 158 Cours Fauriel, 42023 Saint-Étienne Cedex 2, France ; email : laetitial.patural@gmail.com ; govin@emse.fr; grosseau@emse.fr .

ABSTRACT

We show how nuclear magnetic spin-lattice relaxation dispersion of proton-water (*NMRD*) can be used to elucidate the effect of cellulose ethers on water retention and hydration delay of freshly-mixed white cement pastes. *NMRD* is useful to determine the surface diffusion coefficient of water, the specific surface area and the hydration kinetics of the cement-based material. In spite of modifications of the solution's viscosity, we show that the cellulosic derivatives do not modify the surface diffusion coefficient of water. Thus, the mobility of water present inside the medium is not affected by the presence of polymer. However, these admixtures modify significantly the surface fraction of mobile water molecules transiently present at solid surfaces. This quantity measured, for the first time, for all admixed cement pastes is thus relevant to explain the water retention mechanism.

INTRODUCTION

It is known that the presence of cellulose ethers (*CE*) in mortars enhances drastically the water-retention (Mansoutre). Cellulose ethers (*CE*) are water soluble semi-synthetic polymers derived from cellulose, the most abundant polysaccharide in nature. This specific property of *CE* is crucial to achieve sufficient mortar-substrate adhesion when the mortar is applied in thin layers on highly absorbent substrates. Other properties are also affected by *CE*, such as the delay of hydration and setting (Peschard). A significant influence of the polymer molecular parameters like molecular weight and substitution degrees was evidenced (Pourchez, 2006), but no clear water retention mechanism could be clearly identified. During evaporation, no admixture loss is occurring, due to the very low vapor pressure of this admixture and a decrease in the water chemical potential occurs (Pourchez, 2010). A decrease of water mobility due to the jamming of the diffusion space by the polymer molecules is even expected (Patural, 2011). However, a recent pulsed gradient field *NMR* study proved that the macroscopic bulk water self diffusion coefficient is not modified in *CE* solution or in admixed cement pastes (Patural, 2010). Moreover, the

interdiffusion imaging experiments demonstrated also that the water diffusion at the paste interface is not affected by the presence of cellulosic admixture (Patural, 2010). So, the possibility of a potential microscopic diffusion barrier specifically at the cement hydrates interfaces is still controversial and the origin of the mechanism of water retention due to *CE* admixture is still an open question.

Our aim here is precisely to answer the latter question and to propose a realistic mechanism for the water retention in presence of *CE* in mortars and cements. For that purpose, we show how nuclear magnetic spin-lattice relaxation dispersion of protons-water *(NMRD)* can be used to elucidate the effect of cellulose ethers on water retention and hydration delay of freshly-mixed white cement pastes (Patural 2012).

EXPERIMENTS

Mineral and organic products. Cement pastes were prepared with white cement in order to facilitate *NMR* relaxation experiments. However, we showed before by electronic spin resonance (*ESR*) that paramagnetic Fe^{3+} ions were clearly present in white cement (see Figure 6 in (Korb, 2007)). The admixtures used are cellulose ethers (*CE)* of chemical structures given in Figure 1. All the characteristics of the main physical-chemistry properties and labels used for the cellulose ethers studied are described in (Patural, Thesis 2011). Admixture amount (0.27%) was in addition to the total dry mixture (*i.e.* cement, sand and filler). The cellulose ether weight-average molecular mass (M_w) was determined using size exclusion chromatography. We have prepared different samples with increased molecular mass $M_w = \{235,630,910\}$ kDa labeled *J1, J2* and *J3*, respectively. Others starch ethers were also investigated, those are polymers providing very different water retentions

Water retention. For water retention measurements, mortars were prepared according to the *CEReM* mixture proportions consisting in 65% sand, 30% ordinary Portland cement (*CEM I 52.5 R*), 5% calcareous filler with a water to cement ratio w/c=1.

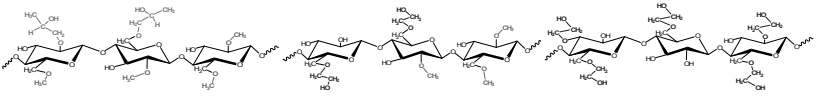

(a) (b) (c)

Figure 1. Structures of cellulose ethers (a) *HPMC*, (b): *HEMC*, (c): *HEC*

The experimental device and way of probing water retention *WR(%)* have been described in (Patural, Thesis 2011). The cellulose ethers improved water retention up to *WR*=98.9% for *HPMC J3*. With respect to the water retention capacity of the non-admixed mortar (64.5%), this represents a very large increase. However the starch ethers procure very different water retention capacities ranging from 66.2% to 92.6%.

Experiments of *NMRD* in admixed cement pastes. We performed proton nuclear magnetic relaxation dispersion (*NMRD*) on a fast-field cycling spectrometer from *Stelar s.r.l., Mede, Italy*, where the polarization magnetic field is 0.5 T while the evolution magnetic field ranges from 0.25 mT to 0.5 T. All samples were introduced into a 7 mm-tube which was inserted into a 10 mm-diameter standard *NMR* tube. Cement pastes were prepared with a water/cement ratio $w/c=0.4$ in order to have an appropriate consistency and for facilitating the *NMR* measurements at low fields. The *NMRD* sequence is very well documented (Kimmich). The experiments were repeated over a large range of proton Larmor frequencies $\omega_I/2\pi$ (10kHz-20MHz) in order to obtain the complete dispersion profile of the longitudinal spin-lattice relaxation rate $1/T_1(\omega_I)$. The temperature was fixed at 298K.

Basically, proton NMR relaxation is a stimulated (non spontaneous) phenomenon driven by the coupling of the proton spins to the magnetic noise induced by molecular motions (translation, rotation, exchange, etc). Varying the magnetic field changes the proton Larmor frequency $\omega_I/2\pi$, and thus allows exploring the time scales of the magnetic fluctuations (noise) to which the nuclear spin relaxation is sensitive. For diffusive liquids, *NMRD* gives also a rich source of dynamical information over a large range of length scales, from localized and fast motions at large frequency to a delocalized and slow motions at low frequency.

We propose two kinds of NMRD experiments for white admixed cement pastes. The first experiment consists of measuring the magnetic field dependence of $1/T_1(\omega_I)$ of various admixtures of different *CE* (Figure 2).

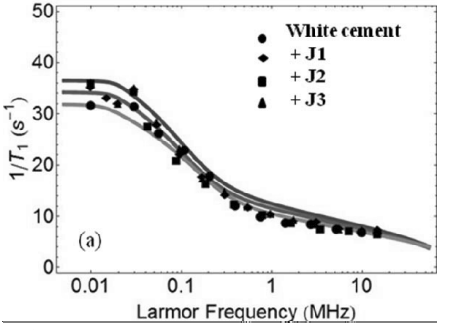

Figure 2. Measured water ^{1}H magnetic relaxation dispersion profiles $1/T_1(\omega_I)$ for hydrated white cement paste (w/c=0.4) as a function of the proton Larmor frequency. The experiments have been realized in the early hydration period (0-45 min). Effect of three cellulose ethers (*HPMC J1, J2 and J3*) compared to the neat white cement paste. The continuous lines are the best fits obtained with our theory of surface relaxation (Barberon and Korb 2009).

The second experiment consists in probing continuously $1/T_1(\omega_I=2\pi\times10kHz, t_{hydr})$ at a fixed and low frequency (10kHz) during the inducing period t_{hydr} of cement paste with various admixtures of different *CE* (Figures 3a, 4a). During this period, we observe a monoexponential longitudinal magnetization decay that rules out any distribution of T_1, the non exponential relaxation only appearing after ten hours of

hydration [see Figure 7 of (Korb, 2007)]. The continuous measurement of $1/T_1(\omega_I=2\pi\times10kHz, t_{hydr})$ in presence of various admixtures of cellulose ethers allows us to monitor the evolution of the specific surface area $S(t_{hydr})/V$, of the material during the hydration.

RESULTS AND DISCUSSION

We proposed previously a theoretical model necessary for interpreting all the *NMRD* relaxation features reported in Figure 2, 3a and 4a (Barberon and Korb 2009). Here, we just outline the basic hypothesis of the model needed for probing the specific surface area and the water surface diffusion coefficients at the growing interface of the admixed and neat cement pastes. Basically, the molecular exchange between the solid and liquid phases is sufficiently fast compared to their respective individual proton relaxation times that a single $1/T_{1,w}(\omega_I)$ exists given by a linear combination of a bulk and a surface contributions. The latter is weighted by the surface to volume ratio *S/V* present at a given time of hydration at the solid/liquid interface. $1/T_{1,w}(\omega_I)$ for the confined proton-liquid has a bilogarithmic frequency dependence (Barberon and Korb 2009) that comes unambiguously from the two dimensional diffusion of the water molecules along the pore surface modulating the dipole-dipole interaction between the proton species and the paramagnetic Fe^{3+} ions fixed at the surface of the pores. On the contrary, in the frequency range studied, the spin-lattice relaxation rate for the solid protons does not depend on the frequency and the bulk relaxation rate $1/T_{1,bulk}$ is frequency independent. The conservation of these frequency dependencies during the progressive hydration and the evolution of $1/T_1(\omega_I, t_{hydr})$ with the hydration time allowed us to renormalize the *NMRD* data to a single master curve $1/T_1(\omega_I, t_{hydr}) \propto [S_{p,NMR}(t_{hydr})]F(\omega_I)$ (Barberon and Korb 2009), where $S_{p,NMR}$ is a *NMR*-based specific surface area of the hydrated cement that appears to be directly proportional to the degree of advancement of chemical reaction.

Surface diffusion coefficient. The surface diffusion coefficient is obtained from a fitting procedure of the *NMRD* profiles of Figure 2 which shows the *NMRD* profiles for different admixed cement pastes with three *HPMC (J1, J2* and *J3)* and neat (without *CE*) white cement pastes. In order to limit the kinetics effect during the measurements, we have decreased the number of frequency points on the profiles. This procedure allows a quite reasonable fit of the plateau dependence at low frequency and the bilogarithmic dependence at higher frequency (Figure 2). The correlation time τ_{trs} for translational diffusion of water-proton is determined using the model described in (Barberon and Korb 2009).

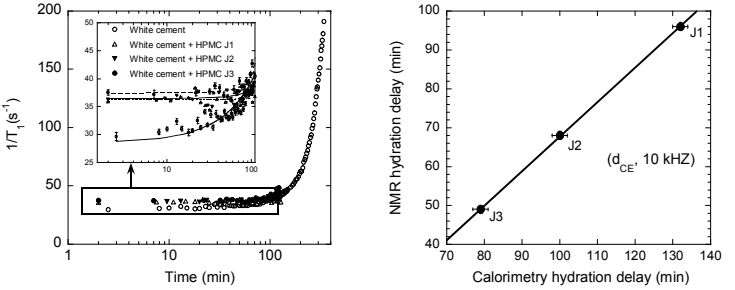

(a) (b)

Figure 3. (a) Water ^{1}H $1/T_1(\omega_I)$ of hydrated cement pastes (w/c=0.4) as a function of hydrating time measured at a Larmor frequency of 10kHz. Effect of three cellulose ethers (*HPMC J1*, *J2* and *J3*). The inset represents a zoom on the frequency range of the plateau. (b) Correlation between the delays obtained by the *NMRD* and isotherm calorimetry.

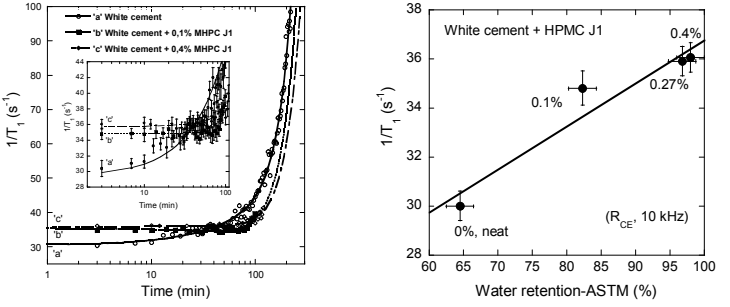

(a) (b)

Figure 4. (a) Comparison of the water ^{1}H $1/T_1(\omega_I)$ of hydrated cement pastes (w/c=0.4) as a function of hydrating time measured at a Larmor frequency of 10kHz. Effect of the *CE* concentration of *HPMC J1*. (b) Correlation between the water retention evidenced from the *NMRD* technique and the macroscopic measurement described in the text (ASTM C1506-09 standard). The different concentrations of *HPMC J1* are indicated.

For these four different cement pastes, we find similar results for the translational surface diffusion $\tau_m \approx 1ns$ and for the time of residence $\tau_s \approx 10\ \mu s$. This suggests a pore scale invariance of water dynamics at the pore surface in *CSH* whatever the paste composition. This value of τ_m is in agreement with previous studies performed on cement pastes or on mortars (Barberon and Korb 2009). The translational diffusion coefficient D_{surf} at the pore surface can be deduced from the Stokes-Einstein relationship: $D_{surf} = \varepsilon^2/(6\tau_m)$ where $\varepsilon = 3\text{Å}$ is the water-molecule size. For all cement pastes (admixed or not), the surface diffusion coefficient is about $D \approx 2.25 \times 10^{-13} m^2.s^{-1}$ *i.e.* about 1/100 of that of bulk water at 23°C. In consequence, the presence of cellulose ethers in cement paste does not modify the surface diffusion coefficient at the pore surface. This result is similar to those obtained in the macroscopic scale by pulsed field gradient *NMR* showing that the *CE*

does not modify the diffusion coefficient of water in the bulk (Patural 2010). We found similar results for starch ethers that present very different water retentions (92.6% and 66.2% respectively). This demonstrates that the translational diffusion coefficient at the surface of the solid interfaces is not affected by starch ether's presence.

These experiments thus demonstrate that cellulose and starch derivatives do not change the surface diffusion coefficient of water. The water mobility at pore surface is thus not modified in presence of such polymers.

Specific surface area and relative quantity of water transiently present at pore surface. On Figure 2, one observes a constant value for $1/T_1(\omega_I)$ when the proton frequency becomes $\omega_{I<}\omega_d=2\pi\times30\,kHz$. Such a cross-over frequency ω_d is of the order of the dipolar interaction in the solid state between two protons separated by *0.155 nm*. On this low frequency range, the confined proton liquid explores relaxation processes induced by characterized long correlation times encountered in the solid state: $\tau_{solide} = 1/\omega_d = 5.3\,\mu s$. We have shown in (Barberon and Korb 2009) that owing to the cross relaxation process, the intermolecular dipole-dipole interaction then couples the water spin relaxation to that of the solid and the magnetic field dependence of the immobilized spin system. The observed data presented in Figure 2 confirms the plateau observed at low frequency (at 10 kHz) for $1/T_1$ during the first hundred minutes. Then, relaxation rate increases due to cement hydration and development of the specific surface area. Moreover, a zoom on the Figure 3a shows that small but significative differences exist between each admixed cement pastes. The observed plateau for frequency below ω_d is thus characteristic of the rigid-lattice limit of the solid-proton hydrates. The absolute value of such a plateau, measured for instance at 10 kHz, is thus indicative of the specific surface area precisely at the solid-liquid interface. The continuous measurement of $1/T_1(\omega_I=2\pi\times10kHz, t_{hydr})$ in presence of various admixtures of cellulose ethers thus allows to monitor the evolution of the specific surface area $S_{P,NMR}(t_{hydr})$, of the material during the hydration.

How NMR relaxation can elucidate water retention mechanisms? In the very early aged of the hydration, the amount of *CSH* is not very large and the admixed polymer is still in the interstitial solution within the pores of the paste, even if the cellulose ethers are rather large. The relaxation of the mobile proton-water thus will be influenced by the presence of the polymer. We show that measuring the time evolution of the spin-lattice relaxation rate $1/T_1(10\,kHz, t_{hydr})$ at 10 kHz, especially in the first minutes of hydration allows probing quantitatively the relative population of water transiently present at the solid hydrate surfaces $N_S/N(t_{hydr})$.

On Figure 3a, the continuous lines exhibit the time evolution of $1/T_1(10\,kHz, t_{hydr})$ for the non admixed (neat) white cement and with *HPMC J1, J2, J3* admixtures. The periods d_{ref} during which the plateau remains constant are evidenced (d_0 is related to neat cement) and ordered as followed:

$$d_0 = 11\,min < d_{J3} = 60\,min < d_{J2} = 79\,min < d_{J1} = 197\,min$$

This period d_{CE}, measured at low frequency, is a clear indicator of the delay of hydration induced by the *CE* polymer introduced into the material. The fact that d_0 stays much smaller than the other d_{CE} is a clear indication of the delayed hydration and setting induced by the *HPMC J1, J2, J3* admixtures. We show on Figure 3b, that one can correlate these delays of hydration measured by *NMRD* to the ones measured from isotherm calorimetry measurements (determined using the method described in Patural Thesis 2011) on similar materials. The quasi linear dependence (r^2=0.99) shows the very good accuracy between the microscopic (NMRD) and macroscopic (calorimetry) measurements.

Another important parameter can be extracted from the behavior of the time evolution of $1/T_1(10\ kHz,\ t_{hydr})$ during the first 100 minutes of hydration. This is the value of the plateau itself, noted, $1/T_{1,CE} = 1/T_{1,observed}(10kHz, t_{hydr})$ which depends critically on the nature of the admixtures. The results found for the neat white cement paste and *HPMC*-admixed cement pastes *J1, J2, J3* are ordered as followed: $1/T_{1,0} = 30s^{-1} < 1/T_{1,J1} = 35.9s^{-1} < 1/T_{1,J2} = 36.3s^{-1} < 1/T_{1,J3} = 37.6s^{-1}$, where $1/T_{1,0}$ is the value of the low-frequency plateau for neat cement. $1/T_{1,CE}$ is proportional to the correlation time τ_m and directly related to the relative amount of water N_s/N transiently present during the first 100 minutes at proximity of solid interfaces that is proportional to the specific surface area. Owing to the observation that $\tau_m \approx 1ns$ and $\tau_s \approx 10\mu s$ are universal for all the cement-based materials, one obtains a proportion $N_S(t_{hydr}=2\ min)/N=1.06\%$ for the neat white cement paste and $N_S(t_{hydr}=2\ min)/N$=1.36% for the admixed cement pastes with *HPMC J3*. One obtains intermediate values for the other admixtures *HPMC J1* and *HPMC J2*.

The fact to probe, in the first minutes of cement hydration, the fraction of mobile water molecules transiently present at solid interfaces N_s/N in presence of different nature and quantity of cellulose ethers is a key result of this study that can be directly linked to the relative amount of water retained on the pores surface.

We have applied the same *NMRD* method for *HPMC J1* with two different concentrations namely 0.1 and 0.4% giving 82.3 and 98.0% macroscopic water retention, respectively (Figure 4a). As expected, the value of the plateau $1/T_{1,CE}$ increases significantly with the concentration of admixture. Finally, on Figure 4b the linear correlation (r^2 = 0.93) of $1/T_{1,CE}$ and water retention of mortar admixed with three different concentrations 0.1, 0.27 and 0.4% of *HPMC J1* proves that our microscopic *NMRD* measurements on cement pastes could be correlated with the macroscopic water retention on mortars.

CONCLUSION

An original method based on two different applications of proton-water magnetic relaxation dispersion (*NMRD*) has been proposed to elucidate the effect of cellulose ethers (*CE*) on water retention of freshly-mixed white cement paste.

The first application of *NMRD* probes directly the proton-water surface dynamics from the magnetic field dependence of the nuclear spin-lattice relaxation rate. In spite of modifications of the solution's viscosity, we find that the cellulosic derivatives do

not modify the surface diffusion coefficient of water that is about two orders of magnitude smaller than that of bulk water.

The second application of *NMRD* concerns the continuous measurements of the spin-lattice relaxation rates at a fixed and very low Larmor frequency. At the very early ages, this application probes continuously and for the first time, the relative population of water transiently present at the surface of the time-growing solid hydrate interfaces. Compared to neat white cement, the *CE* modifies significantly the surface fraction of mobile water molecules transiently present initially at solid surfaces. Our results show that the larger the fraction, the better water-retention capacity of the hydrated cement or mortar samples at proximity of a solid support. This quantity measured for all admixed cement pastes is thus relevant to explain the water retention mechanism. Furthermore, a linear correlation is found between the *NMR* surface fraction and the standard *ASTM* method used by the mortar industry to estimate the water retention capacity of admixed mortars. However for very strong water retention, it seems that the *ASTM* is not able to distinguish polymer's effect while *NMRD* enables to make the difference between two admixtures.

REFERENCES

Barberon, F., Korb, J.-P., Petit, D., Morin, V., Bermejo, E. (2003). "Probing the surface area of a cement-based material by nuclear magnetic relaxation dispersion." *Phys. Rev. Lett.,* 90, 116103-116104.

Kimmich, R., Anoardo, E. (2004). " Field-cycling NMR relaxometry." *Prog. Nucl. Magn. Reson. Spectrosc.* 44, 257-320.

Korb, J.-P. (2009). "NMR and nuclear spin relaxation of cement and concrete materials." *Curr. Opin. in Coll. Int. Sci.*, 14, 192-202.

Korb, J.-P., Monteilhet, L., McDonald, P.J., Mitchell, J. (2007). "Microstructure and texture of hydrated cement-based materials: A proton field cycling relaxometry approach." *Cem. Concr. Res., 37,* 295-302

Mansoutre, S., Colombet, P., Van Damme, H. (1999). "Water retention and granular rheological behavior of fresh C3S paste as a function of concentration." *Cem. Concr. Res.,* 29, 1441-1453

Patural, L., Porion, P., Van Damme, H. Govin, A., Grosseau, Ph., Ruot, B., Devès, O., (2010). "A pulsed field gradient and NMR imaging invsertigations of the water retention mechanism by cellulose ethers in mortars." *Cem. Concr. Res.,* 40, 1378-1385.

Patural, L., Marchal, P., Govin, A., Grosseau, Ph., Ruot, B., Devès, O. (2011). "Cellulose ethers influence on water retention and consistency in cement-based mortars." *Cem. Concr. Res.,* 41, 46-55.

Patural, L., (2011) PhD Thesis, ENSM.

Patural, L., Korb, J.-P., Govin, A., Grosseau, Ph., Ruot, B., Devès, O., (2012). "Nuclear magnetic relaxation dispersion investigations of water retention mechanisms by cellulose ethers in mortars." *Cem. Concr. Res.,* 42, 1371-1378.

Peschard, A., Govin, A., Grosseau, Ph., Guilhot, B. Guyonnet, R. (2004). "Effect of polysaccharides on the hydration of cement paste at early ages." *Cem. Concr. Res.,* 34 2153–2158.

Pourchez, J. Peschard, A, Grosseau, Ph., Guyonnet, R., Guilhot, B., Vallée, F. (2006). "HPMC and HEMC influence on cement hydration." *Cem. Concr. Res.,* 36, 1777-1780.

Pourchez, J., Ruot, B., Debayle, J., Pourchez, E., Grosseau, Ph. (2010). "Some aspects of cellulose ethers influence on water transport and porous structure of cement-based materials." *Cem. Concr. Res.,* 40, 242-252.

.

Water Sorption Hysteresis in Cement Nano Slits

Wen Hui Duan[1], Shu Jian Chen[2], and Mija Hubler[3]

[1] Department of Civil Engineering, Monash University, Clayton, Melbourne, VIC, 3800, Australia; PH (61) 3-99054958; FAX (61) 3-99054944;
email: wenhui.duan@monash.edu
[2] Department of Civil Engineering, Monash University, Clayton, Melbourne, VIC, 3800, Australia; PH (61) 3-99054968; FAX (61) 3-99054944;
email: shujian.chen@monash.edu
[3] Department of Civil & Environmental Engineering, Northwestern University, Evanston, Illinois 60208, USA;
email: m-hubler@u.northwestern.edu.

ABSTRACT

An important feature of the water sorption in cement has been the pronounced hysteresis. The hysteresis in capillary pores has been explained by so-called "ink-bottles" theory and/or the meniscus theory. In contrast, the hysteresis in gel pores (nanopores) received little attention.

This paper investigated the sorption hysteresis in cement slits via atomistic simulations. Tobermorite 11 was adopted to represent the cement atomistic structures. In order to create the surface for adsorption, the Wollastonite chains in Tobermorite 11 were removed and the dangling bonds were saturated with hydrogen atoms. Charges were balanced to be neutral for the whole simulation cell. The sorption isotherms were calculated using the Sorption module in Material Studio (a commercial software for MD simulations), which calculates adsorption isotherms for water in the pores from a series of fixed pressure simulations. Three Tobermorite11 slits of widths H = 10 Å, 20 Å and 30 Å were studied. The temperature was kept at 298 K. The results for all three slits showed significant and slit-size dependent hysteresis sorption-desorption loops. The hysteresis shrinks when the width of the slits decreases. The role of Coulomb interaction in the hysteresis as well as the water molecular density within the slits was discussed.

The results on sorption hysteresis in nano slits can be used to revise/refine the existing water hysteresis models for cement and concrete. This paper provides the pathway towards a better understanding of creep and drying shrinkage of Ordinary Portland cement on the nanoscale.

INTRODUCTION

Creep and shrinkage are the key factors that affect the durability and long-time reliability of concrete structures. Experimental studies show that the creep and shrinkage are associated with moisture loss and gain (Bažant and Robert 1988), which has been extensively investigated via the water sorption isotherms. As porous materials, water adsorption in cement and concrete is governed by the combination of various phenomena including pore condensation, pore blocking, and surface adsorption (free adsorption and hindered adsorption) (Bažant 1972). These complex phenomena, caused by the complication of pore size distribution in cement (Tennis and Jennings 2000), attribute to the hysteresis in water sorption loop.

Based on the Powers-Brownyard model (Taylor 1997), the total porosity of mature cement paste with water/cement ratio of 0.5 is 41%. The large capillary pores occupy 15% and the gel pores 26% of the material volume. The hysteresis in capillary pores can be explained by so called "ink-bottles" theory (Rao 1941) or the non-uniqueness of the surfaces of capillary menisci (Foster 1932). For the sorption in gel pores (or nanopores), Bažant (2001) developed the theory of hindered adsorption for concrete. But this theory of hindered adsorption is reversible and not able to explain the hysteresis. Recently, In order to account for the hysteresis occurring at the gel pores, Bažant (2012) proposed the snap-through instability based on the concept of misfit disjoining pressure and continuum thermodynamics.

With the advancements in nanotechnology and atomistic modeling, sophisticated models of cement nanostructure become possible. For example, first principle calculations and/or Molecular Dynamics (MD) simulations have been used for the calculation of bulk material properties of cement (Manzano et al. 2007; Shahsavari et al. 2009) as well as the interaction between water and cement matrix (Bonnaud et al. 2010; Brochard et al. 2012; Kalinichev et al. 2007; Manzano et al. 2012; Youssef et al. 2011). Interesting MD simulations by MIT researchers (Bonnaud et al. 2010; Bonnaud et al. 2012) demonstrated that there are marked water hysteresis in adsorption and desorption in nanopores of silicon and calcium silicate hydrates.

In this paper, atomistic simulations were implemented to understand the water sorption hysteresis in cement nano slits. The adsorption/desorption of water in cement slits with different widths of 10 Å, 20 Å and 30 Å were calculated. The role of long-range Coulomb force in the hysteresis loop was discussed.

METHODS

Due to the close relationship with the hydrated calcium silicates in cement, Tobermorite groups: Tobermorite9 (Merlino et al. 1999), Tobermorite11 (Merlino et al. 2001) and Tobermorite14 (Bonaccorsi et al. 2005) as well as Jennite (Bonaccorsi et al. 2004) have been widely used in atomistic simulations of cement (Taylor 1997). Recently the Pellenq-Ulm model (Pellenq et al. 2009) has gained attention in the simulations on the interaction between water with cement.

In this paper, three cement slits with the width H = 10 Å, 20 Å , and 30 Å were prepared using Tobermorite 11 as shown in Figure 1. All the coordinates of the atoms for Tobermorite 11 could be found in (Merlino et al. 1999). The sizes of the cell are about 13.470 × 14.770 × 22.487 $Å^3$ with the following angles: α = 90°, β = 90°, and γ = 123.25°. Periodic boundary conditions were used along A, B, and C directions. In order to create the surface for adsorption, the Wollastonite chain and Calcium ions in the interlayer were removed. The silicon and oxygen atoms with a dangling bond were saturated with hydrogen atoms. Partial charges were assigned to the cell as follows: Si (0.445), O_{chain} (-0.445), Ca (1.277), O_{intra} (-0.568), O_w (-0.82), and H_w (0.41). Here the indices "chain", "intra," and "W" refer to silicon chain, intralayer, and water, respectively. This charge distribution ensures that the whole cell remains electroneutral.

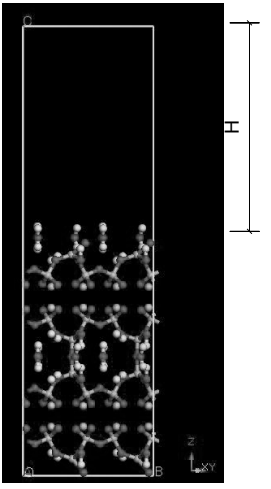

Figure 1. The geometry of simulation cell. Three cases of different slit widths were simulated: H = 10 Å, 20 Å, and 30 Å. Color map for different atoms: Si – yellow, O – red, Ca – green, and H – white. C axis is aligned with Z axis.

The sorption isotherms were calculated using Sorption module in Material Studio (a commercial software for MD simulations), which calculates adsorption isotherms for water in the pores from a series of fixed pressure simulations. The atomic interactions were modeled by the COMPASS force field (condensed-phased optimized molecular potential for atomistic simulation studies) (Rigby et al. 1997), which is the first *ab initio* force field that was parameterized and validated using condensed-phase properties. The detailed contributing forces in the COMPASS force field can be found in (Duan et al. 2011; Duan and Wang 2010). The water model in the COMPASS force field is a simple three-point model (Rigby 2004). However, its saturate pressure is unknown. In our simulations, the sorption pressure was set from 0.1 kPa to 6 kPa considering the saturate pressure 4.4 kPa for SPC water model (Bonnaud et al. 2012).

During the course of the simulation, water molecules within the slits were randomly rotated and translated, and, in addition, water molecules were randomly created in and deleted from the slits. The configuration of the water molecules filling the pores was selected by the Monte Carlo method (Metropolis–Hastings algorithm) based on the minimization of the energy. The temperature was set as 298K in all the simulation cases.

RESULTS AND DISCUSSION

Water sorption isotherms.

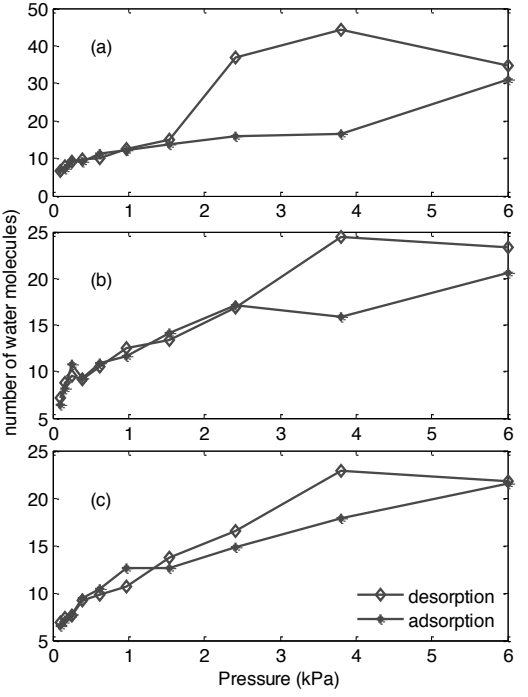

Figure 2. Sorption isotherms of water molecules in cement slits with the width of (a) H = 10 Å, (b) H = 20 Å and (c) H = 30 Å at T = 298 K.

Figure 2 shows the water sorption isotherms at temperature 298 K in Tobermorite 11 slits with the width of H = 10 Å, 20 Å and 30 Å. For all slit sizes, the sorption isotherms represent the typical experimental observations: when the pressure is small, the adsorption and desorption branches follow the same path. The hysteresis region begins at a relatively large pressure, which is around 2 kPa for all three cases. In this region, the desorption branch always corresponds to larger adsorption at a given pressure. Interestingly it should be noted that the slit with the width of 10 Å shows larger hysteresis compared with the other two slits. For example, at the pressure of 3.8 kPa, the difference in the number of water molecules between adsorption and desorption

branches is 28 for 10 Å slit, 9 for 20 Å slit, and 5 for 30 Å slit, respectively. It indicates that when the slit size increases, the hysteresis decreased.

Bonnaud et al. (2010; 2012) calculated the water sorption at temperature 300 K in hydroxylated silica nanopores of a width 10 Å and 20 Å as well as in a cement slit of width H = 10 Å (using Pellenq-Ulm model). They observed that in the case of the silica nanopore with H = 10 Å, the adsorption/desorption cycle is reversible and there is no hysteresis loop. In contrast, the hysteresis loop for the silica nanopore with H = 20 Å started at P = 0.88 kPa and ended at around P = 2.4 kPa. The hysteresis loop for the cement nanopore with H = 10 Å located from 0 kPa to 0.88 kPa. They attributed these observations to the temperature effect, condensations, and surface roughness. Our results showing strong and slit-size dependent hysteresis loops are different to those of Bonnaud et al. These discrepancies are partially attributed to the different force fields and atomistic models of cement used in their simulations.

It is worth noting that in our simulations, the magnitudes of the Coulomb energy were about 4-5 times the respective vdW energies (including Lennard–Jones contribution and hydrogen bond contribution). These ratios are in good agreement with Vorholz et al.'s results on vapor–liquid equilibrium of water (Vorholz et al. 2000). The larger Coulomb energy indicates that the charge-dipole interaction is the dominating factor in our results. Although the silicon chain and intra calcium atoms in our models are electronuetural as a whole, the silicon and oxygen atoms have a net charge when facing water. The inverse-square Coulomb force is much stronger when compared with vdW forces, even stronger than most chemical binding forces (Israelachvili 2011). For example, when we consider the charge-dipole interaction between silicon and oxygen atoms with water molecules, the charge-dipole interaction energy is about 96 kJ/mol, which is much larger than the water-water hydrogen bond 20.4 kJ/mol.

Considering the dominating Coulomb energy in our simulations, the sorption hysteresis can be explained as follows: in the adsorption branch, the water layer on the slit wall is relatively thin. The Coulomb interaction between silicon and oxygen atoms with new water molecules are relatively strong compared with vdW interaction. In contrast, in the desorption branch, the water layer on the slit wall becomes thicker, the large distance between silicon/oxygen atoms with new water molecules makes the Coulomb interaction relatively insignificant. The different Coulomb interaction due to the change in the thickness of water layer in adsorption/desorption branches is the main mechanism for the hysteresis loops in our simulations. It should be noted that the competition between Coulomb interaction and vdW interaction has been discussed to explain the failure modes in the Tobermorite group via first principle calculations (Shahsavari et al. 2009).

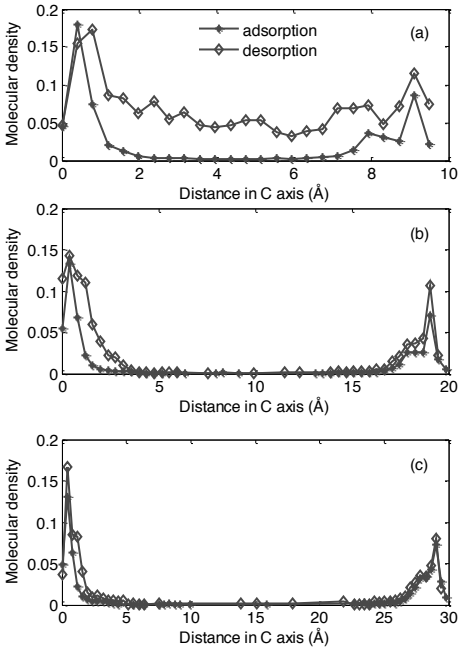

Figure 3. Water molecular density (molecule/Å^3) along C axis of the simulation cell for three cement slits of (a) H = 10 Å; (b) H = 20 Å and (c) H = 30 Å. The pressures for (a) , (b) and (c) are corresponding to 3.8 kPa.

Molecular density profiles.

The water molecular density profiles along the C axis are shown in Figure 3. For all three slits, there are density peaks with similar magnitudes (about 0.15 molecule/Å^3) within 2 Å from the slit walls for both adsorption and desorption branches. This indicates that Coulomb interaction is very strong. It also suggests that the slit wall surface is hydrophilic as illustrated in (Bonnaud et al. 2012). In addition, the density is usually larger for desorption branch within the distance of 5 Å from the slit walls, which is an evidence to back up the sorption hysteresis as shown in Figure 2. The molecular density decrease to about 0.05 under desorption in the middle of the slit with the width H = 10 Å, which is comparable with those calculated by (Manzano et al. 2012; Youssef et al. 2011). It is worth noting that the much larger density for the slit of H = 10 Å is due to the superimposed Coulomb forces from two sides of the slit. The difference of the density between adsorption and desorption shrinks/disappears 5 Å from the slit walls.

Bažant (2012) proposed the snap-through instability to explain the hysteresis for pores with the width smaller than about 3 nm. The snap-through instability is caused by non-uniqueness in the misfit disjoining pressures engendered by a difference between the nanopore width and an integer multiple of the thickness of a monomolecular adsorption water layer. The interaction between the nanopore and water layer was assumed to be a vdW-like potential (Fig. 2 in (Bažant and Bazant 2012)). Our simulation results suggest that for the pore size below 1 nm, the Coulomb interaction is much stronger than the vdW interaction. Therefore there is a research necessity for the theory of hysteresis in a pore below 1 nm width based on the Coulomb interaction.

CONCLUSIONS

The water sorption in three cement slits was investigated by atomistic simulations. The main findings can be summarized as follows: (a) there are strong and slit-size dependent sorption hysteresis loops in three cement slits. The hysteresis loops shrink when the slit size increases; (b) the different long-range Coulomb interactions in adsorption and desorption due to the change in the thickness of the water layer is the main factor for the water sorption hysteresis loops; (c) the molecular density profiles suggest that the Coulomb interaction is significant in pores with thicknesses below 1 nm and that there is a need to develop a Coulomb interaction based theory to complement Bažant's snap-through instability theory for nanopores.

ACKNOWLEDGMENT

WHD is grateful for the financial support provided by the Australian Research Council to conduct this study. WHD would like to thank Professor Zdeněk P. Bažant (Northwestern University, USA) on the discussion of water sorption theory.

REFERENCES

Bažant, Z. P. (1972). "Thermodynamics of hindered adsorption and its implications for hardened cement paste and concrete."*Cem. Concr. Res.*, 2(1), 1-16.

Bažant, Z. P. (2001). "Prediction of concrete creep and shrinkage: past, present and future."*Nucl. Eng. Des.*, 203(1), 27-38.

Bažant, Z. P., and Bazant, M. Z. (2012). "Theory of sorption hysteresis in nanoporous solids: Part I: Snap-through instabilities."*J. Mech. Phys. Solids*, 60(9), 1644 - 1659.

Bažant, Z. P., and Robert, L. (1988). *Mathematical modeling of creep and shrinkage of concrete*, Wiley Chichester.

Bonaccorsi, E., et al. (2005). "The Crystal Structure of Tobermorite 14 (Plombierite), a C--S--H Phase."*J. Am. Ceram. Soc.*, 88(3), 505-512.

Bonaccorsi, E., et al. (2004). "The crystal structure of jennite, Ca9Si6O18(OH)(6)center dot 8H(2)O."*Cem. Concr. Res.*, 34(9), 1481-1488.

Bonnaud, P. A., et al. (2010). "Molecular simulation of water confined in nanoporous silica."*J. Phys. Condens. Matter*, 22, 284110.

Bonnaud, P. A., et al. (2012). "Thermodynamics of Water Confined in Porous Calcium-Silicate-Hydrates."*Langmuir*, 28(31), 11422-11432.

Brochard, L., et al. (2012). "Poromechanics of microporous media."*J. Mech. Phys. Solids*, 60(4), 606-622.
Duan, W. H., et al. (2011). "Controlling the formation of wrinkles in a single layer graphene sheet subjected to in-plane shear."*Carbon*.
Duan, W. H., and Wang, Q. (2010). "Water transport with a carbon nanotube pump."*ACS nano*, 4(4), 2338-2344.
Foster, A. G. (1932). "The sorption of condensible vapours by porous solids. Part I. The applicability of the capillary theory."*Trans. Faraday Soc.*, 28(0), 645-657.
Israelachvili, J. N. (2011). *Intermolecular and surface forces*, Academic Press, Burlington, MA.
Kalinichev, A. G., et al. (2007). "Molecular dynamics modeling of the structure, dynamics and energetics of mineral-water interfaces: Application to cement materials."*Cem. Concr. Res.*, 37(3), 337-347.
Manzano, H., et al. (2007). "Mechanical properties of crystalline calcium-silicate-hydrates: comparison with cementitious C-S-H gels."*Phys. Status Solidi A*, 204(6), 1775-1780.
Manzano, H., et al. (2012). "Confined Water Dissociation in Microporous Defective Silicates: Mechanism, Dipole Distribution, and Impact on Substrate Properties."*J. Am. Chem. Soc.*, 134(4), 2208-2215.
Merlino, S., et al. (1999). "Tobermorites their real structure and order-disorder (OD) character."*Am. Mineral.*, 84(10), 1613-1621.
Merlino, S., et al. (2001). "The real structure of tobermorite 11 normal and anomalous forms, OD character and polytypic modifications."*Eur. J. Mineral.*, 13(3), 577-590.
Pellenq, R. J. M., et al. (2009). "A realistic molecular model of cement hydrates."*PNAS*, 106(38), 16102-16107.
Rao, K. S. (1941). "Hysteresis in Sorption. II. Scanning of the Hysteresis Loop. Titania Gel-Water System."*The Journal of Physical Chemistry*, 45(3), 506-512.
Rigby, D. (2004). "Fluid density predictions using the COMPASS force field."*Fluid Phase Equilib.*, 217(1), 77-87.
Rigby, D., et al. (1997). "Computer simulations of poly(ethylene oxide): Force field, PVT diagram and cyclization behaviour."*Polym. Int.*, 44(3), 311-330.
Shahsavari, R., et al. (2009). "First-Principles Study of Elastic Constants and Interlayer Interactions of Complex Hydrated Oxides: Case Study of Tobermorite and Jennite."*J. Am. Ceram. Soc.*, 92(10), 2323-2330.
Taylor, H. F. W. (1997). *Cement chemistry*, Thomas Telford.
Tennis, P. D., and Jennings, H. M. (2000). "A model for two types of calcium silicate hydrate in the microstructure of Portland cement pastes."*Cem. Concr. Res.*, 30(6), 855-863.
Vorholz, J., et al. (2000). "Vapor+liquid equilibrium of water, carbon dioxide, and the binary system, water+carbon dioxide, from molecular simulation."*Fluid Phase Equilib.*, 170(2), 203-234.
Youssef, M., et al. (2011). "Glassy Nature of Water in an Ultraconfining Disordered Material: The Case of Calcium-Silicate-Hydrate."*J. Am. Chem. Soc.*, 133(8), 2499-2510.

Interpretation of Full Sorption-Desorption Isotherms as a Tool for Understanding Concrete Pore Structure

Matthew B. Pinson[1], Hamlin M. Jennings[2] and Martin Z. Bazant[3]

[1]Department of Physics; email: mpinson@mit.edu
[2]Department of Civil and Environmental Engineering; email: hmj@mit.edu
[3]Departments of Chemical Engineering and Mathematics; email: bazant@mit.edu
Massachusetts Institute of Technology
77 Massachusetts Avenue, Cambridge, MA 02139

ABSTRACT

Sorption isotherms are frequently used to characterize the structure of porous materials such as cement. Their interpretation has been somewhat hindered by the large hysteresis observed between the adsorption and desorption processes. Here we model the hysteresis due to pore blocking, whereby water condensed in small pores prevents propagation of a vapour interface into the pore structure, trapping water condensed in larger pores in a metastable state. The model identifies the adsorption isotherm as more useful in determining the pore size distribution. Additionally, and of particular interest, it provides a way of calculating an additional structural parameter, quantifying the exposure of mesopores (gel pores) to the surrounding atmosphere. This exposure is higher for samples with higher water to cement ratio, suggesting that it is mediated by capillary pores. The model also allows calculation of the connectivity of the pore structure, although the intertwined influences of exposure and connectivity make the latter difficult to interpret.

INTRODUCTION

The measurement of sorbed mass as a function of the partial pressure of the sorbate has long been used to gain information about the structure of porous materials (Pierce 1953; Shull 1948). In particular, adsorption data at low partial pressure are used to calculate internal surface area (Emmett and Brunauer 1937; Harkins and Jura 1944). One difficulty of this approach is that significant hysteresis may be observed in the measured quantity of water in the pores when increasing and decreasing humidity. This hysteresis has caused some confusion in the study of the pore structure of cement. Physical changes in the cement structure have been identified as one cause (Feldman and Sereda 1968; Jennings 2000), but these are expected to be significant only if the cement is dried below 20% relative humidity (Jennings 2008), leaving the bulk of the hysteresis at higher humidity unexplained. The retention of condensed water in a metastable state in large pores located behind smaller pores (Espinosa and Franke 2006; Quenard and Sallee 1992), and the effect of disjoining pressure and

discreteness in the smallest pores (Bažant and Bazant 2012), have also been identified as contributing to the hysteresis. Disentangling each of these effects requires an accurate understanding of each process, including a mathematical model. Here we present a model of the hysteresis caused by pore blocking.

SORPTION MODEL

Adsorption. We consider both the adsorption of water on the internal surfaces, and the filling of pores through capillary condensation. Surface adsorption is treated by the Langmuir equation (Langmuir 1917):

$$\theta = \frac{\alpha h}{1 + \alpha h}, \quad (1)$$

where θ is the proportion of the surface that is covered by water molecules, h is the relative humidity, and α is a constant related to the energy of adsorption. The adsorbed mass is then directly proportional to θ.

Capillary condensation in a pore occurs when the humidity is sufficiently high that the free energy cost of filling the pore is outweighed by the decrease in water surface energy that results from condensing water and forming a curved meniscus. Assuming the system can attain thermodynamic equilibrium, capillary condensation occurs at a humidity given by the Kelvin equation (Feldman and Sereda 1968):

$$\ln h = -\frac{2\gamma v}{rkT}. \quad (2)$$

Here γ is the surface tension of water, v is the molecular volume, k is the Boltzmann constant and T is temperature. r is the radius of curvature of the meniscus separating the condensed water from the vapour: if the meniscus lies perpendicular to the axis of a cylindrical pore and water perfectly wets the pore wall, then r is the effective radius of the pore. The thickness of the adsorbed layer must be subtracted from the physical radius of the pore, in order to obtain the effective radius for use in the Kelvin equation.

Of course, the complexity of the pore structure of concrete means that we cannot assume that every pore is cylindrical and fills through the propagation of a meniscus along its axis at the equilibrium filling humidity. An alternative assumption, still applicable to cylindrical pores, is that filling instead occurs in the radial direction, beginning at the adsorbed layer on the pore wall and proceeding inwards. In this case, filling requires not only that the filled state is at lower free energy than the empty, but that increasing the thickness of the adsorbed layer on the pore wall monotonically decreases free energy (Celestini 1997). In this case, the relationship between radius and filling humidity is (Cohan 1938)

$$\ln h = -\frac{\gamma v}{rkT}$$

Since the humidity at which a pore will fill depends primarily on its radius r, which we can think of as a measure of the volume to surface area ratio in the case of non-cylindrical pores, we can relate these quantities using the general relation

$$\ln h = -\frac{f\gamma v}{rkT}, \quad (3)$$

where f is a parameter related to the shape of the pore and the presence or absence of full neighbouring pores to nucleate condensation. We adopt the simple approximation that f varies from 1 at 0% relative humidity, when there are no full pores, to 2 at 100% relative humidity, when all the mesopores of concrete are full.

Using equations 1 and 3, a measured isotherm can be interpreted in terms of a total surface area and a distribution of pore radii.

Desorption. The desorption process is more complicated than adsorption. In order to empty a pore of its capillary condensed water, it is necessary that the humidity drop below that at which the full and empty states would be in thermodynamic equilibrium, as given by equation 2. Additionally, one of the following criteria must be fulfilled:

1) the pore is in contact with the vapour,
2) the humidity is low enough for cavitation (spinodal decomposition) to occur (approximately 35%), or
3) the vapour phase is nucleated, such as by a heterogeneous surface.

We neglect the latter processes, and focus on the propagation of the vapour phase through the pore network. The model of desorption should thus be valid in the upper and middle parts of the humidity range. To allow interpretation of sorption at low humidity, the model will need to be extended to account for cavitation (Bazant and Bažant 2012).

When the humidity to which a sample of cement paste is exposed is increased to 100%, water condenses in all the mesopores. If the humidity is then decreased, some of these pores are already exposed to the vapour, and hence able to empty once equation 2 is satisfied. We define Q_0 to be the fraction of pores that are directly exposed in this manner.

As humidity is further decreased, pores begin to empty. The emptying of pores results in the exposure of additional pores to the vapour phase. We model this process of gradual exposure of pores by relying on two important assumptions. The first is that of a mean field model, that the properties of a particular pore's neighbours (namely their radii, and whether they are exposed to the vapour via another path) are statistically the same as the properties of all pores, independent of the properties of the central pore. The second is that the pore network can be modeled as a network of cylindrical pores of equal length and connectivity, independent of radius. The connectivity z is defined to be the number of pores exposed to the vapour by emptying a single pore, some of which may already be exposed. The modeled structure is then something like a Bethe lattice with coordination number $z + 1$ (Stauffer and Aharony 1992).

Using the above assumptions, we define $q(h)$, the fraction of pores that would be empty at true thermodynamic equilibrium at a humidity h, and Q, the fraction of pores exposed to the vapour phase. These quantities are related through the differential equation

$$\frac{dQ}{dq} = Qz(1-Q) + \frac{dQ}{dq} qz \frac{1-Q}{1-Qq}. \qquad (4)$$

The two terms on the right hand side correspond to pores becoming exposed as other pores empty for each of two different reasons. The first term accounts for exposed pores emptying as their emptying humidity is reached, the second term for blocked pores emptying as they are exposed to the vapour. Figure 1 gives a schematic illustration of these two processes. Note that an empty pore means a pore emptied of capillary condensed water: it still contains adsorbed water layers on its walls.

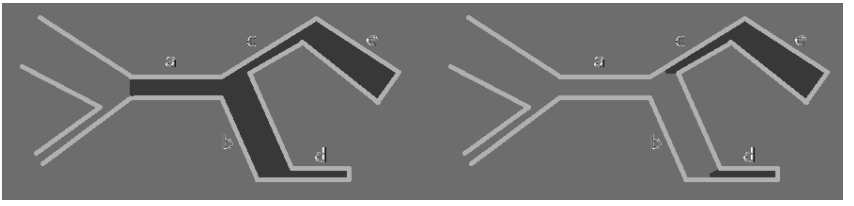

Figure 1. A schematic diagram illustrating two reasons a pore can empty during the desorption process. Between the left and right sections, the humidity was decreased below the value at which pore a, already exposed to the vapour, empties. Pore b empties immediately on being exposed to the vapour, as the humidity is already below the value at which emptying becomes thermodynamically favourable. Pores c and d remain full due to local thermodynamics, while pore e remains full since it is not in contact with the vapour.

Equation 4, with the initial condition $Q(q=0) = Q_0$, can be solved numerically. The product Qq is the proportion of pores that are actually empty. Since q depends on humidity, as described by equation 2, the solution $Q(q)$ allows calculation of the quantity of adsorbed water as a function of humidity.

Application to experimental data. We applied the model described in this section to published adsorption and desorption isotherms for concrete and hardened cement paste samples. After calculating the pore size distribution using the adsorption isotherm, we used a least squares fit to find the value of Q_0 and z for each sample. Since many factors, such as the curing and drying procedures and humidity control, can influence sorption measurements, comparisons between different experiments from a single set are most useful. Here we focus on a recent set of experiments (Baroghel-Bouny 2007) on concrete and cement with a range of water to cement ratios (W/C).

RESULTS AND DISCUSSION

A typical example of the comparison between experimental results and the best fit of the model is shown in figure 2. The experimental adsorption isotherm is used to

determine the pore size distribution, which is shown in figure 3, while the mean field model of pore blocking is fit to the experimental desorption isotherm to determine Q_0 and z. The hardened cement paste sample had W/C of 0.45 (Baroghel-Bouny 2007).

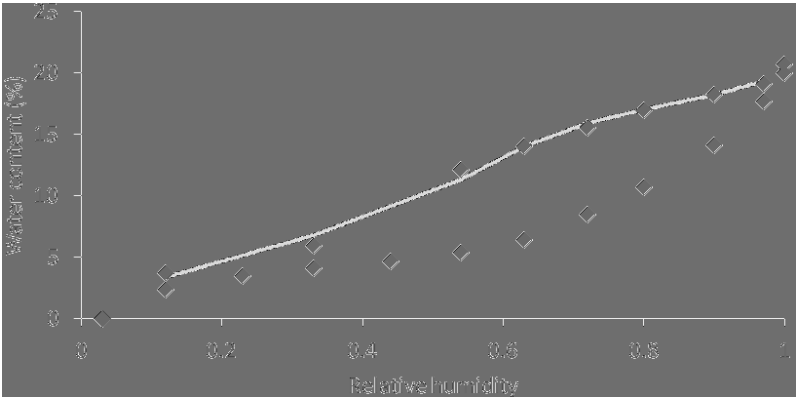

Figure 2. Water content as a function of relative humidity. Points are experimental (Baroghel-Bouny 2007)**. The experimental adsorption data are used as a direct input to determine the pore size distribution. The red line is the prediction of the percolation model of this work, with two parameters Q_0 and z.**

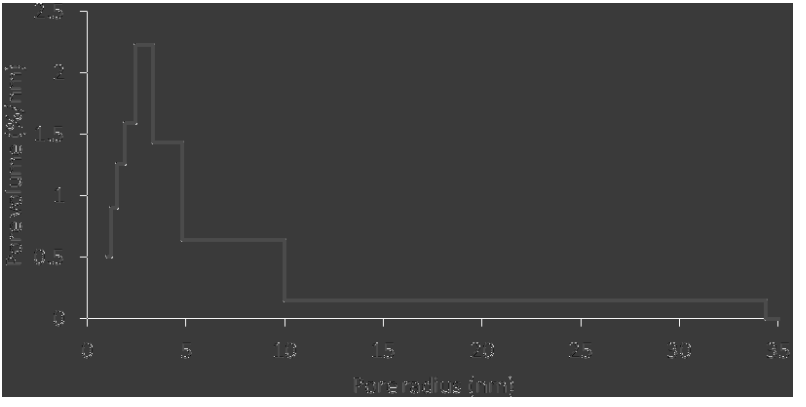

Figure 3. Volume of pores as a function of pore radius, based on the interpretation of experimental adsorption data (Baroghel-Bouny 2007)**.**

Figure 4a shows calculated values of Q_0 as a function of W/C. In general, Q_0 increases as W/C increases. This agrees with what may be expected: higher W/C

leads to a greater quantity of capillary pores (Powers 1958). This provides more large pores that will be empty on desorption even at very high humidity, which increases the probability that a mespore in the cement structure is in contact with the vapour.

Figure 4b shows z as a function of W/C: z decreases as W/C increases. This does not necessarily imply that a sample with higher W/C has lower connectivity. Instead, it is likely to be a result of the variation of Q_0. Higher Q_0 means that more of a particular pore's neighbours are already exposed before that pore empties, decreasing the apparent value of z even if true connectivity is the same. The model takes this into account, but only through a mean field method. The mean field method will be insufficient if there is substantial geometric dependence of exposure to the vapour, as can be expected if this exposure is mediated by capillary pores.

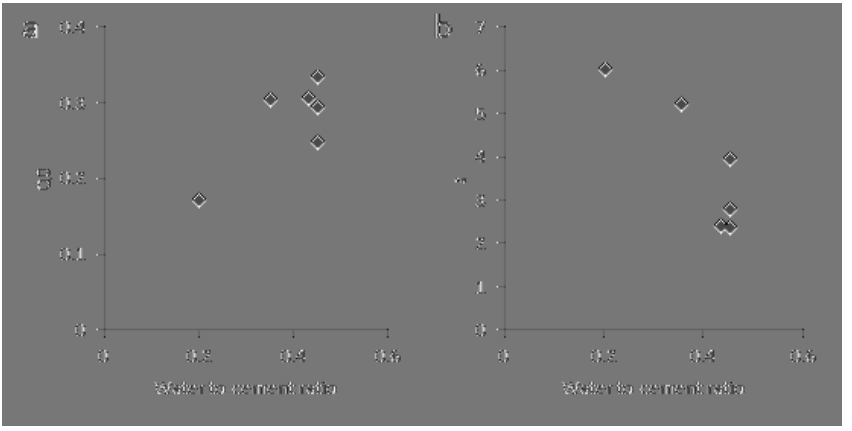

Figure 4. (a) Q_0 and (b) z calculated by applying the model of this paper to experimental results (Baroghel-Bouny 2007)**, as a function of water to cement ratio.**

CONCLUSIONS AND APPLICATIONS

The method outlined here allows additional information to be obtained from sorption isotherms than was previously possible. In addition to the pore size distribution, the method quantifies the exposure of pores to the surroundings (a quantity associated with capillary pore abundance), and the connectivity of the mesopore network. These pieces of information will be of considerable use to the prediction of the properties of a concrete sample. For instance, drying shrinkage behavior is dependent on forces in the mesopores, which depend on pore size and water content (Collins and Sanjayan 2000). Also, permeability is higher for concrete with higher porosity, larger pores and greater pore connectivity (Marsh et al. 1985). The method presented here thus allows the comparison of the suitability of different concretes to a particular application.

REFERENCES

Baroghel-Bouny, V. (2007). "Water vapour sorption experiments on hardened cementitious materials Part I: Essential tool for analysis of hygral behaviour and its relation to pore structure." *Cement and Concrete Research*, 37(3), 414–437.

Bazant, M. Z., and Bažant, Z. P. (2012). "Theory of sorption hysteresis in nanoporous solids: Part II Molecular condensation." *Journal of the Mechanics and Physics of Solids*, 60(9), 1660–1675.

Bažant, Z. P., and Bazant, M. Z. (2012). "Theory of sorption hysteresis in nanoporous solids: Part I." *Journal of the Mechanics and Physics of Solids*, 60(9), 1644–1659.

Celestini, F. (1997). "Capillary condensation within nanopores of various geometries." *Physics Letters A*, 228(1-2), 84–90.

Cohan, L. H. (1938). "Sorption hysteresis and the vapor pressure of concave surfaces." *Journal of the American Chemical Society*, 60(2), 433–435.

Collins, F., and Sanjayan, J. G. (2000). "Effect of pore size distribution on drying shrinking of alkali-activated slag concrete." *Cement and Concrete Research*, 30(9), 1401–1406.

Emmett, P. H., and Brunauer, S. (1937). "The use of low temperature van der Waals adsorption isotherms in determining the surface area of iron synthetic ammonia catalysts." *Journal of the American Chemical Society*, 59(8), 1553–1564.

Espinosa, R. M., and Franke, L. (2006). "Inkbottle Pore-Method: Prediction of hygroscopic water content in hardened cement paste at variable climatic conditions." *Cement and Concrete Research*, 36(10), 1954–1968.

Feldman, R. F., and Sereda, P. J. (1968). "A model for hydrated Portland cement paste as deduced from sorption-length change and mechanical properties." *Matériaux et Construction*, 1(6), 509–520.

Harkins, W. D., and Jura, G. (1944). "Surfaces of Solids. XIII. A Vapor Adsorption Method for the Determination of the Area of a Solid without the Assumption of a Molecular Area, and the Areas Occupied by Nitrogen and Other Molecules on the Surface of a Solid." *Journal of the American Chemical Society*, 66(8), 1366–1373.

Jennings, H. M. (2000). "A model for the microstructure of calcium silicate hydrate in cement paste." *Cement and Concrete Research*, 30(1), 101–116.

Jennings, H. M. (2008). "Refinements to colloid model of C-S-H in cement: CM-II." *Cement and Concrete Research*, 38(3), 275–289.

Langmuir, I. (1917). "The constitution and fundamental properties of solids and liquids. Part I. Solids." *Journal of the Franklin Institute*, 38(11), 2221–2295.

Marsh, B. K., Day, R. L., and Bonner, D. G. (1985). "Pore structure characteristics affecting the permeability of cement paste containing fly ash." *Cement and Concrete Research*, 15(6), 1027–1038.

Pierce, C. (1953). "Computation of pore sizes from physical adsorption data." *The Journal of Physical Chemistry*, 57(2), 149–152.

Powers, T. (1958). "Structure and physical properties of hardened Portland cement paste." *Journal of the American Ceramic Society*, 41(1), 1–6.

Quenard, D., and Sallee, H. (1992). "Water vapour adsorption and transfer in cement-based materials: a network simulation." *Materials and Structures*, 25(9), 515–522.

Shull, C. G. (1948). "The determination of pore size distribution from gas adsorption data." *Journal of the American Chemical Society*, 70(4), 1405–1410.

Stauffer, D., and Aharony, A. (1992). *Introduction to Percolation Theory*. Taylor & Francis, Washington, DC.

Multi-scale hydric transport in hardened cement pastes and reference porous silicate materials

H. Chemmi[1], V. Tariel[1], D. Petit[1], J-P. Korb[1], R. Denoyel[2] and P. Levitz[3]

[1]Laboratoire de Physique de la Matière Condensée, Ecole Polytechnique, UMR 7643 CNRS, Palaiseau 91128, France. email: dominique.petit@polytechnique.fr
[2]MADIREL, Aix-Marseille Université, CNRS-UMR 7246, Centre de St Jérôme, 13397 Marseille Cedex 20, France. email: Renaud.Denoyel@univ-provence.fr
[3]Laboratoire de Physicochimie des Electrolytes, Colloïdes et Sciences Analytiques, UMR 7195 CNRS, Université Pierre et Marie Curie, 4 place Jussieu, 72522 Paris Cedex 5, France. email: pierre.levitz@upmc.fr

ABSTRACT

We show how the pore size and relative humidity are two competitive confinement factors that control the multi-scale water transport in disordered materials. These factors are characterized by proton NMR spectroscopy, relaxometry and diffusometry as well as conductivity and X-ray micro-tomography. We use first MCM41 calibrated micro-porous silicates to focus on the drastic impact of the pores sizes on the moisture transport at micro-scales. Then, we use synthetized control pore glass (CPG) with controlled meso- and macro-pore networks for illustrating the impact of the relative humidity on the moisture transport. These two limiting factors allow understanding the two power-law behaviors found in NMR relaxation distributions used as a robust tool for studying the aging process of cement-based materials. We believe that this approach can be extended to a large class of multi-scale porous materials.

INTRODUCTION

The main objective of this study is to explore the physical processes implied in the moisture transport in hardened cementitious based materials. Understanding such processes is of particular importance for improving the durability of these widely used materials. We focus on grey cement pastes CEM I hardened during long periods of time (up to two years) in controlled atmosphere. In order to decouple the physical processes of moisture transport in the intermixed multi-scales of these cement pastes, we also consider calibrated porous materials in the range of micro, meso and macropores. We use a multi-scale NMR platform including spectroscopy; high and low field relaxometry and diffusometry. Other complementary techniques like conductivity and X-tomography are used. We insist on the possibility of controlling *in situ* the degree of humidity inside the different NMR probes and on the analysis of experimental data to extract representative parameters for the moisture transport.

MOISTURE TRANSPORT CONTROLLED BY LOCAL GEOMETRY

Samples and methods. MCM41 are very well-known calibrated micro-porous. They have been synthetized from the original surfactant template method (Beck) using a sol-gel route (Tourné-Peteilh). The average pore diameters of 3.3 nm have been evidenced by nitrogen and water adsorption. We performed proton nuclear magnetic relaxation dispersion (NMRD) (Kimmich) on a fast-field cycling (FFC) spectrometer. All samples were introduced into a 10 mm diameter-tube where we design an original set up (Chemmi, 2011) ensuring the relative humidity (RH). The temperature was fixed at 298K. The experiment was repeated over a large range of proton Larmor frequencies $\omega_I/2\pi$ (10 kHz - 6 MHz) in order to obtain the dispersion profile of the longitudinal spin-lattice relaxation rate $R_1(\omega_I) = 1/T_1(\omega_I)$.

NMRD results. We show in Figure 1, the NMRD profiles of dry (squares) and hydrated at RH=90% (circles) MCM41 samples. The dry sample has been maintained at 390K during three days under vacuum. For the hydrated sample, we choose a RH of 90% to achieve a Kelvin radius of 10nm that ensure a true saturation of the nano-pores without expelling water outside the 3.3nm channels. In Figure 1.1 the comparison of dry and hydrated samples that shows exactly the same shapes as illustrated by the renormalization labeled by the arrow. This proves the presence of a biphasic fast exchange model (Browstein) that considers a proton dynamics fully controlled by the solid-liquid interface due to the drastic geometric confinement in the channels. According to this model, the spin-lattice relaxation rate is given by $R_1=(1- eS/V)R_{1,bulk} +(eS/V)R_{1,surf} \approx (eS/V)R_{1,surf}$, where e is the size of a surface relaxation layer and S/V is the surface to volume ratio of a channel. $R_{1,bulk}$ and $R_{1,surf}$ are the bulk and surface relaxation rates, respectively. For water, the contribution of $R_{1,bulk} \approx 0.4s^{-1}$ can be neglected in comparison to the $R_{1,surf}$ corresponding to the dry NMRD profile (Figure 1). For a cylindrical channel, one has $S/V=2/r_{pore}$, with $r_{pore}= 1.65nm$. Then the ratio of $R_1(RH=90\%)$ on $R_1(dry)$ leads to $e=0.26nm$. This latter distance is interpreted as an equivalent water layer which is larger than the inter-proton distance of a single water molecule, but smaller than the inter-oxygen distance in bulk water (Gerschel). We show in the inset of Figure 1.2 that the numerical derivative $-dR_1/df$ exhibits two power law frequency behaviors, namely f^{-3} at low frequency below 100 kHz and f^{-1} at high frequency. Then,

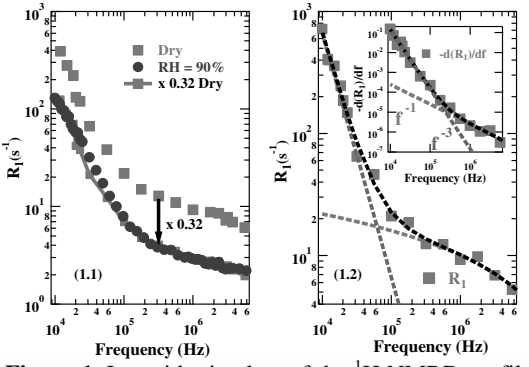

Figure 1. Logarithmic plots of the ^{1}H NMRD profiles of a MCM41 sample at 25°C. **(1.1)** Square, circle and continuous curve stand for dry, hydrated (RH = 90 %) samples and renormalized NMRD profiles respectively. **(1.2)** NMRD profile of the dry sample (square) and of its frequency numerical derivative (inset). The dashed curves represent the best fits obtained with the relaxation model referred in the text.

in Figure 1.2, the low frequency regime follows a f^2 behavior while the high frequency regime varies logarithmically with the frequency. This latter behavior is typical of a surface relaxation model represented by R_1 given as the following linear combination of normalized spectral density for an unlimited surface diffusion process: $J_{n2D}(\omega)=\tau_m ln[1+1/(\omega\tau_m)^2]$ where τ_m represents the translational surface correlation time (Godefroy). From this expression, we separate a slow and fast dynamical regime. For fast diffusion $\omega\tau_m<1$, one has $J_{n2D}(\omega) \approx -2\tau_m ln[\omega\tau_m]$ and for slow diffusion $\omega\tau_m>1$, one has $J_{n2D}(\omega) \approx 1/(\omega^2\tau_m)$. The dashed lines displayed in Figure 1.2 give the best fit achieved with this model leading to the values 1.8 10^{-10} m^2/s and 8.3 10^{-15} m^2/s for the fast and slow diffusion coefficients, respectively (Chemmi, 2011). The fact to find true renormalization and unique theoretical behavior for both dry and hydrated samples shows unambiguously that the geometric confinement is the main factor for limiting the moisture dynamics at micro-scales.

MOISTURE TRANSPORT CONTROLLED BY RELATIVE HUMIDITY

We show now that the relative RH is the main factor for limiting the moisture dynamics at meso and macro-scales.

Samples and methods. We use a synthesis (Chemmi, 2011) involving competition between sol-gel route and spinodale decomposition for controlling the macro-porosity of silica controlled pore glass (CPG) material (Nakanichi). The silica skeleton at the macro-scale presents micro- and meso-porosity characterized by nitrogen adsorption (Chemmi, 2011). At micro and meso scales, mercury invasion and nitrogen adsorption give a meso-pore contribution at about 6 nm. At macro scales, mercury invasion and X-ray tomography give a macro pore contribution at 7 μm. We used a non-invasive multi-scale NMR method including high field spectroscopy with high power probes, FFC relaxometry and diffusometry by the pulsed field gradient (PFG) method. Other complementary techniques like conductivity and X-ray tomography were also used. A key point of our work is the *in situ* control of the RH that allows probing different length-scales by the techniques adapted to the scale of interest.

Dry samples and moisture micro-dynamics. We present in Figure 2.1 the high field ^{1}H NMR spectroscopic data of a dry CPG sample at 360MHz in a static probe. We show the raw experimental spectrum (1) of the dry sample and the analysis based on the sum (2) of two Voigt-profiles components (3 and 4). The peak (3) is an almost Lorentzien peak of relative intensity 57% characteristic of a fast molecular motion. However, the line width of 2 kHz of such a peak is not compatible with a liquid line shape. The peak (4) is almost a Gaussian peak of 4.7 kHz line width typical of static

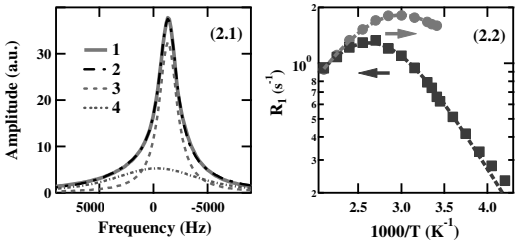

Figure 2. (2.1) ^{1}H NMR spectra of a CPG sample at 25°C (1) and its best fit (2) sum of two Voigt-profiles (3,4). **(2.2)** R_1 temperature dependence during heating (squares) and cooling (circles) with their best fits (dashed curves).

dipolar interaction. A second moment analysis of the Gaussian contribution leads to a static average distance between silanol groups of 0.35nm. This distance is close to the one found in the 100 face of cristobalite silicate (Iler). Moreover, we have analyzed the temperature dependence of R_1 at the same frequency during the increase (squares) and decrease (circles) of this temperature as shown in Figure 2.2. From a classical analysis of these temperature dependences (Abragam), we obtain a distance of minimal approach of 0.2nm between protons. From a precise description of the isolated silanol geometry (Saensawang) and the average distance between two silanol groups given above, we assign the 0.2nm value to inter-protons distance rotating around isolated silanol pairs. This analysis leads to the values of 1.17 10^{-10} m^2/s and 3.35 10^{-11} m^2/s for the surface diffusion coefficients during heating and cooling, respectively. Considering the Larmor frequency and these values of the diffusion coefficients, the protons explore a distance of the order of the nm. For a dry sample, such a dynamical process, about two orders of magnitude slower than the bulk water, is drastically confined by the hydric state.

Hydrated sample and meso-dynamics. We use the NMRD of longitudinal relaxation rate R_1 for studying the dynamics of the proton species at meso-scale close to the solid/liquid interface. We show in Figure 3, the NMRD profiles of the CPG sample at 25°C under an atmosphere with RH=97% which corresponds to the moisture state with silanol and water exchangeable protons. In this experiment, the longitudinal magnetization decay presents a bi-exponential behavior characterized by a fast (circles) and a slow (squares) component with 88% and 12% contributions, respectively. The dispersion over more than a decade for the two components suggests an interpretation in terms of proton transport at meso-scale. These profiles present a plateau at low frequency and a power law, $R_1 \propto 1/\sqrt{f}$, at high frequency. These two NMRD profiles can be fully reduced to a single one by a simple relaxation efficiency rescaling over the whole frequency range. This reveals a biphasic fast exchange process between surface and volume controlled by the same dynamics at the surface of the sample. For the hydrated case these two relaxation efficiencies thus evidence two pore-size populations. The observation of an order of magnitude difference between the fast and slow relaxation rates profiles gives the surface to volume ratio between the meso-porosity at about 6 nm and the Kelvin radius of 38 nm at RH = 97% in large pores of 7 µm. The power law of the NMRD profiles at high frequencies is typical of the $1/\sqrt{f}$ regime of the intermittent surface dynamics model through a succession of Brownian relocations in the proximity of a finite surface (Levitz, 2003). The other frequency regime at higher frequency i.e. $1/f$ and $1/f^{3/2}$ cannot be observed here due to the spectrometer limitation. As shown by the

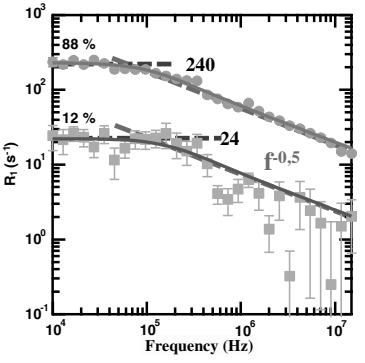

Figure 3. ^{1}H NMRD plots of a CPG sample at 25°C and RH=97%. The longitudinal magnetization decay follows a fast (circle) and slow (square) regime. Continuous curves represent the best fits obtained with the model given in the text.

continuous curves in Figure 3, we have analyzed these profiles with a model that takes into account the two asymptotic behaviors (Chemmi, 2011). This model introduces two time scales. The first one τ_m takes into account the intermittent dynamics in the proximity of the pore surface. The second one, τ_s, reports the finite time of residence at the surface. This analysis leads to τ_m=93ps and τ_s =0.84µs. Since the relaxation behavior is completely controlled by the biphasic fast exchange regime between the surface and bulk, we can use the same distances as in the ones found above in the dry sample. The correlation time τ_m and the 0.35 nm hopping distance lead to a meso-scale diffusion coefficient of 3.5 10^{-10}m^2/s. During τ_s the proton species explore an average distance $\langle r \rangle \approx (4D\tau_s)^{1/2}$ = 34.3nm which is of the order of the Kelvin radius 38nm for RH=97%. For a hydrated sample, such a dynamical process, about one order of magnitude slower than the bulk water, is again confined by the hydric state. As this hydric state has a characteristic length corresponding to the kelvin radius of 38nm at RH=97%, the diffusion process is an order of magnitude more efficient than in the dry sample but an order of magnitude smaller than bulk water. Considering again the Larmor frequency from 20 MHz to 10 kHz and the value of the diffusion coefficient, the protons explore a distance from 8 to 360 nm respectively. This range, which covers the whole IUPAC meso-scale range, illustrates the efficiency of the FFC method to characterize the meso-dynamics controlled by relative humidity.

Saturated sample and macro-dynamics. A CPG saturated with water was used to explore the moisture transport at macro-scale. The diffusion coefficient of confined water is measured at 298K by PFG using a stimulated echo pulse sequence which allows exploring diffusion on a time scale comparable to the longitudinal relaxation time (Callaghan). The diffusion coefficient dependence D(Δ) with the inter echo duration Δ is reported as diamonds in Figure 4. At short time D tends to the bulk diffusion coefficient D_0 = 1.94 10^{-9} m^2/s of the fluid and at long time D tends to the average diffusion coefficient at macro-scale D_∞ = 1.07 10^{-9} m^2/s of the fluid inside the pore network. Then the NMR tortuosity $\tau_{NMR} = D_0/D_\infty$ = 1.81 characterizes the limitation of the diffusive transport by the porous media (Dullien). This experimental tortuosity τ_{NMR} can be impacted by the geometry at all scales and by any adsorption phenomena. Here D_0 is obtained measuring the diffusion coefficient of the supernatant to avoid eddy current problem at short time. In figure 4, the dashed horizontal lines show the average value of D_0 and the asymptotic value D_∞ at long time. Wavelength phase encoding and diffusion length reached during Δ are two ways for evaluating the explored range. In this experiment, the wavelength is scanned from 18 to 368 µm and the diffusion length varies from 8

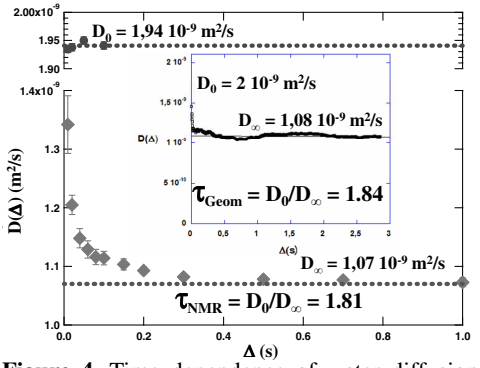

Figure 4. Time dependence of water diffusion coefficient inside CPG (diamond) measured by PFG and its asymptotic behaviors (dashed lines). Dynamic Brownian simulation inside the CPG macro-pore network (inset).

µm to 80 µm (Chemmi, 2011). These ranges underline the efficiency of the PFG method to explore the macro-dynamics of fluids. To obtain a geometric tortuosity factor τ_{Geom}, we have registered an X-ray tomography image of a CPG sample with a 0.7 µm resolution. After segmentation of this image, the macro-pore network was extracted and analyzed (Tariel) (Chemmi, 2011). The time dependence of D with time Δ was computed by dynamic Brownian simulation inside the macro-pore network and is reported in the inset of figure 4. This dependence leads to τ_{Geom} = 1.84 very near the experimental value τ_{NMR} = 1.81. This quasi perfect correspondence demonstrates that porosity below 0.7 µm and adsorptions do not impact the moisture transport at macro-scale. In fact the non-wettability of the surface in this CPG sample was reported elsewhere (Chemmi, 2013). Therefore, in this sample, the water diffusion is mainly controlled by the geometry (morphology and topology) of the macro pore network. Such results, which can be obtained only with this sample saturated by water, demonstrate the drastic impact of the hydric state of the sample and the RH on moisture transport. In this saturated state the diffusivity D_∞ corresponds to the diffusivity of the bulk water limited by the geometric tortuosity at macro-scale which is not so far from unity.

APPLICATION TO CEMENT-BASED MATERIALS

A robust NMR method for probing the hydric state of cement-based materials. A cement paste is prepared at 20°C by mixing anhydrous grey CEM I powder and distilled water with a water-to-cement ratio w/c=0.5. After 24h, the material is kept in saturated lime water solution. After five days of hydration, the evolution of the longitudinal nuclear magnetization $M_z(\tau)$ is recorded at 298 K as shown by the square data in Figure 5.1 using inversion recovery experiments at 360 MHz proton Larmor frequency. Such an evolution can be analyzed by Inverse Laplace Analysis (ILA) (Inset, Figure 5.1) and leads to the longitudinal relation times T_1 distribution of the proton populations as shown by circles in Figures 5.2. From this T_1 distribution a $M_z(\tau)$ magnetization evolution is computed and presented as continuous curve in Figure 5.1. The dashed lines on Figure 5.2 represent the power law analysis of these distributions. According to the biphasic fast exchange model, T_1 is linearly proportional to the average pore sizes for fully saturated pores.

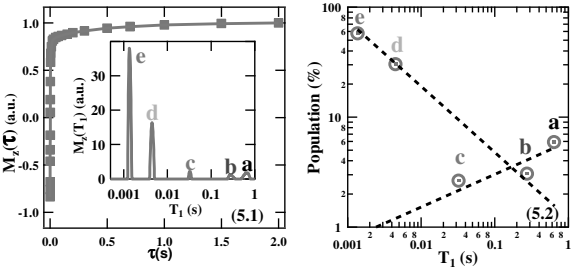

Figure 5. (5.1) Evolution of ^{1}H longitudinal magnetization $M_z(\tau)$ (squares) in CEM I paste at 360 MHz and its ILA curve (inset). Computed $M_z(\tau)$ evolution (continuous curve) **(5.2)** T_1 distribution (circles) coming from surface peaks of ILA curve. Analyze by power law (dashed lines).

In consequence the T_1 distribution shown in Figure 5.2 becomes the pore sizes distribution and characterizes the hydric state of the paste. We have shown in previous publications (Plassais) that the power law with a negative exponent of -0.6 (c, d, e) can be assigned to a surface distribution of pores hierarchy sizes in the micro, meso

length scale range. In Figure 5.2, the ratio between the three successive T_1 (e), (d) and (c) are compatible with the ratio of pore sizes (1.8nm/5nm/50nm) found in earlier work on similar materials (Plassais). Using the same ratio rule for (b) and (a) would lead to 380nm/860nm ratio corresponding to macro-pore sizes. However, in this length-scale, the power law presents a positive exponent of 0.3 which can be assigned to a volume distribution by opposition with the surface distribution associated at micro meso scales. Last, one notes on the inset in Figure 5.1 that the (a) and (b) shapes of the ILA peaks are more distributed than the (e), (d) and (c) ones. Both the concomitant change of exponents and shapes of the ILA peaks reveal the non-fully saturations of the large pores which makes sense since macropores have sizes larger than the Kelvin radii at usual RH. This change shows that the cement paste exhibits a multi-scale distribution of pore sizes which covers the two limiting factors of moisture transport described above, namely geometric confinement at micro-scale and RH at meso and macro scales. This result shows that a complete analysis of the evolution of the longitudinal magnetization is a powerful tool to probe the hydric state of cement-based materials.

Moisture transport across meso-scale porous network. From X-ray tomography records of a gray CEM I (w/c=0.5) obtained 34 h, 83 h and 150 h after hydration with a resolution of 0.7 µm, macro-pore networks are extracted and retraction graphs composed of α_0 vertex and α_1 paths are computed from these networks as well as the porosity above 0.7 µm (Levitz, 2012). The connection number $C_t = -(\alpha_0 - \alpha_1)/\alpha_0$ which is an intensive parameter, allows to characterize the cement past setting by reporting the dependence of C_t with the macro-porosity (Figure 6.1). After 100 h C_t becomes strongly negative showing a depercolation of the macro pore network since $\alpha_1 < \alpha_0$. So the macro pore network cannot ensure alone the moisture transport. Using an original method described elsewhere (Chemmi, 2011), Figure 6.2 presents the dependence of the electrical tortuosity $\tau = \varepsilon\sigma^0/\sigma_\infty$ with NaCl concentration in water of

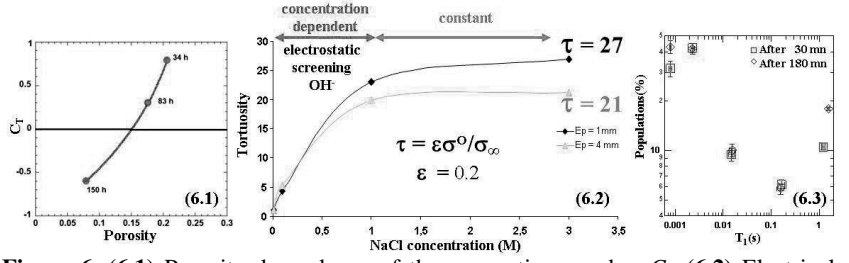

Figure 6. (6.1) Porosity dependence of the connection number C_t. **(6.2)** Electrical tortuosity *vs* NaCl concentration in water. **(6.3)** T_1 distribution of two years aged gray CEM I 30 (square) and 180 mn (diamond) after RH modification around the sample.

a hardened gray CEM I paste (w/c = 0.35) aged during two years in its endogenous humidity. In the expression of τ, ε, σ^0 and σ_∞ stand for the total porosity, the conductivity of the bulk and confined saline solution respectively. The low dispersion of the values of the tortuosity of 27 and 21 with the thickness of 1 and 4 mm of the sample shows that the measure captured the intrinsic tortuosity of the cement paste. Although this tortuosity is higher than that found in the sample CPG, it proves that the moisture transport stays efficient all over the sample even after two years of aging. Given the depercolation after four days, this measure of tortuosity on a two years aged

sample, shows that networks of micro and meso pores are involved in moisture transport on macro-scale. Figure 6.3 reports the T_1 distribution of the same two years aged cement past where we have modified the hydric state by introducing distilled water in a reservoir just above the sample. The square and diamond data was recorded 30 and 180 mn after the change of the hydric state surrounding the sample. On the one hand the hydric state at meso scale does not change; on the other hand the hydric state at macro scale evolves. The increase of both T_1 and the corresponding proton population indicates the filling of macro pores. Since, as mentioned above, the meso pores are not isolated, they are already full after 30 minutes of changing the moisture surrounding. Therefore this last experiment illustrates the impact of both pore size and RH on the hydric state and moisture transport in cement-based materials.

CONCLUSION

Using a multi-scale NMR platform and porous silica with controlled pore size distribution, we separate the impact of the pore size and RH factors on the moisture transport. Then we introduce the T_1 distribution as a robust multi-scale tool to characterize the hydric state and moisture transport of several cement pastes. Given the separation of the effect of the two preceding factors, we illustrate the use of the T_1 distribution by describing the moisture transport in a two years aged cement paste.

REFERENCES

Abragam, A. (1961). “Principles of Nuclear Magnetism.”, Oxford University Press.

Beck J.S., Vartuli J.C., Roth W.J., Leonowicz M.E., Kresge C.T., Schmitt K.D., Chu C.T.-W., Olson D.H., Sheppard E.W., McCullen S.B., Higgins J.B.Schlenker J.L. (1992). “A new family of mesoporous molecular sieves prepared with liquid crystal templates”. *J. Am. Chem. Soc.*, 114(27), 10834-10843.

Brownstein, K. R., Tarr C. E., (1979) “Importance of classical diffusion in NMR studies of water in biological cells” *Phys. Rev. A.,* 19(6), 2446-2453

Callaghan P.T. (2011). “Translational Dynamics & Magnetic Resonance”, Oxford University Press.

Chemmi H. (2011). “Diffusion multi-échelle et sorption hydrique dans les matériaux cimentaires” *Ph.D. Thesis*, Ecole Polytechnique.

Chemmi H., Petit D., Korb J.-P., Denoyel R., Levitz P. (2013). “Impact of wettability on moisture transport at mesoscale in porous materials” *Micropor. Mesopor. Mater.*, http://dx.doi.org/10.1016/j.micromeso.2013.02.045

Dullien F.A.L. (1979). “Porous Media, Fluid Transport and Pore Structure”, Academic Press.

Gerschel A., (1995). “Liaisons Intermoleculaires”, InterEditions.

Godefroy S., Korb J.-P., Fleury M. Bryant R.G. (2001). “Surface nuclear magnetic relaxation and dynamics of water and oil in macroporous media” *Phys. Rev. E* 64(2), 021605 1-13.

Iler R.K. (1979), “The Chemistry of Silica”, John Wiley & Sons.

Kimmich R, Anoardo E. (2004). “Field-cycling NMR relaxometry” Progress in NMR Spectr. 44(3-4), 257-320

Levitz P., Korb J.-P., Petit D., (2003). “Slow dynamics of embedded fluid in mesoscopic confining systems as probed by NMR relaxometry” *Eur. Phys. J. E* 12(1) 29-33 (2003)

Levitz P., Tariel V., Stampanoni M., Gallucci E. (2012). “Topology of evolving pore networks” *Eur. Phys. J. Appl. Phys.* 60, 24202 1-9

Nakanichi, K. (1997). “Pore structure control of silica gels based on phased separation,” *J. Porous Materials,* 4, 67-112.

Plassais A., Pomies M.-P., Lequeux N., Korb J.-P., Petit D., Barberon F., Bresson B. (2005). “Microstructure evolution of hydrated cement pastes”, *Phys. Rev. E*, 72, 041401 1-8.

Tariel (2009) “Image analysis of cement paste: relation to diffusion transport” *Ph.D. Thesis*, Ecole Polytechnique.

Tourné-Peteilh C. (2004). “Etude de l'incorporation de l'ibuprofène dans des matériaux mésoporeux siliciques à tensioactifs structurants: caractérisations et propriétés de liberation” *Ph.D. Thesis*, Université de Montpellier 1.

Water Isotherms, Shrinkage and Creep of Cement Paste: Hypotheses, Models and Experiments

Hamlin M. Jennings[a;b], Enrico Masoero[a;b], Matthew B. Pinson[a;d], Elena G. Strekalova[a;b], Patrick A. Bonnaud[a;c], Hegoi Manzano[f], Q. Ji[g], Jeffrey J. Thomas[h], Roland J.-M. Pellenq[a;b], Franz-Josef Ulm[a;b], Martin Z. Bazant[a;d], and Krystyn J. Van Vliet[a;c]

[a]Concrete Sustainability Hub, [b]Department of Civil and Environmental Engineering, [c]Department of Materials Science and Engineering, [d]Department of Chemical Engineering,
Massachusetts Institute of Technology, Cambridge, MA 02139
[f]Molecular Spectroscopy Laboratory, Department of Physical Chemistry, UPV/EHU, Barrio Sarriena s/n, 48940 Leioa, Bizkaia, Spain
[g]Inspur Group, State Key Laboratory of High-End Server & Storage Technology, Jinan, Shangdong, P. R. China
[h]Schlumberger-Doll Research, Cambridge, MA 02139

ABSTRACT

Cement paste has a complex mesoscale structure, and small changes in its pore network potentially causing large variation in measurements such as the water isotherm (also nitrogen). We deconvolute the water isotherm with the help of advanced computational techniques, hypotheses, and a re-examination of published data. The pore system is divided into four different categories, each containing water with its own physical properties. By viewing the highly interdependent roles of water in each of the pore categories as a system, new insights are gained regarding possible mechanisms that control drying shrinkage and creep, and experimental strategies for verification.

BACKGROUND

While it is widely accepted that mobile and evaporable water can be divided into several distinct pore categories, (i.e. interlayer, gel, capillary), each of which plays an identifiable role that controls properties, there remains significant confusion. Over the years a standard approach to characterizing porous solids, analysis of sorption isotherms, has been applied to cement paste without widely accepted interpretation. The goal, however, of translating information from the water isotherm to a deep understanding of microstructure has not been realized in spite of many decades of research effort. Some of the reasons for this include:

1. Isotherms have a strong dependence on adsorbate: For example BET surface area using nitrogen varies from 20 – 60 m^2/g while using water gives about 200 m^2/g. This paper will only discuss the water isotherm.
2. The shape of the isotherm depends strongly on specimen preparation. The BET surface area for nitrogen is strongly dependent on method of drying. The water isotherm has an unusual hysteresis at relative pressures below 50%, and the shape of this hysteresis depends on specimen preparation.
3. Drying shrinkage strain exhibits a very unusual hysteresis referred to as the "upside down" behavior (Jennings) and there is no relaxation of the bulk sample due to an unstable meniscus.

To address these issues we analyze each pore category with the goal of identifying specific roles and influences on drying shrinkage, and implications for creep. These categories are dictated by the huge range of pore size in cement paste, ranging from sub nanometer to micron, or a span of 10^4, and noting that the physics of water in different size pores depends on size. It is also noteworthy that all of the categories are already discussed in the literature, and we propose here only to consider them together in a new way. The pore system in C-S-H gel, the glue that contains all of the smallest pores in cement paste, has been divided into several categories, depending on size, but separated by physical properties of contained water and dissolved ions, and discussed relationships to drying shrinkage and creep. Specifically the role of the small gel pore, or the pore spaces where the particles contact each other, are of particular interest. These categories are shown in Fig. 1.

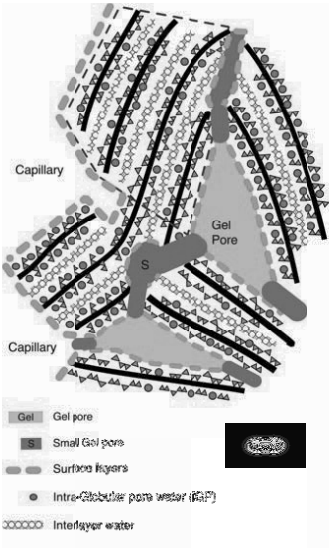

Fig. 1. Schematic of nanometer-scale calcium-silicate-hydrate (C–S–H) gel structure, and associated locations for water. Red triangles are the silicate tetrahedra within the silicate chains, thick black lines are calcium oxide layers within the solid C–S–H. With the simplification that the water content inside the solid C–S–H particles is constant under most conditions, the model focuses on the water in gel pores, the size and volume of which has been discussed elsewhere. There are three identifiable pore types outside the solid C–S–H: 1) Small open spaces between particles (gel pores), 2) defect regions where solid C–S–H particles come into imperfect contact (small gel pores), and 3) much larger capillary pores. Arrow is one nm.

THE PARTICLES AND CONTAINED WATER

We here treat the water inside of the particles separately, with a hypothesis that greatly simplifies the water isotherm. From the perspective of the colloid model there are two types of water within the particles. The hypothesis is that this water (and associated properties of the particles) remains constant as long as the relative pressure outside of the particles is maintained above about 20% (CMII and CCR). The only way of testing this hypothesis (isolating the behavior of the particles of C-S-H independent of the gel pores outside of the particles) is with accurate detailed models. Starting with the model (Pellenq) and Grand Canonical Monte Carlo (GCMC) and Molecular Dynamics (MD) an isotherm for the particles can be simulated as shown in Fig 2.

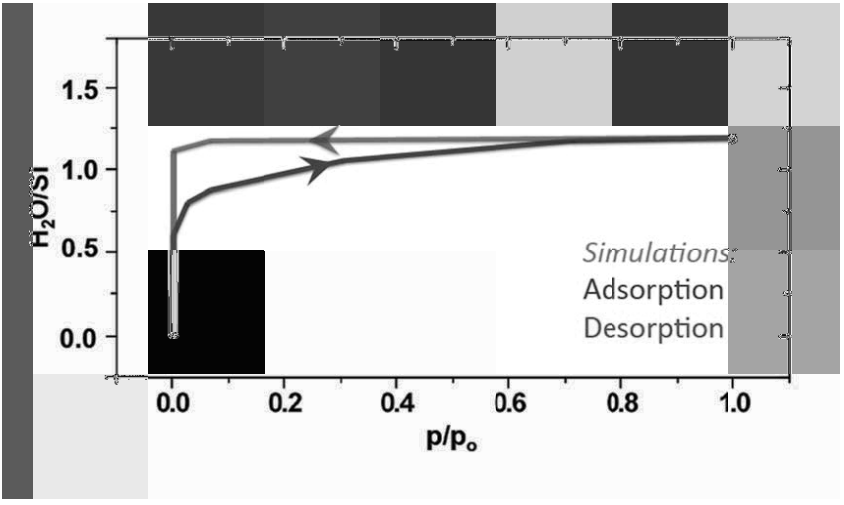

Fig. 2. Simulated isotherms, predicted from atomistic simulations of single C-S-H particles equilibrated sequentially over a range of partial pressures. This desorption/adsorption hysteresis represents loss and gain of intraparticle water from the C-S-H particle, equilibrated initially at 100% RH (i.e., p/po = 1.0). This sharp transition in water content upon desorption in predicts a water mass loss of 7%.

As can be seen from this simulation water does not leave the particle until very low relative pressure, and it also only partially re-enters the particle resulting in a low-pressure hysteresis associated only with the particles. This provides an important simplification when interpreting the water isotherm, but it also suggests that if the pores outside of the particles are of interest, the isotherm should be measured on samples that have not been dried below about 20%. Thus we have proposed that one of the obvious unusual features of the water isotherm for cement paste, the low pressure hysteresis, is addressed by assignment to evaporable water inside the particles, which does not leave until very low pressures. Fig 3 shows

isotherms for Vycor glass and cement paste. The dotted arrow in Fig 3, suggests a possible adsorption path from 20% rh. The hypothesis that the particles remain constant during drying and under creep is further discussed below.

THE GEL PORES: TWO CATEGORIES

Two important pore spaces for water are identified in the gel porosity: 1) the irregular spaces created by mis-orientation of contacting particles (small gel pores in Fig 1.) and 2) the pores formed between the packed particles in the LD and HD arrangements. Water in each of these pore spaces has a unique influence on drying shrinkage.

A striking feature of drying shrinkage of cement paste is that, unlike other materials such as Vycor glass, the strain for adsorption is always below(smaller) than for desorption, as shown in Fig 3: we refer to this as the "upside down" behavior. This means that in cement paste, the extra water present during desorption reduces

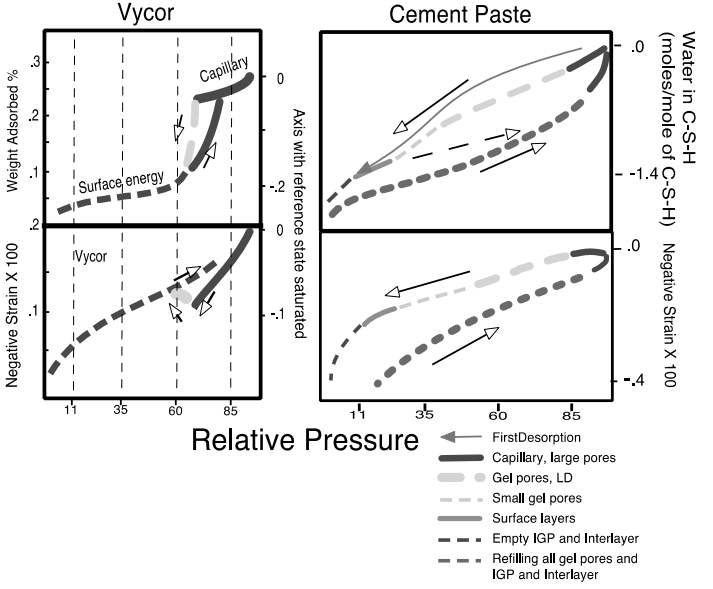

Fig. 3. Water isotherms and strains of Vycor and cement paste. The isotherm for cement paste exhibits a distinct hysteresis over the full relative pressure range. Changes in the packing of particles can be seen between first and second drying. The strain for cement paste is unusually always less on drying (reference is full saturation) than on wetting, referred to here as the "upside down" behavior. There is no evidence of relaxation (reduced strain) when a meniscus becomes unstable, as there is with Vycor glass.

instead of increases shrinkage. This, coupled with the observation that there is almost no evidence for relaxation (expansion) of cement paste at intermediate relative pressures when water is lost from the structure, suggests that there is some sort of overriding expansive pressure: a disjoining pressure.

Disjoining pressure is the origin of swelling in clays such as montmorillomite and certainly must be an important contribution to the "upside down" behavior of cement paste. It is the result of water in tightly confined spaces, and in the case of water hydrophilic surfaces that tend to attract water, it pushes the surfaces apart. The disjoining pressure is defined by:

$$P_{disj} = P_{pore\ pressure\ in\ confined\ space} - P_{bulk}$$

The pore pressure in the bulk is ambient when the pores are saturated. However, for a partially saturated material at higher pressures the pore pressure is dictated by capillary pressure. For a partially saturated material, the bulk pressure is dictated by capillary pressure. Agreement with experiment has been achieved with the following expression for the disjoining pressure in the pores:

$$P_{disj} = -S\left(e/\varepsilon\right)$$

where S is a function of the surface tensions between liquid, solid and vapor (always positive), e is the thickness of the adsorbed layer (a function of relative pressure), and ε is approximately equal to interatomic distance (~0.2 nm). The disjoining pressure increases with relative pressure, interpreted here as the particles being pushed apart as the relative pressure increases. The above equations are simple expressions of an equilibrium state, so what causes the hysteresis? This question has been explored by two modeling approaches.

The first is a thermodynamic approach (discussed in more detail in this conference) that takes into account Langmuir adsorption, and Kelvin condensation. Adsorption and desorption are simulated for a model system with a range of pore sizes, and importantly, during desorption the larger pores in the interior are blocked from completely emptying if they are connected to the surface only through smaller pores. This mechanism is known as pore blocking. During adsorption the pores fill under more or less equilibrium conditions. A schematic of a result is shown if Fig 4. This causes the adsorption branch to be below the desorption branch. Fitting the isotherm produces a model pore system, which characterizes the paste, and provides quantitative parameters that can be used to explore relationships to properties.

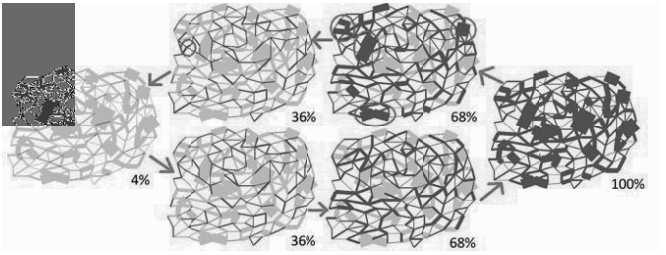

Fig. 4. Schematic illustration of desorption and adsorption of water from a model C-S-H pore system. Blue links represent filled pores, gray links represent mostly empty pores. The width of a link is proportional to pore radius. During desorption (right to left along top figures) some pores remain full below their equilibrium rh value, due to the absence of a continuous path of empty pores leading to the exterior. Some examples of such pores are circled. During adsorption (left to right along bottom figures) some interior pores do not fill because of pore blocking, resulting in hysteresis.

The second approach combines a model that simulates the structure of packed C-S-H particles (Masoero), with a model that simulates the water in the pore system using a mean field density functional analysis of average density of water in the pore system. During desorption water is emptied but some interior pores remain blocked, while during adsorption the water re-enters all of the pores under more or less equilibrium relative pressures (shown in Fig 5). Again, the hysteresis is captured.

It is important to note that neither of these models (not shown here) captures a low pressure hysteresis. Again, this suggests that the low pressure hysteresis can be assigned to water inside of the particles.

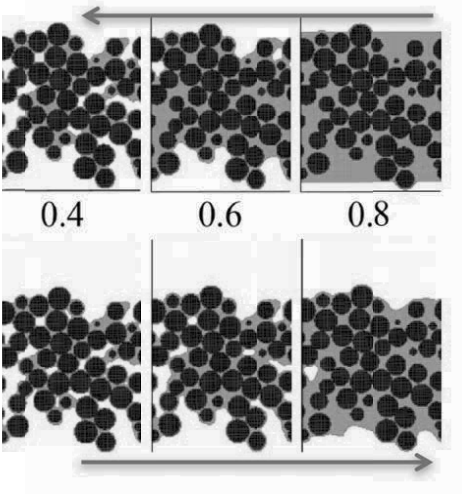

Fig. 5. Cross-sectional snapshots of the simulated particles (black) during desorption and adsorption of water modeled by density functional theory. The important point is that the pores contain more water during desorption than during adsorption.

REVERSIBLE DEFORMATION: UPSIDE DOWN

In the following discussion it is important to note that the reference for strain is saturation. As a consequence, the strain has always a negative value. Both experiment results (isotherm) and the models described above that capture the hysteresis of the water isotherm, clearly show that the water content of the gel pores at any particular relative pressure is higher during desorption than during adsorption, primarily because of pore blocking during desorption.

This increased percentage of full pores, coupled with disjoining pressure that is a direct function of water content in the gel pores, providing a swelling pressure, explains the "upside down" behavior of the strain, compared to Vycor glass. Disjoining pressure first documented for colloids and is responsible for swelling, it must be active in the small gel pores, pushing the particles apart. These contact regions are analogous to grain boundaries and probably represent regions of high energy due to lattice mismatch and very imperfect structure. If the value of disjoining pressure depends on the water content of the adjacent pores, it follows that the pressure will be greater during desorption. In carefully controlled experiments (Beltzung) the disjoining pressure is greater during desorption (almost constant) than during adsorption. During desorption the capillary underpressure, therefore, causes shrinkage with a constant disjoining pressure during desorption, and re-establishing disjoining pressure causes swelling during adsorption when the capillary has not been re-established.

Taking the particle nature of C-S-H to be an important part of its character, there must be significant lattice mismatch at the contact regions, creating the small gel pores. This region is therefore a good candidate for the development of relatively high eigenstress, akin to "microprestress" (Bazant). Combining this structural description of specific regions of water in the pores with poromechanics formulations could allow capturing the shrinkage down to a relative pressure of 50% directly. Below 50% the small gel pores and surface layers only a few molecules thick cause shrinkage by mechanisms other than pore pressure, including surface tension. Below 20% the particles start to empty, which causes them to shrink.

IRREVERSIBLE DEFORMATION

Analysis of neutron scattering experiments (Thomas) has shown that the particles do not change in composition when dried and resaturated, but there is strong evidence for rearrangement of particles during first drying and rewetting. Furthermore, as implied above, the contact regions between the particles is likely to be the point where large deformations, like relative sliding can occur. High positive relative pressures within these small gel pores will assist this process, consistent with the observation that, at constant humidity, creep is highest at high relative pressures.

The region of particle contact has a direct analogy to grain boundaries and therefore to grain boundary sliding in other materials. It is a likely location where stress could be reduced over time (years) with a commensurate reduction in creep under load, or the aging term not associated with increased degree of reaction (Bazant).

CONCLUSIONS

The following conclusions are drawn from models, in consort with hypothesis and experiments.

1. A case has been made that the low pressure hysteresis of the water isotherm is due to water leaving the particles and not reversibly re-entering. This provides an important simplification in that the influence of water on shrinkage and creep is mainly due to gel pores. Subtracting isotherm due to particles may reduce the isotherm to a more conventional form.
2. The high pressure hysteresis is due primarily to pore blocking, with water not able to empty from interior pores when the only channel to the exterior has smaller passages than the pore being emptied.
3. The “upside down” strain on drying and rewetting is due to disjoining pressure that is a direct function of the water content. This prevents deformation on drying. This reduces considerabley the deformation on drying.
4. Reversible strain on drying can be modeled by poro-mechanics down to a relative pressure of 50%.
5. Irreversible strain is due to rearrangement of particles and not to deformation of the particles.
6. Aging may be due to an increased bond strength with passage of time where particles touch at the small gel pores. Like grain boundaries this may be a region of high energy – or adopting the terminology of Bazant et al. (Bazant), a region of micro-prestress, that relaxes by local rearrangement with time.

REFERENCES

Bazant, Z. P., Hauggard, A. B., Baweja, S., and Ulm, F. J. (1997). "Microprestress-solidification theory for concrete creep. I. Aging and drying effects." *Journal of Engineering Mechanics,* 123, 1188-1194.

Beltzung, F., and Wittmann, F. H. (2005). "Role of disjoining pressure in cement based materials." *Cement and Concrete Research,* 35(12), 2364-2370.

Jenning, H. M., Masoero, E., Pinson, M. B., Strekalova, E. G., Bonnaud, P. A., Manzano, H., Ji, Q., Thomas, J. J., Pellenq, R. J.-M., Ulm, F.-J., Bazant, M. Z., and Vliet, K. J. V. (submitted). "Porosity of Cement Paste: Resolving Water Isotherms and Drying Shrinkage with Atomic to Mesoscale Models." *Cement and Concrete Research*.

Masoero, E., Gardo, E. D., Pellenq, R., Ulm, F. J., and Yip, S. (2012). "Nanostructure and Nanomechanics of Cement: Polydisperse Colloid Packing." *Physical Review Letters*, 109(15), 155503 1-4.

Pellenq, R. J.-M., Kushima, A., Shahsavari, R., Vliet, K. J. V., Buehler, M. J., Yip, S., and Ulm, F.-J. (2009). "A Reasistic Molecular Model of Cement Hydrates." *Proceedings of the National Academy of Science USA*, 106(38), 16102 - 16107.

Thomas, J. J., Allen, A. J., and Jennings, H. M. (2008). "Structural changes to the calcium silicate hydrate gel phase of hydrated cement with age, drying and resaturation." *Journal of the American Ceramic Society*, 91(10), 3362-3369.

Diffusion Properties of Sodium and Lithium Silicates through Cement Pastes and its Mitigating Effect on Alkali-silica Reaction

Irfan Prasetia[1], Soyo Asano[2] and Kazuyuki Torii[3]

[1]Graduate School of Natural Science & Technology, Kanazawa University, Ishikawa, Japan, email: irfan@stu.kanazawa-u.ac.jp
[2]Graduate School of Natural Science & Technology, Kanazawa University, Ishikawa, Japan, email: soyosoyo @stu.kanazawa-u.ac.jp
[3]Dep. of Env. Design, College of Science & Eng., Kanazawa University, Ishikawa, Japan, email: torii@t.kanazawa-u.ac.jp

ABSTRACT

The experiments comprised through diffusion cell tests and mortar bar tests with sodium silicate (Na_2SiO_3) and lithium silicate (Li_2SiO_3) solutions, followed by a range of post-analysis such as DSC, XRD and EPMA. The diffusion coefficients of Na^+ ions were 10 times more than Li^+ ions. This result shows that lithium ions are better adsorbed into cement hydration products. The results of mortar bar tests backed up this finding. It was observed that, regardless of Li_2SiO_3 concentration, the specimens did not expand, which suggests no ASR occurrence. However, in the case of Na_2SiO_3 solution, a very interesting phenomenon occurred. Specimens immersed in 0.5 mol/L solution revealed a large expansion. In contrast, an early low expansion in the case of 2.5 mol/L Na_2SiO_3 solution was observed up to 7 days, but subsequently vanished. One explanation is that ASR occurs before CSH gel production halts the reaction process as confirmed by EPMA results.

Keywords: through diffusion cell test, lithium and sodium silicate compounds, diffusion coefficients, ASR mitigation.

1. INTRODUCTION

It is well known that sodium silicate (Na_2SiO_3) and lithium silicate (Li_2SiO_3) have been used in the concrete industry mainly as cement admixtures or sealants, to reduce the porosity and permeability of concrete, thus increasing its overall durability. The mechanism of these silicate-based compounds in concrete consists of its reaction with excess calcium hydroxide (CH), a by-product of cement hydration, leading to the formation of calcium silicate hydrates (CSH gel). By reducing the amount of available calcium hydroxide, they further improve the acid and sulphate resistance of concrete. In addition to the initial chemical reaction, the calcium silicate hydrate gels will also physically absorb the water, preventing it from being

transported through the concrete. However, there are some reports that the silicate-based treatments must not be based on sodium or potassium, which may exacerbate ASR. (NZ Transport Agency, 2010).

As in Japan, the crack injection and surface coating methods were being used for repairing damaged concrete due to ASR since 1988, but cracks and blisters on surface coating almost occurred within 5 years after repairing (Torii et. al, 2008). In Fig. 1 shows a bridge pier repaired with Na_2SiO_3 compound and subsequently re-damaged by a continuous expansion of ASR. A lot of cracks filled with ASR gel can be seen on the area below the expansion joint.

In addition, as for lithium in mitigating ASR, it is not clear whether the sodium or potassium in the ASR gel in concrete is replaced by the lithium supplied from the outside (Kawamura et. al, 2003). Moreover, in the past, only one supplier of lithium-based compounds exists in japan. Thus, this has driven the whole concrete industry into the usage of the highly expensive lithium nitrite ($LiNO_2$) for both, ASR mitigation and control of reinforcing steel bar corrosion (Andrade et. al, 2012).

Therefore, in order to propose a more economical and effective compound for mitigating ASR, the diffusivity of externally supplied lithium and sodium silicate compounds into cementitious materials were investigated. Furthermore, to assess the effects of lithium and sodium silicate compounds on the mitigation of ASR expansion, the accelerated mortar bar test according to ASTM C1260 was carried out for specimens immersed in low and high concentrated lithium and sodium solutions.

2. EXPERIMENTS

2.1 Materials

2.1.1 Diffusion cell test

Cement pastes were prepared with Ordinary Portland cement (OPC), and the water/cement ratio was set at 40%, which the latter is addressed as OPC-0.4. Electrolytes sources selected were Li_2SiO_3 and Na_2SiO_3 solutions. In both cases, the concentrations were set at 0.25 mol/L and 0.5 mol/L.

Figure 1. Bridge pier repaired with Na_2SiO_3 compound and subsequently re-damaged by ASR in Toyama Prefecture.

2.1.2 Mortar bar test

Crushed calcined flint produced from industrial raw materials in England was used as a reactive aggregate, with the grain size ranging from 0.6mm to 2.5mm, and cristobalite as the only reactive component. Regarding the chemical method in accordance to JIS A1145-2007, the dissolved silica content (Sc) and the reduction in alkaline concentration (Rc) were 1063 mmol/L and 70 mmol/L, respectively. Crushed limestone sand with 0.15mm to 5.0mm particle size was used as a non-reactive aggregate and considering the pessimum mixing ratio to this calcined flint, the mass ratio of calcined flint to crushed limestone sand was set at 25%:75% (Yamato et. al, 2009). Ordinary Portland cement (T Corporation, Ltd., density: 3.16 g/cm^3, Blaine specific surface area: 3300 cm^2/g) was used. The alkali content of the cement was 0.42%.

2.2 Test Methods

2.2.1 Diffusion cell test

The cement pastes were cast into PVC acrylic rings, 5mm thick and 30mm internal diameter, placed on glass plates, manually compacted and covered for one day to prevent early dryness and water loss. The cement pastes were then allowed to cure in $Ca(OH)_2$ saturated water solution for 7, 28 and 91 days, under a room temperature of 20ºC and 60% R.H. After diffusion cells were setup, the first sampling was performed after 24 hours and the procedure was repeated every 2 days afterwards. The ionic concentration was measured by a PIA-1000 ion analyzer.

2.2.2 Mortar bar test

In order to assess the effects of lithium and sodium silicate solutions on mitigating ASR expansion, mortar bar tests in accordance to ASTM C1260 method were conducted for specimens immersed in a low (0.5 mol/L) and high (2.5 mol/L) concentrated Li_2SiO_3 and Na_2SiO_3 solutions.

3. RESULTS AND DISCUSSION

3.1 Diffusion Cell Test

3.1.1 Diffusion starting time (DST)

Fig. 2 shows the results of DST subjected to diffusion tests of Li_2SiO_3 and Na_2SiO_3 compounds. In the case of Li_2SiO_3 solutions, DST at 28 days shows a delay compared with others, due to the absorption of Li^+ ions into the cement hydration products. Overall, DST was directly proportional to curing time, especially for 0.25 mol/L Na_2SiO_3 solution. It is also important to note that the determination of DST for Na_2SiO_3 solutions in the latter is fairly a difficult task due to Na^+ ions are immediately released from the pore solution of cement pastes. In addition, the diffusion of SiO_3^{2-} ions did not occur at all, regardless of diffusion solution or curing time, which suggests that it reacts completely with calcium hydroxide.

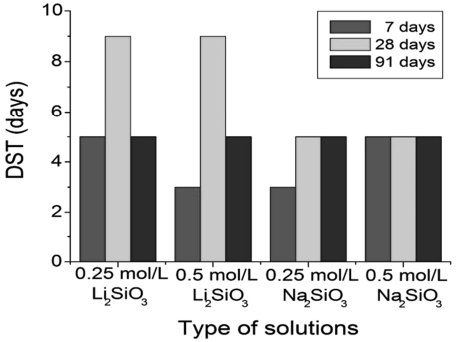

Figure 2. Diffusion starting time of Li_2SiO_3 and Na_2SiO_3 compounds

3.1.2 Diffusion coefficients (D_e)

The effective diffusion coefficients (D_e) of lithium (Li^+) ions from Li_2SiO_3 and sodium (Na^+) ions from Na_2SiO_3 solution in 7, 28 and 91 days cured OPC-0.4 specimens, calculated by Fick's 1st Law are shown in Fig. 3. The diffusion coefficients of Na^+ ions were 10 times more than Li^+ ions, and a slight reduction with curing time was observed in both cases. However, D_e of 0.25 mol/L Li_2SiO_3 was decreasing from 7 days curing time to 28 days curing time, but increased again over time. It might be due to the fact that the formation of calcium silicate have stabled after 28 days curing time. In addition, the result shows that a higher concentration tends to be better absorbed compared with lower ones.

3.1.3 Differential scanning calorimetry analysis (DSC)

Differential Scanning Calorimetry analysis (DSC) was carried out upon diffusion test completion, with a Thermo-plus DSC 8270 equipment. The temperature range was from 20ºC to 1000ºC, with a heating rate of 10ºC/min. The specimens were previously finely ground (<150μm) and vacuum dried for a minimum 24 hour period and each sample weight was set at 42 mg. DSC curves of OPC-0.4 specimens subjected to Li_2SiO_3 and Na_2SiO_3 diffusion tests at 91 days are shown in Fig. 4. The formation of ettringite (Ett) was confirmed by a peak between 100 and 130°C in all specimens. Consistent calcium silicate hydrates (CSH) peaks were observed in all specimens around 160°C to 170°C. Residual calcium hydroxide was confirmed by sharp peaks in the vicinity of 480°C. In the case of specimens subjected to Li_2SiO_3 diffusion test, the amount of residual CH was directly proportional to solution concentration, regardless of curing time. This could be an indication that the exchange ratio of Ca^{2+} in the calcium silicate hydrates by Li^+ ions from the diffusing solution increased with increasing solution concentration and led to the formation of lithium-calcium-silicate-hydrates with the lower Ca/Si ratio and higher Li/Si ratio. Small calcium carbonate peaks ($CaCO_3$) between 680ºC and 740ºC were observed. These peaks are due to material exposure to air and probable contamination of CH with CO_2 during the analysis.

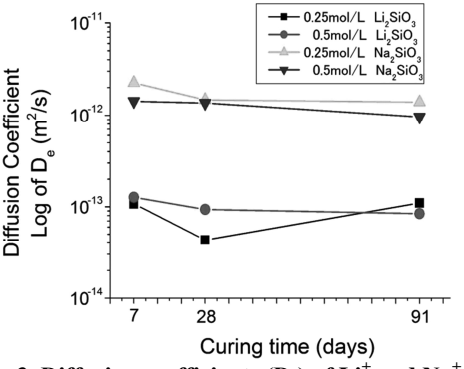

Figure 3. Diffusion coefficients (D_e) of Li^+ and Na^+ ions

3.1.4 X-ray diffraction analysis (XRD)

Powder X-ray diffraction analysis was conducted to investigate the formation of hydration products. The diffraction patterns were recorded by a XD-D1 diffractometer (Shimadzu). CuKα radiation was used at a voltage of 40 kV and a current of 20 mA. The measurements were carried out in a 2θ range of 5º to 40º, with a scan speed of 2 degrees per second. XRD patterns of OPC-0.4 specimens subjected to Li_2SiO_3 and Na_2SiO_3 diffusion tests at 91 days are shown in Fig 5. Etringite peaks (Ett) were observed at 8.8º, 15.6º and 23º in all specimens. Residual calcium hydroxide (CH) was confirmed by sharp peaks at 18º and 34º. Overall, the results obtained from XRD analysis are confirming the DSC analysis.

3.2 Mortar Bar Test

3.2.1 Expansion ratio of mortar bars

The expansion ratio of mortar bars immersed in these solutions is shown in Fig. 6. It was observed that, regardless of Li_2SiO_3 concentration, the specimens did not expand at all, which suggests no ASR occurrence. However, in the case of Na_2SiO_3 solution a very interest phenomenon occurred. Specimens immersed in 0.5 mol/L solution revealed an early expansion that reached 0.1% at 7 days, exceeded 0.2% at 14 days and surpassed 0.4% after 28 days period. Unlike the 0.5 mol/L Na_2SiO_3 solution, which at 80ºC is in the liquid state, 2.5 mol/L Na_2SiO_3 solution revealed a very high viscosity and remained in paste-like state up to 14 days. An early low expansion was observed up to 7 days, but this expansion subsequently vanished and the specimens actually retracted for the remainder of the experimental term. One explanation is that, at the early stages, the ability of this high-concentrated water-glass solution to penetrate the specimens is compromised, if we compare the expansion ratios between mortar bars immersed in 0.5 mol/L and 2.5 mol/L Na_2SiO_3 solutions at 7 days.

At a certain level, in the presence of highly reactive flint aggregates, the rise of alkalinity in the pore solution derived from the hydrolysis reaction between

Na_2SiO_3 and water to produce NaOH, which lead to an increase of OH^- in the solution, triggers the occurrence of alkali-silica reaction, as confirmed by the early expansion of specimens immersed in 2.5 mol/L Na_2SiO_3 solution. This reaction takes precedence, but as the steady supply of highly concentrated Na_2SiO_3 from the external source continues, the reaction between Na_2SiO_3 and $Ca(OH)_2$ takes place and surpasses the pace of alkali-silica reaction. The overwhelming amount of CSH gel produced engulfs and surrounds the ASR gel previous produced, and the ASR-induced expansion is suppressed. This phenomenon is different in nature to that observed in the presence of lithium compounds, because the highly reactive lithium prevents ASR occurrence in the first place, by reacting with CH and exchanging Ca^{2+} ions from CSH gel, thus covering the reactive particles with highly stable and durable layers of lithium-calcium-silicate-hydrates and halting any further steps towards alkali-silica reaction.

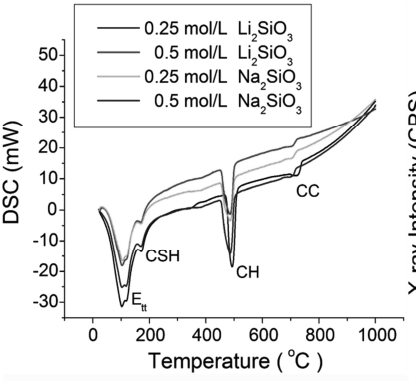

Figure 4. DSC curves of Li_2SiO_3 and Na_2SiO_3 diffusion test (curing time: 91 days)

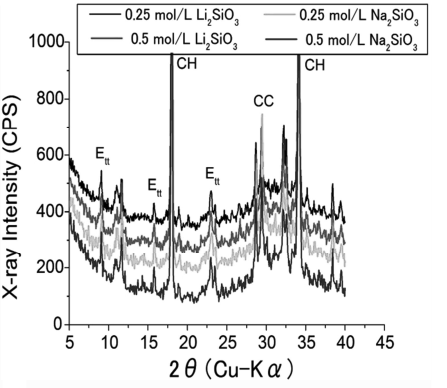

Figure 5. XRD patterns of Li_2SiO_3 and Na_2SiO_3 diffusion tests (curing time: 91 days)

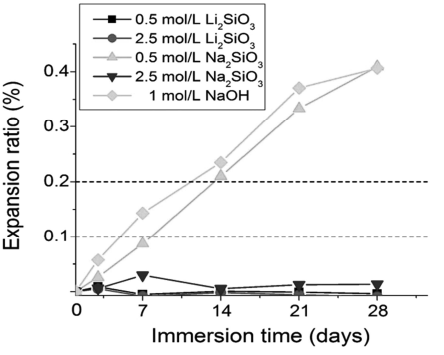

Figure 6. Expansion ratio of mortar bars immersed in 0.5 mol/L and 2.5 mol/L Li_2SiO_3 and Na_2SiO_3 solutions

3.2.2 ASR gel formation of mortar bars

After mortar bars test, a uranyl acetate fluorescence method of coloring area was carried out to measure ASR gel formation in mortar bars immersed in 0.5 mol/L and 2.5 mol/L Li_2SiO_3 and Na_2SiO_3 solutions. The image of ASR gel observation is shown in Fig. 7. Regardless of Li_2SiO_3 concentration, ASR gel was not detected at all, suggesting again, no ASR occurrence in these specimens. One of the interesting properties of lithium ions is that they tend to be incorporated into the cement hydrates to much greater extent than sodium and potassium ions (Feng et. al, 2005). This is one fundamental reason why lithium is effective in ASR prevention.

Moreover, in the case of specimens immersed in 0.5 mol/L Na_2SiO_3 solution, the whole cross-section is covered by dense spots of ASR-gel. Due to the lower Na_2SiO_3 solution, the amount of CSH gel is not enough to halt the ASR process. In addition, for specimens immersed in 2.5 mol/L Na_2SiO_3, ASR gel only observed in the inner-sections of the specimen. The huge amount of CSH gel produced has sunk the ASR-gel, but in the inner-section, where the highly concentrated solution has not reached, dense ASR gel spots can be seen.

3.2.3 Electron probe micro-analysis of mortar bars immersed in Na_2SiO_3 solution

In order to further understand the occurrence of ASR in specimens immersed in sodium silicate (Na_2SiO_3) solution, electron probe microscope analysis (EPMA) of thin sections was conducted for both, 0.5 mol/L and 2.5 mol/L samples. The mapping imagery of silica (Si) and sodium (Na) in the cross-section of mortar bars immersed in 0.5 mol/L and 2.5 mol/L Na_2SiO_3 solutions is shown in Fig. 8. EPMA results confirmed that ASR indeed occurred in these specimens, but was later suppressed in the outer-section of mortar bars immersed in 2.5 mol/L Na_2SiO_3 solutions. In the case of 0.5 mol/L solution, although ASR gel was observed covering the entire section, the amount of Na is quite low and is similar to the one observed in the inner-section of mortar bars immersed in 2.5 mol/L solution. But the reflections of Na in the outer-section were far higher, which combined with the low silica (Si) content in this part, suggests that ASR already occurred. High silica content in the inner-section of specimens immersed in 2.5 mol/L solution is indicative of un-reacted flint particles.

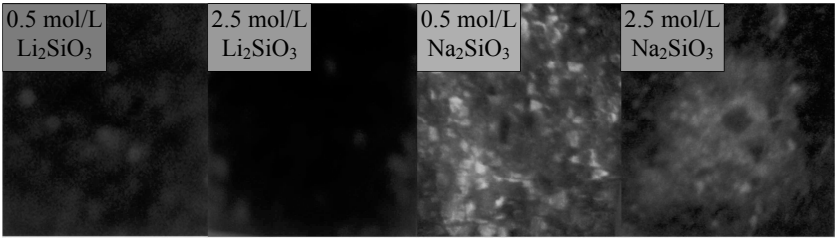

Figure 7. Observation of ASR gel formation in mortar bars immersed in Li_2SiO_3 and Na_2SiO_3 solutions by uranyl acetate fluorescence method (observed area: 25mm x 25mm)

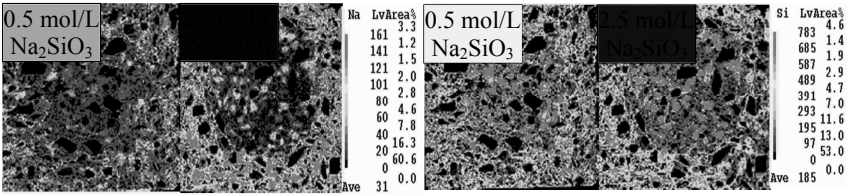

Figure 8. Mapping imagery of sodium (Na) and silica (Si) in mortar bars immersed in 0.5 mol/L and 2.5 mol/L Na_2SiO_3 solutions obtained by EPMA analysis (observed area: 25mm x 25mm)

4. CONCLUSIONS

(1) The diffusion starting time (DST) of Li_2SiO_3 and Na_2SiO_3 was fast around 5 days. However, in term of diffusion coefficients, Na^+ ions were 10 times more than Li^+ ions. This result could be indicative that lithium silicate reacts well and is better absorbed into the hydration products than sodium silicate.

(2) The diffusion of SiO_3^{2-} ions did not occur at all, regardless of diffusion solution or curing time, which suggests that it reacts completely with calcium hydroxide.

(3) Regardless of Li_2SiO_3 concentration, the mortar bar expansion tests show that the specimens did not expand at all, this suggests no ASR occurrence. Thus, it can be recommended for the mitigation of ASR-induced expansion in deteriorated concrete structures.

(4) Although Na_2SiO_3 compounds possess ASR-suppression properties like Li_2SiO_3 compounds investigated, it might not be recommendable for external supply application due to its poor diffusivity, unless it is in high concentration.

ACKNOWLEDGEMENT

The authors would like to express our deep gratitude to Dr. Eng. Osvaldo Andrade.

REFERENCES

Andrade, O., Prasetia, I., and Torii, K. (2012). "The diffusivity of lithium compounds through cement pastes and its effects on ASR mitigation." *Proc. of ASEA-SEC-1*, Perth, pp. 463-468.

Feng, X., Thomas, M.D.A., Bremner, T.W., Balcom, B.J., Folliard, K.J. (2005). "Studies on lithium salts to mitigate ASR-induced expansion in new concrete: a critical review." *Cement and Concrete Research*, Vol. 35, pp. 1789–1796.

Kawamura, M., and Fuwa, H. (2003). "Effect of lithium salts on ASR gel composition and expansion of mortars." *Cement and Concrete Research*, Vol. 33, pp. 913-919.

NZ Transport Agency. (2010). "The influence of surface treatments on the service lives of concrete bridges." *NZ Transport Agency*, Wellington.

Torii, K, Wasada, S, Sasatani, T, Minato, T. (2008). "A Survey on ASR-affected Bridge Piers with Fracture of Steel Bars on Noto Expressway." *Proc. of 13th Inter. Conf. on Alkali-aggregate Reaction in Concrete*, 1304-1311.

New experimental approach to study creep and shrinkage mechanisms of concrete on the nano-scale level

Harald S. Müller[1], Joerg-Detlef Eckhardt[2] and Michael Haist[1]

[1]Institute of Concrete Structures and Building Materials, Karlsruhe Institute of Technology, KIT, D 76128 Karlsruhe, Germany; PH +49 (721) 608-43890; FAX +49 (721) 608-48400; email: sekretariat-bt@imb.kit.edu
[2]Materials Testing and Research Institute, Karlsruhe Institute of Technology, KIT, D 76128 Karlsruhe, Germany; PH +49 (721) 608-44086; FAX +49 (721) 608-47796; email: eckhardt@mpa-karlsruhe.de

ABSTRACT

Small angle X-ray scattering analyses of the nanostructure of hardened cement paste proved to be a highly suitable method to study structural changes due to creep of the material during loading. The short term loading and creep experiments described in this paper were carried out on small hardened cement paste samples (10 x 10 x 0.4 mm³). The specimens were subjected to a compressive load in the plane of the platelets while being penetrated by an X-ray beam perpendicular to the platelet leading to a scattering of the X-ray beam. By using the Bragg's law for X-ray diffraction in combination with Porod's theorem for X-ray scattering these experiments allow for a direct insight into micro-structural processes on the 10^{-9} to 10^{-7} m scale occurring during shrinkage, creep and creep recovery of hardened cement paste specimen stimulated by in-situ drying, loading and unloading of the sample. Whereas previous experiments of the authors were limited to investigation in vacuum, similar experiments can now be performed at any climatic condition. The gained results indicate that creep of hardened cement paste under load leads to an increase of the inner specific surface of the material, probably related to inter-crystalline processes.

INTRODUCTION

The micro-structural mechanisms of hardened cement paste producing macroscopic creep and shrinkage deformations are only qualitatively understood so far. Quantitative information on structural changes is mostly distorted by the fact that originally loaded specimen have to be unloaded and then prepared, e.g. by destroying and pre-drying, for micro-structural analyses, such as MIP or BET measurement or XRD investigations. This problem may be overcome by means of applying small

angle X-ray or neutron scattering (SAXS or SANS) methods. In contrast to conventional methods, no particular specimen preparation, connected with the well-known adverse effects, has to be carried out. In particular small angle scattering techniques allow an insight into the changing structural characteristics of the hardened cement paste while a specimen is under load. Hence, the creep mechanisms, i. e. the related micro-structural alterations of the xerogel within the realm of nanometres, may be studied directly.

For these purposes a loading device for hardened cement paste platelets to be placed in a SAXS apparatus has been developed recently. With respect to the measurement technique the samples had a cross-section of 1 cm² and a thickness of 0.4 mm. They were subjected to sustained loading at a constant stress level of approximately 10 MPa, followed by an unloading of the specimens in order to record creep recovery effects. While earlier experiments required vacuum conditions, the newly developed experimental device allows testing under different constant humidity and temperature conditions. Hence, the creep and shrinkage mechanism under realistic ambient conditions may now be investigated. Trial tests with different mixes applying the new technique – in particular a new type of detector, the new climate box, new data processing software and improved modelling approaches – are under way.

This paper deals with the new measurement technique being under continuous development and presents interesting and auspicious experimental results on micro-structural changes. Theoretical considerations of data interpretation will be outlined. Gained test results are discussed in view of recent and also earlier findings given in the literature, where conventional methods have been applied, being accompanied by a complete destruction of specimens prior to subsequent micro-structural analyses.

THEORY

SAXS is a non-destructive method for the analysis of morphological characteristics of nanostructures. Within a transmission experiment, the different electron densities of particles (i.e. calcium silicate hydrates, calcium hydroxides etc.) in a matrix cause a two dimensional scattering pattern. The structure of a two phased scattering system can be described by a statistical function which is called the correlation function. This mathematical term describes the probability that within the realm of one randomly chosen point of this system, a second point belonging to the same phase (being solid, solid or gaseous, or gaseous) is found. The correlation function has to be derived in such a way that the parameters characterizing the system (e.g. inner surface or mean particle size) are included.

Under the precondition that distinct interfaces between phases of different electron densities exist, it is possible to determine information about the particle characteristics by using the theory of Porod (1951). Porod's law connects the

correlation function with the inner surface of the scattering system and subsequently allows for the determination of the inner surface of the investigated system. In small angle scattering experiments the application of Porod's law is very useful, as it does not require any detailed knowledge of the colloid framework. In this relation it should be possible to evaluate the influence of creep processes on the scattering pattern.

EXPERIMENTS

In the frame of the results presented in this paper, two series of experiments were carried out using two different types of SAXS-instruments. The first group of experiments (series A) used a SAXS-diffractometer equipped with a copper (Cu) tube as X-ray source and an area detector (GADDS). This so-called Kratky-camera system worked with point-collimation, i. e. a focused X-ray beam.

The second series of experiments (series B) took place at the Bruker application laboratory of the Materials Center Leoben (mcl, Austria), using a Bruker Nanostar SAXS instrument with a micro-focus X-ray source and a 2-D Vantec 2000 detector.

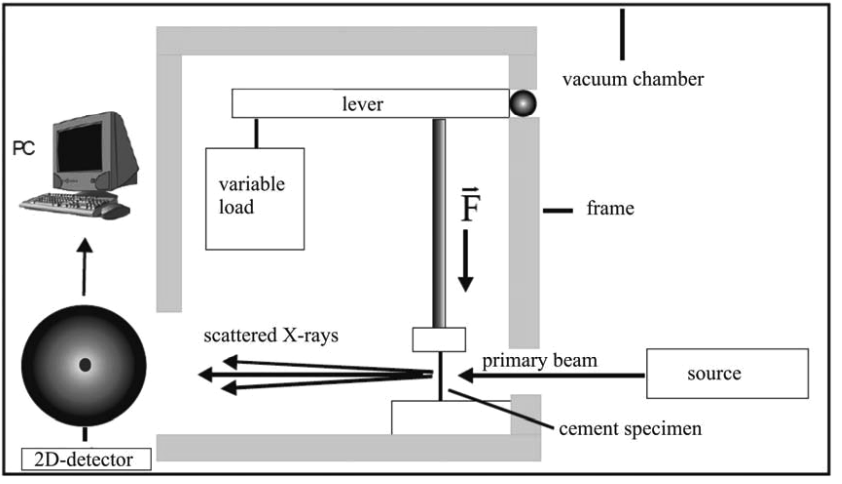

Figure 1. *Sketch of the experimental setup with focus on the loading apparatus*

Both series of experiments were focused on measuring the structural changes during creep of a hardened cement paste sample. For this purpose, an apparatus was developed to apply different compressive loads on cement specimens of dimensions of 10 x 10 mm² and a thickness of 0.4 mm (see Fig. 1). The high slenderness of the samples was chosen to limit the loss of intensity of the X-ray beam during the

radiographing of the sample. The size of the loading apparatus was adapted to the limited dimensions of the measuring chamber. The load exerted onto the hardened cement paste sample was manually varied by applying different weights to the cantilever system shown in Fig. 1. In both test series A and B, compressive loads have been applied to the specimens corresponding to a degree of loading of approx. 40 % (stress/strength ratio). Within series A, in most cases the specimens were sealed with muscovite (mica) platelets of approximately 30 micron thickness to avoid a fast drying of the hydrated cement paste in the evacuated specimen chamber. The specimens were made of Portland cement with a water-cement ratio of 0.4. The duration of observation of the different experiments ranged from 16 to 80 days.

Within series B the sealing of the samples was not necessary as these measurements were performed under non-vacuum conditions in a climate chamber at 20 °C and 65 % rel. humidity. In these experiments, the water-cement ratio was set to 0.6. The time resolution of the data acquisition varied between 300 and 3600 s/frame. The load was increased stepwise until the fracture of the specimen occurred.

RESULTS

The first run of series A was performed without mica plates. After 22 days of aging the hardened cement paste platelet was placed in the vacuum chamber for 12 days before applying the load of 11 MPa. Due to these very harsh environmental conditions in the vacuum chamber, the samples were supposed to be completely dry at the age at loading of 34 days. The creep experiment was finished after 120 days.

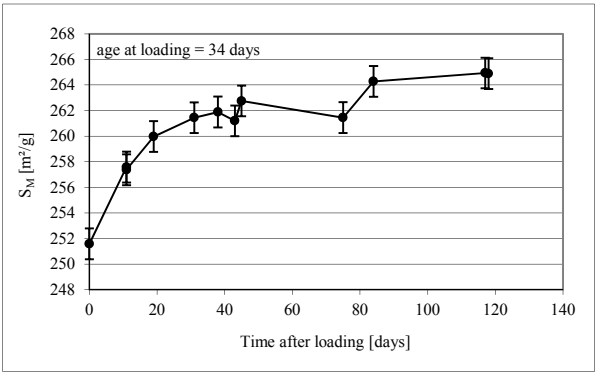

Figure 2. *Development of the specific surface of a specimen subjected to a constant load; dry specimen under vacuum conditions (Neumann et al. 2005)*

The specific surface was calculated according to Porod's law (see Neumann et al. 2005). Figure 2 shows an increase of the specific surface under applied load reaching a boundary value after approx. 40 days. After this time no significant increase or change in the sample characteristics was observed by SAXS. The increase in the specific surface area at the beginning of loading, indicating on-going micro-structural processes, is in so far a somewhat surprising result as absolutely dry specimens are supposed to show no creep.

In the following runs the SAXS diffractometer was equipped with an aperture in order to suppress halo effects in the 2D plot originating from the silhouette of the hydrated cement paste platelets. The specimens were coated with exsiccator fat in order to seal the hydrated cement paste platelets with mica plates to avoid drying under vacuum conditions. The diagram in Fig. 3 shows that at the beginning of the experiment the specific surface of the sample decreases. This turned out to be the result of the loss of moisture during the first 17 days without load which could not be prevented by the aforementioned sealing. This effect of a drastic reduction of the inner surface due to drying is well known by other experiments and already described in literature (e.g. Winslow et al., 1974).

After loading of the sample, the data shows an increase of the specific surface over a time period of 45 days. The last measurement, 12 days after unloading of the specimen, indicates a reduction of the specific surface during creep recovery. These nano-scale effects, visible by SAXS, have to be ascribed to creep and creep recovery processes. They are still not really understood, and further as well as additional structural investigations are necessary to create the basis for a consolidated interpretation.

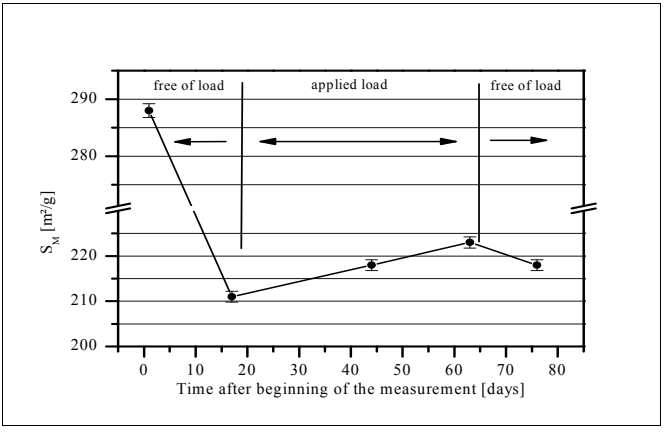

Figure 3. *Specific surface of a specimen subjected to loading and unloading afterwards; the age at loading was 44 days; specimen being sealed and stored under vacuum; sealing proved to be not sufficient (Neumann et al. 2005)*

The experiments of series B were carried out over a much shorter time period. Each measurement point represents a time frame of 1 hour, so that the overall measuring time expands to 14 hours. The specimen was subjected to a compressive load of 16 MPa. Figure 4 shows the integral intensity, which is related to the inner surface of the material by the Porod's law.

Independent of the short loading time, the results are similar to series A. During the first period the inner surface decreases due to drying of the specimen. Under load, the inner surface increases significantly. But, in contrast to former results, after removal of the load a decrease of the inner surface was not observed. On the contrary, not only an on-going, but a steeper increase of the inner surface is analysed by the measurements. This effect could not be analysed in detail so far.

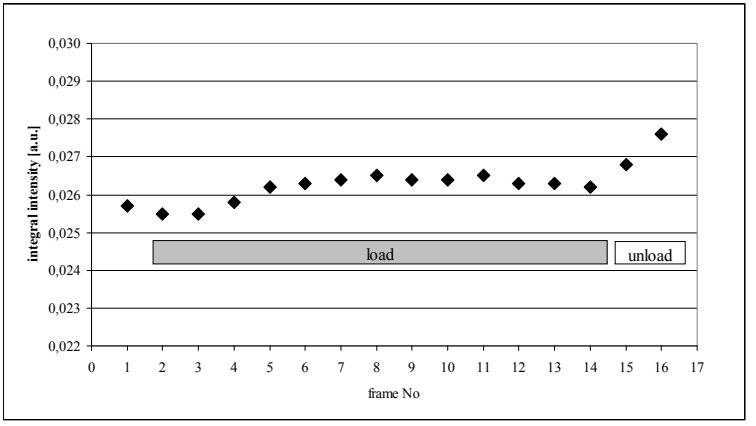

Figure 4. *Integral intensity as a measure for the specific surface of a loaded specimen being unloaded afterwards; each point represents the result of one hour of measuring time*

Though these are only first and still very crude results it has been observed for all experiments that drying and creep have opposite effects on the specific surface of the material. Regarding this, the observed increase of the specific surface due to load should give significantly higher signals if the drying effect would be suppressed, i.e. if basic creep is investigated. Related experiments are planned when the final test set-up will have been installed at the MPA.

CONCLUSIONS AND OUTLOOK

In this paper it is shown that small-angle X-ray scattering is a promising method to investigate structural processes related to creep and shrinkage of hardened cement

paste. The method is in particular well suited to get information about the micro-structural changes of the material on the nano-scale level. Specific experiments on different samples under different ambient and loading conditions applying a former and a newly developed loading and measuring device showed consistently an increase of the inner surface if a hydrated cement paste specimen is subjected to a compressive load. This finding is contrary to some literature data (e.g. Beaudoin, 2001) and therefore has to be validated by further creep experiments.

SAXS is besides SANS the only method which allows observing such nano-scale processes directly, i.e. while specimens are drying and being subjected to loading, respectively. Especially, the progress of instrumental facilities being under way opens the possibility to more detailed experiments and measurements with higher resolution.

The presented results form only the basis for further investigations applying the latest generation of SAXS diffractometer with a much higher sensitivity and highly enhanced modeling software. The new test set-up will allow for the systematic analysis of a larger number of specimens under well controlled and defined conditions (e.g. humidity, temperature) to achieve a fundamental understanding of nano-structural processes occurring during drying and creep of hardened cement paste.

ACKNOWLEDGEMENTS

The authors want to thank N. Dingenouts and A. Neumann for measuring of series A, and G. Maier and his team from the Bruker Application Lab in the Material Center Leoben (mcl) for assistance in measuring and interpreting series B. The first part of the work was funded by the Deutsche Forschungsgemeinschaft (DFG).

REFERENCES

Beaudoin, J. (2001). *Handbook of analytical techniques in concrete science and technology*, William Andrew Publishing/Noyes Publishing, New York/New Jersey.

Neumann, A., Herold, G., Dingenouts, N. and Müller, H. S. (2005). „*Investigation on creep mechanisms of hardened cement paste by means of the small angle X-ray scattering method*." Proceedings of the 7th International Conference on Creep, Shrinkage and Durability of Concrete and Concrete Structures (Concreep-7), 39-44, Nantes.

Porod, G. (1951). "X-Ray small angle scattering of closed packed colloid systems." *Kolloid-Zeitschrift,* 124, 83-96.

Winslow, D. N. and Diamond, S. (1974). "Specific surface of hardened Portland cement paste as determined by small angle X-ray scattering." *J. Amer. Ceram. Soc.* 57, 193-197.

Infinitesimal Shrinkage as Determined by Inverse Analysis Based on Drying and Shrinkage Tests

B. Villmann[1], V. Slowik[1], P. Wang[2], F. H. Wittmann[2,3]

[1]Leipzig University of Applied Sciences, PF 301166, 04251 Leipzig, Germany; email: beate.villmann@fb.htwk-leipzig.de
[2]Qingdao Technological University, Centre for Durability and Sustainability Studies, 11 Fushun Road, Qingdao 266033, China; email: wangpenggang007@163.com
[3]Aedificat Institute Freiburg, Schlierbergstr. 80, 79100 Freiburg, Germany; email: wittmann@aedificat.de

ABSTRACT

The non-uniformity of the moisture distribution in drying concrete specimens results in differential shrinkage. If the specimen thickness tends to zero, theoretically the so-called infinitesimal shrinkage would occur. Since the latter may not be determined directly by experimental means, a method for the inverse analysis of shrinkage tests has been developed. Laboratory sized concrete specimens are subjected to drying whereby the mass loss and the deformation are measured. Then, the material-specific relationship between the unhindered infinitesimal shrinkage strain and the relative humidity is retrieved from the experimental results by inverse analysis of the respective test. Drying is simulated by using the non-linear diffusion theory. In the mechanical model, elastic and viscoelastic strain as well as cracking and strain softening are taken into account in addition to the unhindered local shrinkage. Sensitivity analyses have shown that the measurement of the mass loss and the determination of the desorption isotherm should be conducted with high accuracy in order to obtain reliable inverse analysis results.

INTRODUCTION

Predicting the durability of concrete structures requires the knowledge of the material behavior under changing environmental conditions. Of particular interest in this context are the moisture transport properties and shrinkage deformations. Some of the respective material parameters can not be measured directly or an accurate experimental determination would be too expensive and time consuming. This is the case for the moisture dependent water transport function as well as for the drying shrinkage strain. Drying of laboratory sized specimens will lead to a moisture gradient in the respective specimen and, therefore, to a non-uniform shrinkage, i.e., to the so-called differential shrinkage. Stresses will be built up resulting in elastic and inelastic deformation whereby the latter is mainly caused by cracking and creep. The

measurable global specimen deformation which is partially inelastic will therefore differ from the locally occurring shrinkage strain even after the equilibrium moisture content has been reached. Theoretically, no moisture gradient will occur in drying specimens when their thickness becomes zero. For this reason, the material-specific and geometry-independent local shrinkage is also referred to as infinitesimal shrinkage (Wittmann 2008).

By inverse analysis of drying tests it is possible to determine the water transport properties as well as the moisture distribution in the specimen on the basis of the measured mass loss of this specimen. The desorption isotherm of the material needs to be known for this analysis. Similarly, it is possible to determine the infinitesimal shrinkage by an inverse analysis based on the measured shortening of a drying specimen. In this case, the mechanical as well as the transport properties of the material need to be known. Based on this approach, a two-stage inverse analysis method has been developed.

TWO-STAGE INVERSE ANALYSIS METHOD FOR DETERMINING INFINITESIMAL SHRINKAGE

Figure 1 shows a schematic presentation of the method. Inverse analysis of an experiment means that the latter is repeatedly simulated on the basis of assumed material parameters. Thereby, the deviation between the simulation results and the experimental data is minimized. This allows to identify the best fitting material parameters which will then be the result of the inverse analysis.

In Stage 1 of the proposed inverse analysis method, the moisture transport in a drying specimen is simulated and the material-specific transport properties are determined. In Stage 2, the shrinkage induced deformation of a specimen is simulated and the infinitesimal shrinkage strain is determined. Usually, separate specimens are used for the two analysis stages. A precondition for Stage 2 is a circular cylindrical shape of the specimens. Moisture transport is considered only in the radial direction and plane sections are assumed during the deformation. This restriction allows for a short computing time during the simulations and, consequently, a genetic optimization algorithm may be applied. It has to be pointed out that the restriction does not necessarily lead to an error. The associated assumptions for the analysis are justified if the end faces of the specimens are sealed and the axial displacement is measured between two points sufficiently remote from the end faces.

The genetic algorithm used for the optimization, i.e., for fitting the simulation results to the experimental ones, allows for very good fits with high objectivity and efficiency, but requires a comparatively large number of individual simulations of the respective experiment. This is the reason for the described restriction concerning the specimen geometry. Genetic algorithms are derived from biological concepts like Mendel's laws of heredity and Darwin's model of evolution by natural selection (Schwefel 1981). Another characteristic of these algorithms is the complete separation of the parameter optimization from the underlying physical model. Therefore, the latter may easily be modified while the optimization algorithm remains unchanged. It

has to be pointed out that an efficient optimization requires the formulation and application of appropriate error criteria.

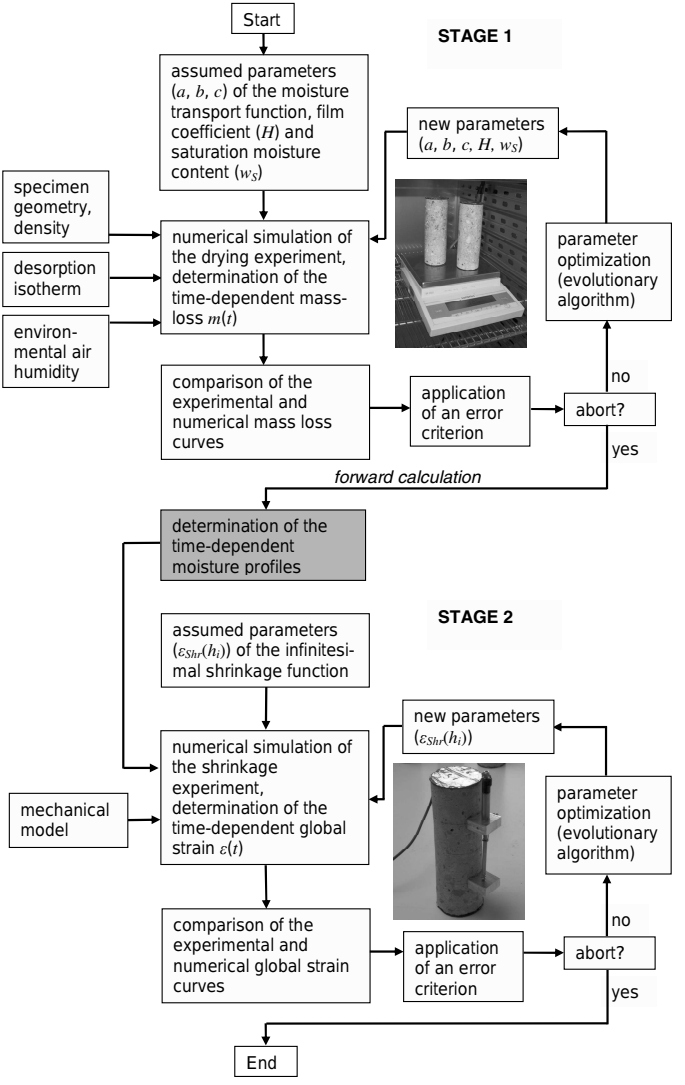

Figure 1. Schematic presentation of the two-stage inverse analysis method for determining the moisture transport properties (Stage 1) and the infinitesimal shrinkage (Stage 2).

The simulation of drying is based on the nonlinear diffusion theory. A proposal by Krus (1995) has been used. Both vapor diffusion and liquid transport are considered by a single moisture-dependent transport coefficient $D(h)$; see eqs. 1 and 2 for the case of axisymmetric transport. The material parameter for the liquid transport is an exponential function of the moisture content and the vapor transport is considered by a constant parameter. A film coefficient H describes the transition at the specimen surface.

$$\rho_B \frac{\partial w}{\partial h}\frac{\partial h}{\partial t} = \frac{1}{r} D(h)\frac{\partial h}{\partial r} + \frac{\partial}{\partial r}\left(D(h)\frac{\partial h}{\partial r}\right) \tag{1}$$

$$D(h) = \rho_B D_l(w)\frac{\partial w}{\partial h} + D_v = \rho_B \frac{\partial w}{\partial h}\cdot b \cdot e^{c\cdot w(h)} + a \tag{2}$$

r … radius
w … moisture content by mass
h … relative humidity
ρ_B … material density
$D(h)$ … transport coefficient (apparent diffusion coefficient)
$D_l(w)$ … moisture-dependent liquid transport coefficient
D_v … vapor diffusion coefficient
a, b, c … parameters to be determined by inverse analysis

The first stage of the analysis yields the parameters a, b, and c (see eqs. 1 and 2), the film coefficient H, and, if necessary, the saturation moisture content w_S of the desorption isotherm. The last-mentioned parameter needs to be determined by inverse analysis in case it was not measured with sufficient accuracy. For validating the numerical analysis procedure comparative Finite Element analyses were performed.

After the transport parameters have been determined, the moisture distribution within the specimens for the shrinkage tests may be calculated. This is Stage 2 of the inverse analysis method. The total strain ε, i.e., the measurable global strain of the specimen, may be decomposed (see eq. 3) into the elastic strain $\varepsilon_{el}(r)$, the unhindered shrinkage strain $\varepsilon_{shrinkage}(r)$, the strain due to smeared cracking $\varepsilon_{crack}(r)$, and the creep strain $\varepsilon_{creep}(r)$. The total strain is independent of the radius r because of the assumption of plane sections.

$$\varepsilon = \varepsilon_{el}(r) + \varepsilon_{shrinkage}(r) + \varepsilon_{crack}(r) + \varepsilon_{creep}(r) \tag{3}$$

In the undamaged state, linear-elastic deformation is assumed. When the tensile strength f_t is reached, the material will crack. A smeared crack approach has been adopted, i.e., the crack opening divided by the crack spacing results in $\varepsilon_{crack}(r)$. For strain softening materials, a bilinear softening curve is used whereby the residual crack opening after unloading is a constant portion of the maximum crack opening (see Figure 2). In strain hardening materials, the softening stress is assumed to remain constant after crack initiation.

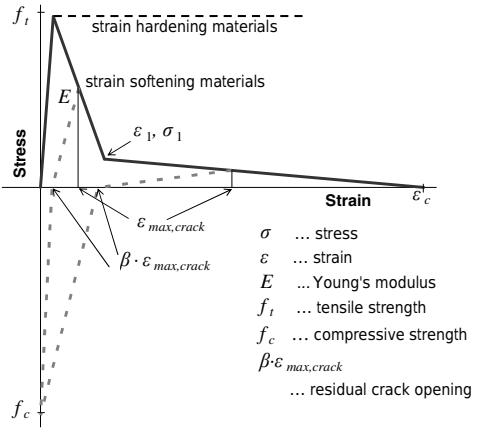

Figure 2. Assumed stress-strain curves for smeared cracking of strain softening and strain hardening materials.

It is well known that the spacing of opening cracks in drying specimens becomes larger with increasing crack depth (Bažant et al. 1982). This is considered in the present model. Crack closing follows the path shown in Figure 2. In the applications described in the following section the assumed ratio of crack spacing and length was equal to one.

In previously performed sensitivity analyses (Villmann et al. 2011), the creep strain $\varepsilon_{creep}(r)$ was found to have a comparatively small influence on the inverse analysis results obtained on the basis of laboratory tests. The viscoelastic deformation has therefore been neglected in the analyses presented in the following section. It should be noted, however, that in full-scale concrete members creep may have a significant influence on the long-term shrinkage deformation.

The function of the moisture-dependent infinitesimal shrinkage strain is described by ten supporting points $\varepsilon(h_i)$ of an interpolating spline. Hence, Stage 2 of the inverse analysis method is aimed towards the determination of the parameters $\varepsilon(h_i)$ which allow for the best fit of the simulated global shortening of the specimen to the corresponding values measured in the experiment.

For Stage 2 of the inverse analysis method, parametric studies were carried out in order to evaluate the sensitivity of the results to the assumed material properties (Villmann et al. 2011). As expected, the given moisture distribution in the specimen strongly influences the obtained infinitesimal shrinkage strain. It is concluded that the transport parameters need to be determined with comparatively high accuracy. The influence of the modulus of elasticity and of the tensile strength is also significant whereas the one of the strain softening parameters appears to be rather small. For a more precise modeling, it would be possible to consider the moisture dependence of the mechanical material properties.

INVERSE ANALYSIS OF EXPERIMENTAL RESULTS

Figure 3 shows the inverse analysis results for three different concrete compositions with w/c-ratios ranging from 0.4 to 0.6. The specimens for both analysis stages had a diameter of 100 mm, a height of 300 mm, and the base length for the displacement measurement was 200 mm. The curves of the experimental results (see Figure 3 (a) and (e)) have been extrapolated by fitting a hyperbola to the last measured data points.

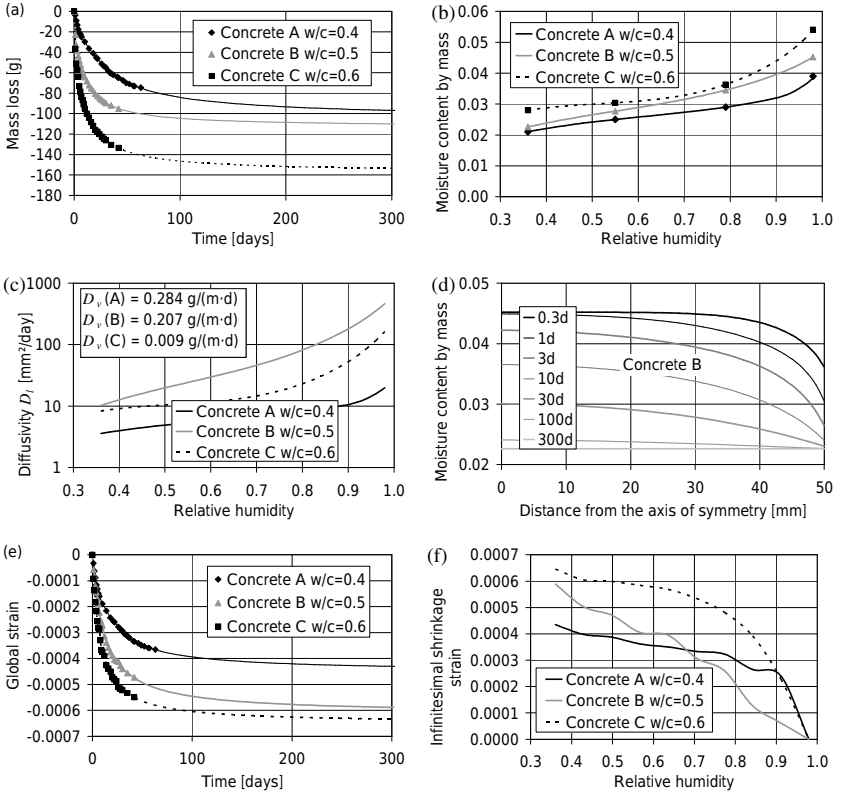

Figure 3. Inverse analysis results for concrete with different w/c-ratios, (a) measured mass loss during drying from 98% to 36% r. H., (b) desorption isotherms, (c) moisture transport parameters as determined by inverse analysis, (d) moisture profile in the specimen made of Concrete B as determined numerically on the basis of the transport parameters, (e) measured global shrinkage strain during drying from 98% to 36% r. H., (f) infinitesimal shrinkages strain as determined by inverse analysis.

The moisture profiles obtained for concrete A and C have a similar shape like those for concrete B (see Figure 3 (d)).

It has to be pointed out that no conditions concerning the shape of the infinitesimal shrinkage curve were enforced. This explains the partially wavy course of the curves. The resulting splines are presented in Figure 3 (f) without any smoothing in order to demonstrate the performance of the inverse analysis procedure.

As expected, the infinitesimal shrinkage tends to become larger with increasing w/c-ratio. More reliable results may be obtained when the assumed desorption isotherms are supported by a higher number of data points, especially in the steep-slope range above 80% relative humidity. As stated before, the moisture distribution in the specimen needs to be determined with high accuracy in order to obtain the correct infinitesimal shrinkage.

In another series of experiments, a fiber reinforced Strain Hardening Cement-Based Composite (SHCC) and its matrix without fiber reinforcement were tested (see Figure 4). In addition, the effect of an integral water repellent agent (IW) on both materials was investigated. The specimen diameter amounted to 50 mm, the height to 300 mm, and the base length for the displacement measurement to 200 mm.

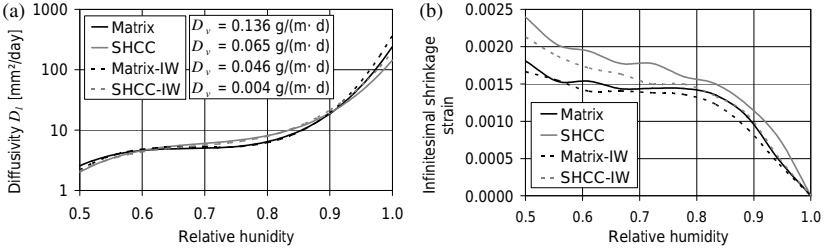

Figure 4. Inverse analysis results for SHCC and its matrix, both with and without integral water repellent agent (IW), (a) moisture transport parameters, (b) infinitesimal shrinkages strain.

When compared to the results for concrete presented in Figure 3, the infinitesimal shrinkage strain of the fine-grained materials investigated here is significantly larger. All curves in Figure 4 (b) show an increasing infinitesimal shrinkage when the relative humidity becomes smaller than about 55%. This may be explained by the shrinkage mechanisms described by Wittmann (2008). The liquid transport appears to be almost identical for all four material compositions whereas the vapor transport seems to be reduced by the water repellent agent. The influence of the latter may also be seen in the infinitesimal shrinkage curves. Especially in the case of the SHCC, the water repellent agent seems to reduce shrinkage.

CONCLUDING REMARKS

It is possible to determine the moisture transport parameters as well as the infinitesimal shrinkage strain by inverse analysis of easy-to-perform laboratory

experiments. The proposed two-stage method has proved to be applicable. For determining the moisture transport properties, there is currently no direct experimental method available. As far as the determination of the infinitesimal shrinkage is concerned, an approximate direct measurement seems to be possible since the cracking and creep strains are comparatively small for usual specimen sizes. It has to be taken into account, however, that such direct shrinkage tests are time-consuming since they can not be terminated before the equilibrium moisture content is reached and hindered shrinkage strains have been relieved. In contrast to that, the proposed two-stage inverse analysis method allows to determine the infinitesimal shrinkage strain on the basis of experimental data acquired before hygral equilibrium is reached. The non-uniform moisture distribution and hindered strains are considered in the underlying model. Furthermore, a direct shrinkage measurement requires multiple specimens being stored under different environmental conditions whereas the proposed inverse analysis yields the complete curve of infinitesimal shrinkage on the basis of just one drying experiment.

In order to obtain reliable inverse analysis results, the experimental data have to meet certain requirements with respect to their accuracy. Especially the quality of the measured desorption isotherm is of high significance. Inaccuracies, in particular in the high-humidity range, will strongly affect the determined transport properties and eventually the infinitesimal shrinkage strain.

The infinitesimal shrinkage as determined by inverse analysis depends noticeably on the assumed values for the modulus of elasticity and for the tensile strength whereas the post-cracking properties do not have a significant influence.

It should finally be mentioned that the computing times for the inverse analysis are comparatively small, hours for Stage 1 and minutes for Stage 2. Besides the inverse analysis, the developed software allows to calculate moisture and stress distributions for various specimen sizes in forward analyses. The program may be downloaded from the website of the first author.

REFERENCES

Bazant, Z.P., Raftshol, W.J. (1982). “Effect of cracking in drying and shrinkage specimens.” *Cement and Concrete Research* 12(2), 209-226.

Krus, M. (1995). „Feuchtetransport- und Speicherkoeffizienten poröser mineralischer Baustoffe. Theoretische Grundlagen und neue Messtechniken.“ Dissertation, Universität Stuttgart, Germany.

Schwefel, H.-P. (1981). *Numerical Optimization of Computer Models*, Wiley & Sons, Chichester.

Villmann, B., Slowik, V. (2011). “Infinitesimal shrinkage as determined by inverse analysis.” *Restoration of Buildings and Monuments* 17(6), 383-396.

Wittmann, F.H. (2008). “Heresies on shrinkage and creep mechanisms.” Proceedings of the 8th International Conference on Creep, Shrinkage and Durability Mechanics of Concrete and Concrete Structures (CONCREEP 8), Sept. 30–Oct. 2, 2008, Ise-Shima, Japan, Taylor & Francis Group, London, vol. 1, 3–9.

Kinetic simulation of the logarithmic creep of cement

E. Masoero[1], H. Manzano[2], E. Del Gado[3], R. J.-M. Pellenq[1,4], F.-J. Ulm[1], and S. Yip[5]

[1]Concrete Sustainability Hub, Department of Civil and Environmental Engineering, Massachusetts Institute of Technology, Cambridge, MA 02139, U.S.A.; emails: emasoero@mit.edu , ulm@mit.edu , pellenq@mit.edu
[2]Laboratory of Molecular Spectroscopy, Department of Physical Chemistry, UPV/EHU Barrio Sarriena s/n, 48940 Leioa, Bizkaia, Spain; email: hegoi.manzano@ehu.es
[3]Group of Microstructure and Rheology, Institute for Building Materials, ETH Zurich, 8093 Zurich, Switzerland; email: delgado@ifb.baug.ethz.ch
[4]CINaM, CNRS and Aix-Marseille University, Campus de Luminy, 13288 Marseille Cedex 09, France
[5]Concrete Sustainability Hub, Department of Nuclear Science and Engineering, Massachusetts Institute of Technology, Cambridge 02139, U.S.A.; syip@mit.edu

ABSTRACT

Many amorphous materials display a logarithmic creep behavior, driven by the rare occurrence of complex, hardly detectable, microscopic structural rearrangements. Following recent developments in experimental techniques and modeling, we develop here a new approach based on transition state theory and on activation energies computed from molecular simulations of shear tests. Our results predict the logarithmic creep of an amorphous, model structure of cement at the molecular and meso- scales. We investigate the interplay of cooperative processes at the different length-scales and establish connections with creep phenomena in other materials.

INTRODUCTION

Creep is the temporal accumulation of irreversible deformation γ under constant stress. It starts with a transient regime of decreasing rate γ' that converges to a constant value at the onset of steady-state creep. The transition state theory (TST, Vineyard, 1957) relates the average occurrence time Δt of a strain accumulation event $\Delta\gamma$ with its activation energy ΔE:

$$\Delta t = \nu_0^{-1} e^{\frac{\Delta E}{k_B T}} \quad (1)$$

ν_0 is a characteristic frequency of attempt, k_B is the Boltzmann constant, and T is the temperature. According to Eq. (1) a transient creep occurs during strain-hardening

regimes (Orowan, 1947) i.e. when ΔE increases with γ. In particular, $\Delta E \sim \gamma$ leads to $\gamma \sim \log(t)$ (Cottrell, 1952), a logarithmic creep shown at all scales by a multitude of materials. Characterizing $\Delta E(\gamma)$ is key to understand the conditions and mechanisms that lead to the logarithmic creep and that control its magnitude. In the simplest cases $\Delta E(\gamma)$ can be estimated analytically (e.g. Cottrell, 1952), but not for amorphous materials with complex, cooperative behavior. Molecular simulations can deal with such complexity, but cannot follow the dynamics of a system for the large time scales (seconds to years) that are relevant to creep (Voter, 2002 and Nabarro, 2002). As an alternative, kinetic approaches can cover much longer time scales by using TST [Eq. (1)] after sampling transitions and associated activation energies on the potential energy surface (PES) (Kushima, 2009, Kushima, 2011, and Mousseau, 2012). These approaches are effective for relatively ordered systems (Lau, 2010, Fan, 2012, and Mousseau, 2012) but their application to amorphous systems has been so far unsuccessful due to the abundance of transitions to be sampled.

Here we propose a new approach based on PES-TST that predicts the logarithmic creep of amorphous materials from simulation. It has the advantage of considering only a small number of possible transitions along one specific trajectory on the PES. This trajectory is generated via progressive increments of applied macroscopic strain, similar to experimental shear tests. The underlying assumption is that the mechanisms activated during creep are the same that cause instantaneous irreversible deformations under mechanical action (Guiu, 1964, Argon, 1982, Fan, 2012). We apply the technique to a multi-scale model of the amorphous molecular (~2 nm) and meso (~100 nm) structure of calcium silicate hydrate (C-S-H), which is the main binder phase of ordinary cements. A logarithmic creep regime emerges at both scales from our calculations. The computed energy barriers confirm that a $\Delta E \sim \gamma$ type of strain-hardening takes place at small γ. We also find a switch to steady-state regime at strain levels that correspond to the onset of stress-induced plastic flow, when ΔE converges to a constant maximum value. This work lays the ground for a broader application to amorphous materials, whose long-term creep behavior can be understood and predicted from the increasing amount of available experimental and simulation data on short-term, mechanically-induced irreversible deformations (Langer, 2006, Schall, 2007, Falk, 2007).

CREEP OF CEMENT

Cement is usually mixed with sand and stones to produce mortars and concretes. It is the most widely used building material on Earth, and its creep has huge practical implications. For example, the creep of prestressed concrete causes a progressive loss of prestress, and a costly maintenance is required to periodically restore it. Therefore a low creep compliance is desirable in bridges made with prestressed concrete. On the other hand, the creep helps buildings and infrastructures accommodate imposed displacements, e.g. due to ground settlement. In this sense, some creep compliance is beneficial to the resilience of concrete structures. Cement normally experiences only a transient, prevalently logarithmic creep (Vandamme, 2009, Bazant, 2012): similar

to many other rocks, a steady-state creep regime does not develop in cement because anticipated by nucleation of cracks and failure. The creep of cement is commonly attributed to that of the calcium silicate hydrate (C-S-H) gel, which is the main binder phase. The C-S-H gel is a highly cohesive, amorphous, mesoporous material, with a disordered arrangement of pores 2 to 50 nm wide, and a solid skeleton that is also amorphous at the molecular level. Hereafter we will focus on the creep of the C-S-H gel, as a prototype of amorphous material at multiple scales.

The microscopic mechanisms of creep in the C-S-H gel are still not known with certainty. Bazant et al. (Bazant, 1997) proposed the "microprestress" mechanism at the molecular scale, according to which an heterogeneous stress field induces molecular rearrangements at randomly located "creep sites", i.e. sub-nanometer regions that are rich in ultra-confined water. This is conceptually similar to the motion of dislocation in metals. To date the microprestress mechanism cannot be confirmed by direct measurements, because experimental techniques are unable to assess the creep of the C-S-H directly at the molecular scale. On the other hand, at the just larger scale of the mesoporous C-S-H gel structure (100 nm - 1 μm), nanoindentation experiments show that a logarithmic creep takes place (Vandamme, 2009) and that gels with a smaller volume fraction of mesopores creep slower. This latter effect can not be predicted by the microprestress argument, and has been interpreted using the free volume theory (Boutreux, 1997, and Vandamme, 2009). Both the microprestress mechanism and the free volume theory have been deduced to interpret qualitatively the experiments, but their predictive ability is limited. Our strategy here, by contrast, is to employ recent models of the molecular (Pellenq, 2009) and mesoporous (Masoero, 2012) structures of the C-S-H gel, predict their deformation mechanisms, quantify the activation energies, and translate all this into creep using Eq. (1).

SIMULATED CREEP OF THE MOLECULAR C-S-H

The molecular structure of the solid C-S-H consists of a disordered arrangement of silica chains and of calcium and water "layers". A model of this structure has been proposed recently (Pellenq, 2009) (see Fig. 1.a) and, coupled with atomistic force fields, it captures and predicts a number of experimentally measured quantities (Pellenq, 2009, Youssef, 2011, Manzano, 2012, and Manzano 2013). In Fig. 1.b, we show the results of a simulated shear test performed on the a molecular structure of C-S-H with Ca/Si = 1.7 (the ratio between the number of calcium atoms and the number of silicon atoms). The protocol of the test consists in a series of increments of the overall imposed simple shear strain $\Delta\gamma_{ext}$. After each increment the interaction energy is minimized at zero kelvin using the conjugate gradient method, and the total interaction energy $E(\gamma_{ext})$ and (virial) shear stress τ after minimization are computed. During the test, we observed that large non-affine deformations tended to accumulate in correspondence of the most water-rich region, which confirms the "creep site'" activation argument of the microprestress creep theory (Manzano 2013).

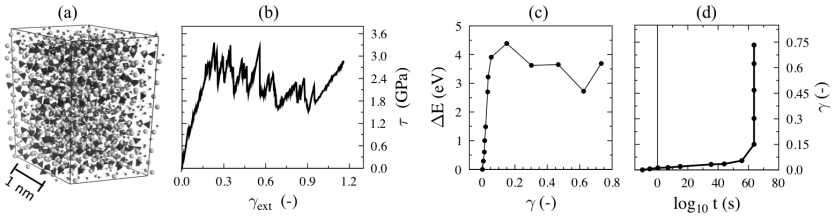

Figure 1. (a) Snapshot of the molecular structure of C-S-H employed. Silica tetrahedra are shown in blue, calcium atoms as yellow spheres, and OH bonds as white and red sticks. One can appreciate a horizontal water-rich layer in the middle. (b) Shear stress τ versus applied strain γ_{ext} curves at zero kelvin. (c) Energy barriers ΔE overcome at different levels of accumulated irreversible shear deformation γ. (d) Creep curves with the time evolution of the irreversible deformation computed applying Eq. (1) to the information in (c).

The sudden drops of τ in Fig. 1.b suggest that irreversible rearrangements may be occurring. In order to verify whether a drop of τ is actually accompanied by an accumulation of irreversible strain, the configurations corresponding to each point in Fig. 1.b have been unloaded by applying an increasingly negative simple shear strain until $\tau = 0$ was recovered (Manzano, 2013). The residual shear strain after minimization back to $\tau = 0$ is indicated with γ. These analyses showed that the residual γ increases discontinuously, jumping up suddenly in correspondence only of some drops of τ. These drops, for which γ increases, define a chain of discrete events of irreversible deformation. The activation energy $\Delta E(\gamma)$ of one such event can be evaluated from the molecular configuration at γ_{ext} just prior to the event triggering. In order to compute $\Delta E(\gamma)$, we first take the negative difference between the total interaction energy in that configuration, and the total interaction energy in that same configuration after it is unloaded back to $\tau = 0$. Subsequently, we divide this value times the number of particles in the simulation box N, and we multiply it times the number of particles M that take active part in the irreversible rearrangement. M is estimated from the local non-affine strain field, and for this simulation we have M = 200. Fig. 1.c shows that ΔE initially increases with γ (strain-hardening) and then converges to a constant maximum value when the stress-strain curve reaches the plateau of the plastic flow regime.

Fig. 1.d is the calculated creep curve of C-S-H at the molecular scale. The time increment Δt corresponding to each increment of irreversible strain $\Delta\gamma$ is obtained applying \Eq. (1) to the series of energy barriers in Fig. 1.c, and using $\upsilon_0 = 10^{10}$ s^{-1} and T = 300 K. Fig. 1.d shows a logarithmic $\gamma \sim \log(t)$ regime that extends over many orders of magnitude in time, before the upturn of $\gamma(t)$ at the onset of steady-state creep. Contrary to the common issue of molecular simulations that cannot access sufficiently large time scales, here we confront with an excessively large one compared to creep experiments. We will discuss this issue later in the manuscript.

SIMULATED CREEP OF THE C-S-H GEL AT THE MESO-SCALE

The same procedure employed for the molecular structure of the C-S-H is now applied to the mesoporous gel structure, at the larger scale of ~100 nm. The meso-structure of the C-S-H gel can be modeled as a disordered packing of nanoparticles with polydisperse diameters, that interact via a highly cohesive, spherical pair potential (Masoero, 2012). Here we will use the interaction potential in (Masoero, 2012): a modified single-well Lennard-Jones potential with single energy well of depth ε that scales as the volume of the interacting particles ($\varepsilon \sim \sigma^3$ with σ being the particle diameter). This implies that large particles stick to each other more strongly than small ones. Monodisperse systems (e.g. in Fig. 2.a) have maximum packing fraction $\phi = 64\%$ and represent the experimentally observed "low-density" C-S-H gel. Polydispersity instead enables more efficient packing, with ϕ up to 1, which can model the experimentally detected "high-density" C-S-H gel. The interactions between the nanoparticles are key to quantifying the activation energy for the irreversible deformations. Hereafter we will estimate ε from the results obtained previously at the smaller, molecular scale. This provides a truly multi-scale and cross-scale character to the present study.

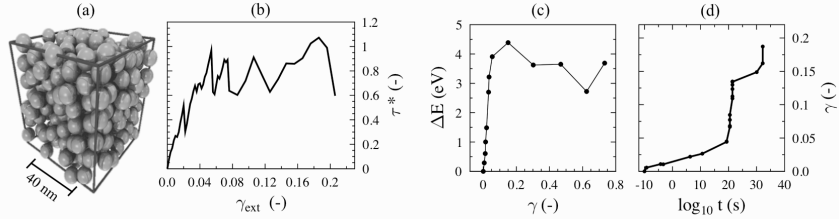

Figure 2. (a) Snapshot of the meso-structure of low-density C-S-H gel employed, with monodisperse nanoparticles. (b) Shear dimensionless stress vs. strain curves and (c) energy barriers for the activation of irreversible shear deformation mechanisms. (d) Creep curve computed using Eq. (1).

Fig. 2.b shows the results of a shear test simulation on a monodisperse model structure of the C-S-H gel. The test protocol is analogous to the one that led to Fig. 1.b, with applied shear strain increment $\Delta\gamma_{ext}$ between 0.005 and 0.01. We plot the dimensionless shear stress $\tau^* = \tau \cdot \sigma^3/\varepsilon$, because the simulation was performed in dimensionless units. Similar to the case of the molecular C-S-H structure, sudden drops of τ* indicate the triggering of deformation mechanisms, some of which correlate with a discontinuous accumulation of irreversible shear strain γ (Masoero, 2013). The energy barriers ΔE for the activation of such events are shown in Fig. 2.c. Similar to the molecular case, we rescaled the energy barrier computed over the whole simulation box dividing it by the number of particles in the box N = 1700 and multiplying it times the number M of particles actively involved in the irreversible rearrangement. The analysis of the local non-affine strain indicated M ~ 20

nanoparticles, independent of the system size. In Fig. 2.c we switched to real unit by employing $\varepsilon = 0.036\ \sigma^3$ eV, with σ expressed in nanometers. This energy scale implies that nanoparticles with $\sigma = 5$ nm, similar in size to the molecular structure in Fig. 1.a, interact with $\varepsilon = 4.5$ eV. This value corresponds to the activation of steady-state creep at the molecular scale (see plateau in Fig. 1.c). We are therefore effectively assuming that the unit events that control the energy scale of the gel deformations are plastic flows at the molecular scale, at the interface between nanoparticles. In general one cannot activate only one sliding event at a time, in the jammed meso-scale structures. Rather, cooperative mechanisms take place that involve several particles and activate multiple unit events of local slidings. Therefore one would expect an increase of the energy barriers at the gel scale. By contrast, we obtain energy barriers at the meso-scale that are smaller than those at the molecular scale, which is probably due to the eigenstresses in the meso-structure that can favor the activation of local mechanisms. Similar to the molecular scale, in Fig. 2.c we observe again an initial strain-hardening regime followed by the convergence of ΔE to a constant maximum value, at the onset of plastic flow in Fig. 2.b.

Fig. 2.d is the calculated creep curve of the low-density C-S-H gel, obtained analogously to Fig. 1.d. In order to apply Eq. (1) to the energy barriers in Fig. 2.c, we still employ $\nu_0 = 10^{10}\ s^{-1}$ and T = 300 K. Such high value of ν_0 is consistent with our assumption that the rearrangements at the molecular scale are the unit events for the rearrangements at the larger meso-scale. It is also worth noting that the choice of ν_0 affects the time scale only linearly, hence it can not change a qualitative logarithmic behavior and is also quantitatively less important that the exponential part of Eq. (1). Similar to Fig. 1.d, also Fig. 2.d shows an extended logarithmic regime and a subsequent upturn at the onset of steady-state creep. As a result of the smaller energy barriers, the time scale for the creep of the C-S-H gel is smaller than that for the C-S-H at the molecular scale.

CONCLUSION

Our results indicate that the energy barrier for accumulation of irreversible deformation increase with the applied strain both at the molecular scale and at the larger scale of the mesoporous gel. This is a signature of cooperative mechanisms whose activation energy increases until a regime of plastic flow is established. We argued that the mechanisms at the molecular scale could be considered as unit processes that set the energy scale of the relative sliding of nanoparticles at the larger meso-scale. Interestingly, we found that the heterogeneous stress field at the gel scale can result into an effective reduction of the energy barriers, despite what one would expect from the cooperative nature of the rearrangements.

Our simple approach brings out the connection between creep and mechanisms of instantaneous irreversible deformation. We applied it to the multi-scale amorphous structure of the C-S-H gel in cement, but the extension to other materials is straightforward. For the first time molecular simulations predict the logarithmic creep

of an amorphous material, which spans many orders of magnitude in time, and relate it with the strain-hardening behavior postulated in the 1940s by Orowan (Orowan, 1947). The advantage compared to previous phenomenological approaches is that now creep can be related quantitatively to the series of microscopic mechanisms through which it develops. This understanding is prerequisite to new solutions for designing materials with improved creep behavior.

Several aspects of this work can benefit from refinements and extensions. Above all, Fig. 1.d and Fig. 2.d show clearly that the time scale of creep is overestimated, compared to that of macroscopic creep in cement. A time scale of years ($\sim 10^8$ s), using $\nu_0 = 10^{10}$ s^{-1} and T = 300 K K in Eq. (1) implies activation energies ΔE of the order of 1.2 eV $\sim$ 46.5 $k_B T$. Fig. 2.c shows that the activation energy from our calculation is overestimated, and there are multiple possible sources of such result that are worth being investigated in future works. Among such possibilities, there is the effect of the external load (here tending to zero), the constraint of considering only one trajectory in the phase space, and the possible contribution to the free energy coming from chemical reactions or water dynamics (for example, in relation with the Pickett effect). On the other hand, already at the present state our protocol captures robustly the absence of a characteristic time scale that is distinctive of logarithmic creep, and can be employed for comparative studies between different systems. All this favors a technological transition toward including the predicted creep response as a new design variable for cement and other amorphous materials.

This work is supported by Schlumberger (SDR Cambridge, U.S. / SRPC Clamart, France) and by the CSHub at MIT. EDG is supported by the SNSF (Grant No. PP002_126483/1).

REFERENCES

Argon, A. S. (1982). “Mechanisms of inelastic deformation in metallic glasses.” *J. Phys. Chem. Sol.*, 43(10), 945-961.

Bazant, Z. P., Hauggaard, A. B., Baweja, S., and Ulm, F. J. (1997). “Microprestress-solidification theory for concrete creep. I: Aging and drying effects.” *J. Eng. Mech.*, 123(11), 1188-1194.

Bazant, Z. P., Yu, Q., and Li, G. H. (2012). “Excessive Long-Time Deflections of Prestressed Box Girders. I: Record-Span Bridge in Palau and Other Paradigms.” *J. Struct. Eng.*, 138(6), 676-686.

Boutreux, T., and de Geennes, P. G. (1997). “Compaction of granular mixtures: a free volume model.” *Phys. A: Stat. Mech.,* 244(1), 59-67.

Cottrell, A. H. (1952). “The time laws of creep.” *J. Mech. Phys. Solids* 1(1), 53-63.

Falk, M. L. (2007). “The Flow of Glass.” *Science*, 318(5858), 1880-1881.

Fan, Y., Osetsky, Y. N., Yip, S., and Yildiz, B. (2012). “Onset Mechanism of Strain-Rate-Induced Flow Stress Upturn.” *Phys. Rev. Lett.*, 109(13), 135503.

Guiu, F., and Pratt, P. L. (1964). “Stress relaxation and the plastic deformation of solids.” Phys. Stat. Sol., 6(1), 111-120.

Kushima, A., Lin, X., Li, J., Eapen, J., Mauro, J. C., Qian, X., Diep, P., and Yip, S. (2009). "Computing the viscosity of supercooled liquids." *J. Chem. Phys.*, 130, 224504.

Kushima, A., Eapen, J., Li, J., Yip, S., and Zhu, T. (2011). "Time scale bridging in atomistic simulation of slow dynamics: viscous relaxation and defect activation." *Eur. Phys. J. B*, 82(3-4), 271-293.

Langer, J. S. (2006). "Shear-transformation-zone theory of deformation in metallic glasses." *Scripta Mater.*, 54(3), 375-379.

Lau, T. T., Kushima, A., and Yip, S. (2010). "Atomistic simulation of creep in a nanocrystal." *Phys. Rev. Lett.*, 104(17), 175501.

Manzano, H., Moeini, S., Marinelli, F., Van Duin, A. C., Ulm, F. J., and Pellenq, R. J. M. (2012). "Confined water dissociation in microporous defective silicates: Mechanism, dipole distribution, and impact on substrate properties." *J. Am. Chem. Soc.*, 134(4), 2208-2215.

Manzano, H., Masoero, E., Arbeloa, I. L., and Jennings, H. M. (in press, 2013). "Molecular modelling of shear deformations in ordered and disordered Calcium Silicate Hydrates." *Soft Matter*.

Masoero, E., Del Gado, E., Pellenq, R. M., Ulm, F. J., and Yip, S. (2012). "Nanostructure and Nanomechanics of Cement: Polydisperse Colloidal Packing." *Phys. Rev. Lett.*, 109(15), 155503.

Masoero, E., Del Gado, E., Pellenq, R. M., Ulm, F. J., and Yip, S. (2013). "Nano-scale mechanics of colloidal C-S-H gels." *Soft Matter*, under review.

Mousseau, N., Béland, L. K., Brommer, P., Joly, J. F., El-Mellouhi, F., Machado-Charry, E., Mihai-Cosmin, M., and Pochet, P. (2012). "The Activation-Relaxation Technique: ART Nouveau and Kinetic ART." *J. At. Mol. Opt. Phys.,* 2012.

Nabarro, F. R. N. (2002). "Creep at very low rates." *Metall. And Mater. Trans. A*, 33(2), 213-218.

Orowan, E. (1947). J. West Scotland Iron and Steel Inst., 54.

Pellenq, R. J. M., Kushima, A., Shahsavari, R., Van Vliet, K. J., Buehler, M. J., Yip, S., and Ulm, F. J. (2009). "A realistic molecular model of cement hydrates." *Proc. Natl. Acad. Sci.*, 106(38), 16102-16107.

Schall, P., Weitz, D. A., and Spaepen, F. (2007). "Structural rearrangements that govern flow in colloidal glasses." *Science*, 318(5858), 1895-1899.

Vandamme, M., and Ulm, F. J. (2009). "Nanogranular origin of concrete creep." *Proc. Natl. Acad. Sci.*, 106(26), 10552-10557.

Vineyard, G. H. (1957). "Frequency factors and isotope effects in solid state rate processes." *J. Phys. Chem. Solids*, 3(1), 121-127.

Voter, A. F., Montalenti, F., and Germann, T. C. (2002). "Extending the time scale in atomistic simulation of materials." *Annu. Rev. of Mater. Res.*, 32(1), 321-346.

Youssef, M., Pellenq, R. J. M., and Yildiz, B. (2011). "Glassy Nature of Water in an Ultraconfining Disordered Material: The Case of Calcium− Silicate− Hydrate." *J. am. Chem. Soc.,* 133(8), 2499-2510.

Recent developments in durability mesomechanics of concrete, including cracking via interface elements

Joaquin Liaudat, Mariana Rodriguez, Carlos Lopez and Ignacio Carol

Department of Geotechnical Engineering and Geo-Sciences
ETSECCPB (School of Civil Engineering)-UPC (Technical Univ. of Catalonia)
08034 Barcelona
e-mail: joaquin.liaudat@upc.edu, mariana.rodriguez@upc.edu,
carlos.maria.lopez@upc.edu, ignacio.carol@upc.edu.

ABSTRACT

The mesomechanical model for concrete previously developed for purely mechanical actions, is used as the basis for coupled durability mechanics calculations. Until now, the phenomena studied include drying shrinkage, external sulfate attack and mechanical effects of high temperatures. On-going work is focusing on alkali-silica reaction (ASR). From the chemical viewpoint, ASR is represented with a three-field diffusion-reaction chemical model, which is shown to qualitatively and quantitatively reproduce some experimental measurements of sandwich-type specimens subject to standardized accelerated ASR tests. The model developed includes the recently identified role of Calcium in this type of expansive reactions.

INTRODUCTION

Constantly increasing computer power is fostering the development of sophisticated material degradation models including phenomena such as humidity, temperature and/or chemical processes coupled with mechanical behavior. On the other hand, micro/meso-level analysis of heterogeneous and quasi-brittle materials such as concrete or rock has emerged as a powerful tool for the modeling of the cracking and fracture processes under different loading situations. During over a decade, the group of Mechanics of Materials at UPC (Barcelona) has been developing such type of combined tools with the distinctive feature of representing cracks via zero-thickness interface elements, for progressively more complex loading/environmental scenarios. The approach was first applied to the purely mechanical behavior in 2D (López et al, 2000, 2008) and 3D (Caballero et al, 2007), then to basic creep (López,et al, 2001)., drying shrinkage (Idiart et al, 2011a) and external sulfate attack (Idiart et al, 2011b). In this paper, the latest of those applications are briefly summarized, and the most recent developments are described in more detail: the application to the mechanical effects of high temperatures, and the on-going work on alkali-silica reaction.

MESOMECHANICAL MODEL

The models developed for coupled durability phenomena are based on an underlying meso-mechanical model in which the largest aggregate particles are represented explicitly, surrounded by a homogeneous matrix representing the average behavior of mortar plus the smaller aggregates. In order to capture the main potential crack trajectories, zero-thickness interface elements are inserted *a priori* of the analysis, and are equipped with a nonlinear constitutive law based on elasto-plasticity with concepts of fracture mechanics (Carol et al., 1997; Carol et al., 2001). Results of the meso-mechanical model for normal concrete specimens subject to a variety of loading cases in 2D and 3D can be found elsewhere (Carol et al., 2001; Caballero et al., 2007; López et al., 2008).

HYGRO- AND CHEMO-MECHANICAL PROBLEMS

Transport model and coupling strategy. The diffusion analysis of moisture or ionic species in the concrete is based on Fick's second law, with a variable coefficient of diffusivity. The diffusion analysis is combined efficiently with the mechanical analysis by using the same mesh for both. This requires interface elements with double nodes also for the diffusion analysis, as proposed by Segura and Carol (2004). Such interface elements for diffusion incorporate longitudinal as well as transversal diffusivities K_l and K_t. In the absence of specific information, the latter may be given a very high value, while K_l is assumed to increase with a law proportional to the cube or square of the crack opening (Idiart et al., 2011a). The diffusion of moisture or ions drives chemical and/or physical processes that lead to volume changes in the cement paste, which in general are not uniform and therefore lead to stresses and possibly cracks. These cracks are the vehicle for coupling, ie. they represent an easier way for moisture or ionic species to move through the specimen, thus accelerating the volume changes and therefore increasing cracking again. The coupling is implemented *via* staggered strategy for each time step of the time discretization.

Drying shrinkage. Drying shrinkage is phenomenon driven by the loss of moisture, of the initially saturated concrete, to the environment. In the model developed, the moisture movement is represented by a diffusion equation in terms of relative humidity in the pores, H (Eqn. 1a), in which the diffusivity coefficient is not constant (Eqn. 1b). Once this equation solved with the appropriate boundary conditions, the water loss ω_e (mass of water per unit volume of concrete) can be calculated as a post-processing of the resulting H, by using a desorption isotherm curve. Water loss causes volume reductions ε_{sh} in the cement paste, which as a first approach may be assumed linear (Eqn. 1c). Further details of the shrinkage model and examples of application may be found in (Idiart et al., 2011a).

$$\frac{\partial H}{\partial t} = \frac{\partial}{\partial x}\left(D_H \frac{\partial H}{\partial x}\right) \;\; ; \;\; D_H(H) = D_0 + (D_1 - D_0) f(\beta, H) \;\; ; \;\; \varepsilon_{sh} = \alpha(\omega_e) \cdot \omega_e \qquad \text{(1a,b,c)}$$

External sulfate attack. This degradation phenomenon is originated by the ingress of sulfate ions from the environment into the cement pores. These ions then react

with solid ingredients of the cement paste leading to volume expansion. It seems accepted that the reaction takes place in two steps: first, sulfate ions react with the portlandite and/or calcium silicate hydrates of the cement paste leading to gypsum, and second, gypsum reacts with various kinds of calcium aluminates leading to formation of secondary ettringite, which is really the expansive product. In the model developed, this mechanism is represented via equation (2), which is mathematically similar to (1) except for the extra sink term which corresponds to the consumption of sulfate ions. Isotropic expansion of the cement paste due to secondary ettringite precipitation is obtained from equation (3), as the product of the total aluminate reacted C_{eq}^{react} by an equivalent molar volume α_s. The second term in the equation accounts for the volume of capillary pores $f\Phi_{\text{ini}}$ that has to be filled before any macroscopic expansion is observed.

$$\frac{\partial U}{\partial t} = \frac{\partial}{\partial x}\left(D_U \frac{\partial U}{\partial x}\right) - kUC; \;\; D_U(H) = D_0 + (D_1 - D_0) f(\beta, \Phi_{cap}) \tag{2}$$

$$\varepsilon_v(t) = max\left|\alpha_s \cdot C_{eq}^{react} - f\Phi_{\text{ini}}, 0\right| \tag{3}$$

A simple application example of the model is shown in Figure 1. A square concrete specimen is subject to sulfate attack from its perimeter, under both coupled (top diagrams of the figure) and uncoupled analysis (bottom diagrams). In the uncoupled analysis, diffusion is unaffected by cracking, while in the coupled analysis cracks work as penetration channels for sulfate ions. Note that, in the coupled case, the emerging perimetral crack eventually becomes a new attack front, leading to the total penetration of the sulfates, while in the uncoupled analysis penetration is limited to a layer near the surface. Further details of the formulation and examples of application may be found in Idiart et al. (2011b).

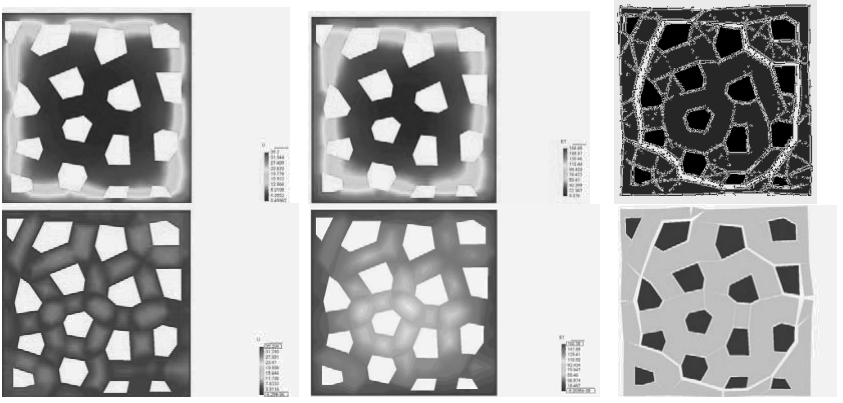

Sulfate concentration

Ettringite Concentration

Mechanical response: expansion, cracking and spalling

Figure 1: Simulations at the meso-level of external sulfate attack to concrete. Final stage: 4,600days; high C3A content: 9,13%. Uncoupled (first row) and coupled analysis (second row).

Alkali Silica Reaction. The reaction mechanism proposed involves three coupled diffusion processes, two in-going and one out-going from the aggregate viewpoint. Alkali (Na^+ and K^+) and Calcium (Ca^{2+}) ions diffuse "inwards", from high molar concentration sites in the pores of the cement paste phase of the concrete specimen or at its boundaries, towards the aggregate-cement paste interfaces or the inner cracks of the aggregates. The OH^- ions associated with alkali and calcium ions attack certain forms of silica in the aggregates (the "reactive silica"), dissolving it in the form of silicate ions which in turn diffuse back to the cement paste phase ("outwards"). The final potentially deleterious ASR precipitation process involves those silicate ions, plus calcium and alkalis. It takes place wherever the reactants are available by precipitating Calcium-Alkali-Silicate-Hydrates (CASH) with a molar volume depending on the reactants concentrations. These diffusion- reaction processes are summarized in the following system of equations (4) where *a*, *c* and *s* are the molar concentrations of alkali, calcium and silicate ions respectively. The source/sink terms are given by chemical kinetics equations (reactive silica dissolution, CASH formation) and chemical equilibrium equations (water self-ionization and portlandite dissociation).

$$\frac{\partial a}{\partial t} = \frac{\partial}{\partial x}\left(D^a \frac{\partial a}{\partial x}\right) + \dot{a} \;;\; \frac{\partial c}{\partial t} = \frac{\partial}{\partial x}\left(D^c \frac{\partial c}{\partial x}\right) + \dot{c} \;;\; \frac{\partial s}{\partial t} = \frac{\partial}{\partial x}\left(D^s \frac{\partial s}{\partial x}\right) + \dot{s} \tag{4}$$

During the development of the reaction the volume fractions of the solid components in the material are not constant. Portlandite and reactive silica are progressively dissolved reducing their volumes and increasing the capillary porosity of the material. The CASH formed occupies this empty volume, leading to a net volumetric expansion when the volume of CASH produced exceeds the available pore space. The volume fraction $u_k(x)$ corresponding to the solid component k is calculated by means of the molar volume and concentration of the chemical species associated to the component, so that the total volume *V(x)* is given by equation (5a). Then, the net isotropic expansion due to ASR is obtained from equation (6). The volumetric distribution of the solid components at each location determines the overall diffusion coefficients by equation (6) (similar equations are considered for $D^a(x)$ and $D^c(x)$) where d_k is the diffusion coefficient of the solid phase k, and m_s is a coefficients that introduces the effect of the ion type (electric charge, ionic radius). Further details of the formulation may be found in Liaudat et al. (2013).

$$V(x) = \sum_{k=1}^{8} u_k(x) \quad ; \quad D^s(x) = \frac{m_s}{V(x)} \sum_{k=1}^{8} u_k(x) \cdot d_k \tag{5a,b}$$

$$\varepsilon_{ASR}(x) = V(x) - 1 \quad if\ V(x) > 1\ (and\ \ 0\ otherwise) \tag{6}$$

An example of application in 1D which simulates an ongoing experimental test is presented to illustrate the capabilities of the model to reproduce realistically the ASR process. The experimental test has been set up to measure ASR expansions at the level of single interface between the hardened cement paste (HCP) and aggregate. Cylindrical "sandwich" specimens of 33 mm of diameter and 64 mm of total height, with a borosilicate glass disc in the middle as reactive aggregate, and HCP on top and bottom, are exposed to a 1M NaOH solution at 60ºC for a period of 14 days during which expansions are measured regularly.

The overall expansion curve obtained with the model is plotted together with the experimental results in Figure 2. The main trend of experimental behavior is caught by the model. The volumetric solid phase distribution in the area near the HCP-glass interface, for different exposure times, is represented in Figure 3. There, the progressive glass and portlandite depletion near the interface becomes apparent, as well as the CASH precipitation, first filling the capillary pores and finally producing a volumetric expansion.

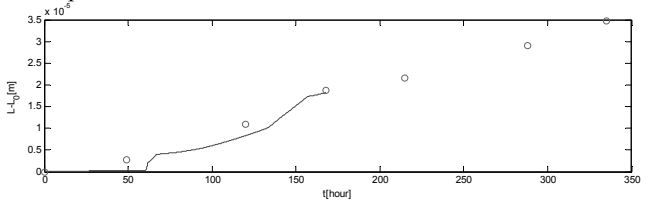

Figure 2: Experimental ASR expansion test at the level of a single aggregate-HCP interface. Length change from experiment (circles) and model (line).

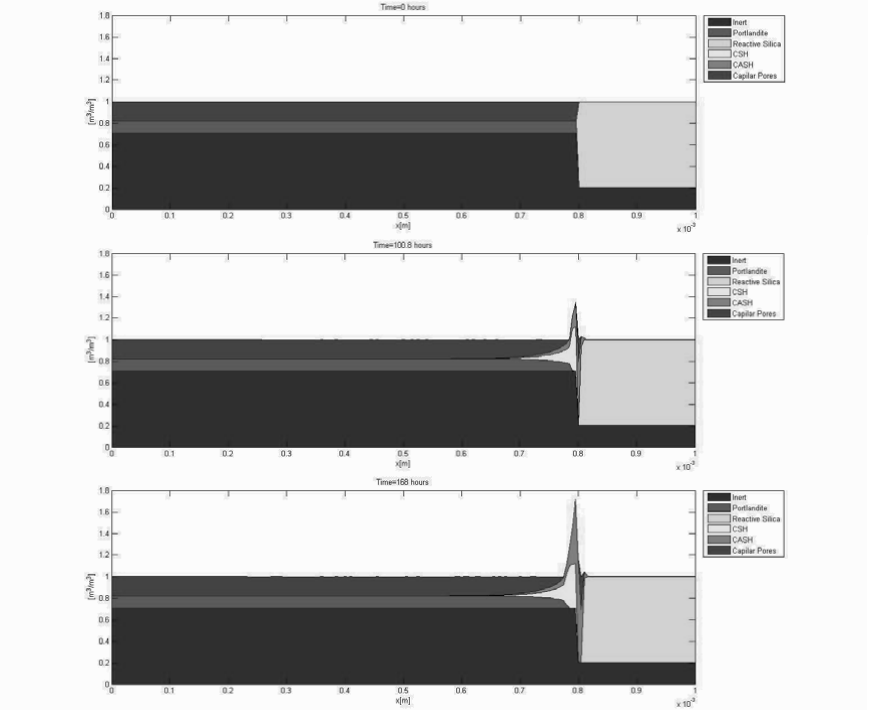

Figure 3: Volumetric solid phase distribution in the interface zone of HCP-glass for different exposure times. Note the gel formation (non-expansive CSH in yellow, and expansive CASH in orange) and the reduction of Portlandite ($Ca(OH)_2$) and pore space, near the cement-glass interface.

CONCRETE SUBJECT TO HIGH TEMPERATURES

The effects of temperature changes on heterogeneous materials such as concrete, may include internal stresses, cracking and degradation, even if the temperature remains constant thought the specimen cross-section. This is due to the expansion mismatch between components. Those effects are studied by a coupled thermo-mechanical model, where the main material heterogeneities with their detailed (or at least approximate) geometry are represented, and applying to phase the appropriate thermal expansion and material behavior laws. The cause of coupling in this case is given by the thermal boundary conditions as spalling occurs: for the first time step temperature distributions are computed with the boundary conditions applied on the original specimen boundary, but this situation changes as the time goes on and layers of material start dissapearing. Then, the new temperature b.c.s for each time increment are applied onto the new updated domain boundaries.

The example of application presented consists of to a 10x30cm^2 rectangular 2D specimen of concrete subject to prescribed temperature increments on the right vertical edge of the domain only, while thermal flow is assumed null on the other three faces. The displacements normal to the surface are also restrained along those faces. The time-dependent imposed temperature values correspond to the standard curve given in the fire-resistance tests recommendation ISO834-1 which are defined by $T = 345\log_{10}(8t + 1) + 20$, where T is the temperature in ºC and t is the time in minutes. In the numerical analysis, concrete is represented by large aggregates particles of dolomite rock surrounded by a matrix that represents mortar and smaller aggregates. The specimen considered has volume fraction of large aggregates 28% and maximum aggregate size 14mm (average aggregate size 10.4mm). A variable coefficient of thermal expansion has been used for mortar. It has been extracted from a volume expansion vs. temperature curve obtained numerically in (Rodriguez et al., 2011). For the aggregate a constant coefficient of thermal expansion extracted from the experimental results of (Cruz & Guillen, 1980), who obtained independent expansion curves for aggregates, cement, mortar and concrete, are used.

Figure 4 depicts the temperature distribution (top) and cracking/spalling situation (bottom) obtained for four different calculation times, which correspond to prescribed temperatures of 420, 660, 680 y 720ºC, respectively. As already mentioned, the analysis includes the thermo-mechanical coupling due to the evolving geometry and boundary conditions of the thermal action, which, at each stage of the calculation are moved to the new boundary resulting from the mechanical spalling. More details of these calculations, including the extension to 3D, can be found in Perez et al. (2013).

CONCLUDING REMARKS

The mesomechanical model for concrete previously developed for purely mechanical actions, which is based on Voronoi-generated geometries of the larger aggregates and cracking via fracture-based zero-thickness interface elements, seems to provide a convenient basis for extensions to coupled durability mechanics calculations. Until now, the model has been developed for drying shrinkage, external sufate attack and

mechanical effects of high temperatures. On-going work devoted to alkali-silica reaction (ASR) seems very promising, with a three-field diffusion-reaction chemical model which has yet to be coupled to the mechanical analysis, but that has already been shown to qualitatively and quantitatively reproduce some experimental measurements of sandwich-type specimens subject to standardized accelerated ASR tests. From the chemical viewpoint, the formulation has the advantage that it incorporates the recently identified role of Calcium in ASR expansions (Leeman et al, 2011) , i.e. depending on local conditions (including pH and Ca^{++} concentration) the model can lead to either generation of non-expansive CSH, expansive CASH, or a mix of both in varying proportion.

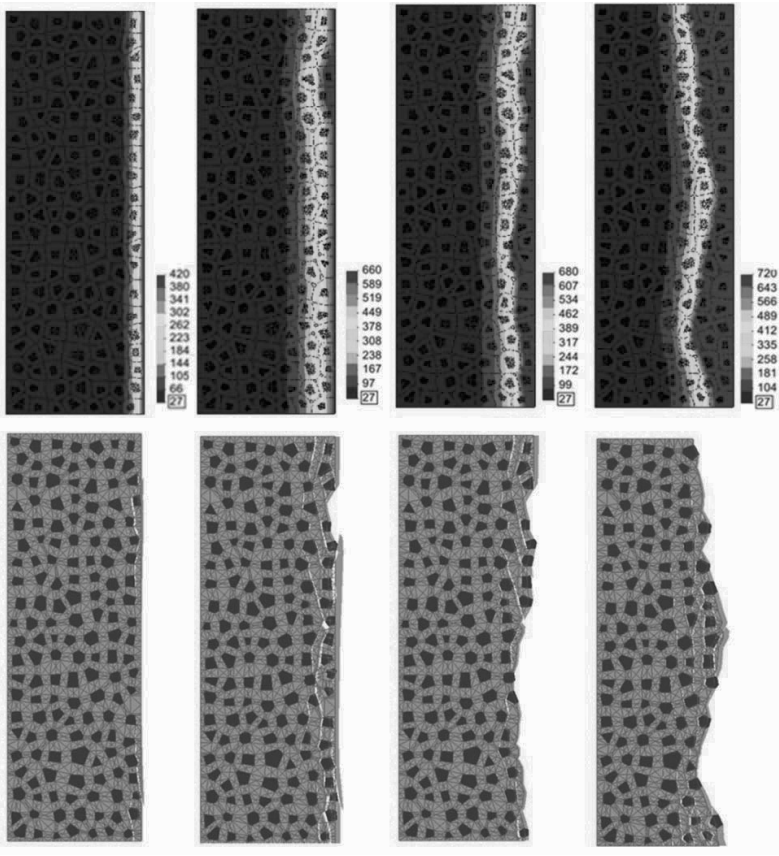

Figure 4: Evolution of temperature and deformation for the prescribed boundary values: T = 420, 660, 680 y 720ºC, corresponding to the ISO curve times: t = 1.68; 8.82; 10.10 and 13.23 minutes.

ACKNOWLEDGEMENTS

Partial support comes from grants BIA-2012-36898 from MEC (Madrid), including FEDER funds, and 2009SGR-180 from AGAUR-G. de Catalunya (Barcelona). The first author also thanks MICINN (Madrid), for his FPI doctoral fellowship.

REFERENCES

Caballero, A., Carol, I., López C. M. (2007). "3D mesomechanical analysis of concrete specimens under biaxial loading". *Fatigue and Fracture Engng. Mat. and Structures*, **30**: 877-886.

Carol, I., Prat, P. C., López, C.M. (1997). A normal/shear cracking model. Application to discrete crack analysis*. Engng. Mech. ASCE*, **123**: 765–773.

Carol, I., López, C.M. and Roa, O. (2001). Micromechanical analysis of quasi-brittle materials using fracture-based interface elements. *Int. J. Num. Meth. Engng.,* **52**:193-215.

Cruz, C. R., and Gillen, M. (1980). "Thermal expansion of Portland cement paste, mortar and concrete at high temperatures". *Fire and materials*, **4**:66-70

Idiart, A., López, C.M., Carol, I. (2011a). "Modeling of drying shrinkage of concrete specimens at the meso-level". *Materials and structures RILEM*, **44**: 415–435.

Idiart, A., López, C.M., Carol, I. (2011b). "Chemo-mechanical analysis of concrete cracking and degradation due to external sulfate attack: A meso-scale model". *Cement & Concrete Composites*, **33**:411–423.

Leemann, A., Le Saout, G., Winnefeld, F., Rentsch, D., & Lothenbach, B. (2011). Alkali–Silica Reaction: the Influence of Calcium on Silica Dissolution and the Formation of Reaction Products. *J. Am. Ceram. Soc.* **94**: 1243-1249.

Liaudat, J., López, C.M. and Carol, I. (2013)."Diffusion-reaction model for alkali-silica reaction in concrete". In Proc. *COMPLAS XII*. E. Oñate, D.R.J. Owen, D. Peric and B. Suárez (Eds). CIMNE (2013) (in press).

López, C.M., Carol, I., and Aguado, A., (2000). Microstructural analysis of concrete fracture using interface elements. In O˜nate, E. et al., editors, Proc. *ECCOMAS 2000*.CIMNE (Barcelona, Spain). ISBN 84-89925-70-4 (in CD-ROM).

López, C.M., Carol, I., and Murcia, J, (2001). Mesostructural modeling of basic creep at various stress levels. In Ulm, F.J., Ba˘zant, Z.P., and Wittmann, F.H., editors, Creep and Shrinkage of Concrete Structures, pp. 101–106. John Wiley (New York).

López C.M., Carol I., Aguado A. (2008). "Meso-structural study of concrete fracture using interface elements. I: numerical model and tensile behavior" and "II: compression, biaxial and Brazilian test". *Materials and Structures*, **41**: 583-620.

Pérez, A., Rodriguez, M., Lopez, C.M. and Carol, I. (2013). "3D Meso-mechanical analysis of cracking and spalling of concrete subject to high temperatures". In *Proc. COMPLAS XII*. E. Oñate, D.R.J. Owen, D. Peric and B. Suárez (Eds). CIMNE (2013) (in press).

Rodríguez, M., López, C.M., Carol, I., and Murcia, J. (2011). "High temperature effects in mortar and concrete specimens using a meso-mechanical model with fracture based zero-thickness interface elements". *Proc. COMPLAS XI*, Barcelona, Spain.

Segura, J. M. and Carol, I. (2004). "On zero-thickness interfase elements for diffusion problems". *International Journal for Numerical and Analytical Methods in geomechanics,* **28**: 947-962

Finite Element Based Characterization of the Creep Properties of the Cement Paste Phases by Coupling Nanoindentation Technique and SEM-EDS

L. Sorelli[1], D.-T. Pham[2], D. Vallée[3], J. Chen[4], M. Fafard[5]

[1] Université Laval, Department of Civil and Water Engineering, 1065 av. de la Médecine, PLT2928-A, Quebec, QC, CANADA; PH (418) 656-3060; FAX (418) 656-2928; email: luca.sorelli@gci.ulaval.ca
[2] Université Laval, Department of Civil and Water Engineering, 1065 av. de la Médecine, Quebec, QC, CANADA; email: duc-tho.pham.1@ulaval.ca
[3] Université Laval, Department of Civil and Water Engineering, 1065 av. de la Médecine, Quebec, QC, CANADA; email: daniel.vallee.1@ulaval.ca
[4] Lafarge Centre de Recherche, 95, rue du Montmurier - B.P 70, 38291 St Quentin Fallavier, France email: jeffrey.chen@lafarge.com
[5] Université Laval, Department of Civil and Water Engineering, 1065 av. de la Médecine, PLT 2926-B, Quebec, QC, CANADA; PH (418) 656-7605; FAX (418) 656- 2928; email: mario.fafard@gci.ulaval.ca

ABSTRACT

This work aims to characterize the creep behavior of the major microstructure constituents of cement paste by means of a novel approach which combines Nanoindentation Technique (NT) and Scanning Electron Microscopy with X-ray microanalysis (SEM-EDS).
We first performed a large grid of nano-indentation tests on different cement paste samples. The tests were carried out in displacement-control by imposing a maximum penetration depth of 150 nm for 600 seconds. The surface was finely polished according to an optimized protocol to reach very low roughness, verified by Atomic Force Microscopy (AFM) techniques. Then, we performed the chemical analysis of all the indented points by SEM-EDS. The chemical analysis allowed selecting the indentation tests which corresponding to likely pure phase. One of the advantages of such coupling technique is that there is no need of statistically deconvoluting the distributions of the measured properties to estimate the property of the phases. For instance, the relaxation curves load-time for the C-S-H phase was selected with and without carbonation. Finally, we perform a finite element analysis of the relaxation behavior of the selected points by means of a viscous model for concrete which splits the deviatoric long term creep and the volumetric short term creep. Eventually, this simplified model-based approach provided the creep coefficient of the so-identified Calcium-Silicate-Hydrates (C-S-H), Calcium-Hydroxide (CH) and belite (C2S), monosulfoaluminate (AFm) phases. The conclusions of this work provided new insights on the identification of the creep properties of the sub-micrometer phase composing the cement phase.

INTRODUCTION

Nanoindentation techniques have recently advanced the limit of material science in characterizing the microstructure properties. First application of nanoindentation techniques in concrete science allowed to characterize the mechanical properties of the clinker phases (Sorrentino et al. 2001), as well as the Calcium-Silicate-Hydrates for both the low and high density morphology (Constantinides, 2006). Constantinides (2006) extended the nanoindentation techniques to heterogeneous material by applying a grid of nanoindentation tests over a sufficiently large area to be considered as statistically representative. The deconvolution technique allows identifying the normal distribution of the mechanical properties (indentation modulus, hardness and creep compliance) of each phase by simply minimizing the difference between the experimental distribution and a mixture distribution. As an important advancement, Krakowiak (2011) extended the deconvolution technique by considering joint distribution functions of the measured indentation. He employed a multi-variate cluster analysis based on the minimization of the maximum-likelihood estimation.

The premise of statistical indentation technique is that the volume probed by a single indentation test is made of a pure phase. However, for highly heterogeneous material, the heterogeneity size may be smaller than the volume probed by an indentation test. By applying a Focused Ion Beam (FIB) test on a cement paste, Lura and Trtik (2009) showed that the likelihood of testing a micrometer volume of pure C-S-H is less than 10%; that is, the volume probed by an indentation test is most likely composed by an intermix of phases. One μm is also roughly the dimension of the probed volume underneath an nanoindentation test, the exact dimension depending on the maximum penetration depth h_{max}. To bypass this issue, Vanzo (2009) carried out a decoupled chemo-mechanical analysis by testing carbonated cement pastes with nanoindentation tests and a chemical analysis based on Wavelengh Diffration Spectroscopy. As the mechanical and chemical characterization were carried out on a different grid of points of the sample surface, their results did not allow to clearly relate the distribution of the mechanical properties of each phase with the distribution of the chemical composition. Chen et al. (2010) carried out a fully coupled analysis on a cement paste with very low water-to-cement ratio by analyzing the chemical composition of the volume underneath each nanoindentation test with a Scanning Electron Microscopy-Energy Dispersion Spectroscopy (SEM-EDS). Each indentation imprint was analyzed in the SEM-EDS to study the chemistry of the underneath volume. As a major result, this approach allowed understanding the stiffening role of the CH crystals embedded in the C-S-H matrix.The scope of this work is to further apply this coupled chemo-mechanical approach to characterize the mechanical properties of the cement paste microstructure, especially alite (C2S), belite (C3S) and an Ordinary Portland Cement (OPC) paste, with a stoichiometric w/c ratio in between 0.40 and 0.50. The section 2 describes the test methodology and the tested materials. Section 3 presents the results based on a deterministic analysis. Section 4 presents the conclusions with future perspectives of research.

MATERIALS AND METHODS

Material preparation and mix designs. Table 1 reports the samples which were prepared by Lafarge Centre Research (LCR): a hydrated belite, a hydrated alite, and a

hydrated ordinary Portland cement (OPC). Belite and alite were cured in an environment with a relative humidity (RH) equal to 100%, while the OPC type 1 ordinary Portland cement was cured into water. All samples were mixed using a waring blender. The samples were cast and cured into plastic cylinder with a diameter of approximately 10 mm. They were cast in October 2010 and cured until November 2011 before being cut into pieces with a height of approximately 8 mm and polished.
The surface topography was investigated by atomic force microscopy using the tapping mode of a Dimension TM 3100 Atomic Force Microscope with an etched silicon tip (OTESPATM, tip radius < 10 nm, aspect ratio=1.6/1). The images were taken with 256x256 data acquisitions at a scan rate of 1 Hz at room temperature in air. The surface topography was evaluated for areas of 80x80 μm which is close to the size of the indentation grid. Image processes (i.p.) were applied on the images generated from the raw elevation data over their respective position in order to be considering the only roughness that may affect the nanoindentation measurements. A linear slope correction with a least-squares polynomial of order 3 was performed in order to make horizontal the reference plane of the AFM. A Gaussian filter was also applied to eliminate wave effects larger than 8.0 μm. These processes were realized with the software TrueMap. RMS before and after the i.p. are shown in Table 1.

Table 1. Sample choice and roughness.

Materials	w/c [-]	RMS [nm]	RMS i.p. [nm]
Hydrated belite (C2S)	0.45	91	23
Hydrated alite (C3S)	0.42	51	11
Hydrated Ordinary Portland cement (OPC)	0.51	64	18

SEM-EDS

The chemical analysis employs scanning electron microscope with energy-dispersive X-ray spectroscopy (SEM-EDS). The tests were performed on a Quanta FEG 200 by FEI Company and conducted with an accelerating voltage of 15 kV, a beam current of 1 nA and a 10 mm working distance. Calibrations were made on specimens with well-known stoichiometry allowing precise quantitative analysis: Ca2SiO4, Ca3Al2O6, Fe2O3, MgO, KSi, Mn, Ti and Ca as suggested by Chen et al. (2010). This calibration allows quantitative analysis of the following chemical elements: O, Na, Mg, Al, Si, P, S, K, Ca, Ti, Mn, Fe. Each SEM-EDS measurement was executed directly on the indentation imprints in the grid of indentations. With an average residual depth below 125 nm for the tested samples and a micro-volume of about 2 μm for the SEM-EDS, the roughness effect of the nanoindentation imprint on the EDS measurements were considered negligible

Instrumented nanoindentation technique (NT). Nanoindentation technique allows extracting the mechanical properties of a material at the microstructure scale. The nanoindentation consists of setting up a contact between a rigid diamond indenter with a known geometry and a material sample, while measuring the applied load P in function of the penetration depth h (Constantinides, 2006). For an elastic material, the

analysis of the P-h curve provides the indentation modulus M and the indentation hardness H as follows:

$$M = \frac{\sqrt{\pi}}{2}\frac{S}{A_C} \quad (1)$$

$$H = \frac{P_{max}}{A_C} \quad (2)$$

where P_{max} is the maximal load applied, A_C is the projected contact area and S is the initial slope of the unloading P-h curve, which is defined as $S = [dP/dh]_{h=hmax}$. The maximum penetration depth h_{max} is determined with the Oliver and Pharr method (Oliver and Pharr, 1992). For homogeneous isotropic linear elastic material, the indentation modulus M can be linked to the Young's modulus E as follows:

$$\frac{1}{M} = \frac{1-\upsilon^2}{E} + \frac{1-\upsilon'^2}{E'} \quad (3)$$

where ν is the Poisson ratio of the indented material, ν' is the Poisson ratio of the indenter and E' is the Young's modulus of the indenter, which for a diamond indenter. The penetration depth was rapidly applied and then kept constant (h_{max}) for 600 seconds to allow a viscous material to relax.

Table 2. Nanoindentation testing parameters

Type of loading:	Displacement control
Indentation Matrix	20×20
Max depth	150 nm
Loading time	5 s
Holding time	600 s
Unloading time	5 s
Interdistance	5 μm

We first performed a 20x20 grid of nano-indentation tests on a finely polished surface samples. The tests were carried out in displacement-control by imposing a maximum penetration depth of 150 nm for 600 seconds (Table 2). Displacement control tests allow avoiding delayed plasticity during the holding phase (Vandamme et al. 2012). The surface was finely polished with an optimized protocol which was checked by Atomic Force Microscopy (AFM) techniques (REF). The surface image was analyzed to assess the mean square roughness (RMS) after having applied the following operations: (i) flip the surface horizontally; (ii) filter of the Gaussian smoothness with wavelength larger than 8 μm. We employed a UHNT nanoindentation platform available at the $L(CM)^2M$ laboratory of the Université Laval which is endowed with a double reference system to reduce the thermal drift to less than 1 nm over 500 seconds without need of post-processing correction of the thermal drift.

Finite Element model. The Finite Element Method (FEM) Code_Aster (2001) was employed to analyze the nanoindentation results. The material model is composed by two parts, a plasticity model for the loading phase and a creep model for both the holding and unloading phase. The FEM mesh is shown in Figure 1: 2112 contact element were employed to model the contact problem, 36917 nodes and of 36709 Q4 axisymmetric elements were used with an adapted mesh density to the problem.

Plasticity model. The loading curve is modeled with a Drucker-Prager model with associated plasticity flow rule implemented in Code_Aster (2001). The yielding function reads:

$$f(\sigma) = \sigma_{VM} + \frac{2\sin\varphi}{3-\sin\varphi} I - \frac{6\,c\,\sin\varphi}{3-\sin\varphi} \leq 0$$

where σ_{VM} is the von Mises stress, I is the 1st stress invariant, φ is the friction, and c is the cohesion.

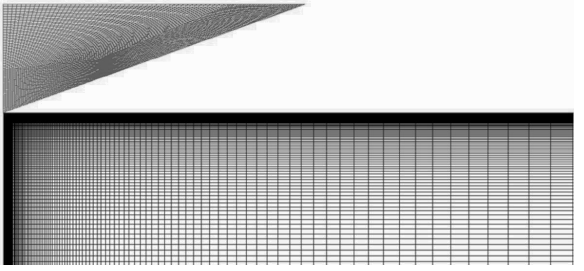

Figure 1. Finite element mesh employed for the indentation test.

Creep model. To model the holding and unloading phase, we employed the creep model of Benboudjema (1999) available in Code_Aster developed which makes a physical distinction between the deviatoric and the volumetric creep. Briefly, the former is associated to the reversible mechanism of water diffusion in the sub-capillary pores, while the latter is associated to the irreversible mechanisms of slippage at the scale of the hydrates (Benboudjema, 1999). The model is based on the decoupling of the creep strain into the volumetric and deviatoric parts as follows:

$$\underline{\underline{\varepsilon}}^{c} = \varepsilon^{c}_{V,rev}\,\underline{\underline{I}} + \underline{\underline{\varepsilon}}^{c}_{d,irrev} \tag{5}$$

where the volumetric and deviatoric parts are:

$$\varepsilon^{c}_{V,rev} = tr(\underline{\underline{\varepsilon}}^{c})/3 \qquad \underline{\underline{\varepsilon}}^{c}_{d,irrev} = \underline{\underline{\varepsilon}}^{c} - \varepsilon^{c}_{V}\,\underline{\underline{I}} \tag{6}$$

It is assumed that the volumetric creep, related to the water diffusion, is purely volumetric and that the deviatoric creep, which is as due to slippage at the level of hydrates, which is purely irreversible. The evolution law of the reversible creep is

$$\dot{\varepsilon}^{c}_{V,rev} = \frac{1}{\eta_{V,rev}}\left[\sigma_{V} - k_{V,rev}\varepsilon^{c}_{V,rev}\right] \tag{7}$$

where $k_{V,rev}$ is the the apparent stiffness associated to the skeleton composed by hydrates at the meso-scale and $\eta_{V,rev}$ the apparent viscosity associated to the diffusion mechanisms in the capillary pores. σ_{V} and $\underline{\underline{\sigma}}_{d}$ are respectively the volumetric and deviatoric part of the stress tensor. The evolution law of the irreversible deviatoric creep is described by a linear law:

$$\eta_{d,irrev}\,\dot{\underline{\underline{\varepsilon}}}^{c}_{d,irrev} = \underline{\underline{\sigma}}_{d} \tag{8}$$

which depends on one parameter $\eta_{d,irrev}$, which is a viscosity associated to the irreversible mechanisms at the hydrate creep sites, Finally, for the reversible volumetric creep we can define a characteristic time as follows:

$$\tau_{V,rev} = \eta_{V,rev} / k_{V,rev} \quad (9)$$

Results and discussion

Chemical analysis.

Figure 2 displays the chemical results of the SEM-EDS for the belite and alite samples in terms of Si/Ca ratio and Mass Oxide Total. The stoichiometric theoretical values of the pure phases are identified with cross shaped markers. As the experimental points are close to those markers but not exactly located over them, we need to define a satisfactory range with a margin of error. We decided to at the points must be in an absolute circle of interval range with a radius of 2%, 5% or 10% for all 3 different chemical plots, where the center of these circles being the single phase. For instance, we filtered out points with values within the ranges with radius of ±0.02, ±0.05, ±0.10 for the Si/Ca, (Fe + Al)/Ca and S/Ca atomic ratios and for ±2%, ±5%, 10% for the mass of oxides total. Figure 2 shows the identification of the C-S-H (C/S=1.8) for the belite sample. Analogously, we carried out the same point selection to identify the C-S-H carbonated (C/S=1.4), Portlandite (CH) and monosulfoaluminate (AFm) for the 3 samples.

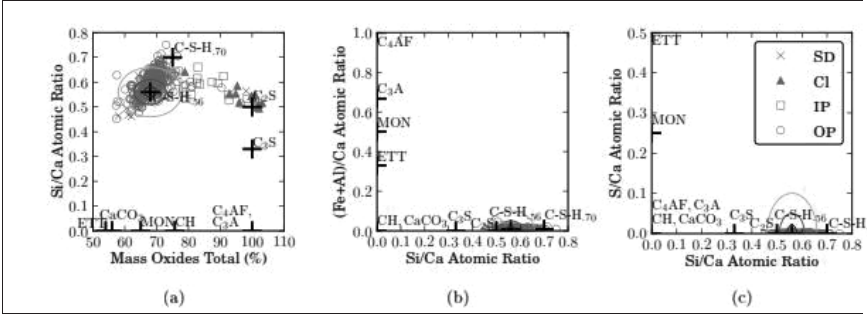

Figure 2. Chemical analysis for identifying C-S-H in the belite sample: (a) plot Si/Ca vs. MOT; (b) plot (Fe+Al)/Ca vs. Si/Ca; (c) plot S/Ca vs. Si/Ca.

Mechanical analysis. Figure 3 shows the relaxation curve P-t during the holding time for the indentation points belonging to pure phases as identified with the chemical analysis for the 3 samples. The experimental curves are plotted in grey, the average one is in black and the numerical one is circle-dashed. Table 3 reports the creep parameters needed to fit the creep curves for the pure phases shown in Figure 3 as well as for AFm and CH.

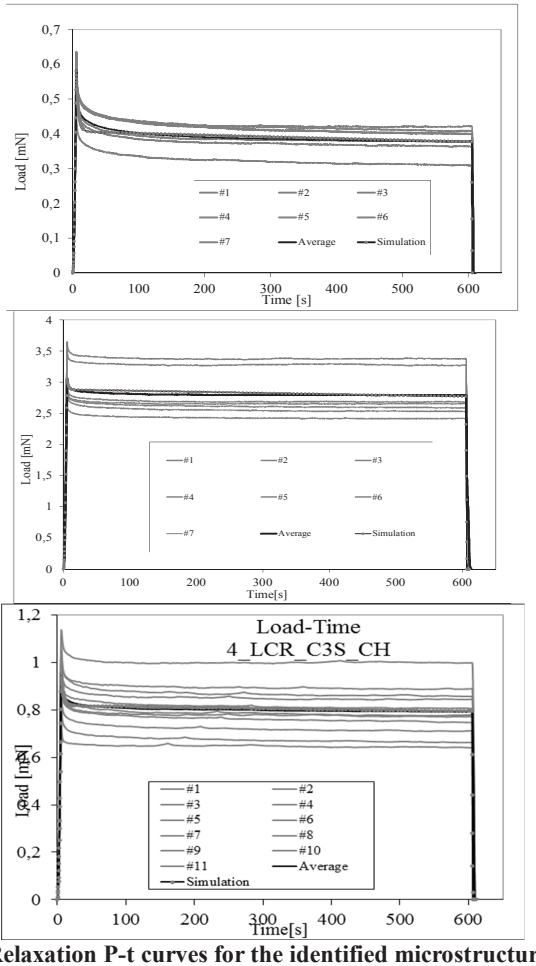

(a)

(b)

(c)

Figure 3. Relaxation P-t curves for the identified microstructure phases for (a) C-S-H (C/S=1.8), (b) C2S, and (c) CH (C/S=1.4).

Table 3. Creep properties of the microstructure phases.

Phase	Sample	E [GPa]	$k_{V,rev}$ [GPa]	$\eta_{V,rev}$ [GPa sec]	$\tau_{V,rev}$ [sec]	$\eta_{d,irrev}$ [GPa sec]
C-S-H(C/S=1.8)	Belite	26	26	150	5.8	96e+04
C_2S	Belite	112	1000	2200	2.2	96e+05
C-S-H(C/S=1.4) belite	Belite	29	115	200	1.7	20e+05
CH	Alite	45	130	500	3.8	46e+05
AFm	OPC	22	22	100	4.5	96e+04

CONCLUDING REMARKS AND RESEARCH OUTLOOK

This work shows a new approach to couple nanoindentation technique and SEM-EDS to identify the chemistry and the mechanical response of the pure phases composing a cement paste. The results were analyzed using FEM and provide the creep coefficient of the pure phases composing the cement paste. Based on those results, the volumetric viscosity (η_V^r) for the C-S-H, CH and C2S is 150:500:2200 GPa sec, respectively while the deviatoric viscosity η_d^i is 96:460:960 GPa sec. The decalcification of C-S-H increases the volumetric (short term) viscosity from 26 to 125 GPa sec, and the deviatoric (long term) viscosity from 96e+04 to 200e+04 GPa sec. The ongoing research is focusing on the experimental characterization of the creep at different humidity and the model enhancement for the creep mechanisms.

ACKNOWLEDGEMENTS

We acknowledge the support of the LCR in the sample preparation as well as FRQNT-BMP for the financial support. We also acknowledge CSM Instruments for supporting in the use of the UHNT-CSM platform available at Université Laval.

REFERENCES

Benboudjema, F. (2002) "Modélisation des déformations différées du béton sous sollicitations biaxiales. Application aux bâtiments réacteurs de centrales nucléaires. " PhD Thesis, Université Marne La Vallée, France.

Chen, J.J., et al. (2010). "A Coupled Nanoindentation/SEM-EDS Study on Low Water/Cement Ratio Portland Cement Paste: Evidence for C-S-H/Ca(OH)(2) Nanocomposites." *J. of the Am. Cer. Soc.*, 93(5), 1484-1493.

Code_Aster (2001) http://www.code-aster.org/V2/doc/default/fr/

Constantinides, G. (2006). Invariant Mechanical Properties of Calcium-Silicate-Hydrates in Cement-Based Materials: Instrumented Nanoindentation and Microporomechanical Modeling." PhD thesis, Massachusetts Institute of Technology, Cambridge, MA.

Krakowiak K.J., (2011) "Assessment of the mechanical microstructure of masonry clay brick by nanoindentation", PhD Thesis University of Minho, Portugal.

Lura P., Trtik P., Munch B. (2009). "A critical examination of statistical nanoindentation on model materials and hardened cement pastes based on virtual experiments." *J. Cem Concr Comp*, 31(10), 705-714.

Oliver W., Pharr G. (1992) "An improved technique for determining hardness and elastic modulus using load and displacement sensing indentation experiments.", *J Mat Res* (7), 1564 – 83.

Sorrentino F., Velez K., Maximilien S., et al. (2001) "Determination by nanoindentation of elastic modulus and hardness of pure constituents of Portland cement clinker." *J. Cem Concr Res*, 31(4), 555–561.

Vandamme M., et al. (2012) "Quantifying plasticity-independent creep compliance and relaxation of viscoelastoplastic materials under contact loading" J. Mat Res 27(01):302-312.

Vanzo J.F., (2009) "A nanochemomechanical investigation of carbonated cement paste." MSc thesis, Massachusetts Institute of Technology, Cambridge, MA.

In-situ Chemo-Mechanical Characterization of Cementitious Microstructures with Coupled X-Ray Microanalysis and Indentation Technique.

Konrad J.Krakowiak[1], William Wilson[2], Simon James[3], Franz.-J. Ulm[4]

[1]Civil and Environmental Engineering Department, Massachusetts Institute of Technology, 77 Massachusetts Avenue, Cambridge, MA 02139-4307, USA; email: kjkrak@MIT.EDU

[2]Civil and Environmental Engineering Department, Massachusetts Institute of Technology, 77 Massachusetts Avenue, Cambridge, MA 02139-4307, USA; email: wilsonw@MIT.EDU

[3]Schlumberger Riboud Product Center, 1 rue Henri Becquerel, Clamart, 92140, France; email: james6@slb.com

[4]Civil and Environmental Engineering Department, Massachusetts Institute of Technology, 77 Massachusetts Avenue, Cambridge, MA 02139-4307, USA; email: ulm@MIT.EDU

ABSTRACT

This work is focused on the chemo-mechanical characterization of cement-based materials. A novel approach is presented, which combines the classical grid indentation technique with x-ray energy dispersive microanalysis method. Two oil-well cement systems with different combination of silicious filler are examined, both, from mechanistic and chemical point of view. The characteristic x-rays of major elements, silicon, calcium and aluminum, are measured over the indentation region and mapped back on the indentation points. Measured intensities together with indentation hardness and modulus are considered as the set of observables used in the deconvolution analysis. Inference of the number of phases, their average properties and clustering of experimental observations is executed in the framework of Finite Mixture Models with Gaussian component density function. The calcium-silica-hydrate gel is successfully isolated at the indentation scale from other phases of cement hydration, and its mechanical response linked to the calcium-to-silicon ratio quantified with x-ray wavelength dispersive spectroscopy.

INTRODUCTION

Introduction of the grid indentation technique to the experimental filed of cement-based materials gave access to the characterization of cementitious microstructures at different length and time scales (Constantinides 2004, 2006, Hughes 2004, Vandamme 2009, 2013). In the method's framework, the large set of measurements carries the statistical information about each mechanical phase of the

bulk, which may be inferred via statistical deconvolution (Ulm 2007). Therefore, the method is able to examine cement systems beyond laboratory conditions, where the hydration products are created in the unique local environment. However, the inference is purely based on the mechanical response, therefore, the direct correlation of measured properties to the local chemistry is only possible with comparison to reference. Additionally, phases of different stoichiometry, which represent similar mechanical response, may manifest as one single microstructural component, what could bias the entire analysis.

To address these problems, this work combines the indentation measurement with the energy dispersive x-ray microanalysis technique, in order to link the indentation response to in-situ chemistry. The applicability of the method is demonstrated for two oil-well cement systems with different combinations of silicious additive, and curing conditions. The multivariate Gaussian Mixture Model is applied to model experimental data obtained in both measurements, and to infer the phase's redistribution. The indentation response of the C-S-H solid is linked to its stoichiometry via quantitative wavelength dispersive spectroscopy (WDS) microprobe analysis.

MATERIALS

Table 1 outlines cement systems selected for this experimental study. Portland Cement Class G is used in both pastes as a hydraulic binder, but, they differ in the type and the fraction of the siliceous material used as filler. The silica flour (α-quartz), with the median particle size d_m=30μm and in the amount 35% by weight of cement (bwoc) is used as an inert filler in G-1 system, while the combination of silica fume (SF, 14.4% bwoc) and quartz (17.4% bwoc) is incorporated in the G-2 sample.

Table 1. Investigated cement-based systems

Sample Name	Binder Type	w/c	Curing Conditions
G-1	cement Class G + quartz**	0.43	T=60°C, p=20.7 MPa
G-2	cement Class G + quartz + SF	0.55	T=30°C, p=20.7 MPa

METHODS

Sample Preparation

Samples for Instrumented Indentation, SEM imaging and x-ray spectrometry were prepared via a semi-automatic polishing procedure. In the first stage, cylindrical sub-samples, ≈1.0 cm in diameter and 0.5 cm in height, were cut from each bulk material, with the IsoMet diamond saw, Buehler (Lake Bluff, USA). After that, each sample was mounted with cyanoacrylate glue on the AFM disk (Ted Pella, USA), and leveled and ground in a specially designed jig and the post system (Miller 2008). A perforated cloth TexMetP (Buehler, USA) with a 9 μm oil-based diamond suspension MetaDi (Buehler, USA) was used for grinding. Grinding passes lasted approximately 20 min. in total, with four stops for 3 min. of the ultrasonication in Isopropanol.

Finally, the ground and cleaned samples were manually polished on the alumina disks FibrMet, Buehler (Lake Bluff, USA), with abrasive sizes 9, 3 and 1 μm, respectively. At each abrasive size the samples were polished for around 5 min.. Fine polishing was accompanied by 1 min. cleaning of the sample in the ultrasonic bath with Isopropanol.

Wavelength Dispersive X-ray Spectrometry (WDS)

A quantitative analysis of the chemical composition was carried out with the electron probe micro-analyzer (EPMA) JEOL JXA-8200 Superprobe. The polished specimens were analyzed by WDS under the following analytical conditions: an accelerating voltage 15 keV, a beam current of 10 nA, a beam diameter 1 μm and a counting time per element of 10sec. The background correction was applied at each spot. The mass fractions were calculated with CITZAF package (Armstrong 1995), using the *$\phi(\rho z)$-method* (stopping power, back-scatter corrections and *$\phi(0)$* from Love and Scott, mean ionization potential from Berger and Seltzer, Heinrich's tabulation of mass absorption coefficients, and Armstrong's modified equations for absorption and fluorescence corrections (Goldstein 2007, Heinrich 1991).

Elemental Mapping with Energy Dispersive X-ray Spectrometry (EDS)

Electron micrographs and EDS elemental maps were acquired with the JEOL 5910 general purpose scanning electron microscope equipped with Bruker EDX system for elemental analysis. The backscattered images of the region of interest (ROI) were obtained at beam voltages of 15 and 10 kV and working distance of 10mm. Elemental maps of major constituents, silicon (Si), calcium (Ca), aluminum (Al) and iron (Fe) were collected at the count rate 15kpcs and a current of 40nA.

Instrumented Grid Indentation

Instrumented indentation tests were carried out in the standard nanoindentation tester, CSM Instruments, equipped with the environmental control enclosure (18±1°C, 21±2%RH) and the damping system. Force controlled tests were run to the prescribed maximum force F_{max}=3 mN, with the linear loading and unloading at constant rate 12 mN/min and dwell time of 5 sec. Tip area function of the diamond indenter, Berkovich type, was calibrated on the standardized fused silica block (E=73.1±0.7 GPa, v=0.16), at 18 different loads ranging from 0.5 to 100 mN, and cross-validated on the natural α-quartz [0001] sample as an auxiliary reference material, H=14.5±0.5 GPa and M=124.5±4 GPa. Indentation penetration – force curves were corrected w.r.t. point of contact as well as the frame compliance and analyzed for indentation hardness, H, and plain stress modulus, M, according to the Oliver and Pharr method (Oliver 1992, Fischer-Cripps 2004).

Single indentation grid comprises N=576 measurement points minimum, arranged in the rectangular grid and spaced regularly around 10 μm apart in each direction, to assure the independency of successive measurement. The indentation tests carried out on the G-1 sample were executed on freshly exposed polished surface, while for the G-2 sample the surface was spotted with 20nm thick carbon layer prior the mechanical testing.

Linking Indentation Properties to Local Chemistry: Deconvolution Model

Mechanical properties obtained in the instrumented indentation, are directly linked to the local phase chemistry, which is assessed qualitatively at each point of the indentation grid with SEM-EDS elemental mapping technique. For statistical data modeling, each *j-th* point of the grid is associated with the n-tuple vector $\boldsymbol{y}_j=\{H_j;M_j;I_{j,1};\ldots;I_{j,n}\}$, where H and M correspond to local hardness and indentation modulus, while $I_{j,1}$*'s* stand for raw or autoscaled intensities. Given the uniqueness of the chemical composition of phases in the investigated cement systems, as well as similar scaling applied to counts at each pixel and for every element of interest, each phase will be associated with one and only one combination of the $I_i's$, H and M on average, represented by mean vector $\boldsymbol{\mu}_i$, with $i=1,\ldots,g$. In this work, the inference of the mean vectors $\boldsymbol{\mu}_i$ is carried out in the framework of Finite Mixture Models (Eq. 1a) with the multivariate normal p.d.f., f_i, as the component density function (see Eq. 1b). Therefore, the standard deviations on each of the variables, as well as eventual variable correlations are captured by the covariance matrix $\boldsymbol{\Sigma}_i$, while π_i, represents the surface fraction of a given phase. All unknown parameters $\boldsymbol{\Psi}=(\pi_1,\ldots,\pi_g,\boldsymbol{\mu}_1,\boldsymbol{\Sigma}_1,\ldots,\boldsymbol{\mu}_g,\boldsymbol{\Sigma}_g)$ are estimated based on the maximum likelihood (ML) via the expectation maximization (EM) algorithm. The probabilistic clustering of the IND-EDX observations into g groups, selected according to Bayesian Information criterion (BIC), is carried out following the Bayes rule of allocation. The reader is referred to references (Dempster 1977, Schwartz 1978, McLachlan 2000) for detailed discussion of Mixture Modeling and ML parameter estimation method together with EM algorithm.

$$f(\boldsymbol{y}_j;\boldsymbol{\Psi})=\sum_{i=1}^{g}\pi_i f_i(\boldsymbol{y}_j;\boldsymbol{\theta}_i),\ 0\le\pi_i\le 1\ (i=0,\ldots,g),\qquad \sum_{i=1}^{g}\pi_i=1 \qquad \text{Eq. 1a}$$

$$f_i(\boldsymbol{y}_j;\boldsymbol{\mu}_i,\boldsymbol{\Sigma}_i)=(2\pi_i)^{-\frac{p}{2}}|\boldsymbol{\Sigma}_i|^{-\frac{1}{2}}exp\{-\tfrac{1}{2}(\boldsymbol{y}_j-\boldsymbol{\mu}_i)^T\boldsymbol{\Sigma}_i^{-1}(\boldsymbol{y}_j-\boldsymbol{\mu}_i)\} \qquad \text{Eq. 1b}$$

RESULTS AND DISCUSSION

General Characteristics of the Indentation Region: BSE Micrographs

The electron micrographs of the indentation regions are presented in Figure 1. Each phase in the investigated microstructures corresponds to its unique average atomic number, which results in the different gray level contrast (Goldstein 2007, Scrivener 2004). Therefore, the brightest regions indicate of the residual ferrite (C_4AF) commonly found in the close proximity of residual belite (C_2S) or alite (C_3S) minerals. The rounded morphology of belite helps further to identify this phase in both microstructures. Additionally, regions of portlandite (CH) are also apparent, especially at the boundaries of the siliceous aggregates incorporated in the G-2 paste, while lower contrast in micrograph of G-1 paste makes this phase less apparent. This microstructural components, together with the siliceous aggregates, α-quartz (Q) and

fume (SF) in G-2 system are embedded in the matrix of C-S-H gel which may be intermixed with submicron scale AFm/AFt phases (Taylor 1997, Richardson 1993).

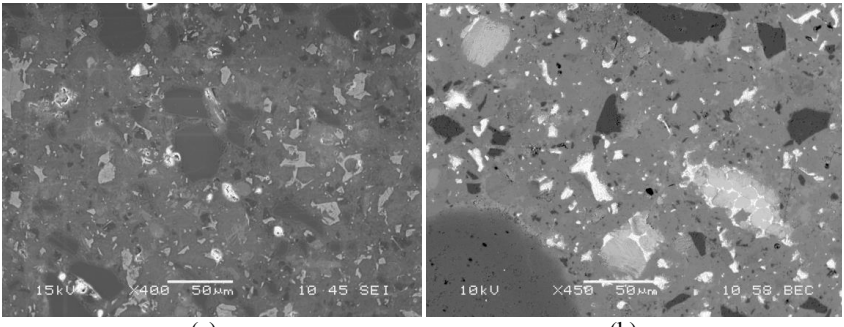

(a) (b)

Figure 1. SEM-BSE micrographs of the indentation region: (a) G-1 system with crystalline silica enrichment, (b) G-2 paste with combination of crystalline and amorphous silica bearing additive.

Elemental Mapping and Chemistry Assessment with EDS and WDS techniques

The spatial distribution of phases inferred from EDS elemental mapping is presented in Figure 2. As expected, the composite EDS maps highlight the siliceous aggregates represented as red color dominated regions, which is in complete agreement with the backscattered micrographs. On the other hand, the calcium dominated regions, which likely correspond to portlandite are outlined as irregular patches dominated by blue, and regions of ferrite corresponding to cyan. The most apparent microstructure component, the C-S-H matrix is defined by the purple color in both samples. The residual belite is also apparent in the G-2 microstructure. In summary, each of the microstructural components present in the indentation ROI is associated with the set of autoscaled intensities of characteristic x-rays, on average, which correspond to unique set of numbers in the color scale used for a display (Goldstein 2007, Newbury 1999). It must be mentioned, the current analysis is restricted to three major elements, silicon, calcium and aluminum, which are displayed as red, green and blue, respectively. This analysis may be easily extended to additional elements as well.

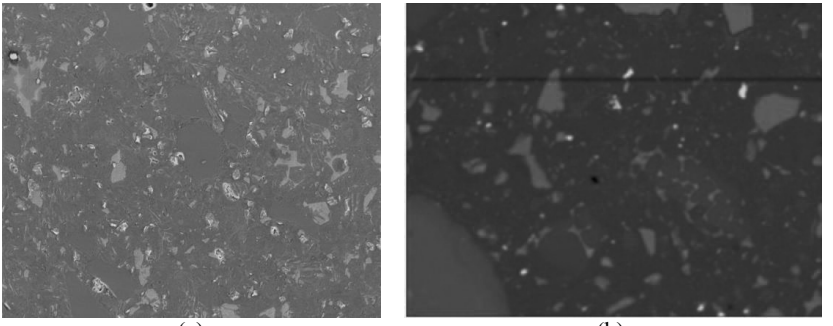

(a) (b)

Figure 2. The elemental composite maps showing the redistribution of phases with different stoichiometry over the ROI: a) the composite of {Si;Ca;Al} and BSE micrograph for G-1 paste, b) the composite map of {Si;Ca;Al} for G-2 paste with mixed crystalline and amorphous siliceous filler.

Figure 3 presents the scatter diagrams of characteristic x-ray intensities of silicon and calcium at each point of the indentation grid extracted from EDS elemental maps. The grouping of the experimental records around several poles becomes apparent suggesting redistribution of the indentation measurements among numerous phases with distinctive chemistries, as expected.

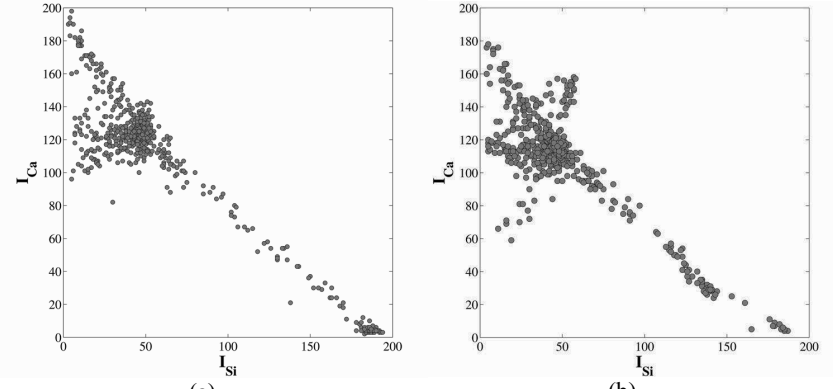

(a) (b)

Figure 3. Scatter diagrams of the autoscaled intensities of major elements, silicon and calcium, obtained at the locations of the indentation points: a) G-1 paste, b) G-2 paste.

Indentation Properties

Typical imprint of the grid indentation is obtained for both cement pastes (Figure 4). Therefore, the majority of experimental points are located in the mechanical domain H=[0.5;2.0] and M=[15.0;50.0] GPa., which is commonly attributed to the products of cement hydration (Constantinides 2004, 2006, Hughes 2004, Vandamme 2009, 2013), C-S-H gel and portlandite, respectively. Because of relative close proximity of the indentation properties between C-S-H gel and porltandite (Constantinides 2006), as well as the smeared characteristics of the spatial distribution of CH, indentation records of these two phases may lack sufficient mechanical contrast to allow clear phase distinction based on the raw experimental observations (Figure 4). Additional components of the indentation results are observations with much higher values on both properties, which tend to originate from the indentation on the residual clinker phases, or crystalline silica.

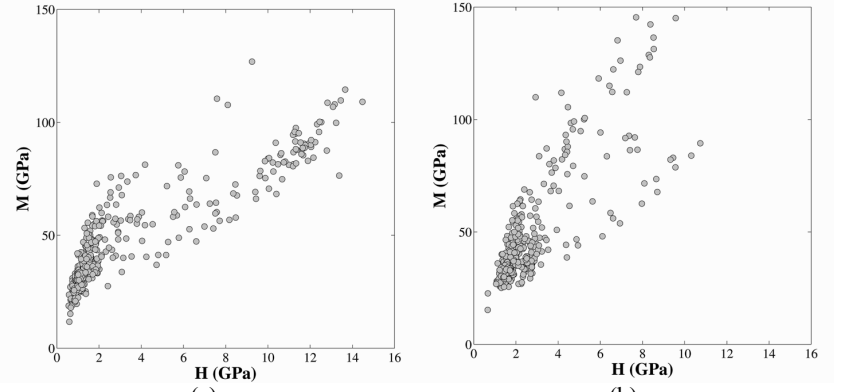

Figure 4. Scatter diagrams of indentation responses corresponding to: a) G-1 paste, b) G-2 paste.

Linking Indentation Properties to Phase Chemistry

As discussed in the previous paragraphs, in the proposed experimental approach each measurement point on the grid is associated with the vector of measured mechanical properties (Figure 4) and intensities (Figure 3) corresponding to major elements, silicon, calcium and aluminum. Therefore, the statistical inference was carried out with respect to these observables and its outcome is presented in Figure 5.

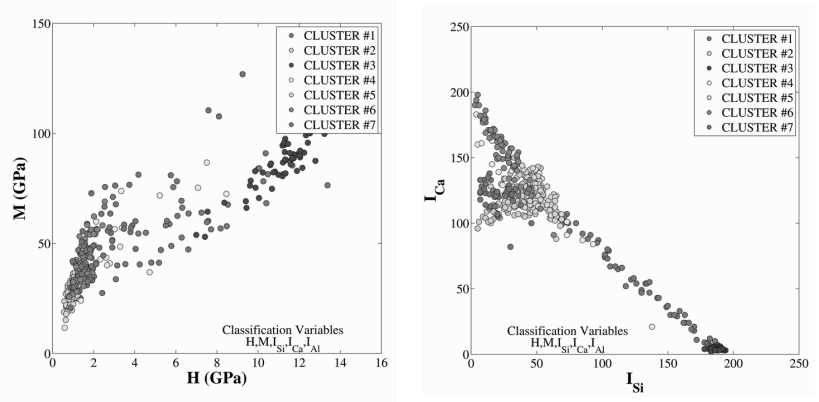

(a)

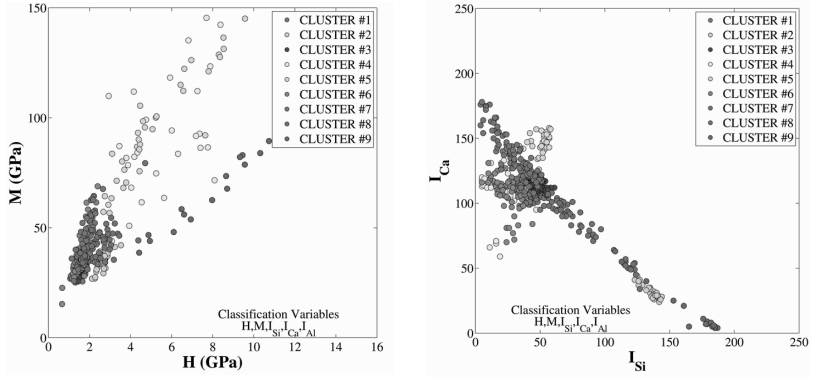

(b)

Figure 5. Results of the coupled indentation-EDS statistical deconvolution with the clustering of observations into distinct phases as assessed with the Gaussian Mixture Modeling.

The optimum model with seven different families corresponds to experimental data obtained on the G-1 paste (Figure 5a). The products of cement hydration are represented by clusters #5, 2 and 6, which are C-S-H gel, AFm like phase and portlandite, respectively. The mean indentation hardness and modulus of C-S-H matrix are 1.07 GPa and 29.5 GPa, respectively, with estimated volume fraction of 28%. Additionally, the quantitative WDS analysis, carried out independently on G-1 paste, confirms its mean calcium-to-silicon ratio ≈2.1 (see Figure 6a). The mechanical response of AFm phase is similar to the indentation

response of C-S-H matrix, as indicated on Figure 5a, namely, 1.1 GPa for mean hardness and 31.1 GPa for modulus. Although this phase tends to show chemical affinity to AFm hydration products, the possibility of indentation on Al-substituted C-S-H, or intermixing with normal C-S-H cannot be excluded in the current analysis. The last product of hydration is a portlandite, with the estimated properties H=1.5 GPa and M=40.1GPa, and volume fraction of 14%. Lastly, cluster #1 tends to be a composite response of a cementitious matrix and quartz, cluster #3 represents quartz while family #7 circumvents all indentation records linked to residual clinker phase C_4AF. It is interesting to notice than only a few of experimental points in the last group record values of hardness, ≈9.5 GPa, and modulus, ≈125 GPa, typical for aluminoferrite crystals (Veleza 2001). Therefore, it is very likely that majority of records in this group are affected by the more compliant surrounding matrix or grain boundaries. This hypothesis tends to be supported by the fine crystal size of this phase present in both pastes as observed under SEM microscope (see Figure 1).

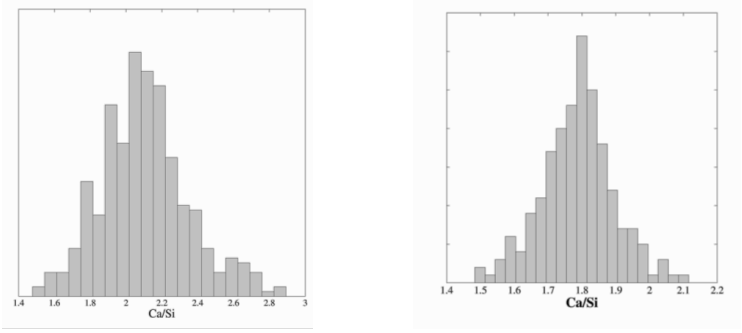

(a) (b)

Figure 6. Distribution of the calcium-to-silicon ratio of the C-S-H measured with the WDS microanalysis technique on a) G-1 and b) G-2 paste.

The chemo-mechanical deconvolution of sample G-2 follows the qualitative trend as previously discussed on the sample G-1, however, several differences are apparent (Figure 5b). First, the number of optimum clusters is increased suggesting more heterogeneous structure of the experimental data, as well as the microstructure of G-2 paste what is in line with the slurry design (see Table 1). The extra components recorded both, mechanically and chemically, relate to the aggregates of silica fume, clusters #2 and 8. The C-S-H solid, with Ca/Si=1.8 (see Figure 6b), is clearly distinguishable and corresponds to clusters #1, 3, with the first one showing slight chemical affinity to Al-bearing hydration products. Despite this apparent chemical difference, the mean indentation properties are quite similar, ≈1.6 GPa for hardness and ≈33 GPa for modulus, on average. Lastly, the chemo-mechanical response of residual belite phase is captured and identified as family #5.

SUMMARY AND CONCLUSIONS

This work presents an original chemo-mechanical approach to the problem of phase characterization in cement-based materials. Such materials represent complex systems, which require experimental and statistical methods able to address heterogeneous microstructures as well as experimental data structures.

It is shown, that the combination of widely accepted grid indentation technique together with EDS elemental mapping provide suitable base of observables to identify microstructural components by their unique chemo-mechanical footprint. The insight into the chemistry of the indentation volume, coined here "chemical eye", appears to be central to the problem of separation of cement hydration products with different stoichiometry, yet very similar indentation responses at submicron scale. Therefore, the C-S-H solid with high chemical affinity to its pure member can be isolated at the scale of indentation as we demonstrated on selected engineering examples. The current approach uses WDS technique to quantify the stoichiometry of the C-S-H solid, however, the future extension of the proposed technique to quantitative EDS appears possible.

The inference of the phase properties as well as their abundance was carried out in the framework of the Gaussian Mixture Model, which represents an efficient approach to the data deconvolution. Such statistical data modeling, with long standing achievements in other fields (McLachlan 2000), reduces much of the ambiguity related to the choice of the number of phases as well as the impact of the user on the deconvolution process and analysis, which have been points of contention for some critics in the past (Lura 2011).

ACKNOWLEDGEMENT

The authors would like to acknowledge the important role of Schlumberger-MIT cement research collaboration, X-CEM, in the presented developments. We also would like to thank Concrete Sustainability Hub at MIT, with sponsorship provided by the Portland Cement Association (PCA) and the RMC Research & Education Foundation. The authors are grateful for this support.

REFERENCES

Armstrong, J. T. (1995) "CITZAF - A package of correction programs for the quantitative electron microbeam X-ray analysis of thick polished materials, thin films, and particles," Microbeam Analysis, 4(3), pp. 177–200.

Constantinides, G. and Ulm, F. –J. (2004) "The effect of two types of C-S-H on the elasticity of cement-based materials: results from nanoindentation and micromechanical modeling", Cem. Concr. Res. 34, pp. 67–80 (2004)

Constantinides, G. (2006) "Invariant mechanical properties of calcium-silicate-hydrates (C-S-H) in cement-based materials: Instrumented nanoindentation and micromechanical modeling", PhD Thesis, Massachusetts Institute of Technology.

Dempster A. P., Laird N. M., and Rubin D. B., (1997) “Maximum likelihood from incomplete data via the EM algorithm,” Journal of the Royal Statistical Society, Series B, 39, pp. 1–38.

Fischer-Cripps, a. C., (2006), Nanoindentation, 2nd ed., Springer.

Goldstein, J., Newbury D. E., Joy, D., Lyman, Ch., Echlin, P., Lifshin, E., Sawyer, L., Michael, J., (2007) Scanning Electron Microscopy and X-ray Microanalysis, 3rd ed., Springer.

Heinrich, K. H. J., Newbury, D. E. Eds., (1991) Electron Probe Quantitation.

Hughes, J. J., and Trtik, P., (2004) "Micro-Mechanical Properties of Cement Paste Measured by Depth-Sensing Nanoindentation: A Preliminary Correlation of Physical Properties with Phase Type," Mater. Charact., 53, pp.223‑31.

Lura, P., Trtik, P., Münch, B., (2011) “Validity of recent approaches for statistical nanoindentation of cement pastes”, Cem. Concr. Compos. 33, pp. 457-465.

McLachlan, G. J., Peel, D., (2000) “Finite Mixture Models’, Wiley Series in Probability and Statistics, A Wiley-Interscience Publication.

Miller, M., Bobko, C., Vandamme, M., Ulm, F. –J., (2008) “Surface roughness criteria for cement paste nanoindentation”, Cem. Concr. Res. 38 (4), 467-476.

Newbury, D. E., Bright, D. S. (1999) “Logarithmic 3-band encoding: a robust method for display an dcomparison of compositional maps in electron probe x-ray micronalaysis”, Microsc. Microanal., 5(5), pp. 333-343.

Oliver, W. C., Pharr, G. M., (1992) “An improved technique for determining hardness and elastic modulus using load and displacement sensing indentation experiments,” J. Mater. Res., 7, p. 1564-83.

Richardson, I. G., Groves, G. W., (1993) “Microstructure and microanalysis of hardened ordinary Portland cement pastes”, J. Mater. Sci. 28, pp. 265-277.

Schwartz, G., (1978), “Estimating the dimension of the model,” Ann. Statist., 6 461-64.

Scrivener, K. L., (2004) "Backscattered electron imaging of cementitious microstructures: understanding and quantification." Cem. Concr. Compos. 26(8): 935-945.

Taylor, H. F. W., (1997) “Cement Chemistry”, 2nd ed., Thomas Telford.

Ulm, F. –J., Vandamme, M., Bobko, Ch., Ortega, J. A., (2007) “Statistical indentation techniques for hydrated nanocomposites: concrete, bone, and shale”, J. Am. Ceram. Soc. 90, pp. 2677-2692.

Vandamme, M., Ulm, F.–J. (2009) “Nanogranular origin of concrete creep”, PNAS, 106 (26), 10552-10557.

Vandamme, M., Ulm, F.–J., (2013) “Nanoindentation investigation of creep properties of calcium silicate hydrates”, Cem. Concr. Res., 52, 38-52.

Veleza, K., Maximiliena, S., Damidot, D., Fantozzia, G., Sorrentinob, F., (2001) “Determination by nanoindentation of elastic modulus and hardness of pure constituents of Portland cement clinker”, Cem. Concr. Res., 31, pp. 555-561.

Efficient homogenization of ageing creep of random media: application to solidifying cementitious materials

J. Sanahuja[1]

[1]EDF R&D - département MMC, Site des Renardières - Avenue des Renardières - Ecuelles, 77818 Moret sur Loing cedex, FRANCE; PH (33) 1-60-73-79-92; FAX (33) 1-60-73-65-59; email: julien.sanahuja@edf.fr

ABSTRACT

The correspondence principle is widely used to estimate the effective behaviour of non ageing linear viscoelastic composites, as it allows to take advantage of homogenization approaches originally developed in the elastic framework. However, this principle is no longer valid when the phases exhibit ageing. An approach recently proposed overcomes this limitation: homogenization of random media can be used on composites made up of isotropic ageing linear viscoelastic phases. In this paper, the latter is applied to estimate the effective viscoelastic behaviour of solidifying composite materials, that is porous materials subjected to gradual precipitation of solids into pore space. This theory developed by Bažant shows that even if the behaviour of the precipitated material is non ageing, the effective behaviour exhibits ageing due to the microstructure evolution with time. Modelling the solidifying material as a set of fictitious ageing linear viscoelastic phases, homogenization can be taken advantage of to estimate the effective behaviour. This allows to investigate other precipitation mechanisms than the parallel arrangement initially considered by the solidification theory, such as a rough, simplified, model of cement paste. The effective ageing creep is found to be highly dependent on both the precipitation mechanism and kinetics.

INTRODUCTION

Ageing linear viscoelasticity

The mechanical behaviour considered in this paper is linear viscoelasticity with ageing. This behaviour is written as a Stieltjes integral relating the stress tensor $\boldsymbol{\sigma}$ evolution to the strain tensor $\boldsymbol{\varepsilon}$ history:

$$\boldsymbol{\sigma}(t) = \int_{-\infty}^{t} \mathbb{C}(t,t') : \mathrm{d}\boldsymbol{\varepsilon}(t') \tag{1}$$

where $\mathbb{C}(t,t')$ is the relaxation tensor. The component $C_{ijkl}(t,t')$ gives the stress along i,j at time t resulting from a unit strain step along k,l occurring at t'. As $\boldsymbol{\sigma}(t)$ cannot

depend on $\varepsilon(t')$ for $t' > t$ (causality principle), $\mathbb{C}$ can be extended as $\mathbb{C}(t,t') = 0$ when $t' > t$.

The specific case of the (non ageing) linear elastic behaviour can be represented with a relaxation tensor written as $\mathbb{C}(t,t') = \mathbb{C}_0 \mathrm{H}(t-t')$, where $\mathbb{C}_0$ is the stiffness and H is the Heaviside function.

Homogenization of ageing linear viscoelastic composites

A new approach to upscale ageing linear viscoelastic behaviours in the framework of homogenization of random media has been recently proposed [Sanahuja(2013)]. Contrary to existing approaches [Ricaud and Masson(2009), Masson et al.(2012)Masson, Brenner, and Castelnau], the so-called strain localization tensor is derived directly in the ageing linear viscoelastic context. The latter is a linear integral operator, in the sense of (1). Then, classical homogenization schemes (namely the dilute, Mori Tanaka and self-consistent schemes) commonly used in elasticity can be straightforwardly extended to ageing linear viscoelastic behaviours. This approach is nearly as easy to use as the correspondence principle in the non ageing case, and directly outputs the effective bulk and shear relaxation functions. As a side effect, the (often numerical) inversion of the Laplace-Carson transform is avoided. This approach is used but not detailed here: for complete description and validation, see [Sanahuja(2013)].

FROM A TENSORIAL EXTENSION OF SOLIDIFICATION THEORY TO FICTITIOUS AGEING PHASES

Effective ageing behaviours can arise from non ageing ones at the lower scale, if the underlying morphology of the composite material evolves with time. We here refer to the solidification theory from Bažant [Bažant(1977)]: some phases are expected to precipitate at given times.

Without entering into details, before the precipitation time, the phase behaves as a void (zero stiffness), and after the precipitation time, the phase exhibits a solid behaviour. At solidification time, the phase is stress-free. The original solidification theory only considered a monodimensional parallel arrangement of precipitating layers (figure 1). Here, a tensorial extension is proposed.

To take advantage of homogenization, the solidifying material is modelled as ageing linear viscoelastic. In the most general case, its relaxation tensor takes the form:

$$\mathbb{C}_{t_s}(t,t') = \mathbb{C}^s(t-t')\mathrm{H}(t'-t_s) \tag{2}$$

where t_s is the solidification (or precipitation) time and $\mathbb{C}^s$ is the relaxation tensor of the solidified material, whose behaviour is non ageing (after precipitation). In the particular case of an isotropic elastic behaviour once precipitated, the bulk and shear relaxation functions take the form:

$$k_{t_s}(t,t') = k^s \mathrm{H}(t-t')\mathrm{H}(t'-t_s) \quad \text{and} \quad g_{t_s}(t,t') = g^s \mathrm{H}(t-t')\mathrm{H}(t'-t_s) \tag{3}$$

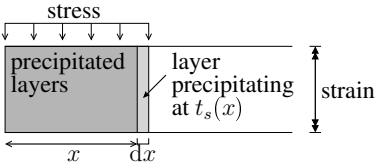

Figure 1. Bažant's original solidification theory: underlying precipitation mechanism

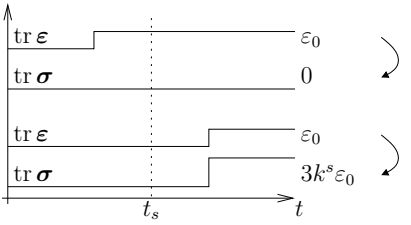

Figure 2. Relaxation experiments (for an isotropic strain loading) on the ageing viscoelastic material modelled by (3)**.**

where k^s and g^s are the bulk and shear elastic moduli of the precipitated material. As illustrated on figure 2, this behaviour models a solidifying material according to the solidification theory.

Going back to viscoelastic behaviours, let us show that in the particular case of a morphology as a parallel arrangement of layers of solidifying material (figure 1), the effective behaviour from Bažant's solidification theory is retrieved. The relaxation function of the layer precipitating at time t_s, as the one dimensional counterpart of (2), reads:

$$R_{t_s}(t,t') = R^s(t-t')\mathrm{H}(t'-t_s) \tag{4}$$

where R^s is the non ageing relaxation function of the solid phase. Note that the expression of the relaxation function $R_{t_s}(t,t')$ is valid whatever t and t'. Taking advantage of the parallel arrangement of the layers (every layer is subjected to the macroscopic strain) and assuming that the layers (including the not yet precipitated ones) occupy the domain $0 \leqslant x \leqslant 1$ (and that the solidification front increases from 0 to 1 as a function of time), the effective relaxation function of the set of layers reads:

$$R^{eff}(t,t') = \int_0^1 R_{t_s(x)}(t,t')\,\mathrm{d}x = \int_0^1 R^s(t-t')\mathrm{H}(t'-t_s(x))\,\mathrm{d}x \tag{5}$$

where $t_s(x)$ is the (supposedly known) solidifying time of the $\mathrm{d}x$ layer found at x. In

the last integrand, the Heaviside function is equal to 1 when $t_s(x) < t'$, that is for layers that have already solidified at time t'. In other words, $t_s(x) < t' \Leftrightarrow x < f(t')$ where $f(t')$ denotes the volume fraction already solidified at t'. Thus (5) becomes:

$$R^{eff}(t,t') = f(t')R^s(t-t') \tag{6}$$

which is the exact counterpart of equation (15) in [Carol and Bažant(1993)], up to notation changes.

Note that a micromechanical technique to homogenize solidifying composites made up of non ageing viscoelastic phases has already been proposed [Scheiner and Hellmich(2009)]. The idea is to consider auxiliary homogenizations performed at fixed volume fractions of phases, thus taking advantage of the correspondence principle. Then the effective viscoelastic behaviour is built referring to each one of these auxiliary results around its domain of validity. Compared to this technique, the approach proposed in this paper does not make use of the Laplace-Carson transform, is also able to deal with local ageing behaviours, and directly outputs the effective bulk and shear relaxations as functions of both times t and t' (in discretized form).

APPLICATION TO EFFECTIVE CREEP OF A SOLIDIFYING COMPOSITE

Homogenization of random media made up of ageing linear viscoelastic phases makes possible the estimation of the effective ageing behaviour of solidifying materials. This is useful to improve the prediction of the ageing behaviour of materials whose microstructure is subjected to phase changes, such as cementitious materials (see for example [Bernard et al.(2003)Bernard, Ulm, and Lemarchand, Sanahuja et al.(2007)Sanahuja, Dormieux, and Chanvillard]). Indeed, during hydration of cement paste, and this continuous process can last several monthes, species progressively dissolve and precipitate.

Application to complex materials such as concrete or cement pastes is beyond the scope of this paper. Thus, the first application proposed here considers a simplified material where a fictitious precipitation process occurs. The aim is to evaluate the influence of the precipitation mechanism and kinetics over the effective ageing behaviour. Investigation of real cementitious materials can be viewed as prospects of the current study.

Morphology of composite and solidifying mechanisms investigated

This section is devoted to a first application over a simplified microstructure: a porous media where a solid material progressively solidifies into pores (modelled as spheres). As information about morphology can be integrated thanks to homogenization of random media, it is possible to investigate the influence of the precipitation mechanism on the effective ageing behaviour. Two solidifying scenarios are investigated (figure 3):

- precipitation in whole pores, one pore after the other, in random order,

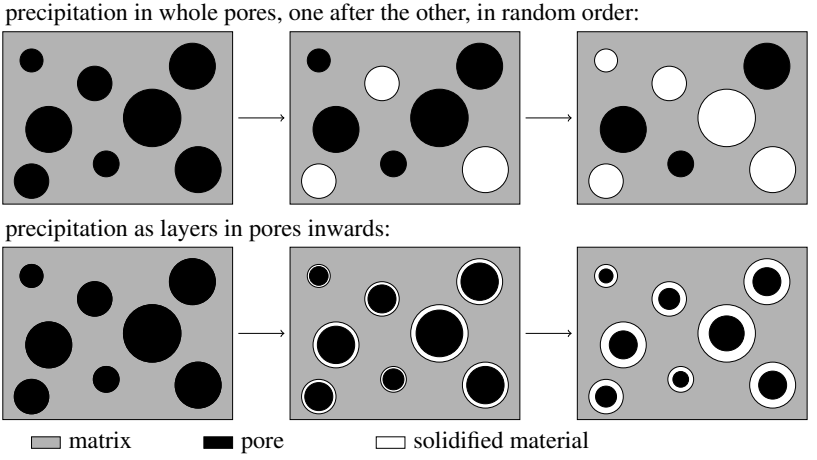

Figure 3. Schematic representations of the solidifying mechanisms investigated.

- precipitation at the boundary of pores inwards, forming layers whose diameter decreases with time (the evolution of the local volume fraction of solidified material is assumed to be the same in every pore, for simplification purposes).

The matrix and the solidified material are respectively denoted by subscripts 0 and s. The volume fraction f_0 of matrix is constant. As pores are progressively invaded by solidified material s, the volume fraction f_s of the latter increases up to f_s^∞, while porosity $\varphi = 1 - f_0 - f_s$ decreases. For the sake of simplicity, the kinetics of the precipitating process is modelled through an "S-shaped" curve (figure 5):

$$f_s(t) = f_s^\infty \frac{(t/\tau)^\alpha}{1 + (t/\tau)^\alpha} \tag{7}$$

where τ and α are the characteristic time and a kinetic parameter of microstructure evolution (ageing). More realistic evolutions could come from chemical and kinetic models of the precipitation processes occurring in the investigated composite material, but this is beyond the scope of this paper.

Behaviour of phases

The spherical and deviatoric behaviours of both matrix and solidified material are modelled by Maxwell rheological models for the sake of simplicity, even if *any* linear viscoelastic behaviour (including ageing) could be used:

$$\mathbb{C}(t - t') = 3k\mathrm{e}^{-\frac{t-t'}{\eta/k}}\mathrm{H}(t - t')\mathbb{J} + 2g\mathrm{e}^{-\frac{t-t'}{\gamma/g}}\mathrm{H}(t - t')\mathbb{K} \tag{8}$$

where the stiffness and viscosity of the spherical (resp. deviatoric) part of the Maxwell behaviour are denoted by k and η (resp. g and γ). The numerical parameters used in the simulations are gathered on table 1. The stiffness is defined by the Young's modulus E and the Poisson ratio ν, instead of k, g.

Table 1. Material parameters used in the application (stresses are normalized by the matrix Young's modulus E_0, and times are normalized by the characteristic ageing time τ), both matrix and precipitate being represented by a Maxwell rheological model.

	stiffness		characteristic time		volume fraction	kinetic parameter
	$\frac{E}{E_0}$	ν	$\frac{\eta/k}{\tau}$	$\frac{\gamma/g}{\tau}$	f	α
matrix	1	0.2	0.2	0.133	0.6	n/a
precipitate	5	0.3	1	1.67	from 0 to $f_s^\infty = 0.3$	1, 4 or 7

Modelling solidification resorting to fictitious ageing phases

The microstructure evolution (precipitation into pores) is not taken into account directly. Rather, several solidifying phases are considered, whose precipitating time is derived from the volume fraction evolution. More precisely, the final volume fraction of precipitate is divided into N equal volume fractions. The final volume fraction being denoted by f_s^∞, N solidifying materials are introduced, the i^{th} ($i \in \{1, \dots, N\}$) having the volume fraction f_s^∞/N and precipitating at time t_i such that:

$$f_s(t_i) = \left(i - \frac{1}{2}\right)\frac{f_s^\infty}{N} \tag{9}$$

Thus the volume fraction evolution of solidified material is discretized as N cumulative vertical steps (see dotted line on figure 5). Phase i occupies in the fictitious REV the domain invaded by the part of precipitate which appears when the volume fraction of solidified material increases from $(i-1)f_s^\infty/N$ to if_s^∞/N. Its solidifying behaviour, modelled as an ageing linear viscoelastic behaviour, is defined by the relaxation tensor:

$$\mathbb{C}_i(t, t') = \mathbb{C}_s(t - t')\mathrm{H}(t' - t_i) \tag{10}$$

where t_i is the precipitation time from (9) and $\mathbb{C}_s(t-t')$ is the relaxation tensor of the solidified material (8).

The estimation of the effective ageing viscoelastic behaviour of the composite where precipitation occurs reverts to the homogenization of a fictitious composite made up of $N+1$ ageing viscoelastic phases, with N sufficiently large. The latter is performed taking advantage of the approach proposed in [Sanahuja(2013)].

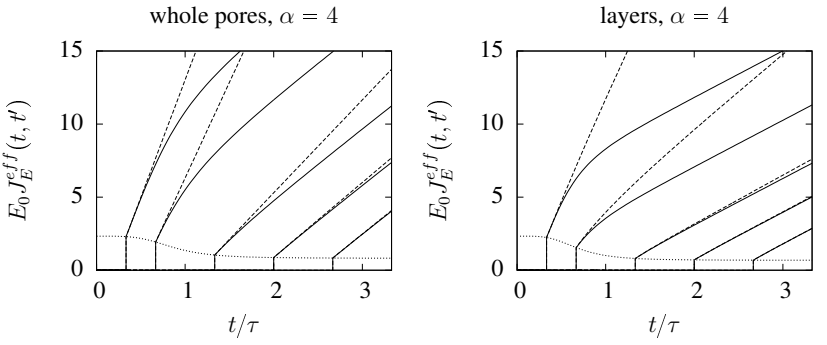

Figure 4. Ageing effective compliance functions (uniaxial stress case), when solids precipitate in whole pores (left part) or as layers in pores inwards (right part), for $\alpha = 4$ and $N = 100$ fictitious ageing phases.

Influence of the precipitation mechanism

Effective uniaxial compliance functions are plotted on figure 4, for both precipitation mechanisms, as plain lines. The kinetic parameter is the same in both cases: $\alpha = 4$. Dotted lines represent the evolution of the instantaneous elastic compliance (inverse of the effective Young's modulus), estimated from usual homogenization schemes in the framework of elasticity, taking into account the current morphology of the matrix-pore-precipitate composite. The initial elastic strain observed on compliance curves matches these elastic predictions. Dashed lines represent the effective creep functions estimated under the assumption of a frozen microstructure (i.e. which does not evolve any more) once the loading stress step has started, which allows to take advantage of the correspondence principle. Clearly enough, when the microstructure is expected to evolve once the loading step has been applied, the discrepancy between both creep functions can be very large.

Even if the materials and volume fraction evolutions are the same in both cases, the effective ageing creep curves highly depend on the precipitation mechanism. This is also the case when the microstructure evolution during loading becomes negligible, as both morphologies differ even when $t \to \infty$ (remember that the final porosity is 0.1, as $f_0 = 0.6$ and $f_s^\infty = 0.3$). Homogenization of solidifying materials, allowing to estimate the influence of the precipitation scenario over the effective ageing creep, could help to design materials optimizing the effective creep behaviour towards a given criterion. For example, in the present case, one would try to favour the precipitation mechanism as layers in pores inwards if one would want to minimize the effective creep strain.

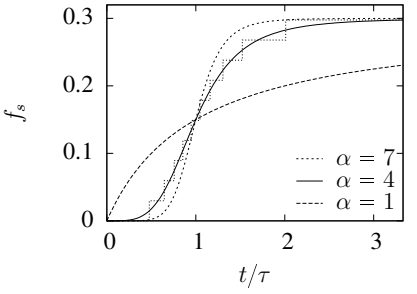

Figure 5. Volume fraction of precipitate, depending on the kinetic parameter α; and as a dotted line the discretized volume fraction as considered by the homogenization model (here with $\alpha = 4$ and for $N = 10$ fictitious phases).

Influence of the precipitation kinetics

Only considering the mechanism of precipitation in whole pores one after the other, the effect of precipitation kinetics is now investigated through the parameter α. Other parameters are kept equal, and results are presented on figure 6 in the same manner as on figure 4. The left part of figure 6, the left part of figure 4 and the right part of figure 6 respectively represent results from $\alpha = 1, 4$ and 7.

Even if the materials and solidifying mechanism are the same in the three cases, the effective ageing creep curves highly depend on the precipitation kinetics. For example, comparing results from $\alpha = 4$ to $\alpha = 7$, creep is lower for a loading at $t'/\tau = 0.33$ but higher for a loading at $t'/\tau = 1.33$. Thus concluding on the relative creep behaviour of two solidifying materials from creep tests performed at only one age is highly questionable. Indeed, analysing creep curves for $t'/\tau = 0.33$ only, one may conclude that "material with $\alpha = 4$ exhibits lower creep than material with $\alpha = 7$", while this is not the case at later ages.

CONCLUSION AND PROSPECTS

The development of a straightforward approach to homogenize ageing viscoelastic behaviours [Sanahuja(2013)] paves the way to the estimation of the effective viscoelastic behaviour of solidifying materials. Bažant's solidification theory [Bažant(1977)] considers that the effective ageing behaviour of a composite does not come from ageing of the elementary phases (which are considered as non ageing linear viscoelastic) but emerges from the gradual evolution of its microstructure. Replacing the solidifying material by many fictitious ageing linear viscoelastic phases with varying precipitation times allows to take advantage of homogenization of ageing linear

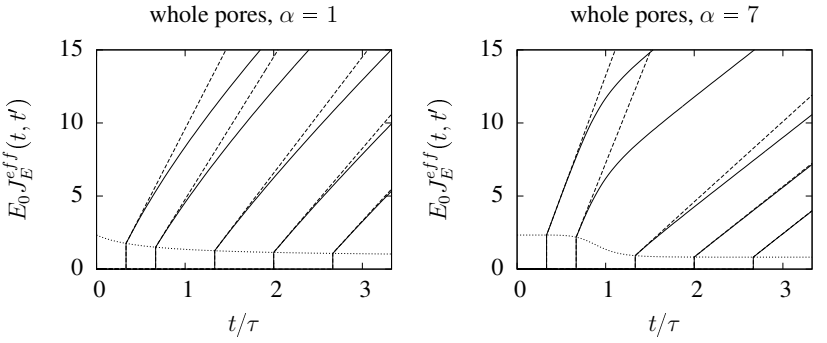

Figure 6. Ageing effective compliance functions (uniaxial stress case), when solids precipitate in whole pores (kinetic parameter $\alpha = 1$ or 7), for $N = 100$ fictitious ageing phases.

visco-elastic composites. As a first application, the influence of two simple precipitation mechanisms and of the precipitation kinetics over the effective creep is investigated. Despite that the materials are the same in every cases, significant differences are found as far as the effective creep behaviour is concerned.

The first application proposed in this paper considers simplified precipitation mechanisms, far from the complexity of real cementitious materials. To be able to model the ageing creep of concrete as a solidifying material, two kind of developments are required. Firstly, improvements in the homogenization technique [Sanahuja(2013)] are necessary to be able to model the complex evolving morphologies of cement pastes. Then it would be possible to extend homogenization schemes designed to estimate the elastic behaviour of cement pastes (for example [Bernard et al.(2003)Bernard, Ulm, and Lemarchand, Sanahuja et al.(2007)Sanahuja, Dormieux, and Chanvillard]) to ageing creep. Secondly, concrete can be modelled as a multi-scale material, embedding aggregates into the cement paste. Contrary to the first point, the latter is straightforward, at least considering aggregates as spheres, since the homogenization approach [Sanahuja(2013)] can be readily used in a multi-scale context.

The design of such a micromechanical ageing model of cementitious materials may also help to transpose the creep strain evolution for loading at a given time to the evolution for loading at another time. It would be rather tedious without a model based on physical assumptions on the microstructure evolution. This would then allow to start creep tests without waiting for the hydration process of the cement paste to stabilize itself.

REFERENCES

[Bažant(1977)] Z. Bažant. Viscoelasticity of solidifying porous material—concrete. *Journal of the Engineering Mechanics Division*, 103:1049–1067, 1977.

[Bernard et al.(2003)Bernard, Ulm, and Lemarchand] O. Bernard, F.-J. Ulm, and E. Lemarchand. A multiscale micromechanics-hydration model for the early-age elastic properties of cement-based materials. *Cement and Concrete Research*, 33(9):1293–1309, 2003.

[Carol and Bažant(1993)] I. Carol and Z. Bažant. Viscoelasticity with aging caused by solidification of nonaging constituent. *Journal of Engineering Mechanics*, 119 (11):2252–2269, 1993.

[Masson et al.(2012)Masson, Brenner, and Castelnau] R. Masson, R. Brenner, and O. Castelnau. Incremental homogenization approach for ageing viscoelastic polycrystals. *Comptes Rendus Mécanique*, 340:378–386, 2012.

[Ricaud and Masson(2009)] J.-M. Ricaud and R. Masson. Effective properties of linear viscoelastic heterogeneous media: Internal variables formulation and extension to ageing behaviours. *International Journal of Solids and Structures*, 46:1599–1606, 2009.

[Sanahuja(2013)] J. Sanahuja. Effective behaviour of ageing linear viscoelastic composites: homogenization approach. *International Journal of Solids and Structures*, 2013. accepted for publication.

[Sanahuja et al.(2007)Sanahuja, Dormieux, and Chanvillard] J. Sanahuja, L. Dormieux, and G. Chanvillard. Modelling elasticity of a hydrating cement paste. *Cement and Concrete Research*, 37(10):1427–1439, 2007.

[Scheiner and Hellmich(2009)] S. Scheiner and C. Hellmich. Continuum microviscoelasticity model for aging basic creep of early-age concrete. *Journal of Engineering Mechanics*, 135(4):307–323, 2009.

Multi-scales characterization of the early-age creep of concrete

M. Farah[1], F. Grondin[1], M. Matallah[1,2], A. Loukili[1], J. Saliba[1]

[1]Institut de Recherche en Génie Civil et Mécanique (GeM), UMR-CNRS 6183, Ecole Centrale de Nantes, 1 rue de la Noé, F-44321 Nantes ; email: {mounia.farah, frederic.grondin, mohammed.matallah, ahmed.loukili, jacqueline.saliba}@ec-nantes.fr.

[2]RiSAM, Université de Tlemcen BP 230 Tlemcen, Algérie, e-mail: matallah@mail.univ-tlemcen.dz

ABSTRACT

Concrete is a heterogeneous material that develops delayed strains under a constant load. These deformations are related to micromechanisms which occur in its microstructure. To model this behaviour a new numerical multi-scales method is suggested. Based on a method for the calculation of the effective response for a non-aging material, an extension to aging materials has been developed. This method operates directly in space-time and avoids the difficulties of Laplace Carson transform inversion. The delayed strains are calculated in a representative elementary volume thanks to classical finite elements method which allows determining the components of the creep compliance tensor. First of all, calculations have been performed for an uni-axial loading to model the creep strain at different scales in order to give the visco-elastic property of calcium silicate hydrates. Then, the evolution of the microstructure with age has been considered to model the creep at early-ages of concrete.

1. Introduction

The prediction of creep of concrete is a major challenge for the civil engineering structures. In fact, concrete is a heterogeneous visco-elastic material that develops delayed deformations. According to several studies, the visco-elastic behaviour is strongly linked to calcium silicate hydrates (C-S-H). Because of their solid sheets composition separated by adsorbed water, they can be deformed due to the movement of water causing the sliding of the solid layers. During the solidification of the cement paste at early-ages, a maximum deformation is observed (Bazant, 1988). These important deformations restrained by the presence of aggregates cause microcracks in the paste witch can be prejudicial to a good performance of the structure (Saliba et al., 2012).

The study of the cement paste morphology is of particular interest to evaluate the macroscopic behaviour of concrete (Sanahuja, 2009). For this reason, homogenization techniques seem to be the best method to calculate the effective behaviour from the description of the local behaviour. Indeed, for a visco-elastic heterogeneous material, the

correspondence principle between elasticity and linear visco-elasticity through the Carson-Laplace transform is used. This allows using classical homogenization schemes (Mori-Tanaka, self-consistent scheme, etc.) directly in the transformed space (Christensen, 1969) and (Hashin, 1962). Effective visco-elastic properties are derived by inverting the Laplace-Carson transform. Most of these techniques are limited to non-aging materials and the extension to aging materials is rarely dealt (Briffaut et al., 2011) due to difficulties of inverting the Laplace-Carson transform. Within this framework, the aim of this work is to introduce an original multi-scales method for creep of concrete at early-ages taking into account the evolution of the microstructure (Grondin et al., 2010). This method operates directly in time domain (Tran et al., 2011) and avoids difficulties of inverting the Laplace-Carson transform.

To model the cementitious materials at different scales it is possible to represent at each scale the material by a matrix and inclusions of different sizes. To simulate the creep, a constant load is applied to the volume and local stresses and strains fields are calculated. The relation between the average of stresses and strains allows deducing the effective tensor of creep compliance. This work is divided into two parts: the determination of creep properties of the concrete constituents and the evolution of creep in terms of the age of concrete. Here, the first part highlights the evaluation of creep compliance of the C-S-H which could be considered intrinsic in the second part. For this, their visco-elastic parameters are estimated by inverse approach starting from an experimental comparison made on concrete.

2. Multi-scales model of creep for a non-aging material

The volume V of the studied material is formed by two phases: a matrix volume V_m and inclusions volume V_i. Locally, only the matrix is considered visco-elastic and its compliance is defined for a model of Kelvin-Voigt with three chains (Figure 1), with E the elastic modulus, k_i the stiffness and τ_i the characteristic time:

$$J(t) = \frac{1}{E} + \sum_{i=1}^{i=3} \frac{1}{k_i}(1 - e^{\frac{-t}{\tau_i}}) \qquad [1]$$

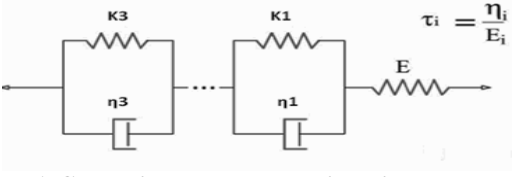

Figure 1. Generalized bounded Kelvin-Voigt model.

A constant load F is applied on one of the surface boundary Γ_1 of V according to the unit normal vector $\underline{n}$. This load implies local displacements fields $\underline{u}(\underline{y})$, local strain

fields $\underline{\underline{\varepsilon}}(\underline{y})$ and local stress fields $\underline{\underline{\sigma}}(\underline{y})$ in each point $\underline{y}$ of V. The non-linear visco-elastic problem is written as follows:

$$\underline{div}\,\underline{\underline{\sigma}}(\underline{y}) = \underline{0} \qquad \underline{y} \in V \qquad [2]$$

$$\underline{\underline{\sigma}}(\underline{y}) = C\left(\underline{\underline{\varepsilon}}(\underline{y}), \underline{y}\right) : \left(\underline{\underline{\varepsilon}}(\underline{y}) - \underline{\underline{\varepsilon}}^{v}(\underline{y})\right) \qquad \underline{y} \in V \qquad [3]$$

$$\underline{\underline{\varepsilon}}(\underline{y}) = \frac{1}{2}\left(\underline{\underline{\nabla u}}(\underline{y}) + {}^{t}\underline{\underline{\nabla u}}(\underline{y})\right) \qquad \underline{y} \in V \qquad [4]$$

$$\underline{F} = \underline{\underline{\sigma}}\,\underline{n} \qquad \underline{y} \in \Gamma_1 \qquad [5]$$

$$\underline{u} = 0 \qquad \underline{y} \in \Gamma_2 \qquad [6]$$

Where $C(\underline{\underline{\varepsilon}}(\underline{y}), \underline{y})$ is the secant stiffness tensor depending on the local strains and damage (Saliba et al., 2013), $\underline{\underline{\varepsilon}}^{v}(\underline{y})$ the local visco-elastic strain fields (for inclusions $\underline{\underline{\varepsilon}}^{v}(\underline{y}) = 0$) and Γ_2 the boundary of V on which macroscopic displacements conditions are applied. The chosen damage model is the isotropic model developed by Fichant (Fichant et al., 1997) based on the microplan theory.

The volume is modeled by finite elements. The resolution of the local problem gives a relation between the average stresses $\langle\sigma\rangle_V$ and the average strains $\langle\varepsilon\rangle_V$ linked by the effective creep tensor $J^{\hom}$:

$$\left\langle \boldsymbol{\varepsilon} \right\rangle_V = \boldsymbol{J}^{\boldsymbol{hom}} : \left\langle \boldsymbol{\sigma} \right\rangle_V \qquad [7]$$

To determine the visco-elastic properties of the concrete components, an inverse approach is used. At each step the visco-elastic coefficients of the matrix are calibrated to adjust the result of the material volume. At the first step, concrete is represented by a mortar matrix and the real aggregate size distribution is generated in the volume. The visco-elastic coefficients of mortar are adjusted from experimental results on concrete. These coefficients allow defining the creep compliance of mortar (equation [1]). At the second step, mortar is represented by a cement paste matrix and the real sand grains size distribution. The inverse approach is used to characterize the visco-elastic coefficients of the cement paste. Then, at the lower scale, an assumption is made on the visco-elasticity of the cement paste to be strictly dependent on that of the C-S-H. Thus, the cement paste is represented as a heterogeneous medium formed by a matrix of C-S-H and inclusions composed by the other hydrated phases and residual clinkers (CH, Ettringite, gypsum, C_3AH_6, FH_3, C_3S, C_2S, C_3A, C_4AF). In this case, only one type of particle is considered with a unique size and their elastic characteristics are derived from the average of the elastic characteristics of the different hydrates and clinkers. The visco-elastic parameters of C-S-H are then calibrated to find the creep compliance $J^{\hom}$ defined in the previous

step for the cement paste. The volume fraction of each component of the cement paste is determined by a hydration model (Grondin et al., 2010).

Volumes are generated by using a digital concrete model developed by (Mounajed, 2002). Geometries are showed in figure 2.

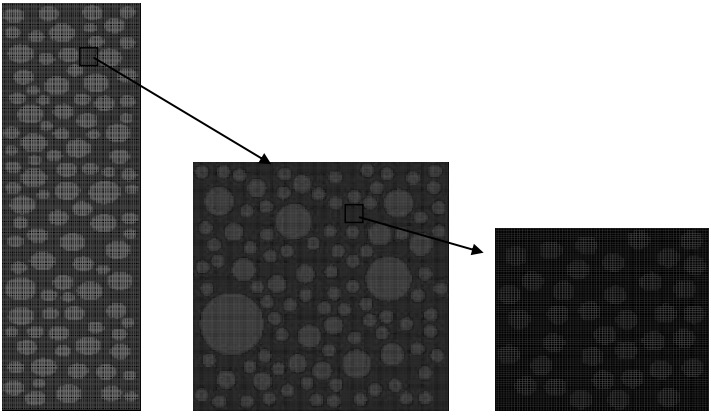

Figure 2. Geometry descriptions of concrete, mortar and cement paste.

3. Results for a non aging material

Direct tensile tests have been realized on cylindrical specimens of concrete (Saliba et al., 2013). The experimental results achieved for a load of 70% of the tensile strength have shown with the help of acoustic emission technique that the damage did not develop during creep, but only during the instantaneous loading. This allows characterizing the creep compliance regardless of the damage. The composition of concrete is given in detail in (Saliba et al., 2012). The visco-elastic coefficients of mortar are calibrated to well reproduce the evolution of the creep compliance of concrete for a load of 70% of its tensile strength (2.5MPa) (Figure 3).

According to these results, the visco-elastic parameters of cement paste are then calibrated for calculations made on the mortar volume (Figure 4). Finally, for the cement paste volume the volume fraction of C-S-H is assessed equal to 70% (including pores), corresponding to a hydration degree of 0.78. The inclusions have a unique size equal to 30μm with a volume fraction of 30%. The visco-elastic matrix coefficients are calibrated to obtain the creep compliance of the cement paste determined in the previous step (Figure 5). The material parameters obtained are presented in Table 2 (ft: tensile strength, $\nu 0$: Poisson coefficient; G_f: fracture energy).

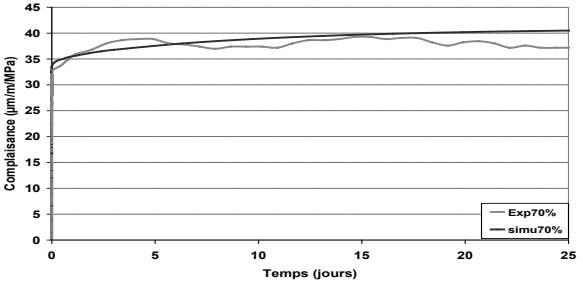

Figure 3. Comparison between the measured concrete compliance and that obtained with the calibrated coefficients of mortar.

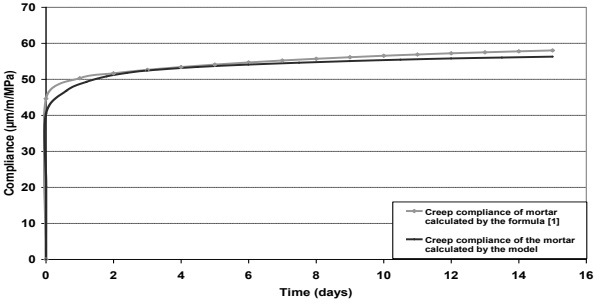

Figure 4. Comparison between the creep compliance of mortar obtained at the previous step and that obtained with the calibrated coefficients of the cement paste.

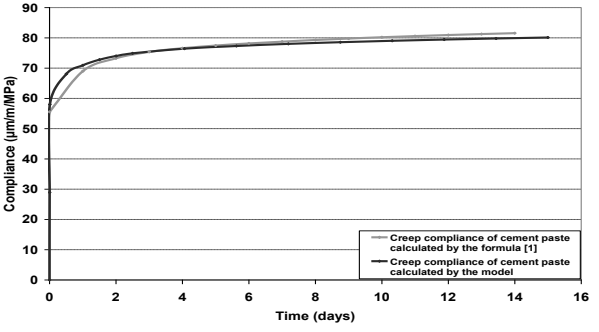

Figure 5. Comparison between the creep compliance of the cement paste obtained at the previous step and that obtained with the calibrated coefficients of C-S-H.

Table 1. Model parameters for mortar and aggregates

	E(GPa)	ν0	ft(MPa)	Gf(J/m2)	k^1_{fp} (GPa)	k^2_{fp}(GPa)	k^3_{fp}(GPa)
Mortar	22.4	0.24	2.0	45	776.7	472	98.1
Aggregates	60	0.24	6	80	-	-	-
Cement Paste	18	0.2	1. 9	15	300	100	90
Sand grains	80	0.24	4	40	-	-	-
C-S-H	12	0.13	1. 6	0.5	150	50	65
Inclusions in CP	45	0.3	3	5	-	-	-

4. Suggestions for aging material

The volume fractions of the constituents of the cement paste change with the evolution of the degree of hydration. Thus, the visco-elastic parameters are dependent on the pores volume fraction. An analytical method (Ricaud and Masson, 2009) is used to find the intrinsic value (k^i_{int}) of C-S-H, independent of the pores volume (p):

$$k^i_{\text{int}} = k^i_{fp}\frac{3.A(f_p)}{4} \qquad \textit{with} \quad A(f_p) = \frac{f_p}{1-f_p} \qquad [8]$$

k^i_{int} is obtained for C-S-H for ages after 48h of hydration. Then, knowing the pore volume fraction at different ages, calculated with the hydration model presented in (Grondin et al., 2010), k^i_{fp} at different ages is calculated (table 7). The creep compliance of cement paste is calculated on the REV and the figure 7 shows that it is more important at early ages. The evolution of the effective creep parameters of cement paste and mortar are calculated on REV (table 7). As well as the compliance of the cement paste the creep compliance of mortar (Figure 6) and concrete are more important at early ages (Figure7).

Table 2. Evolution of the C-S-H parameters

	Age	E(GPa)	k^1_{fp} (GPa)	k^2_{fp}(GPa)	k^3_{fp}(GPa)	p(%)
C-S-H (excluding pores)	16h	9.5	66.46	22.15	28.8	63
	24h	10.5	142.74	47.58	61.84	44.2
	>48h	12	148.24	49.41	64.24	43.29
Cement paste	16h	13.12	170.43	56.81	51.13	43
	24h	15.85	286.18	95.39	85.85	31
	>48h	16.7	300	100	90	30
Mortar	16h	17	483.91	294.07	61.12	28.38
	24h	21	745.46	453.02	94.15	20.46
	>48h	24	776.7	472	98.1	19.8

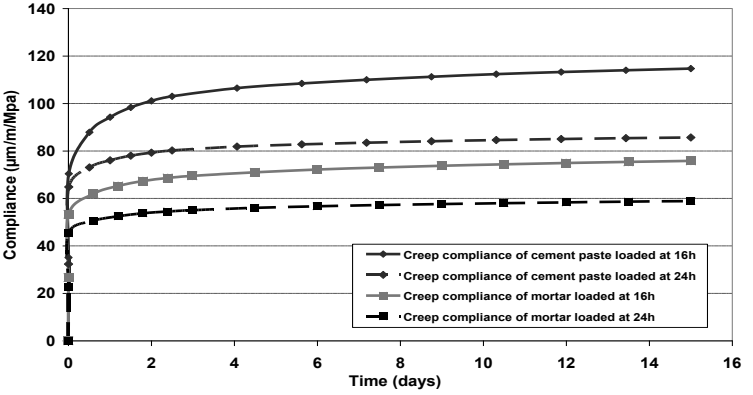

Figure 6. Influence of age on the creep compliance of cement paste and mortar.

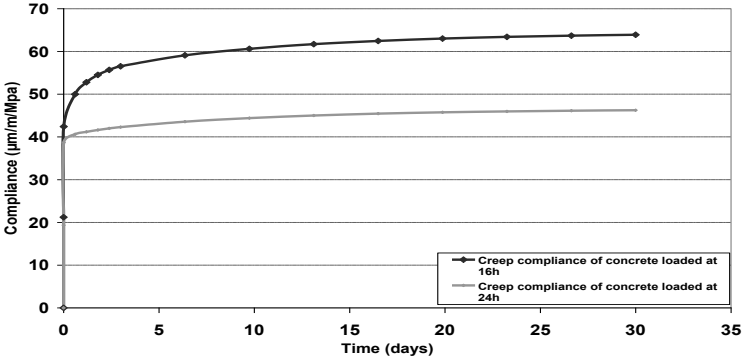

Figure 7. Influence of age on the creep compliance of concrete.

5. Conclusion and perspectives

The proposed multi-scales model allows taking into account the different phases of concrete. The major goal was first to determine the visco-elastic parameters which could be considered intrinsic. The objective is the checking of the solidification theory (Bazant, 1988) considering that only the volume fraction of cement paste components determines the viscosity as a function of the age of concrete. Another point will be dealt on consideration of the presence of the interface transition zone between aggregates and the matrix. Also, experimental tests will be made to compare numerical results.

6. References

Bazant Z.P., Prasannan S. (1988). "Solidification theory for aging creep", *Cement and Concrete Research*, 18, 923-932.

Briffaut M., Benboudjema F., Torrenti J.M., Nahas G. (2011). "Numerical analysis of the thermal active restrained shrinkage ring test to study the early age behavior of massive concrete structures", *Engineering Structures*, 33, 1390–1401.

Christensen R.M. (1969). "Viscoelastic properties of heterogeneous media", *Journal of Mechanics and Physcis of Solids*, 17, 23–41.

Fichant, S., Pijaudier-Cabot, G., La Borderie, C. (1997). "Continuum damage modeling: approximation of crack induced anisotropy", *Mechanical Research Communications*, 24 (2), 109–114.

Grondin F., Dumontet H., Ben Hamida A., Mounajed G., Boussa H. (2007). 'Multi-scales modelling for the behaviour of damaged concrete', *Cement and Concrete Research*, 37 (10), 1453-1462.

Grondin F., Bouasker M., Mounanga P., Khelidj A., Perronnet A. (2010). "Physico-chemical deformations of solidifying cementitious systems: multiscale modeling", *Materials and Structures*, 43 (1), 151-165.

Hashin Z. (1962). "The elastic moduli of heterogeneous materials", *Journal of Applied Mechanics*, 29, 143–150.

Mounajed G. (2002). *Exploitation du nouveau modèle Béton Numérique dans Symphonie : Concept, homogénéisation du comportement thermomécanique des BHP et simulation de l'endommagement thermique*, Cahiers du CSTB n° 3421, septembre.

Ricaud J.M., Masson R. (2009). "Effective properties of linear viscoelastic heterogeneous media: Internal variables formulation and extension to ageing behaviours", *International Journal of Solids and Structures*, 46, 1599–1606.

Saliba J., Loukili A., Grondin F., Regoin J;-P. (2012). "Influence of basic creep on cracking of concrete shown by the Acoustic Emission technique", *Materials and Structures*, 45, 1389-1401.

Saliba J., Grondin F., Matallah M., Loukili A., Boussa H. (2013). "Relevance of a mesoscopic modelling for the coupling between creep and damage in concrete", *Mechanics of Time-Dependent Materials*, DOI 10.1007/s11043-012-9199-4.

Sanahuja J., Dormieux L., Le pape Y.,Toulemonde C. (2009). « Modélisation micro-macro du fluage propre du béton », 19éme Congrès Français de Mécanique, Marseille, 24- 28 août.

Tran A.B., Yvonnet J., He Q.-C., Toulemonde C., Sanahuja J. (2011). « A simple computational homogenization method for structures made of linear heterogeneous viscoelastic materials", *Computer Methods in Applied Mechanical Engineering*, 200, 2956–2970.

Coupled damage and multiscale creep model applied to cementitious materials

B. Bary[1*], Q.-C. He[2], M.-Q. Thai[1,2]

[1]CEA, DEN, DPC, SECR, Laboratoire d'Etude du Comportement des Bétons et des Argiles, F-91191 Gif-sur-Yvette, France. PH (33) 169082383; FAX (33) 169088441; email: benoit.bary@cea.fr
[2]University of Paris-Est, Laboratoire de Modélisation et Simulation Multi Echelle, MSME UMR 8208 CNRS, 77454 Marne-la-Vallée Cedex, France.

ABSTRACT

We present in this study a coupled creep and damage model for describing the behavior of cementitious materials. The creep model is based on a multiscale approach where the material is represented as a composite made of a linear viscoelastic matrix with distributed spherical elastic inclusions and pores. The Mori-Tanaka scheme is then applied in the Laplace-Carson space to this composite material. Exact analytical expressions of the moduli in the time space are derived in simpler cases when a limited number of Maxwell elements are involved to describe the matrix behavior. The model is compared to finite element simulations results carried out on 3D mesostructures. Several configurations of mesostructures with different volume fractions of spherical inclusions ranging from 25 to 40% and boundary conditions are analyzed. The creep model is further coupled to the isotropic damage model due to (Mazars 1986) at the macroscale, based on the concept of pseudo-strains which allows reformulating the initial viscoelastic problem as an equivalent elastic one. The evolutions of the damage variable are governed by an equivalent pseudo-strain calculated from the pseudo-strains tensor. The model is then applied to the simulation of concrete basic creep tests at different temperatures.

INTRODUCTION

Concrete is a common construction material, including in the context of nuclear waste storage structures. For these applications, its durability and long-term performance are essential to ensuring the protection against radionuclide migration. Among the important mechanisms to be accounted for, the differed deformations are known to considerably alter the long-term response of structures and their service life due to the resulting redistributions of strains and stress which may lead to damage initiation and growth. The precise knowledge of creep phenomenon and related induced damage appears then of particular importance regarding such structures. In the literature, few models are based on micromechanical approaches and associated upscaling techniques. It is however well-known that cementitious materials exhibit a heterogeneous and hierarchical microstructure, and that their main phases behave

differently: viscoelastic behavior for the cement paste, linear elastic for the aggregates. The problem is even more complicated when cracking is considered, since damage growth becomes also time-dependant and its coupling with strain or stress rate difficult to describe. We present in this paper a coupled basic creep-damage model based on the pseudo-strain approach due to (Park et al. 1996; Schapery 1984), and the use of the isotropic damage model of (Mazars 1986). The application of an equivalence principle allows obtaining a particularly simple formulation. Another characteristic of the proposed model resides in the application of analytical upscaling techniques to obtain the evolution of the linear viscoelastic bulk and shear moduli of the concrete. This procedure relies on the description of the material as a linear viscoelastic matrix in which are randomly distributed spherical elastic inclusions representing aggregates, and pores. The Mori-Tanaka (MT) scheme is applied in the LC space to estimate the mechanical parameters, and their inversion into the time space is achieved semi-analytically. The model is further compared to results obtained with finite element (FE) simulations performed on 3D mesostructures. Several configurations with different inclusion volume fractions and various boundary conditions are considered. Finally, basic concrete creep tests at different temperatures are simulated and the results are analyzed and compared to experimental data.

CREEP-DAMAGE MODEL

We describe in this section the coupled creep-damage model proposed for concrete materials. A key feature of this model is the use of the pseudo-strains concept introduced in (Park et al. 1996; Schapery 1984). This approach is extended here to the 3D isotropic case such that the viscoelastic creep model is written in a form equivalent to the Hooke's law via an elastic-viscoelastic correspondence principle:

$$\boldsymbol{\sigma} = 3k_R \boldsymbol{L} : \boldsymbol{\varepsilon}^R + 2\mu_R \boldsymbol{J} : \boldsymbol{\varepsilon}^R$$

where $\boldsymbol{\sigma}$ is the stress tensor, k_R et μ_R are the reference elastic bulk and shear moduli, respectively, $\boldsymbol{L}$ and $\boldsymbol{J}$ are the projection operators defined by $\boldsymbol{L} = 1/3\boldsymbol{1} \otimes \boldsymbol{1}$ and $\boldsymbol{J} = \boldsymbol{1} \overline{\otimes} \boldsymbol{1} - \boldsymbol{L}$ with $\boldsymbol{1}$ the second-order identity tensor, and $\boldsymbol{\varepsilon}^R$ is the tensor of pseudo-strains incorporating all the loading history and defined by:

$$\mathrm{tr}\left[\boldsymbol{\varepsilon}^R(t)\right] = \frac{1}{3k_R}\int_0^t k(t-\tau)\,\mathrm{tr}\left(\frac{d\boldsymbol{\varepsilon}}{d\tau}\right)d\tau \text{ and } \boldsymbol{\varepsilon}^R_{dev}(t) = \frac{1}{\mu_R}\int_0^t \mu(t-\tau)\frac{d\boldsymbol{\varepsilon}_{dev}}{d\tau}d\tau$$

in which $k(t)$ and $\mu(t)$ are the isotropic bulk and shear moduli, $\mathrm{tr}(\cdot)$ designates the trace, $\boldsymbol{\varepsilon}_{dev}$ and $\boldsymbol{\varepsilon}^R_{dev}$ are the deviatoric part of the tensors of strains and pseudo-strains, respectively. We consider in the following isotropic viscoelastic materials with potentially different time functions for $k(t)$ and $\mu(t)$, i.e. the Poisson ratio may also be time-dependant. The above formulation is particularly simple, and allows a direct coupling with damage mechanics in the same way as elastic-damage models. We choose for representing the effects of cracking the well-known damage approach

proposed by (Mazars 1986), due to its simplicity and robustness. Introducing the scalar damage variable D into the creep formulation, we obtain:

$$\boldsymbol{\sigma} = \left(1 - D(\tilde{\varepsilon}^R)\right)\left(k_R \,\mathrm{tr}\left(\boldsymbol{\varepsilon}^R\right)\boldsymbol{I} + 2\mu_R \boldsymbol{\varepsilon}^R_{dev}\right)$$

with $\tilde{\varepsilon}^R$ the equivalent strain obtained from (Mazars 1986) by $\tilde{\varepsilon}^R = (\sum_i < \varepsilon_i^R >_+^2)^{1/2}$, where ε_i^R stands for the eigenvalues of $\boldsymbol{\varepsilon}^R$ and $<.>_+$ designates the Macauley brackets. The evolutions of the damage variable are then controlled by the pseudo-strains, and the following law initially proposed by Mazars in the context of time independency is retained:

$$D(\tilde{\varepsilon}^R) = 1 - \frac{\varepsilon_d (1 - A_{t,c})}{\tilde{\varepsilon}^R} - A_{t,c} \exp\left[-B_{t,c}(\tilde{\varepsilon}^R - \varepsilon_d)\right]$$

in which A and B are adjusting parameters, with the subscripts t and c indicating tension and compression states of stresses, respectively, and ε_d is the initial damage threshold. The model developed for estimating the linear viscoelastic bulk and shear moduli of the concrete is based on the application of the MT scheme in the LC space to the heterogeneous material defined by an isotropic linear viscoelastic matrix with distributed spherical isotropic elastic inclusions and voids representing aggregates and pores, respectively. The bulk $k^m(t)$ and shear $\mu^m(t)$ moduli of the matrix are assumed to be described by a generalized Maxwell model with 4 elements (one with only a spring), so that they can be expressed by:

$$k^m(t) = k_\infty^m + \sum_{i=1}^{3} k_i^m e^{-\frac{t}{\tau_i^{m,k}}} \quad \text{and} \quad \mu^m(t) = \mu_\infty^m + \sum_{i=1}^{3} \mu_i^m e^{-\frac{t}{\tau_i^{m,\mu}}}$$

where k_∞^m, k_i^m, μ_∞^m and μ_i^m are the elastic moduli in the Maxwell models and $\tau_i^{m,k}$ and $\tau_i^{m,\mu}$ are the relaxation times. In the following, we assume that $\tau_i^{m,k} = \tau_i^{m,\mu} = \tau_i^m$, i.e. the relaxation times for both bulk and shear moduli are equal. It is showed in (Thai 2012) that k^{hom} and μ^{hom} may be expressed by the following exact semi-analytical formulae in the time space:

$$k^{hom}(t) = k_\infty + \sum_{i=1}^{9} k_i e^{-\frac{t}{\tau_i^k}} \quad \text{and} \quad \mu^{hom}(t) = \mu_\infty + \sum_{i=1}^{12} \mu_i e^{-\frac{t}{\tau_i^\mu}}$$

In these equations, k_∞, k_i, μ_∞ and μ_i are the coefficients derived explicitly in function of the mechanical parameters and volume fractions of the different phases composing the material; τ_i^k and τ_i^μ are the relaxation times which are also calculated from the microscopic phase characteristics (see (Thai 2012) for further details). We observe that the number of relaxation times defining the macroscale behavior is much higher than that at microscale, indicating an enrichment of the relaxation spectra due to the homogenization procedure.

COMPARISON WITH 3D NUMERICAL SIMULATIONS

In this section, we propose to compare the response of the model developed in the preceding section to FE simulations performed on 3D microstructures. The main objective is to investigate and quantify the accuracy of the model and in particular the estimation procedure based on the application of the MT scheme. The microstructures consist in a linear viscoelastic matrix in which are dispersed spherical inclusions of various diameters. Three volume fractions of particulate phase are considered: 0.25, 0.32 and 0.40, resulting in three different configurations. As it is well-known that the boundary conditions (BL) applied on such numerical specimens affect significantly the results obtained, two types of homogeneous BL will be analyzed. They consist in applying a homogeneous stress (σ_{cr} = -25.8 MPa) and strain (ε_{rel} = -5×10^{-4}), respectively, in direction 1, on the sample boundaries. Such BL are typical of a creep loading and of a relaxation loading with overall prescribed strains, respectively. The procedure for generating the numerical cubic samples is detailed in (Bary et al. 2009; de Larrard et al. 2013). In order to reduce the number of elements in the meshes and then the calculation time, the number of spherical particles is voluntarily reduced. The characteristics of the geometries and meshes (number of tetrahedral elements) are indicated in Table 1 for the 3 considered configurations. The dimension of the cubic samples edge is 100, while the diameters of the spherical particles range between 8 to 16 (with arbitrary unit). The mechanical parameters retained for the Maxwell models with 4 chains are listed in Table 2; the ones of the elastic aggregate phase are set to E = 60 GPa and ν = 0.25. Note that these values are identified from the data of a classical concrete creep test.

Table 1. Characteristics of the geometries and corresponding meshes.

Inclusion volume fraction	Number of inclusions	Number of tetrahedrons
25%	210	1881552
32%	315	2336636
40%	400	2373712

Table 2. Mechanical properties of the matrix Maxwell models.

Chain	0	1	2	3
k_i^m (GPa)	6.27	2.93	4.21	6.93
μ_i^m (GPa)	3.41	7.77	3.54	3.32
τ_i^m (days)		2	20	150

Fig. 1 shows the meshes of the inclusions for the 25% and 40% mesostructures. Fig. 2 presents the numerical results obtained with the model presented in the preceding section (lines) and with the FE simulations (symbols), in terms of longitudinal and transversal strains (creep test, up) and stresses (relaxation-like test, down). To ease the comparison, only the cases with volume fraction of 25 and 40% are reported. It appears that both results agree well, in particular for the creep test, with a maximum

difference of 3% at 250 days. A slightly lesser agreement is generally observed for the 40% case with respect to the 25% one. We then consider that the creep model provides sufficiently accurate results. In a future contribution, the effects of the mesh refinement, of the inclusions shape and on the phase contrast will be investigated, and a comparison with other approximation schemes will be carried out.

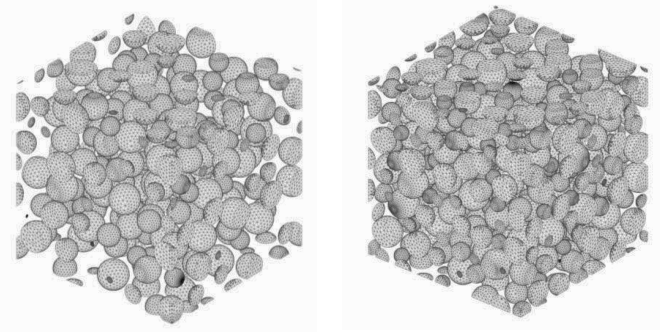

Figure 1. Meshes of the particles for the 25% (left) and 40% (right) cases.

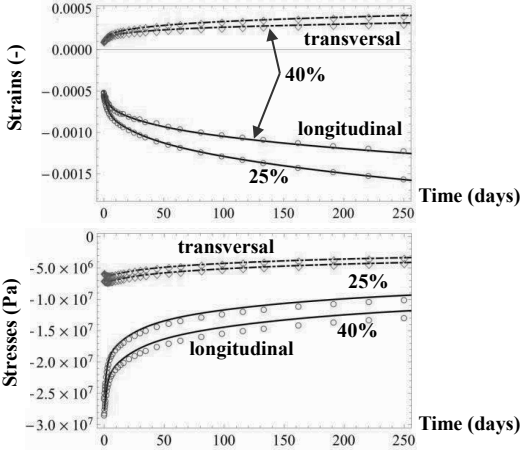

Figure 2. Numerical FE results (symbols) and model response (lines) for a creep test (up) and relaxation-like prescribed strains test (down).

APPLICATION TO THE SIMULATION OF A CONCRETE CREEP TEST

We apply here the model presented in the previous section to the simulation of the tests performed by (Arthanari and Yu 1967). They consist in classical axial basic creep tests on ordinary CEM I concrete specimens at different constant temperatures

ranging from 20 to 80°C. The main data regarding the concrete are defined as follows: Young modulus E = 28 GPa; Poisson ratio ν = 0.25; estimated volume fractions of aggregate and pore phases ϕ_a = 0.62 and ϕ_p = 0.12; parameters of the damage evolution law adjusted on a standard static compression test A_c = 0.8, B_c = 1289 and ε_d = 1×10^{-4}. The compressive stress applied during the creep tests is σ_f = 6.9 MPa and represents 30% of the material strength. The identification of the viscoelastic parameters of the model is carried out by making use of the experimental longitudinal creep strains at 20°C. Since the creep model assumes two different time functions for the bulk and shear moduli, the identification process also requires a priori two distinct experimental time-dependant data. Typically this consists of the measured values of both longitudinal and transversal strain evolutions. However in the creep tests by (Arthanari and Yu 1967), only the longitudinal strains were monitored. We then make the hypothesis that the Poisson ratio of the material evolves as experimentally reported in the study by (Parrott 1974). This allows defining the time evolutions of both moduli of the model. The microscopic parameters identified with this method are listed in Table 3. The macroscopic parameters calculated from all these coefficients are given in Table 4.

Table 3. Microscopic parameters of the Maxwell models at 20°C.

Chain	0	1	2	3
k_i^m (GPa)	4.86	5.60	3.98	2.94
μ_i^m (GPa)	3.09	4.48	2.24	1.50
τ_i^m (days)		1	5	20

Table 4. Macroscopic parameters of the creep model at 20°C.

Chain	0	1	2	3	4	5	6	7	8	9	10	11	12
k_i (GPa)	6.68	3.60	1.02	1.11	3.63	1.02	0.937	3.70	0.57	0.40			
μ_i (GPa)	4.79	1.60	0.11	0.051	0.011	1.86	0.54	0.65	0.173	2.00	0.60	0.963	0.251
τ_i^k (days)		1.0	1.24	1.52	5.0	5.79	7.33	20.	22.5	32.5			
τ_i^μ (days)		1.0	1.29	1.47	1.50	5.0	6.01	7.31	7.33	20.0	23.3	33.0	33.4

The extension of the formulation to non isothermal cases with moderate temperature increases is achieved by applying the equivalent time method consisting in replacing the time variable t by an equivalent one $t_e(t)$ expressed by:

$$t_e(t) = \int_0^t \exp\left[-\frac{Q}{R}\left(\frac{1}{T(\tau)} - \frac{1}{T_{ref}}\right)\right] d\tau$$

with T and T_{ref} the current and initial temperatures, Q the activation energy of the process and R the gas constant. Once the model parameters are identified, the activation energy Q can be adjusted by appealing to the experimental creep strains measured at another temperature. We then chose the results at 40°C to obtain the value Q = 50803 J/mol. The Fig. 3 left reports experimental (symbols, (Arthanari and Yu 1967)) and numerical (curves) creep strains at different temperatures. As the

transversal strains were not measured during the tests, only the simulated curves are shown. Notice that to ease comparison, we have chosen to exclude the thermal strains from this figure. We observe a good concordance between experimental and numerical longitudinal strains for all the considered temperatures, indicating that the proposed model is able to correctly reproduce the concrete behavior. The Fig. 3 right presents the evolutions of the damage variable D. At 20°C D increases from about 0.15 due to the instantaneous loading at t = 0, to 0.175 at 60 days, while at 80°C it reaches 0.195. We can conclude from the model response to the considered creep tests that the damage growth is not very sensitive to moderate temperature increases, and that at ambient temperature its evolution is limited. Fig. 4 shows the evolutions of bulk (left) and shear (right) moduli at different temperatures. We remark that both parameters decrease rapidly the first 10-20 days, then more slowly. We also notice that an elevation of the temperature accelerates the decrease of the moduli.

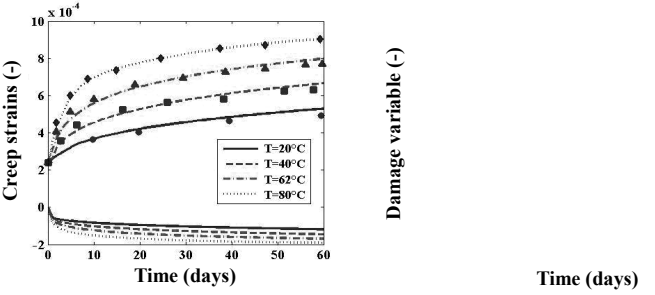

Figure 3. Left: experimental (symbols, (Arthanari and Yu 1967)) and numerical (curves) creep strains at different temperatures. Right: corresponding evolutions of the damage variable.

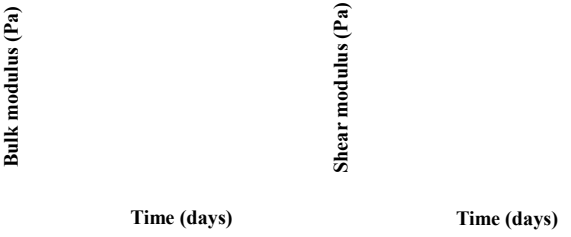

Figure 4. evolutions of bulk (left) and shear (right) moduli at different temperatures.

CONCLUSION

We have presented in this study a creep-damage model based on the pseudo-strain approach of Schapery coupled with the isotropic damage model of Mazars. A simple

formulation analogous to a damage-elastic model is obtained. Further, the MT scheme is applied in the LC space to estimate the evolutions of the linear viscoelastic bulk and shear moduli of the concrete. This procedure relies on the material representation as a composite consisting in spherical elastic aggregates and voids embedded in a linear viscoelastic matrix. Analytical expressions of the time-dependant effective mechanical properties are then derived. The model is then successfully compared to FE computations performed on 3D mesostructures with inclusion volume fractions of 25, 32 and 40%. It is next extended to the case of moderate heating by making use of the equivalent time method. Finally it is applied to the simulation of standard creep tests at different temperatures ranging from 20 to 80°C. A good agreement is obtained between experimental and numerical results of creep strains. The model response tends to show that the creep strains result mainly from the viscous characteristics of the material, and to a minor extent to the damage growth. As perspectives, we intend to investigate the effects of the shape and volume fraction of the aggregates and pores on the macroscopic properties of the material. The influence of the relative humidity on the estimated mechanical properties and the explicit introduction of the capillary pressure in the formulation will also be considered.

ACKOWLEDGMENTS

ANDRA is gratefully acknowledged for its financial support.

REFERENCES

Arthanari, S., and Yu, C. W. (1967). “Creep of concrete under uniaxial and biaxial stresses at elevated temperatures.” *Magazine of Concrete Research*, 19(60), 149–156.

Bary, B., Ben Haha, M., Adam, E., and Montarnal, P. (2009). “Numerical and analytical effective elastic properties of degraded cement pastes.” *Cement and Concrete Research*, 39(10), 902–912.

De Larrard, T., Bary, B., Adam, E., and Kloss, F. (2013). “Influence of aggregate shapes on drying and carbonation phenomena in 3D concrete numerical samples.” *Computational Materials Science*, 72, 1–14.

Mazars, J. (1986). “A description of micro-and macroscale damage of concrete structures.” *Engineering Fracture Mechanics*, 25(5-6), 729–737.

Park, S. W., Kim, R. Y., and Schapery, R. A. (1996). “A viscoelastic continuum damage model and its application to uniaxial behavior of asphalt concrete.” *Mechanics of Materials*, 24(4), 241–255.

Parrott, L. J. (1974). “Lateral strains in hardened cement paste under short-and long-term loading.” *Magazine of Concrete Research*, 26(89), 198–202.

Schapery, R. A. (1984). “Correspondence principles and a generalized J integral for large deformation and fracture analysis of viscoelastic media.” *International Journal of Fracture*, 25(3), 195–223.

Thai, M.-Q. (2012). “Modélisation micromécanique et simulation numérique du fluage des bétons avec prise en compte de la microfissuration et des effets thermohydriques.” PhD thesis (in French), Université Paris-Est.

Micromechanical Model of Concrete Creep

Lev Khazanovich[1] and Kairat Tuleubekov[2]
[1]Associate Professor, Department of Civil Engineering, University of Minnesota, 160 Civil Engineering Building, 500 Pillsbury Drive S.E., Minneapolis, MN 55455, USA, email: khaza001@umn.edu
[2]Senior Research Engineer, SRA, Inc., 1201 New Road, Suite 242, Linwood, NJ, 08221, USA

ABSTRACT

The paper presents a three-dimensional micromechanical model for concrete creep at early age. In this model concrete is treated as a two-phase composite material with an aging matrix (cement paste) and inclusions (aggregates). The uniaxial creep behavior of the aging matrix is described by Bazant's solidification theory, which models aging by volume growth of nonaging viscoelastic products of cement hydration. However, the bulk modulus of the matrix is assumed to be time-independent and the inclusion behavior is assumed to be elastic. The Mori-Tanaka scheme is adapted for determining the effective shear and bulk creep operators of the composite material. To enable numerical determination of concrete creep compliance and relaxation functions, continuous integral operators are approximated by matrix operators acting in finite-dimensional spaces. Effective creep operators (which represent overall properties of the composite) are evaluated as rational functions with matrix arguments.

INTRODUCTION

The response of young concrete to sustained loading depends not only on the loading duration, but also on the age of the concrete at loading. Many authors (Bažant 1977; Ulm and Coussy 1996; Scheiner and Hellmich 2009) explain the time-translation non-invariance of concrete properties as a consequence of the cement hydration process. Bažant's solidification theory (Bazant 1977, Bazant and Prasannan 1998) is the most widely used model for describing concrete creep behavior at early age. Concrete aging is modeled as volume growth of the hydrated cement with visco-elastic properties that are nonaging (time-translation invariant). This is likely the dominant mechanism of aging in the first few days and weeks after concrete sets, although several other aging mechanisms have been identified (Bazant et al. 1997).

According to the Bazant's solicitation theory, the constitutive equation for a statistically homogeneous material may be express as follows:

$$V(t)\left(\dot{\varepsilon}(t)-\dot{\varepsilon}_0(t)\right)=\int_0^t \Phi(t-\tau)d\dot{\sigma}(\tau) \qquad (1)$$

where t is the elapsed time; $\sigma(t)$ and $\varepsilon(t)$ are time-dependent uniaxial stress and strain, respectively; $V(t)$ is the aging function that represent the degree of solidification, $\Phi(t-\tau)$ is the

micro-compliance function of the non-aging solid, $\varepsilon_0(t)$ is the free strain; and the overhead dots denote the partial derivative with respect to time.

For an isotropic material with Poisson's ratio $\nu(t)$ depending on the elapsed time but independent from the time history, Kharlab (1980) obtained the following solution for the lateral creep compliance $J_\perp$ under a uniaxial loading:

$$J_\perp(t,t') = \Phi(0)\frac{\nu(t')}{V(t')} + \int_{t'}^{t} \frac{\nu(\tau)}{V(\tau)} \frac{\partial \Phi(\tau - t')}{\partial \tau} d\tau$$

Bažant *et al.* (1997) extended the solidification theory to the multiaxial creep law as follows:

$$\varepsilon_{ij}(t) = \int_0^t J(t,\tau) G_{ijkl} d\sigma_{kl}(\tau)$$

where $\sigma_{ij}(t)$ and $\varepsilon_{ij}(t)$ are stress and strain tensors, respectively; G_{ijkl} depends only on Poisson's ratio, ν ,which does not depend on time.

The equations above describe behavior of a statistically homogeneous material. Granger and Bažant (1995) proposed treating concrete as a two-phase composite material: aging matrix (cement mortar) with properties described by the solidification theory and elastic phase (coarse aggregates).

The effective creep compliance function $J_e(t,\tau)$ in this uniaxial model is determined as follows (Granger and Bažant 1995):

$$J_e(t,\tau) = \frac{\xi}{\chi E_p + (1-\chi)E_{ma}(\tau)} \left(1 + \frac{(1-\chi)(E_{ma}(\tau) - R_{ma}(t,\tau))}{\chi E_p + (1-\chi)(E_{ma}(\tau) - R_{ma}(t,\tau))} \right) + (1-\xi) J_{ma}(t,\tau)$$

where $R_{ma}(t,\tau)$ and $J_{ma}(t,\tau)$ are relaxation and creep compliance functions of the matrix, respectively, $E_{ma}(\tau) \equiv R_{ma}(\tau,\tau)$, E_p is Young's modulus of the elastic phase, and ξ is the model parameter.

This model comprehensively describes the creep compliance response to uniaxial loading, but does not capture the triaxial behavior.

GENERALIZED MODEL

In this paper, Bažant's one dimensional composite model is generalized for a three dimensional case. Following Bažant (1977) as well as Granger and Bažant (1995), consider concrete as a two-phase composite material with an aging matrix (cement paste) and elastic inclusions (aggregates). Assuming that the aging matrix phase has time-independent bulk modulus K_{ma}, rates of stresses and strains are related as follows:

$$\dot{\sigma}_{ij}(t) = K_{ma}\dot{\varepsilon}_{kk}(t)\delta_{ij} + 2\underline{\mu}_{ma}\underline{V}_{ma}\left(\dot{\varepsilon}_{ij}(t) - \frac{1}{3}\dot{\varepsilon}_{kk}(t)\delta_{ij}\right) \tag{2}$$

where $\underline{V}_{ma} = V(t)\underline{I}$, $\underline{I}$ is the identity operator, i.e. $\underline{I}f(t)=f(t)$; operator $\underline{\mu}_{ma}$ is defined as:

$$\underline{\mu}_{ma} = 3K_{ma}(9K_{ma}\underline{V}_{ma}^{-1}\underline{\Phi}_{ma} - \underline{I})^{-1} \tag{3}$$

and $\underline{\Phi}_{ma}$ denotes an integral operator corresponding to micro-compliance function, $\Phi(t-\tau)$:

$$\underline{\Phi}_{ma}f(t) \equiv \int_0^t \Phi_{ma}(t-\tau)df(\tau) \tag{4}$$

Function *V(t)* and operator $\underline{\Phi}_{ma}$ describe the relationship between stresses and strain for the matrix (cement paste). The form of operator $\underline{\mu}$ ensures that equation (2) can be reduced to equation (1) of Bazant's solidification theory for a uniaxial loading of the matrix.

Another phase of the composite material (inclusions) is elastic, therefore

$$\dot{\sigma}_{ij}(t) = K_p\dot{\varepsilon}_{kk}(t)\delta_{ij} + 2\mu_p\left(\dot{\varepsilon}_{ij}(t) - \frac{1}{3}\dot{\varepsilon}_{kk}(t)\delta_{ij}\right)$$

where K_p and μ_p are bulk and shear modulus of the elastic phase.

Although it can be shown that the operator $\underline{\mu}_{ma}$ can be presented in the integral form, $\underline{\mu}_{ma}f(t) \equiv \int_0^t \mu_{ma}(t-\tau)df(\tau)$, an analytical determination of function $\mu_{ma}(t)$ can be very difficult for important practical problems. This obstacle can be overcome by replacing the integral operators with their finite dimensional analogs (Pyatigorets et al 2010).

Consider a discrete set of time moments: $t_1 = 0, t_2, ..., t_{n-1}, t_n = t$ with uniform step h. The strain $\dot{\varepsilon}(t)$ and stress $\dot{\sigma}(t)$ rate histories can be represented by vectors $\{\dot{\boldsymbol{\varepsilon}}\} = \{\dot{\varepsilon}(t_k)\}_{k=1}^n$ and $\{\dot{\boldsymbol{\sigma}}\} = \{\dot{\sigma}(t_k)\}_{k=1}^n$, respectively. To obtain a matrix representation for the integral operator $\underline{\Phi}_{ma}$, the integral in equation (4) can be evaluated numerically using the trapezoid rule (Bazant 1972).

$$\begin{aligned}\int_0^{t_k} \Phi_{ma}(t_k-\tau)d\dot{\sigma}(\tau) &= \Phi_{ma}(0)\dot{\sigma}(t_k) - \int_0^{t_k}\dot{\sigma}(\tau)\frac{\partial\Phi_{ma}(t_k-\tau)}{\partial\tau}d\tau = \dot{\sigma}(t_k)\Phi_{ma}(0) + \\ &+ \frac{h}{2}\dot{\sigma}(t_1)\dot{\Phi}_{ma}(t_k-t_1) + h\sum_{i=2}^{k-1}\dot{\sigma}(t_i)\dot{\Phi}_{ma}(t_k-t_i) + \frac{h}{2}\dot{\sigma}(t_k)\dot{\Phi}_{ma}(0) + O(h^2)\end{aligned} \tag{5}$$

In the absence of free strains, relationship (1) can be rewritten in the following form:

$$[V]\{\dot{\boldsymbol{\varepsilon}}\} = [\Phi_{ma}]\{\dot{\boldsymbol{\sigma}}\}$$

where $[V]$ is a diagonal matrix with values $V_{ma}(t_k)$ (k=1, …, n) on the diagonal and $[\Phi_{ma}]$ is a lower-triangular matrix consisting of the weight coefficients from the quadrature rule (5):

$$[\Phi_{ma}] = \begin{bmatrix} \Phi_{ma}(0) & 0 & 0 & \ldots & 0 \\ \frac{h}{2}\dot{\Phi}_{ma}(t_2 - t_1) & \Phi_{ma}(0) + \frac{h}{2}\dot{\Phi}_{ma}(0) & 0 & \ldots & 0 \\ \frac{h}{2}\dot{\Phi}_{ma}(t_3 - t_1) & h\dot{\Phi}_{ma}(t_3 - t_2) & \Phi_{ma}(0) + \frac{h}{2}\dot{\Phi}_{ma}(0) & \ldots & 0 \\ \ldots & \ldots & \ldots & \ldots & \ldots \\ \frac{h}{2}\dot{\Phi}_{ma}(t_n - t_1) & h\dot{\Phi}_{ma}(t_n - t_2) & h\dot{\Phi}_{ma}(t_n - t_3) & \ldots & \Phi_{ma}(0) + \frac{h}{2}\dot{\Phi}_{ma}(0) \end{bmatrix}$$

Replacement of the operators $\underline{V}_{ma}$ and $\underline{\Phi}_{ma}$ by their matrix analogous in equation (3) leads to the following matrix operator:

$$[M] = 3K_{ma}(9K_{ma}[V]^{-1}[\Phi_{ma}] - [I])^{-1}$$

The stress strain relationships for the matrix and inclusions can then be re-written in the following form:

$$\{\dot{\sigma}_{ij}\} = K_p\{\dot{\varepsilon}_{kk}\}\delta_{ij} + 2\mu_p\left(\{\dot{\varepsilon}_{ij}\} - \frac{1}{3}\{\dot{\varepsilon}_{kk}\}\delta_{ij}\right)$$

$$\{\dot{\sigma}_{ij}\} = K_{ma}\{\dot{\varepsilon}_{kk}\}\delta_{ij} + 2[M][V]\left(\{\dot{\varepsilon}_{ij}\} - \frac{1}{3}\{\dot{\varepsilon}_{kk}\}\delta_{ij}\right)$$

The product of matrices $[M]$ and $[V]$ is a lower triangular matrix with increasing diagonal elements. Therefore, there exists a matrix $[\Psi]$, along with an inverse matrix $[\Psi]^{-1}$, such that $[M][V] = [\Psi]^{-1}[D][\Psi]$, where [D] is a diagonal matrix. By introducing transformed stresses and strains, $\{\sigma_{ij}{}^*\} = [\Psi]\{\sigma_{ij}\}$ and, $\{\varepsilon_{ij}{}^*\} = [\Psi]\{\varepsilon_{ij}\}$, the stress-strain relationships in the transformed variables can be re-written as follows:

$$\{\dot{\sigma}^*_{ij}\} = K_p\{\dot{\varepsilon}^*_{kk}\}\delta_{ij} + 2\mu_p\left(\{\dot{\varepsilon}^*_{ij}\} - \frac{1}{3}\{\dot{\varepsilon}^*_{kk}\}\delta_{ij}\right)$$

$$\{\dot{\sigma}^*_{ij}\} = K_{ma}\{\dot{\varepsilon}^*_{kk}\}\delta_{ij} + 2[D]\left(\{\dot{\varepsilon}^*_{ij}\} - \frac{1}{3}\{\dot{\varepsilon}^*_{kk}\}\delta_{ij}\right)$$

An advantage of this representation is that the stress-strain relationships in the transformed variables comprise of a combinations of independent elastic stress-strain relationships. In addition, the boundary conditions on the interfaces between the matrix and inclusions are satisfied in the transformed variables. Therefore, the original boundary value problem was transformed into a set of independent quasi-elastic boundary value problems

(BVPs). For each BVP, stress-strain relationships can be homogenized using an appropriate equivalency technique. If the Mori-Tanaka scheme is used the relationship between bulk stresses and strains for the homogenized material has the following form:

$$\{\dot{\sigma}_{kk}^{*}\} = 3\left(K_{ma}[I] + c(K_p - K_{ma})(4[D] + 3K_{ma}[I])\right)\left(3K_p[I] + 4[D] + 3c(K_{ma} - K_p)[I]\right)^{-1}\{\dot{\varepsilon}_{kk}^{*}\}$$

where [*I*] is the identity matrix.

Multiplying both sides of this relationship by matrix $[\Psi]^{-1}$ from the right and performing simple manipulations with the matrices we obtain the following relationships for bulk stresses and strains:

$$\{\dot{\sigma}_{kk}\} = 3\left(K_{ma}[I] + c(K_p - K_{ma})(4[M][V] + 3K_{ma}[I])\right)\left(3K_p[I] + 4[M][V] + 3c(K_{ma} - K_p)[I]\right)^{-1}\{\dot{\varepsilon}_{kk}\}$$

where c is the concentration of inclusions.

Therefore, the matrix analogy of the composite material bulk operator,$[K_e]$, can be expressed as;

$$[K_e] = \left(K_{ma}[I] + c(K_p - K_{ma})(4[M][V] + 3K_{ma}[I])\right)\left(3K_p[I] + 4[M][V] + 3c(K_{ma} - K_p)[I]\right)^{-1}$$

Similarly, the matrix analogy of the shear operator relating rates of deviatoric stresses and strains for the composite material is given below:

$$[\mu_e] = [M][V] + c(\mu_p[I] - [M][V])$$
$$\left([I] + (1-c)(\mu_p[I] - [M][V])([M][V](9K_{ma}[I] + 8[M][V])(6K_{ma}[I] + 12[M][V])^{-1} + [M][V])^{-1}\right)^{-1}$$

Finally, the relationship between the rates of stresses and strains under the uniaxial loading is described by the matrix [*J*]:

$$[J_e] = [V]((9[K_e])^{-1} + (3[\mu_e])^{-1})$$

NUMERICAL EXAMPLE

To illustrate how the approach above can be used to predict creep behavior of concrete, consider the following example: 80% of the volume is occupied by aggregates with Young's modulus and Poisson's ratio of 60 GPa and 0.15, respectively; the cement paste (matrix) bulk modulus is 33.3 GPa and the matrix creep compliance (in 1/GPa) is described by the Bazant's B3 (Bazant and Baweja 1995) model with the following coefficients:

$$J_{ma}(t,t') = \frac{(10.43/t)^{0.5} + 1.30}{12.34} + 0.211\int_{t'}^{t} \frac{1}{\tau^{0.5}} \frac{10.43^{0.5}(\tau - t')^{-0.9}}{10.43^{0.1} + (\tau - t')^{0.1}} d\tau + 2.74 \ln\left[1 + \left(\frac{t - t'}{10.43}\right)^{0.1}\right]$$

Figure 1 presents predicted axial strain histories under sustained uniaxial loadings applied at various concrete ages. Figure 1 also shows predictions of these strains from Bazant's B3 model with the following coefficients:

$$J_{B3}(t,t') = \frac{(1/t)^{0.5}+1.1}{41.52} + 0.016\int_{t'}^{t} \frac{(\tau - t')^{-0.9}}{\tau^{0.5}(1+(\tau-t')^{0.1})} d\tau + 0.18\ln(1+(t-t')^{0.1})$$

As can be observed from figure 1, for uniaxial compression applied at various concrete ages, the predictions of the proposed composite model agree very well with the predictions of Bazant's B3 model which, in turn, is in a good agreement with experimental data. However, unlike a uniaxial B3 model, the proposed model also predicts lateral strains, which are not proportional to axial strains (see figure 2). Figure 3 shows the apparent Poisson's ratios. It can be observed that the value depends on duration of the loading as well as the time of load application. As expected, an increase in concrete age, and associated increasing degree of solidification, leads to a decrease in apparent Poisson's ratio. This illustrates that the model eliminates the need to assume a constant Poisson's ratio.

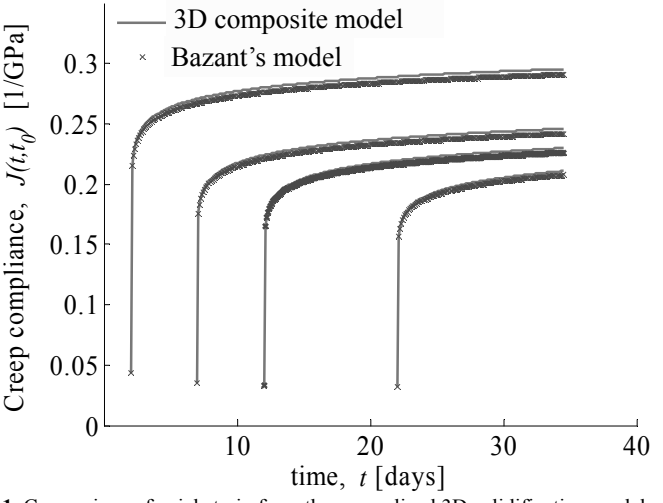

Figure 1. Comparison of axial strain from the generalized 3D solidification model and Bazant's B3 model.

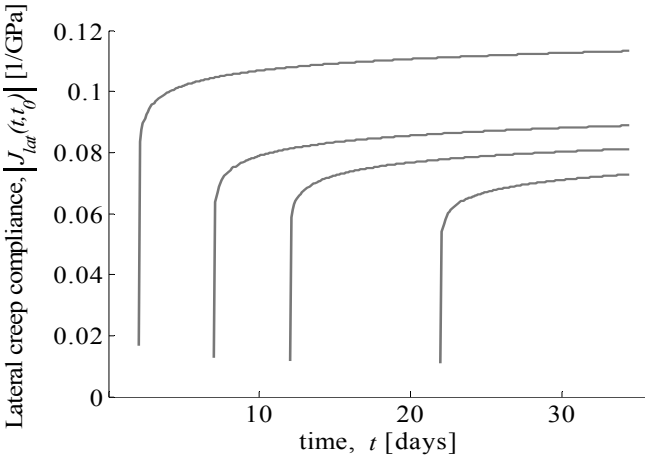

Figure 2. Lateral creep compliance.

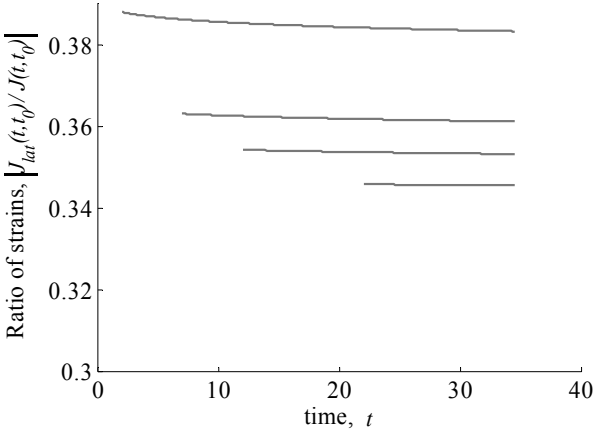

Figure 3. Apparent Poisson's ratio.

CONCLUSIONS

The paper presents a three-dimensional micromechanical model for a two-phase composite material with an aging matrix and elastic inclusions. The aging matrix uniaxial creep behavior is described by Bazant's solidification theory, which models aging by volume growth of nonaging viscoelastic products of cement hydration. To enable numerical determination of concrete creep compliance functions, continuous integral operators are approximated by matrix operators acting in finite-dimensional spaces. The Mori-Tanaka scheme is adapted for determining the effective shear and bulk creep operators of the composite material. Effective creep operators (which represent overall properties of the composite) are evaluated as rational functions with matrix arguments. A numerical example demonstrates that the model can adequately describe both axial and lateral strains in concrete under uniaxial loading.

ACKNOWLEDGEMENTS

The authors acknowledge the support from the Strategic Highway Research Program 2 (SHRP2) project R21 "Composite Pavements."

REFERENCES

Bažant, Z.P. (1972). "Matrix differential equation and higher order numerical methods for problems of nonlinear creep, elasto-plasticity and visco-elasticity." *International Journal for Numerical Methods in Engineering*, 4, 11-15.

Bažant, Z.P. (1977). "Viscoelasticity of solidifying porous material - concrete." *J. Eng. Mech.*, 103(6), 1049-1067.

Bažant, Z.P and Baweja, S. 1995 "Creep and shrinkage prediction model for analysis and design of concrete structures - model B3". *Materials and Structures*, 28, 357–365.

Bažant, Z.P. and Prasannan, S. 1989 "Solidification theory for concrete creep," *J. Eng. Mech*., 115(8), 1691-1703.

Bažant, Z.P., Hauggaard, A.B., and Baweja, S. and Ulm, F.-J. *(*1997). "Microprestress-solidification theory for concrete creep. I: aging and drying effects. *J. of Eng. Mech,* 123(11), 1188-1194.

Granger, L.P. and Bažant, Z.P. (1995.) "Effect of composition on basic creep of concrete and cement paste." *J. of Eng. Mech,* 121(11), 1261-1270.

Kharlab, V.D. (1980). "The linear creep theory of growing bodies," *Mekhanika Sterzhnevyh System i Sploshnyh Sred* (in Russian), 13 (1980), 149–156.

Pyatigorets, A.V., Marasteanu M. O., Khazanovich, L., Stolarski, H. K. (2010)**. "**Application of a matrix operator method to the thermoviscoelastic analysis of composite structures," *J. Mechanics of Mat. and Struct.* 5, 837–854.

Scheiner, S. and Hellmich, C. (2009). "Continuum Microviscoelasticity Model for Aging Basic Creep of Early-Age Concrete," *J. Eng. Mech.*, 135(4), 307-323.

Sercombe, J., Hellmich C., Ulm F.-J., and Mang, H. (2000). "Modeling of early-age creep of shotcrete. I: Model and Model Parameters." *J. Eng. Mech.*, 126(3), 284-291.

Ulm, F.-J. and Coussy, O. (1996) "Strength growth as chemo-plastic hardening in early age concrete," *J. Eng. Mech,* 122(12), 1123-1132.

Experimental analysis of drying shrinkage cracking in coating mortars by digital image correlation

F. Benboudjema[1], T. Mauroux[2], P. Turcry[3], A. Ait-Mokthar[3] and O. Deves[4]

[1]LMT-Cachan, ENS-Cachan, Paris 6 University, CNRS, UniverSud Paris PRES, France; email: farid.benboudjema@ens-cachan.fr
[2]SITES, 2 bis Avenue du Centre 92500 Rueil Malmaison, France
[3]University of La Rochelle, LaSIE – CNRS FRE 3474, France
[4] CSTB Marne-la-Vallée, France

ABSTRACT

Since drying is a very slow process, a strong gradient of drying shrinkage occurs in concrete members leading, at the macroscopic level, to the rise of tensile stresses at the surface and compressive stresses at the core. Therefore, it may lead to superficial cracking. In addition, crossing cracks and/or debonding (at the interface with a substrate) may also occur in thin members if drying shrinkage is restrained. In order to study these phenomena, a new device based on digital image correlation (DIC) was set-up. A post-processing tool is then proposed to capture the mapping of shrinkage strains and to determine the evolution of the cracking patterns. It was used successfully to observe, quantify and analyze cracking of a coating mortar, due to the restraint of drying shrinkage by a rigid substrate (concrete block).

INTRODUCTION

Since drying is a very slow process, a strong gradient of drying shrinkage occurs in concrete members leading, at the macroscopic level, to the rise of tensile stresses at the surface and compressive stresses at the core. Therefore, it may lead to superficial cracking. In addition, crossing cracks and/or debonding (at the interface with a substrate) may also occur in thin members if drying shrinkage is restraint (like in reparation, coating mortar, slabs, tile mortar, by a concrete lift …). The consequences are the reduction of the durability of the construction, since the apparent permeability and diffusivity are increased. In cladding unit (using rendering mortar), the efficiency of the insulating material may be reduced if it comes in contact in water (in the case of external thermal insulation), the loss of adhesion of the rendering mortar may occur and associated esthetical considerations may force the constructor to remove and lay again the rendering mortar.
In order to study these phenomena, a new device based on digital image correlation (DIC, developed by Besnard et *al.*, 2006) was set-up. The DIC method is based on the comparison of two images (shot with a CANON EOS 450D camera) with two

random gray levels recorded before and after a displacement. Compared to intrusive devices (SEM, embedded gauges …), parasite cracks are not induced. Moreover, representative geometries and restraint conditions of rendering mortars can be used. Finally, it is here possible to obtain field of displacements and not only local information.
A post-processing tool is then proposed to capture the mapping of shrinkage strains (computed after interpolation of the displacement using quadrangular functions) and to determine the evolution of the cracking patterns. Besides, this enables also to quantify cracks openings, depths inside the mortar and debonding.
The device was validated by comparison with measurements of drying shrinkage using LVDT and investigations with an optical microscope. It was used successfully to observe, quantify and analyze cracking of cement-based materials (coating mortar, w/c =1, containing cellulose ether) due to the restraint of drying shrinkage by a rigid substrate (concrete block of controlled roughness). The mortar was dried at the age of 1 day, as the concrete substrate is at least 1 month old. Micro-cracks were detected going from the drying surface to the interface. The shrinkage of the mortar layer induces shear stress at the mortar/concrete interface, which results in debonding. Each one of these cracks was confirmed by optical microscopy observations.

EXPERIMENTAL PROGRAM

Mortar mix, geometry and conditions.

The mix of the studied mortar is given in the Table 1. The high value of the water to cement ratio (w/c = 1) has been fixed by the industrial consortium CEReM who supported this research program. The mortar contains a hydroxyl-methyl-propyl cellulose (HMPC) addition, which has water retention properties and is classically used in mortar used in cladding unit.

Table 1. Mortar mix.

Siliceous Sand	Portland cement (CEM I 52.5)	Siliceous Filler (Sifraco)	Cellulosic ether (MHPC)	w/c
650 kg/m^3	300 kg/m^3	50 kg/m^3	0.11%*	1

* % by weight of the cement content

Tested mortar specimens were protected from drying by a cellophane film and kept at 25±2°C for 24 hours after mixing. After demoulding, they were placed in a room at 25°C and 30±5% of relative humidity (RH).
Three types of elements have been casted (note that a thickness of 1 cm is used classically for the rendering mortar in industrial applications):

- 2×4×16 cm prismatic specimens (free drying shrinkage): the two opposite lateral faces (2×16 cm) and the two end faces (2×4 cm) were insulated by adhesive aluminum foils in order to prevent drying by these faces. These hydric boundary conditions were adopted in order to have a symmetrical

drying problem and to avoid curling. Drying shrinkage strains are measured using LVDT;

- 1×20×20 cm prismatic specimens (free drying shrinkage): the drying is allowed only by the 2 faces of 20 by 20 cm. Drying shrinkage is measured by DIC;
- 2×20×20 cm prismatic specimens (restrained drying shrinkage): the drying shrinkage is restraint by standardized concrete blocks with cubic dimensions ($20×20×20\ cm^3$) used as substrate.

The concrete blocks have been provided by Rocholl GMBH company and they comply with the European Standard EN 1766:2000 on concrete substrates designed for repair materials testing. Since the roughness of the substrate is a major parameter involved in adherence and cracking (Garbacz et *al*., 2008), its control is crucial to obtain reproducible test. The surfaces of the blocks were sandblasted with a blasting depth of 1-2 mm. Concrete blocks were kept for at least two weeks in the testing room.

DIC principles.

The digital image correlation method is based on the comparison of two images with two random gray levels recorded before and after a displacement. The first picture is called "reference" and the second "deformed". The correlation consists in determining the degree of similarity (in terms of conservation of optical flux) between these two pictures. The displacement measurement consists in finding the best displacement field which allows overlying the pattern of the "reference" image and those of the "deformed" image using a pattern-matching algorithm.

In the present study, DIC is carried out using Correli-Q4-LMT, software developed in the LMT laboratory (see http://www.lmt.ens-cachan.fr/PDFs/HILD.2008.7.pdf and Besnard et *al.*, 2006)

DIC measurements

The optical device (a CANON EOS 450D camera placed above the mortar surface) was used to monitor the evolution of the surface displacement. From the beginning of drying, images (1157×1737 pixels) of the surface were recorded every ten minutes for ten days. The time exposure was set to 1 second and the surface was lighted up by several LED lights in order to limit the optical noise.

In the restraint test, the adopted device, displayed in Figure 1, allows for following surface and in-depth displacements (and cracking).

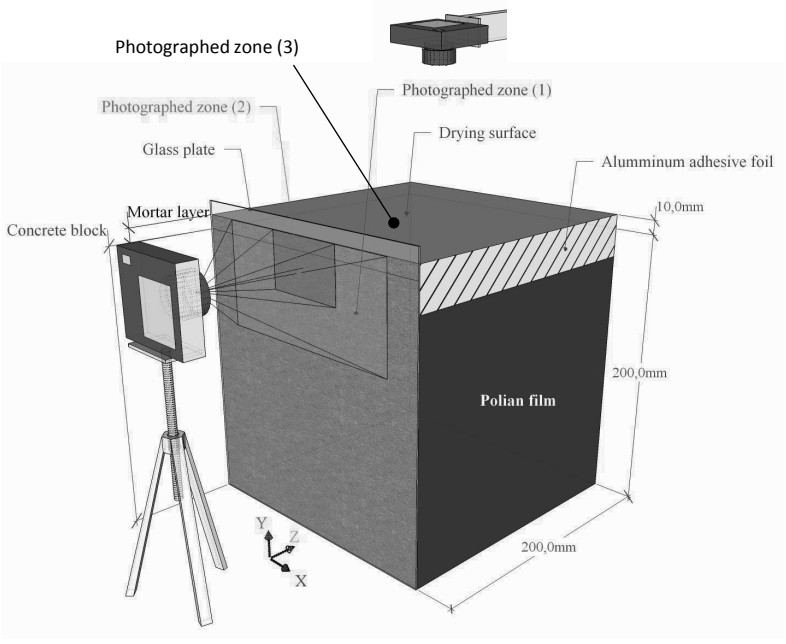

Figure 1. Experimental devices in the restrained shrinkage test: measurement of the surface and in-depth displacement.

Post-processing.

Strain tensor is calculated thanks to the small strain hypothesis (the displacement gradient is computed after interpolation of the displacement by Q4 finite elements):

$$\boldsymbol{\varepsilon}(\mathbf{x}) = \frac{1}{2}\left(\mathbf{Grad}(\mathbf{U}(\mathbf{x})) + {}^{T}\,\mathbf{Grad}(\mathbf{U}(\mathbf{x}))\right) \text{ with } \mathbf{U}(\mathbf{x}) = \sum_{i=1}^{i=n} N_i(\mathbf{x})\mathbf{U}_i^e \qquad (1)$$

where $\boldsymbol{\varepsilon}$ is the strain tensor (2D) and $\mathbf{U}$ is the displacement vector depending upon the position vector $\mathbf{x}$. N_i are Q4 (linear) scalar shape function (the same function as in finite element calculations), n is the number of nodes and $\mathbf{U}^e$ are the nodal displacements obtained by digital image correction

Cracking due to restraint of shrinkage (cracking in mode I) is related to 1D tension. As conventionally done in continuum damage mechanics for cement-based materials, an equivalent tensile (positive) strain was computed as follows in order to characterize cracking with a single scalar value (Mazars, 1986):

$$\hat{\varepsilon} = \sqrt{\langle \boldsymbol{\varepsilon} \rangle_+ : \langle \boldsymbol{\varepsilon} \rangle_+} \qquad (2)$$

where $\langle\ \rangle_+$ is the positive part operator. From this equivalent strain, the following criterion f can be derived:

$$f = \hat{\varepsilon} - \kappa_0 \qquad (3)$$

where κ_0 is the tensile strain threshold. This allows us to assess accurately damage/cracking in tension knowing the 2D strain tensor.
This criterion, used previously by Lagier et *al.* (2011) for studying drying cracks in cement pastes, is relevant for cement-based materials due to their very low tensile deformability (and low tensile strength).

EXPERIMENTAL RESULTS

Validation of DIC by comparison in free shrinkage test

It should be note that autogeneous shrinkage was found to be largely negligible for such high w/c ratio (Monge, 2007). The final displacement field (after 11 days, along the **x** direction), calculated by Corelli_Q4_LMT, is given in Figure 2(a). Almost uniform gradients of displacement field along the **x** axis and (the **y** axis, not represented) can be observed (by plotting displacements U_x/U_y versus x/y coordinates, respectively). It should be noticed that, in each direction, iso-values of displacement were slightly incurved on the sides of the plate. This phenomenon may be due to a slight drying of the lateral sides (induced by the peeling of aluminum adhesive foils) or by slight curling (induced by the presence of wood sticks which modify partially drying). DIC measurements depend strongly on the frame surface quality (Hild et al., 2002). In order to validate the proposed procedure, the displacement measured by DIC was used to determine the "mean" strain in the mortar specimen. The comparison with measurements with a classical LVDT is plotted in Figure 2(b). The rather good agreement between the two measurement methods indicates that the DIC method is efficient for obtaining displacement and strain fields during drying for several days.

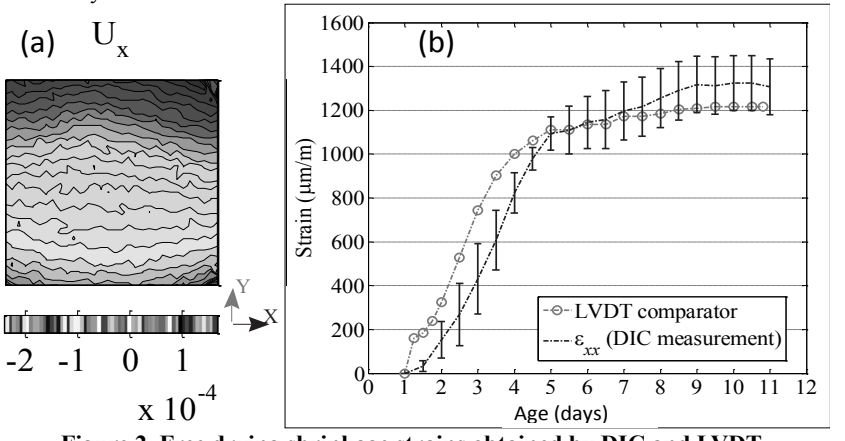

Figure 2. Free drying shrinkage strains obtained by DIC and LVDT

Surface cracking in restraint tests

At the end of the restrained shrinkage test, no macro-crack (i.e. visible to naked eye) was observed. Only micro-cracks (i.e. only visible with optical microscope) on the whole surface were detected. These qualitative observations have been retrieved quantitatively by DIC. The post-processing tool displays the field of the criterion (see Eq. 2 and 3, only positive values are displayed), which reveals the apparition of a micro-cracking network at the surface (Figure 3). The pattern of cracks (3 joining cracks) is typical of cracking due to the restraint of drying shrinkage. After cracking initiation, the global shape of the cracks network remained the same throughout the test. However, the intensity of the equivalent tensile strain (Eq. 2) increased during the test, corresponding to an increase of the crack widths. The method does not allow us to determine accurately the time of cracking initiation. Indeed, at this time, the tensile strains are of the same order of magnitude than the resolution of the measure.

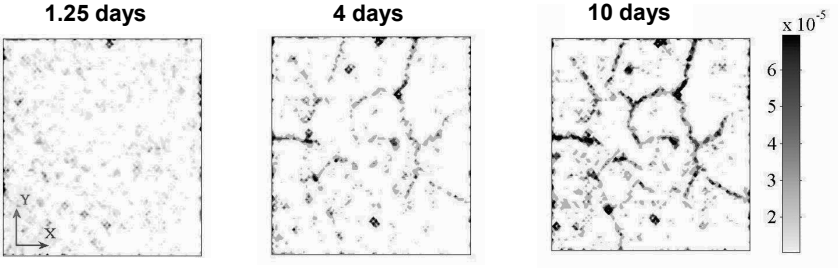

Figure 3. Micro-cracking pattern on the mortar surface (20×20 cm) during the restrained shrinkage test (Figure 1, photographed zone 3) – Iso-values of equivalent strain of Mazars (1986) in m/m at different ages.

In-depth cracking in restraint tests

The previous results do not give any information on the depth of cracks in the mortar and on the cracking at the interface between mortar and substrate. The observation shown below gives more insight on these aspects. However, it should be emphasized that the zone observed by camera through the glass plate is not representative of the material core (photographed zone (2) in Figure 1). In the studied area, three tensile cracks propagated through the mortar layer and reached the interface with the concrete support.

Crack widths were determined at the middle of the mortar layer (line A'-B' in the cartography of equivalent strain given in Figure 4). In order to obtain an accurate measurement, some precautions should be taken. Indeed, the image texture of the ZOI where the crack occurred is modified by the presence of the crack. The observed displacement gaps correspond to the cracks. Then, the crack width can be calculated as the difference of displacement between the interpolated displacements along the line A'-B'. This interpolation method allows us to determine crack widths, for

instance 25.6, 16.6 and 14.6 µm (Figure 4) after 10 days. These values are of the same order of magnitude than those found by optical microscopy.
The same method has been used to determine the debonding at the interface between the mortar layer and the concrete support. For instance, a displacement gap of 25 µm has been found.
Three experiments were conducted on concrete blocks with controlled roughness in order to assess the reproducibility. Due to material heterogeneities and random location of defaults, the crack locations and widths observed were variable from one sample to another.

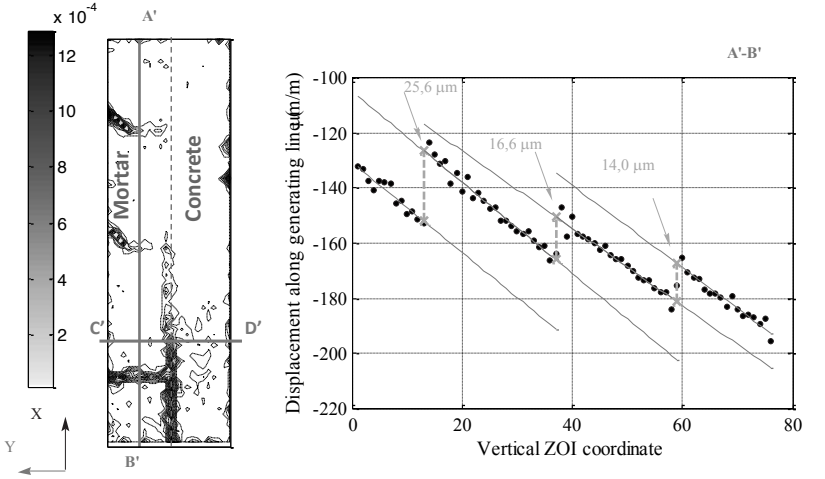

Figure 4. Micro-cracking pattern during the restrained shrinkage test (Figure 1, photographed zone 2) – Iso-values of equivalent strain of Mazars (1986) in m/m (left hand side). Determination of crack openings by interpolation from the displacement field (right hand side) after 10 days.

CONCLUSION

The cracking evolution due to restrained drying shrinkage is hardly measurable but its monitoring is necessary to improve the understanding of mortar/substrate systems behavior. For this purpose, a new experimental method using Digital Image Correlation (DIC) was presented. Based on a post-processing of images obtained by a camera, after painting a random pattern on the studied surface, the device was developed in order to monitor 2D displacements fields. The proposed method enables also a mapping of the cracking surface and a quantification of cracks openings (in-depth cracking, debonding at the interface). Based on these results, it can be

concluded that DIC method is a promising tool to study coating mortar cracking with representative geometries and in restraint conditions.
Besides, almost all relevant material parameters (related to the evolutions of hydration degree, Young modulus, tensile strength, drying, drying shrinkage …) have been measured. The next objective is then to perform numerical simulations in order to validate a model which is currently under improvement. In contrary to previous studies, it is possible using DIC to compare experimental with predicted displacements, not at predefined locations (corresponding to sensors), but in the whole surface. Furthermore, since cracks initiate at random areas, depending on local defaults, it is difficult to discriminate models. Using DIC, it is possible to extract the boundary conditions in term of displacements and to impose them for finite element calculations.

REFERENCES

Besnard, G., Hild, F., and Roux, S. (2006). “Finite-element" displacement fields analysis from digital images: Application to Portevin-Le Châtelier bands.” *Exp. Mech.*, 46, 789-804.

Garbacz, A., Courard, L., and Kostana, K. (2006). “Characterization of concrete surface roughness and its relation to adhesion in repair sytems.” *Mater. Charact.,* 56, 281-289.

Lagier, F., Jourdain, X., De Sa, C., Benboudjema, F., Colliat, J.-B. (2011). “Numerical strategies for prediction of drying cracks in heterogeneous materials: comparison upon experimental results.” *Engineering Structures*, 33(3), 920 – 931

Mazars, J., “A description of micro and macroscale damage of concrete structures.” *Eng. Fract. Mech.*, 25, 729-737.

Monge, J. (2007). *Fissuration des mortiers en couches minces - Effets de l’hydratation, du séchage et de la carbonatation*, PhD Thesis, ENS Cachan, in french.

Hild, F., Raka, B., Baudequin, M., Roux, S., Cantelaube, F. (2002). “Multi-scale displacement field measurements of compressed mineral wool samples by digital image correlation.” *Appl. Opt.*, 32, 6815-6828.

Numerical analysis of cracking induced by drying shrinkage in concrete using a mesoscopic approach: influence of aggregates restraint and skin effect

M. Briffaut[1] and F. Benboudjema[2]

[1]University Joseph Fourier-Grenoble I , Grenoble-INP, , CNRS UMR 5521, Laboratoire 3S-R,
Domaine Universitaire, BP53, 38041 Grenoble Cedex 9, France,
Email : matthieu.briffaut@3sr-grenoble.fr
[2]LMT-Cachan, ENS-Cachan, Paris 6 University, CNRS, UniverSud Paris PRES, France

ABSTRACT

Drying shrinkage is a very slow process, leading to self-equilibrated stresses and eventually to cracking, which can be observed at two scales. On the one hand, at the macroscopic scale, the concrete skin shrinkage is restrained by the concrete core. On the other hand, at the mesoscopic scale, the cement matrix shrinkage is restrained by the aggregates.
To study simultaneously the influence of the two aforementioned phenomena (self-restraint at the macroscopic and mesoscopic scale), numerical simulations have been performed on a mesostructure (including explicitly the aggregates and mortar).
Results show on an ordinary concrete that when creep is not taken into account, drying shrinkage leads to misleading results: an important damage field arises rapidly, whereas taking into account creep changes and delays the cracking pattern. The consequences are a reduction of the apparent Young modulus and tensile strength which are slightly more important when skin effect is taken into account.

KEYWORDS : drying shrinkage, cracking, mesoscopic approach, creep

INTRODUCTION

After its casting, ordinary concrete is generally protected from drying by formwork or curing products and remains saturated or close to saturation (self-desiccation occurs). After the formwork removal, the concrete skin is exposed to the relative humidity of the environment which can be highly lower than the inner concrete one. Therefore, water movements occur (from concrete to the surrounding environment) leading to a drying shrinkage of the cement matrix. Since drying shrinkage is at least self-restrained (the case of an external restraint, *i.e.* by a concrete lift, in reparation, by a support in tile/coating mortars etc… will not be considered in this study), stresses are generated and cracking may occur. This restraint and the associated cracking can be observed at two scales. On the one hand, at the macroscopic scale, the concrete skin shrinkage (which dries first) is restrained by the concrete core (which undergoes a

slow drying). On the other hand, at the mesoscopic scale, the shrinkage of the cement matrix is restrained by the aggregates.

This communication is the second step of a multi-scale approach which aims to predict the cracking of concrete structures adopting evolving mechanical properties. The first step allows studying strain incompatibility (autogeneous shrinkage/thermal strain) between aggregates and cement paste (Briffaut et *al.*, 2013). Indeed, this may lead to cracking (mesoscopic scale), especially in the concrete structure core (which does not undergo significant drying at this time) and reduce mechanical properties (apparent Young modulus, tensile strength …).

The aim of this communication is now to focus on the skin of concrete structures. Indeed, it is submitted rapidly to drying after formwork removal and the content of cement paste is higher (due to wall effect), leading to more drying shrinkage. Induced superficial cracking may increase local transfer properties (diffusivity and permeability), leading to sooner deterioration (penetration of CO_2 and associated corrosion of reinforcement) or reduction of the tightness. To study simultaneously the influence of the two aforementioned phenomena (self-restraint at the macroscopic and mesoscopic scale), numerical simulations have been performed on a mesostructure (which contains the aggregates and the mortar and represents a concrete REV), using Cast3m finite element code.

In a first part, drying calculations are performed. A simplified drying model, based on mass balance equations of water, is used. The influence on the hydric profile of the skin effect is studied, showing that the rate of the drying process is increased, as expected. The second part is dedicated to the study of the consequences of drying on the mechanical behavior using a viscoelastic damage model for the mortar behavior. Both creep strains (which relax the induced stresses) and skin effect influences are highlighted.

MODELLING PRESENTATION

Drying and drying shrinkage model.

The hydric model is based on the conservations equations of the liquid water mass, water vapor and dry air (with some validated assumptions (De Sa et al., 07)). Relations between the relative permeability of the cement matrix and the degree of saturation and between the degree of saturation and capillary pressure (desorption isotherm) are coming from the ones proposed by Van Genuchten (80).

The model of drying shrinkage is based on the theory of unsaturated porous media (Benboudjema and Torrenti, 13).

Creep and damage models.

The basic creep model which renders most of known and admitted features (partially reversible strain, effects of hydration, aging, drying, temperature …) is based on the use of an adaptated Burger element. Drying creep strains (intrinsic to the cement paste (Day et al., 84)) are taken proportional to the variation of relative humidity of the material (Bazant and Chern, 85).

The damage is calculated from the equivalent strain defined by Mazars (Mazars, 86) and modified by Mazzotti and Savoia (Mazzotti and Savoia, 03) to take into account a part of the creep strains in the calculation of the damage variable (*D* used thereafter). Finally the damage model is regulated by the introduction of a characteristic length of the elements to dissipate energy constant even after a refinement of the mesh (Chiumenti and Cervera, 06).

Mesoscopic mesh.
The mesoscopic mesh generation algorithm was developed by Nguyen (Nguyen et al., 10). Numerical simulations are performed on two-dimensional VER of concrete (100 × 100 mm²) for which the cement matrix and aggregates are represented. The calculations are carried out under the assumption of plane stresses. The mesh is not adapted to the presence of aggregates, but the material properties are projected into a fine finite element mesh. Figure 1 shows an example of the mesh used. Only the coarser granular classes are used. Indeed, as the ITZ in our approach is not explicitly taken into account, no percolation path appears if the finest aggregates are represented. It should be noted that a second mesostructure was used to introduce a side effect to the drying face (at the right side in the Figure 1a) to reproduce the effect of the formwork.

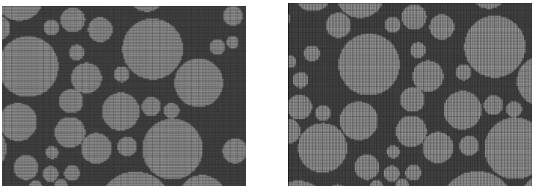

(a) *(b)*

Figure 1. Mesoscopic mesh : with side effect (a), without side effect (b)

Boundaries conditions. A solid concrete wall is considered. An area on the surface is removed and becomes our VER concrete by the use of suitable mechanical boundary conditions (Figure 2). The right side is free to deform and displacement of the other three sides is partially restricted (same uniform movement along an axis is imposed). Other boundary conditions are used to eliminate the movement of rigid bodies. It should be noted that the boundary conditions used are not exactly representative of real ones because displacements allowed are purely vertical or horizontal when in reality, it depends on the location of the VER in the wall.

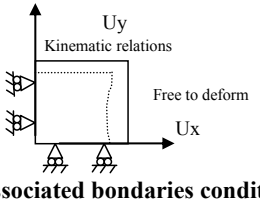

Figure 2. Associated bondaries conditions

Parameters calibration. The use of mesoscopic simulations requires a relevant parameters calibration in roder to avoid reaching flawed conclusions. Indeed, obtaining experimental information on VER located within a massive wall is not easy. To identify the parameters (essentially the mortar ones) virtual tests were therefore carried out on mesosctructure to reproduce the experimentally identified macroscopic behavior of ordinary concrete (w / c = 0.57) (Reviron, 09) (Briffaut *et al.*, 10) (Briffaut *et al.*, 12). Some results of these calibrations on hydric parameters and creep parameters are shown in Figure 3. The mechanical parameters (Young's modulus, tensile strength, cracking energy) are coming from the literature and pre-cited studies and are presented in Table 1.

Table 1. Used mechanical parameters

	Young modulus	**Tensile strength**	**Fracture energy**
Mortar	30GPa	2.1 MPa	40 J/m²
Aggregates	60 GPa	-	-

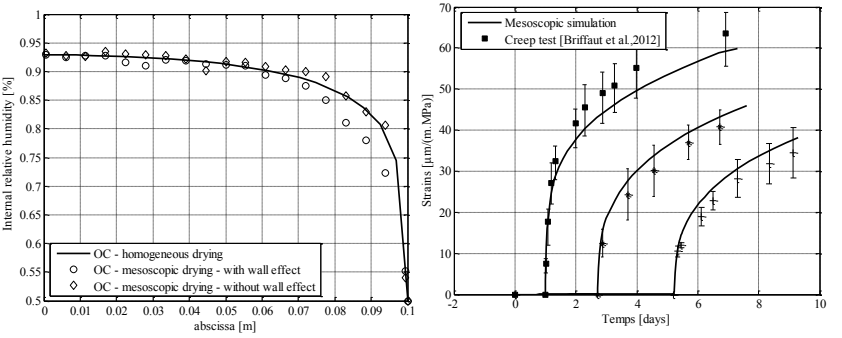

Figure 3. Results of calibration of hydric and creep parameters

Damage fields during drying.

Numerical simulations are performed on the VER concrete to calculate the evolution of the damage field during drying due to incompatibilities deformation (autogenous shrinkage and drying shrinkage of mortar) between the cement matrix and aggregates. The outer relative humidity is equal to 50 %.

Figure 4 to 6 shows the evolution of the damage field during drying for the two aforementioned meshes (with and without side effect). Figures 4 and 5 also highlight the effect of creep consideration. The probability of crack growth is the result of a competition between the generated stresses induced by differential shrinkage (due to drying), creep deformations and mechanical properties.

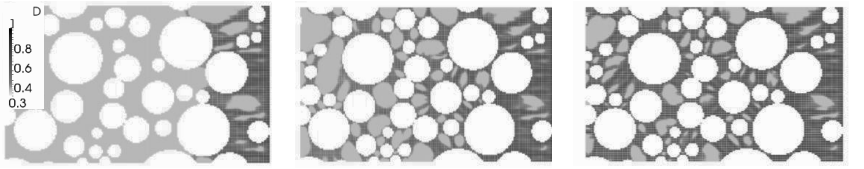

Figure 4. Damage fiels evolution (D) during drying (t represents the time in days after the formwork removal) with side effect consideration without taking into account creep.

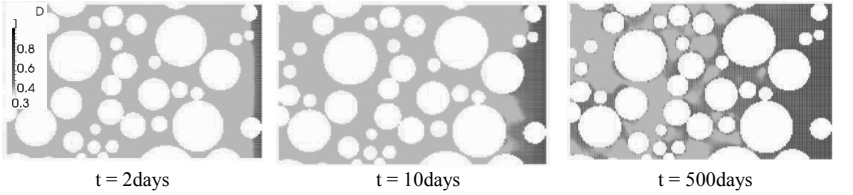

Figure 5. Damage fiels evolution (D) during drying (t represents the time in days after the formwork removal) with side effect consideration with the the take into account of creep.

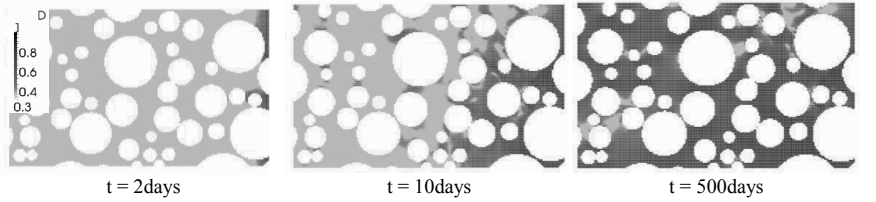

Figure 6. Damage fiels evolution (D) during drying (t represents the time in days after the formwork removal) without side effect consideration with taking into account creep.

During the first days of drying, the simulations results show that a significant but localized damage in skin appears in each situation. Except for the case in which creep is not taken into account, it is only after more than a year that the mesostructures are significantly damaged. It is worth noting that the damage patterns are consistent with those observed experimentally namely cracking around the coarse aggregates (debonding) and radial cracks perpendicular to coarse aggregates (Lagier et *al.*, 12). One result which may be unexpected is the fact that the damage develops faster when side effect is not taken into account whereas internal relative humidity is lower (see figure 3) leading to higher drying shrinkage. The result is explained by the presence of aggregates on the skin which increases the strains incompatibilities and cracking.

GLOBAL BEHAVIOUR AFTER DRYING

After calculating the internal strains and initial stresses (and associated damage) in concrete REV (see previous section), the overall behavior of concrete is calculated by a simulation of a unilateral loading (uniaxial tensile followed by compressive stresses). The purpose of these simulations is to study the influence of drying on the macroscopic behavior, in particular tension (global restrained shrinkage mainly generates tensile stresses).

In the case of unilateral loading, during the reversal of load, microcracks gradually close and the tangential stiffness of the material must increase. Damage model used in the previous simulation is not able to reproduce this increase in stiffness. Thus, for the following simulations, the unilateral effect is taken into account by a separation of the stress tensor in positive and negative parts (Fichant et al., 99).

As irreversible deformations are not taken into account in the damage model used, the stress closure cracks must be equal to $\sigma_c = 0$ MPa.

Figure 7 shows the stress - strain relationships of ordinary concrete in the cyclic tensile and compression test for different drying period and for the three situations studied in the previous section. Although damage appears from the first moments of drying, this skin damage has only a small influence on the law of behavior predicted by our simulations. Indeed, it is only when the damage penetrates throughout the mesoscopic structure that a visible impact on the behavior law is obtained.

A decrease of apparent Young modulus and tensile strength is predicted, which is consistent with most of available experimental data (de Sa et *al.*, 08). When a large initial damage due to drying is taken into account, an increase in the ductility of the material related to the multiplication of locations where micro-cracking in the cracking process of the virtual test is noted. The same results were obtained by Heinfling (Heinfling et al., 98) on simulations of concrete at high temperature.

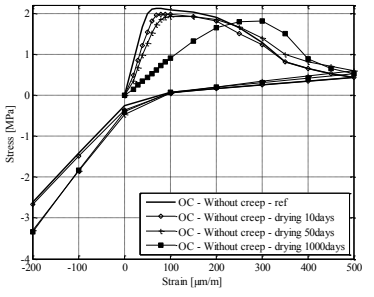

(a)

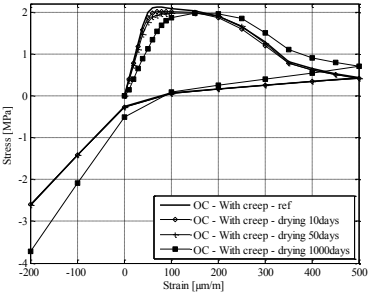

(b)

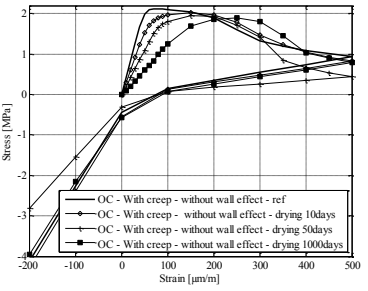

(c)

Figure 7. Global behaviour during the cyclic virtual test; with side effect consideration and without creep (a), with side effect consideration and with creep consideration (b) without side effect consideration and with creep consideration (c)

CONCLUSION

A mesoscopic approach has been used to study the effect of strains incompatibilities due to drying and their effect on the concrete behaviour. The results show that for an ordinary plain concrete when creep strains are not taken into account, the differential drying behavior leads quickly to an important damage while taking into account the creep delays the cracking and the amplitude of the damage.

In skin members, the mechanical concrete behavior is only slightly modified in the first days of the drying process (only a thin layer of concrete is damaged) but the apparent Young modulus and the tensile strength can be strongly modified after several hundred days, due to drying shrinkage incompatibility between mortar and aggregates.

Although the hydric profile evolves more rapidly when wall effect is taken into account, it seems that the cracking due to drying is lower. Nevertheless, this observation need to be validated by coupled simulation. Indeed, in the presented simulation, the mortar permeability is not affected by the damage. Moreover, it is supposed that mechanical behavior of mortar is not sensitive to drying, whereas it undergoes the same phenomena that are presented in this communication.

REFERENCES

Bažant Z. P., Chern J. C. (1985), Concrete Creep at Variable Humidity : constitutive law and mechanism, Materials and Structures, 18 (103), p. 1-20

Benboudjema F., Torrenti J.-M. (2013), Modelling desiccation shrinkage of large structures, accepted in European Physics Journal

Briffaut, M., Benboudjema, F., Torrenti, J.-M. and Nahas, G. (2011), Numerical analysis of the thermal active restrained shrinkage ring test to study the early age behavior of massive concrete structures, Engineering Structures, vol. 33(4) pp.1390-1401.

Briffaut, M., Benboudjema, F., Torrenti, J.-M. and Nahas, G. (2012), Concrete early age basic creep : experiements and test of rheological modelling approches, Construction and buildings materials, Vol. 36, pp. 373-380.

Briffaut M., Benboudjema F., Laborderie C., Torrenti J.-M. (2013), Prediction and impact of internal stresses in concrete due to restraint of autogeneous and thermal shrinkage by aggregates, Journal of Engineering Mechanics, 10.1061/(ASCE)EM.1943-7889.0000607.

Cast3m, Commissariat à l'Energie Atomique CEA - DEN/DM2S/SEMT, Cast3m finite element code, available at http://www-cast3m.cea.fr/.

Cervera, M. & Chiumenti, M. 2006. Mesh objective tensile cracking via a local continuum damage model and a crack tracking technique. Computat. Methods Appl. Mech. Engrg. 196, p.304-320.

Day R.L., Cuffaro P., Illston J.M. (1984), The effect of drying on the drying creep of hardened cement paste, Cement and Concrete Research, 14 (3), p. 329-338

De Sa C., Benboudjema F., Thiery M. and Sicard J. (2008), Analysis of microcracking induced by differential drying shrinkage, Cement and Concrete Composites, 30(10), p. 947-956.

Heinfling G., Stabler J., Baker G. and Reynouard J.M. (1998), Effects of high temperatures on the fracture energy of concrete, International Conference on Fracture Mechanics of Concrete Structures, FRAMCOS 3 (3rd).

Lagier F., Jourdain X., De Sa C., Benboudjema F., Colliat J.B. (2011), "Numerical strategies for prediction of drying cracks in heterogeneous materials: comparison upon experimental results", Engineering Structures, Volume 33, issue 3, Pages 920 – 931.

Mazars J. (1986) A description of micro and macroscale damage of concrete structures, Engineering Fracture Mechanics, 25(5:6), p. 729-737.

Nguyen T.D., Lawrence C., La Borderie C., Matallah M. and Nahas G. (2010), A mesoscopic model for a better understanding of the transition from diffuse damage to localized damage, European Journal of Environment and Civil Engineering, 14(6-7), p. 751-776.

Reviron N. (2009), Study of creep of concrete in tension. Application to the nuclear pressurized water containment, PhD thesis ENS Cachan, LMT, in French.

Van Genuchten M. Th. A closed-form equation for predicting the hydraulic conductivity of unsaturated soils. Soil Science Society of America 1980,44, p.892-898.

Delayed strains of cementitious materials – Impact of heterogeneities and creep on cracking induced by drying

C. De Sa[1], C. Benboudjema[1] and A. Michou[2]

[1]LMT-Cachan (ENS Cachan/CNRS/UPMC/PRES UniverSud Paris), 61 avenue du Président Wilson, 94235 Cachan cedex, France; email: desa, benboudjema, michou@lmt.ens-cachan.fr

ABSTRACT

The behaviour of cementitious materials under drying depends on the behaviour of each phase of this material (cement paste and aggregates mainly), which are very different. Indeed, cement paste shrinkage is restrained by the aggregates under drying. The stresses induced by these strain incompatibilities between these two components at meso scale are added to the ones due to macroscopic drying shrinkage gradients. These stresses lead to debonding at the cement paste/aggregate interfaces (circumferential cracks) and to the growth of intergranular cracks (radial cracks). Influence of size and volume fraction of granular inclusions on cracking induced has already been experimentally studied, showing cracking patterns function of volume fraction and size of inclusions.

The aim of this paper is to numerically simulate this hydro-mechanical behaviour at meso scale by taken into account the heterogeneity at this scale. A simplified representation of the mesostructure is adopted, using a spherical inclusions scheme of various sizes and volume fractions. A weakly hydro-mechanical coupling is used. Drying and basic creep are also taken into account. A discrete representation of cracking is adopted permitting to represent the failure due to the hydric loading appearing at the interface between aggregate and cement paste and inside the cement paste.

INTRODUCTION

During drying (due to hygrometrical imbalance between concrete and external environment) concrete undergoes an apparent shrinkage called drying shrinkage. The latter leads to self-stresses induced at different scales. At macro scale, hydric gradient leads to microcracking at the surface of the structure (Bazant, 1982), (Sicard, 1992), (Benboudjema, 2005), (Burlion, 2005), (De Sa, 2008), (Bisschop, 2011), (Yurtdas, 2011). At meso scale, cement paste shrinkage is restrained by the aggregates leading to debonding at the cement paste/aggregates interfaces (Bisschop, 2002), (Lagier, 2011). All these mechanical effects can be prejudical for the durability of concrete structures. To accurately predict the durability of these structures requires the development of a powerful numerical tool to account for the influence of drying loadings on the mechanical response. But this numerical tool should also be able to

describe additional effects of creep (basic and drying creep), which will relax the stresses and so change the cracking pattern due to drying inside the structure.
Most of numerical drying simulations in concrete structures are nowadays based on a macroscopic scale modelling, taking only into account the drying shrinkage gradients. Whereas, some experimental studies have already shown the significant influence of inclusions on cracking during drying loadings (Bisschop, 2002), (Lagier, 2011), (Hobbs, 1974), (Hubert, 2003), (Szczesniak, 2007), (Grassl, 2010), (Idiart, 2012). The aim of this work is so to improve a predictive numerical modeling which will be able to account for the influence of both macroscopic and mesoscopic effects on the mechanical response.

NUMERICAL TOOL DESCRIPTION

Hydric modelling. For "natural" drying (i.e. at ambient temperature), using liquid water mass balance equation and Darcy's law, one obtains the following equation for the evolution of the capillary pressure inside the structure :

$$\frac{dS_l}{dp_c}\frac{dp_c}{dt} = div\left(k_{rl}(S_l)\frac{K}{\mu_l \phi}.grad(p_c)\right)$$

The capillary pressure can be calculated using Kelvin's law, which assumes equilibrium between the gazeous phase (dry air and water vapor, pressure p_g) and the liquid phase (pressure p_l) :

$$p_c = p_l - p_g = \frac{\rho_l RT}{M_l} ln(h)$$

where R is the perfect gas constant, T the absolute temperature, h the relative humidity and M_l the molar mass of water.

The saturation degree is related to the capillary pressure through van Genuchten's relation (van Genuchten, 1980) :

$$p_c(S_l) = a\left(S_l^{-b} - 1\right)^{1-1/b}$$

where a and b are parameters of the material.

The relative permeability is related to the saturation degree through the same model without any additional material parameter (van Genuchten, 1980) :

$$k_{rl}(S_l) = \sqrt{S_l}\left[1 - \left(1 - S_l^b\right)^{1/b}\right]$$

Hydro-mechanical coupling. A weakly hydro-mechanical coupling is used. Coupling effect between hydric and mechanical behaviours (drying shrinkage modelling) is based on capillary pressure mechanism, which seems to prevail in the

current relative humidity scale 50–100% (Soroka, 1979). Such approach is related to the mechanics of non saturated porous media. The drying shrinkage may be computed, in a incremental way, with the following relation (similar to the one used by (Baroghel-Bouny, 1999)) :

$$d\varepsilon_{ds} = \frac{1-2\nu}{E} \times bi \times S_l \times dp_c$$

where ν is the Poisson ratio and E is the Young modulus of the cement paste.

Drying creep is also taken into account. We will be using the stress-induced shrinkage model proposed by (Bazant, 1985) :

$$\varepsilon_{dc} = \dot{\mu}\left|\dot{h}\right|\sigma$$

where ε_{dc} is the stress-induced shrinkage strain, σ is the stress (induced here only by drying loading) and μ a material parameter.

Material's heterogeneity meshing. The strategy we choose here to describe explicitely the material's heterogeneity employs a non-adapted mesh. The mesh nodes positions are fully independent from the meso-scale phases morphology. Hence each element may be split into two parts, each of them lying inside different materials (e.g. here the cement paste or the aggregates). The main advantage of such meshing strategy is flexibility along a new geometry (inclusions shapes and size changes). Nevertheless, this point of view requires to develop kinematics enhancements inside the cut elements by adding a discontinuity within its strain field ("weak discontinuity"). Local kinematics enhancements are incorporated inside the cut elements, based on incompatible modes method (Hautefeuille, 2009), (Benkemoun, 2010). In order to model the homogeneous isotropic media, we used a tridimensional truss built of "bar" finite elements, based on Benkemoun et al. works (Benkemoun, 2010). This approach has been developed in order to decrease the mesh size and so the computation time and size. So as to be representative of the media isotropic behavior, the tridimensional truss is built on the spatial Delaunay triangulation and its corresponding Voronoi tessellation. To be able to introduce material heterogeneity (the two phases aggregates and cement paste) in the truss mesh, the enhanced kinematics introduced concern both the hydric gradient field (in order to represent permeability jump) and the strain field (in order to represent and elastic modulus jump).

Cracking modeling. Cracks are represented by introducing strong discontinuities inside all truss bar elements. These displacement discontinuities can so be activated at the interface between the two phases or inside the matrix, so as to take into account respectively the debonding or the global micro cracking.

APPLICATION TO MODEL MATERIAL DRYING – SIMULATIONS FRAMEWORK

The objective of this numerical study is to improve the capacity of the numerical modeling presented above to analyze the influence of granular inclusions on drying of cementitious materials. This study is based on experimental results obtained by (Bisschop, 2002). Some controlled materials specimens, constituted of cement paste and glass spherical inclusions, are submitted to drying on one of their faces, the other ones remaining protected from desiccation.

Numerical protocol. The size of the mesostructures tested is 40 × 40 × 40 [mm]. Twelve types of mesostructures (see Figure 1) are considered, of different diameters and volume fractions of inclusions.

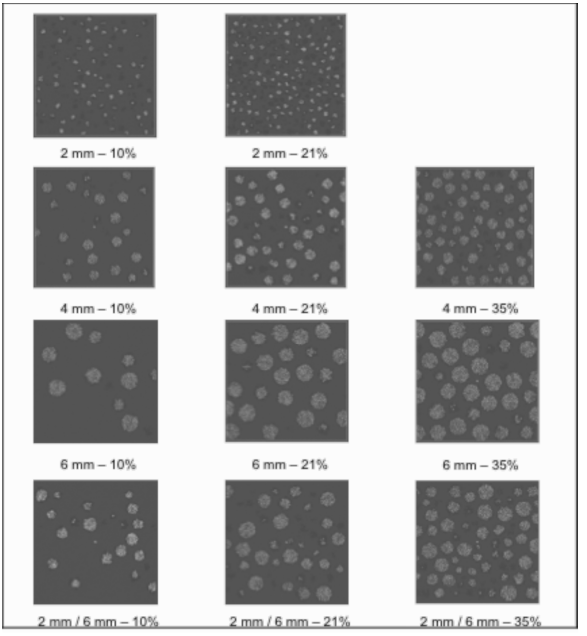

Figure 1. Slices of the tested mesostructures. The notation "Xmm - Y%" refers to the inclusions diameter X in millimeters and the inclusions volumic fraction Y in percentage of the total volume of the mesostructure considered. Concerning the last line the mesostructures contain a uniform distribution of different inclusions diameters (between 2 and 6 mm).

The mesostructures, initially saturated are submitted on the face x = 40 [mm] at a relative humidity of 30% (see Figure 2). The other faces are protected from drying. No mechanical conditions are imposed, the mesostructures can so deform freely

(without any external restraint, so as only self-restrain occurs) in all directions (see Figure 2). The cubic lattice mesh realized for these simulations is constituted of 338436 nodes and 2 326 217 elements, with 338436 × 3 mechanical degrees of liberty and 338 436 × 1 hydric degree of liberty.

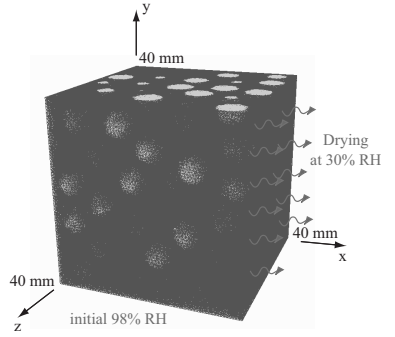

Figure 2. Boundary conditions imposed.

Parameters identification. The hydric parameters of cement paste have been identified, according to the experimental mass loss of the cement paste alone due to drying. The permeability of inclusions is estimated to be largely lower than the cement paste one. The mechanical parameters have been identified to obtain the experimental Young modulus of cement paste and glass inclusions. We can note that the inclusions are considered to remain elastic. The drying shrinkage and creep coefficients are obtained from literature results (Day, 1984), (Lagier, 2011). The identified parameters are given in Table 1.

Table 1. Parameters identification.

Phase	K [m^2]	ϕ [-]	b [-]	a [MPa]
Cement paste	12.10^{-21}	0,6	0,32	30
Inclusions	12.10^{-30}	-	-	-
Phase	E [GPa]	f_t [MPa]	α_{rd} [-]	μ [GPa^{-1}]
Cement paste	8	3,6	1,2	3
Inclusions	70	∞	-	-

APPLICATION TO MODEL MATERIAL DRYING – SIMULATIONS RESULTS

Representation of hydric gradient and strain incompatibilities effects. The simulations performed on cement paste and on heterogeneous material (cement paste and inclusions) underline the influence of the heterogeneity on the hydric gradient and on the cracking patterns observed numerically (see Figure 3). There are almost no

mass transfers in the aggregates since their permeability and porosity are weaker than the cement paste ones. Moreover we can observe in the cement paste and in the mortar, cracking coming from the drying face due to the hydric gradient. For the mortar only, the strain incompatibilities effects are added, with cracking observed numerically around the aggregates. Such numerical observations are very close to experiments findings (Bisschop, 2002).

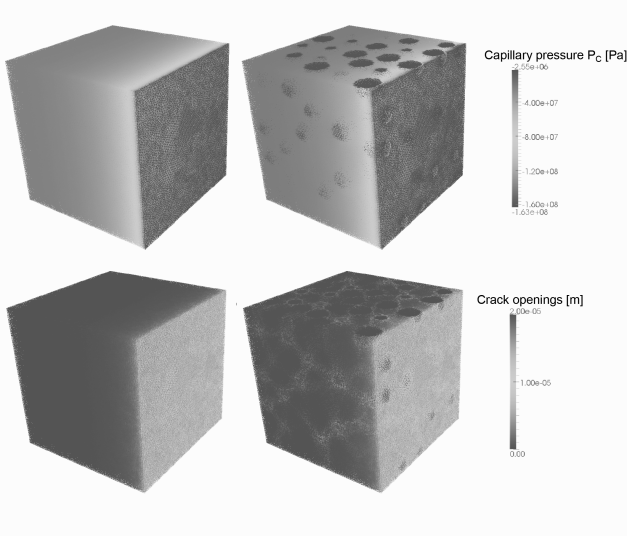

Figure 3. Capillary pressures and crack openings patterns for cement paste without and with inclusions at 80 days of drying.

Cracking patterns. Experimental cracking patterns have been retrieved numerically (see Figure 4), with different patterns observed depending on the presence or not of inclusions. For mesostructures of cement paste only, cracks are localized at the surface of the specimens (due to gradients of drying shrinkage). For the mesostructures including inclusions, cracking is more diffuse and isotropic, with circumferential and radial cracks growthing at the interface between matrix and inclusions. Taking into account drying creep induces for the same drying conditions and the same mesostructures tested a decrease of induced cracking, due to stress relaxation due to drying creep (see Figure 5).

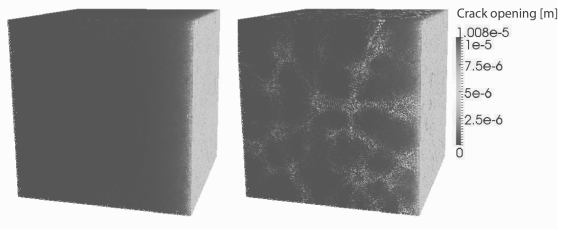

Figure 4. Cracking patterns induced by drying in the different mesostructures at final time (no drying creep taken into account).

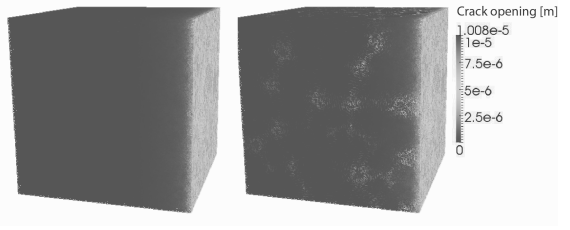

Figure 5. Cracking patterns induced by drying in the different mesostructures at final time (with drying creep taken into account).

"Volume" of cracks. Figure 6 shows the evolution of volume of cracks along time for the different mesostructures tested. Volume of cracks depends on the volume fraction and on the inclusions size. The cracks growing inside the mesostructure constituted of cement paste only are induced by the hydric gradients appearing due to the superficial drying of cement paste. The localization of these cracks is limited to the surface dried, due to the stop of the propagation as soon as the hydric gradients decrease. This explains that the volume of cracks tends so to a constant value during drying. On contrary, for the heterogeneous mesostructures, it can be observed a permanent increase of the cracking during drying. Moreover, volume of cracks seems to increase with inclusions volume fraction and inclusions size even if these conclusions are not confirmed for the highest volume fraction (of 35% of inclusions). Figure 7 underlines also the influence of drying creep, volume of cracks being less important, as expected, if drying creep is taking into account.

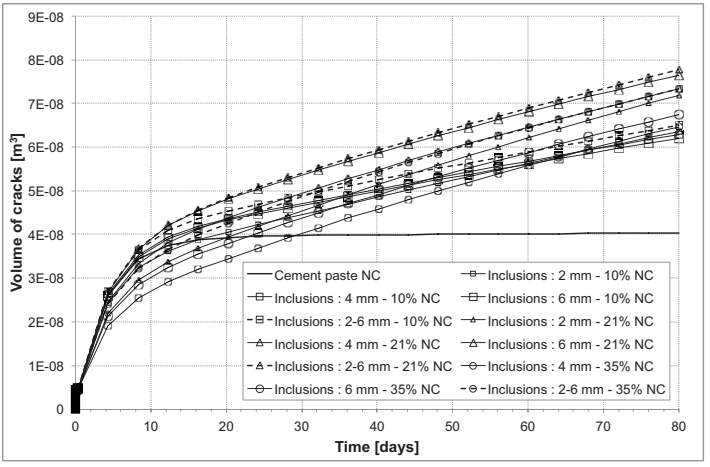

Figure 6. Evolution of the volume of cracks during drying for the different mesostructures, without taking into account drying creep (NC: No Creep), with time.

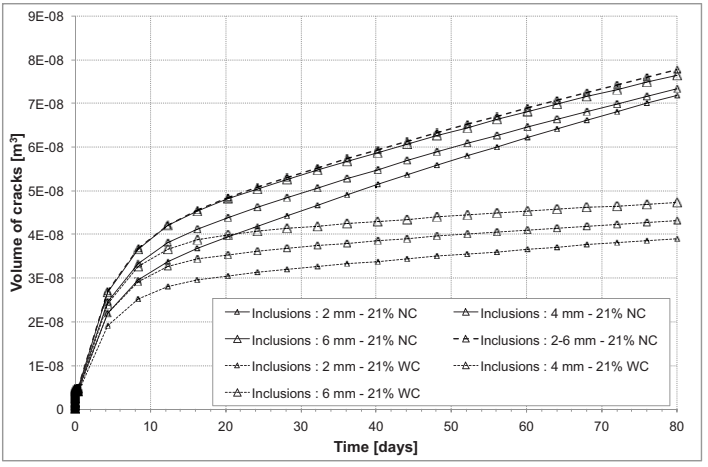

Figure 7. Evolution of the volume of cracks during drying for the different aggregates diameters for 21% of inclusions with time (NC: No Creep, WC: With Creep).

CONCLUSION

An hydro-mechanical coupled FE model has been presented in this paper which differs from traditional ones using smeared cracking representation. The model introduced here is based on a discrete representation of cracking, realized by

introducing strong discontinuities in the displacement field. A non adapted truss mesh is employed. Drying creep is also taken into account in this model. This model has been set up so as to be able to study the effects of heterogeneity in cementitious materials on mechanical responses to drying. The aim of this study was to be able to show the influence of the strain incompatibilities between matrix and inclusions appearing during drying and inducing non negligible cracking. This phenomena has successfully been shown. A numerical study considering different volume fractions and size of inclusions has been developed to quantify this influence of heterogeneity in terms of hydric evolutions induced and so mechanical responses evolutions (cracks volume and apparent young modulus). The simulation results obtained by using this model lead to the following conclusions: drying gradient effects occurring are limited in time in terms of volume of cracks increase. The cracking continuation during drying can be explained by drying strain incompatibilities being observed between cement paste and aggregates during all the drying process and generating cracking at the interfaces between these two phases. Moreover, the necessity of taking account of the drying creep effects is underline, leading to weaker values of volume of cracks. These numerical results are in agreement with experimental results from literature. The next step of this numerical work, already begun, consists on evaluating this effects of cracking due to drying on the transfers properties of an heterogeneous material submitted to drying loadings.

REFERENCES

Baroghel-Bouny, V., Mainguy, M., Lassabatère, T. and Coussy, O. (1999). "Characterization and identification of equilibrium and transfer moisture properties for ordinary and high-performance cementitious materials." *Cement and Concrete Research*, 29, 1225-1238.

Bazant, Z.P., and Raftshol, W.J. (1982). "Effect of cracking in drying and shrinkage specimens." *Cement and Concrete Research*, 12, 209-226.

Bazant, Z.P., and Chern, J.C. (1985). "Concrete creep at variable humidity: constitutive law and mechanism." *Materials and Structures*, 18, 1-20.

Benboudjema, F., Meftah, J.M., and Torrenti, J.M. (2005). "Interaction between drying, shrinkage, creep and cracking phenomena in concrete." *Engineering Structures*, 27, 239-250.

Benkemoun, N., Hautefeuille, M., Colliat, J.B., and Ibrahimbegovic, A. (2010). "Failure of heterogeneous materials: 3D meso-scale FE models with embedded discontinuities." *Int Jal for Numerical Methods in Engineering*, 82, 1671-1688.

Bisschop, J., and van Mier, G.M. (2002). "Effect of aggregates on drying shrinkage microcracking in cement-based composites." *Materials and Structures*, 453-461.

Bisschop, J., and Wittel, K. (2011). "Contraction gradient induced microcracking in hardened cement paste." *Cement and Concrete Composites*, 33, 466-473.

Burlion, N., Bourgeois, F., and Shao, J.F. (2005). "Effects of desiccation on mechanical behaviour of concrete." *Cement and Concrete Composites*, 367-379.

Day, R.L., Cuffaro, P., and Illston, J.M. (1984). "The effect of drying on the drying creep of hardened cement paste." *Cement and Concrete Research*, 14(3), 329-338.

De Sa, C., Benboudjema, F., Thiery, J. and Sicard, J. (2008). "Analysis of microcracking induced by differential drying shrinkage." *Cement and Concrete Composites*, 30, 947-956.

Grassl, P., Wong, H.S., and Buenfeld, N.R. (2010). "Influence of aggregate size and volume fraction on shrinkage induced micro-cracking of concrete and mortar." *Cement and Concrete Research*, 40, 85-93.

Hautefeuille, M., Melnyk, S., Colliat, J.B., and Ibrahimbegovic, A. (2009). "Failure model for heterogeneous structures using structured meshes and accounting for probability aspects." *Engineering Computations*, 26, 166-184.

Hobbs, D.W. (1974). "Influence of Aggregate Restraint on the Shrinkage of Concrete." *ACI Journal,* 71, 445-450.

Hubert, F.X., Burlion, N., and Shao, J.F. (2003). "Drying of concrete: modelling of a hydric damage." *Materials and Structures*, 36, 12-21.

Idiart, A., Bisschop, J., Caballero, A. and Lura, P. (2012). "A numerical and experimental study of aggregate-induced shrinkage cracking in cementitious composites." *Cement and Concrete Research*, 42, 272-281.

Lagier, F., Jourdain, X., De Sa, C., Benboudjema, F., and Colliat, J.B. (2011). "Numerical strategies for prediction of drying cracks in heterogeneous materials: Comparison upon experimental results." *Engineering Structures*, 33, 920-931.

Sicard, V., Francois, R., Ringot, E., and Pons, G. (1992). "Influence of creep and shrinkage on cracking in high strength concrete." *Cement and Concrete Research*, 22, 159-168.

Soroka, I. (1979). *Portland cement paste and concrete,* Macmillan.

Szczesniak, M., Burlion, N., and van Mier, G.M. (2007) *An experimental study of the roles of water saturation degree and aggregate size in the mechanical response of cement based composites,* in: Proceedings of FraMCoS-6 - Fracture Mechanics of Concrete Structures, Italy.

van Genuchten, M.T. (1980). "A closed-form equation for predicting the hydraulic conductivity of unsaturated soils." *Soil Science Society of America,* 44, 892-898.

Yurtdas, I., Burlion, N., Shao, J.F., and Li, A. (2011). "Evolution of the mechanical behaviour of a high performance self-compacting concrete under drying." *Cement and Concrete Composites*, 33, 380-388.

Influence of the initial water saturation of aggregates on concrete shrinkage

E. Roziere[1], R. Cortas[1], A. Loukili[1], A. Hamami[2], S. Staquet[2]

[1]Civil Engineering and Mechanics Research Institute, Ecole Centrale de Nantes, 1 rue de la Noë, BP 92101, 44321 Nantes, France; PH (33) 2 40 37 16 62; FAX (33) 2 40 37 25 35; email: Emmanuel.Roziere@ec-nantes.fr
[2]BATir, Building, Architecture & Town Planning BATir service, Université Libre de Bruxelles, CP194/4, 87, A.Buyl Avenue, 1050 Bruxelles, Belgium; PH (32) 2-6502758; FAX (32) 2-6502782; email: sstaquet@ulb.ac.be

ABSTRACT

The study presented in this paper deals with the influence of the water saturation of natural aggregates on shrinkage and cracking sensitivity of concrete at early age. Limestone crushed gravels were specially chosen for this study due to their high porosity. The degree of water saturation of gravels varied, from a given concrete mixture, keeping the total water content constant. Significant variations of the plastic shrinkage and early age autogenous deformations were observed. Due to the kinetics of absorption of gravels, the water content remaining in cement paste was different from the effective water content. This was confirmed by the values of mechanical properties and porosimetry. The evolutions of elastic modulus and tensile strength were experimentally assessed and used to compare the cracking sensitivity of the three studied concretes by evaluating the self generated stresses.

INTRODUCTION

After site investigation, short term cracks across a 20 cm thick slab were observed. In this slab, the used concrete was ordinary vibrated concrete with a water to cement ratio (W/C) varying from 0.45 to 0.6. After composition analysis, the effect of gravel water saturation was found an important parameter to understand the cracking risk of these concretes subjected to restrained shrinkage. The concrete cracking phenomena depends on the kinetics of shrinkage and the mechanical behavior of the concrete. Both properties can be influenced by aggregates. The fine and coarse aggregates generally occupy 60% to 75% of the concrete volume. Even if they are usually considered as inert material, aggregates are actually porous materials and their properties vary with water saturation. How could this supplied or absorbed water be taken into account? The effective water used in the mix design of concrete is the amount of water available for the hydration of cement. In other words it is the theoretical total water (mixing water + water supplied by aggregates + water provided by admixtures) from which the water absorbed by the aggregates is subtracted. This concept remains theoretical because it does not take into

consideration the aggregates absorption kinetics and the cement hydration. The theoretically absorbed water is different from the actually absorbed water. As a result, the actual paste porosity is quite different from the corresponding theoretical one and particularly in the zones surrounding aggregates, where an interfacial transition zone is likely to appear (Ollivier, 1995). Aggregates have a significant influence on the shrinkage, strength, and other concrete properties (Verbeck, 1960, Fujiwara, 2008), and thus on the concrete cracking. The effect of lightweight aggregate saturation on the concrete shrinkage has been investigated in literature (Zhutovsky, 2002), whereas few studies on more commonly used aggregates can be found. The study presented in this paper deals with the effect of the degree of water saturation of porous limestone aggregates on the early-age shrinkage and mechanical behavior of concrete.

1. MATERIALS AND CONCRETE MIXTURES

Three concretes were designed from one theoretical concrete mixture by varying the initial degree of saturation of gravels. The compositions of the concrete mixtures are given in Table 1. Limestone crushed gravels from Beauvilliers, France were specially chosen for this study due to their high porosity. The water absorption coefficient (WA24) of these gravels is 3.2 % (in percentage of dry mass after 24 hours after immersion during 24 hours) according to EN 1097-6 (2000), thus their porosity represents 7.9 % in volume. Added water was adjusted taking into account the initial water content of gravels.

Table 1: Composition and properties of concrete mixtures (kg/m^3)

(kg/m^3)	BV 0%	BV 50%	BV 100%
Gravel - Limestone (4/22.4) Absorption coefficient: 3.2 % - density : 2.46	1000	1016	1032
Sea sand (0/4) Absorption coefficient: 0.6 % - density : 2.58	382	382	382
Crushed limestone (0/4) Absorption coefficient: 0.77 % - density : 2.65	397	397	397
Cement CEM I 52.5 N	350	350	350
W_{eff} [a]	175	175	175
W_{total} [b]	211	211	211
W_{sand}	35	35	35
$W_{gravels}$	0	16	32
W_{added}	176	160	144
Sp	1	1.25	1.5
W_{eff}/C	0.50	0.50	0.50
Slump (mm)	160	170	160
$f_{c,\,1d}$ (MPa)	15.5	20.5	17.0
$f_{c,\,2d}$ (MPa)	22.6	31.4	26.9
$f_{c,\,28d}$ (MPa)	42.6	50	47.5

[a] $W_{eff} = W_{added} + W_{aggregate} + W_{absorption}$ [b] $W_{total} = W_{sand} + W_{gravels} + W_{added}$

2. EXPERIMENTAL PROCEDURES

2.1 Plastic shrinkage

The development of plastic shrinkage was measured using a prism-shaped steel mould device (70x70x280 mm^3). The upper face of the concrete prism is exposed to drying (Turcry, 2006). The fresh concrete is poured into an envelope built using two PVC plates (70x68x5 mm^3) also used as reflecting plates. These reflecting plates are stuck to a plastic sheet and they are placed in the steel mould which is covered with PTFE in order to limit the friction between the concrete and the walls of the mould. The horizontal movement of the reflecting plates anchored to the ends of the sample is monitored using two laser sensors. The sample temperature is controlled using water circulation in both the side walls and the steel mould bottom (Saliba, 2010). In this study tests were performed at 20C° and 50% RH.

2.2 Early age autogenous deformation

The autogenous deformation measurements of the studied concretes were carried using a *BTJADE* device (Boulay, 1993). This latter is composed by a corrugated PVC mold in which the concrete is casted. The base length is 250 mm. The sample and the mold are maintained vertically by means of a metal frame. The vertical deformation of the sample is measured by means of an external displacement sensor. The device is completely immersed inside a temperature controlled bath and totally surrounded by water to ensure isothermal conditions. A thermocouple is inserted into the concrete specimen to measure the temperature variation of the concrete during the test. The specimen autogenous deformations are obtained from the recorded data (displacement and temperatures) after correction with the thermal variations.
In order to verify the repeatability of measurements, this test was carried out on 3 specimens. Autogenous deformation curve is reinitialized to the time of setting thus it does not take into account deformations related to fresh concrete like bleeding.

2.3 Porosity and pore size distribution

The porosity and pore size distribution were determined from mercury intrusion porosimetry (MIP) on a single crushed sample of about 3 mm^3. The hydration of the studied materials was stopped, by immersing them in two solvents (acetone and ether), at 24 hours and the samples were dried under vacuum (2 mmHg) at 40°C for 24 hours before the test. (MIP) was carried out with a *Micromeritics* porosimeter (*Autopore IV 9500*) whose range of pressure reached more than 400 MPa. This pressure range allows the mercury to penetrate pores ranging between 0.003 µm and 360 µm diameter, according to Laplace law.

2.4 Tensile strength

The tensile strength of early age concrete was assessed through direct tensile testing (Roziere, 2012) at 3, 5, 10, 15, and 24 hours. The load is applied horizontally by an electric displacement-controlled actuator. The mould actually comprises two halves with curved transitions to a central part with reduced constant section, 100 mm high, 100 mm long, and 105 mm wide. The specimen is protected from drying with thin polyethylene sheets before testing.

2.5 Ultrasonic monitoring of elastic modulus

The *FreshCon* system was used to monitor the early age behavior of concrete using ultrasonic compression (p) and shear (s) waves. More detailed information on this device can be found in (Reinhardt and Grosse, 2004). It consists in a specific mold equipped with two piezoelectric transducers (one transmitter and one receiver). The test was carried out in an air-conditioned room at 20°C and that the concrete sample was protected from desiccation by the use of a plastic foil.
The evolution of the dynamic Poisson ratio υ_{dyn} and the dynamic elastic modulus E_{dyn} are deterdimned using the ultrasonic device. Their values are obtained as a function of the p and s wave velocities (Krauß and Hariri, 2006). P-waves and S-waves were simultaneously measured on the same concrete with dedicated FreshCon molds.

3. RESULTS AND DISCUSSION

3.1 Plastic shrinkage and early age autogenous deformations

Relatively high magnitudes were deduced from the plastic shrinkage measurements. The deformation reached 1200 (µm/m) at the age of 24 hours (figure 1). (BV 50%) showed the highest plastic shrinkage (Figure 1). Significant differences were observed. The shrinkage of (BV 50%) was almost the double of the case (BV 0%). (BV 0%) contained more added water, and thus it was likely to draw benefits from bleeding water on the surface which mitigated the plastic shrinkage. (BV 50%) had the largest plastic shrinkage because it could not draw benefit from the bleeding water as in the case of (BV 0%) and from the internal curing of saturated aggregates as in the case of (BV 100%).

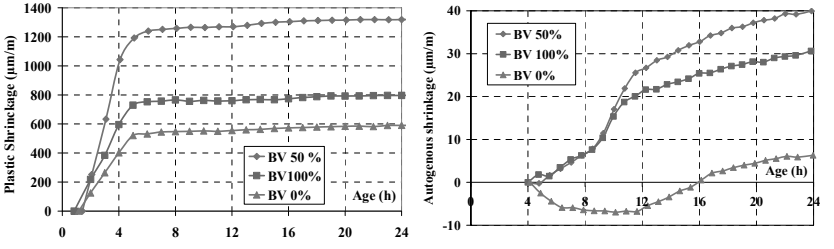

Figure 1. Plastic shrinkage (left) and autogenous deformations (right).

Even thought the autogenous shrinkage of concretes with a water to cement ratio equal to 0.5 is relatively low, it was measured. This is because cracking of this concrete observed on a building site was not limited to the drying surface but crossing through the slab. Thus the purpose was to 'eliminate/reduce' autogenous shrinkage as the main cause of cracking. As shown in figure 1, the autogenous deformations relatively change with respect to the variation of gravels saturation. These magnitudes are very low compared to those obtained when monitoring the plastic shrinkage. However the same trends and ranking can be observed. (BV 0%) concrete exhibited during the 12 first hours a swelling phase which is absent in the case of saturated (BV 100%) and intermediate concrete (BV 50%). In concrete made of initially dry gravels (BV 0%), the paste contains more added water than for the two other concretes. The (W_{added} / C) is higher than the one obtained in the cases of (BV50%) and (BV100%). The concrete made of initially saturated aggregates (BV 100%) contains less water in the paste and thus it performs greater autogenous shrinkage compared to the concrete made of dry gravels (BV 0%). The intermediate concrete (BV 50%) showed the highest autogenous shrinkage. This can be explained by the fact that the cement paste of the intermediate concrete (i) contains less water than the dry concrete (BV 0%) and, (ii) benefits less from the internal curing of saturated gravel compared to the made of saturated gravels (BV 100%). As a conclusion, the intermediate concrete (BV 50%) is the most sensitive to the autogenous shrinkage.

3.2 Compressive strength and porosity

The influence of the added water to cement ratio (W_{added} / C) on the behavior of concrete can be confirmed by the compressive strength and MIP data (Figure 2). The trends and the classification are actually the same as for early age shrinkage.

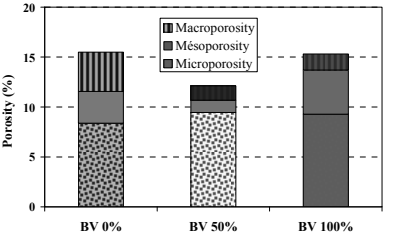

Figure 2. Porosity of the three concretes at 24 hours.

According to Table 1 (BV 100 %) had a higher compressive strength than concrete made of dry gravels (BV0 %). The paste of concrete (BV 100 %) actually contained less water than concrete (BV0 %), because the (W_{added}/C) was lower. The added water W_{added} was actually assessed from the effective water W_{eff} by taking into account the 24-hour absorption of gravels. If the gravels are initially dry (BV0 %), their absorption at the time of setting is not complete because of the kinetics of

absorption, thus the water content of cement paste is higher than W_{eff}. Referring to capillary porosity, the macroporosity of the concrete (BV 0%) was higher which weakened its mechanical strength. (BV 50%) showed the highest strength, this can be explained by the following assumptions (i) it contained less added water than the concrete (BV 0%), (ii) and showed lower mesoporosity than (BV 100%) (Figure 2).

3.3 Assessment of the cracking sensitivity

From the early age properties, the developed internal elastic stresses in the concrete may be calculated using the elastic model (equation 1). The dynamic modulus evolution and the autogenous shrinkage were both determined previously. The obtained values of the developed internal stresses provide data about the potential cracking risk of these compositions due to autogenous shrinkage by comparing the internal stresses to concrete tensile strength (Hammer, 2007).

$$\sigma(t) = \varepsilon(t).E(t) \tag{1}$$

With $\sigma(t)$: Evolution of the estimated internal stresses,
$\varepsilon(t)$: Autogenous shrinkage,.
$E(t)$: Evolution of the modulus of elasticity.

Figure 3 shows the evolution of the dynamic elastic modulus as a function of the age of concrete. This dynamic elastic modulus was slightly larger in the case of (BV 50%) and (BV 100%) compared to (BV 0%). It should be noticed here that at the age of 6 hours the difference of modulus between (BV 0 %) and the BV (100 %) was 70% whereas at the age of 24 hours the difference was only 10 %.

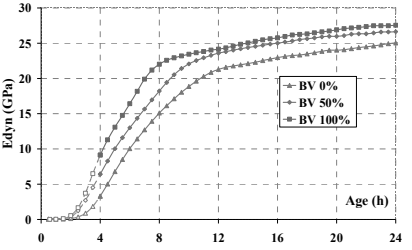

Figure 3. Evolution of the modulus of the three concretes at early age.

The comparison presented on figure 4 shows that the internal stresses due to total restraint of autogenous shrinkage would remain much lower than the tensile strength of concrete (BV0%), thus the potential risk of cracking was relatively low. This comes from the early age swelling due to higher bleeding. As shown in figures 5 and 6, internal stresses due to autogenous shrinkage are likely to become higher than the tensile strength of (BV50%) and (BV100%) at early age. (BV 100 %) would show the highest stresses development before 8 hours. This is due to the prevailing influence of the rapid increase of the elastic modulus during the first hours, whereas

the tensile strength remained relatively low. As a consequence, the potential risk of cracking by restrained autogenous shrinkage of these formulations was high relatively to strength at this age. (BV 0%) remained the safest concrete comparably to (BV 50%) and (BV 100%), dealing with the potential risk of cracking by restrained autogenous shrinkage. It is important to note that such results do not take into account the creep and relaxation phenomena of the concrete and any coupling between shrinkage and strength development.

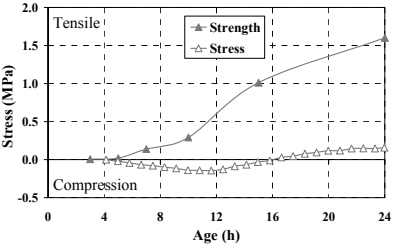

Figure 4. Evolution of the predicted internal stresses and the experimental values of the tensile strength of (BV0%)

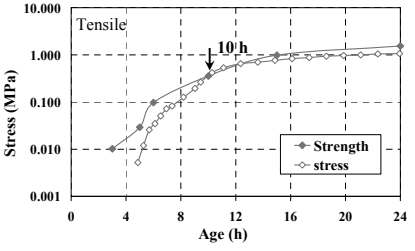

Figure 5. Evolution of the predicted internal stresses and the experimental tensile strength of (BV50%)

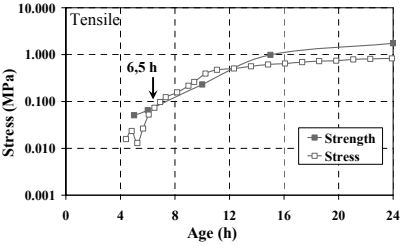

Figure 6. Evolution of the predicted internal stresses and the experimental tensile strength of (BV100%)

CONCLUSION

In this paper, a comprehensive set of experimental data about the effect of initial degree of water saturation of porous limestone gravels on shrinkage is presented. The main conclusions of this study can be summarized as follows:

- The concept of the effective water remains theoretical. The behavior of the same theoretical concrete mixture depends on the initial water saturation of gravels. Considering precisely the water content of gravels and the kinetics of absorption is a very important task.
- Concrete made of partially saturated gravels (BV 50%) does not have intermediate behavior between (BV 0%) and (BV 100%). It showed the highest autogenous and plastic shrinkage at early age, and the highest compressive strength. (BV 50%) contains less added water than (BV 0%) and

does not take advantage of the internal curing by saturated gravels of (BV 100%).

- As the risk of cracking of the concrete due to restraint shrinkage depends on the free shrinkage evolution but also on the mechanical properties, the elastic modulus and the tensile strength were monitored since setting time to assess the relative cracking sensitivity of the concretes with regard to the initial water saturation of gravels. Concrete made of saturated aggregates showed the highest risk of cracking.

Further works are being done to take into account the influence of creep and relaxation phenomena on the cracking sensitivity of early age concrete.

REFERENCES

Boulay, C., Patiès, C., 'Mesure des déformations du béton au jeune âge', *Materials and Structures*, 26, (1993) 307-311.

BS EN 1097-6: 2000, Tests for mechanical and physical properties of aggregates, Determination of particle density and water absorption.

Fujiwara, T., 'Effect of aggregate on drying shrinkage of concrete', *Journal of Advanced concrete Technology*, 6 (1) (2008) 31-44.

Hammer T.A., Fossa, K.T., Bjøntegaard, Ø. 'Cracking tendency of HSC: Tensile strength and self generated stress in the period of setting and early hardening', *Materials and structures*, 40 (2007) 319-324.

Krauß, M., Hariri, K. 'Determination of initial degree of hydration for improvement of early-age properties of concrete using ultrasonic wave propagation', *Cement and Concrete Composites*, 28 (2006) 299-306.

Ollivier, J. P., Maso J.C., Bourdette B., 'Interfacial transition zone in concrete', *Advn. Cem. Bas. Mat.* 2 (1995) 30-38.

Reinhardt, H.W., Grosse, C.U. 'Continuous monitoring of setting and hardening of mortar and concrete', *Construction and Building Materials*, 18 (2004), 145–154.

Roziere, E., Cortas, R., Loukili, A., 'How to investigate the tensile behaviour of early age concrete?' Microdurability, Amsterdam, 11-13 April 2012, 8 p.

Saliba, J., Roziere, E., Grondin, F., Loukili, A., 'Influence of shrinkage-reducing admixtures on plastic and long-term shrinkage', *Cement and Concrete Composites* 33 (2010) 209–21

Turcry, P., Loukili, A., 'Evaluation of plastic shrinkage cracking of self-consolidating concrete', *ACI Mater J* 103 (4) (2006) 272–9.

Turcry, P., Loukili, A., Haidar, K., Pijaudier-Cabot, G., Belarbi, A., 'Cracking tendency of self-compacting concrete subjected to restrained shrinkage: Experimental study and modelling'. *J Mater Civ Eng* 18 (1) (2006)

Verbeck, G., Landgren R., 'Influence of physical characteristics of aggregates on frost resistance of concrete', ASTM, Philadelphia 3, 60 (1960) 1063-1079.

Zhutovsky, S., Kovler, K., Bentur, A., 'Efficiency of lightweight aggregate for internal curing of high strength concrete to eliminate autogenous shrinkage', *Materials and Structures*, 35 (2002) 97-101.

Freeze-Thaw Resistance of Fiber Reinforced Composites with Superhydrophobic Admixtures

Scott Muzenski[1], Ismael Flores-Vivian[2], Konstantin Sobolev[3]

Department of Civil Engineering and Mechanics
University of Wisconsin-Milwaukee, 3200 N. Cramer Street,
Milwaukee, WI 53211-3029

ABSTRACT

Freezing and thawing cycles in northern regions lead to serious deterioration in bridges and dictate the need for early repair or replacement. The use of polyvinyl alcohol (PVA) fibers in cementitious composites improves durability because of its ability to withstand large deformations due to its strain hardening and multi-cracking ability. However, the addition of fibers alone to a cementitious matrix may not be adequate in providing resistance to freezing and thawing beyond the standard 300 cycles. The addition of superhydrophobic admixtures to fiber reinforced composites results in an air void system with small, well-dispersed air voids allowing for better resistance to freezing and thawing. Moreover, the superhydrophobicity of the of the air void surface provides a water repellant effect ensuring that water does not attach to the surface of the air voids. This research demonstrates that the addition of superhydrophobic admixtures to fiber reinforced composites provides improved freeze-thaw resistance by demonstrating a durability factor of 100 through as many as 700 accelerated (-50°C to 20°C) freeze-thaw cycles in fresh water and 5% NaCl solution. Additionally, the accelerated freeze-thaw testing provides a more efficient method for testing freezing and thawing in cementitious materials.

INTRODUCTION

Infrastructure and especially, reinforced concrete bridges in the United States are displaying great need for repair or replacement due severe weathering such as salt scaling and freezing and thawing deterioration. In these key infrastructure elements, cracks within concrete allow chlorides to penetrate, reaching the enclosed steel reinforcement and accelerating corrosion. With this process, cracks and voids within the concrete become even more pronounced and water that occupies these flaws expands during freezing resulting in internal stresses, thus accelerating the deterioration of structure.

[1] Ph.D. Student/Research Assistant, Email: swm@uwm.edu, PH: 1-414-229-4377
[2] Post-Doctorate Research Associate, Email: ismaelfv@uwm.edu, PH: 1-414-229-3229
[3] Associate Professor, Email: sobolev@uwm.edu, PH: 1-414-229-3198

A construction material that is not susceptible to corrosion and displays extremely high freeze-thaw resistance is needed for northern regions to improve the nation's failing infrastructure. The addition of polyvinyl alcohol (PVA) fibers to a cementitious matrix has proven to be a more durable alternative to conventional concrete and exhibits high ductility and strain hardening performance under tension and bending similar to steel (Li, 2002). However, to achieve high ductility and strain hardening behavior, the strength of the cementitious matrix must be reduced so that the maximum tensile cracking strength of the matrix does not exceed the maximum fiber bridging strength (Yang et al., 2009). This reduction in matrix performance would lead to lower freeze-thaw resistance as well (Skalny et al., 1973). The use of PVA fibers within a strong cementitious matrix designed for optimal packing with ultrafine particles (Amirjanov and Sobolev, 2006; Sobolev and Yeginobali, 2005) can still provide high ductility through the addition of superhydrophobic admixtures which are capable of creating the artificial flaws to initiate cracking, allowing for strain hardening and multi-cracking behavior (Muzenski et al., 2013). Although it was found that fiber reinforced concrete with high volumes of fly ash can adequately survive a standard freeze-thaw test (Wang and Li, 2005), 300 freeze-thaw cycles may be sufficient for a concrete to survive only 20 years in some regions. Some regions can experience up to 46 freeze-thaw cycles per year (Janssen et al., 1986), therefore, a material that is designed to withstand 300 cycles would only last about 6 years. In order for a material to last 50 or more years it must be able to survive several thousands of freeze-thaw cycles. ASTM C666 specifies that the center of the specimen must reach a minimum temperature of -18 ± 2° C and a maximum temperature of 4 ± 2° C. However, due to the complexity of measuring the internal temperature of samples, these temperatures are often interpreted as the temperature inside the freeze-thaw chamber. Moreover, the length of time that the material must remain at these temperatures can be fairly short which could result in incomplete thawing of the entire sample as ice near the top surface is usually last to thaw. This being said, many standard freeze-thaw testers do not provide adequate thawing and thus the actual number of freeze-thaw cycles would then be reduced. By allowing the samples to freeze at lower temperatures, a freezing of water in very small capillaries is ensured. The low temperatures provide an accelerated deterioration of the samples as water enclosed in higher pressure areas, such as capillaries, will begin to freeze. Moreover, by allowing the samples to thaw at higher temperatures a full thaw can be guaranteed and a complete freeze-thaw testing is realized.

In northern regions, air entraining admixtures are used to improve freeze-thaw resistance by creating air voids used to allow an escape for water within capillary voids to expand upon freezing. However, many air entraining admixtures create air voids with large, irregular shaped and poorly dispersed air voids (Figure 1). Moreover, a loss of intended air is seen and the surface of the air void is hydrophilic. All of these parameters would lead to lower resistance to freeze-thaw. The use of superhydrophobic admixtures as an alternative to typical air entraining admixtures provides a "desired" air void structure with small, evenly spaced air voids to allow a

shorter distance for water trapped within the capillaries to travel to be able to expand upon freezing (Figure 2). The water repellant surface of the air void can also ensure that water within the air voids is not pulled into the capillary voids through suction. Unlike typical air entraining admixtures, superhydrophobic admixtures demonstrate little to no reduction in compressive strength of the cementitious matrix.

The addition of superhydrophobic admixtures to cementitious materials, (known as superhydrophobic hybridization) combines interdisciplinary work of biomimetics (lotus effect), chemistry (the use of siloxane polymers), and nanotechnology (the use of nano-SiO_2 particles) to solve concrete's fundamental problems such as insufficient durability (Sobolev and Bartrakov, 2007; Sobolev and Gutierrez, 2005; Sobolev and Bartrakov, 2009; Kock et al., 2008). To manufacture superhydrophobic admixtures, the hydrogen-containing admixture (polymethyl hydrosiloxane, PMHS) is combined with small quantities of submicro- and nano-sized particles (Figure 2) (Flores-Vivian et al., 2013). This PMHS admixture can be used at a dosage of 0.01 to 0.1% of cement weight to release hydrogen that forms small (10-100 μm), uniform air voids within the hardened cement phase. For optimal performance, more than 70% of the PMHS must be dispersed to the size of less than 10 μm (Sobolev and Bartrakov; 2007, Sobolev and Bartrakov, 2009). Submicro- and nano-sized particles are then distributed on the surface of these voids to create surface roughness and the hydrophibization effect.

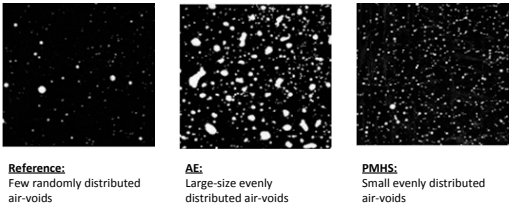

Figure 1. Air Void Structure of Reference, Air Entrained, and PMHS-Based Samples (Sobolev et al., 2013)

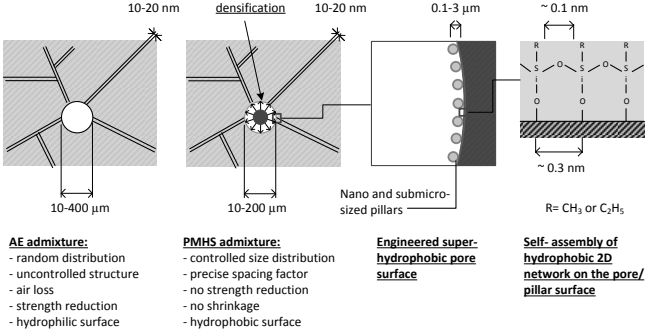

Figure 2. How the Superhydrophization of Concrete Works (Sobolev et al., 2013)

EXPERIMENTAL PROGRAM

The Kuralon K-II RECS 15 x 12 PVA fibers used within this study had a length 12 mm and a diameter of 15 dtex (0.04 mm). These fibers had a Young's modulus of 40 GPa and a tensile strength of 1.6 GPa. Other materials that were used within this study include: Type I portland cement conforming with ASTM C150, ground granulated blast furnace slag (GGBFS), standard graded silica sand conforming with ASTM C778, and commercially available polycarboxylate ether superplasticizer (PCE/SP) with a 31% solid concentration.

The water-based admixtures used to create superhydrophobic air voids were composed of 4.4% polyvinyl alcohol surfactant (PVAS) and 25% PMHS as primary ingredients (Sobolev et al., 2013). To improve the hydrophobicity of the admixture, submicro- and nano-sized particles were added. These consisted of 0.4% (by weight of the total superhydrophobic admixture) metakaolin, and 0.1% SiO_2.

The ECC/SECC material was prepared in a 19 liter mixer as follows: first, 75% of tap water at room temperature was added to the mixing bowl along with the PCE/SP. Then, standard-graded silica sand was added and mixed at a low speed (107 rpm) for 30 seconds. Half of the PVA fibers were then added and mixed for 30 seconds, followed by the remaining PVA fibers for another 30 seconds. Half of the cementitious materials were added next and mixed for one minute, followed by the remaining cementitious materials for another minute. Finally, the remaining water along with the PMHS admixture was added and mixed at low speed for one minute, followed by 30 seconds of mixing on medium speed (198 rpm) (Sobolev et al., 2013). A portion of ECC/SECC was then tested for flow, followed by mixing for 30 seconds at a medium speed before placing into the molds.

Specimens consisted of 40 x 40 x 160 mm beams for durability factor evaluation. Carbon fiber based, dog-boned shaped coupons were instrumented to serve as a sensor; these were embedded in the specimens (Figure 3). The 120 ohm strain gauges with a gauge factor of 2.05 ± 0.28% were mounted on these coupons, while the coupons were embedded within the fiber reinforced composite so that the deformation of the carbon fiber would be equal to the deformation of the fiber reinforced composite. Carbon fiber beams were chosen because of their low coefficient of thermal expansion to ensure that readings from the strain gauge could correlate to the performance of the fiber reinforced composite.

The samples were then covered with glass plates and placed in a curing room at standard temperature (20 ± 3°C) and a relative humidity of no less than 90%, per ASTM C192. The samples were removed from the molds after 24 hours and placed in a lime water bath for an additional 13 days until the time of testing.

TESTING METHODS

Freeze-thaw tests were performed in an accelerate manner (which is different from standard ASTM C666 procedures) with temperatures oscillating between -50°C

(0% relative humidity) and 20°C (95% relative humidity) (Figure 4) (Sobolev et al., 2013). Temperatures were held at the extreme points for just under 2 hours and the temperature change occurred rapidly (approximately 15 - 25 minutes from minimum to maximum temperature and vise versa). This provided a single cycle with a total duration of 4 hours. Samples were tested in both fresh water and salt water (5% NaCl) media. Samples were tested every 50 or 100 cycles for durability factor while readings for electrical resistivity were continuously taken every 5 minutes. The fresh water and 5% NaCl solution was changed every time the samples were tested.

The durability factor was calculated based on standard calculations of relative dynamic modulus of elasticity from ASTM C215. The internally placed strain gauges were used to measure the resistivity of the sample during freezing and thawing cycles. This provided a response of the material's strain during freezing and the change of response during cycling without the need for manual evaluation every 50 to 100 cycles.

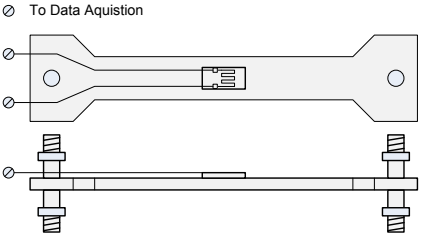

Figure 3. Schematic of Strain Gauge Placed within Samples

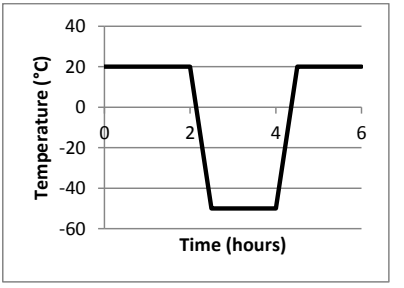

Figure 4. Temperature Range for Freezing and Thawing Cycles

Mixtures were prepared with 2.75% by volume PVA fibers. Samples were created at a water to cementitious material ratio of both 0.30 and 0.45 with a sand to cementitious material ratio of 0.5 and 1.0 respectively. Each mixture was created with and without a single dose of PMHS (0.25 g of siloxane to 1 liter of entire composite mix). The experimental mixtures are summarized in Table 1.

Table 1. Experimental Program.

MIX ID	W/CM	S/CM	GGBFS (%)	PMHS Dosage (g / liter)	PCE/SP Content (%)
REF30	0.30	0.5	50	0	0.125
REF45	0.45	1.0	50	0	0.05
E30	0.30	0.5	50	0.25	0.125
E45	0.45	1.0	50	0.25	0.05

RESULTS AND DISCUSSION

Results from the freeze-thaw testing demonstrate that the main factor affecting the durability of the material is the w/cm ratio (Figure 5). All samples with a lower w/cm ratio displayed exceptional performance through as many as 700 cycles by maintaining of durability factor of 100 or more, meaning that the dynamic modulus of elasticity is the same if not higher through cycling compared to untested specimens. For these samples an increase in durability factor can be seen through the first 200 cycles. This can be attributed to the continued strength gain (since the samples were placed in the chamber at 14 days). This, however, was not the case for higher w/cm ratio samples, demonstrating that the weaker matrix with larger capillary porosity was subjected to immediate deterioration due to severe exposure. Samples with a lower w/cm, tested in water, did not display many variations when comparing samples with and without superhydrophobic admixtures. This experiment demonstrates that the strong matrix is essential for the samples to survive 700 accelerated freeze-thaw cycles; however if tested further, deterioration of these samples may still begin and, in this case, the superhydrophobic admixtures may improve the durability. This can be seen as the deteriorated samples with a higher w/cm ratio and superhydrophobic admixtures (E45 Salt) displayed better performance compared to the samples without (REF45 Salt). This was not the case however in fresh water as the reference displayed slightly better results.

Resistance values from strain gauge reading were taken every five minutes. This allowed the response of the samples to be seen throughout cycling which can give an indication of the strain response. From this data the peaks of minimum and maximum strain envelope values corresponding to minimum temperatures and maximum temperatures can be observed to find the general trend of resistance values through cycling (Figure 6). From this, the difference between maximum and minimum resistance values is increasing through cycling, correlating to the fact that the material is becoming more deteriorated and forming larger voids saturated with water. Additional research work must be performed to calibrate these readings and to correlate them to deformation and dynamic modulus of elasticity values.

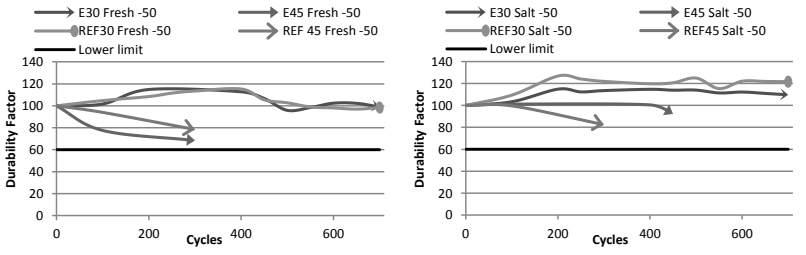

Figure 5. Durability Factor for Samples test for Freeze-Thaw in Fresh Water (left) and 5% NaCl Solution (right)

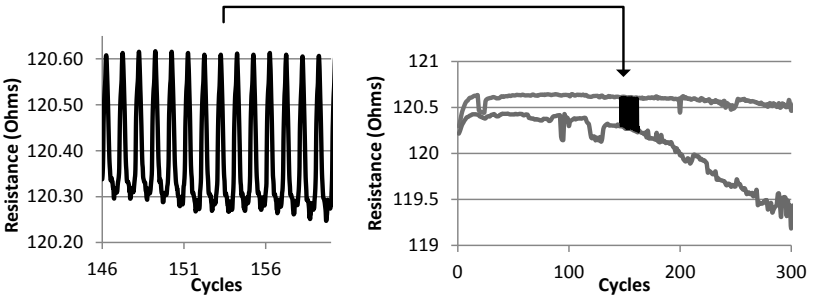

Figure 6. Resistance Values of "REF45 Salt" Specimen through Freezing and Thawing Cycles

CONCLUSION

Based on the durability factor results, it is clear that a lower w/cm ratio provides a better freeze-thaw response. Although from low w/cm results it is not clear that the addition of superhydrophobic admixtures improves the durability; however as seen with higher w/cm, the addition of superhydrophobic admixtures improves performance in salt water cycling. Knowing this, it can be assumed that as lower w/cm ratio samples become more deteriorated, and begin to have similar void structures as higher w/cm ratios, the addition of superhydrophobic admixtures will provide extended durability. Future freeze-thaw tests will be performed through more cycles to verify this hypothesis.

The use of an accelerated freeze-thaw test method proved to be very beneficial since there is an assurance that the samples are completely subjected to freezing and thawing for the prescribed number of cycles, however more testing needs to be done in order to verify the use of an appropriate multiplication factor for the accelerated method compared to conventional methods.

The use of internally placed strain gauges allows the strain response of material to be visualized during freezing whereas in the past, the material's performance could only be tested in the thawed state. This method also allows the performance to be measured without having to manually test the samples frequently. Additional tests will be performed to correlate the resistance readings from the strain gauges to deformation of the samples and to durability factors.

ACKNOWLEDGEMENTS

The authors thank the National Center for Freight & Infrastructure Research & Education for funding this project through grants CFIRE 04-09 and CFIRE 05-10. Support from the University of Wisconsin-Milwaukee Research Growth Initiative and the National Science Foundation is acknowledged. The authors also thank Kuraray, Nycon, Lafarge, and Handy Chemicals for donation of materials used in this study.

REFERENCES

Amirjanov, A., and Sobolev, K. (2006) "Fractal properties of dense packing of spherical particles." *Modeling and Simulation in Materials Science and Engineering*, 14, 789-798.

Flores-Vivian I., Hejazi V., Nosonovksy M., and Sobolev K. "Towards superhydrophobic self-assembled coatings for cement based materials." *Submitted for publication,* 2013.

Janssen, D. J., and Dempsey, B. J. (1986). "Predicting the progression of D-cracking." *Urbana, 51*, 61801.

Koch, K., Bhushan, B., and Barthlott, W. (2008). "Diversity of structure, morphology and wetting of plant surfaces." *Soft Matter, 4*(10), 1943-1963.

Li V. (2002). "Advances in ECC research." *ACI Special Publication on Concrete: Material Science to Applications*, SP206-23:373-400.

Muzenski, S., Flores-Vivian, I., and Sobolev, K. (2013). "Hydrophobic engineered cementitious composites for highway applications." Submitted for publication in *Cement and Concrete Composites*.

Skalny, J., Phillips, J. C., and Cahn, D. S. (1973). "Low water to cement ratio concretes." *Cement and Concrete Research, 3*(1), 29-40.

Sobolev, K., and Gutierrez, M. F. (2005). "How nanotechnology can change the concrete world: Part two of a two-part series." *American Ceramic Society Bulletin, 84*(11), 16-19.

Sobolev, K., and Batrakov, V. G. (2007). "Effect of a polyethylhydrosiloxane admixture on the durability of concrete with supplementary cementitious materials." *Journal of Materials in Civil Engineering, 19*(10), 809-819.

Sobolev, K., and Batrakov, V.G. (2009). "The development of high-performance concrete with polyethylhydrosiloxane-based admixture." ConcreteLife'09: 2nd International RILEM Workshop on Concrete Durability and Service Life Planning, Haifa, Israel

Sobolev, K., and Yeginobali, A. (2005) "The development of high-strength mortars with improved thermal and acid resistance." *Cement and Concrete Research, 35*(3), 578-583.

Sobolev, K., Tabatabai, H., Zhao, J., Oliva, M., Flores-Vivian, I., Muzenski, S., and Rauf, R. (2013). "Superhydrophobic engineered cementitious composites for highway applications: Phase II" (CFIRE 05-10). *National Center for Freight & Infrastructure Research & Education*. Madison, WI.

Wang, S., and Li, V. C. (2005, May). "Polyvinyl alcohol fiber reinforced engineered cementitious composites: material design and performances." In *Proc., Int'l Workshop on HPFRCC Structural Applications, Hawaii*.

Yang E.H., Yang Y., and Li V.C. (2009). "Use of high volumes of fly ash to improve ECC mechanical properties and material greenness." *ACI Materials Journal, 104*(6), 620-628.

Experimental Study on Effect of Internal Cracking on Corrosion Rate of Reinforcement in Concrete

Isao Ujike[1], Shinichiro Okazaki[2] and Ryoichi Sato[3]

[1]Department of Engineering for Production and Environment, Graduate School of Science and Engineering, Ehime University, 3 Bunkyo, Matsuyama, Ehime, 790-8577, Japan; TEL +81(89) 927-9819; FAX+81 (89)927-9842; e-mail: iujike18@ehime-u.ac.jp

[2]Structural Mechanics Group, Structural Engineering Field, Port and Airport Research Institute, 3-1-1 Nagase, Yokosuka, Kanagawa, 239-0826 Japan; TEL +81(46) 844-5059; FAX+81 (46)844-0255; e-mail: okazaki-s@pari.go.jp

[3]Department of Civil and Environmental Engineering, Graduate School of Engineering, Hiroshima University, 1-4-1, Kagamiyama, Higashi-Hiroshima, Hiroshima, 739-8527, Japan; TEL & FAX +81(82)424-7787; e-mail: sator@hiroshima-u.ac.jp

ABSTRACT

In this study, two types of accelerated tests were conducted to determine the corrosion rate of a reinforcing bar in concrete. Tensile test specimens were used for these accelerated tests. In one test, the chloride content of the concrete in the specimens was varied at three levels. The corrosion rate of the reinforcing bar increased with the chloride content. The increasing ratio of the corrosion rate with increase in the chloride content became large when the specimens were subjected to repeated loadings before the start of testing. The corrosion rate was promoted by the generation of internal cracking. In the other accelerated test, two types of aggregates were used for the concrete of the tensile test specimens to change the shrinkage characteristics. Repeated loading was also employed. The test results show that corrosion was initiated in a shorter time period when the width of internal cracking was large.

INTRODUCTION

A purpose of a concrete cover is to prevent the corrosion of the reinforcing steel bar (rebar). The cover of a reinforced concrete structure is determined by considering the quality of the concrete, rebar diameter, environmental conditions, errors in construction, and the importance of the structure, assuming that no defects exist in the concrete cover. However, it has been reported that internal cracks are generated at the transverse ribs of a tension deformed bar and do not appear on the surface of a reinforced concrete member (Goto et al. 1980). The generation of internal cracks cannot be avoided under normal service load conditions, because internal cracks are induced around a tensile rebar before the tensile stress in rebar reaches about 100 N/mm^2. In addition, it has been clarified that the tightness of a

cover concrete deteriorates owing to the generation of internal cracking (Ujike et al. 2010).

The present study aims to clarify the influence of internal cracking on the corrosion rate of a deformed rebar, because internal cracking decreases the mass transfer resistance of a cover concrete. Two types of accelerated tests on the rebar corrosion rate in concrete were conducted. The tensile test specimens modelled after the tension zone in a reinforced concrete member were used for the accelerated corrosion tests. The difference in corrosion rate caused by the presence or absence of internal cracking is examined.

EXPERIMENTS

The tensile test specimens of dimensions 100 mm × 100 mm × 200 mm, as shown in Fig.1 were used in this study. A deformed bar of diameter 25 mm was used in the tensile test specimen. The specimens were covered with a wet cloth for 28 days after casting of the concrete. Two types of accelerated tests were conducted on the corrosion rate of rebar in the tensile test specimens. One is an experiment for the effect of internal cracking on rebar corrosion, called test A. Another is an experiment for the effect of volume change of the concrete on rebar corrosion, called test B.

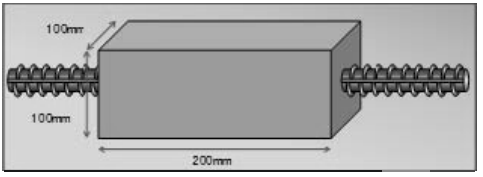

Fig.1 Tensile test specimen

The water cement ratios of the concrete for Test A were 40, 50 and 60%. Moreover, to promote the rebar corrosion in the concrete, NaCl at 0.3, 0.5 and 1.0% of the weight of the fine aggregate was mixed with each concrete. Eighteen specimens were manufactured. After curing with a wet cloth, nine specimens were subjected to a repeated load (ten times) of a maximum of 200 N/mm^2 in terms of reinforcement stress. After loading, the rebar projecting from the concrete of tensile test specimens was cut, and four surfaces of the specimens (all except the two side surfaces parallel to the reinforcement) were covered with an epoxy resin adhesives. The treated specimens were placed in the vessel, water was collected in the vessel so as to not touch the specimens, the cover was fixed with tape, and the vessel was sealed shut. The sealed vessel was placed in an oven at 40°C.

To evaluate the corrosion situation in the concrete, an electrochemical technique (polarization resistance method) was adopted in this study. An electric current from a counter electrode with a potentiostat is passed through the rebar in the concrete and the alternating current of a specific frequency is measured. From this measurement, the apparent polarization resistance and apparent concrete resistance can be obtained. The polarization resistance was measured at intervals of about 7 days at 20°C in the laboratory. The polarization resistance was converted to the polarization resistance per unit area by the method proposed in a previous study (Kanada et al. 2011).

Furthermore, the corrosion current density per unit area was calculated by substituting the polarization resistance in the Stern-Geary equation.

The water cement ratio of the concrete for Test B was 50%. Sandstone and limestone were used as fine and coarse aggregates, respectively to vary the shrinkage of the concrete. It had been confirmed by a prior experiment that concrete made with limestone shrinks less. Four specimens were manufactured. After curing with a wet cloth, all specimens were subjected to a repeated load (ten times) of 200 N/mm^2 at the maximum in terms of reinforcement stress. After loading, to conduct the accelerated test, the same treatment as that in Test A was performed on the specimens. The specimens were soaked in 3% NaCl solution for two days, and dried for five days. This cycle was repeated in an oven at 40°C. The corrosion rate was evaluated in the same manner as in Test A. After soaking at each cycle, the polarization resistance was measured. Furthermore, the volume change due to the repeated wet and dry cycling was measured using the same size specimens without a rebar.

In addition to the accelerated corrosion tests, an experiment was conducted for the effect of shrinkage of concrete on the width of internal cracking. Time-dependent changes in the width of internal cracking were observed by use of the tensile test specimens shown in Fig.2. Internal cracks can be observed on the concrete surface where the rebar appears. The specimen was subjected to a sustained load of 120 N/mm^2 in terms of reinforcement stress by fixing both ends of the rebar to a reaction frame. The observation surface was always covered with latex resin except at the observation time. A microscope was used to observe internal cracking. The picture of the internal cracking observed with the microscope was recorded, and the width of the internal cracking was calculated from the ratio to the standard length displayed in the picture. Furthermore, the drying shrinkage strain was measured by on the same size specimen without a rebar.

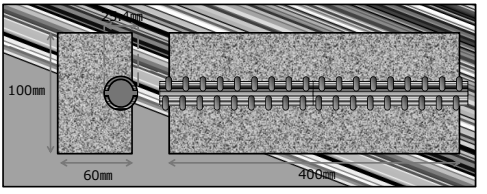

Fig.2 Tensile test specimen for observation of internal cracking

RESULTS AND DISCUSSION

Fig.3 shows the time-dependent changes in the corrosion rate of the tensile test specimens. The marks painted out indicate the results of the specimens subjected to repeated loadings and the outline marks indicate the results of the specimens without loading. The broken line shows a corrosion rate of 1.8 mg/cm^2/year. This value is calculated on the basis of the judgment criterion of the CEB. When the corrosion rate is less than this value, it is evaluated as no corrosion or an extremely slow corrosion rate. The corrosion rate of all specimens increases with time. Except for the loaded

specimen with a water cement ratio of 40%, the rebar does not corrode by the addition of 0.3% or 0.5% NaCl. However, the corrosion rate exceeds 1.8 mg/cm^2/year from an early time by adding 1.0% NaCl, and rebar corrodes. In the case of 1.0% NaCl, the corrosion rate of the specimen subjected to repeated loadings is larger than that of the no load specimen. This tendency is remarkable at a water cement ratio of 40%. These increases in corrosion rate are thought to be caused by the development of internal cracking.

Fig.4 shows the rate of rebar corrosion for the specimens subjected to 1.0% NaCl. The values indicated in Fig.5 are the average after 200 days from the start of the accelerated test. The difference of corrosion rate depends on concrete quality because the environmental conditions of the accelerated test are the same. In this study, concrete quality is evaluated using the prediction model for the corrosion rate of a rebar in concrete proposed by previous study (Yokota et al. 2006). Yokota et al. thought that the corrosion rate of reinforcement in a concrete structure is governed by the concentration of chloride ions at the surface of the reinforcement, the temperature and the apparent diffusion coefficient of the chloride ions in the concrete, and formulated it as follows.

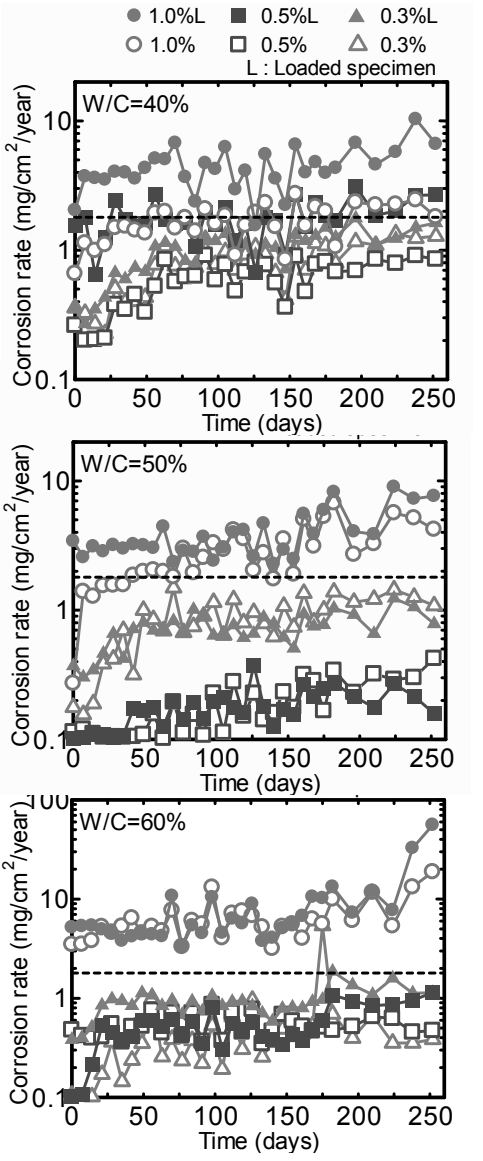

Fig.3 Time-dependent changes in corrosions rate for Test A

$$R(T,C,D)=R(T,C)\cdot C_D(D) \quad (1)$$

Where, $R(T,C,D)$ is the corrosion rate, $R(T,C)$ is the concentration of chloride ions

and temperature, and $C_D(D)$ is the apparent diffusion coefficient of chloride ions. Details of the two terms on right hand side are described in the reference though it omits here. In this study, the values based on the experimental conditions were substituted in the above equations, and the apparent diffusion coefficient of the chloride ions was determined to agree with the corrosion rate shown in Fig.4.

Fig.5 shows the apparent diffusion coefficient of the chloride ions in the loaded specimens and in the no load specimens. The solid curve indicates the regressive equation proposed to predict the diffusion coefficient of concrete on basis of the investigative results of the Japan Society of Civil Engineers (JSCE). The diffusion coefficients for the no load specimen are close to the curve proposed by JSCE. The diffusion coefficients for the loaded specimen are higher than those for the no load specimen. The diffusion coefficient increases by about 1.5 – 3 times owing to loading. The increase in this diffusion coefficient might indirectly suggest a decrease in the tightness of the cover concrete by the generation of internal cracking.

Fig.6 shows the drying shrinkage strains of concrete used for the tensile test specimens in Test B. Although the concrete mixture is the same, the drying shrinkage of the concrete with sandstone is about double at a drying time of 100 days compared with that of the concrete with limestone.

Fig.7 is a picture of internal cracking

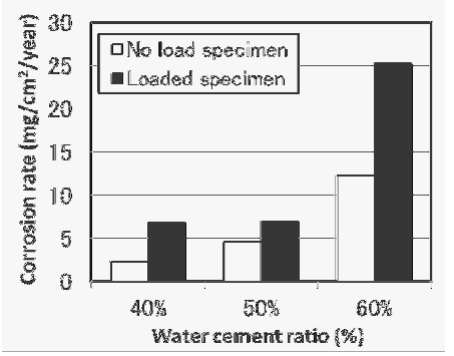

Fig.4 Corrosions rate of no load specimen and loaded specimen

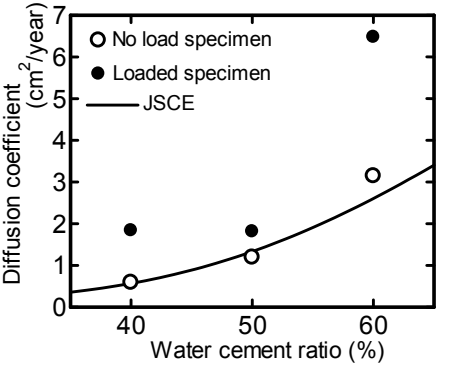

Fig.5 Diffusion coefficient of no load and loaded specimens

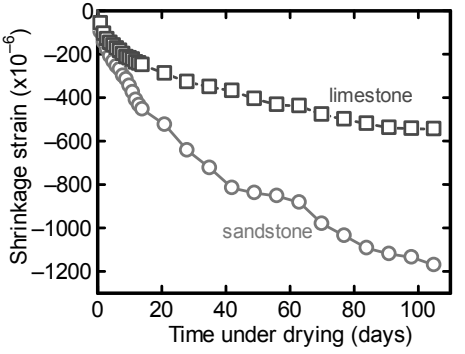

Fig.6 Effect of aggregate kind on drying shrinkage

observed on the surface of the tensile test specimen by a microscope. The cracks that reach the concrete surface are primary cracks, and the cracks that generate from the top of the rebar ribs are internal cracks. The change in the width of the internal cracking was measured from a picture taken by the microscope.

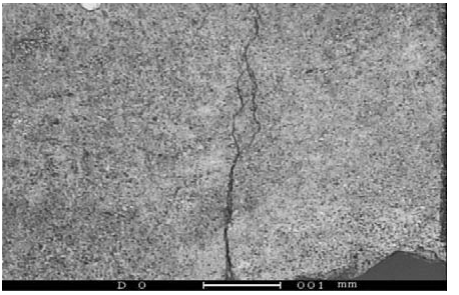

Fig.7 Example of picture taken by a microscope

Fig.8 shows the increment in internal cracking width in the tensile specimens manufactured from the concrete with limestone and sandstone. The crack width is measured in the vicinity of the reinforcement, and the measured positions are not united at a constant distance from the reinforcement. In general, the widths of the primary cracks expand owing to drying shrinkage of the concrete. As is obvious from Fig.8, the width of the internal cracking also increases by drying shrinkage of the concrete. The increment in the crack width in the concrete with sandstone is larger than that in the concrete with limestone. This tendency corresponds to that of the drying shrinkage shown in Fig.6.

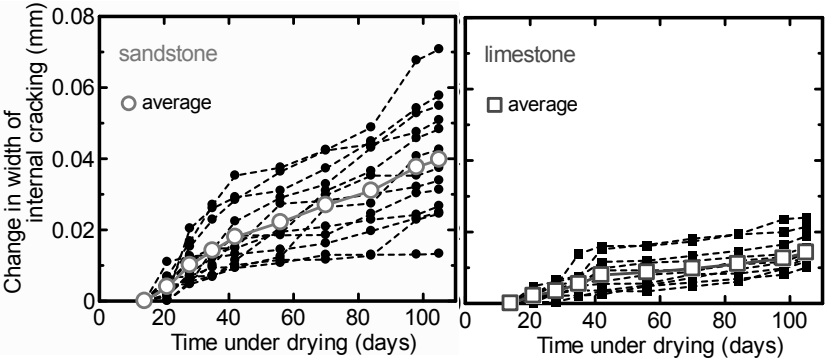

Fig.8 Change in width of internal cracking

Fig.9 shows the corrosion rate of the loaded specimens of the concrete with sandstone and limestone. As in Fig.7, the broken line shows a corrosion rate of 1.8 mg/cm^2/year based on the judgment criterion of the CEB. The corrosion rate increases gradually with time by repeated immersions in 3% NaCl solution for two days and drying for five days in a 40°C environment. The rebar corrosion rate in the concrete with sandstone is still in the passive state or in the state of extremely slow corrosion rate. However, the corrosion rates for the loaded specimens of the concrete with limestone exceed the criterion value of 1.8 mg/cm^2/year at 21 days and 56 days from the start of

the accelerated test. This tendency does not correspond to the tendency of the width of internal cracking to increase with time, as mentioned above. The specimens for the measurement of crack width are exposed to drying conditions, whereas the specimens for the measurement of corrosion rate are exposed to dry and wet cycling.

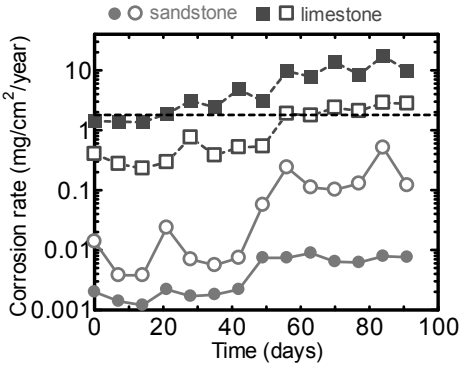

Fig.9 Corrosion rate of loaded specimen with sandstone and

Fig.10 shows the volume change of the concrete under dry and wet cycling. The outline and painted marks indicate the measured values after drying for five days and after soaking for two days, respectively. Although the five-days drying period is longer than the two-days wetting period, the concrete gradually expands with time. The specimens are not saturated with water at the start of the accelerated test because they were cured with a wet cloth before the test. The degree of volume change of the concrete by dry and wet cycling is larger for the concrete with sandstone than that for the concrete with limestone.

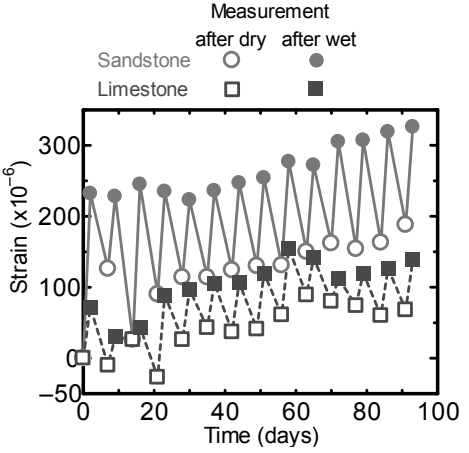

Fig.10 Volume change of concrete under repeated drying and wetting

The difference in the corrosion rate according to the type of aggregate, shown in Fig.9, was determined by considering the behavior of the volume change of the concrete shown in Fig.10. Time-dependent change in the width of the internal cracking relates to the volume change of the concrete, as shown in Figs.7 and 8. The width of the internal cracking in the accelerated test of dry and wet cycling is thought to narrow because of the expansion of the concrete. The width of the internal cracking that occurs from repeated loads before the accelerated test is considered to be the same in each concrete specimen. Therefore, it can be extrapolated that the width of the internal cracking of the concrete with sandstone is narrower than that of the concrete with limestone for specimens exposed to dry and wet cycling. As a result, the rebar corrosion in the specimens with limestone may be promoted.

CONCLUSION

This study investigates the effect of the internal cracking in a cover concrete on the corrosion rate of the rebar. The following conclusions were drawn within the scope of the study.

1) The rate of rebar corrosion in concrete with internal cracking is greater than that in concrete without internal cracking.
2) The rebar corrosion is promoted by a decrease in the mass transfer resistance of a cover concrete as a result of internal cracking. The apparent diffusion coefficient of chloride ions is about 1.5 – 3 times higher.
3) Change in internal cracking width depends on the volume change of the concrete. The width of internal cracking is greatly increased in concrete with much drying shrinkage.
4) These results suggest that the rate of rebar corrosion in concrete accelerates as the width of internal cracking increases.

ACKNOWLEDEGMENTS

The authors would like to thank the Japan Society for the Promotion of Science for the financial support provided by JSPS KAKENHI Grant Number 24246077, 24360172, as a part of the present study.

REFERENCES

Goto, Y. and Ohtsuka, K., (1980) Experimental studies on cracks formed in concrete around deformed tension bars, *Proceeding of JSCE*, No.294, 85-100.

Kanada, H., and Matsuoka, K., (2011) Current distribution simulation and estimation of rebar polarization resistance by BEM, *Proceedings of the Japan Concrete Institute*, No.33, 1715-1720.

Ujike, I., Sato, R. and Okazaki, S., (2010) Proposal of Effective Concrete Cover in Consideration of Deterioration by Internal Cracking, *Proceedings of 2nd Internationsal Symposium on Service Life Design for Infrastructure* Oct. 4, Delft, Netherlands, CD-ROM .

Yokota, M., Nakagawa, H. and Matsushima, M., (2006) Prediction of progress of reinforcement corrosion in concrete structures by external chloride attack based on exposure test, *Proceedings of the Concrete Structure Scenarios, JSMS*, Vol.10, 67-74.

Mechanical properties of deteriorated hardened cement paste

K.Kurumisawa[1], H. Owada[2] and M. Shibata[3]

[1] Faculty of engineering, Hokkaido University, Kita 13, Nishi 8, Kita-ku, Sapporo, Hokkaido, Japan; PH +81(11) 706-6319; email: kurumi@eng.hokudai.ac.jp
[2] Radioactive Waste Management Funding and Research Center, 1-15-7 Tsukishima, Chuo-ku, Tokyo, Japan; PH +81(3) 3534-4537; email: owada@rwmc.or.jp
[3] Taiheiyo Consultant Co.,Ltd., 2-4-2, Ohsaku, Sakura-city, Chiba, Japan; PH +81(43)498-3858 ; email: Masahito_Shibata@taiheiyo-c.co.jp

ABSTRACT

The porosity of hardened cement paste changes when it is exposed to the actual environments, and it may be expected that the chemical structure of the C-S-H undergoes changes. The C-S-H is the main component, comprising 60% or more by volume of hardened cement paste, and this study focuses on changes in the chemical structure of C-S-H. Deterioration induced by ammonium nitrate solution was accompanied by changes in the pore structure as well as structural changes in the C-S-H in the hardened cement paste. It was ascertained that when evaluating the decreases in the elastic modulus of the hardened cement paste, both the pore structure and the structure of the C-S-H must be considered.

Introduction

When concrete structures are exposed to actual environments for long periods of time, the concrete deteriorates, and the mechanical characteristic of the concrete changes. For example, the storage of radioactive waste is necessary for tens of thousands of years, and the performance of the concrete structures holding it must be maintained during this length of period. It is possible to know the early performance of concrete structures, but it is difficult to know the long-term performance. Therefore, it is very important to know and be able to predict the long-term behavior of concrete, and it is important to clarify the mechanisms involved which are working on the concrete (Heukamp 2001, Carde 1996). Much study focusing on the pore structure has been reported (Faucon 1998, Adenot 1992), but there are not many investigations focusing on the calcium silicate hydrate (C-S-H) structure in hardened cement paste (HCP), the matrix of the concrete. The C-S-H is the main component comprising 60% or more by volume of hardened cement paste. The porosity of concrete changes when concrete is exposed, and it may be expected that the chemical structure of the C-S-H changes. Therefore this study focuses on the changes in the chemical structure of C-S-H. Here, X-ray photoelectron spectroscopy (XPS) and solid state nuclear magnetic resonance (NMR) was used for the determination of the C-S-H structure.

Experimental

Specimen preparation Hardened cement paste (W/C 0.6) was used as specimens. Ammonium nitrate solution was used to accelerate the deterioration of the hardened cement paste, and the degree of deterioration of the hardened cement paste was simulated by changing the concentration of ammonium nitrate solution. It was possible to produce hardened cement pastes with different CaO/SiO_2 ratios by varying the concentration of ammonium nitrate solution where the specimens were immersed, here for 7 days.

CaO/SiO_2molar ratio by EDX. The CaO/SiO_2 (C/S) of the hardened cement paste was analyzed by SEM with energy dispersive electron spectroscopy (EDX). A 3 mm thick specimen plate was cut from the dried samples of the hardened cement pastes, and used for the observations. The C/S was calculated from the data for the EDX analysis for ten points.

X-ray diffraction (XRD) measurements. Samples for the measurements were powder that was crushed by ball mill and mixed with 10%wt of corundum (Al_2O_3) as an internal standard. The conditions of the XRD measurements were 40kV, 40mA, and with an CuKα X-ray monochrometer attached. The Rietveld method was used for the quantitative analysis of the composition of the hydrated cement (C_3S, C_2S, C_3A, C_4AF, AFm, AFt, and CH), and was performed with the Siroquant software.

Mercury intrusion porosimetry (MIP). Crushed freeze dried samples were used for the MIP. The porosity and pore size distribution determination was carried out by a mercury intrusion porosimeter capable of generating pressures in the range from subambient to 33,000 psi (227 MPa). The pore radius calculations were performed with the Washburn equation.

BET surface area measurements. The BET surface area of the hydrated cement paste was measured with the water vapor isotherm (Hydrosorb1000, Quantachrome). The samples used in the measurements were powder that had been crushed with a ball mill and dried by freeze-drying. Sample was placed in a vacuum at 105 degrees Celsius for 1hour before the measurements, and measurements were at 0.05-0.98 relative pressures. The surface area was determined from an adsorption curve established by the BET multi point analysis.

Microelastic modulus measurement by microindentation. The mechanical characteristic of the hardened cement paste was determined by micro indentation. Experiments were performed using a depth-sensing microindentation apparatus. The load and depth (or displacement) of the indenter were continuously monitored during a programmed microindentation load cycle. In this study, the maximum applied load was 20 mN, the load speed was 1 mN/s, and 100 points were measured in a 10 × 10 grid (10μm intervals). Poisson's ratio for samples was assumed to be 0.25 to simplify the calculations.

NMR measurements. Measurement of the ^{29}Si-NMR(MAS) was performed at a frequency of 60.6MHz, acquisition time of 30 seconds, and number of points 2000 (MSL 400, Bruker). When the ^{29}Si nuclei are subjected to NMR, the silicate anions (SiO_4^{4-}) in a calcium silicate compound show Q^0 to Q^4 peaks in the spectrum

representing their chain structures. In C-S-H, the major constituent of HCP, the Q^1(chain end) and Q^2(within chain) are the major chain structures and neither Q^3 (branching chain) nor Q^4(networked chain) can be observed. The mean chain length (MCL) or number of SiO_4 tetrahedra in C-S-H can be calculated from Richardson's equation (Richardson 1999),

$$MCL = \frac{2 \times (Q^1 + Q^2)}{Q^1} \quad (1)$$

XPS measurements. A plate sample (5*5*1mm) that was polished was used for the XPS measurements. Analysis was performed using a JEOL JPS-9200 fitted with a Mg K_α (hv=1253.6eV) X-ray source operating at 100 W (10 kV, 10 mA). The area for the XPS analysis was 3mm in diameter with a high vacuum condition ($<10^{-6}$Pa). Spectra were corrected for charging effects using the adventitious hydrocarbon peak at 284.8 eV binding energy.

Results and Discussions

XRD and CaO/SiO_2. Table 1 shows the results of mineral composition determinations in the HCP specimens measured by the XRD Rietveld method, and the CaO/SiO_2 molar ratio (C/S) of the C-S-H measured by EDX. It was confirmed that the calcium hydroxide and AFm in deteriorated specimens disappeared from the XRD results, as in previous reports. In Table 1, the quantity of amorphous compounds including C-S-H and Katoite increased. The C/S of the C-S-H decreased with the increases in NH_4NO_3 concentration in the immersion solution, showing that it is possible to produce specimens with different C/S ratios by adjusting the concentration of the NH_4NO_3 solution.

Table 1. Mineral compositions (wt%) and CaO/SiO_2 molar ratios of HCP.

	Non-deteriorated	0.25M NH4NO3	0.4M NH4NO3	0.6M NH4NO3
Unhydrated cement	2.52	5.53	5.12	6.02
CH	19.04	0	0	0
AFm	5.29	0.39	0.69	0.09
AFt	0.09	3.16	1.53	0.69
Katoite	4.44	6.52	8.22	9.66
Amorphous	68.32	82.93	82.15	81.37
CaO/SiO2	1.83	1.62	1.04	0.83

Pore structure. Figure 1 shows results of the pore size distribution determinations of the specimens measured by MIP. The porosity of the hardened cement paste increased with the increases in the concentration of the ammonium nitrate solution. The threshold diameter of pore is 0.1 μm in the non-deteriorated specimens, while it is about 1 μm in the deteriorated specimens, showing that deteriorated specimens have a coarser structure. The porosity of the hardened cement paste increases with increases

in the concentration of the ammonium nitrate solution. The BET surface area of the hardened cement paste calculated from the water vapor adsorption also increases with the increases in the concentration of ammonium nitrate solution.

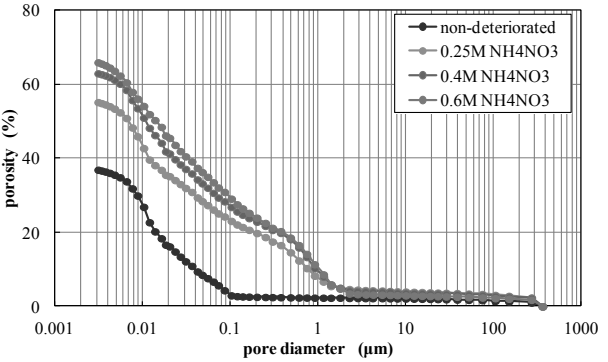

Figure 1. Pore size distribution in specimens.

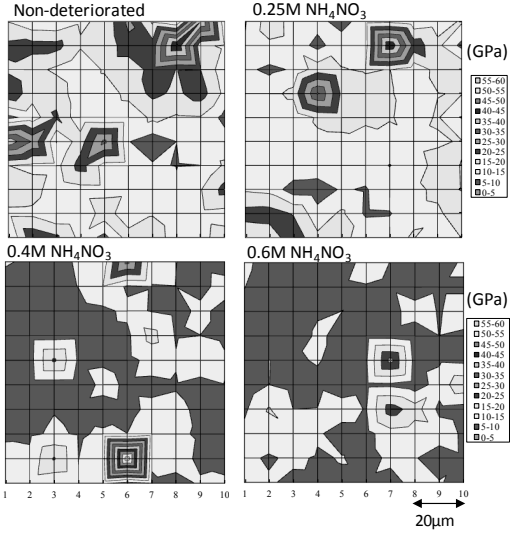

Figure 2. Distribution of elastic modulus in HCP

Micro indentation test. The median value of the micro elastic modulus of non-deteriorated, 0.25M, 0.4M, and 0.6M NH_4NO_3 immersed specimens was 14.3, 14.2, 9.5, and 9.4 GPa respectively. The micro elastic modulus of specimens was determined by the micro indentation, and the elastic modulus of the hardened cement paste decreases with the decreases in CaO/SiO_2 in the C-S-H. Figure 2 shows the distribution of elastic modulus of the hardened cement pastes. The specimens become

more homogeneous with the progress of deterioration. The relationship between porosity and elastic modulus of the hardened cement pastes is shown in Figure 3. The elastic modulus decreased with the increases in porosity. The relationship between porosity and elastic modulus of the deteriorated specimens is different from that of the non-deteriorated specimens. These results show that it is not possible to determine the decrease of elastic modulus by the porosity alone.

^{29}Si NMR. The fractions of the chemical states of silicate anions in HCP are shown in Figure 4. The ^{29}Si-NMR results indicate that Q^2 increased with decreases in C/S, Q^1 decreased with the decreases in C/S. This shows that the polymerization of silicate in deteriorated specimens increases. The spectrum of Q^3 that is not detected in non-deteriorated specimens appeared at C/S 0.8. However, there is no Q^3 spectrum of synthesized C-S-H in a previous report (Viallis 1999). This suggests that the chemical bonding state of Si in deteriorated and synthesized C-S-H is different. The calculated mean chain lengths of non-deteriorated, 0.25M, 0.4M and

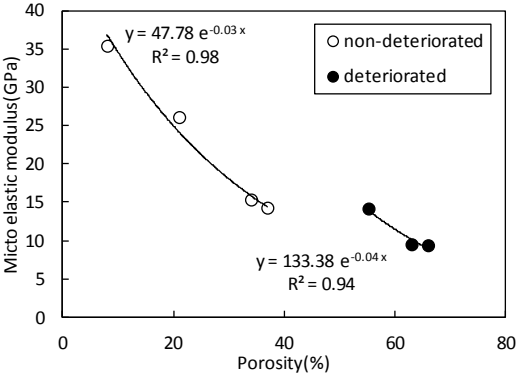

Figure 3. Relationship between porosity and micro elastic modulus of HCP

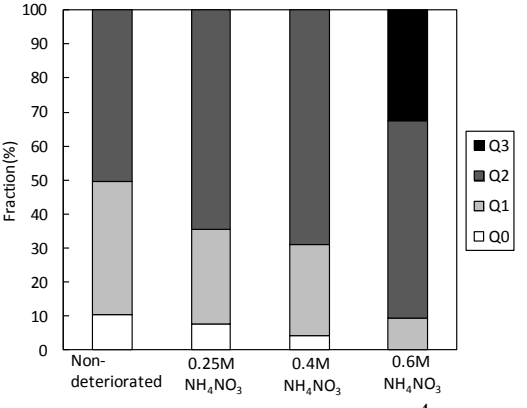

Figure 4. Fraction of chemical bonding of SiO_4^{4-} by NMR

0.6M NH_4NO_3 immersed specimens from the NMR was 4.5, 6.6, 7.1, and 14.3 respectively. The chain length of the C/S 0.8 specimen is 3 times longer than that of non-deteriorated specimens, suggesting the progress of the polymerization. Figure 5 shows the correlation between $Q^1/\sum Q^i$ and the C/S ratio for C-S-H, determined in this study and for 1.4nm Tobermorite and Jennite reported in a previous study (Cong 1996). It shows that the structure of the C-S-H immersed in 0.4 and 0.6M NH_4NO_3 is similar to tobermorite and the C-S-H in the previous study, the specimens immersed in 0.25M NH_4NO_3 and the non-deteriorated specimens are similar to jennite. It is considered that the structure of C-S-H varied due to the differences in the NH_4NO_3 concentrations of the immersion solutions.

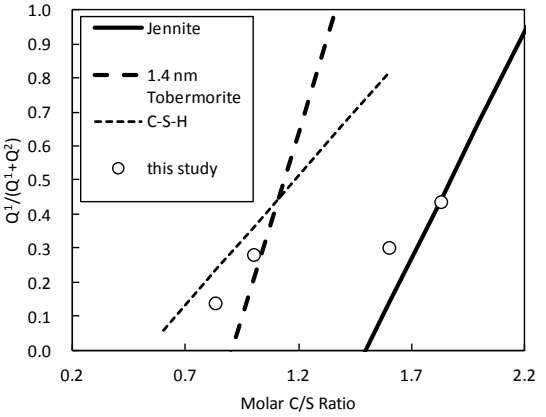

Figure 5. Correlation between $Q^1/\sum Q^i$ and C/S ratios for C-S-H, 1.4nm tobermorite and Jennite

X-ray photoelectron spectroscopy. Figure 6 shows the Si 2p spectra of the non-deteriorated and deteriorated samples. The binding energy of Si 2p was shifted, and increased with the increases in NH_4NO_3 concentration of the immersing solution, this may show that Si is chemically combined with oxide (Okada 1998, Seyama 1985). The difference in the binding energy of Si 2p between C/S 1.8 and 0.8 is more than 1.0eV. It was shown that the silicate chain length in the deteriorated specimens that were immersed in ammonium nitrate solution is longer than that in the non-deteriorated specimens. This result is in good agreement with the results determined by ^{29}Si-NMR. It was shown that it is possible to determine the polymerization of silicate in C-S-H by XPS like in the measurements of NMR. Figure 7 shows the relationship between CaO/SiO_2 and the Si 2p binding energy of C-S-H plotted together with the results of previous reports (Black 2003, 2008). Here the binding energy of the C-S-H immersed in 0.4 and 0.6M NH_4NO_3 is close to that in the previous studies. However, the binding energy of C-S-H immersed in 0.25M NH_4NO_3 and the non-deteriorated specimens is different from those in the previous reports. It was considered that the effect of the binding energy in the unhydrated cement is

included in the results, and that the structure of the C-S-H is different as suggested in Figure 5. Therefore, it was suggested that the structure of the C-S-H in the deteriorated specimens may be similar to that of the synthetic C-S-H.

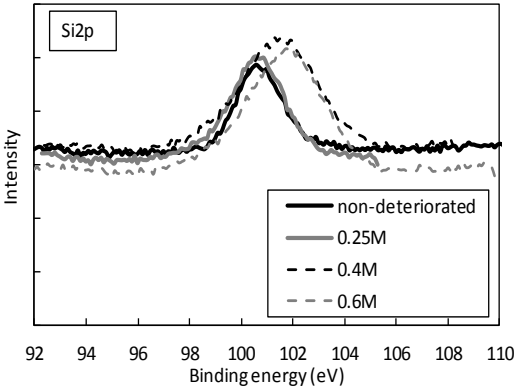

Figure 6. Photoelectron spectra （Si2p）

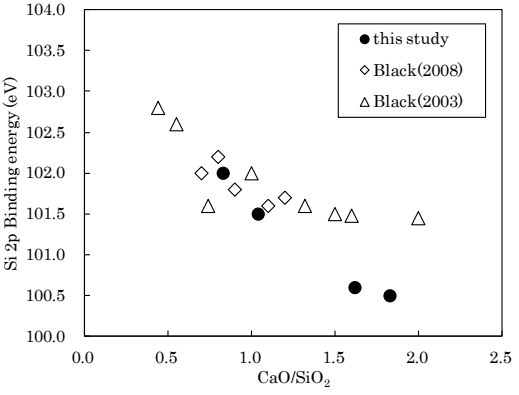

Figure 7. Plot of CaO/SiO_2 vs. Si 2p binding energy of C-S-H

CONCLUSIONS

In conclusion, the deterioration by the ammonium nitrate solution measured by ^{29}Si-NMR and XPS was accompanied by changes in the pore structure as well as structural changes in the C-S-H of the hardened cement paste. It was shown that the binding energy of Si in deteriorated specimens is shifted to higher energies by XPS, and the mean chain length of the C-S-H in deteriorated specimens is longer than that of non-deteriorated specimens by NMR. In evaluating the decreases in the elastic

modulus of the hardened cement paste, both the pore structure and the structure of the C-S-H must be considered.

Acknowledgments

This research include and is a part of the results of "Evaluation Experiments of Long-Term Performance of Engineered Barriers System, FY2012" under a grant from the Agency for Natural Resources and energy in the Ministry of Economy, Trade and Industry (METI) of Japan. And we also thank Mr. Suzuki and Mr. Kurosawa of Hokkaido University for help with the measurements.

REFERENCES

Adenot, F. Buil, M. (1992). "Modelling of the corrosion of the cement paste by deionized water." Cem Concr Res, 22, 489–96.

Black, L. Garbev, K. Stemmermann, P. Hallam, K.R. Allen, G.C. (2003) "Characterisation of crystalline C-S-H phases by X-ray Photoelectron Spectroscopy (XPS)." Cem. Concr.Res, 33 (6), 899–911.

Black, L. Stumm, A. Garbev, K. Stemmermann, P. Hallam, K.R. Allen, G.C. (2003) "X-ray photoelectron spectroscopy of the cement clinker phases tricalcium silicate and β-dicalcium silicate." Cem. Concr. Res., 33, 1561–1565.

Black, L. Garbev, K. Gee, I. (2008) "A Comparison between Fresh and Aged C–S–H Using X-ray Photoelectron Spectroscopy." Cem. Concr. Res., 38, 745–50.

Carde, C. Francois, R. Torrenti, J.M. (1996) "Leaching of both calcium hydrate and C-S-H from paste: modeling the mechanical behavior." Cem. Concr. Res. 26 (8). 1257–1268.

Cong X. Kirkpatrick, R.J. (1996) "29Si MAS NMR study of the structure of calcium silicate hydrate." Advn. Cem. Bas. Mat, 3, 144-156.

Faucon, P. et.al. (1998). "Long-term behavior of cement pastes used for nuclear waste disposal: review of physic-chemical mechanisms of water degradation." Cement and Concrete Research, 28(6), 847-857.

Heukamp, F.H. Ulm, F.J. Germaine, J.T. (2001) "Mechanical properties of calcium-leached cement pastes Triaxial stress states and the influences of the pore pressures." Cem Concr Res, 31, 767–74.

Okada, K. Kameshima, Y. Yasumori, A. (1998) "Chemical shifts of silicon X-ray photoelectron spectra by polymerization structures of silicates." J. Am. Ceram. Soc., 81 (7), 1970–1972.

Richardson, I.G. (1999) "The nature of C-S-H in hardened cements." Cem.Concr.Res., 29, 1131-1147.

Seyama, H. Soma, M. (1985). "Bonding-state characterization of the constituent elements of silicate minerals by X-ray photoelectron spectroscopy." J. Chem. Soc. Faraday Trans., 81, 485–495.

Viallis, H. Faucon, P. Petit J.-C. Nonat, A. (1999) "Interaction between Salts (NaCl, CsCl) and Calcium Silicate Hydrates (C-S-H)." J.Phys. Chem. B, 103, 5212-5219.

Microstructure improvement of cementitious systems using nanomaterials: A key for enhancing the durability of concrete

L.P. Singh*, S.K. Bhattacharyya, U. Sharma, G. Mishra and S. Ahalawat
CSIR-Central Building Research Institute,
Roorkee, India
E-mail: lpsingh@cbri.in; director@cbrimail.com; geetika.mishra30@gmail.com: srv.cbri@gmail.com

Abstract

Nanotechnology is providing challenging research avenues in the field of construction materials as the developed materials exhibit novel physical and chemical properties. In the present studies, sol-gel process has been employed to prepare amorphous, dispersed, spherical silica nanoparticles. Further, these silica nanoparticles were supplemented to cementitious system for comparative mineralogical and morphological attributes of calcium-silicate-hydrate (C-S-H) gel. The results of these studies showed that the addition of silica nanoparticles up to 3.0% significantly improved the compressive strength of cement mortar. Addition of silica nanoparticles into cement paste improves the micro-structure of the cement system and calcium leaching is significantly reduced as silica nanoparticles reacts with calcium hydroxide (CH) and thereby forming a denser C-S-H gel. It was found that, CH content in silica nanoparticles incorporated cement paste reduced 90% at 1 day and up to 59% at 28 days. Further to investigate the durability aspects, chloride permeability of cement mortar was assessed using accelerated electro migration experiment with a glass cell apparatus. To find the chloride ion concentration at different interval of time a UV-Visible spectrophotometer was used. It was observed that incorporation of nanosilica in cement mortar significantly improved resistance to chloride ion diffusion as compared to silica fume samples. Silica nanoparticles with 3% addition improved the chloride ion resistance up to ~43% whereas silica fume improved only 15%. Therefore, it can be concluded that the microstructure of the cement can be tuned with the help of nanoparticles and thus producing more durable and sustainable cementitious materials. SEM and TGA techniques have been employed for the comparative morphological and mineralogical aspects of cementitious system.

Keywords: Nanosilica; Mechanical properties; Calcium leaching; Chloride Permeability

Introduction

In the construction sector, nanotechnology is being used in a variety of ways to produce innovative materials. If nano-materials are integrated with cement-based materials, the new composites might possess some interesting and enhanced properties. Cement is one of the most widely used man made materials and present focus is on the investigation of the structure of cement-based materials and their fracture mechanisms [1-5]. The performance of cementitious materials is controlled by physical and chemical processes occurring at nano level. Hydrated cement has a complex nanostructure, which still remains to be fully understood. The hydrates (C-S-H) are formed by chemical processes that can be modified and controlled at nano-scale level. With emerging sophisticated instrumentation, it is possible to understand the structure of C-S-H gel at its atomic level and even measure the strength, hardness and other basic properties of the micro and nano-scopic phases of the material. Advancement in microscopy has helped in investigating the amorphous C-S-H gel at nano level and these investigations revealed that C-S-H has an ordered structure at the nano-scale. C-S-H particles which are about 5 nm across in all the cement samples can be considered as a 'nano-signature' for these materials [6]. Better understanding of nano-structure of cement

based materials helps to control the processes related to hydration, strength development, fracture, and corrosion. For instance, the development of materials with new properties such as self-cleaning, discoloration resistance, anti-graffiti protection, and high scratch and wear resistance, is extremely important for many construction applications [7-11]. High strength concrete and mortar with high strength and durability properties offer many advantages. They have been gradually replacing normal strength concrete due to their improved mechanical characteristics and low permeability. The mechanical behavior of concrete depends on the nano-sized calcium-silicate-hydrate (C-S-H) gel produced as a result of hydration process in the cement. The partial replacement of cement with nanophase particles improves the mechanical properties of cementitious system. The effect of nano silica on the refinement in pore structure of cement paste has been studied by Gaitero [12]. The addition of nanosilica improved the performance of cementitious system by controlling the C-S-H degradation under aggressive condition of calcium leaching process [13]. Durability of cementitious materials has attracted a lot of attention from many researchers, because it has critical influence on the service life of structure of the cement based materials. Chloride permeability is one of the major causes affecting the corrosion of steel rebars embedded in concrete. An important process in the corrosion propagation is the migration of chloride ions from the cathode to anode in the electrical field, which generates the corrosion cell. Therefore, the resistance to chloride ion penetration into concrete is a crucial parameter affecting the durability of reinforced concrete structures. A number of ways have been attempted so far to prevent the chloride permeability by the use of additives (like fly ash, silica fume, ground blast furnace slag and metakaolin) and cathodic protection etc [14-17].
In the present work, we have reported the preparation of amorphous dispersed, spherical, stable dry powder form of silica nanoparticles by sol-gel method and further, the effect of addition of these nanoparticles in cement system for mineralogical and morphological attributes was investigated.

Experimantal
Materials

In the present studies, ordinary Portland cement (OPC), 43 grade, conforming to IS: 8112 was used. The chemical and mineralogical characteristics of the OPC are given in Table 1.

Table 1. Chemical and mineralogical properties of OPC.

Minerals	SiO_2	Al_2O_3	Fe_2O_3	CaO	MgO	SO_3	LOI	C_3S	C_2S	C_3A	C_4AF
Content (%)	22.3	6.1	2.2	61.1	3.1	2.1	2.3	49.4	27.2	10.9	11.3

In the preparation cetrimonium bromide (CTABr), hydrochloric acid (HCl) and deionized water were mixed and stirred for 45 min. Cetrimonium bromide (CTABr) was used as dispersing agent and 1N HCl used as catalyst. Then 1M solution of sodium silicate was added drop wise with stirring at room temperature until the pH of reaction system was reached upto 8-10 then stops adding sodium silicate solution. The sol-gel mixture was then washed well with deionized water to remove all the sodium chlorate formed. The synthesized powder was dried at ~50-60 and then muffled at 700 for 4h.
Four series of fresh cement mortar with varying composition of silica nanoparticles (0.5, 1.0, 2.0, and 3.0%) were casted with moulds (50 x 50 x 50 mm) to prepare specimens keeping water cement ratio (w/c 0.4) for the measurement of compressive strength. After being demoulded at the age of 24 h, all specimens were cured in water and three cubes were tested at a given age (3, 7 & 28 days) using HEICO make UTM. Morphological attributes of silica nanoparticles and hydrated cement mortar were measured using Scanning Electron

Microscope (LEO-438 VP) at an accelerating voltage of 20 kV. The samples were analysed under Variable Pressure (VP) mode by depositing on a sample holder with a double stick conducting carbon tape. Powder X-ray diffraction data were recorded at 30kV and 40 mA on a Rigaku D-Max 2200 X-ray Diffractrometer using Cu-Kα radiation at a scanning rate of 1°/min. TGA studies were performed on a Perkin Elmer (TG/DTA) analyser at a heating rate of 25 °C/ min.

Results and Discussion

These prepared silica nanoparticles (~50 nm) were incorporated into the cementitious system to improve the mechanical properties of cement system. The mechanical properties of cement mortar are enhanced by the addition of silica nanoparticles as compressive strengths after 3, 7 and 28 days are substantially enhanced (Fig 1). It can be inferred from fig 3 that;

(i) Early strength is achieved at 3 & 7 days (254 Kg/cm^2) as compared to control sample at 28 days (252 Kg/cm^2).

(ii) By adding 1% silica nanoparticles and 12% less cement content, same strength is observed as in case of control sample at 28 days of hydration.

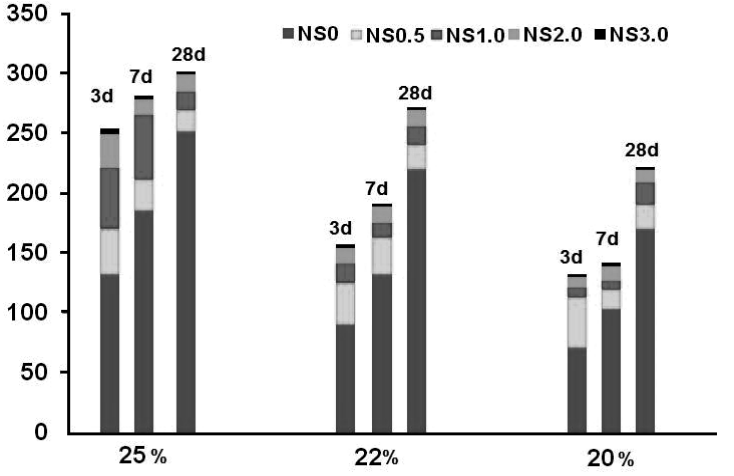

Fig 1. Compressive strength (Kg/cm^2) of cement mortar (i) 25% cement, (ii) 22% cement and (iii) 20% cement with different amount of silica nanoparticles, respectively.

The nanoparticles have high surface energy and atoms at the surface have a high activity, leading the atoms to react rapidly. The compressive strength of cement paste containing silica nanoparticles is higher than that of control cement paste. The difference in the strength development of the paste is attributed to the pozzolanic reaction of silica nanoparticles with CH and forming a denser C-S-H structure. To verify this mechanism of increased compressive strength by formation of denser structure of C-S-H, SEM and TGA studies were carried out for the morphological and mineralogical attributes of cement pastes. It was observed that the compressive strength of cement mortar with silica nanoparticle is higher than that of plain cement mortar and gradually increases with an increase in the amount of silica nanoparticles. Increase in the silica nanoparticles content beyond 3% did not change the compressive strength significantly. It was found that large amounts of silica nanoparticles

decrease the compressive strength of the composites instead of improving it, which is probably due to the fact that when the content of silica nanoparticles is high, nanoparticles are difficult to disperse uniformly. Two fundamental mechanisms can be assumed for strength enhancement by silica nanoparticles, first is strength enhancement by matrix densification and another is by reduction in the content of $Ca(OH)_2$.

Two major products of cement hydration are C-S-H and CH, respectively. C-S-H which is produced by hydration of C_3S and C_2S plays a vital role in mechanical characteristics of cement mortar. Whereas, calcium hydrates which is also formed by hydration of cement does not have cementing property. It contains about 20-25% of the volume of the hydration products. Calcium hydrates due to their morphology are relatively weak and brittle. Cracks can easily propagate through regions populated by them, especially at the aggregate cement mortar matrix interface. Silica nanoparticles react with calcium hydrates formed during hydration of cement rapidly and produce C-S-H with cementitious properties which is beneficial for enhancement of strength in concrete/mortar. The C-S-H gel being the main component of cement hydration is responsible for the strength and microstructure of the cement paste. The amount of CH formation in cement paste was evaluated by thermogravimetric analysis (TGA) during hydration process. This was characterized by CH residue determination in cement paste admixture. Further, silica fume was also added to cement paste for comparison. Hydrated cement shows a reduction in weight up to 200°C due to surface water desorption as well as loss of water from C-S-H gel layer and from the dehydration of ettringite. Further, weight loss ~400-500°C is due to the thermal decomposition of CH followed by the decomposition of carbonated phases and calcite. The amount of CH in the specimen is calculated directly from the TG curves using the following equation:

$$CH(\%) = WL_{CH}(\%) \times \frac{MW_{CH}}{MW_{H}}$$

where WL_{CH} corresponds to the weight loss attributable to CH dehydration and MW_{CH} and MW_H are the molecular weights of CH (74.01 g/mol) and water (18 g/mol), respectively [18]. TGA curves of pure, silica nanoparticles and silica fume incorporated cement pastes are shown in Fig 2 at 28 days of hydration. At early stage of hydration plain cement paste has 4.1% of CH whereas silica fume incorporated cement paste has 2.1% and silica nanoparticles incorporated paste has only 0.4% CH content. During the hydration, CH is continuously formed and at 3, 7 and 28 days it amounts to 7.4%, 12.3% and 20.0%, respectively in plain cement paste. Whereas the CH content, in silica fume incorporated cement paste is upto 15.9% at 28 days. Silica nanoparticles has much significant effect as compared to plain and silica fume incorporated cement paste and at 28 days of hydration only 8.2% CH content was observed (Table 3).

Table 3: CH content (%) in cement pastes.

	CH content (%) at			
	1 day	**3 days**	**7days**	**28 days**
Plain cement paste	4.1	7.4	12.3	20.0
Cement + SF (5%)	2.1	5.7	9.4	15.9
Cement + NS (5%)	0.4	3.3	4.9	8.2

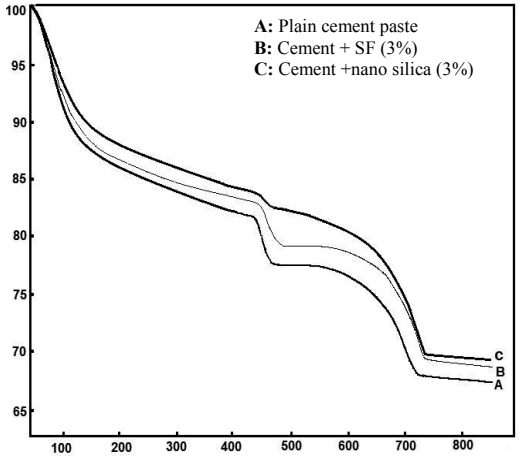

Fig. 2. TGA curves of cement pastes at 28 days of hydration.

Chloride permeability of cement mortars was carried out using accelerated chloride migration method i.e. electromigration test. In this method, a glass cell assembly consisting two-compartment separated by mortar specimen, where one of the cells was filled with 3% NaCl solution and the other cell was with 0.3N NaOH solution as per ASTM C1202. Two platinum electrodes placed in both sides of the specimens served as working electrodes whereas saturated calomel electrode (SCE) placed in analyte worked as reference electrode to monitor the potential applied (Fig 3).

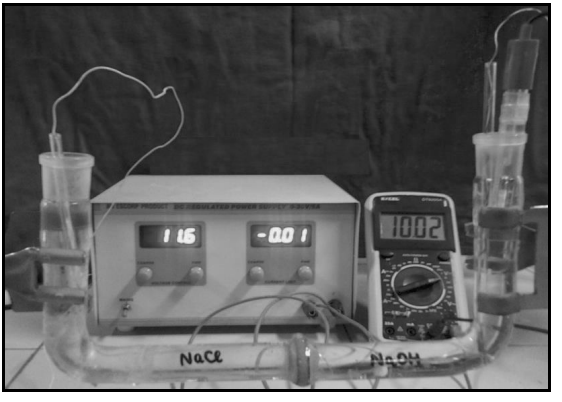

Fig. 3. Experimental st-up for chloride penetration

Once the mortar specimen disc, solutions and electrodes were in place, the cells were connected with 7V power source in which the NaCl solution electrode becomes cathode and the NaOH solution electrode become anode. During the test, small aliquot from destination

solution (0.3 NaOH) was taken periodically to measure the evolution of free chloride anions concentration in destination solution using UV-VIS spectrophotometer. The incorporation of nanosilica and SF improved the penetration resistance of cement mortar as indicated by the reduction in chloride ion concentration in destination solution. The 3% addition of nanosilica developed chloride ion resistance ~43%, where as silica fume able to reduce only ~15% (Fig 4). These results signifies that the incorporation of nanosilica promote the formation of more hydration product and developed denser microstructure as compared to silica fume.

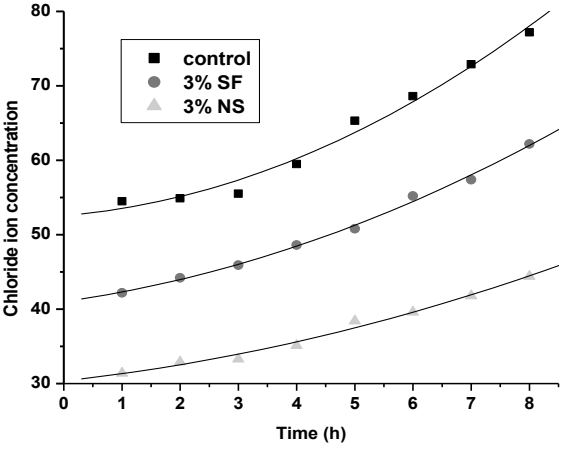

Fig. 4. Chloride ion concentration in anodic cell at 7V.

SEM micrographs of plain cement paste, silica fume and with silica nanoparticles (3%) at 7 and 28 days are shown in Figure 5. Depending on the time of hydration and the cement composition, several crystalline phases can be observed in hydrated cement paste. Secondary electron images show the hexagonal plates of calcium hydroxide, needle-like habit of ettringite and the sheet-like, flaky habit of calcium-silicate-hydrate. The dimensions, of course, depend on the concentration in aqueous solution and the age of the crystal. The dominating phase in forming the shape in the contact surface is C-S-H probably due to its significantly higher strength. It was observed that in the microstructure of the plain cement mortar and silica fume incorporated cement mortar, the C-S-H gel existed along with needle and plate shaped hydrates of CH. The deposited CH around the C-S-H gel is uniformly distributed among the entire cement phase (Figure 5). The microstructure of the cement mortar with the addition of silica nanoparticles revealed that the formation of hydration products was denser, becomes significantly different and showing absence of the needle and hexagonal plate shaped crystals of CH.

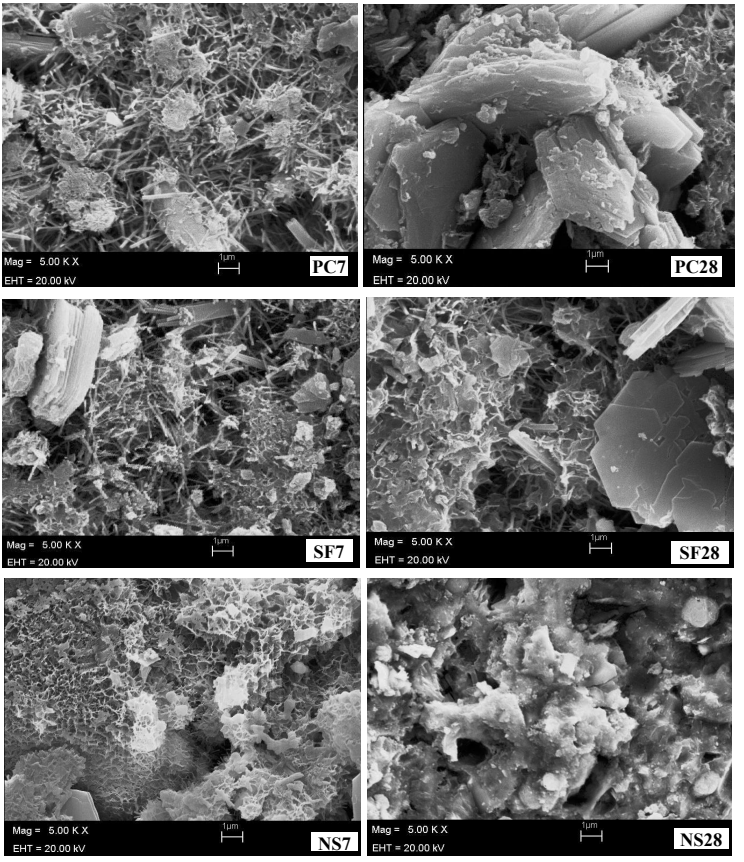

Fig. 5. SEM micrographs of plain cement mortar (PC7&PC28), silica fume incorporated cement mortar (SF7&SF28) and nano silica incorporated cement mortar (NS7&NS28) at 7 and 28 days of hydration, respectively.

4. Conclusion

Spherical, amorphous and dispersed silica nanoparticles (~50 nm) were prepared using sol-gel method. Further, these silica nanoparticles were supplemented to cementitious system for comparative mineralogical and morphological attributes of calcium-silicate-hydrate gel. Results of these studies showed that the compressive strength of nano-modified cement system is higher than that of plain cement mortar and significantly increases with an increase in the amount of silica nano-particle. It was observed from SEM, XRD and TGA studies that addition of silica nanoparticles to cement reduced CH leaching by reacting at early stage of hydration and forming denser C-S-H gel. It was found that, CH content in silica nanoparticles incorporated cement paste reduced 90% at 1 day and upto 59% at 28 days. Silica nanoparticles with 3% addition improved the chloride ion resistance up to ~43% whereas silica fume improved only 15%. Therefore, addition of nanoparticles significantly improves the engineering properties of the cementitious materials.

References

[1]. Sobolev K., Gutiérrez FM. How nanotechnology can change the concrete world: Part 1. Am. Ceram. Soc. Bull.; 2005.10, 14–17.

[2]. Sobolev K., Gutiérrez FM. How nanotechnology can change the concrete world: Part 2. Am. Ceram. Soc. Bull.; 2005. 11, 16–19.

[3]. Mondal P., Shah SP, Marks LD, Gaitero JJ. Comparative Study of the Effects of Microsilica and Nanosilica in Concrete. Transportation Research Record: Journal of the Transportation Research Board, No. 2141, Transportation Research Board of the National Academies, Washington, D.C.; 2010, pp. 6–9.

[4]. Thoma JJ, Jennings HM, Allen AJ. Relationships between Composition and Density of Tobermorite, Jennite, and Nanoscale $CaO\text{-}SiO_2\text{-}H_2O$, J. Phys. Chem. C; 2010. 114, 7594–7601.

[5]. Nonat A. The structure and stoichiometry of C-S-H, Cement and Concrete Research; 2004. 34 1521–1528.

[6]. Plassard C., et al. Investigation of the surface structure and elastic properties of calcium silicate hydrates at the nanoscale. Ultramicroscopy 100, 331–338 (2004).

[7]. Bjornstrom J, Martinelli A, Matic A, Borjesson L and Panas I Accelarating effects of colloidal nano-silica for beneficial calcium-silicate-hydrate system. Chemical Physics Letter; 2004. 392, 242-248.

[8]. Watanabe, T., et al. Multi-functional material with photocatalytic functions and method of manufacturing same. US patent 6294247 (2001).

[9]. Vittoria DM, Ormellese M and Pedeferri M Characterization of photocatalyticnext term and superhydrophilic properties of mortars containing titanium dioxide. Cement and Concrete Research; 2008. 38, 1349–1353.

[10]. Ying LG, Ming WP and Zhao X. Pressure-sensitive properties and microstructure of carbon nanotube reinforced cement composites. Cement & Concrete Composites; 2007 29: 377–382.

[11]. Chung DDL. Comparison of submicron-diameter carbon filaments and conventional carbon fibers as fillers in composite materials. Carbon (2001) 39: 1119–1125.

[12]. Gaitero JJ, Campillo I and Guerrero. A Reduction of the calcium leaching rate of cement paste by addition of silica nanoparticles. Cement and Concrete Research (2008) 38: 1112–1118.

[13]. Berra M., Carassiti F., Mangialardi T., Paolini A.E. and Sebastiani M., "Effects of nanosilica addition on workability and compressive strength of Portland cement pastes," Construction and Building Materials, 2012, 35, 666-675.

[14]. K. A. Gruber, T. Ramlochan, A. Boddy, R. D. Hooton, M. D. A. Thomas. Increasing concrete durability with high-reactivity metakaolin, Cem. Concr. Compos. 23 (6) (2001) 479–84.

[15] Y. S. Choi, J. G. Kim, K. M. Lee, Corrosion behavior of steel bar embedded in fly ash concrete, Corros. Sci. 48 (7) (2006) 1733–1745.

[16] M. I. Khan, Nanostructure and microstructure of cement concrete incorporating multicementitious composites, Transp. Res. Rec.: J. Transp. Res. Brd. 2141 (2010) 21–27.

[17] H. W. Song, S. W. Pack, S. H. Nam, J. C. Jang, V. Saraswathy, Estimation of the permeability of silica fume cement concrete, Constr. Build. Mater. 24 (2010) 315–321.

[18]. Jain J, Neithalath N. Analysis of calcium leaching behaviour of plain and modified cement pastes in pure water. Cement Concrete Research; 2009. 31, 176.

The use of superabsorbent polymers to mitigate shrinkage of concrete

A. Assmann and H.W. Reinhardt

Department of Construction Materials, University of Stuttgart, Pfaffenwaldring 4, 70569 Stuttgart, Germany, PH (49) 711 6856-3323; FAX (49) 711 6856-7681; email: reinhardt@iwb.uni-stuttgart.de

ABSTRACT

Superabsorbent polymers (SAP) are a new type of admixture. They can store many times more water than their own weight. They can be used for internal curing of concrete and for mitigation of shrinkage. By adding 0.7 % SAP by mass of cement, autogenous shrinkage of low water-cement ratio concrete can be suppressed completely. By adding only 0.35 %, autogenous shrinkage can be reduced by 80 % compared to concrete without SAP. Total shrinkage of drying concrete (the sum of autogenous and drying shrinkage) is also reduced considerably.

The paper reports about experimental investigations on cement paste and concrete which show the favorable effect of SAP on shrinkage. Results will be shown and discussed in the light of the mechanism of autogenous shrinkage and the effect of SAP on the water balance in concrete.

INTRODUCTION

Superabsorbent polymers (SAP) are a type of addition which can be used in concrete for various purposes. Due to its ability to absorb water it can assist curing and can mitigate shrinkage. Before the action of SAP will be exemplified, SAP will be described in general. SAP is a cross-linked copolymer frequently built up of acrylic acid and sodium acrylate. The polymer chains contain functional side groups which attract water. Sodium ions are trapped inside the network resulting in a mismatch of concentration between the polymer and the outside water. Therefore an osmotic pressure builds up which sucks water into the interior of the polymer molecule. Ionic side groups are able to store large quantities of water. Figure 1 gives an impression.

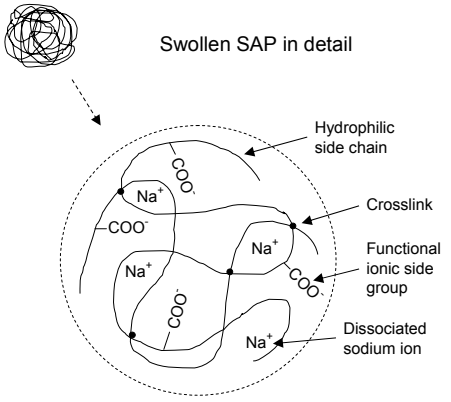

Figure 1. Superabsorbent polymer particle, schematically

Dependent on the way of production, the SAP particles are angular (from gel-polymerization) or spherical (from suspension polymerization) (Mechtcherine & Reinhardt 2012). The size of the particles in dry condition varies between several microns to a few hundred microns. The water absorption capacity is strongly dependent on the ambient aqueous solution: In pure water, SAP can absorb several 100 g water per g SAP, if the salt concentration of the water goes up (for instance hydrated cement pore solution) the absorption is reduced to a few g/g. For this reason, especially designed salt-insensitive SAP have to be used for the application in concrete. Added dryly to the concrete mix, they absorb a part of the mixing water which is later released in the course of hydration.

Usually, five types of shrinkage are differentiated, i.e. plastic shrinkage (capillary shrinkage), chemical shrinkage, autogenous shrinkage, drying shrinkage, and carbonation shrinkage. In the following, these types will be addressed as far as SAP can play a part.

PLASTIC SHRINKAGE

Plastic shrinkage is the result of capillary pressure between the solid particles in fresh concrete. When concrete is mixed and placed the system can be regarded as suspension with solid particles in water. The solid particles which have a greater density than water sink and water rises and accumulates at the concrete surface (this phenomenon is called bleeding). As long as there is a closed water layer on the surface there is no tension between the aggregate grains. When the water evaporates, preferably with strong wind and high temperature, menisci develop between the particles at the drying surface and the suspension consolidates. This phenomenon is called plastic shrinkage (or physically correct “capillary shrinkage”) and the contraction amounts to about 1 to 2 x 10^{-3}. When the movement of the concrete is restraint, tensile stresses develop which may lead to cracks. Plastic shrinkage can be prevented by spraying water (external curing).

Water supply can also be achieved by an internal water source. SAP is such a possibility which can store about 2 to 20 dm^3 water per m^3 concrete. (The numbers depend of course on the quantity of SAP and the absorption ratio.) This water keeps the concrete wet and helps to avoid plastic shrinkage until the concrete has set so much that a contraction in the fluid state is not possible anymore.

Wind-tunnel tests have been carried out on cement pastes (Dudziak & Mechtcherine 2010) which show the beneficial effect. The setup used was similar to (Slowik et al. 2008). Figure 2 shows how the capillary pressure is building up. Further, the diagram reports on plastic deformation and settlement of the pastes. The black lines refer to a control paste without SAP made with a water-cement ratio of 0.30. The grey lines refer to a cement paste produced at water-cement ratio of 0.39, modified with 0.6% SAP with respect to the cement content. While the plastic shrinkage amounts to 5 mm/m after 8 hours in the control paste, the plastic shrinkage of the SAP modified paste is only half this value. The capillary pressure, which is to some extent an indication for the cracking susceptibility of the young material, is negligible in the paste containing SAP and extra water, whereas the settlement is increased compared with the control paste.

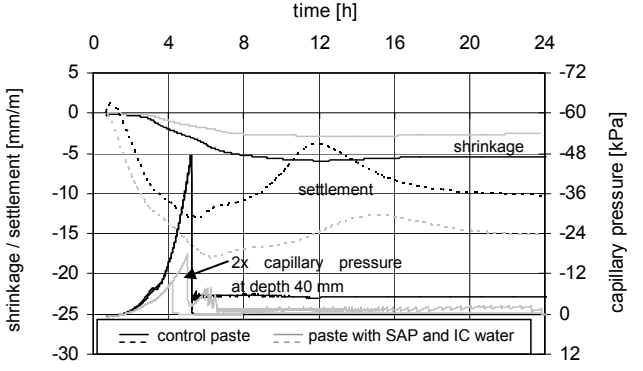

Figure 2. Capillary pressure, shrinkage and settlement of cement paste without SAP (black lines) and with SAP and extra water (grey lines). Data from Dudziak & Mechtcherine (2010) as cited in Mechtcherine & Reinhardt (2012)

CHEMICAL SHRINKAGE

Chemical shrinkage is due to the fact that the absolute volume of cement and water in the fresh cement paste decreases when the cement hydrates. The reduction depends on the mineral composition of the cement but an average value amounts to 0.07 ml per gram of cement reacted. For a water/cement ratio of 0.42 and a degree of hydration of one, one can calculate the volume reduction to about 8 % (Powers & Brownyard 1946/1947). The volume reduction can only lead to a reduction of the apparent volume as long as the cement paste is fluid which means in the first stage of reaction. As soon as the cement paste stiffens, chemical shrinkage results in the

creation of water-air menisci forming small capillary pores and the apparent volume stays constant.

AUTOGENOUS SHRINKAGE

The small capillary pores due to chemical shrinkage are water filled if there is a surplus of water with respect to the quantity of water which is needed for complete hydration of the cement. This is the case for water/cement ratios of 0.42 and greater. If the water/cement ratio is smaller the system will dry out internally which is called self-desiccation. The consequence of the reduction of the internal relative humidity is twofold: First, the disjoining pressure between hydrated particles decreases and, second, the menisci radii of pore water decrease. Both effects lead to a reduction of apparent volume.

Autogenous shrinkage is usually defined as the bulk deformation of a sealed, isothermal cementitious material system not subject to external forces (Jensen & Hansen 2001). A small part is due to chemical shrinkage and another part is due to self desiccation. In practice, autogenous shrinkage was not important as long as rather large water/cement ratios were used for good workability. With the emergence of superplasticizers which secured good workability with low water/cement ratios and, consequently, high-performance concretes, the aspect of autogenous shrinkage becomes substantial in concrete technology. Autogenous shrinkage occurs after setting of the cement and manifests itself in the entire volume of concrete at the same time.

To mitigate self-desiccation the relative humidity of the system should be maintained at almost 100 %. That can be achieved by adding superabsorbent polymers (SAP) to concrete which create an internal water reservoir. This method of water supply is called internal curing. The SAP used has to have sufficient water absorption and slow water release.

Figure 3 shows an example of autogenous shrinkage of concrete during the first 7 days of hydration (Igarashi & Watanabe 2010).

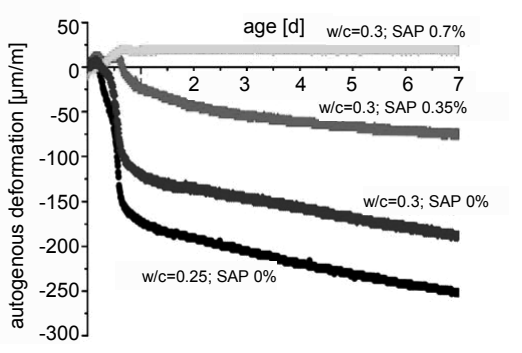

Figure 3. Effect of SAP on autogenous shrinkage of concrete vs. time (Igarashi & Watanabe 2010)

The water-cement ratio of 0.25 led to a deformation of 250 μm/m and the water-cement ratio of 0.30 to 200 μm/m. Adding 0.35 % SAP with respect to the mass of cement reduced the deformation to 75 μm/m and the addition of 0.7 % caused an elongation (swelling) of 25 μm/m. The diagram shows that autogenous shrinkage can be suppressed with SAP. The degree of suppression depends clearly on the quantity of SAP used and on the water retention capability. An average value is 0.4 % addition of SAP with respect to the mass of cement.

DRYING SHRINKAGE

Concerning reference concretes without SAP, there is a linear relationship between cement paste content and drying shrinkage (Grube 1991). Increasing amount of water leads to a larger capillary pore system while increasing amount of water stored in SAP causes a larger number of uniformly distributed SAP pores. Usually, the weight loss caused by evaporation determines the rate of drying shrinkage.

Figure 4 (left) shows the total deformation of two reference concretes with water-cement ratios of 0.36 and 0.42, respectively, and one concrete with total water-cement ratio of 0.42 containing 0.25 % SAP by mass of cement. The concrete specimens were exposed to drying at 20°C and 65% RH either directly after demoulding (24 hours after casting) or after 28 days of sealed storage. The reference concretes show that increasing the water content leads to higher total shrinkage whereas the SAP-modified concrete shows reduced total shrinkage. In case of early drying this reduction is caused by suppressed autogenous shrinkage (measured on sealed companion specimens) as can be seen from Figure 4 (right). The diagram shows the total minus autogenous shrinkage strain.

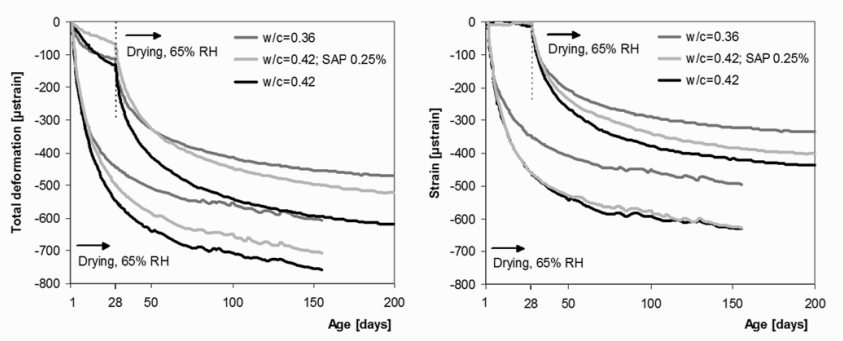

Figure 4. Total shrinkage strain of concrete specimens exposed to early drying(as of demoulding) and retarded drying (as of 28 days of sealed storage) at 20°C and 65% RH (left) and drying shrinkage as the result of total minus autogenous shrinkage strain (right)

However, in case of delayed drying, the SAP-modified concrete shows less drying shrinkage compared to the control concrete with same amount of mixing

water. It is expected that the difference in microstructure formation caused this effect. At the beginning of delayed drying, the SAP-modified concrete possesses less capillary porosity and, at the same time, the higher water saturation degree due to internal water reservoirs. In consequence, more water is drained via the larger capillaries which causes less drying shrinkage compared to drainage of finer pores. In case of early drying, drainage will start at complete saturation in both concretes and the effect will vanish.

To get a general idea which amount of total shrinkage is due to autogenous shrinkage and which to drying shrinkage, the numbers given by Eurocode (2004) were evaluated. Table 1 reports on the results.

Table 1. Shrinkage of concrete according to Eurocode (2004) (based on samples of 400 mm in size, produced with type 42.5 cement, stored at 20°C / 70 % RH)

Strength class	Autogenous ε_a	Drying ε_d	$\frac{\varepsilon_a}{\varepsilon_a + \varepsilon_d}$
C 30	0.07×10^{-3}	0.40×10^{-3}	0.15
C 50	0.12×10^{-3}	0.35×10^{-3}	0.26
C 70	0.17×10^{-3}	0.28×10^{-3}	0.38
C 90	0.22×10^{-3}	0.20×10^{-3}	0.52
C 110	0.25×10^{-3}	0.17×10^{-3}	0.60

At C 30 autogenous shrinkage amounts to 15 % of total shrinkage. At C 70 the ratio is 38 % and at C 110 it is 60 %, i.e. autogenous shrinkage is greater than drying shrinkage. This means that the addition of SAP can reduce total shrinkage considerably because it can suppress autogenous shrinkage completely, which is important for high-performance concrete in particular.

CONCLUSIONS

On the basis of the results presented, the indicated effects of superabsorbent polymers on shrinkage of cement paste and concrete can be summarized as follows:

- Wind tunnel tests performed on cement pastes indicated that capillary pressure and related plastic shrinkage is reduced due to addition of SAP and extra water.
- Internal curing with SAP can mitigate autogenous shrinkage, e.g. addition of 0.7 % SAP with respect to cement content completely suppressed autogenous shrinkage of concrete produced at w/c ratio of 0.30.
- Total shrinkage of concrete exposed to drying is reduced due to addition of SAP. The reduction is mainly due to suppressed autogenous shrinkage which can be larger than the share of drying shrinkage in total deformation as far as high-strength concrete is considered.

REFERENCES

Dudziak, L., and Mechtcherine, V. (2010). "Enhancing early-age resistance to cracking in high-strength cement-based materials by means of internal curing using SAP. *RILEM PRO 77*, Vol. III, Bagneux, 129-139.

EN 1992-1-1:2004-12 Eurocode 2: *Design of concrete structures* – Part 1-1: General rules and rules for buildings

Grube, H. (1991) *Causes for shrinkage of concrete and effects on structural components*, (in German). Beton-Verlag, Düsseldorf

Igarashi, S., and Watanabe, A. (2010) "Experimental study on prevention of autogenous deformationby internal-curing using SAP particles". *RILEM PRO 74*, Bagneux, 77-86

Jensen, O.M., and Hansen, P.F. (2001). "Autogenous deformation and RH change in perspective". *Cement and Concrete Research* 31(12), 1859-1865.

Mechtcherine, V., and Reinhardt, H.-W. (2012) *Application of superabsorbent polymers (SAP) in concrete construction*. RILEM State-of-the-Art Reports, Vol. 2, Dordrecht

Powers, T.C., and Brownyard, T.L. (1946/1947) "Studies of the physical properties of hardened Portland cement paste" (9 parts). *J ACI* 43(10) to 44(4)

Slowik, V., Schmidt, M., and Fritzsch, R. (2008) "Capillary pressure in fresh cement-based materials and identification of the air entry value". *Cement and Concrete Composites* 30(7), 557-565.

Measuring the Chemical Shrinkage of Alkali-Activated Slag Cements Using the Buoyancy Method

Christopher P. Cartwright[1], Farshad Rajabipour[2], and Aleksandra Radlińska[3]

[1]Corresponding author, Graduate Research Assistant, The Pennsylvania State University, 3127 Research Drive, State College, PA 16801, USA. (814)-421-2830. cpcartwright@gmail.com

[2]Assistant Professor, The Pennsylvania State University, 223B Sackett Building, University Park, PA 16802, USA. (814)-863-0601. farshad@engr.psu.edu

[3]Assistant Professor, The Pennsylvania State University, 231D Sackett Building, University Park, PA 16802, USA. (814)-865-9427. ara@engr.psu.edu

ABSTRACT

Recent incentives to reduce the carbon footprint of Portland cement (PC) concrete have sparked the research and development of eco-friendly products such as alkali-activated slag (AAS) concrete. AAS is a promising product capable of developing compressive strengths comparable to PC concrete; however, its large drying and autogenous shrinkage (the latter being the focus of this paper) have impeded its marketability and use in the construction industry. The mechanisms and parameters that control the self desiccation of AAS are relatively unknown. Chemical shrinkage, the driving force of autogenous shrinkage, has never been measured for AAS systems; however, it has been theoretically estimated to be much higher than that of PC. The first step in determining why the autogenous shrinkage of AAS is so large is to investigate its chemical shrinkage. This research focuses on proper measurement of the chemical shrinkage of AAS and the parameters that affect the results.

INTRODUCTION

Concrete production utilizes the most abundant natural materials present on the Earth's surface. However, the high temperatures (~1400°C) required during production of Portland cement in the kiln result in a significant energy use (embodied energy = 5.7MJ/kg of cement) and a large CO_2 footprint (0.95kg CO_2/kg of cement) (Ashby 2009, Marinshaw and Wallace 1994). Recent global initiatives to reduce the carbon footprint and harmful emissions into the Earth's environment have ignited the research to develop new environmentally friendly and sustainable construction materials. The annual production of concrete exceeds 10^{10} tonnes/year, more than all other manmade materials combined (Ashby 2009). This large production rate results

in a large carbon footprint of Portland cement, resulting in approximately 5% of the total anthropogenic GHG emissions (Damtoft et al. 2008).

Multiple eco-friendly products have been researched up to date to partially or fully replace Portland cement in concrete. Research has shown (Ben Haha et al. 2011, Shi et al. 2006) that industrial waste products, e.g. blast furnace slag from steel manufacturing, can be used to successfully produce a Portland cement-free concrete.

Alkali activation is the process of exposing a glassy silica-based material (e.g., slag) to a high pH environment to promote the congruent dissolution of alumino-silicates. These dissolved products can then react with water and the available alkali and calcium ions to form calcium silicate hydrate (C-S-H) and calcium-aluminum-silicate hydrate (C-A-S-H) gels that provide the binder phase in concrete (Ben Haha et al. 2011). The process of alkali activation of these amorphous materials allows for the development of a Portland cement-free binder (Shi et al. 2006).

The marketability and acceptance of alkali-activated slag (AAS) in the industry have been hindered by concerns related to their volumetric instability and risk of cracking. Many researchers (Shi et al. 2006, Palacios et al. 2007, Collins et al. 2000, Chen et al. 2007) have shown that AAS concrete has significantly higher shrinkage strains (both autogenous and drying) than ordinary Portland cement (OPC) mixtures. This large deformation can lead to concrete durability issues, as cracking is expected to occur when volumetric changes are restrained. These cracks allow salts and other harmful chemicals to penetrate the concrete and corrode the reinforcing steel.

Figure 1 shows the autogenous shrinkage strains of several AAS and a control OPC mixture (all having a sand volume fraction of 50.7%). It can be seen that the autogenous shrinkage strains of AAS are significantly higher than those found in OPC. While limited data related to shrinkage performance of AAS do exist (Shi et al. 2006, Palacios et al. 2007), the scientific reasoning and mechanisms of large autogenous strains in AAS have not been explained. For instance, many authors (Melo Neto et al. 2008, Collins et al. 2000, Palacios et al. 2007) suggest that a refined pore structure creates large capillary stresses, resulting in a significant shrinkage of AAS systems. Others (Thomas et al. 2012) have theoretically estimated the chemical shrinkage values of AAS paste to be between 0.107 and 0.139 ml/g_{slag} and suggested that a large chemical shrinkage (in comparison with that of Portland cement: ~0.064 ml/g_{cem}) could be responsible for large autogenous shrinkage. However, a comprehensive study that physically measures the chemical shrinkage of AAS, and investigates the parameters affecting the results, has not been performed. In order to properly analyze and understand the autogenous shrinkage of AAS systems, the first step is to properly quantify and evaluate their chemical shrinkage.

This paper focuses primarily on chemical shrinkage and the role it plays in the self desiccation of AAS systems. It provides the results for chemical shrinkage and other tests used to analyze and understand the hydration of several AAS mixtures. Chemical shrinkage and degree of hydration experiments were conducted on four unique AAS mixtures, and the results were compared to those of a typical OPC mix.

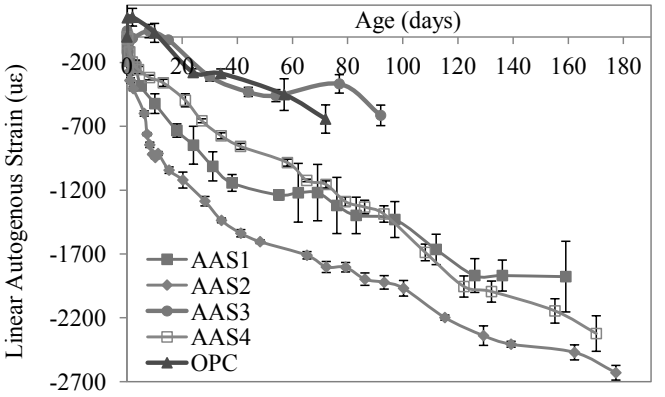

Figure 1. Autogenous shrinkage strains of AAS mortars

MATERIALS

Alkali-activated slag pastes were investigated in this study. The grade 120 ground granulated blast-furnace slag used (ASTM C989M-12a) had a density of 2.89 g/cm^3, and an oxide composition as shown in Table 1. A particle size analysis (using laser diffraction) showed that 50% of slag particles were smaller than 7.4μm and 10% of slag particles were smaller than 1μm. Portland cement was ASTM C150 type I cement with a density of 3.14 g/cm^3 and an oxide composition as shown in Table 1.

Table 1. Oxide compositions of slag and cement (mass%)

	CaO	SiO_2	Al_2O_3	MgO	SO_3	Fe_2O_3
Slag	39.20	33.22	20.56	2.86	4.16	0
Type I cement	62.50	19.90	5.44	2.31	4.93	2.26

Four AAS mixtures and a control OPC mixture were designed using a constant volumetric liquid (water + activator) to solid (slag or cement) ratio of 1.30, yielding an initial binder porosity of 56.5%. For the control OPC mixture, this is equivalent to a mass-based w/c = 0.414. For the AAS mixtures, the mass-based liquid to solid ratio was in the range 0.489-0.510, depending on the concentration and density of the alkali activating solutions (Table 2).

Mixtures AAS1 (low silica concentration) and AAS2 (high silica concentration) were activated using an alkaline solution containing a combination of dissolved sodium hydroxide (NaOH) pellets, aqueous sodium silicate ($Na_2O(SiO_2)_n$), and water. The other two mixes, AAS3 and AAS4, were activated using only a solution of NaOH in water (either a 2M or 4M). The aqueous sodium silicate (($Na_2O(SiO_2)_n$) had the modulus n = 1.6, pH = 13.7, and specific gravity = 1.60 at 20°C. It contained 53.2% water, 28.8% SiO_2, and 18.0% Na_2O by mass. To prepare the activating solutions, reagent NaOH pellets were dissolved in water at room temperature and covered to prevent carbonation. The solution was shaken for 5 minutes and then set aside for

approximately two hours to allow for heat dissipation and a return to room temperature. For mixtures AAS1 and AAS2, the sodium hydroxide and sodium silicate solutions were kept separate. The sodium hydroxide solution and slag were added to the mixing bowl and mixed according to ASTM C305-12. In order to allow the solution to properly dissolve the slag, the sodium silicate was excluded from the mixture until 15 minutes after mixing.

Table 2. Activating Solution Properties for AAS Mixtures

Mix ID	$n = (SiO_2/Na_2O)$ molar-based	pH	Density (g/cc)
AAS1	0.41	14.31	1.09
AAS2	1.22	13.78	1.13
AAS3	0	14.30	1.04
AAS4	0	14.60	1.09

EXPERIMENTAL METHODS

Chemical shrinkage was measured using the buoyancy method (Sant et al. 2005). After mixing slag with the activating solution, a slag paste sample (both 10 and 25 gram samples were tested) was placed in a crystallizing dish (70 mm diameter × 50 mm height). A 10 mL solution composed of NaOH and water, with the equivalent pH of the activating solution, was placed on top of the sample. The dish was then filled with low density paraffin oil (0.863 g/cm^3). The sample was placed on a wire mesh and lowered into a stainless steel bucket filled with the oil. The bucket was placed in a water bath which was kept at constant temperature of 23±0.5°C. The wire mesh was attached to a string mounted to the underside of a high precision balance, capable of measuring mass with an accuracy of 0.0001g. The entire system was surrounded by a clear acrylic shield to prevent wind currents from interfering with the mass measurements. Mass measurements were recorded every five minutes using an automatic data acquisition system. Chemical shrinkage strains were calculated using equation 1 (Sant et al. 2005) where $W_{sub}(30)$ is the submerged weight of the sample 30 minutes after mixing, $W_{sub}(t)$ is the submerged weight of the sample at any time t, ρ_{oil} is the density of the paraffin oil, and g_{slag} is the mass of slag in the paste sample.

$$V_{cs} = \frac{\Delta V_{paste}}{g_{slag}} = \frac{W_{sub}(t) - W_{sub}(30)}{\rho_{oil} * g_{slag}} \quad (1)$$

Degree of hydration was measured using selective acid dissolution (Luke and Glasser 1987). Hydration products of AAS systems dissolve in acid; therefore, any remaining residue after acid dissolution tests represents unhydrated slag. After the chemical shrinkage test had concluded, the paste sample was removed from the setup and oven dried to constant mass. Next, the sample was crushed to a powder, and a 0.5g sample was added to a solution of EDTA, Na_2CO_3, triethanolamine, and distilled water (as prepared by Luke and Glasser, 1987). Before adding the powder, the solution was adjusted to a pH of 11.6 using 1M NaOH. The solution was shaken for 30 minutes and then filtered through a Gooch crucible with GF/F (0.7μm diameter) filter paper and dried to constant mass.

RESULTS & DISCUSSION

Chemical shrinkage results for 25g (5mm thick) samples are reported in Figure 2. The values reported are in ml of chemical shrinkage per gram of cement or slag mixed. This does not account for the actual fraction of the cement or slag that has reacted at a given age; therefore, degree of hydration is needed to correct the chemical shrinkage for the actual amount of reacted slag or cement. It can be seen that AAS3 and AAS4 mixtures have comparable chemical shrinkage values that are lower (0.03 ml/g_{slag}) than the control OPC paste (0.055ml/g_{cem}) at 150 hours. AAS4 was tested up to 14 days (336 hours); and the final measured chemical shrinkage was recorded to be 0.045 ml/g_{slag}. Mixtures activated only by NaOH have slightly higher chemical shrinkage than those activated by NaOH and $Na_2O(SiO_2)_n$. This may be due to the coarser porosity (and therefore higher permeability) of NaOH activated systems.

The values of chemical shrinkage at complete hydration of OPC are reported (Powers et al. 1948, Jensen et al. 2001) to be approximately 0.064 ml/g_{cem}. Similarly, the theoretical chemical shrinkage of AAS at complete hydration has been estimated (Chen 2007) to be between 0.107 and 0.139 ml/g_{slag}, depending on the concentration and type of activator used. Other authors (Thomas et al. 2012) calculated a similar value of 12.2 ml/g_{slag}. Hypotheses as to why measurements of AAS chemical shrinkage in this study do not match the theoretical estimations are discussed below.

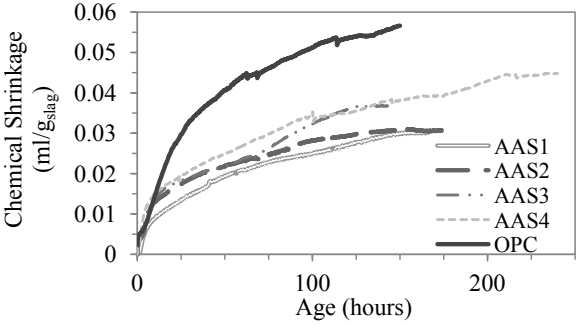

Figure 2: Chemical shrinkage of 25g samples

Three possible explanations for inconsistencies between the measured chemical shrinkage and the theoretical models are provided as follows: (1) only a percentage of slag particles has reacted and is available to form C-S-H and C-A-S-H products. The theoretical models assume full hydration of slag, yet previous tests (Ben Haha et al. 2011) show that AAS systems only reach approximately 40% hydration, (2) the low permeability of AAS pastes is preventing the top layer of solution in the test setup from permeating into the entire thickness of the paste and reaching all air pockets that form during slag hydration and the resulting chemical shrinkage, and (3) the large thickness (5mm) of the paste sample exacerbates the low AAS permeability and further reduces the ability of the test setup to effectively measure chemical shrinkage.

Adjustments were made to sample preparations during the chemical shrinkage test setup to test hypotheses (2) and (3). First, the sample thickness was reduced from

5mm to 2mm. This will help by eliminating the need for the top solution layer to have to permeate the entire 5 mm thickness of the AAS paste. Second, the porosity of the mixtures was doubled to increase the paste permeability. The chemical shrinkage is reported on a "per gram of slag" basis; therefore, theoretically, the chemical shrinkage should be independent of water/solid and the porosity. An increase in the porosity, however, will increase the permeability and allow easier moisture transport from the top layer of solution into the AAS paste sample.

To evaluate hypothesis (1), tests for measuring the degree of hydration of slag were performed on each mixture after the termination of chemical shrinkage tests (typically 7 days). A low degree of hydration, as suggested by the literature, would help resolve the resounding issue as to why the chemical shrinkage values of AAS binders are significantly lower than what the theoretical models suggest.

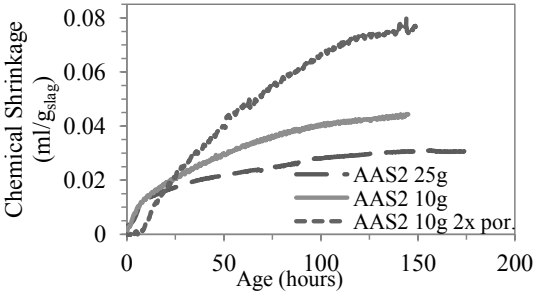

Figure 3: Chemical shrinkage of mix AAS2 using a thinner sample (10 grams) and a higher porosity (2x por.)

The paste AAS2 was selected for testing of a 2mm sample thickness (10 grams), an increase (2x's) in porosity, and comparison of results with those for 5 mm thick sample. The chemical shrinkage measurements for "AAS2 25g", "AAS2 10g", and "AAS2 10g 2x por" are shown in Figure 3. As shown previously in Figure 2, the 7 day chemical shrinkage of AAS2 25g is approximately 0.03 ml/g_{slag}. When the thickness of the sample was reduced to 2mm, the measured chemical shrinkage of AAS2 at 7 days increased to 0.045 ml/g_{slag}. Although this is a modest increase, the measured values are still significantly lower than the theoretical estimates. When the porosity was doubled, the chemical shrinkage for "AAS2 10g 2x por" increased to 0.08 ml/g_{slag}. This most likely occurs because the paste permeability is increased, which facilitates better moisture transport through the paste thickness. It is also possible that the hydration reactions and therefore, the degree of hydration of slag have increased due to improved accessibility of slag particles to the activating pore solution. A higher degree of hydration of slag would further increase the chemical shrinkage. These results suggest that the thickness and permeability of the AAS paste have a considerable impact on the measured value of chemical shrinkage.

Table 3 shows the results of selective dissolution tests to determine the degree of slag hydration for 6 AAS pastes. The tests were performed immediately after termination of the chemical shrinkage tests (typically 7 days). In addition, the raw CS results at

the conclusion of the test are included, as well as the normalized results, which were adjusted based on the slag degree of hydration. Clearly, these AAS systems have a very low degree of hydration. As such, it is misleading to assume that the raw CS results from the buoyancy test can represent the true chemical shrinkage corresponding to 100% hydration of slag in alkali activated mixtures. After 7 days, half of the mixtures failed to reach 15% hydration. AAS2 10g had a slightly higher degree of hydration than AAS2 25g, most likely because a larger percentage of the thinner sample was accessible to the top layer of solution. Similarly, AAS2 10g 2x por (25.18%) had a higher degree of hydration than AAS2 10g (13.33%), due to the improved accessibility of slag particles to the activating pore solution. AAS4 had the highest degree of hydration (24.47%) among the binders with an equivalent initial capillary porosity, most likely due to its high pH and fast dissolution of slag powder.

Table 3: Degree of hydration of AAS pastes

	AAS1 25g	AAS2 25g	AAS2 10g	AAS2 10g 2x por	AAS3 25g	AAS4 25g
Slag Degree of Hydration	13.99%	12.03%	13.33%	25.18%	13.80%	24.47%
Raw CS (ml/g_{slag})	0.03	0.03	0.045	0.08	0.03	0.045
Normalized* CS (ml/g_{slag})	0.214	0.249	0.337	0.319	0.217	0.184

* Assumes 100% hydration of slag

The normalized chemical shrinkage values of AAS pastes are ranging from 0.184 to 0.337 ml/g_{slag} (averaged 0.253 ml/g_{slag}). These are considerably higher than the theoretical estimations, and further research is needed to determine the causes of disagreement. One reason for this discrepancy could be that absorption of free water by the aqueous sodium silicate pore solution in pastes AAS1 and AAS2 could by itself result in chemical shrinkage independent of degree of slag hydration. Another possibility could be that lower porosity AAS pastes may never reach 100% hydration due to running out of capillary pore space to form the hydration products.

CONCLUSIONS

- Chemical shrinkage (CS) of alkali activated slag (AAS) paste, when measured using the buoyancy method, is substantially lower than the values estimated based on theory. Possible reasons for such low CS measurements include: (1) low permeability of AAS paste, (2) large sample thickness, and (3) incomplete hydration of slag particles.
- Increasing the porosity of the paste sample and reducing the sample thickness both resulted in considerable increase in the chemical shrinkage results.
- At the conclusion of CS buoyancy test, only 12% to 25% of slag had reacted. Therefore, the raw chemical shrinkage results cannot represent the true CS values of slag corresponding to 100% reaction.
- After adjusting for the degree of hydration, the average chemical shrinkage of AAS paste is determined as 0.253 ml/g_{slag}. This is 3.95 times larger than the

chemical shrinkage of Portland cement, and contributes directly to the large autogenous shrinkage of AAS materials.

ACKNOWLEDGEMENTS

Financial support from the National Science Foundation (NSF) under Grant No. CMMI 1265789 granted to the last two authors is greatly appreciated. Any opinions, findings and conclusions or recommendations expressed in this material are those of the authors and do not necessarily reflect the views of the NSF.

REFERENCES

Ashby, M. (2009) *Materials and the Environment*, Elsevier, Inc, Burlington, MA

Ben Haha, M., Le Saout, G., Winnefeld, F., Lothenbach, B. (2011), "Influence of activator type on hydration kinetics, hydrate assemblage and microstructural development of alkali activated blast furnace-slags." Cem Conc Res, 41: 301-310.

Chen, W., Brouwers, H.J. (2007), "The hydration of slag, part 1: reaction models for alkali-activated slag." J Mater Sci, 42: 428-443.

Collins, F., Sanjayan, J.G. (2000), "Effect of pore size distribution on drying shrinkage of alkali-activated slag concrete." Cem Conc Res, 30: 1401-1406.

Damtoft, J., Lukasik, J., Herfort, D., Sorrentino, D., Gartner, E. (2008) "Sustainable development and climate change initiatives." Cem Conc Res, 38: 115-12.

Marinshaw, R., Wallace, D., (1994). "Emission factor documentation: Portland cement manufacturing." United States Environmental Protection Agency (EPA), www.epa.gov/ttn/chief/ap42/ch11/bgdocs/b11s06.pdf (accessed May 15, 2013).

Jensen, O.M., Hansen, P.F. (2001) "Water-entrained cement-based materials: Principles and theoretical background." Cem Conc Res, 31: 647-654.

Luke, K, Glasser, F.P. (1987) "Selective dissolution of hydrated blast furnace slag cements." Cem Conc Res, 17: 273-282.

Melo Neto, A.A, Cincotto, M.A., Repette, W. (2008) "Drying and autogenous shrinkage of pastes and mortars with activated slag cement." Cem Conc Res 38(4): 565-574.

Palacios, M., Puertas, F. (2007) "Effect of shrinkage-reducing admixtures on the properties of alkali-activated slag mortars and pastes." Cem Conc Res 37: 691–702.

Powers, T.C., Brownyard, T.L. (1948) "Studies of the physical properties of hardened portland cement paste." Bulletin 22, Research Laboratories of the Portland Cement Association, Chicago.

Sant, G., Lura, P., Weiss, J. (2005) "Measurement of volume change in cementitious materials at early ages." Trans Res Board. No. 1979, pp. 21-29.

Shi, C., Krivenko, P., Roy, D. (2006) *Alkali-Activated Cements and Concrete*, Taylor & Francis. New York, NY.

Thomas, J.J., Allen, A.J., Jennings, H.M. (2012) "Density and water content of nanoscale solid C-S-H formed in alkali-activated slag (AAS) paste and implications for chemical shrinkage." Cem Conc Res 42: 377-383.

An Apparatus for Dissecting Volumetric Changes in Hydrating Cement Paste

M. Abuhaikal[1], S. Musso[2], J. Thomas[2] and F.-J. Ulm[1]

[1]Department of Civil and Environmental Engineering, Massachusetts Institute of Technology, Cambridge, MA 02139, USA; Email: muhannad@mit.edu, ulm@mit.edu
[2]Schlumberger-Doll Research, Cambridge, MA 02139, USA; Email: SMusso@slb.com, JThomas39@slb.com

ABSTRACT

An apparatus has been designed to study the volumetric changes under controlled curing conditions. The apparatus is capable of measuring the chemical shrinkage as well as the macroscopic volumetric changes of sealed and saturated specimens under controlled pressure and temperature. Specifically, when measuring separately the macroscopic deformation (bulk shrinkage) and the water absorption of a saturated specimen, we find that the sum of the bulk deformations and water absorption adds up to the chemical shrinkage. Furthermore, while we observe pore pressure drops in the hydrating cement paste even in the presence of an infinite supply of pressurized water (i.e. chemical shrinkage test conditions), bulk shrinkage occurs even in the absence of negative liquid pressure and at (almost) zero effective stress. That is, at (very) early ages, other driving forces than capillary forces are at work to cause bulk shrinkage.

INTRODUCTION

The volume of the hydration products of a cement paste is smaller than the initial volume of cement and water reacted to form these products. This reduction in volume is referred to as chemical shrinkage, also known as Le Chatelier contraction. Since the early 1900's, chemical shrinkage has been measured by covering the cement sample with water and measuring the drop in water level in a burette mounted on top of the sample container (Powers, 1935). Although the fundamental technique has not changed over time, other researchers measured the change in the pressure at the bottom of a burette placed on the top of the cement container (Zhang et al., 2010). Another method consists in measuring the change in buoyancy force on an immersed specimen in direct contact with water (Sant et al., 2006). A standard test method is also available for the measurement of chemical shrinkage: ASTM (C01 Committee, 2007).

Macroscopic volumetric deformation refers to the macroscopic volumetric changes (either shrinkage or swelling) associated with the hydration of cement. These changes depend on the mix design and the curing conditions. The driving force that causes macroscopic deformation can be eigenstresses or external stresses, where eigenstresses can be, short-range colloidal forces, capillary pressure or temperature changes. Macroscopic deformation of a sealed specimen measured at isothermal room temperature and under atmospheric pressure is referred to as autogeneous shrinkage. Capillary forces are commonly assumed to be the driving force behind the autogeneous shrinkage in cement-based materials (Hua et al., 1995)(Barcelo et al., 2005). A typical method to measure the volumetric autogeneous shrinkage involves casting the cement paste inside a rubber membrane and measuring the change in buoyancy forces on the submersed specimen (Bouasker, 2006). The goal of this study is to build an apparatus to measure volumetric changes under controlled curing conditions in order to separate the different types of volumetric changes based on the driving forces.

MATERIALS AND METHODS

Class G cement is used in this study. Samples are mixed manually with a stirring rod in a glass beaker for 5 minutes.

Apparatus and test procedures. Fig. 1 shows a cross section through the apparatus built for this study. The apparatus consists of a pressure vessel with top and bottom caps. The bottom cap has a single port in the center and is connected to a syringe pump. The top cap has two ports: an eccentric port connected to a syringe pump, and a concentric port to let the air out of the vessel prior to testing. To facilitate the air exit, the bottom surface of the top cap is slightly tapered towards the outlet port. Syringe pumps can deliver a pressure up to 69 MPa and a flow rate up to 30 mL/min. Pumps can be run under controlled pressure or controlled flow rate. De-aeration of the specimen is achieved by applying vacuum and vibration to the specimen after casting inside the vessel. A vacuum cap is designed with a geometry matching the top cap, and is designed for the ease of use and to prevent splatter of slurry on the inside walls of the vessel during de-aeration. A vibrator is attached to the body of the vessel via an aluminum collar. The vibrator is operated at 100 Hz providing 15 g acceleration amplitude.

Test procedures

1. Preparing the vessel for testing: The inner wall of the vessel is covered with a thin layer of grease. The lower part of the vessel (everything between valve 3 and the top surface of the filter in Fig. 1) is saturated with water under vacuum and vibrations.

2. Preparing the slurry: cement is added to water and mixed manually with a stirring rod for 5 minutes.
3. Placing and degassing: slurry is poured inside the vessel and degassed under vacuum and vibration for 10 minutes.
4. Pressurizing the vessel: before sealing the vessel with the top cap, the specimen is covered either with water or the liquid barrier depending on the purpose of the test.

The liquid barrier is a hydrophobic liquid with viscosity of 10,000 cSt and a density of 1.3 g/mL. The high viscosity associated with large molecular weight prevents the liquid from permeating through the hydrating cement paste while the density of 1.3 g/mL is necessary to prevent water from reaching the cement paste. The possible test configurations are as follows (Fig. 2):

Chemical shrinkage test. In this test, the top surface of the specimen is exposed directly to pressurized water. Valve-1 is open and the volume injected through port 1 is recorded. Valve-3 is closed and the pressure measured by pressure transducer-3 (PT-3) is recorded.

Sealed specimen test. In this test, a 10 mm layer of the liquid barrier is placed on top of the specimen and water is injected through port-1 to fill the rest of the vessel. Similar to the chemical shrinkage test, the pressure measured by PT-3 is recorded while valve-3 is closed. When the test is carried out under pressure load, the bulk deformation measured consists of both creep and autogeneous shrinkage.

General test. Similar to the sealed test, a 10 mm layer of the liquid barrier is placed on top of the specimen; but water is injected through port-1 to fill the rest of the vessel. Initially, V-3 is closed and pressure reading of PT-3 is monitored. Onset of percolation is recognized by a sharp drop of the pressure reading, at which point, the desired effective stress is achieved by applying the corresponding water pressure through port-3.

RESULTS

Chemical shrinkage results for w/c = 0.30, 0.35, 0.42 and thickness of 45 mm under 5 MPa curing pressure is shown in Fig. 3. Pressure at the bottom of the specimens is shown in Fig. 4.

A sealed experiment under 5 MPa is shown in Fig. 5. The chemical shrinkage under similar conditions is shown for reference. Since macroscopic volumetric changes cannot be measured for bleeding samples with the current design, water-to-cement ratio of 0.3 was used to avoid the bleeding problem.

A general test result for a w/c=0.3 cement paste subjected to a 5 MPa pressure is shown in Fig-6, together with the result of a chemical shrinkage test for reference.

As described in the procedures above, valve-3 is opened after the pressure at the bottom of the specimen dropped to 0.96 MPa.

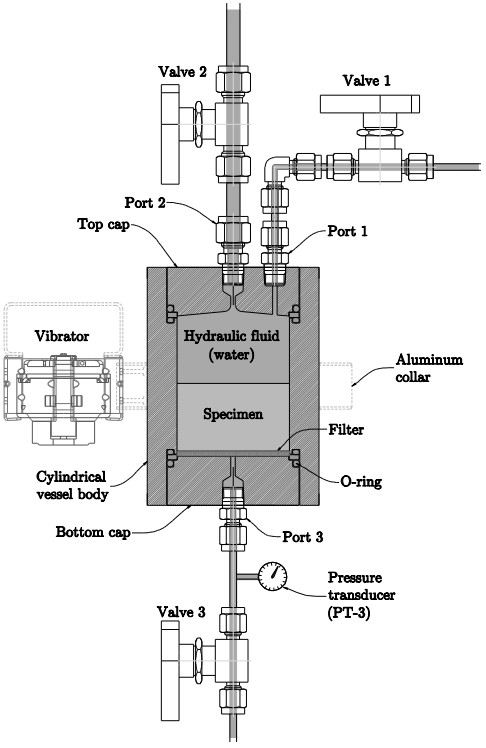

Fig. 1: Cross section of the apparatus.

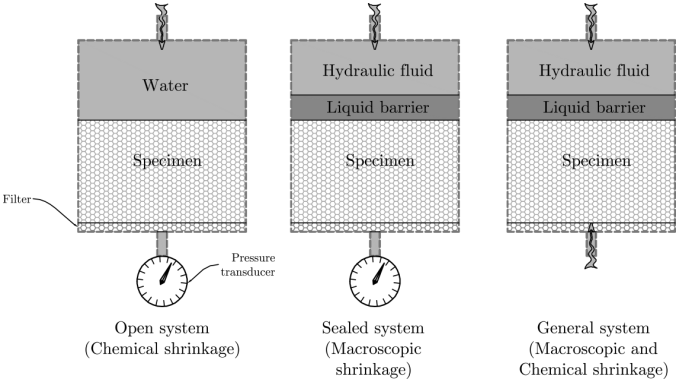

Fig. 2: Different Test configurations.

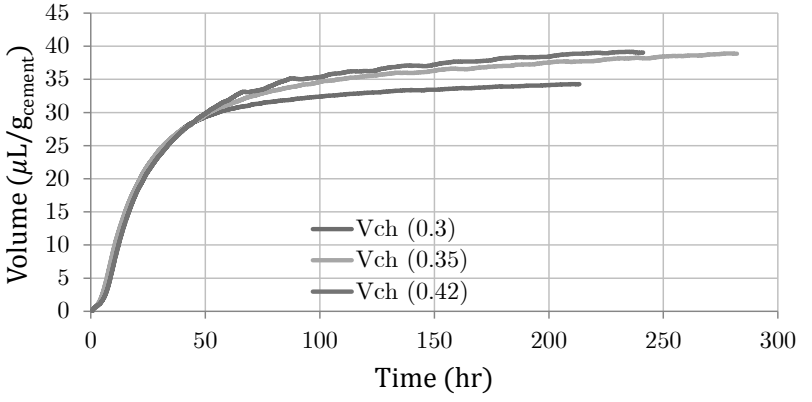

Fig. 3: Chemical shrinkage test under 5 MPa for different w/c ratios. V_{ch} is the total volume injected into the vessel.

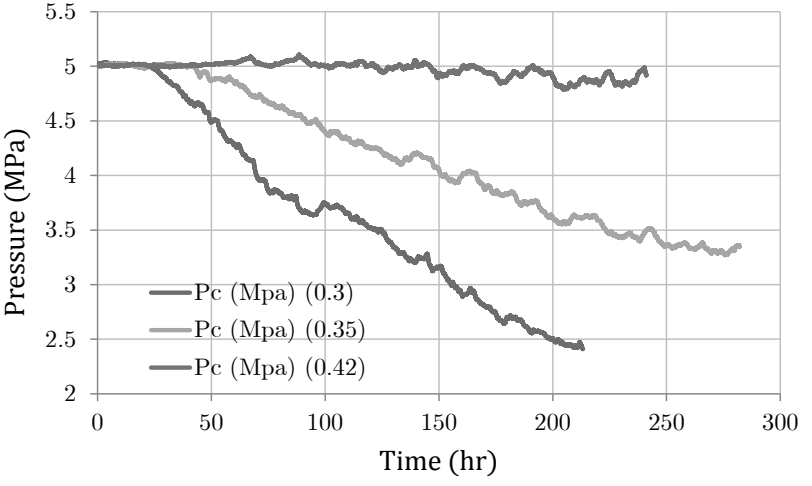

Fig. 4: Corresponding pressure measurement of samples shown in Fig. 3. P_c is the liquid pressure measured at the bottom of the specimen measured by PT-3.

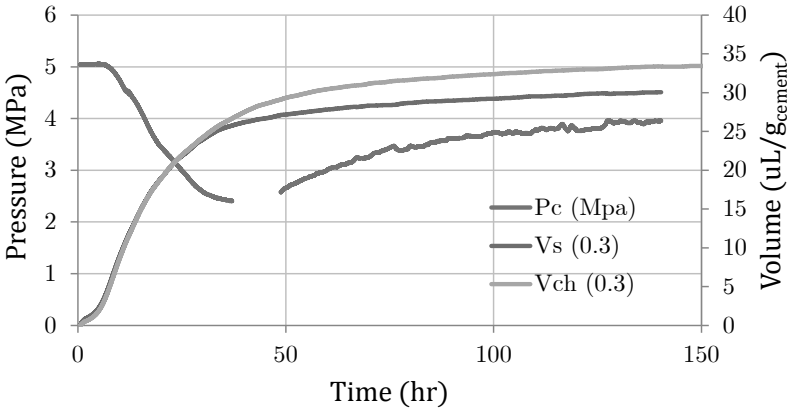

Fig. 5: Macroscopic volumetric changes under sealed conditions with 5 MPa applied pressure load. P_c is the pressure at the bottom of the specimen measured by PT-3 under sealed conditions. V_s is the volume injected inside the vessel through port-1 under sealed conditions. V_{ch} is the volume injected inside the vessel under open conditions (chemical shrinkage) measured in a separate experiment under the same conditions.

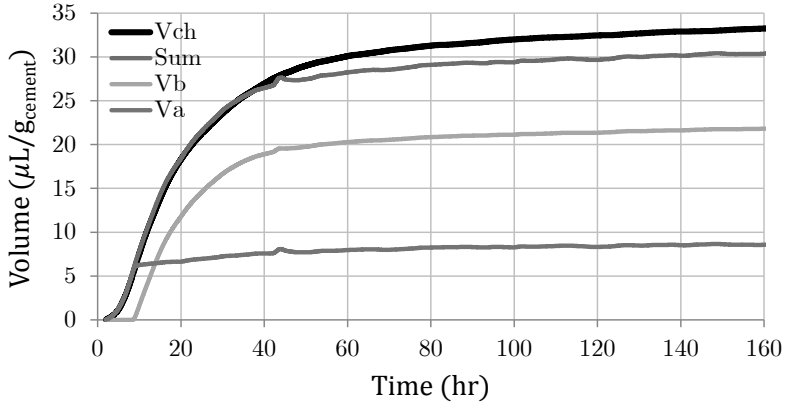

Fig-6: A general test run under 1 MPa with valve-3 closed until the pressure measured by PT-3 dropped to 0.96 MPa at around 8.5 hours. V_b is the volume injected through port-3. V_a is the volume injected through port-1. $Sum = V_a + V_b$. V_{ch} is the chemical shrinkage measured in a separate experiment under the same conditions.

DISCUSSION

In this study, chemical shrinkage is quantified by measuring the volume of water injected inside the vessel under controlled pressure as shown in Fig. 2 (a). In addition to the measured volume, a pressure transducer mounted at the bottom of the specimen, allows monitoring the evolution of the pore pressure as the specimen hydrates, as shown in Fig. 4 for three different water-to-cement ratios. The time at which the pressure drops appears to be related to the de-percolation of the capillary porosity. In fact, Bentz (Bentz, 2006), estimates the complete de-percolation of OPC samples with w/c = 0.35 to occur at around 72 hours. The results show that the rate of pressure decrease is the higher the lower the w/c ratio. Yet, it should be noted that during the observation period, no negative liquid pressure was measured. Otherwise said, capillary effects can be excluded.

Such a liquid pressure drop is also observed under sealed conditions as shown in Fig. 5, with an onset of the pressure drop that relates most likely to the percolation of the solid skeleton. It should be also noted that the pressure rise observed after 30 hours is attributed to a leakage of liquid from the top flowing around the (shrinking) specimen. In all cases, during the observation period, no negative pre pressure was recorded, which excludes for the w/c=0.3 material capillary forces as a driving force of skeleton deformation. It should be noted that the bulk deformation recorded in this test includes possible autogeneous shrinkage deformation and creep deformation under the 5 MPa pressure load.

The general test separates, by design, volume change measurements from the water mass absorbed; as shown for a w/c=0.3 cement paste subjected to a $\sigma = -1$ MPa (compressive) stress in Fig-6. To achieve this separation, the test starts as a sealed test. As in the sealed test, a pressure drop is recorded. When the pore pressure drops to $p = 0.96$ MPa, valve-3 is opened to deliver pressurized water at exactly this pressure, $p = 0.96$ MPa. That is, in contrast to both the chemical shrinkage test and the autogeneous shrinkage test, the pore pressure is controlled in this test, and allows achieving a constant effective stress, here $\sigma + p = -0.04$ MPa. At this (close-to-zero) effective stress, a small volume change still occurs (curve V_a in Fig. 6), which could be considered as the true skeleton shrinkage at (almost) zero effective stress. In return, a substantial amount of water is absorbed by the sample (curve V_b in Fig. 6). Interestingly, the sum of both curves (curve SUM in Fig. 6) almost perfectly matches the results of the chemical shrinkage test for the same material and testing conditions up to 50 hrs. The slight divergence, thereafter, may be due to an evolving effective stress under chemical shrinkage conditions (analogous to Fig. 4). As the pressure drops, the effective stress magnitude increases, causing creep of the hydrating solid in chemical shrinkage conditions; in excess of the sum of the true skeleton shrinkage (curve V_a in Fig. 6) and water absorption (curve V_b in Fig. 6).

CONCLUSIONS

An apparatus was designed and built to measure the volumetric changes occurring in hydrating cement pastes at early ages. With this apparatus, volumetric changes can be measured under sealed or saturated conditions while simultaneously measuring the bulk shrinkage and the water absorption. While we observe pore pressure drops in the hydrating cement paste even in the presence of an infinite supply of pressurized water (i.e. chemical shrinkage test), bulk shrinkage occurs even in the absence of negative liquid pressure. That is, at (very) early ages, other driving forces than capillary forces are at work to cause bulk shrinkage. The identification of these driving forces is focus of ongoing research.

REFERENCES

Barcelo, L., Moranville, M., Clavaud, B., (2005). Autogenous shrinkage of concrete: a balance between autogenous swelling and self-desiccation. Cement and Concrete Research 35, 177–183.

Bentz, D.P., (2006). Capillary Porosity Depercolation/Repercolation in Hydrating Cement Pastes Via Low-Temperature Calorimetry Measurements and CEMHYD3D Modeling. Journal of the American Ceramic Society 89, 2606–2611.

Bouasker, M., (2006). Improved measurement methods for autogenous shrinkage of cement mortars at very early age. RILEM Publications.

C01 Committee, (2007). Test Method for Chemical Shrinkage of Hydraulic Cement Paste. ASTM International.

Hua, C., Acker, P., Ehrlacher, A., (1995). Analyses and models of the autogenous shrinkage of hardening cement paste: I. Modelling at macroscopic scale. Cement and Concrete Research 25, 1457–1468.

Powers, T., (1935). Absorption of Water by Portland Cement Paste during the Hardening Process. Ind. Eng. Chem. 27, 790–794.

Sant, G., Lura, P., Weiss, J., (2006). Measurement of volume change in cementitious materials at early ages: Review of testing protocols and interpretation of results. Transportation Research Record: Journal of the Transportation Research Board 1979, 21–29.

Zhang, J., Weissinger, E.A., Peethamparan, S., Scherer, G.W., (2010). Early hydration and setting of oil well cement. Cement and Concrete Research 40, 1023–1033.

Effectiveness of various superabsorbent polymers (SAP) in mitigating autogenous shrinkage of cement-based materials

V. Mechtcherine[1], C. Schroefl[2], and M. Gorges[3]

[1]Prof. Dr.-Ing., Director of the Institute of Construction Materials, Faculty of Civil Engineering, Technische Universität Dresden, 01062 Dresden, Germany; phone: +49(0)351-463-36311; email: mechtcherine@tu-dresden.de
[2]Dr. rer.nat. Dipl.-Chem., Head of Research Group for Microstructural Analysis at the Institute of Construction Materials, TU Dresden, Germany
[3]Dipl.-Ing., PhD student at the Faculty of Civil Engineering, TU Dresden, Germany

ABSTRACT

Synthetic superabsorbent polymers (SAP) were studied here as chemical admixtures in mitigating autogenous shrinkage of high-strength concrete or mortar. The sorptivity of the SAPs was quantified in saline solutions which mimicked the ionic composition of cement pore solution and in the cement pore solution itself. Ca^{2+} ions essentially modified this sorptivity. SAPs of maximum anionicity released the stored ionic solution swiftly to a large extent, whereas SAPs containing acrylamide as a comonomer retained the liquid over a longer term. These kinetics could be directly linked to the efficiency of the SAPs in mitigating autogenous shrinkage of high-strength mortar. The SAPs which released liquid freely reduced autogenous shrinkage significantly less than the more retentive SAPs. Finally, the compressive strength of the mortars under investigation was determined. It became obvious that only a well-balanced selection of SAP type and dosage in conjunction with the most appropriate amount of extra water for internal curing has no negative effect but can even lead to an increase in compressive strength.

INTRODUCTION

LYMAN described the phenomenon of autogenous shrinkage of Portland cement-based concrete in 1934 for the first time (*Lyman 1934*). This mode of intrinsic volume change is defined as the bulk deformation of a closed, i.e., sealed, isothermal, cementitious material system not subject to external forces (*Kovler and Jensen 2007*). Autogenous shrinkage is considerably smaller than drying shrinkage in normal-strength concrete and practically irrelevant in most applications. However, high-strength concrete (HSC), with a characteristic water-to-cement ratio (w/c) of far below 0.4, tends to intense autogenous shrinkage deformations as a consequence of self-desiccation (*Jensen and Hansen 2001*). Autogenous shrinkage gives rise to great cracking potential in the case of restraint (*Cusson and Hoogeveen 2007*). In contrast to drying shrinkage, autogenous shrinkage occurs over the entire volume of the specimen and thus cannot be mitigated by surface treatment, especially considering the dense microstructure of HSC. This "internal curing" (IC) by additives or

admixtures containing water was developed as an addition to classical "external curing". Polymer hydrogels, commonly called "superabsorbent polymers" (SAP) in concrete technology, evolved to be most appropriate as water-regulating admixtures apart from porous saturated light-weight aggregates (*Jensen and Hansen 2001, Mechtcherine and Reinhardt 2012*). The principle of their functioning is quite well understood to be a steady release of internally stored water into the matrix (e.g. *Lura et al. 2006, Trtik et al. 2010*, *Schroefl and Mechtcherine 2012*). In cement-based matrices, covalently crosslinked polymers of acrylic acid and acrylamide, neutralized by alkaline hydroxides, have proven efficient. They are chemically stable and can absorb the liquid portion of cement pastes during concrete preparation in significant amounts of up to several times their tenfold dry weight (*Buchholz and Graham 1998*).

The present study illustrates the structure-effect-relation among the two main chemical characteristics of acrylic acid-based SAPs (level of anionicity and degree of crosslinking) on the one hand and their performance as internal curing admixtures in HSC on the other.

EXPERIMENTAL

Materials

Nine SAP samples made of acrylic acid and acrylamide were considered (**Figure 1**). Homopolymers of acrylic acid, containing only an initiator and a crosslinker as further ingredients, correspond to the level of anionicity of one. SAP 1 has a spherical particle form whereas all others are irregularly shaped. SAPs 8 and 9 have the least feasible, near zero, anionicity.

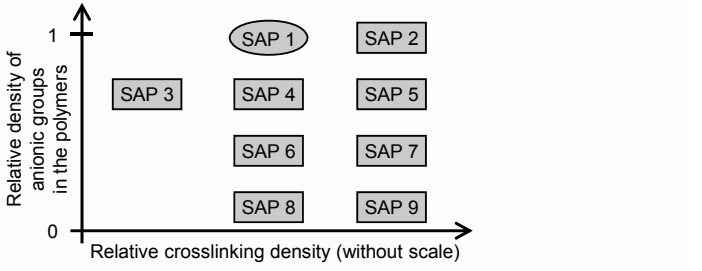

Figure 1. SAP structures with respect to anionicity and crosslinking density (polymers synthesized from the monomers acrylic acid and acrylamide)

Cement pore solution was filtered from a cement suspension prepared with distilled water (w/c = 4.3). A normal Portland cement CEM I 42.5 R according to EN 197-1 was used. Saline solutions were prepared to mimic the ionicity of the filtrate:

- pH 12.2: KOH dissolved in distilled water,
- sulphate concentration of 7 g/L and high pH value: Na_2SO_4 and KOH in dist. water,
- calcium concentration of 1 g/L and high pH value: $Ca(NO_3)_2 \cdot 4H_2O$ and KOH in distilled water.

The high strength mortar was composed according to **Table 1**.

Table 1. Mortar composition

Material	Unit mass, kg/m^3
Cement CEM I 42.5 R	700.0
Silica fume	70.0
Quartz sand 0.06/0.2	121.8
Aggregate sand 0/4	1218.0
Water (for W/C = 0.30)	210.0
PCE superplasticizer (solution, solids content 35 wt-%)	12.6

Methods and specimens

The size distributions of the SAPs were measured in a laser granulometer.

The kinetics of absorption/desorption of the SAPs were determined by the so-called "teabag method" according to the literature (*Edana 2002*, *Schroefl et al. 2012*).

The high-strength mortar (**Table 1**) was prepared in an ordinary concrete mixer. After completing the mixing, the mortar was poured into a HÄGERMANN cone (height 60 mm; upper diameter 70 mm; bottom diameter 100 mm) and the flowability tested according to DIN EN 1015-3, but without the prescribed beats. The slump flow value was registered 17 to 20 min after the initial contact of the dryly preblended powders (incl. SAPs) with the mixing water and its predissolved superplasticizer.

For internal curing the mortar was modified with SAP and extra water. Due to the absorption by the SAPs the slump flow would diminish as expected. To compensate for this and to assess the amount of liquid taken up, a series of slump flow experiments with predefined amounts of nominally increased w/c was performed. A slump flow value corresponding to that of the reference mortar of 19 ± 1 cm indicated a well-balanced mortar composition with regard to the type of SAP and the amount of IC water. After mixing, the mortar was transferred into corrugated tubes, which were immediately placed in a dilatometer and free autogenous shrinkage was recorded following ASTM C 1698-09. The recorded values were later referenced to the time of the final set (VICAT needle test). Furthermore, compressive strength was measured according to EN 1015-11.

RESULTS AND DISCUSSION

Absorption/desorption kinetics in saline solutions

Table 2 summarizes the particle size distributions of the SAPs. The particle size distributions can affect the sorption kinetics in the early minutes of the contact with liquids. However, the authors are convinced that the different chemical designs outweigh this effect by far in the medium and long terms, and such an appropriate chemical design is essential for the efficiency of the SAPs as IC agents.

Table 2. Particle size distributions of SAP samples in the dry state

	1	2	3	4	5	6	7	8	9
d10, µm	178	224	246	386	136	236	201	114	359
d50, µm	324	586	631	903	357	683	596	417	803
d90, µm	582	1029	1052	1446	555	1205	1130	828	1232

The principle behind the efficiency of SAPs as IC agents in concrete is their functioning as temporary reservoirs of water. The SAP particles absorb the water by osmosis. Pore solutions of Portland cement-based construction materials feature a high pH value, Ca^{2+} at saturation levels (typically about 1 g/L) and significant amounts of SO_4^{2-}, K^+ and Na^+. To characterise the effects of each of these ions on absorption/desorption kinetics of the SAP samples, saline model solutions and extracted cement pore solution were used as liquid media. KOH provided the alkaline pH value. Sulphate and calcium were then introduced separately. In each case monovalent counter-ions were present, which did not significantly screen more intense interactions between the bivalent ions and the SAPs. In KOH solution only and in that containing sulphate, K^+ and Na^+, all SAPs absorbed the liquid rapidly within a few minutes and retained it for more than three hours.

On the contrary, Ca^{2+} decisively altered the sorptivity of most SAP samples. SAPs 1 and 2, with the highest level of anionicity, i.e., with the highest density of anionic functional groups, released the majority of initially absorbed liquid from 15 minutes onwards. The other SAPs either lost just a very minor portion (SAP 4) or kept the mass constant for the time of the measurement. Any one of the SAPs behaved similarly to this alkaline Ca^{2+} solution in the cement pore solution (**Figure 2**), which proves that Ca^{2+} is the pivotal ion with respect to sorptivity. A mechanistic explanation can be given according to *Plank and Sachsenhauser 2009*, who published results of a comparable study with polycarboxylate-based superplasticizers. Ca^{2+} will efficiently screen the anionic groups of the SAPs by thorough complexation. This causes a decrease in the osmotic pressure and consequently the collapse of the storage function. This is most pronounced in the highly anionic SAPs 1 and 2. To a very little extent this can be observed with SAPs 4 and 5 as well. The SAPs with the least anionicity are unaffected by Ca^{2+}. They swell much more slowly and to a significantly lesser degree in principle because they generate only a quite weak osmotic pressure in any case. The crosslinking density determines the final, achievable level of absorption of the SAPs. It plays a minor role compared to that of the anionicities, and Ca^{2+} has no influence.

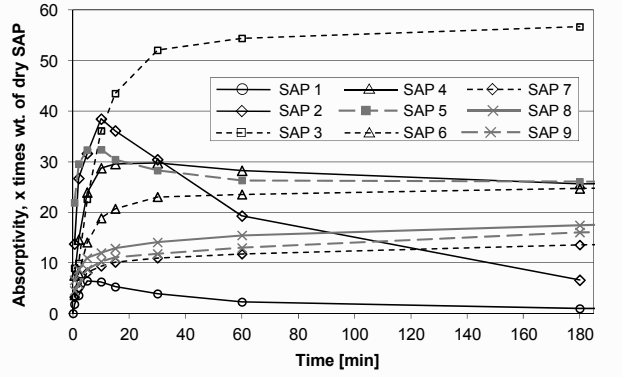

Figure 2. Absorptivity of SAP samples in cement pore solution

Influence of the SAPs on the workability of high-strength mortar

In mortar SAPs take up distinct amounts of water, which they withdraw from the cement matrix and which accordingly cannot support the flowability of the paste. To compensate for this, an additional amount of mixing water was added in the present study; **Figure 3** shows a representative selection. This water is called "IC water" because it is provided to the matrix over time, especially after the final set. All SAPs were dosed 0.3 wt-% by weight of cement because it had been proven that this dosage mitigates autogenous shrinkage efficiently (cf. **Figure 4**). The w/c had to be increased by 0.02 to 0.06 units except SAP 3, whose absorptivity was excessive, leading to a w/c = 0.56.

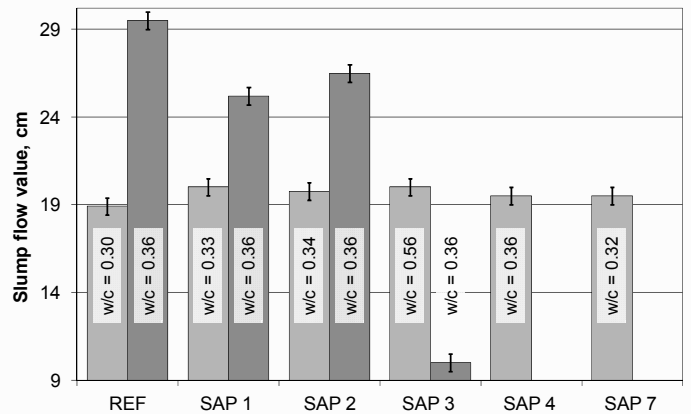

Figure 3. Slump flow from HÄGERMANN cone for a selection of the mortars with 0.3 wt-% SAP by weight of cement and adjusted w/c

The absorptivity and, thus, the molecular structure of the SAPs are directly linked with the workability of the mortar. The absorptivity should be considered in the time span from 17 to 20 minutes after the initial contact of the dry mortar components (including SAP) with water. This time interval is indeed that of the slump flow test. Until this time, SAP 3 had absorbed the largest amount of liquid, and absorption continued steadily on. In contrast, SAPs 7 to 9 absorbed just a minor amount and further absorption proceeded very slowly and quite weakly. Consequently, they needed the least increments in the w/c. The other SAPs were situated between SAP 3 on the upper and SAPs 7 to 9 on the lower level.

Mitigation of autogenous shrinkage by SAP

The main focus of the present study lay on the propensity of the SAPs to mitigate free autogenous shrinkage of the high-strength mortar; see **Figure 4**, each curve being the average of three independent measurements. All types of SAP significantly reduced autogenous shrinkage. The excessively high w/c of 0.56 (SAP 3) would practically by itself not cause autogenous shrinkage (*Jensen and Hansen 2001*). When dosages lower than 0.3 % are used, e.g., 0.1 or 0.2 %, and the w/c is

adjusted according to the flowability test, the mitigation of autogenous shrinkage is still very pronounced (*Schroefl et al. 2012)*. The mechanisms causing the apparent expansion are a topic of ongoing scientific research and discussion (cf. e.g. *Sant et al. 2011)*.

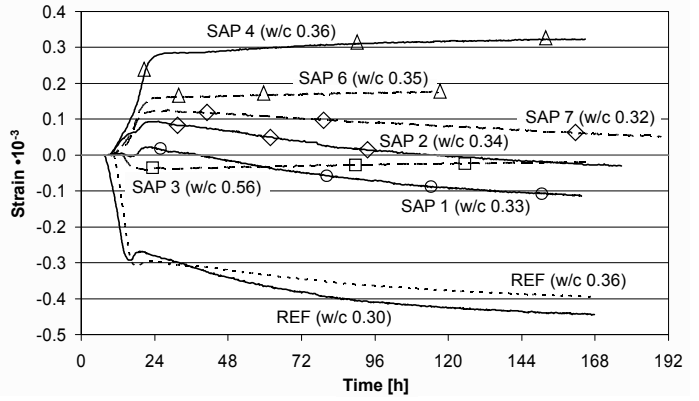

Figure 4. Free autogenous shrinkage of the mortars (according to ASTM C 1698-09); SAP dosage 0.3 wt-% bwoc, w/c adjusted according to Figure 3

Effect of SAP and extra water on the compressive strength of the mortar

Each SAP particle introduces into the binder matrix a void that may cause a distinct degrading of its mechanical performance when compared to a SAP-free reference mortar. Compressive strength was tested to assess this concern (**Figure 5**).

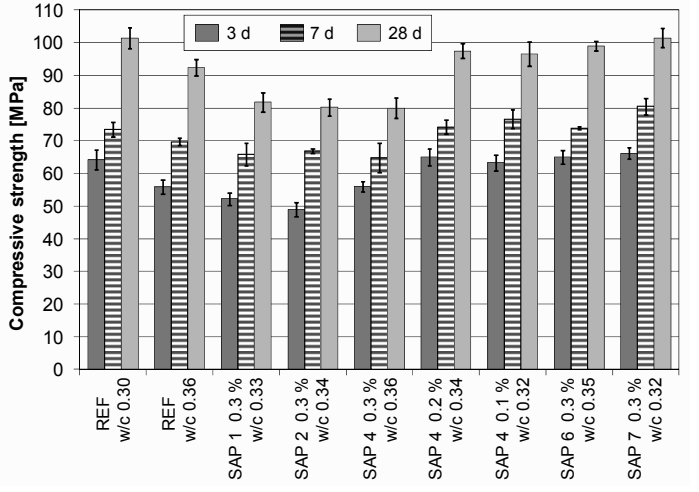

Figure 5. Compressive strength of the mortars (according to EN 1015-11)

None of the highly efficient SAPs with respect to mitigation of autogenous shrinkage, especially SAPs 4, 6 and 7, led to severely diminished compressive strengths. The kinetics of ab- and desorption inherent in the SAPs thus play a decisive role for their performance in the high-strength mortar. Obviously, the freely releasing SAPs 1 and 2 set their water free too readily. This weakens the matrix due to an apparently increased w/c, in addition to weakening the matrix because of the voids left behind by the SAPs. Some positive effects of IC on mechanical properties may result from continuous hydration and therefore a denser microstructure as well as from the decrease in internal stresses caused by the different propensities to shrinkage of matrix and aggregates. All retentive SAPs have the potential rather to improve than worsen the mechanical properties of HPC if their dosage and the amount of IC water are carefully equilibrated.

SUMMARY AND CONCLUSIONS

Various synthetic superabsorbent polymers based on acrylic acid and acrylamide have been investigated with respect to their structure-effect-relation in mitigating autogenous shrinkage of a Portland-cement-based, high-strength mortar.

The kinetics of free absorption and, potentially, desorption, are decidedly determined by the presence of Ca^{2+} ions dissolved in the cement pore solution as well as by the relative level of anionicity and crosslinking density of the polymers themselves. These kinetics could be directly related to the efficiency of the mitigation of autogenous shrinkage.

All SAPs under investigation efficiently counteracted free autogenous shrinkage of the high-strength mortar; even expansion of the mortar was observed. Over the long term, the freely releasing SAPs lost their efficiency after the first day and the strain-time curves turned parallel to the SAP-free references. But even in this way autogenous shrinkage was reduced to a large extent. On the contrary, mortars prepared with non-free-releasing SAPs remained in the “expanded” state for at least the duration of the measurements (7 days).

Finally, the compressive strengths of the high-strength mortars were recorded. SAP and a well balanced amount of extra water for internal curing did not negatively affect this crucial property.

In conclusion it should be pointed out which aspects should be considered for a most beneficial use of SAP to mitigate autogenous shrinkage and provide efficient internal curing in high-strength mortar:

- The SAP should quickly absorb a significant but not exaggerated amount of cement pore solution and keep this stored for several hours;
- A SAP dosage of some 0.1 to 0.3 wt-% by weight of cement is well suitable;
- The most important point is a careful adjustment of internal curing water to the sorption capacity of the SAP. This amount can, e.g., be estimated via a mini-slump test. The w/c may be increased by 0.02 to 0.06 units based on an initial w/c of 0.30. This does not affect the compressive strength of the mortar negatively.

ACKNOWLEDGMENTS

The authors gratefully thank SNF Floerger (Andrézieux Cedex, France) for the generous supply of SAP samples.

REFERENCES

Buchholz, F. L., and Graham, A. T. (1998). "Modern superabsorbent polymer technology", WILEY-VCH, New York, 304 pp

Cusson, D., and Hoogeveen, T. (2007). "An experimental approach for the analysis of early-age behaviour of high-performance concrete structures under restrained shrinkage", *Cem. Concr. Res.,* 37(2), 200-209

Jensen, O. M., and Hansen, P. F. (2001). "Water-entrained cement-based materials: I. Principle and theoretical background", *Cem. Concr. Res.*, 31(4), 647-654

Kovler, K., and Jensen, O. M., eds. (2007). "Internal curing of concrete. State-of-the-art report of RILEM Technical Committee 196-ICC. RILEM Report 41", RILEM Publications, Bagneux, 161 pp

Lura, P., Durand, F., and Jensen, O. M. (2006). "Autogenous strain of cement pastes with superabsorbent polymers", *RILEM Proceedings PRO 052*, O. M. Jensen, P. Lura and K. Kovler, eds., RILEM Publications, Bagneux, pp. 57-66.

Lyman, G. C. (1934). "Growth and movement in portland cement concrete", Oxford University Press, London, 139 pp

Mechtcherine, V., and Reinhardt, H.-W., eds. (2012). "RILEM State-of-the-art report: Application of super absorbent polymers (SAP) in concrete constructions, state of the art report prepared by Technical Committee 225-SAP", Springer, Heidelberg, 164 pp

Plank, J., and Sachsenhauser, B. (2009). "Experimental determination of the effective anionic charge density of polycarboxylate superplasticizers in cement pore solution", *Cem. Concr. Res.*, 39(1), 1-5

Sant, G., Lothenbach, B., Juillant, P., Le Saout, G., Weiss, J., and Scrivener, K. (2011). "The origin of early expansions induced in cementitious materials containing shrinkage reducing admixtures", *Cem. Concr. Res.,* 41(3), 218-229

Schroefl, C., Gorges, M., and Mechtcherine, V. (2012). "Relation between the molecular structure and the efficiency of superabsorbent polymers (SAP) as concrete admixtures to mitigate autogenous shrinkage", *Cem. Concr. Res.*, 42(6), 865-873

Schroefl, C., and Mechtcherine, V. (2012). "Superabsorbent polymers to mititgate autogenous shrinkage of cement mortar", Malhotra, V. M., ed., 10th international conference on superplasticizers and other chemical admixtures in concrete, *SP-288-18*, ACI, Farmington Hills (MI), pp. 265-278

Edana (2002). "Recommended test method: superabsorbent materials – polyacrylate superabsorbent powders – free swell capacity in saline solution by gravimetric determination, 440.2-02", European disposables and nonwovens association, ed., Edana recommended test methods, Brussels, pp. 297-301

Macrocrack propagation in a concrete specimen subjected to a sustained loading: influence of tensile creep

Pierre Rossi, Jean-Louis Tailhan

Institut Français des Sciences et Technologies des Transports, de l'Aménagement et des Réseaux (IFSTTAR), Université Paris-Est, cité Descartes, 4-20 bd Newton, 77447 Champs-sur-Marne-Marne-la-Vallée Cedex2,France; PH :33-680017226; email : pierre.rossi@ifsttar.fr

ABSTRACT

Structures managers need a better prediction of the delayed failure of concrete structures, especially for very important structures like nuclear power plant encasement. Sustained loadings at high level (above 75% of loading capacity of the structure), can lead to structure failure after some time. In this study, a series of 4-point bending tests were performed in order to characterize the creep behaviour of pre-cracked beams under high load level. The specimens were made of normal strength concrete. A power law relationship is observed between the secondary deflection creep rate and the failure time. It is also shown that when crack propagation occurs during the creep loading, the creep deflection rate increases with the creep loading level and with the crack propagation rate.

INTRODUCTION

The delayed failure of concrete structures under sustained loading has been an important issue for researchers and structure managers for a long time. Among other topics, the progression to failure of a structure with a localized macrocrack, subjected to a sustained loading, needs a better understanding.

In the past some researchers worked on the interaction between crack propagation and time dependence behaviour of concrete (Rüsch (1960), Smadi et al. (1985), Rossi (1989), Rossi and Boulay (1990), Bazant and Gettu (1992), Zhou (1992), Carpinteri et al. (1997), Denarié (2000), Mazzotti and Savoia (2002), Denarié et al. (2006), Omar et al. (2009)).

The scientific objective of the present work is to understand the physical mechanisms involved in the possible coupling between crack propagation and delayed behaviour of concrete.

The industrial objective is more concerned with the case of the containment vessel of a nuclear power plant.

As regards nuclear civil engineering, safety requirements specify durability of

then containment vessel functionalities in terms of stability and confinement. This requirement is very different from classical functionalities in buildings and can be very demanding.

To operate nuclear power plants (NPP), EDF (the French operator) must justify to the French safety authority the capability of the containment to ensure, in case of an accident, a leak rate lower than 1.5% per day of the total mass of fluids. To evaluate, this possible leak rate, experimentally, each containment structure undergoes every 10 years a leakage test at 0.53 MPa in dry air and at atmospheric temperature (the duration of this leakage test is around 3 days). In this case the leak rate should not exceed 1% (in total). If it is not the case, repairs are needed to improve the tightness of the containment. Of course, these repairs in a nuclear context are very expensive and if the nuclear power plant is not allowed to operate, the losses are very important (about 1 M€ per day).

During this leakage test, existing cracks in the structure can propagate. So, it is very important to evaluate the cracking evolution.

CONCRETE STUDIED

In order to evaluate the basic mechanical characteristics (compressive and tensile strengths) of the studied concrete, uniaxial tensile and compression tests were performed. Compression tests were carried out at different ages, 7, 14, 28, 64, 90, 180 days, to study the evolution of the concrete strength. For the uniaxial tension tests, 1 expiry at 64 days was taken into account. Six specimens per concrete age were tested both for compression and uniaxial tension tests. Table 1 summarizes the results obtained

Table 1. Concrete mechanical characteristics in static

Mechanical characteristic (MPa)	Compression						Tension
Concrete age (days)	7	14	28	64	90	180	64
Average value (MPa)	31.2	35.1	39.9	42.2	44.4	51.2	2.8

EXPERIMENTAL PROGRAM AND SET-UPS

This experimental study focuses on 4-point bending tests of one beam size: 200 mm height, 150 mm width and 700 mm face to face. Twenty-four hours after casting, the specimens were demolded and protected from drying by two layers of an auto-adhesive aluminum and stored in a temperature and humidity controlled room.

The beams were bended under a 4-point loading, each point load spaced at 200 mm. The beams under high-creep load level were tested under a 100 kN hydraulic testing machine. This set-up is also used for pre-cracking of beams and beam characterization. The beams are instrumented with a deflection measurement at mid-point of the beam. This apparatus is fixed at two points directly upon the lower bearings (figure 1). This disposition ensures that there is no influence of bearing deformations on the measurements. Another measurement system (LVDT) is used to evaluate the horizontal displacement (displacement parallel to the specimen length) at a certain level of the specimen width in the tensile zone. This measurement is made at 25 mm of the inferior fibre of the specimen (figure 1). The measurement basis of this horizontal displacement, called in this work D25, is 200 mm.

Figure 1. Test set-up for bending creep test on cracked specimens

Concerning the static test for beam characterization, six specimens were tested. The concrete age when these specimens are loaded is 28 days.

Concerning the step related to the pre-cracking of the specimens, the strategy adopted is the following:

- From the bending stress versus deflection average curve (obtained with the static tests), a deflection value related to the post-peak behaviour is chosen. It is called δ_0. This value corresponds to a certain length of macrocrack and to a certain value of loading force on the specimen, called P_0.
- So, for the specimens which will be loaded in creep, the first step corresponds to a static loading until the deflection δ_0.

After having created the initial crack, the specimen is unloaded. From this point, the specimen is reloaded until a force corresponding to a given percentage of P_0. This force is called P_S (Figure 2). The maximal duration of the creep loading on this machine does not exceed 3 days. After this duration, the test is stopped.

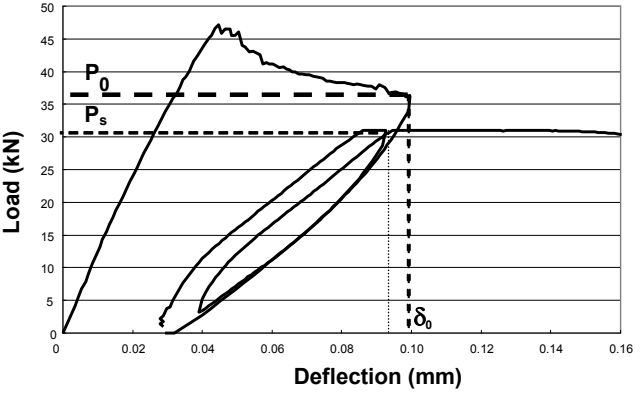

Figure 2. Load-deflection curve – Procedure adopted for the creep loading

During the creep loading, unloading/reloading cycles are performed to follow the compliance evolution of the specimen (Figure 3). The objective is to determine eventual crack propagation during creep.

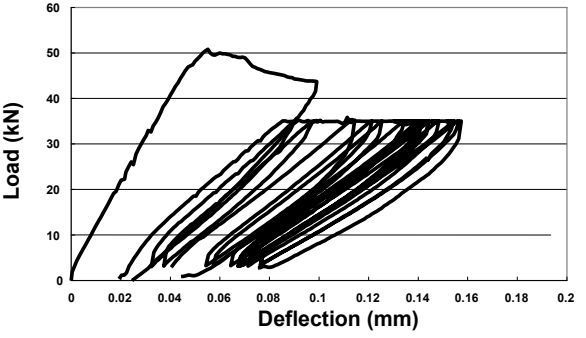

Figure 3. Example of unloading/reloading procedure during the creep loading

EXPERIMENTAL RESULTS

Figure 4 provides relation (in log-log scale) between time to failure and the secondary deflection creep rate. This secondary deflection creep rate is not available for all tests (see table 2) due to problems with the deflection measurement. Table 2 provides all the results related to the tests.

Figure 5 provides the curves of the compliance evolution during time. The compliance evolution is equal to C (t) – C_S where C (t) is the specimen compliance at time t during the creep loading and C_S is the specimen compliance just before the creep loading.

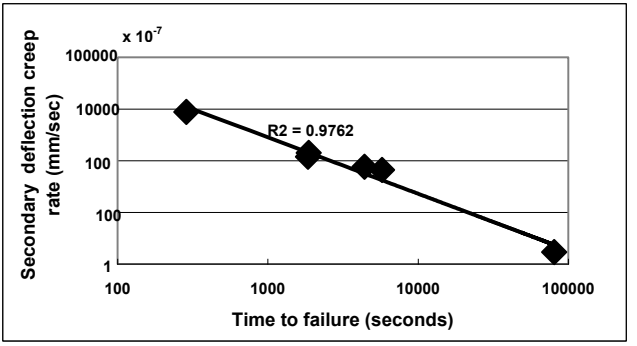

Figure 4. Secondary deflection creep versus time to failure

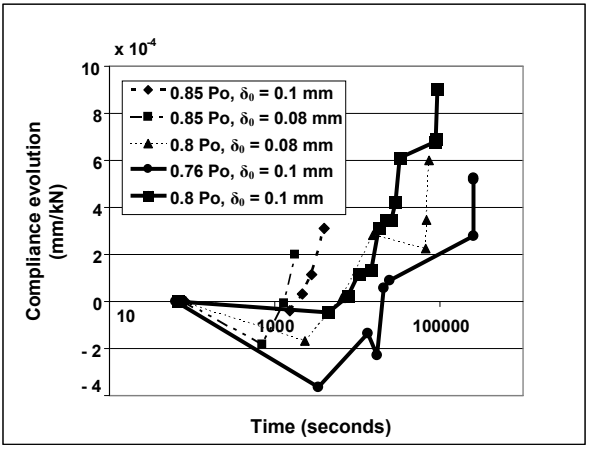

Figure 5. Compliance evolution versus time

ANALYSIS OF RESULTS

Figure 4 proves that crack propagation is strongly linked to the delayed behaviour of concrete.

A look of Figure 5 leads to the following remark: crack propagation (at time t of the creep loading, positive evolution of the compliance is only attributable to macrocrack propagation) always occurs after negative evolution of the compliance.

Table 3 provides the relationship among the relative evolution rate, the creep loading level and the secondary displacement (D25) creep rate (The number of values related to the secondary deflection rate are not sufficient, see Table 3). This relative evolution rate is given by $C(t) - C_S / C_S$.

Figure 6 provides the curve related to the relative evolution rate of the compliance as a function of the secondary displacement (D25) creep rate.

Table 2. Series of bending creep test - Different results

Concrete age at loading (days)	P_S/P_0	δ_0 (mm)	Time to failure (Seconds)	Cycles Yes/No-Number	Secondary deflection creep rate (x 10^{-7}mm/s	Secondary displacement (D25) creep rate (x 10^{-7}mm/s)
60	0,80	0,1	Stop of the test (80575)	No	1.7	1.7
56	0,85	0,1	1852	No	119	151
67	0,85	0,1	4400	Yes - 4	75.9	86.5
68	0,88	0,1	287	No	877	1070
68	0,85	0,1	5750	No	66.5	80.7
80	0,85	0,08	1874	Yes - 3	142	231
84	0,80	0,08	72716	Yes - 6	No	2.7
88	0,76	0,1	Stop of the test (252594)	Yes - 8	No	0.311
86	0,80	0,1	93713	Yes - 12	No	6.15
187	0,85	0,1	533	No	306	378
189	0,84	0,1	590	No	190	225

Table 3. Relative evolution rate of the compliance

P_S/P_0 (%)	80	80	85	85
$[(C(t)-C_S)/ C_S] \times t^{-1}$ (x 10^{-4} s^{-1})	0.02	0.03	0.5	1
Secondary displacement (D25) creep rate (x 10^{-7}mm/s)	2.7	6.15	86.5	231

From Table 3 and figures 6, the following remarks can be made when the crack propagates continuously during the creep loading (continuous increasing of the compliance):

- Crack propagation rate (represented by the relative evolution rate of the compliance) increases with the creep loading level.
- Crack propagation rate increases with the secondary displacement (D25) rate.
- Macrocrack propagation being directly (locally) linked to the displacement (D25) evolution, it is reasonable to make the following proposal: during creep loading, the secondary concrete specimen creep is the consequence of stable macrocrack propagation.

In others words, stable macrocrack propagation is at the origin of the secondary cracked specimen creep. This conclusion has to be linked to the fact that basic creep of concrete in tension is very low compared with basic creep in compression. As a matter of fact, an experimental study previously performed at IFSTTAR (Rossi et al. (2012)) on the same concrete has clearly shown that basic creep in tension is 3 times lower than in compression. Figure 7 provides this comparison between basic creep in tension and in compression.

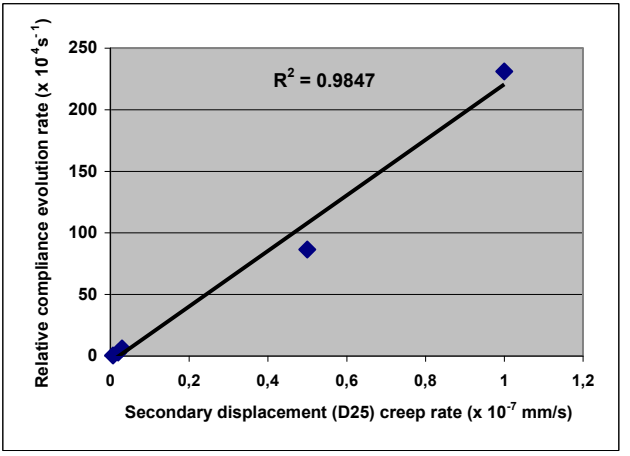

Figure 6. Relative evolution of the compliance rate versus the secondary creep displacement (D25) rate

The proposed physical approach permitting to explain this result can be summarized as follows: that ***basic creep is mainly due to microcracking which induces additional self-drying shrinkage.***

If this physical assumption is considered at the level of the process zone (microcracking zone at the macrocrack front tip), it is easy to understand why concrete creep can not explain the delayed behaviour of the cracked specimen and why before the crack propagation, a decrease of the specimen compliance is observed.

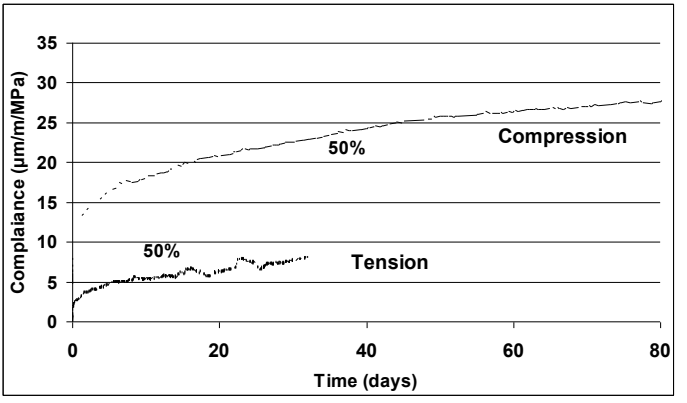

Figure 7. Comparison between basic creep in tension and in compression (after Rossi et al. [12])

REFERENCES

Bazant, Z.P., and Gettu, R. (1992) "Rate effects and load relaxation in static fracture of concrete." *ACI Materials Journal*, 89(5).

Carpinteri, A., Valente, S., Zhou, F.P., Ferrara, G., and Melchiorri, G. (1997) "Tensile and flexural creep rupture tests on partially-damaged concrete specimens." *Materials and Structures,* 30, 269-276.

Dénarié, E. (2000) "Etude expérimentale des couplages viscoélasticité-croissance des fissures dans les bétons de ciment." *Swiss Federal Institute of Technology, Lausanne*, Doctoral Thesis no. 2195 (in french).

Denarié, E., Cécot, C., and Huet, C. (2006) "Characterization of creep and crack growth interactions in fracture behavior of concrete." *Cement and Concrete Research*, 36, 571-575.

Mazzotti, C., and Savoia, (2002) M. "Nonlinear creep, Poisson's ratio, and creep-damage interaction of concrete in compression", *ACI Materials Journal*, 99(5).

Omar, M. et al. (2009) "Creep-damage coupled effects: experimental investigation on bending beams with various sizes." *Journal of Materials in Engineering*, ASCE 21 (65).

Rossi, P. (1989) "Coupling between the crack propagation velocity and the vapour diffusion in concrete." *Materials and Structures*, 22, 91-97.

Rossi, P., and Boulay, C. (1990) "Influence of free water in concrete on the cracking process." *Magazine of Concrete Research*, 42(152), 143-146.

Rossi, P., Tailhan, J.L., Le Maou, F., Gaillet, L., and Martin, E. (2012) "Basic Creep Behaviour of Concretes. Investigation of the physical mechanisms by using acoustic emission." *Cement and Concrete Research*, 42, 61-73.

Rüsch, H. (1960) "Researches toward a general flexural theory for structural concrete." *ACI Journal*, Proceedings, 57, 1-28, July.

Smadi, M.M,. Slate, F.O., and Nilson, A.H. (1985) "High-, medium-, and low-strength concretes subject to sustained overloads- strains, strengths, and failure mechanisms." *ACI Journal*, 657-664.

Zhou, F.P. (1992) "Time-Dependent Crack Growth and Fracture in Concrete.(1992)." *TVBM-1011, University of Lund, Sweden*, Ph.D. Thesis.

Experimental Research and Numerical Simulation of Post-Crack Creep Behavior of SFRC Loaded in Tension

Guanyu Zhao[1], Marco di Prisco[2] and Lucie Vandewalle[1]

[1]Department of Civil Engineering, KU Leuven, Kasteelpark Arenberg 40, Heverlee, B3001, Belgium; email: guanyu.zhao@bwk.kuleuven.be, lucie.vandewalle@bwk.kuleuven.be
[2]Department of Civil and Environmental Engineering, Politecnico di Milano, Piazza Leonardo da Vinci, 32 20133 Milano; email: marco.diprisco@polimi.it

ABSTRACT

This paper mainly studies uniaxial tensile creep behavior of pre-cracked steel fiber reinforced concrete (SFRC). A series of uniaxial tensile creep tests were carried out on SFRC cylinder specimens which were pre-cracked at 0.2mm. The pre-cracked specimens were loaded at the load level of 30% of maximum pre-cracking load for three months under constant temperature of 20 degrees and relative humidity of 60%. Time dependent crack opening displacements (COD) were continuously measured by LVDTs. For the specimens with pre-cracking COD of 0.2mm, the maximum creep deformation is almost the same as the initial elastic deformation. Among the various rheology models, Burgers model was employed to describe the creep behavior. A damage factor was introduced in order to consider the gradual debonding behavior at the fiber/matrix interface.

INTRODUCTION

In order to improve the durability and structural integrity of building materials, steel fiber reinforced concrete (SFRC) has been developed over the past decades. SFRC has great advantages over traditional concrete in terms of crack resistance ability and ductility under tensile loading. The load bearing capacity of SFRC in tension is improved due to fiber pullout behavior. Moreover, as steel fibers are randomly distributed and oriented, it can be considered as a smeared reinforcement, which will ensure a more favorable crack distribution and limit crack width at serviceability limit states (SLS). Although FRC has a better performance in the post-crack regime, it still suffers from time dependent deformations under sustained tensile load. This time dependent deformation is considered as tensile creep behavior of cracked FRC, which will lead to serviceability problems such as stress redistribution, significant crack width increase and even creep failure.

The study on creep behavior of compressed concrete has been carried out for several decades. Detailed discussions of this phenomenon can also be found in Bazant [1]. Differently from compressive creep of concrete, the tensile creep of cracked SFRC is actually considered as a time dependent fiber pullout which is influenced by the debonding behavior at the fiber/matrix interface. In order to study

such behavior at the macro level, an artificial crack opening needs to be introduced before the creep test. Some research could be found on the flexural creep behavior of cracked FRC beams and shotcrete panels. Kurtz [2] studied post-crack flexural creep behavior of polypropylene and nylon fiber reinforced concrete at different stress levels. He found that sustainable stress levels for both fibers are less than 38% of average residual strength (ARS) which is much lower than the post-crack strength. MacKay [3] reported one year flexural creep results of pre-cracked steel and synthetic FRC beams under different load levels (20, 40 and 60% ARS). He found that the cracked synthetic FRC specimens failed no more times due to flexural creep than the cracked steel FRC specimens. Bernard [4] did flexural creep test on cracked fiber reinforced shotcrete (FRS) panels with steel fibers and macro-synthetic fibers respectively. He found post-crack creep for macro-synthetic FRS panels is more sensitive to load level than steel FRS panels. Kusterle [5] tested flexural creep behavior on cracked beams reinforced with steel fiber and synthetic fibers respectively at the same load level of 50% ARS. The midspan deflection was measured continuously for 3 years. He found cracked beams reinforced by synthetic fibers had higher deformation. He also observed tertiary creep and rupture of beams with polymer fibers at a load level of 60% ARS after 500 days.

The main scope of this study is to investigate the uniaxial tensile creep behavior of cracked SFRC in the softening branch. The SFRC specimens were firstly pre-cracked at 0.2mm before the creep test. A robust pre-cracking setup and the creep frame with a lever system were developed and validated previously. The notched SFRC specimen could be successfully pre-cracked at 0.2mm with combination of load and crack opening control. During the creep test, the time dependent crack opening and the drying shrinkage were measured continuously. A uniaxial tensile test was performed with several unloading-reloading loops in order to study the damage development at the fiber/matrix interface in terms of the stiffness degradation at different COD levels.

EXPERIMENTAL PROGRAM

The experimental program investigates the uniaxial tensile creep behavior of cracked steel fiber reinforced concrete specimens. 16 and 14 prismatic specimens with dimension of 150×150×660mm were cast respectively in two times. The concrete mixture design is the same for the two batches of concrete as shown in table 1. The prismatic specimens were demoulded one day after the casting, and they were cured for 28 days in the environmental chamber with temperature of 20 degrees and a relative humidity of 90%.

The fiber used is a hooked-end steel fiber (RC65/60BN). The fiber content is equal to 80kg/m^3. Steel fibers are low-carbon, 60mm long and with aspect ratio (length/diameter) of 65. The average compressive strength after 28 days is around 45MPa and the density is around 2.45g/cm^3.

The whole experimental program of post-crack creep testing of SFRC specimen consists of 3 different phases as shown in figure 1. The first phase refers to the mechanical characterization of the material; three point bending tests were carried out on the notched prismatic specimens according to EN14651. Once tested, two

cylinder specimens with dimension of 100mm in diameter and 300mm in length were cored from each prismatic specimen. In the second phase, the pre-cracking test was executed. The cylinder specimen was pre-cracked manually at a certain crack opening before the creep test. The last phase is the long-term creep test. The cylinder specimen was mounted on the tensile creep frame immediately after the pre-cracking. The time-dependent crack opening under uniaxial tension was continuously measured for 3 months in the environmental curing chamber with constant temperature of 20 degrees and a relative humidity of 60%.

Table 1. Concrete mixture design

Constituent	Type	Content(kg/m^3)
Cement	I 42.5R	350
Aggregates	0/4 sand	835
	4/14 gravel	1099
Water		175
Superplasticizer	G51	1.05
Fiber	RC65/60BN	80

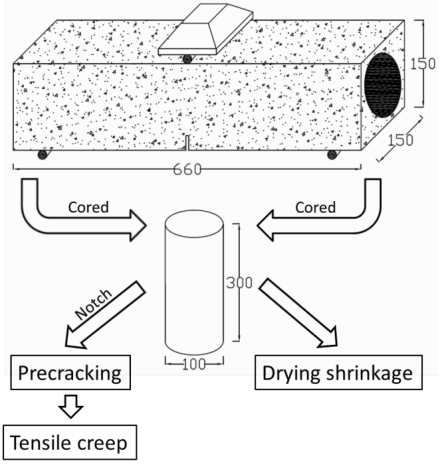

Figure 1. Experimental Progam

THREE POINT BENDING TESTS

Three point bending tests were carried out according to the EN14651 (figure 2) on notched specimens with dimension of 150*150*660mm and a notch depth of 25mm at midspan. The test results of three point bending tests are shown in figure 3. It can be seen there is a big deviation in residual strength due to the fiber orientation and distribution.

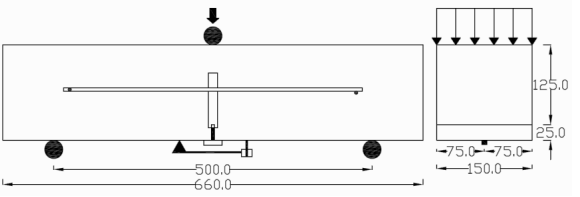

Figure 2. 3-point-bending test setup

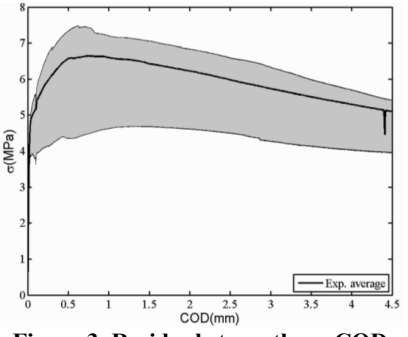

Figure 3. Residual strength vs. COD

PRE-CRACKING

The purpose of pre-cracking is to introduce a certain crack opening in the cylinder specimen by applying a uniaxial tensile load. The pre-cracking setup is shown in figure 4. It is composed of 3 loading bars, 3 fastening bolts, and 3 LVDTs. Three LVDTs are mounted around the notch at 120 degree between each other to measure the crack opening displacement during the pre-crack loading. The three loading bars are used to measure the reaction force during the pre-crack loading. Each loading bar has three strain gauges glued on it. All the loading bars were calibrated with load cells before pre-cracking, a good linear relationship between applied load and deformation of strain gauges was observed.

The specimen was glued to both top and bottom steel plates with epoxy resin. The pre-cracking load was applied by turning the three fastening bolts on the loading bars simultaneously. As the top steel plate is forced up, the tensile load is successfully

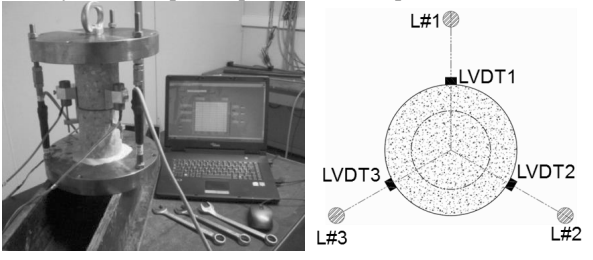

Figure 4. Pre-cracking setup (Left) and topview (Right)

imposed on the cylinder specimen, which is equal to the total reaction force taken by the three loading bars. In order to make sure the pre-cracking is accurate and stable, both load control and COD control were adopted. Before the cracking of concrete, load control was used, the tensile load was applied by several load steps at 0.5kN per load step. After the cracking of concrete, COD control was used, the crack was forced open at 0.01mm per load step until the target pre-cracking COD was reached.

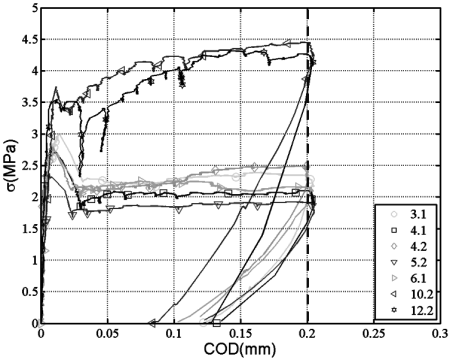

Figure 5. Pre-cracking stress vs. COD

The pre-cracking results of 0.2mm are shown in figure 5. The load was plotted against the average value of the three LVDTs. It can be seen that specimens 10.2 and 12.2 have a hardening behavior after cracking.

UNIAXIAL TENSILE CREEP TEST

A tensile creep frame with a lever system was developed to apply a constant tensile load. With this lever system, only 70kg weight is needed to make a 4.2kN tensile load on the specimen as shown in figure 6. This whole system is convenient to assemble and it is easy to maintain a constant load. After the pre-cracking, the cylinder specimen with two steel plates can be mounted on the creep frame. The steel plates were connected with the frame by two strong rings, in order to prevent any additional moments introduced on the specimen. During the creep test, the same 3 LVDTs from the pre-cracking test are used again to measure the creep deformation. The tensile creep load was applied gradually on the cylinder specimen with a hydraulic jack as shown in figure 6. The specimen was loaded at 30% of the maximum pre-cracking load for creep test, and the tensile creep loads for all the specimens are summarized in table 2.

The irreversible COD is also measured before the creep loading as shown in table 2. The creep results of 4 different specimens after 80 days loading are shown in figure 7. It should be noted that the normalized crack opening is calculated as $COD_{norm} = (COD - w_{irr}) / \sigma_{creep}$ and represents the average of the three LVDTs.

Figure 6. Tensile Creep frame (Left) and Hydraulic jack (Right)

Table 2. Pre-cracking stress and creep loading stress

Specimen	12.2	4.1	5.2	3.1	6.1	10.2	4.2	Mean
σ_{crk}	3.57	2.71	2.35	2.99	2.73	3.78	2.85	3.00
σ_{max}	4.49	2.71	2.35	2.99	2.73	4.62	2.85	3.25
σ_{creep}	1.35	0.81	0.71	0.90	0.82	1.39	0.86	0.97
$w_{irr}(mm)$	0.12	0.12	0.11	0.11	0.098	0.085	0.10	0.11

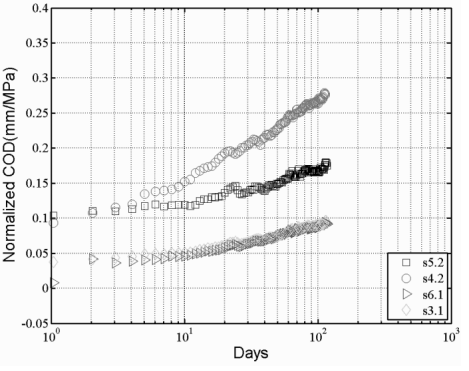

Figure 7. Creep results after 80 days

NUMERICAL SIMULATION

A one-dimensional viscoelastic model is used to describe the time dependent behavior of cracked SFRC under uniaxial tensile load. This type of basic rheological models has been used extensively by researchers to explain and describe creep in concrete, rock and masonry. Two creep phases can be observed in the tests: primary creep phase during which the strain rate decreases in time, a secondary phase or steady-state creep with a constant strain rate. The primary creep phase can be modeled using a Kelvin component. This component is placed in series with a Maxwell spring-dashpot configuration as shown in figure 8. This combination, also

known as Burgers model, is able to simulate the elastic deformations and first two stages of creep curve.

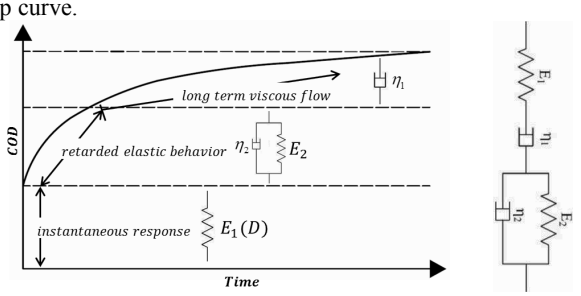

Figure 8. Burgers Model

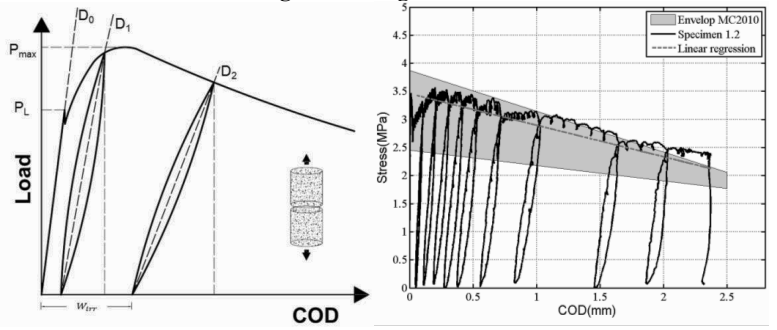

Figure 9. Stiffness degradation

In order to consider the gradual debonding behavior at fiber/matrix interface as the fiber is gradually pulled out, a damaged elastic module $E(D)$ is introduced instead of a constant value in Burgers model. The damage factor D is defined as the stiffness degradation and evolves in function of COD from zero (no damage) to 1 (total material failure). The stiffness degradation is calculated based on uniaxial tensile test as shown in figure 9. Nine hysteresis loops were carried out at nine different COD levels. The irreversible COD w_{irr} was measured by each unloading-reloading cycle. The damage evolution law is formulated according to the concrete damage model (in tension) proposed by Mazars [6] in 1986 as following:

$$F(w) = 1 - \frac{(1-A)w_0^{irr}}{w} - \frac{A}{\exp[B(w - w_0^{irr})]}$$

In the model, the equivalent strain $\tilde{\varepsilon}$ is replaced by the irreversible COD w_{irr}, and w_0^{irr} is the initial irreversible COD, $w_0^{irr} = 0.11mm$ in the case shown in Fig.10. A and B are parameters which can be determined by the experiments (A=0.056; B= 0.79). The damage evolution with different irreversible crack openings is then shown in figure 10. The time dependent behavior was simulated by the damaged Burgers model, the initial input parameters were obtained by curve fitting of the first 30 days' creep deformation. The results are shown in figures 11.

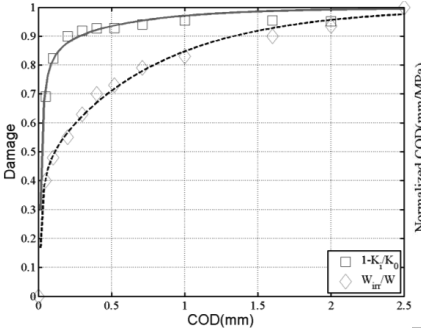

Figure 10. Damage evolution

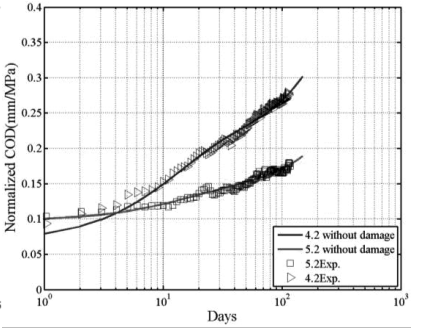

Figure 11. Specimen 4.2, 5.2

CONCLUSION

An experimental program was carried out to investigate the post-crack behavior of SFRC. It can be seen that the creep deformation after 80 days loading is significantly increased even if only 30% of the peak strength was considered as applied stress value. The damaged Burgers model can be used to simulate the stiffness degradation evolved in the creep process. Long-term creep results are still needed to validate the proposed model.

REFERENCES

[1] Bazant, Z.P.(1988), *Mathematical Modelling of Creep and Shrinkage of Concrete*,

[2] Kurtz,S., Balaguru P (2000), *Post-crack creep of Polymeric Fiber Reinforced Concrete in Flexure, Cement and Concrete Research*, V.30, , pp.183-190.

[3] MacKay J, Trottier J-F, (2004) *Post-crack Creep Behaviour of Steel and Synthetic FRC under Flexural Loading, Shotcrete : More Engineering Developments*, pp.183-192

[4] Bernard E.S, (2004) *Creep of Cracked Fiber-Reinforced Shotcrete Panels, Shotcrete: More Engineering Developments*, pp.47-58.

[5] Wolfgang Kusterle (2009). "*Viscous material Behavior of Solids- Creep of Polymer Fiber Reinforced Concrete" 5th Central European Congress on Concrete Engineering.*

[6] J. Mazars. (1986) "*A description of Micro and Macroscale damage of concrete structures*" *Journal of Engineering Mechanics, Vol. 115, No.2*

Analysis of concrete creep in compression, tension and bending: Numerical modeling

A. Hilaire[1], F. Benboudjema[1], A. Darquennes[1], Y. Berthaud[2] and G. Nahas[1,3]

[1]LMT, ENS CACHAN, 61 Avenue du Président Wilson, 94230 Cachan, FRANCE;
email: adrien.hilaire@ens-cachan.fr
[2]Université Paris 6, 4 place Jussieu, Paris, FRANCE
[3]IRSN, Fontenay-aux-Roses, FRANCE

ABSTRACT

Concrete structures with a long-term serviceability may be impacted by the time-dependent strains. In this study, creep strains modeling is performed by a rheological model, the long-term viscoelasticity and the influence of the loading on the specific creep are taken into account. The impact of the dissymmetry between tensile and compressive creep is studied with the numerical simulation of a four-point bending creep test. According to the results, a reliable long-term structural analysis has to consider this possible dissymmetry of basic creep.

INTRODUCTION

Prediction of creep in tension may be of great interest in special structures, where a tightness criterion must be respected. For instance, the concrete containment of the nuclear power plant is the last barrier to nuclear release. For safety reasons, a high level of tightness is required during its designing life (40 years for now, with a possible extension up to 60 years which is under evaluation). Prestressed concrete is consequently used in order to ensure the containment of the structure. This material has been chosen for its low hydraulic conductivity (for example: around 10^{-11} m/s for a standard concrete). However, cracks may appear at early age due to shrinkage restraint, in singular areas (around the access areas, for instance) or at long term if a loss of coolant accident occurs, even if prestress is used. Thus, this property may increase by several orders of magnitude and the containment may not be longer guaranteed.
Creep is one of these time-dependent deformations. This strain has to be considered to assess the risks of cracking of the nuclear containment during its life time. Unfortunately, several questions about the physical origins of creep are not yet solved. Consequently, creep modeling is still a current topic. Moreover, there is not any consensus about the relationship between compressive and tensile creep (Figure 1).

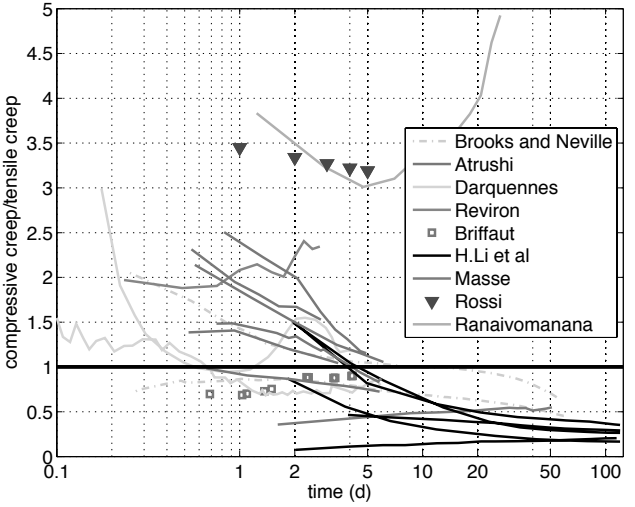

Figure 1: Evolution of the ratio of compressive basic creep on tensile basic creep

A macroscopic numerical modeling is proposed to differentiate tensile and compressive creep. At this stage, the influence of this dissymmetry on the long-term behavior of structures is assessed quantitavely through the simulation of a four-point creep bending test.

MODELING OF BASIC CREEP

Usually, basic creep is explained by two physical mechanisms with different kinetics (Ulm et al, 1998): the short-term micro-diffusion of water between capillary pores and the long-term sliding of C-S-H sheets characterized by a non-asymptotic aging. They are common to tensile and compressive creep; furthermore, it seems that a non-negligible micro cracking occurs during tensile creep. An adapted simple rheological Burger model with only 4 parameters is used to predict creep strains (Figure 2). This modeling is able to consider the ageing of concrete and consequently to simulate both early-age creep and long-term creep. In this study, only the behavior of mature concrete is simulated. Consequently, the part of the modeling linked to the early-age behavior is not presented (for more details, see (Hilaire et al 2013)).

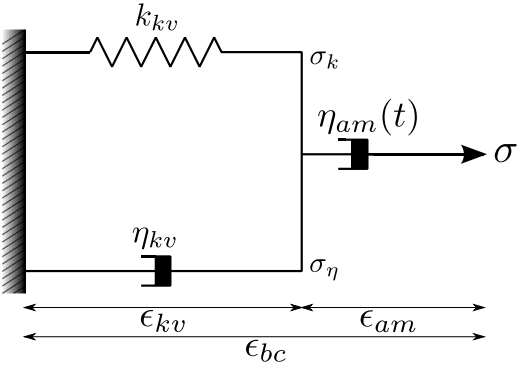

Figure 2: Rheological modeling

Short-term micro-diffusion of water between capillary pores. The hydrates lose their thermodynamic equilibrium when a stress is applied to concrete. Water molecules diffuse from layers of free adsorbed water to free zones in order to reestablish this equilibrium. This water displacement leads to a deformation of the solid skeleton.
A Kelvin-Voigt chain is used to model this micro-diffusion where the parameters k_{kv} and η_{kv} are proportional:

$$\eta_{kv} = k_{kv} \,.\, \tau$$

Sliding of C-S-H sheets. The sliding of the C-S-H is often used to explain long-term creep; this mechanism is characterized by its irreversibility and its logarithmic evolution. It is modeled by a dashpot $\eta_{am}(t)$; its viscosity is a function of time (it allows for retrieving age effect after hydration reaction stops) according to the following equation:

$$\eta_{am}(t) = \eta_{am} . t$$

This model turns out to be particularly accurate when considering a very long time creep, and is in good accordance with experimental results (cf. the experimental campaign by Brooks (2005) for 30 years creep).

Micro-cracking. According to several authors (Al-Kubaisy et al, 1975)(Rossi et al, 2012), micro cracking appears when concrete is under tensile load. During a compressive loading, basic creep strain and the total number of micro-cracks created in the material seem to be proportional (Rossi et al, 2012). Besides, the cement paste content has an opposite effect depending on the type of loading: in tension, creep increases with a reduction in the paste content (Bissonnette et al, 2007) when in compression it decreases. Moreover, presence of steel fibers contributes to increase tensile creep (Bissonnette et al, 2007). These observations make manifest that the interfaces cement paste-aggregate or cement paste-fibers have a large influence. The

relative weakness of these zones makes them very sensitive to micro-cracking and a significant part of tensile creep could then be explained by the growth of micro-cracks. Finally, autogeneous shrinkage of cement paste, restrained by the aggregates, leads prior to the loading, to smeared cracking (Briffaut et al, 2013). The dashpot $\eta_{am}(t)$ is used to describe this phenomenon; the dissymmetry between tension and compression is expressed thanks to the coefficient α:

$$\dot{\epsilon}_{am} = \alpha \frac{<\sigma>_+}{\eta_{am}(t)} + \frac{<\sigma>_-}{\eta_{am}(t)}$$

where the positive part operator is $<>_+$ and the negative part is $<>_-$.

3D-Modeling. The three dimensional problem is dealt by solving the following system of equations where ν_{bc} is the creep Poisson's coefficient, $\boldsymbol{D}$ are the principal stresses of $\boldsymbol{\sigma}$ and $\boldsymbol{P}$ is the transformation matrix:

$$\dot{\boldsymbol{\epsilon}}_{\boldsymbol{bc}} = \dot{\boldsymbol{\epsilon}}_{\boldsymbol{bc}} + \dot{\boldsymbol{\epsilon}}_{\boldsymbol{am}}$$

$$\dot{\boldsymbol{\epsilon}}_{\boldsymbol{kv}} = \frac{1+\nu_{bc}}{k_{kv}}\dot{\boldsymbol{\sigma}}_{\boldsymbol{kv}} - \frac{\nu_{bc}}{k_{kv}}\boldsymbol{Tr}(\dot{\boldsymbol{\sigma}}_{\boldsymbol{kv}})\mathbb{I}$$

$$\dot{\boldsymbol{\epsilon}}_{\boldsymbol{kv}} = \frac{1+\nu_{bc}}{\eta_{kv}}\boldsymbol{\sigma}_{\boldsymbol{\eta}} - \frac{\nu_{bc}}{\eta_{kv}}\boldsymbol{Tr}(\boldsymbol{\sigma}_{\boldsymbol{\eta}})$$

$$\dot{\boldsymbol{\epsilon}}_{\boldsymbol{am}} = \frac{1+\nu_{bc}}{\eta_{am}}\boldsymbol{\sigma}_{\boldsymbol{\alpha}} - \frac{\nu_{bc}}{\eta_{am}}\boldsymbol{Tr}(\boldsymbol{\sigma}_{\boldsymbol{\alpha}})$$

$$\boldsymbol{\sigma}_{\boldsymbol{\alpha}} = \boldsymbol{P}\boldsymbol{D}_{\boldsymbol{\alpha}}\boldsymbol{P}^{-1}$$

$$\boldsymbol{D}_{\boldsymbol{\alpha}} = <D>_- + \alpha <D>_+$$

MECHANICAL SIMULATION OF FOUR-POINT BENDING CREEP TEST

A numerical analysis of a beam under bending is carried out. The dimensions of the problem are presented on the Figure 3. The cross section of the beam is squared. The numerical problem is a three-dimensional visco-elastic problem. The ambient conditions induce that basic creep strain is the only time-dependent strain. The beam is approximately loaded 28 days after its casting; consequently, the phenomena linked to the hydration of concrete are neglected.

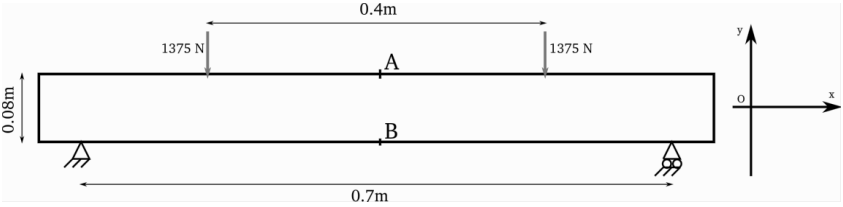

Figure 3: Geometry of the four-point bend creep test

Elastic and creep parameters. The elastic parameters are given in Table 1. The creep parameters are identified from the experimental campaign performed by Reviron (Reviron, 2009). The tests were undertaken 90 days after the casting of the specimens and they last 3 days (expected duration of a coolant loss accident). The identification of the parameters of the Kelvin-Voigt chain (associated to the short-term creep) is done by using the creep recovery.

Table 1. Elastic parameters.

E (GPa)	ν
30	0.2

Strains evolutions predicted by the parameters in the Table 2 are plotted on the Figure 4. The concrete of this experimental campaign creeps more in compression than in tension.

Table 2. Creep parameters.

k_{kv} (GPa)	$\tau(h)$	η_{am}(GPa)	α	ν_{bc}
30	8	3.5	1/4.5	0.2

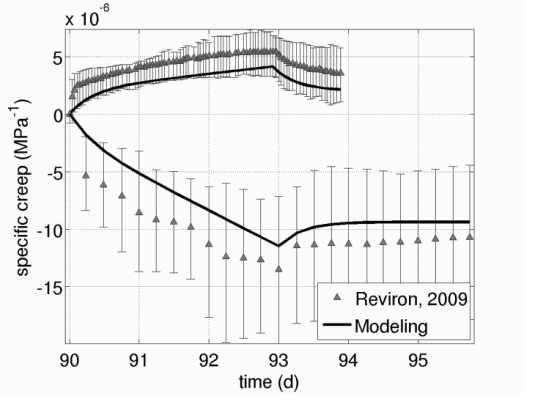

Figure 4: Comparison between simulated and experimental evolutions of strains.

Results. The total strains $\boldsymbol{\epsilon^{xx}}$ is equal to the sum of the elastic $\boldsymbol{\epsilon_{el}^{xx}}$ and basic creep $\boldsymbol{\epsilon_{bc}^{xx}}$ strains. The figure 5 shows the evolution of the total strain $\boldsymbol{\epsilon_{xx}}$ along the vertical axis AB (Figure 3) just after the loading (elastic phase) and at the end of the simulation. After 6 days, the neutral axis drifts towards the initial tensile zone.

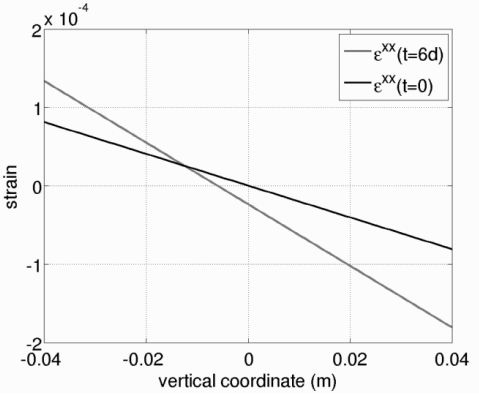

Figure 5: Strains of cross-section of the bending specimens.

The figure 6 shows the evolution of the position of the neutral axis versus time. The neutral axis diverges towards the area with the lower creep compliance. It is logical since creep strains are more important in compression. However, this result is in contradiction with the ones obtained by Ranaivomana (2013).

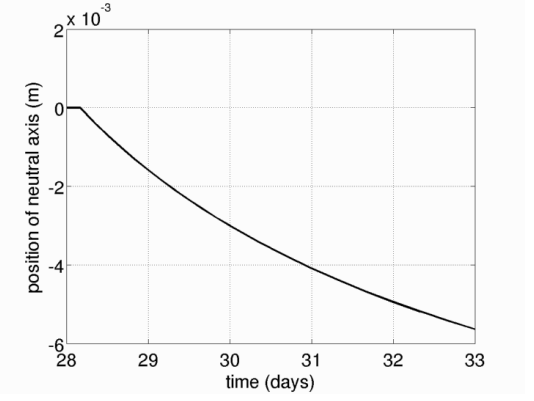

Figure 6: Evolution of the position of the neutral axis vs time

The figure 7 shows the evolution of the stress $\boldsymbol{\sigma_{xx}}$ along the vertical axis AB just after the loading (elastic phase) and at the end of the simulation. After 6 days, the gradient of the stress is not constant along the vertical axis. It is relevant to notice that the

tensile stresses increase progressively. This may explain the failure of beams tested by Omar (2004) during the loading.

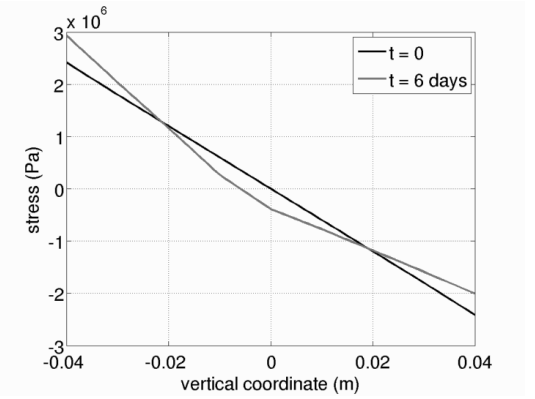

Figure 7: Stress of the cross-section

This non-linearity explains why the experimental specific bending creep varies often between the specific compressive creep and the specific tensile creep. The figure 8 shows the evolution of the bending induced compressive creep (point A) and tensile creep (point B). After 6 days under loading, the specific creep is calculated with two methods. Firstly, the elastic stress field is used to obtain a physical quantity with the same dimensions as specific creep (black lines); this method is used to process experimental data. Secondly, the specific creep is calculated with the real stress field (red lines), the compliances obtained with this method are equal to the direct compressive and tensile ones.

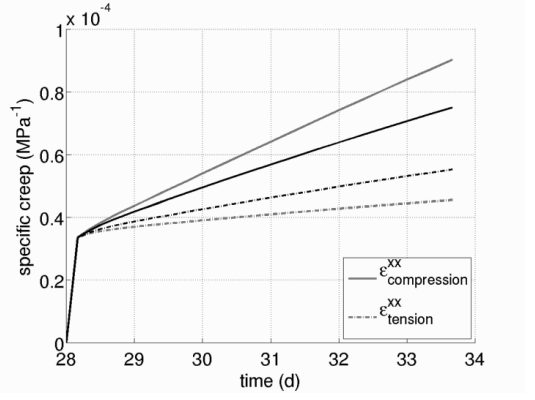

Figure 8: Creep compliance of concrete calculated in the initial compressive and tensile area with two methods.

CONCLUSION

The influence of the loading on the creep's compliance is not widely accepted by the scientific community and most of the known modeling does not considered it. The difference between compression and tension is introduced with the parameter α.

A four-point bend creep test is simulated. The choice of the parameters induce that this concrete creeps more in compression than in tension. After 6 days under loading, the neutral axis diverges towards the tensile zone and the plane cross-section remains plane during the creep phase. However, the stress field is no longer linear. This change explains why specific creep compliances cannot be calculated with experimental data from a bend testing.

The analysis of a simple four-point bend creep test makes evident the importance of the creep dissymmetry to have reliable structural analysis. The serviceability of a nuclear containment may be impacted by a more accurate consideration of the delayed strains in concrete. Previous studies demonstrate that the choice of the creep's modeling has a huge influence to estimate the life expectancy of complex structures (Bazant et al, 2008).

An experimental campaign has been launched to validate numerical results: sealed specimens of mature concrete are loaded in compression, in tension and in bending.

REFERENCES

Al-Kubaisy MA. and Young AG. (1975) Failure of concrete under sustained tension. Magazine of Concrete Research, 27.

Bazant, ZP., Li GH., Yu Q., Klein G. and Krıstek V. (2008) Explanation of excessive long-time deflections of collapsed record-span box Girder Bridge in Palau.

Bissonnette B, Pigeon M, Vaysburd AM. (2007) Tensile creep of concrete: study of its sensitivity to basic parameters, ACI Materials, 10.

Briffaut M., Benboudjema F., Torrenti J.-M., Laborderie C., (2013) Creep consideration effect on meso-scale modelling of concrete hydration process and consequences on the mechanical behavior, ASCE J. Eng. Mech., 10.1061/(ASCE)EM.1943-7889.0000607

Brooks, J. J. (2005). 30-year creep and shrinkage of concrete. Magazine of Concrete Research, 57(9): 545–556.

Hilaire, A. Benboudjema, F. Darquennes, A. Berthaud, Y and Nahas G. (2013) Some issues on prediction of massive structures cracking at early age. Framcos-8

Omar M. (2004). Déformations différées du béton : étude expérimentale et modélisation numérique de l'interaction Fluage – chargement, PhD thesis, ECN Nantes, France. (In French).

Ranaivomana N. (2013). Etudes expérimentale et numérique des interactions entre le fluage en traction et l'endommagement du béton, Université Paul Sabatier de Toulouse, France. (In French).

Reviron, N. (2009). Étude du fluage des bétons en traction. Application aux enceintes de confinement des centrales nucléaires à eau sous pression, PhD thesis, ENS Cachan, (In French).

Rossi P, Tailhan JL, Le Maou F, Gaillet L and Martin E. (2012) Basic creep of concretes investigation of the physical mechanisms by using acoustic emission. Cement and Concrete Research, 42.

Ulm, F-J. and Acker, P. (1998). Le point sur le fluage et la recouvrance des bétons. Bulletin des Laboratoires des Ponts et Chaussées, (Spécial XX):73–82.(In French)

Improvement of Crack Resistance of Slag Concrete by Utilizing High Alite Cement

Huynh Phuong NAM[1] and Akira HOSODA[2]

[1]Institute of Urban Innovation, Yokohama National University (79-5, Tokiwadai, Hodogaya-ku, Yokohama-shi, Kanagawa 240-8501, Japan); email: hphuongnam@gmail.com
[2]Institute of Urban Innovation, Yokohama National University; email: concrete@ynu.ac.jp

ABSTRACT

In this study, microcracks in slag concretes with water-to-binder ratio (w/b) of 0.5 and 0.3 subjected to temperature regime simulated steam curing in early ages were characterized by the combination of acoustic emission (AE) technique and mechanical tests. By using a new-shaped wave-guide, which reduced the distance from cracking points to wave-guide, effect of attenuation in detecting AE signals was significantly mitigated. Due to analysis of AE parameters, crack mode in slag concretes was clarified. The result showed that they were very different in each stage of temperature history and in each type of concrete. This research also revealed the capacity of high alite cement (HAC) in improving resistance against microcracking of slag concrete. However, cracking resistance of HAC slag concrete in case of w/b of 0.3 was higher than that in case of w/b of 0.5.

1. INTRODUCTION

In the early ages from concreting, hydration process of cement produces a large amount of heat leading to deformation of main constituents of concrete such as coarse aggregate and cement paste. Because of the difference in deformation capacity of them, microscopic stresses occur in concrete. They result in cracking inside concrete even without the application of external load. Microscopic thermal stresses appear significantly in case of massive concrete and heat curing.

Nowadays, because of its advantages such as better workability, high compressive strength, environmental conservation and high durability, concrete using ground granulated blast furnace slag (GGBFS) has been widely applied on the world. Unfortunately, it is also subjected to severer microcracks than normal concrete.

There are some approaches to investigate microcracking in concrete. Due to its sensitivity and rich information from collected parameters, AE technique has been widely used to detect deterioration of hardened concrete. Nevertheless, AE sensors can not be directly attached on the surface of concrete in very early ages. Therefore,

a wave-guide embedded inside concrete was utilized. However, attenuation of acoustic wave was a problem. In this study, a combination of AE technique using a new-shaped wave-guide with mechanical tests was used to clarify the characteristics of microcracks in slag concrete subjected to temperature variation in early ages.

This research also investigated the effects of chemical properties of cement on controlling microcracking of slag concrete. For this purpose, HAC was utilized and it showed better resistance against microcracking than normal cement when used in slag concrete.

2. EXPERIMETAL SETUP

2.1 Materials and mix proportions

In this study, three types of binder were used: Ordinary Portland Cement (OPC), HAC, and GGBFS. HAC is newly developed special cement with very high content of alite ($3CaO.SiO_2$) and almost no belite ($2CaO.SiO_2$) (Hashimoto et al, 2012). Chemical composition and physical properties of binders are presented in Table 1. Limestone and andesite were two types of coarse aggregate with the same maximum particle size of 19mm. Fine aggregate was pit sand. All the materials were placed in a curing room with temperature of around 20^{o}C before mixing.

Mix proportions of mortars and concretes are given in Table 2. Proportion of mortars was calculated from that of respective concretes by removing coarse aggregates while keeping the proportion of other components.

2.2 Acoustic emission system

The experimental system of AE tests is described in Figure 1. Two-channel AE system and R15-Alpha sensors were used. In each test, two sensors were coupled on a sensor seat located at the top of a stainless steel wave-guide, whose design is clarified in section 2.3. The wave-guide was embedded in the specimen and the assembly was placed in a temperature controlled chamber.

Noise deriving from the dynamic parts of the temperature controlled chamber and the operation of other surrounding machines is a big problem. Son and Hosoda (2010) were successful in using damping buffer to isolate the unexpected noises. By setting a threshold value of 40dB, sound from the outside ambient transmitting through air was rejected. During tests, the change of electric pulses from electrical facilities can cause jam in detecting AE signal. To avoid this phenomenon, all sensors, pre-amplifiers, and connectors were wrapped by alumina sheets.

Cylindrical tin molds with 100mm diameter and 200mm height were used for all tests. In order to eliminate noises induced from the friction between concrete and the mold due to their different deformation under temperature variation, the inside face of the mold was covered with 0.5mm thick teflon sheet (Figure 2a).

Time for preparing the specimen including installation of wave-guide and sensors was around 30 minutes. Right after finishing preparation, concrete was sealed by polyethylene film inside the mold and placed in the temperature controlled chamber, which had been maintained at 20^{o}C. The heating began at 2 hours after adding water into the mix. Temperature regime applied for the specimens is shown in Figure 3. The record of AE signals started at 1.5 hours after mixing.

Table 1 Chemical composition and physical properties of binders

Binder	Chemical composition (%)								Density	Specific area
	SiO_2	Al_2O_3	Fe_2O_3	CaO	MgO	SO_3	Na_2O	K_2O	(g/cm^3)	(cm^2/g)
OPC	20.36	5.33	3.04	64.09	1.50	2.13	0.28	0.36	3.16	3310
HAC	18.76	5.18	2.85	64.16	1.88	3.97	0.42	0.38	3.11	5480
GGBFS	32.30	14.20	0.31	43.40	5.70	1.93	0.26	0.27	2.90	4030

Table 2 Mix proportions (kg/m^3)

Mixture	Water	OPC	HAC	GGBFS	Pit-sand	Lime stone	Andesite	SP	w/b
M-O-30	251	418	-	418	1229	-	-	4.2	0.3
M-H-30	250	-	417	417	1225	-	-	5.8	0.3
M-O-50	265	265	-	265	1454	-	-	-	0.5
M-H-50		-				-	-	-	0.5
C-O-L-30	165	275	-	275	810	838	-	2.8	0.3
C-O-A-30	165	275	-	275	810	-	816	2.8	0.3
C-H-L-30	165	-	275	275	808	836	-	3.9	0.3
C-H-A-30	165	-	275	275	808	-	814	3.9	0.3
C-O-L-50	165	165	-	165	904	936	-	-	0.5
C-O-A-50	165	165	-	165	904	-	911	-	0.5
C-H-L-50	175	-	175	175	-			-	0.5
C-H-A-50	175	-	175	175		-		-	0.5

2.3 Wave-guide

Since concrete is in plastic form in very early ages, AE sensors cannot be coupled directly on the surface of the specimens. To deal with this problem, AE wave-guide was applied (Son, Hosoda, & Watanabe, 2010). This wave-guide was a stainless steel rod with 250mm length and 4mm diameter, with a sensor seat on the top (Figure 4a). In case of concrete with w/b of 0.5; however, this wave-guide did not work properly due to the attenuation of acoustic wave in a high moisture content ambient (Landis & Shah, 1995).

In order to solve the matter of attenuation, a new-shaped wave-guide was employed in this research (Figure 4b). It was made from a stainless steel plate with 4mm thickness. The section of the wave-guide is square with dimension of 4x4mm. The rod is 250mm in length with two horizontal bars located at 50mm and 150mm from the bottom. On the top, 25x50mm plate is perpendicularly bent to the vertical rod making a sensor seat. Since two sensors can be coupled on the seat at a time, only one specimen was used in each experiment. The method for coupling sensors to the sensor seat is found in elsewhere (Son, Hosoda, & Watanabe, 2010).

2.4 Test of CTEs

Coefficients of thermal expansion (CTE) of mortar were measured by using an embedded I-shaped strain gage PMFL-60-2LT with 4mm diameter and 60mm length. Figure 2b describes the setup for measuring the CTE of mortar. Two

specimens of one mix were tested at the same time and the mean value was calculated. Tests of CTE were conducted at one day after being subjected to heat curing. Specimens were heated from 20°C to 50°C in two hours, and maintained at 50°C in two hours, and then cooled down to 20°C in two hours. CTE of mortar was calculated separately for heating and cooling stages and the average was taken.

For coarse aggregates, CTEs were directly measured on the particles. The flat-type strain gauges FLG-1-11 with 1mm length were attached on the smooth surfaces in three orthogonal directions of one particle. The temperature regime was the same as that applied for mortar. The particles were sealed to prevent evaporation. Three particles of each type of coarse aggregate were used in a test and then the mean value was taken.

2.5 Tensile strength test

Tensile strength of concretes and mortars were investigated at the age of one day following heat curing. Specimens were cylinders with 100mm diameter and 100mm height. The method for direct tensile strength test was proposed by Son and Hosoda (2010).

3. RESULTS AND DISCUSSION

Under curing temperature and heat from hydration process of binders, temperature inside concrete changed throughout two periods: the increasing period (expansion period) from mixing up to eight hours and the decreasing one (shrinkage period). Due to the incompatibility in CTE between mortars and aggregates shown in Figure 5, microcracks occurred in concrete in both periods. The development of AE hits of three types of slag concrete with andesite is presented in Figure 6.

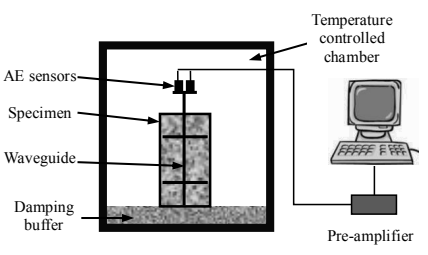

Figure 1. AE testing system

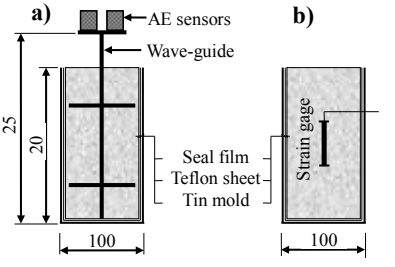

Figure 2. Specimen preparation for (a) AE test, and (b) CTE test

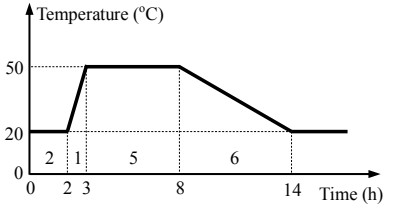

Figure 3. Temperature regime simulating heat curing

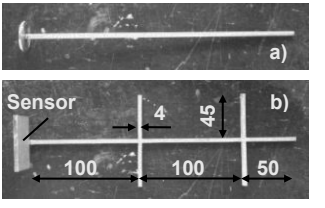

Figure 4. AE wave-guide (a) previous, and (b) present

3.1 Effectiveness of new-shaped wave-guide

In previous research, the numbers of AE hits of concrete with w/b of 0.5 were extremely smaller than those of concrete with w/b of 0.3 (Son & Hosoda, 2010). However, with new-shaped wave-guide, concretes with w/b of 0.5 presented much more microcracks, especially in the temperature increasing stage (Figure 6). To clarify the reason of this difference, amplitude distribution of microcracks was analyzed. Figure 7 reveals that microcracks in concrete with w/b of 0.5 mostly occurred at low amplitudes. The low amplitudes in concrete with w/b of 0.5 can be explained by the attenuation of acoustic waves when they transmitted throughout a moist ambient caused by a large amount of remained water in concrete in very early ages (Aggelis, Polyzos, & Philippidis, 2005). Because of far distances from cracking points, when acoustic waves touched to the wave-guide in the former study, attenuation made their amplitude lower under the threshold value of 40dB. Thus, AE sensors could not detect these microcracks. By using two additional horizontal bars in new wave-guide, the distances became shorter and hence the effect of attenuation must have been significantly decreased. The comparison of AE hits collected by the old and the new wave-guide in concrete with w/b of 0.5 was shown in Figure 8. The number of hits recorded by the new wave-guide was considerably higher than that recorded by the old one. It can be clearly said that the new one is more effective.

3.2 Characterization of crack mode during heat curing

Two possible crack modes can appear during heat curing of concrete are tensile and shear. In expansion period, tensile-mode cracks are caused by the separation between aggregates and mortar while shear-mode cracks caused by the slippage of aggregates. In shrinkage period, crack mode depends on the strength of ITZ. If it is strong enough, crack is open mode (tensile). Conversely, crack is both open mode and debonding-slip mode (shear) (Son, 2010).

Rise time in milliseconds over peak amplitude in volts (RA value) and average frequency have been applied to classify crack mode (Aggelis, 2011). Cracks in tensile mode tend to have higher average frequency and smaller RA value while longer rise time were observed in shear mode (Soulioti et al., 2009). Crack modes in three concretes with limestone were classified in Figure 9. In C-O-L-50, most of cracks were tensile mode and most of shear-mode cracks generated in expansion period. In both concretes with w/b of 0.3, the number of cracks in tensile mode was not much larger than that in shear mode. Nevertheless, while shear-mode cracks in C-O-L-30 occurred in two periods of heat curing, those in C-H-L-30 mostly fell in to the shrinkage stage. Deeply analysis revealed that all shear-mode cracks in expansion stage appeared at very early age. It can be explained that in very early age, cement paste is not sufficiently hardened. In such an unhardened state, slippages between coarse aggregates and matrix must have led to shear-mode cracks. On the other hand, all shear-mode cracks in shrinkage period generated from the age of 10 hours to 14 hours after mixing. This was because in that time interval, mortars shrank largest and induced the stresses exceeded bond strength. These cracks were also expected to appear around large-size particles due to the fact that larger size of aggregate causes greater stresses (Elices & Rocco, 2008). Because of their small level; however, shear-mode cracks had an inconsiderable effect on cracking of slag concretes.

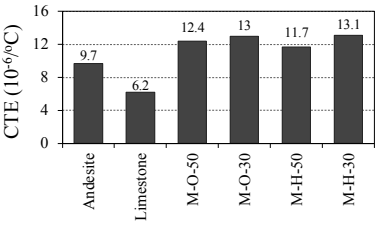

Figure 5. CTE of coarse aggregates and mortars

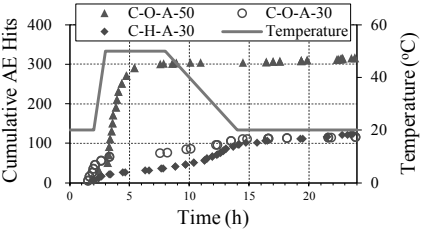

Figure 6. AE hits of concretes with andesite

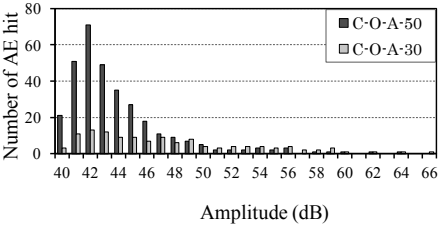

Figure 7. Amplitude distribution of microcracks of C-O-A-50 and C-O-A-30

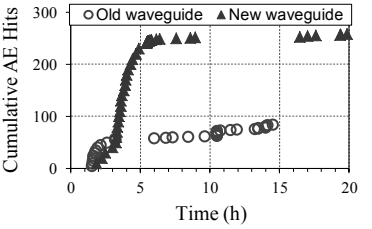

Figure 8. Comparison of new and old wave-guide in C-O-A-50

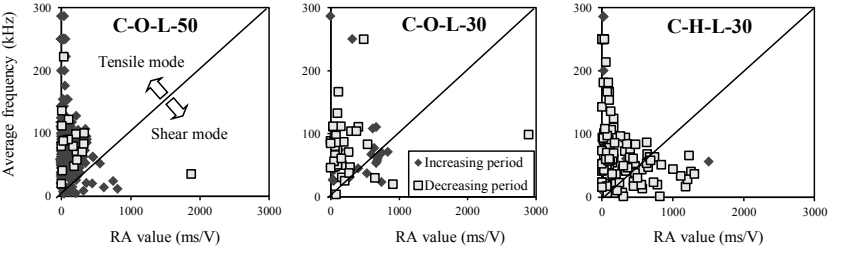

Figure 9. Classification of crack mode of concretes with limestone

3.3 Capacity of HAC slag concretes in resisting against microcracking

Ductility of materials can be qualified by duration of AE events. It was found that AE events recorded in ductile materials were characterized by longer durations than those in brittle materials (Kuksenko et al., 1987). In both cases of w/b of 0.5 and 0.3, AE events in HAC slag concretes showed the significant longer average duration than that in OPC ones (Figure 10). This reveals that HAC slag concretes are more ductile than OPC ones. As the result, HAC slag concretes presented a higher tensile strengths than those of OPC ones. Moreover, while tensile strength of OPC slag concretes were much smaller than respective mortars, tensile strength of HAC slag concretes were just a bit smaller (w/b=0.5) or even larger (w/b=0.3) than respective mortars (Figure 11). Figure 12 also shows the good correlation between tensile strength rate and AE duration of slag concrete. The higher the average duration was, the less the loss of tensile strength was.

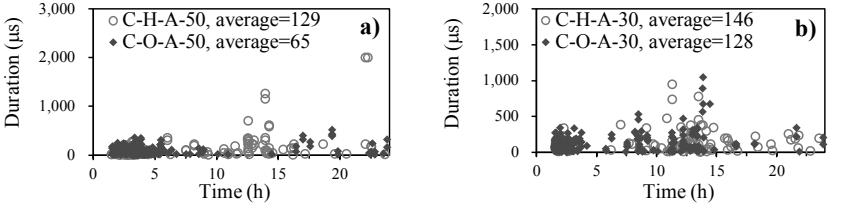

Figure 10. Comparison of event durations between HAC and OPC slag concretes with andesite: (a) w/b = 0.5 and (b) w/b = 0.3

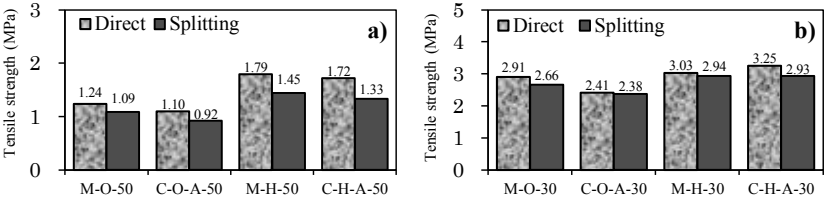

Figure 11. Tensile strength of slag concretes with andesite and respective mortars: (a) w/b = 0.5 and (b) w/b = 0.3

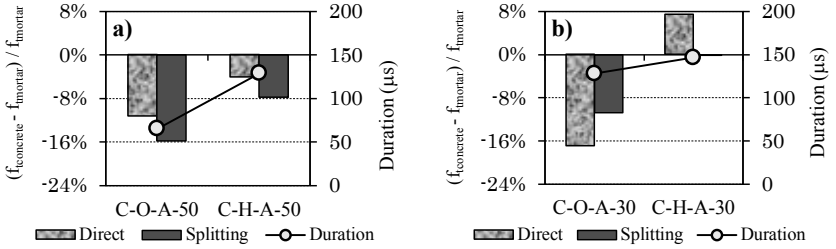

Figure 12. Correlation between tensile strength rate and AE duration of concretes with andesite: (a) w/b = 0.5 and (b) w/b = 0.3

The effectiveness of HAC in improving resistance against microcracking may be explained by the role of $Ca(OH)_2$. In hydration of cement, alite produces three times as much $Ca(OH)_2$ as is formed by the hydration of belite (Neville, 1996). Therefore, HAC will create more $Ca(OH)_2$ than OPC in hydration. $Ca(OH)_2$ will grow where free space is available and hence they distribute evenly in concrete. Because of their weak strength, even distributed $Ca(OH)_2$ crystals might have become a kind of buffers to prevent propagation of microcracking leading to the higher ductility of HAC slag concrete. In addition, although tensile strength of M-H-30 was a bit higher than that of M-O-30, tensile strength of C-H-A-30 was much larger than that of C-O-A-30 (Figure 11b). Because ductility of C-H-A-30 was not much higher than that of C-O-A-30 (Figure 10b), the aforementioned difference in tensile strength of concrete also inferred that bond strength in C-H-A-30 might be higher than that in C-O-A-30. The combined effect of ductility and bond strength resulted in the better microcracking resistance capacity of C-H-A-30. The role of bond strength was not observed in case of w/b of 0.5.

4. CONCLUSION

The conclusions obtained from this research are as follows:

1. New-shaped wave-guide had a great effectiveness on detecting AE signals in high moisture medium due to the short distance from cracking points to wave-guide.
2. By analyzing AE parameters, crack mode in slag concretes was clarified. The result showed that the number and time point of occurrence of shear-mode cracks were very different in each type of slag concretes. However, these shear-mode cracks had not remarkable effect on cracking of concrete.
3. HAC can improve the cracking resistance of slag concrete with w/b of 0.5 and 0.3. The role of $Ca(OH)_2$ layers as a kind of buffers resulting in higher ductility of HAC slag concrete might be the reason. In case of HAC slag concrete with w/b of 0.3, bond strength might be also an important factor. However, to grasp about characteristics of HAC in slag concrete, more studies need to be investigated.

REFERENCES

Aggelis, D. G. (2011). "Classification of cracking mode in concrete by acoustic emission parameters." *Mechanics Research Communications 38*, 153–157.

Aggelis, D. G., Polyzos, D., & Philippidis, T. P. (2005). "Wave dispersion and attenuation in fresh mortar: theoretical predictions vs. experimental results." *Journal of the Mechanics and Physics of Solids*, 53(4), 857–883.

Elices, M., & Rocco, C. G. (2008). "Effect of aggregate size on the fracture and mechanical properties of a simple concrete." *Engineering Fracture Mechanics*, 75(13), 3839–3851.

Hashimoto, A. et al (2012). "Properties of high alite cement", *Annual Meeting of JCA*, 66 (in Japanese)

Kuksenko, V. S. et al (1987). "Investigation of fast processes during stable growth of a wedge-shaped crack in steel by the method of acoustic emission." *Strength of Materials*, 19(7), 901–905.

Landis, E. N., & Shah, S. P. (1995). "The influence of microcracking on the mechanical behavior of cement based materials." *Advanced Cement Based Materials*, 2(3), 105–118.

Neville, A. M. (1996). "Properties of Concrete." John Wiley & Sons, 867-869.

Son, H. N. (2010). Ph.D Thesis submited to Yokohama National University.

Son, H. N., & Hosoda, A. (2010). "Detection of Microcracking in Concrete Subjected to Elevated Temperature at Very Early Age by Acoustic Emission." *Journal of Advanced Concrete Technology*, 8(2), 201–211.

Son, H. N., Hosoda, A., & Watanabe, T. (2010). "Characterization of microcracking in very early age concrete subjected to elevated temperature by AE." *Proceeding of the JCI Annual Convention,* 32(1), 323–328.

Soulioti, D. et al (2009). "Acoustic emission behavior of steel fibre reinforced concrete under bending." *Construction and Building Materials*, 23(12), 3532–353.

Experimental Determination of Early Age Fracture Toughness and Fracture Process Zone Size in Cement Pastes

C. Hoover[1]

[1]Department of Civil and Environmental Engineering, Massachusetts Institute of Technology, Cambridge, MA 02139, USA; Email: cgh2@mit.edu

ABSTRACT

The micro-scratch test and its analysis continue to grow in the fields of material science and engineering, particularly as it relates to materials at smaller scales being used for fracture resistance. In this study, white cement paste specimens were cast, extracted and their hydration was stopped at desired curing ages. A Rockwell probe was used to scratch the surface of the specimens to determine the fracture toughness at that age. Classical Brazilian split-cylinder were also performed to compliment the scratch tests. The excellent convergence of the raw data allows the increase of fracture toughness and splitting strength over time to be determined. Finally Irwin's characteristic length, which is proportional to the fracture process zone size, is determined and shown to asymptotically reach a constant size.

INTRODUCTION

Scratch testing is one of the oldest material classification experiments, dating back to the early 1800's, with Mohs scale of mineral hardness used scratching resistance as a classification of material (Broz et al. 2006, D. Tabor 1954). The scratch test itself simply involves cutting a material with a blade and relating the resulting horizontal force with a hardness value (Williams 1996) by dividing the horizontal force by the projected contact area of the blade or a probe orthogonal to the direction of the scratch. The scratch test is highly sought after as a means of classification of materials due to its simplicity (it is almost non-invasive) and ease of application to only a small amount of many different materials including metals, polymers, rocks and coatings (Wredenberg and Larson 2009, Akono et al. 2012, Ollendorf and Schneider 1999, Richard et al. 1998 and Schei et al. 2000).

This study presents an application of the scratch test to early age cement pastes. It is well known that the compressive strength and stiffness of cement pastes increases with curing time. However, currently, no study exists that relates the effect of curing time to the development of fracture resistance or to the evolution of the fracture process zone (FPZ) size. To determine this trend, the fracture toughness is evaluated by the microscratch test on specimens of various curing ages, and the tensile strength of the material is then determined through a collection of Brazilian split cylinder tests. When the tensile strength and fracture toughness are known, the characteristic length l_{ch}, which is proportional to the size of the FPZ, can be determined though Irwin's relation (Irwin 1958).

REVIEW OF THE TESTS AND ANALYTICAL MODELS

Micro-Scratch Test

In this investigation, we first apply a simple microscratch technique, developed and explained in (Akono et al. 2011, Akono and Ulm 2011, Akono and Ulm 2012 and Akono et al. 2012), that extracts the fracture toughness from the measured forces and depth of penetration during a microscratch test carried out with a Rockwell probe. The test itself creates a scratch groove in the sample by drawing a probe across a sample surface with a prescribed constant or increasing vertical force, which would lead to a wider scratch trough and deeper penetration into the specimen, and horizontal velocity. The horizontal force, penetration depth and acoustic emissions are recorded. If the material is homogeneous, linear elastic and isotropic, the stress field ahead of the crack can be approximated (ignoring the effects of the vertical force on the fracture process) as $\sigma_{xx} = -F_T/A$ where F_T is the tangential (horizontal) force and A is the projected contact area of the probe orthogonal to the scratch direction. The model assumes the existence of semicircular horizontal crack planes, emanating from the probe tip (Akono et al. 2012). Applying a contour integral method (Barenblatt 1962) to evaluate the energy release rate of the system, the following expression was derived that relates F_T, $A(d)$, the contact perimeter $p(d)$, and the fracture toughness K_c of the material (Akono et al. 2011, Akono et al. 2012):

$$K_c = \frac{F_T}{\sqrt{2p(d)A(d)}} = \frac{F_T}{\sqrt{f(d)}} \qquad \text{(eq. 1)}$$

The perimeter and projected contact area are both functions of the penetration depth d and take into account the geometry of the probe. If $f(d), d$ and F_T are known, obtaining K_c becomes trivial. If $f(d)$ is not known, it must first be determined by performing a series of scratches on a material of a known fracture toughness.

Brazilian Split-Cylinder Test

This standard test involves placing a cylinder on its side and compressing it until it splits laterally to the applied load. The classical equation for tensile Brazilian split-cylinder strength is calculated as

$$f_t = \frac{2P_u}{\pi D t} \qquad \text{(eq. 2)}$$

where P_u is the maximum load, t is the thickness of the specimen and D is the diameter of the cylinder (Timoshenko and Goodier, ASTM C496). A wooden bearing strip was placed between the cylinder and the loading platens of the testing machine to help distribute the line load uniformly on the cylinder and to help eliminate any stress concentrations between the machine loading platens touching the cement specimen (ASTM C496). The splitting strength was shown to also depend on the width of a wooden bearing strip and the following modification factor was introduced (C. Rocco et al. April 1999, C. Rocco et al. July 1999).

$$f_{st} = \frac{f_t}{\left(1-\beta^2\right)^{3/2}} \qquad \text{(eq. 3)}$$

Where $\beta = b/D$ and b is the bearing strip width.

EXPERIMENTAL PROGRAM

Casting and Curing

The main goal was to cast a collection of sample from different curing ages starting with the earliest age possible and up through 28 days. All samples were cast in batches consisting of 100 grams of White Ordinary Portland Cement (WOPC) at a 0.4 water to cement (w/c) ratio. The constituents were homogenized using a mixer and impeller from Heidolph, then cast into 20 mm x 55 mm cylindrical molds. The paste was tamped and vibrated to help work the paste into the molds and to expel air. Finally the molds were capped and stored in a sealed container to help prevent evaporation.

All specimens were de-molded after 8 hours and stored in lime water. Just prior to the desired age, disk specimens were cut with an average thickness of about 8.5 mm from the parent samples using a drop saw with a diamond coated blade. The hydration was stopped at the desired time by immersing the specimens into isopropanol alcohol for 1 hour to replace the free water in the paste. A regular replacement of the isopropanol and stirring was applied to ensure a sufficient extraction of water from the specimens. Finally, the specimens were stored in isopropanol until the time of preparation. At each curing time, at least 12 specimens were created, 4 were used for determining fracture toughness and 8 for tensile strength using Brazilian split tests, the curing ages investigated were 7, 8, 18, 24, 36, 48, 96, 168, 336 and 672 hours. The 7 and 8 hour old specimens were extracted from their parent cylinders without being submerged in the lime water. The quality of the sample needed to be kept consistent throughout all specimens and a detailed preparation procedure was followed.

Sample Preparation

Sample surface preparation is essential to ensure the accuracy and repeatability of the scratch tests. The surface to be tested should be as flat as possible, parallel with the bottom surface of the sample and have a small roughness. The procedure used to achieve these criteria, inspired by (Miller et al. 2009), is describes how to accomplish this.

During specimen extraction, the drop saw should be as orthogonal to the sample as possible, which helps to ensure that the top and bottom surfaces of the specimen are parallel to each other. The specimens are then ground, to further improve the parallelism of the top and bottom faces, and finally polished until the surface becomes reflective. The older specimens were ground using a 15 μm and 9 μm diamond/oil suspension on a polishing table with a jig to hold the specimen in place. The polishing procedure then consists of using 9, 3 and 1 μm alumina pads. The microstructure of the younger specimens is too fragile for the polishing table, so the alumina pads were used for the grinding and polishing process. In between each preparation step, the specimens were ultrasonicated in isopropanol to clean and remove debris.

The surfaces of the Brazilian cylinders did not have to have polished, so only the grinding procedure was used to help achieve a uniform specimen thickness. The wooden bearing strips were cut to be less than 2.5 mm wide and placed on top and bottom of the cylinder as per (ASTM C496).

EQUIPMENT AND TESTING PROCEDURE

Calibrating the Tip Shape Function

The probe tip shape function $f(d) = 2p(d)A(d)$ needs to be calibrated before K_c can be predicted. It was shown in (Akono and Ulm 2012) that a conical shaped probe depends on d^3 and a spherical tip on d^2. Since the Rockwell tip consists of a conical and spherical region, the following function was used:

$$f\left(\frac{d}{R}\right) = R^3\left[\alpha\left(\frac{d}{R}\right)^3 + \delta\left(\frac{d}{R}\right)^2 + \gamma\left(\frac{d}{R}\right)\right], \alpha \geq 0, \delta \geq 0, \gamma \geq 0 \quad \text{(eq. 4)}$$

Where α and δ capture the conical and spherical shape, respectfully, and γ accounts for any blunting of the tip, although in all calibrations performed in this investigation, $\gamma = 0$. Lexan was used as a reference material because the maximum penetration depth in the Lexan is comparable to the cement pastes presented here. Lexan is very sensitive to environmental conditions and so a rigid preparation procedure (Akono 2013) was performed to help ensure repeatability. First, blocks of Lexan about 25 mm x 25 mm were cut from a parent sample by a water jet, and their surfaces were thoroughly cleaned. The blocks were then dried in an oven at 120°C for 24 hours, and then placed in a sealed container to cool at room temperature for another 24 hours before testing began.

Just prior to testing, the Lexan block is glued to a 4 mm thick piece of steel with cyanoacrylate ("super glue"). The steel base is then tightly secured in the jaws of the MCT testing machine. The specimen is oriented inside the machine to ensure that if there is a slope to the surface, the probe will scratch "down-hill". The testing procedure consists of making 24 scratches in 3 different rows one of the surfaces according to the following protocol: Loading rate = 60 N/min, Maximal vertical force = 30 N, Scratch speed = 6 mm and Scratch length = 3 mm. The K_c of Lexan is 2.69 $MPa\sqrt{m}$ (Hill 1990). The parameters of the shape function are then determined by re-arranging equations 1 and 4 and plotting ${F_T}^2/R^3{K_c}^2$ vs d/R, the parameters α, δ and γ are then calibrated from the curve fitting. Once the shape function parameters are calibrated, equation 1 can then be used to predict K_c of the cement pastes.

Micro-scratch Testing

A CSM Instruments Micro Scratch Tester (MCT) (Randall et al.) with a load cell capacity up to 30 N was used with a 200 μm Rockwell diamond probe. The probe is a cone, with a half-apex angle of $\theta = 60°$ that terminates in a hemisphere of radius $R = 200\ \mu m$. The depth where the tip transitions from a cone to a sphere is $26.8\mu m$ (Akono and et al. 2012). The tests were performed by first probing the location of the reference surface by applying a 0.03 N load. Once the unscratched surface was located, the test began and the penetration depth d was determined according to the

reference surface. After the test was completed, some of the scratch grooves were then photographed, see figure 1. Some selected plots showing the raw data and excellent convergence to a constant value of K_c can be seen in figure 2. Note that some curves had to be removed from the analysis if the raw data was contaminated, for example if the probe passed through a pore.

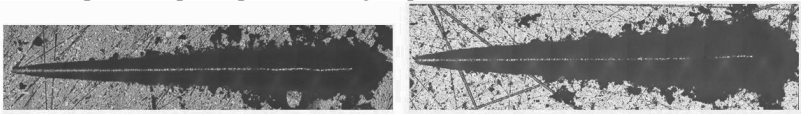

Figure 1: Scratch groove of in a sample cured for (left) 2 weeks and (right) 1 day. The scratch cured for 1 day is wider because the probe penetrated deeper into the material.

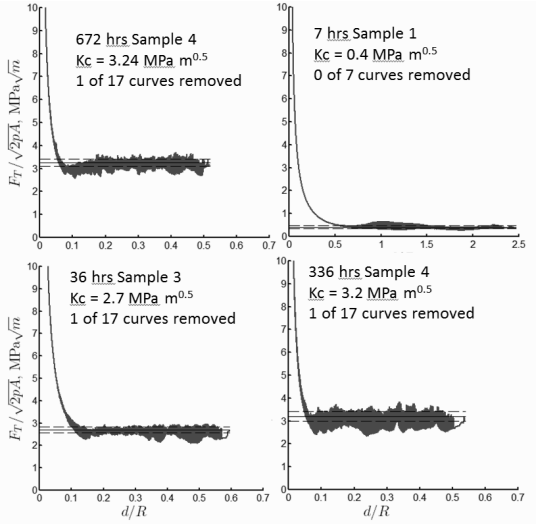

Figure 2: Select raw data curves from a collection scratch tests.

Brazilian Split Cylinder Testing

The cylinders were tested in a screw-driven testing machine from Instron with a 20,000 lb (89 kN) capacity load cell. A constant vertical displacement rate of 0.2 mm/min was used. The typical load vs vertical displacement curve is shown below in figure 2. It consists of different behaviors: 1) an initial linear range when the entire system is elastic 2) a ductile 'hardening' zone where the bearing strips are compressing inelastically 3) a final loading stage after the bearing strips have completely compressed and 4) a brittle 'snap-down' stage when a macro-crack is formed.

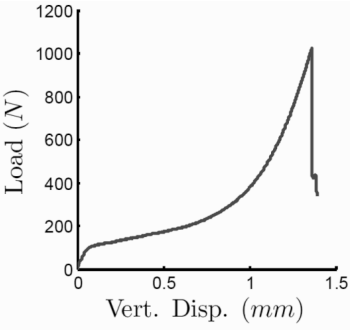

Figure 3: Load vs Vertical Displacement of a 24 hr old split cylinder sample

RESULTS AND DISCUSSION

The evolution of fracture toughness versus Log of curing time (in hours) and the evolution of splitting strength vs Log of curing time are shown in figure 4. Both trends closely follow a simple asymptotic equation of the form $y = Ax^B + c$, which are shown by the red lines in the graphs. The parameters of these equations, determined using the trust-region reflective algorithm implemented in MatLab, are: for the fracture toughness evolution $A = -16.67$, $B = -0.91$ and $c = 3.24$ and for the splitting strength evolution $A = -32.78$, $B = -1.18$ and $c = 4.1$. Note that in the fracture toughness evolution plot, at 169 hours, the point which shows a much smaller fracture toughness compared to the rest of the family of points had a large sloped surface and should not be considered in further analysis.

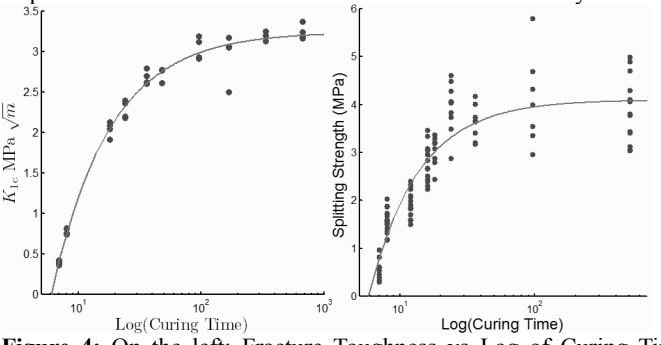

Figure 4: On the left: Fracture Toughness vs Log of Curing Time, On the right: Splitting Strength vs Log of Curing Time

As the curing time approaches infinity, the parameter c governs the asymptotically approached limit for both the fracture toughness and splitting strength. With these two trends defined, it is now possible to show the evolution of the FPZ size which is proportional to the characteristic length l_{ch} given by (Irwin, 1958), see figure 5:

$$l_{ch} = \frac{K_1^2}{f_t^2} \qquad \text{(eq. 5)}$$

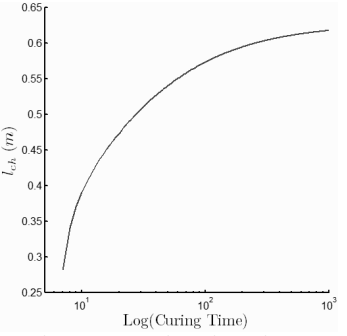

Figure 5: Evolution of FPZ Size vs Log of Curing Time

This trend clearly shows that l_{ch} increases with the curing age of the cement paste and is approaching a finite value of 0.62 m. This is proportional (within a multiplying factor) to the size of the FPZ of the cement paste.

CONCLUSION

The micro-scratch testing and its analysis continue to grow in the fields of material science and engineering, especially when it comes to using materials at smaller scales being used for fracture resistance. In this study, white cement paste specimens were created at different curing ages to use in the scratch test as well as the classical Brazilian split cylinder test. The excellent convergence of the raw data allows the increase of fracture toughness and splitting strength at different curing ages to be determined, both approached an asymptotic value for larger curing times. Finally Irwin's characteristic length, which is proportional to the fracture process zone size, was determined and also shown to asymptotically reach a constant size for large curing times.

REFERENCES

ASTM (2011). Standard Test Method for Splitting Tensile Strength of Cylindrical Concrete Specimens. C496/C496M - 11.

A-T. Akono, P.M. Reis, and F-J. Ulm (2011). "Scratching as a Fracture Process: From butter to steel." Phys. Rev. Lett. 106, 204302.

A-T. Akono and F-J. Ulm (2011). "Scratch Test Model for the Determination of Fracture Toughness." Eng. Fract. Mech. 78, 334.

A-T. Akono and F-J. Ulm (2012). "Fracture Scaling Relations for Scratch Tests of Axisymmetric Shape." J. Mech. Phys. Solids 60(3), 379-390.

A-T. Akono, N.X. Randall, and F-J. Ulm (2012). "Experimental Determination of the

Fracture Toughness via Microscratch Tests: Application to Polymers, Ceramics, and Metals." J. Mat. Res. 27(2), 485-493.

A-T Akono, (2013). *Micro Scratch Tests as an Alternative Means to Assess the Fracture Properties of Materials*, Ph.D. Thesis, Massachusetts Institute of Technology.

G.I. Barenblatt (1962), "The Mathematical Theory of Equilibrium Cracks in Brittle Fracture." Adv. Appl. Mech. 7, 55.

M.E. Broz, R.F. Cook, D.L. Whitney (2006) "Microhardness, Toughness and Mohs Scale Minerals." Am Mineral 91, 135–42.

M. Miller, C. Bobko, M. Vandamme, and F-J. Ulm (2008). "Surface Roughness Criteria for Cement Paste Nanoindentation." Cem. Concr.Res. 38(4), 467-476.

N.X. Randall, G. Favaro, and C.H. Frankel (2001). "The Effect of Intrinsic Parameters on the Critical Load as Measured with the Scratch Test Method." Surf. Coat. Technol. 137, 146.

D. Tabor (1954). "Mohs's Hardness Scale – a Physical Interpretation." Proc. Phys. Soc. 67, 249.

J.A. Williams (1996). "Analytical Models of Scratch Hardness." Tribol. Int. 29:675–694.

F. Wredenberg, P-L. Larrson (2009). "Scratch Testing of Metals and Polymers: Experiments and Numerics." Wear 266, 76–83.

H. Ollendorf, D. Schneider (1999). "A Comparative Study of Adhesion Test Methods for Hard Coatings." Surf Coat Technol 113, 86–102.

T. Richard, E. Detournay, A. Drescher, P. Nicodeme, D. Fourmaintraux (1998). "The Scratch Test as a Means to Measure Strength of Sedimentary Rocks." SPE/ISRM 47196.

G. Schei, E. Fjær E. Detournay, C.J. Kenter, G.F. Fuh (2000). "The Scratch Test: An Attractive Technique for Determining Strength and Elastic Properties of Sedimentary Rocks." SPE 63255.

A.J. Hill and C.M. Agrawal (1990). "Positron Lifetime Spectroscopy Characterization of Thermal History Effects on Polycarbonate." J. Mater. Sci. 25, 5036.

G.R. Irwin. Fracture (1958). *Handbuch der physik*, 6:551-590. S. Flügge, Springer, Berlin.

C. Rocco, G.V. Guinea, J. Planas and M. Elices (April 1999). "Size Effect and Boundary Conditions in the Brazilian test: Experimental Verification" Mat. Str. 32, 210-217.

C. Rocco, G.V. Guinea, J. Planas and M. Elices (July 1999). "Size Effect and Boundary Conditions in the Brazilian test: Theoretical Analysis" Mat. Str. 32, 437-444.

S.P. Timoshenko and J. N. Goodier (1951). *Theory of elasticity*, McGraw-Hill, New York.

C.G. Rocco, (1995). *Size Dependence and Fracture Mechanisms in the Diagonal Compression Splitting Test*. Ph.D. Thesis, Dept. Ciencia de Materiales, Universidad Politecnica de Madrid.

The Significance of Nanosilica on Degradation of Oil Well Cement in Carbonated Brine Environments

Andrew S. Griffin[1], Muhammad K. Rahman[2], Jung J. Kim[3], Mahmoud Reda Taha[1*]

[1] Dept. of Civil Engineering, University of New Mexico, MSC01 1070 1 University of New Mexico, Albuquerque, NM 87131-0001, USA; email: mrtaha@unm.edu
[2] Research Center, King Fahd University of Petroleum and Minerals (KFUPM), Dhahran, Kingdom of Saudi Arabia, email: mkrahman@kfupm.edu.sa
[3] Department of Civil Engineering, Sejong University, Seoul, South Korea, email: jungjkim@sejong.ac.kr

ABSTRACT

Emergent interest in geological carbon dioxide (CO_2) sequestration has brought a need for understanding the mechanism of potential degradation of oil well cement (OWC) in carbonated brine. In this paper, Type G OWC paste specimens produced with water to binder (*w/b*) ratio of 0.45 and incorporating 0, 1 and 3% nanosilica by weight of cement are hydrated for 28 days under two conditions, room condition (20 °C with 0.1 MPa pressure) and an oil well simulated condition (80 °C with 10 MPa pressure). Conditions of geosequestration in a sandstone formation at a depth of 1 km, were simulated by bubbling CO_2 into a heated vessel containing 0.5 M NaCl (brine). Fresh cured OWC cylindrical specimens were exposed to this environment. Slices of the cement specimens were taken periodically, during and after exposure to quantify degradation progression. The modulus of elasticity of the specimens was examined prior to and after exposure, and a damage metric was computed. The results show that the addition of 1% nanosilica can significantly limit OWC degradation in carbonated brine environments. Furthermore, microstructural characterization using BET-N2, X-ray diffraction (XRDA) and ^{29}Si nuclear magnetic resonance (NMR) was performed to explain the macroscale observations.

INTRODUCTION

Carbon capture and storage (CCS) is an international effort that targets reducing carbon dioxide (CO_2) in the atmosphere by capturing and storing it in deep geological formations (Cailly et al. 2005). A major concern in the CO_2 sequestration process is to ensure the integrity of existing oil wells and to confirm their ability to confine CO_2 storage. It is well accepted that wellbore integrity is strongly dependent on the quality of the oil well cement (OWC) in the annulus and the quality of the bond between this annulus and the rock formation on one side and between the annulus and the steel casing on the other side. Researchers have shown that combining elevated temperature and pressure conditions with continuous CO_2 exposure in deep oil wells can result in debonding of the steel casing from the cement annulus (Wong and Yang 2006). It has also been demonstrated that degradation of the

cement adjacent to the rock formation is much more possible than that adjacent to the steel annulus (Zhang and Bachu 2011).

Many researchers conducted experiments to simulate OWC degradation due to exposure to saturated carbonated brine (e.g. Huet et al. 2010 and Duguid and Scherer 2009). Zhang and Bachu (2011) explained that the process of carbonation might not be harmful to OWC. While carbonation means the reaction of CO_2 with Calcium Hydroxyl (CH) in hydrated cement, this results in the formation of $CaCO_3$ (Calcite) which might fill the pores of cement and reduce its porosity and thus increase its integrity. Carbonation in and of itself, therefore, is argued not to be dangerous to the quality of OWC. However, CO_2 bicarbonation, which results in dissolving $CaCO_3$ from cement and leaching out of the cement, is a dangerous mechanism that can significantly affect OWC integrity. This difference was confirmed by field measurements by Crow et al. (2010). The differentiation of these two steps in the degradation process is important. Bicarbonation is dependent on the chemistry of the environment which is strongly dependent on the nature of the rock formation. Degradation testing was implemented here to quantify the specimen's resistance to attack from carbonated brine formed during carbon sequestration following the set-up developed by Duguid and Scherer (2009) with some modifications. This system was designed to simulate the characteristics of geosequestration conditions at a depth a 1 km below ground level (Hitchon 1996). The system simulates sandstone-like conditions of 50 °C and pH 5 at the same depth.

EXPERIMENTAL METHODS

Materials. Water to binder ratio (*w/b*) of 0.45 was used for the neat and nanosilica incorporated OWC paste specimens. Type G OWC was used incorporating 0, 1 and 3% nanosilica by weight of cement. Mixing quantities were determined after American Petroleum Institute's (API) Specification 10A for Cements and Materials for Well Cementing (API, 2009). API's specifications provide the slurry requirements for Class G OWC as 349±5 g of deionized mixing water and 792±5 g of OWC. Special molds were fabricated out of hardened plastic to cast 25 mm. diameter, 50 mm. tall cylinders for one day and then cure up to 28 days of age. The uncommon specimen size was selected in order to accommodate the restrictive dimensions of the high pressure and temperature curing vessel described in the next section.

Curing set-up. Specimens were cured in a curing room under tap water containing lime with a controlled temperature of 20 °C and pressure 0.1 MPa (1 atm) for the ambient curing condition. A special set-up for the elevated temperature 80 °C and pressure 10 MPa (98.7 atm) curing conditions was prepared as shown in Figure 1. The special set-up and process were created in order to simulate actual OWC curing conditions. An enlarged 900 ml *Parr*® pressure vessel was used. Two-thirds of the vessel was filled with tap water containing lime and the specimens were cured in the water under elevated temperature and pressure. Pressure was applied by injecting nitrogen gas from a compressed Nitrogen cylinder at 10 MPa while the temperature was kept constant using the heater surrounding the pressure vessel controlled with

thermocouple sensors. All specimens were cured under ambient or elevated curing conditions for 28 days with subsequent monitoring of the temperature and pressure.

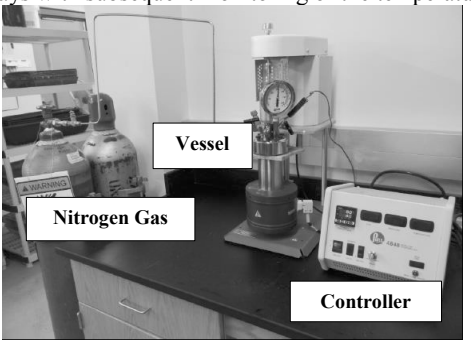

Figure 1. Elevated curing reactor set-up.

Degradation testing. After 28 days of curing and appropriate cooling techniques, four visually comparable samples from each specimen category were selected for subsequent degradation testing. The uneven top surfaces of the specimens were cut (3 mm. slice) and prepared using a Buehler® Isomet low speed saw and Buehler® 6 inch diamond wafering blade. Specimens were then placed in a 0.5 M NaCl solution in a sealed chamber with a nitrogen induced environment for 28 days of conditioning prior to the start degradation testing. A schematic of the set-up and flow through the degradation testing system simulating sandstone-like conditions is shown in Figure 2. The degradation-testing set-up is shown as an insert in Figure 2. Before the start of testing, the 5 gallon brine reservoir was filled with 0.5 M NaCl (brine) solution and heated to 50 °C. CO_2 was then bubbled at the bottom of the reservoir at approximately 5-10 psi for the remainder of the testing period.

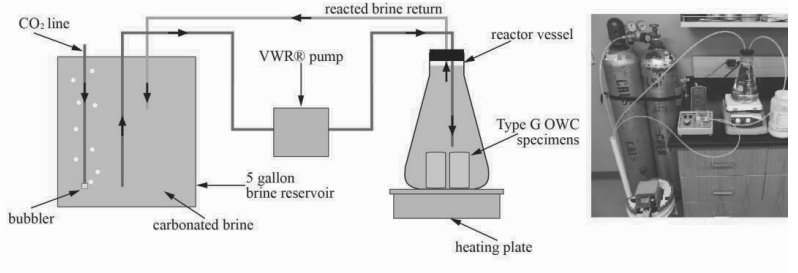

Figure 2. Schematic of set-up and flow through degradation testing system.

The specimens were then placed inside the sealed reactor vessel and the VWR® variable flow pump was then set to a flow rate of approximately 8 mL/min to initiate the testing process. The influent carbonated brine from the reservoir then entered the bottom of the sealed reactor forcing the reacted brine to exit through the return line at the top. This process ensured that the specimens would react with fresh solution throughout the test. The degradation test ran for 28 days. The temperature was held constant at 50 °C ± 0.2 °C. The pH of the system was initially 5.05 but

reached a measured value of 4.16 after 28 days of testing. Samples were collected at specific time intervals starting at the beginning of the test and ending after 28 days. Samples were obtained by cutting small slices, around 5 mm in height, from the cylindrical cement specimens in the reactor. A high resolution scan was taken of each of the specimens to visually examine the degradation progression. Collected samples were then preserved in 0.5 M NaCl in a nitrogen environment until being used for microscopic analysis. Uniaxial compression testing was performed on OWC specimens before and after degradation in order to determine the modulus of elasticity and quantify damage due to carbonated brine exposure. Microstructural characterization of the OWC specimens with and without nanosilica before and after carbonated brine exposure was performed using BET-N2 techniques, X-ray diffraction (XRDA) and ^{29}Si nuclear magnetic resonance (NMR).

RESULTS AND DISCUSSIONS

Slices of the specimens taken throughout the experiment showed that a dark grey degradation ring had formed and progressed inward for the neat specimen type cured under both conditions. However, specimens incorporating 1% and 3% nanosilica displayed no visual degradation or degradation progression. This comparison is presented in Figure 3. The rate of degradation advance was calculated from plots of the degradation reaction depth versus time by fitting a straight line to the data; Figure 4. The neat specimen type cured under ambient (N) conditions exhibited a degradation advance rate of 0.173 mm/day throughout the entire experiment and the neat specimen type cured under elevated (H) conditions displayed a slightly higher rate of 0.198 mm/day. Both specimen types showed no visual degradation advance until 10 days of exposure and then exhibited rapid degradation advance until day 15 of exposure at a rate of 0.469 and 0.458 mm/day for the ambient and elevated cured conditions respectively. From day 15 to day 28 the degradation rate slowed considerably to 0.072 and 0.118 mm/day for the ambient and elevated curing conditions. Specimens incorporating nanosilica are shown as a solid line at the zero mark in the figure as they showed no visual sign of degradation. Neat specimens cured under ambient conditions had a statistically significant increase in modulus of elasticity, around 31%, after degradation testing.

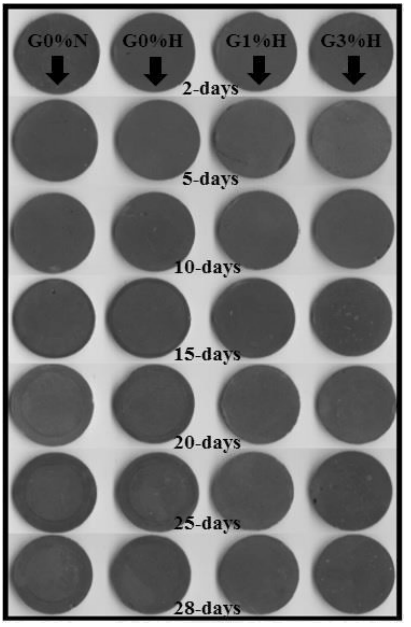

Figure 3. Degradation progression.

The neat specimen type cured under elevated (oil well simulated) conditions showed a slight statistically insignificant increase, less than 5%, in static modulus of elasticity after degradation testing. Specimens incorporating 1% nanosilica addition produced a statistically significant increase in modulus of elasticity of almost 50%. Specimens incorporating 3% nanosilica addition exhibited a statistically insignificant decrease in modulus of just over 5%. The results are shown in Figure 5. The increase in the modulus of elasticity can be attributed to the exposure of OWC specimens to a relatively high temperature (50 °C ± 0.2 °C) during carbonated brine degradation. This is explained by the ability of high temperatures to stimulate further cement hydration. The combined observation of damage progression at the surface and the increase in modulus of elasticity might be explained by considering two interacting mechanisms occurring simultaneously: a degradation mechanism that quickly affects the surface and an elevated temperature curing effect that further strengthens the core by producing calcium carbonate. While the above hypothesis might explain the significant increase in modulus of elasticity of the OWC cured under ambient (N) conditions without nanosilica, it cannot explain the increase in OWC specimens including 1% nanosilica and/or cured at high temperature and pressure.

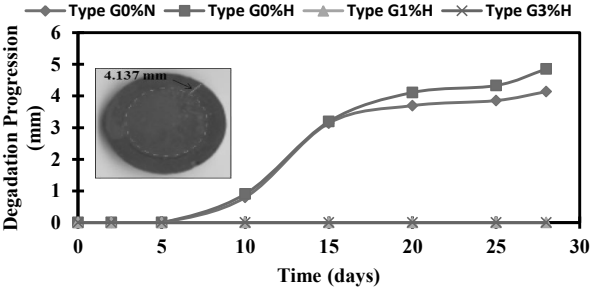

Figure 4. Degradation progression for the specimen types.

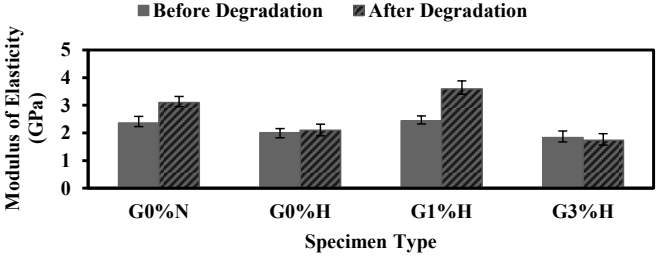

Figure 5. Modulus of elasticity before and after carbonated brine degradation.

To further explain our degradation observations, microstructural investigation of the porosity using BET N2 technique indicated type IV isotherm classification for all isotherms produced for the varying specimen types, according to IUPAC recommendations. Type IV isotherms are characteristic of solids having mesopores (2-50 nm) and macropores (> 50 nm) (Aligizaki, 2006). The sub classification of the

pore system is type H3 which describes mesopore structures with very wide capillaries having narrow openings and an interstice between the parallel plates. This sub classification type is typically found in sheet-like material shapes, which we believe describes calcium silicate hydrate (CSH). Comparison of the porosity observations showed a decrease in pore volume and peak pore size (pore volume= 0.028 cm^3/gm at d_{peak}=310 nm) for 1% nanosilica specimens when compared with OWC without nanosilica cured under elevated temperature (pore volume= 0.053 cm^3/gm at d_{peak}= 321 nm). However, specimens incorporating 3% nanosilica exhibited an increase in porosity (pore volume=0.078cm^3/gm at d_{peak}=328 nm). The absence of visual degradation in OWC specimens incorporating 1% nanosilica can be explained by the significant reduction in porosity of these specimens.

X-ray diffraction analysis results are shown in Figure 6. It can be observed that calcium carbonate ($CaCO_3$) peaks at $2\theta = 23^o$ are only distinct in OWC specimens without nanosilica. Peaks located at $2\theta = 23^o$ for specimens incorporating nanosilica were also identified to be for Hatrurite and Brownmillerite as shown in Figure 6. The relatively low amount of $CaCO_3$ in OWC with nanosilica can be explained by the low permeability of OWC incorporating nanosilica and the lack of free lime (CH crystals) consumed by nanosilica. It is therefore evident that using nanosilica significantly reduced the carbonation mechanism. The significant increase in modulus of elasticity of OWC specimens without nanosilica cured under ambient conditions can partly be explained by the $CaCO_3$ formation as a result of CO_2 reaction with CH. $CaCO_3$ has a higher modulus of elasticity than CH and CSH. With the relatively low amount of $CaCO_3$, the risk of bicarbonation is significantly reduced when nanosilica is used.

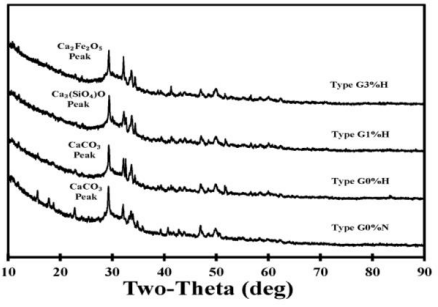

Figure 6. XRDA of OWC specimens after carbonated brine exposure.

Furthermore, ^{29}Si MAS NMR was used to examine the polymerization of a silicate tetrahedron in synthetic CSH (Lippmaa et al. 1980). The results of ^{29}Si MAS NMR spectra for all specimens before and after degradation were deconvoluted after Saoût et al. (2006). Figure 7 compares the NMR spectra and silicate polymerization fraction Q^n (Taylor 1997) for all OWC specimens before and after degradation. From Figures 7 (a) and (b), it can be observed that Q^0 fraction, which is observed typically in alite (C_3S) and belite (C_2S), decreased significantly after exposure to carbonated brine. Therefore, it is evident that the unhydrated cement components in hydrated cement pastes react with CO_2 and produce calcium carbonate. One can also observe an increase of Q^2 (the middle chain of C-S-H layer) over Q^1 (the end chain of C-S-H) fractions after carbonated brine exposure. This increase is observed in all OWC

specimens with and without nanosilica. The formation of Q^2 might occur due to CO_2 reaction with CSH forming calcium carbonates and thus connecting two CSH layers. There is a slight increase in Q^3 and Q^4 as well. High level polymerization can happen due to combining multi layers in CSH.

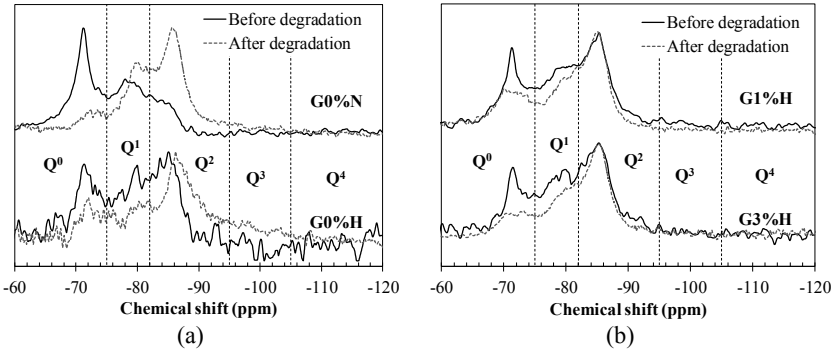

Figure 7. Comparison of NMR spectra before and after carbonated brine exposure for OWC specimens (a) G0%N vs. G0%H (b) G1%H and G3%H.

NMR observations indicate that carbonated brine exposure of OWC can lead to forming a high degree of silicate polymerization Q^2 and typically non-observed Q^3 and Q^4 in OWC specimens. The change of Q^0 to high order polymerized silicate might explain the increase in the modulus of elasticity of OWC specimens incorporating 1% nanosilica. The significance of increasing polymerized silicate with Q^2, Q^3 and Q^4 content compared with Q^0 and Q^1 on the modulus of elasticity of cement needs to be further investigated. It is important to note that increasing silicate polymerization increases brittleness and thus the chance of cracking under thermal stress fluctuation in deep oil wells. The significant increase in porosity of OWC specimens incorporating 3% nanosilica might explain the limited change in its modulus of elasticity in spite of the increase in its silicate polymerization.

CONCLUSION

Degradation of OWC in carbonated brine is a complex process that is affected by many interacting factors including the cement paste porosity, the existence of free lime (CH) and degree of hydration of OWC prior to carbonated brine exposure. It is evident that nanosilica at the appropriate content limits OWC porosity and consumes almost all free lime and therefore limits the carbonation mechanism. Adding nanosilica eliminated any visually observed damage at the outer surface of the OWC specimens compared with OWC specimens without nanosilica. No decrease in the modulus of elasticity after carbonated brine exposure was observed in all OWC specimens with and without nanosilica. Some specimens showed an increase in the modulus of elasticity after exposure. Microstructural analysis showed that the increase in modulus of elasticity could be attributed to the formation of calcium carbonate in CSH and/or to an increase in the level of silicate polymerization. While both reasons can contribute to OWC specimens without nanosilica, only the latter

affects OWC specimens with nanosilica. No mechanical degradation was observed in any of the tested OWC specimens, however, OWC specimens without nanosilica will have high risk of bicarbonation if continued to be exposed to carbonated brine. This risk is significantly reduced for OWC incorporating nanosilica. Further research is warranted to examine the long-term effect of carbonated brine exposure on OWC.

ACKNOWLEDGMENT

The authors would like to acknowledge the support to the University of New Mexico team by US National Science Foundation (NSF) Award # 1131369. The support provided to KFUPM, Project #09-NAN754-04 by King Abdulaziz City for Science and Technology (KACST), is greatly acknowledged.

REFERENCES

Aligizaki, K. K. (2006) *Pore structure of cement-based materials*, Taylor and Francis, New York.

API (2009) *RB 10A Specification for cements and material well cementing*, 24th ed., American Petroleum Institute, Washington, DC.

Crow, W., Carey, J.W., Gasda, S., Williams, D.B., and Celia, M. (2010) "Wellbore integrity analysis of a natural CO2 producer." *Int. J. of Greenhouse Gas Control*, 4(2), 186–197.

Cailly, B., Le Thiez, P., Egermann, P., Audibert, A., Vidal-Gilbert, S., and Longaygue, X. (2005) "Geological storage of CO2: A state-of-the-art of injection processes and technologies." *Oil & Gas Science and Tech.*, 60(3), 517–525.

Deguid, A., and Scherer, G. W. (2009) "Degradation of oilwell cement due to exposure to carbonated brine." *Int. J. of Green Gas Control*, V. 4, 546–560.

Hitchon, B. (1996) *Aquifer disposal of carbon dioxide*, Geoscience Publishing Inc., Sherwood Park, Alberta, Canada.

Huet, B. M., Prevost, J. H., and Scherer, G. W. (2010) "Quantitative reactive transport modelling of Portland cement in CO_2 saturated water." *Int. J. of Greenhouse Gas Control*, 4(3), 561–574.

Lippmaa, E., Mägi, M., Samoson, A., Engelhardt, G. and Grimmer, A. R. (1980) "Structural studies of silicates by solid-state high-resolution 29Si NMR." *American Chemical Society*, 102, 4889–4893.

Saoût, G. L., Le´colier, E., Rivereau, A., and Zanni, H. (2006) "Chemical strucutre of cement aged at normal and elevated temperatures and pressures. Part II: Low permeability class G oilwell cement." *Cem. & Conc. Res.,* 36, 428–433.

Taylor, H. F. W. (1997). *Cement chemistry*, Vol 1, 2nd ed., Thomas Telford, London.

Wong, R. C. K., and Yeung, K. C. (2006) "Structural integrity of casing and cement annulus in a thermal well under steam stimulation*." J. of Canadian Pet. Tech.*, 45(12), 6–9.

Zhang, M., and Bachu, S. (2011) "Review of integrity of existing wells in relation to CO2 geological storage: what do we know?" *Int. J. of Greenhouse Gas Control*, 5, 825–840.

Optimization of Anti-creep Admixtures for Plasterboards

J. Colombani[1] and M. Bellotto[2]

[1]Institut Lumière Matière, Université de Lyon, Université Claude Bernard Lyon 1, CNRS UMR5306, campus de la Doua, F-69622 Villeurbanne, France; PH (+33) 4 72 44 85 70; FAX (+33) 4 72 43 26 48; email: jean.colombani@univ-lyon1.fr
[2]Giovanni Bozzetto S.p.A., via Provinciale, 12, I-24040 Filago (BG), Italy; email: maurizio.bellotto@bozzetto.it

ABSTRACT

We have measured by digital holographic interferometry the dissolution rate constant of gypsum in water containing various phosphonates, small molecules or polymers, known to adsorb at the gypsum crystal surface. According to the assumption of reaction-driven pressure solution creep, dissolution inhibitors of gypsum should also inhibit humid creep of gypsum plaster. This was checked by measuring by rheometry the shear creep rate of gypsum plaster containing these phosphonates in a saturated humid environment. Validating the assumption, all these phosphonates appear to be efficient anti-creep admixtures of humid set plaster, the polymeric ones having the complementary advantage to be easier to use, with a less delicate dosage.

INTRODUCTION

Plasterboard is a universally employed building material. It is a cheap, light, insulating and fireproof solid, which compensates for its weak mechanical strength. One striking weakness is the enhancement of the creep of set plaster by a humid environment. It constitutes a strong limitation of the durability of this material, especially in regions with a humid climate.

It has been recently demonstrated that the creep strain rate of wet set plaster is driven by the water dissolution kinetics of gypsum (Pachon-Rodriguez et al., 2011). This knowledge has enabled us to propose a model for the creep mechanism (reaction-driven pressure solution creep) and to give elements to improve the humid gypsum plaster long-term mechanical behavior. Indeed the dissolution properties of gypsum are modified by the presence of foreign ions in the solution which adsorb at the surface and thus, according to the model, should modify the creep rate of the material. For example, phosphate and phosphonate salts are known to be effective crystal growth modifiers for calcium containing crystals, affecting dissolution as well as growth (Liu and Nancollas, 1973), therefore being likely to slow down humid creep of polycrystalline gypsum.

To identify new potential anti-creep admixtures in this product family, we measure in this work the dissolution rate constant, relevant for quantifying the reaction kinetics, of gypsum in aqueous solutions of different phosphonates, both of

simple molecular structure and of polymeric nature. As the variation of the dissolution rate constant among these products may be tiny, a non-standard experiment (holographic interferometry) has been used for the measurements. This convection-free technique gives access with unprecedented accuracy and precision to the dissolution rate constants (Pachon-Rodriguez, 2013).

The anti-creep performance of these admixtures is then tested by recording the strain evolution vs. time of samples of set plaster submitted to a constant stress under water vapor saturated conditions in a rheometer. The anti-creep efficiency is obtained by comparison with the creep curves of set plaster produced without admixtures. These experiments have led to the confirmation of our assumption on the origin of the humid creep, and to the finding of new anti-creep admixtures. In addition the importance of the texture of the polycrystalline material on the total creep strain has been evidenced.

CHOICE OF ANTI-CREEP ADMIXTURES FOR GYPSUM PLASTER

Set plaster is made of intricate micrometric gypsum needles ($CaSO_4{\cdot}2H_2O$), obtained from the hydration of plaster, i.e., calcium sulfate hemihydrate ($CaSO_4{\cdot}½H_2O$). Adjacent crystallites are considered to be linked either via a solid junction, or via a thin water film. In water, the nanometric thickness of this water slab stems from the balance between the dispersive attraction between the crystallites and the repulsion of the Debye layers present in the liquid film close to the surfaces, as in flocculated colloids (Chappuis, 1999; Gartner, 2009). In a humid atmosphere, capillary forces at the liquid film extremities contribute also to the attraction between needles and increase the stiffness and strength of the material. If the water layer thickens (due to the increase in relative humidity or the material soaking in water) the intercrystalline interaction is weaker and gypsum needles may slide. Various mechanical properties of set plaster in the presence of water can find explanation in this behavior (fall of rigidity, compressive strength, and bending strength).

But the equilibration of the water film thickness with the ambient humidity, so the increase of the inter-needle sliding, is quite instantaneous. Therefore it cannot account for the very slow strain encountered in the creep of wet gypsum plaster. We have proposed recently that this phenomenon finds its origin in a phenomenon called reaction-driven pressure solution creep. When a sample is submitted to an external load, local stresses appear at the needle contacts. These stresses increase the solubility of gypsum, which accordingly dissolves in the liquid films. The dissolved gypsum then diffuses, and precipitates when arriving in non-stressed regions, where it recovers its initial solubility. This transfer of matter leads to a macroscopic plastic strain of the sample. The thicker the liquid slab, the faster the matter transfer, the larger the creep strain. The phenomenon is said reaction-driven, because the chemical reactions (dissolution and precipitation) are the slowest steps, and then control the kinetics of the creep. Therefore when calcium-complexing chemicals adsorb at the crystals surface, thus hindering these heterogeneous reactions, creep has been seen to be slowed down (Pachon-Rodriguez et al., 2011).

In order to find the best potential anti-creep products, we measure here the dissolution kinetics of gypsum in various aqueous solutions of phosphonates, both simple molecules and polymers, well known for their calcium-chelating action. This scan of numerous phosphonates leads to the identification of the best dissolution inhibitors. The actual anti-creep effect of these phosphonates is tested in a humidity-controlled rheometer on gypsum plaster samples manufactured with these phosphonates. In addition to these parameters, also the texture of the poly-crystalline assemblage, as determined by crystal habit and dimensions, has been found to play a role in the macroscopic mechanical behavior of gypsum-based materials.

MATERIALS

The investigated additives are the following phosphonates:

- HEDP (hydroxyethylidene – 1.1 diphosphonic acid), sodium salt at pH 11.5
- ATMP (aminotrimethylenephosphonic acid), sodium salt at pH 10.5
- EDTMP (ethylenediaminetetramethylenephosphonic acid), sodium salt at pH 7.0
- DTPMP (diethylenetriaminepentamethylenephosphonic acid), sodium salt at pH 7.0
- HMDTMP (hexamethylenediaminetetramethylenephosphonic acid), potassium salt at pH 7.0
- Four different poly-aminophosphonates with alkylene oxide functional groups of increasing molecular weight – from 2 ethylene oxide groups per molecule to 45 alkylene oxide groups per molecule, named P1, P2, P3 and P4. All of them neutralized as sodium salts at pH 7.0.

The plaster used is an industrial plaster from a plasterboard production plant, with high purity hemihydrate and minor components of dihydrate and soluble anhydrite.

HOLOINTERFEROMETRIC EXPERIMENTS

To measure the dissolution rate constant, representative of the reaction kinetics of gypsum in contact with the additive aqueous solution, we have made use of digital holographic interferometry, a non-conventional optical technique. This device is often used in solid mechanics for study vibrations and in fluid mechanics to study flows. We have adapted the method in order to access in real time to the bidimensional concentration field in an aqueous solution above a dissolving gypsum single crystal (Colombani and Bert, 2007).

During an experiment, a digital hologram, i.e., a tridimensional phase picture, of a 10x10x40 mm^3 transparent cell containing the aqueous solution is first recorded, constituting the so-called reference hologram. Subsequently a 6x6x0.5 mm^3 sample of a cleaved gypsum single crystal from Mazan quarry (France) is placed at the bottom of the cell. Digital holograms are then recorded during the dissolution of the crystal in the liquid (typically during one day). The interference between these holograms and the reference hologram are carried out numerically and brings the phase difference in the liquid between time t and the reference time, from which the concentration evolution in the cell with time is deduced. The fit of the concentration curves in the

liquid with their theoretical expression, brings the dissolution rate constant of the mineral in the aqueous solution. The first advantage of this technique is that it is carried out in a quiet liquid, no flow blurring the dissolution rate as in standard solution chemistry dissolution experiments. So the measured coefficient is a pure surface reaction rate constant. Its second main advantage is that it enables to observe the interface where the dissolution proceeds, instead of computing the dissolution rate from concentration measurements far from the surface.

The dissolution rate constants from all the investigated admixtures are collected in Table 1. It can be immediately seen in these results, from the lower value of the rate constant in presence of phosphonate, that all these chemicals influence the gypsum-solution reaction in slowing down the transfer from solid to liquid. All measurements have been performed with a concentration of product of 1%. It should be noted that for two products, precipitates appeared during the experiment, making the rate constant measurement impossible.

Table 1. Dissolution rate constant of the various phosphonates.

Product	Dissolution rate constant (mol m^{-2} s^{-1})
set plaster as it is	$4.6 \cdot 10^{-5}$
P1	$4.5 \cdot 10^{-6}$
P2	$1.6 \cdot 10^{-5}$
P3	$8.9 \cdot 10^{-6}$
P4	$8.3 \cdot 10^{-6}$
EDTMP	$4.9 \cdot 10^{-6}$
ATMP	$7.1 \cdot 10^{-6}$
DTPMP	precipitation observed
HEDP	precipitation observed

HUMID CREEP EXPERIMENTS

The measurements have been performed with a rotational rheometer (Physica MCR 301), with a plate-plate measuring system. The plates used are serrated (rough surface) plates of 25 mm diameter. The gap has been set for all the experiments to 3 mm, the sample thus being a disk 25 mm in diameter and 3 mm in height. The plaster has been mixed with water in a water-to-plaster ratio of 0.7 by weight. The phosphonates have been added at two different dosages: 0.1% and 0.3% active phosphonic acid over plaster weight. The plaster slurry has been mixed in a mechanical stirrer with turbine blade for 1 minute at 1200 rpm and loaded in the measuring system while still plastic. The measurements have started 3 minutes after the first contact of plaster and water. The measuring system is contained in a chamber saturated with water vapor (humidity measured at 92% to 95%). The plaster has been allowed to set in the measuring system. After the setting it has been allowed a resting/curing time of 30 minutes to completely develop the microstructure of gypsum, before starting the creep experiment. The sample has been subject at a shear stress of 10 kPa while being subject to an axial compression of 10 kPa for a duration

of 2h25. Subsequently the shear stress has been removed and the relaxation of the sample has been recorded.

Setting time. The setting of plaster is followed through its volume changes. All the phosphonates cause an increase in setting time, which is larger the higher the dosage. The variation of setting time shows almost the same trend with the molal concentration of the phosphonate in solution for all the products, except for HEDP and DTPMP which show a smaller increase on increasing dosage, as reported in Figure 1. These products, HEDP and DTPMP, are the ones for which a precipitation is observed in the experiments of holographic interferometry, and we may suggest that it is the Ca salt of the phosphonate which is precipitating, thus reducing its effect at the highest concentration.

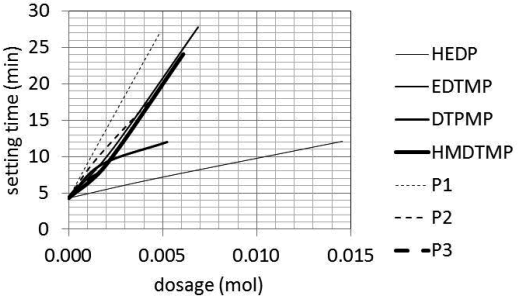

Figure 1. Setting time as a function of concentration.

Creep. The creep and relaxation of gypsum without admixtures is shown in Figure 2 (a). The deformation has an important elastic contribution, which is recovered upon removal of the stress. A visco-elastic deformation is also present which is slowly recovered upon unloading of the sample. Finally there is an irreversible plastic deformation, and the strain rate measured on the final linear portion of the curve is $2{,}165 \cdot 10^{-9}$ s^{-1}. The compliance of the sample is $J = 7.70 \cdot 10^{-8}$ Pa^{-1}, a value which corresponds to the complex modulus G^* measured in a frequency sweep within the linear domain, as shown in Figure 2 (b). The measurement has been performed at an imposed stress of 10 kPa resulting in a strain of $2.7 \cdot 10^{-4}$. The complex compliance $J^*(\omega)$, reciprocal of the complex modulus $J^*(\omega) = 1/G^*(\omega)$, is related to the creep compliance by Fourier transform, and the correspondence between the two indicates that the measurement is not affected by instrumental artifacts.

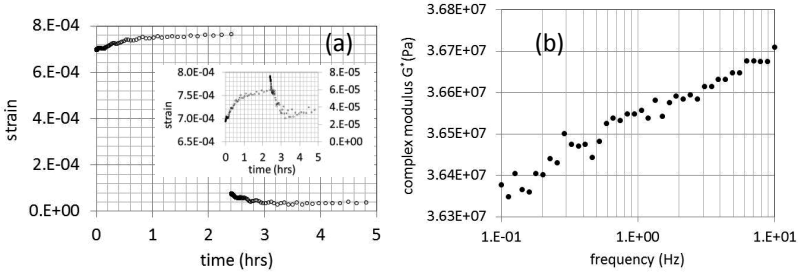

Figure 2. Creep and relaxation for the set plaster without admixtures. In the inset the curves are shown on two different scales (a). Complex modulus as a function of frequency (b).

The qualitative creep behavior of set plaster with the phosphonate admixtures is similar, with differences in the instantaneous elastic deformation and in the long term plastic creep rate. In Figure 3 (a) and (b) are reported the creep curves for the small molecule phosphonates at dosage 0.1% and 0.3% respectively.

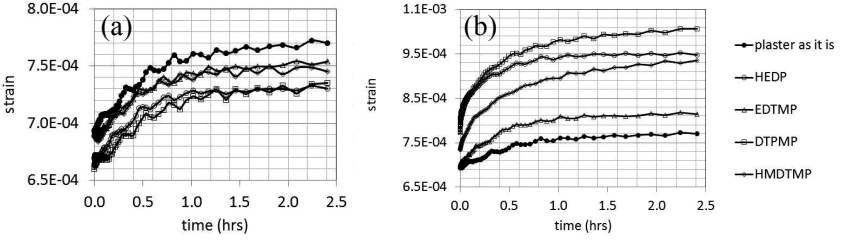

Figure 3. Creep behavior of set plaster with small molecule phosphonates at dosage 0.1% active matter (a) and 0.3% active matter (b).

The long term plastic creep rate is reported in Table 2. It appears that while at low dosage the compliance is lower in the presence of the phosphonates than in their absence, the opposite is true at higher dosage. Apart from the case of EDTMP the instantaneous elastic deformation is increasing with the admixture dosage. The strain rate is also increasing on increasing dosage, being higher in the presence of phosphonates than for the sole set plaster, again with the exception of EDTMP.

The picture is different in the case of set plaster with the addition of the polymeric phosphonates, as shown in the creep curves reported in Figure 4 and in the plastic strain rates reported in Table 2. In the case of products P1 and P2, at lower dosage the creep behavior is similar to the one of set plaster without admixtures, while on increasing the dosage the overall compliance reduces and the strain rate gets

smaller. The product P3 behaves differently, with performance getting better on increasing the dosage, still being however worse than the plain plaster.

Table 2. Plastic strain rate for set plaster with and without phosphonates.

Product	strain rate (s^{-1})	
set plaster as it is	$2.165 \cdot 10^{-9}$	
	dosage 0.1%	dosage 0.3%
HEDP	$1.048 \cdot 10^{-9}$	$3.202 \cdot 10^{-9}$
EDTMP	$1.942 \cdot 10^{-9}$	$2.096 \cdot 10^{-9}$
DTPMP	$1.719 \cdot 10^{-9}$	$4.378 \cdot 10^{-9}$
HMDTMP	$1.438 \cdot 10^{-9}$	$5.252 \cdot 10^{-9}$
P1	$1.534 \cdot 10^{-9}$	$8.841 \cdot 10^{-10}$
P2	$1.921 \cdot 10^{-9}$	$1.083 \cdot 10^{-9}$
P3	$3.363 \cdot 10^{-9}$	$2.825 \cdot 10^{-9}$

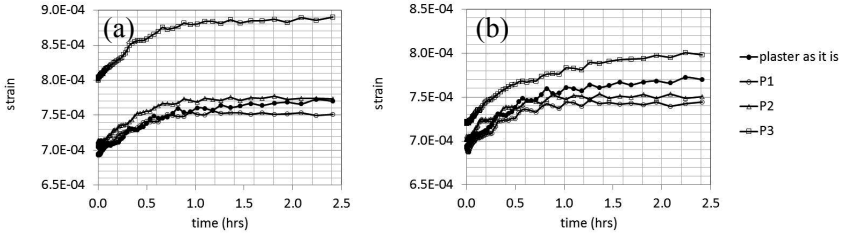

Figure 4. Creep behavior of set plaster with the polymeric phosphonates at dosage 0.1% active matter (a) and 0.3% active matter (b).

DISCUSSION

The creep behaviour of set plaster in the presence of phosphonates confirms the mechanism of pressure dissolution creep, the phosphonates lowering parallely the dissolution rate and creep rate. However the overall creep is composed of the sum of an elastic component, a visco-elastic component and a plastic flow. While plastic flow is determined by the pressure dissolution mechanism, the first two components are deeply influenced by the texture of the polycrystalline assemblage, i.e. by the crystal shape and dimensions. Phosphonates are known crystal habit modifiers for calcium dihydrate. This may explain that the dissolution rate and total creep strain rate are not strictly correlated, the admixtures acting both on the dissolution and microstructure.

Concerning the use of the products, the case appears to be different for small molecule and polymeric phosphonates. The first ones precipitate the Ca salt of the phosphonate on increasing concentration in the presence of high Ca contents. This precipitation most probably disturbs the development of the gypsum microstructure during setting at high dosage, which negatively affects the mechanical behavior of set plaster. Therefore overdosing of these products may affect the set plaster performance, which makes their use quite difficult in practice.

The polymeric phosphonates never precipitate even at high concentration and high Ca loadings and their performance gets better on increasing the dosage. This makes them good candidates as anti-creep admixture. Among them, the best product, easy to use and very effective, is the lowest molecular weight polymer P1, with the highest molal concentration at a given dosage and the best influence of the mechanical behavior.

CONCLUSION

Relying on the assumption that humid creep of gypsum plaster originates in the dissolution of the material, we have measured the dissolution rate constant of gypsum in aqueous solutions of various phosphonates, known to adsorb on calcium containing crystal like gypsum. All of them have been seen to slow down the dissolution. Therefore the shear creep of gypsum plasters containing these admixtures has been investigated by humidity-controlled rheometry in humid saturated conditions. All of them but one have been found to lower the creep rate, validating our assumption. Dissolution rate and creep rate are not strictly proportional because the phosphonate influence not only dissolution but also the microstructure of the samples, modifying its mechanical behaviour. Polymeric phosphonates have been found to be better anti-creep candidates, their dosage being less delicate.

REFERENCES

Chappuis, J. (1999). “A new model for a better understanding of the cohesion of hardened hydraulic materials.” Colloids Surf. A 156, 223-241.

Colombani, J. and Bert, J. (2007). “Holographic interferometry study of the dissolution and diffusion of gypsum in water.” Geochim. Cosmochim. Acta 71, 1913-1918.

deMeer, S. and Spiers, C. (1997). “Uniaxial compression creep of wet gypsum aggregates.” J. Geophys. Res. 102, 875-891.

Gartner, E.M. (2009). “Cohesion and expansion in polycrystalline solids formed by hydration reactions — The case of gypsum plasters.” Cem. Concr. Res. 39, 289-295.

Jørgensen, K.D. and Posner, A.S. (1959). “Study of the setting of plaster.” J. Dental Res. 38, 491-499.

Liu, S.T. and Nancollas, G.H. (1973). “The crystal growth of calcium sulfate dihydrate in the presence of additives.” J. Coll. Int. Sci. 44(3), 422-429.

Pachon-Rodriguez, E.A., Guillon, E., Houvenaghel, G., Colombani, J. (2011). “Pressure solution as the origin of the humid creep of a mineral material.” Phys. Rev. E 84, 066121.

Pachon-Rodriguez, E.A., Colombani J. (2013). "Pure dissolution kinetics of anhydrite and gypsum in inhibiting aqueous salt solutions.” AIChE J. 59, 1622-1626.

Van’t Hoff, J.H., Armstrong, E.F., Hinrichsen, W., Weigert, F., Just, G. (1903). “Gips und Anhydrit.” Zeitschr. f. Physik. Chem. 45, 257-298.

Role of recycled concrete aggregates on the long-term behavior of structural concrete

C. Mazzotti[1], S. Manzi[1] and M.C. Bignozzi[1]

[1]DICAM, Department of Civil, Chemical, Environmental and Materials Engineering, University of Bologna, Viale Risorgimento 2, 40136 Bologna, Italy, PH (+39) 051-2093237; FAX (+39) 051-2093236; Email: claudio.mazzotti@unibo.it, stefania.manzi4@unibo.it, maria.bignozzi@unibo.it

ABSTRACT

The effects of coarse recycled concrete aggregates on long-term behavior of concrete (shrinkage and creep) are investigated. Most important corresponding prediction models have been compared with experimental findings obtaining a systematic underestimation of results. The adhered mortar of the recycled concrete aggregates is determined and its influence on the final concrete properties is investigated as its content and porosity can influence the final properties of the new concrete.

INTRODUCTION

The increasing charges for landfill, as well as the shortage of natural resources for aggregates production are encouraging the sustainable use of waste from construction sites as a source of new aggregates. Indeed, the use of construction and demolition waste (C&DW) for the production of new concrete has become popular in the last years (Rao et al. 2007), in accordance with the possibility of using recycled concrete aggregates in the European standards and Eurocodes. When demolished concrete is crushed, a certain amount of mortar and cement paste from original concrete remains attached to stone particles in recycled aggregates. It is well known that attached mortar is the main reason for the lower quality of C&DW (low density, high water absorption, etc.) compared to natural aggregates.

While a certain number of studies can be found in literature describing the fresh state properties and instantaneous mechanical behavior of this type of concretes (Etxeberria et al. 2007, Rahal 2007) very few information are available concerning their long-term performances, like shrinkage and creep (Manzi et al. 2013*a*). In this framework, it is not clear yet if conventional predictive models, calibrated on databases coming from concretes with natural aggregates, could be successfully applied to this type of concrete.

In this paper, the effects of coarse recycled concrete aggregates on long-term mechanical and physical properties of new structural concrete are investigated. Moreover, particular attention has been addressed to the adhered mortar of the

recycled concrete aggregates. Indeed, adhered mortar and its porosity can greatly influence the final properties of the new concrete, particularly long-term ones (Fathifazl et al. 2011). Correlations between porosity of concrete made of recycled concrete aggregates and both creep and shrinkage have been also described, verifying that the amount of recycled aggregates alone is not sufficient to comprehensively understand the long-term behavior. Finally, experimental results in term of creep and shrinkage have been compared with prediction rules provided by the most important International Guidelines and Codes, in order to verify their applicability even to this type of sustainable construction material.

EXPERIMENTAL CAMPAIGN

Materials. Conventionally available concrete components were used to prepare the mixes; as for the natural aggregates, sand (0 - 6 mm), fine gravel (6 - 16 mm) and gravel (16 - 25 mm) were used with a cumulative grain size distribution (sand: 48 vol%, fine gravel: 25 vol% and gravel: 27 vol%) complying with Fuller distribution (see Manzi et al., 2013a for further details). Cement type CEM II-A/LL 42.5 R and an acrylic based superplasticizer were used as binder and mixture, respectively, for all the concrete mixes.

Concrete waste coming from the demolition of a never finished concrete construction was used as recycled aggregates (fcm ≈ 36 MPa). The demolished concrete underwent a number of crushing in different stages (see Manzi et al., 2013a for further details) finally obtaining chunks with size and grain size distribution similar to the coarse natural aggregates (fraction 16 – 25 mm).

The coarse recycled aggregates exhibit sharp contours and are similar in appearance to the coarse natural crushed aggregates, however their texture is rougher due to the adhered mortar, with higher water absorption and lower density than natural aggregates.

Specimens preparation and testing. Composition of three considered concrete mixes are reported in Table 1. Cement content (350 kg/m^3) and D_{max} (25 mm) were constant for all the formulations. Reference mix, named M0, was prepared with 100 % natural aggregates and water/cement ratio w/c = 0.48. In order to investigate the effects of total coarse aggregate substitution on the concrete properties, two different concrete mixes were studied. A first concrete mix, named M1, was prepared replacing all the natural gravel (27 vol% on the total volume of aggregates) with the coarse recycled aggregates and with workability similar to that of the reference mix (M0). Therefore a slightly higher w/c ratio (0.52) than M0 was necessary. A further concrete mix, named M2, was prepared with the same content of coarse recycled aggregates of M1 but with the same w/c ratio of M0, thus characterized by a reduced workability. Mix procedure can be found in Manzi et al. (2013a).

For each formulation, water absorption (w_a), concrete compressive strength (f_{cm}) and secant elastic modulus (E) at 28 days from casting were measured and can be found in Manzi et al. (2013b). The long-term behavior of the recycled aggregates concretes was investigated by creep and shrinkage tests. Two cylinders for each mix

were subjected to creep test according to ASTM C512/C512M-10 and two cylinders were subjected to shrinkage test. All the tests were performed in a climate chamber (T=20 ± 1 °C and RH=60 %) for nearly two years with specimens in drying conditions. The longitudinal strain variation with time of each cylinder was measured by using electrical strain gauges connected to a digital acquisition system (Mazzotti and Savoia, 2012). Shrinkage measures started after two days from casting while for creep tests, a compression stress of about 30 % of the strength at the time of loading (f_{cm}=41, 44 and 52 MPa, respectively for M0, M1 and M2) was applied at 28 days from casting. The content of adhered mortar in the recycled aggregates was determined with thermal treatments (see Manzi et al., 2013a for further details). Pore size distribution was investigated by mercury intrusion porosimeter (MIP) equipped with a macropore unit on samples constituted by the adhered mortar detached from recycled aggregates and samples of the new cement matrix.

Table 1. Concrete mix-design.

	M0	M1	M2
Cement (kg/m^3)	350	350	350
Water (kg/m^3)	168	182	168
Water/cement ratio	0.48	0.52	0.48
Natural aggregates[(a)] (kg/m^3)	1800	1331	1331
Recycled aggregates[(a)] (kg/m^3)	0	419	419
Superplasticizer[(b)] (%)	1.0	0.8	1.2
Slump (cm)	19	23	10

[(a)] saturated surface-dried (ssd) conditions; [(b)] mass% on cement amount

SHRINKAGE PREDICTION MODELS

In order to verify the suitability of current shrinkage prediction models to describe the shrinkage behavior of concretes containing recycled aggregates, a comparison between numerical and experimental results was made by using the following recognized models available in literature.

Model Code 2010 – final draft. Total shrinkage can be calculated according to the expression $\varepsilon_{cs}(t,t_s)=\varepsilon_{cas}(t)+\varepsilon_{cds}(t-t_s)$, where the autogenous contribution is:

$$\varepsilon_{cas}(t)=\varepsilon_{cas0}(f_{cm})\cdot\beta_{as}(t) \text{ being} \tag{1}$$

$$\varepsilon_{cas0}(t)=-\alpha_{as}\left(\frac{f_{cm}/10}{6+f_{cm}/10}\right)^{2.5}\cdot 10^{-6} \text{ and } \beta_{as}(t)=1-\exp(-0.2\cdot\sqrt{t}). \tag{2}$$

Coefficient α_{as} depends from the type of cement, t is the concrete age in days, t_s is the concrete age at the beginning of drying in days and f_{cm} is the 28 days mean compressive strength. Drying part is $\varepsilon_{cds}(t,t_s)=\varepsilon_{cds0}(f_{cm})\cdot\beta_{RH}(RH)\cdot\beta_{ds}(t-t_s)$ with

$$\varepsilon_{cds0}(f_{cm})=\left[(220+110\,\alpha_{ds1})\cdot\exp(-\alpha_{ds2}\cdot f_{cm})\right],\ \beta_{RH}=-1.55\cdot[1-(RH/100)^3] \tag{3}$$

and

$$\beta_{ds}(t-t_s)=\left(\frac{t-t_s}{0.035\cdot h^2+(t-t_s)}\right)^{0.5}. \quad (4)$$

Previous expressions depend from relative humidity *RH*, wet perimeter *h* (in mm) and coefficients α_{ds1} and α_{ds2} properly defined as a function of cement type.

ACI 209. The ACI prediction model follows a different analytical structure, combining the two shrinkage components into the following single expression:

$$\varepsilon_{cs}(t,t_0)=\frac{t}{35+t}\varepsilon_{cs,u}\ , \quad (5)$$

where the shrinkage strain limit value $\varepsilon_{cs,u}$ under standard conditions can be defined as $780\cdot\gamma_{sh}$; eq. (5) is valid only when considering 7 days of moist curing.

$$\gamma_{sh}=\gamma_{cp}\cdot\gamma_{\lambda}\cdot\gamma_{h}\cdot\gamma_{s}\cdot\gamma_{\psi}\cdot\gamma_{cc} \quad (6)$$

represents the product of the applicable correction factors which are able to taken into account a number of environmental, geometric and mix-design parameters. In more details, γ_{cp} depends from the curing period, γ_{λ} is related to the environmental relative humidity, γ_h depends from the element notional size $h=2A/u$, γ_s is related to the concrete workability (slump), γ_{ψ} accounts for the amount of fine aggregate content and γ_{cc} introduces the effect of the cement content (absolute amount). All these coefficients are linear functions of the considered parameters and corresponding expressions (not reported here for reason of space) have been numerically calibrated.

CREEP PREDICTION MODELS

As for the creep behavior, the following models were considered.

Model Code 2010 – final draft. Starting from the specific creep function defined as

$$C(t,t_0)=\frac{\Phi(t,t_0)}{E_{c,28}}, \quad (7)$$

the final draft of the Model Code 2010 (fib, 2012), suggests to obtain the concrete creep coefficient $\Phi(t,t_0)$ by considering its two fundamental components referring to the basic and the drying creep contributions as follow:

$$\Phi(t,t_0)=\Phi_{bc}(t,t_0)+\Phi_{dc}(t,t_0), \quad (8)$$

where the basic creep is computed as a function of concrete strength, age at loading and time interval according to the expression:

$$\Phi_{bc}(t,t_0)=\beta_{bc}(f_{cm})\cdot\beta_{bc}(t,t_0), \quad (9)$$

being

$$\beta_{bc}(f_{cm}) = \frac{1.8}{(f_{cm})^{0.7}} \text{ and } \beta_{bc}(t, t_0) = \ln\left(\left(\frac{30}{t_{0,adj}} + 0.035\right)^2 \cdot (t - t_0) + 1\right). \quad (10)$$

The drying creep contribution is defined as:

$$\Phi_{dc}(t, t_0) = \beta_{dc}(f_{cm}) \cdot \beta(RH) \cdot \beta_{dc}(t_0) \cdot \beta_{dc}(t, t_0), \quad (11)$$

where

$$\beta_{dc}(f_{cm}) = \frac{412}{(f_{cm})^{1.4}}, \ \beta(RH) = \frac{1 - \frac{RH}{100}}{\sqrt[3]{0.1 \cdot \frac{h}{100}}}, \ \beta_{dc}(t_0) = \frac{1}{0.1 + t_{0,adj}^{0.2}} \text{ and} \quad (12)$$

$$\beta_{dc}(t, t_0) = \left[\frac{(t - t_0)}{\beta_h + (t - t_0)}\right]^{\gamma(t_0)}. \quad (13)$$

The exponent $\gamma(t_0)$ is a function of the age at loading t_0 according to the expression:

$$\gamma(t_0) = \frac{1}{2.3 + 3.5/\sqrt{t_{0,adj}}}, \text{ being } t_{0,adj} = t_0 \cdot \left[\frac{9}{2 + t_0^{1.2}}\right]^{\alpha}, \quad (14)$$

where the parameter α depends from the type of cement, assuming values of -1, 0 and 1 when using 32.5 N, 32.5 R or 42.5 N, 42.5 R or 52.5 cement types, respectively. β_h is a function of the relative humidity and of concrete strength (not reported here for brevity). Previous equations are all dependent from the general time t, age at loading t_0 (both in days) and $E_{c,28}$ is the concrete elastic modulus after 28 days from casting.

ACI 209. The ACI prediction model, like for shrinkage, suggests a single creep contribution according to the following creep coefficient:

$$\Phi_t(t, t_0) = \frac{t^{0.6}}{10 + t^{0.6}} \Phi_u, \quad (15)$$

where the creep coefficient limit value Φ_u under standard conditions can be defined as $2.35 \cdot \gamma_c$; Eq. (15) is valid only when considering a loading age of 7 days.

$$\gamma_c = \gamma_{la} \cdot \gamma_{cp} \cdot \gamma_\lambda \cdot \gamma_h \cdot \gamma_s \cdot \gamma_\psi \cdot \gamma_{cc} \quad (16)$$

represents the product of the applicable correction factors which have the same meaning of those in Eq. (6). In addition, γ_{la} accounts for loading ages different from 7 days. All these coefficients have specific expressions for creep, different from those for shrinkage (and not reported here for brevity).

RESULTS AND COMPARISONS WITH PREDICTIVE MODELS

Shrinkage. The total shrinkage (autogenous and drying contributions) of the three considered mixes over a period of almost two years is reported in Figure 1. Mix M0 shows the smallest strains, in accordance with literature data (Rao et al. 2007). Concrete with coarse recycled aggregates, in fact, usually leads to larger values of

shrinkage because the recycled aggregates have a lower modulus of elasticity than the natural ones and offer less restraint to the potential shrinkage of the cement paste. At the same time, mixes M1 and M2 exhibit almost the same shrinkage strain trend, irrespective of the different *w/c* ratio used in the two mixes.

Comparison with prediction models (Figure 1) shows that they provide for an acceptable description of experimental finding when considering reference concrete (M0) only, while a strong underestimation (30%) can be observed with respect to recycled aggregate concretes (RAC). In particular, MC2010 model suggests three very similar curves, having only the compressive strength as variable parameter among the three; on the contrary, the ACI 209 model includes some further mix-design parameter dependency, obtaining a better result for M1 but not for M2. Moreover, experimental curves become quite flat after about one year while the models predictions keep increasing more rapidly. It is apparent like present models are not able to properly take into account the contribution of the adhered mortar and should be revised, at least increasing their absolute values when dealing with RACs.

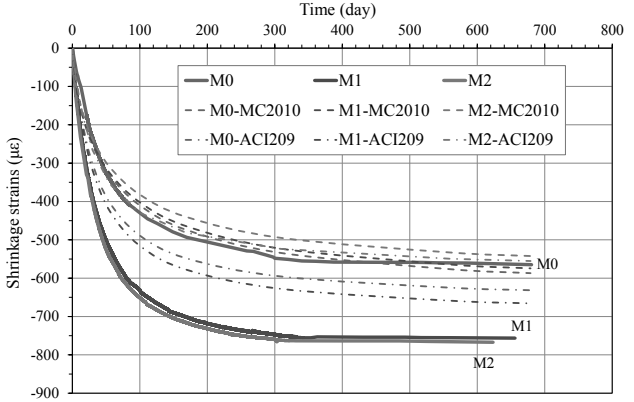

Figure 1. Shrinkage strains: comparison between experimental data and models predictions.

Creep. Specific creep curves (creep strain per unit of applied stress, basic and drying contributions together) provided by all mixes are shown in Figure 2. The slope of all the curves (reference included) is still appreciable after nearly two years, meaning that the creep phenomenon is still quite active and not only related to the presence of recycled aggregates; mix M1 shows the largest creep behavior due to its larger *w/c* ratio with respect to M2. Results show that creep is more sensitive to the *w/c* ratio than shrinkage. Among the three mixes, M2 provided for the lowest creep values; indeed, the total replacement of the coarse natural aggregates with recycled ones can lead to positive effects on creep if comparable *w/c* ratio is used, depending on the type of recycled aggregates adopted.

Comparison with prediction models (Figure 2) shows that, in all cases, they provide for a strong underestimation of experimental results (50%). Even the ACI

209 model, which contains a number of governing mix-design parameters, performs not satisfactorily. Nevertheless, a proper calibration of the models could strongly improve their performances without the necessity of introducing new dependencies.

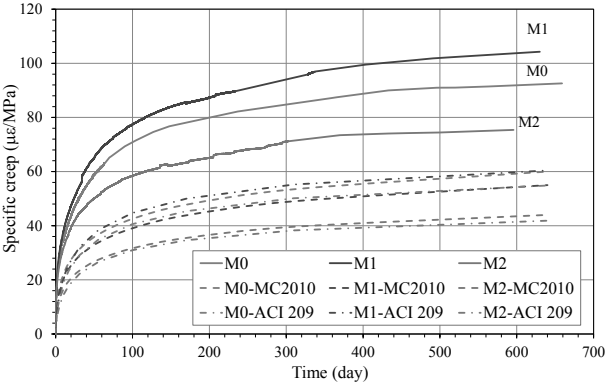

Figure 2. Specific creep: comparison between experimental data and models predictions.

Porosity. The content of adhered mortar determined in the coarse recycled aggregates is about 72 %: a high level of separation between aggregates and cement mortar was reached. The cumulative pore size distributions (determined by MIP) show that the cement mortar samples coming from M2 and M1 are less porous than those coming from M0 and the adhered mortar covering the recycled aggregates (values of total intruded volume are 56, 60, 68 and 111 mm^3/g respectively). When coarse recycled aggregates are used for the preparation of RAC, the fresh cement mortar adheres on the adhered mortar of the aggregates, filling their porosity and creating a new cement matrix very compact. Moreover, porosity data for M2 agree with the good concrete performances observed during the creep tests, confirming that microstructural properties are the basis of the macroscopic behavior of concrete structures. Table 2 reports the IUPAC classification of the pore size and the relevant data of porosity determined for the investigated samples. The amount of mesopores strongly influences the shrinkage, indeed shrinkage strain increases with the increasing content of mesopores (M2 > M1 >> M0). This trend confirms the results previously reported in Fig. 1.

Table 2. Classification of porosity in the investigated samples according to IUPAC pore size classification.

Designation	Porosity Range (nm)	M0 (mm^3Hg/g)	M1 (mm^3Hg/g)	M2 (mm^3Hg/g)
Mesopores	1.25 - 25	10.6	14.1	17.6
Macropores	25 - 5000	57.1	45.1	37.0
Directly accessible large pores	5000 - 50000	1.2	0.5	1.8

CONCLUSIONS

In this study the long-term behavior of concrete made with coarse recycled concrete aggregates were compared with those of conventional concrete. Based on the results of the investigation, the following conclusions are obtained:

- shrinkage strain is negatively influenced by the use of recycled concrete aggregates, regardless the water/cement ratio used. On the contrary, creep results appear to follow general rules also valid for conventional concretes.
- According to previous remark, to improve shrinkage prediction models a more complex dependency from porous structure (or similar) is required while for creep models a simple recalibration could be sufficient, since the underestimation involves conventional and recycled mixes similarly.

REFERENCES

American Concrete Institute Committee 209 (1992). "Prediction of creep, shrinkage, and temperature effects in concrete structures", ACI 209R-92.

American Society for Testing and Materials (2002). "Standard Test Method for Creep of Concrete in Compression", ASTM C512-02, West Conshohocken.

Etxeberria, M., Vázquez, E., Marí, A., and Barra, M. (2007). “Influence of amount of recycled coarse aggregates and production process on properties of recycled aggregate concrete”. *Cement and Concrete Research*, 37, 735-742.

Fathifazl, G., Razaqpur, A. G., Isgor, O. B., Abbas, A., Fournier, B., and Foo, S. (2011). “Creep and drying shrinkage characteristics of concrete produced with coarse recycled concrete aggregate”. *Cement and Concrete Composites*, 33, 1026-1037.

fib (2012). Model Code 2010 final draft, fib.

Manzi, S., Mazzotti, C. and Bignozzi M.C. (2013a). "Short and long-term behavior of structural concrete with recycled concrete aggregate." Cement and Concrete Composites 37(1), 312-318.

Manzi, S., Mazzotti, C. and Bignozzi, M.C. (2013b). Effect of adhered mortar of recycled concrete aggregates on long-term concrete properties. SCMT 2013 - 3rd International Conference on Sustainable Construction Materials and Technology. Kyoto. **1**: 1-8 (on CD).

Mazzotti, C., and Savoia, M. (2012). An experimental campaign on the long-term properties of self-compacting concretes. *Advances in Structural Engineering*, 15, 1155-1166.

Rahal, K. (2007). “Mechanical properties of concrete with recycled coarse aggregate”. *Building and Environment*, 42, 407-415.

Rao, A., Jha, K. N., and Misra, S. (2007). “Use of aggregates from recycled construction and demolition waste in concrete”. *Resources Conservation Recycling*, 50(1), 71-81.

Effects of Poly Vinyl Alcohol Fibers on Fracture Energy of Concrete

H.R.Ahmadian [1] and M.Ganji [2]

[1]Tehran Science and Research University, Artman Construction Company, unit 20, no.6, Azad alley, south Kamranieh Street, Shemiranat, Tehran. P.O. Box195187698, TEL/FAX (+9821)22570350; CELL PHONE (+98912) 61999420 email: hamidreza_ahmadian@hotmail.com
[2] Artman Construction Company, unit 20, no.6, Azad alley, south Kamranieh Street, Shemiranat, Tehran. P.O. Box 195187698 TEL/FAX (+9821) 22570350; CELL PHONE (+98912) 1393581 email: Miladganji@gmail.com

ABSTRACT

Among all the advantageous of concrete elements improving ductility and energy absorbent has always been a great challenge. These papers reports on an experimental study of poly vinyl alcohol fibers effects on fracture energy of concrete and its comparison with steel fiber reinforced concretes. Energy absorbent of the concrete were measured according to ACI544 impact test code. Compressive and impact resistance of poly vinyl fiber reinforced concretes were also measured. Stress strain curve in compressive tests are reported.

INTRODUCTION

Concrete has been introduced as a most popular material in recent decades. Achievements on concrete technology lead to high strength concretes with great compressive strength but meanwhile with brittle behavior. Recent researches has demonstrated that fibers can improve ductility and flexibility of concrete elements especially high strength ones. It is almost what Persian and romans did thousand years ago to improve mechanical properties of their materials by using straw in clay. This phenomena appears by bridging effect of fibers so the fibers should be stronger than the concrete itself and also be able to make good connection with cementitious matrix and do not slip under high stresses. Generally the mechanical properties of concrete will improve by increasing compressive strength. In high strength concretes this improvement will decrease specially in ductility and energy absorbent factors. To make up this defect we use fibers.it has been suggested that the impact test by ACI-544 can be used to characterize the fracture energy of concrete (FRC) which describes the material ability to absorb energy. Regarding to high modulus and high strength of the fibers used in batches we had to use high strength concrete to see the maximum effect of the fibers. This paper reports on an experimental study about fracture energy of poly vinyl alcohol fiber reinforced concretes. Fibers used in FRC test specimens were PVA high-modulus high strength fibers product of kurrary Ltd. and steel fibers

from BASF in order to compare the results with another FRC. The properties of both fibers are presented. The fracture energy of the FRC were studied by the compressive strength stress strain cure and impact resistance test results. Stresses versus crack separation curves are also reported. Observations on effect of both fibers on workability of freshly mixed FRC and on the drying shrinkage of FRC are also described.

MATERIALS AND PROPERTIES

The following materials were used throughout to form the mortar matrix of FRC:

- Cement: Tehran Portland cement Type 1-425
- Gravel: Aggregates passing through sieve 3/8" (9.5 mm)
- Sand: Aggregates passing through sieve no.4 (4.75 mm)
- Water: Drinkable local tap water at room temperature
- Super plasticizer: Glenium 51 High Range Water Reducing Super plasticizer BASF Ltd. admixture based on modified polycarboxylic ether (PCE) polymers classified as ASTM C-494 type A, F or G.
- Steel fibers: steel fibers product of BASF Co. with 0.5 mm diameter and 30 mm length, tensile strength 1900 MPa , length to diameter relation of 60 , circle cross section shape and 7850 kg⁄m^3 density.
- PVA fibers: poly vinyl alcohol fibers product of Kuraray Ltd. With 0.04 mm diameter and 8 mm cut length, 1600 MPa tensile strength and length to diameter relation of 200 and circle cross section shape with 1300 kg⁄cm^3 density.

FRC Mix Design. The mix design for the tests are listed in table 1

Concrete Type	**HSC-Control**	**SFRHSC**	**PVFRHSC**
Cement (kg)	550	550	550
Gravel (kg)	686	686	686
Sand (kg)	935	935	935
Steel Fibers (kg)	-	157 (%2)	-
PVA Fibers (kg)	-	-	26 (%2)
Water (lit)	220	220	220
W/C	0.4	0.4	0.4
Super plasticizer	% 0.1	% 0.15	% 0.3

Table 1.Concrete mix designations

Workability of Fresh Concrete. In this study Glenum-51 poly carboxylate super plasticizer was used to improve the workability of fresh FRC mixes. The workability was judged by the deformability of fresh mixes during molding. Good workability was observed in control mixes and samples with steel fibers but mixes with PVA fibers had less workability and used double dosage of super plasticizer (%0.3-%0.4)

to keep w/c ratio constant. All the mixes were compacted by vibrating table for 30 minutes except mixes with PVA fibers which had to be hand-filled and compacted because regard to using higher dosages of super plasticizers but because regard to using higher dosages of super plasticizers but we faced weaker workability in PVAFRHSC mixes.

Specimen Preparation and Test Procedure. Mixing procedure consisted of mixing dry cement sand and gravel in the beginning with blade mixer, followed by adding water and super plasticizer which was mixed together before, and mixing them with cement and aggregates for 3 minutes. For FRC mixes, we add fibers little by little during the mixing process and scattered them throughout the batch. This type of adding fibers helps fibers dispersion and prevents clumping phenomena.

This technique works well for steel fibers because of their size and rigidity, but for PVA fibers we need more precaution and care to prevent clumping of fibers. For this purpose, we mixed PVA fibers with water and super plasticizer and mixed them for 5 minutes to disperse fibers in water and open their bunches. 15X30 cm cylinders were used for molding impact test discs and 10X20 cm cylinders were used to make compressive samples. All the samples were covered by nylon to prevent water evaporation, and were demolded after 24 hours. All the specimens were cured in 23 C water for 28 days. After 28 days moist curing, samples were kept in room temperature for 2 days before final tests.

RESULTS AND ANALYSIS

Compressive Strength and Stress-Strain Curves. Compressive strength values shown in Table 2 are the average strength of three cylinders. In order to measure total compressive toughness we used the area under stress-strain curve until 40% of maximum load in downward part. The compressive strength of STFRHSC is more than HSC because of steel fibers and their effect in improving tensile strength. Compressive strength increases indirectly due to Poisson's phenomena under compression. Steel fibers are tough and hard enough as aggregates so they won't decrease compressive strength of the concrete. PVA fibers are not as tough as steel fibers so they will act as voids in compression. As a consequence, compressive strength of HSC decreases. After reaching maximum stress with increasing strain, stress in HSC samples will decease faster in comparison with SFRHSC and PVAFRHSC; and SFRHSC will decrease faster than PVAFRHSC. This happens because of brittle nature of HSC and more ductility of FRC. PVA fibers have better bonding with cementitious composites and they won't slip from broken section so they will last longer and the slope of PVAFRHSC stress strain curve after maximum stress in downward slope is less than SFRHSC. But because of problems in dispersing PVA fibers and their negative effects on compressive strength with partially and localized unwanted clumping and overdose of super plasticizer and its negative consequences on strengths to keep W/C ratio fixed, they will reach less stresses in comparison with HSC and SFRHSC. By using 2% volumes of PVA fibers all the parameters of concrete will increase significantly except compressive strength

and the compressive toughness is equivalent to maximum stress. In SFRHSC all the parameters will increase.

Effect of fibers on rising part of the stress-strain curve is negligible. But fibers will increase maximum stress and equivalent strain in SFRHSC and they will increase strain equivalent with maximum stress in PVAFRHSC. The fibers' effect on compressive behavior of concrete is dependent on properties of cementitious matrix and properties of fibers. After failure of specimens, visual inspection on cracked parts showed that steel fibers had been separated from cementitious matrix by slipping the fibers because a lack of friction between surface of fibers and cementitious matrix so we should increase the ratio of l/d in fibers and use fibers with hook and more effective shape but PVA fibers had been separated by ripping and some of they were torn after loading. This was because of better connection between fibers and cementitious matrix.

Concrete type	**HSC**	**SFRHSC**	**PVAFRHSC**
Average of Maximum Stress	58	69.3	54.5
Strain Equivalent with maximum stress	0.0034	0.0046	0.0038
Total Compressive Toughness(N-M)	153.9	485.3	256.7
Compressive Toughness equivalent maximum stress(N-M)	123.4	188	121.7
Compressive Ductility	1.25	2.58	2.2
Final Strain	0.0037	0.0085	0.0067

Table 2. 15X30 Cylindrical specimens compressive test result

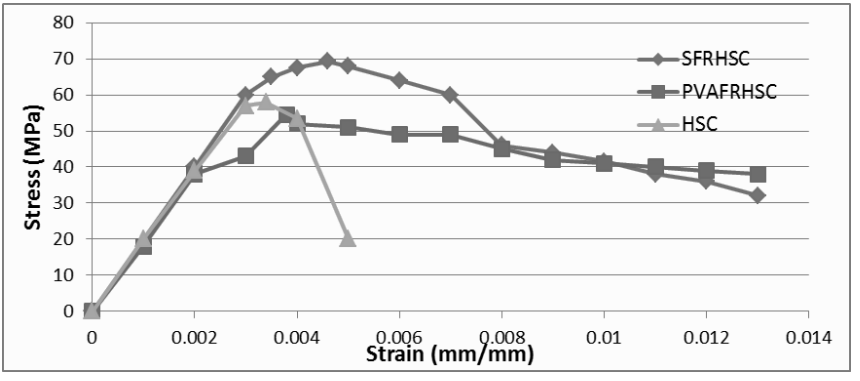

Figure 1.Stress strain curves for cylindrical samples, compressive test

CONCRETE SPECIMENS	MAXIMUM STRESS	STRAIN EQUIVALENT WITH MAXIMUM STRESS	TOTAL COMPRESSIVE TOUGHNESS	COMPRESSIVE TOUGHNESS TILL MAXIMUM STRESS	COMPRESSIVE DUCTILITY	FINAL STRAIN
SFRHSC	19	35	315	152	224	229
PVAFRHSC	-6	12	176	-9	176	181

Table 3.Effect of fibers on compressive strength of HSC in percent.

Effect of fibers on strain equivalent with maximum stress is more than maximum stress; so the greatest influence is observed for total compressive toughness and ductility.

Compressive strength and compressive toughness equivalent with maximum stress in SFRHSC is much more than PVAFRHSC but final strain and compressive ductility of concretes are almost in the same range. This happens because PVA fibers will endure and transfer stresses by bridging actions until they fail but steel fibers will slip because of higher modules of elasticity and weaker connection with cementitious matrix and high ratio of l/d. For concrete with coarse aggregates, this ratio should be more than 100. Steel fibers used in the research has l/d ratio of 60 and most of steel fibers has l/d ratio under 100.

The steep shape of stress-strain curve in downward part is higher for SFRHSC in comparison with PVAFRHSC. This is due to better performance of PVA fibers in transferring stresses by bridging action and preventing cracks to open. In SFRHSC, because of smaller l/d ratio and smaller stress transfer area intensity of forces that must be carried by steel fibers between cracked surfaces, the chance of slip in fibers will increase after reaching maximum stress in comparison with PVAFRHSC so ductility of concrete with PVA fibers which has l/d ratio of 200 is higher in compression mode.

Bending and Impact Tests. Bending test (indirect tensile strength) was carried out according to ASTM C293-79, and impact test according to ACI 544. Specimens for bending test were prismatic 4X4X16 cm, and for impact test discs with 15 cm diameter and 6.35 cm thickness were used. For bending test, prismatic specimens were made by fine aggregates (0-4.75 mm) prepared according to ASTM C33 because of limitation of size in small concrete sample. For impact test, it was made by combination of fine and coarse aggregates (0-9.5 mm) prepared according to ASTM C33. Impact discs were made from slices of 15X30 cm cylinders. Results of flexural strengths and its ratio with compressive strength are presented in Table 4.

CONCRETE TYPE	MODULUS OF FAILURE (MPa)	Percent ratio modulus of failure with cylindrical compressive strength
HSC	4.59	7.9
SFRHSC	9.58	13.8
PVAFRHSC	6.93	12.7

Table 4. Flexural strength and percent of its ratio with cylindrical compressive strength

The greatest flexural strength is found for SFRHSC with 9.58 MPa. PVAFRHSC comes in second place. The efficiency of PVA fibers are better in flexural stresses and flexibility and energy absorbent. Yet, because the higher compressive strength of SFRHSC and the direct relation between compressive strength and other mechanical parameters of concrete specimens, we see a greater modulus of failure among SFRHSC specimens. Modulus of rupture for SFRHSC and PVAFRHSC are greater than HSC control by 200% and 151%, respectively. With increases in compressive strength of the concrete, the ratio of flexural strength to compressive strength becomes smaller. This effect is observed for both plain concrete and fiber reinforced concretes. Because fibers increase more the flexural strength than the compressive strengths, the ratio of flexural strength to compressive strength is greater in fiber reinforced concretes. Figure 2 displays load-displacement curves for HSC, SFRHSC and PVAFRHSC. Table 5 compares the flexural behavior of SFRHSC and PVAFRHSC.

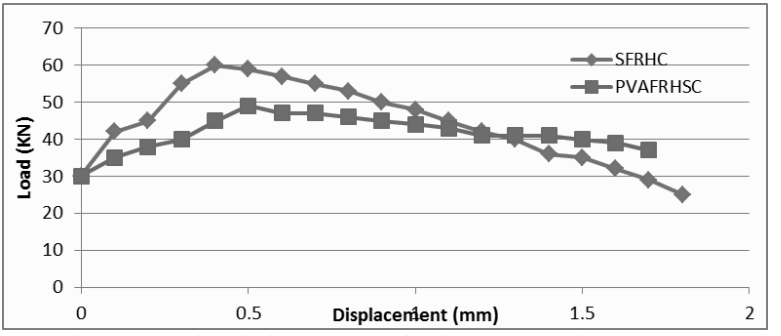

Figure 2. Load - Displacement graph of SFRHSC and PVAFRHSC

	SFRHSC	**PVAFRHSC**
Displacement equivalent with first crack (mm)	0.037	0.035
Strength equivalent with first crack (MPa)	8.55	6.18
Modulus of failure (MPa)	9.58	6.93
Toughness index I_5	5.6	4.88
Toughness index I_{10}	11.36	10.23
Toughness index I_{20}	22.1	18.90
Toughness index I_{30}	31.12	28.25
Toughness index I_{40}	40.52	38.91
Toughness index I_{50}	48.61	45.18
Flexural toughness T_{JCI} (N-M)	52.2	51.26
Flexural ductility	88	70

Table 5.Comparisson between flexural behavior of SFRHSC and PVAFRHS

Concrete type	HSC-CONTROL	SFRHSC	PVFRHSC
Number of impacts for first crack	35.2	78.4	54.3
Number of impacts for final failure	37.9	189.3	97.5

Table 6. Impact test results according to ACI-544 code.

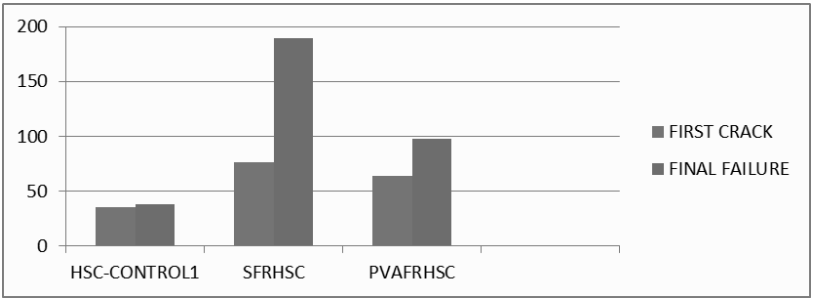

Chart 1.impact test results (first cracks and final failure)

Impact resistance of fiber reinforced concretes is much more than control plain HSC, and the difference between first crack and final crack is significant. Impact resistance of SFRHSC is more than PVAFRHSC. This difference is due to the length of PVA fibers and the size of aggregates used in concrete. The length of fibers must be at least twice the size of aggregates to make good connection with concrete to transfer stresses by bridging effect. Although the efficiency of PVA fibers are lower than steel fibers, the final price and their durability and their resistance against corrosion make it a good choice to use instead of steel fibers. The reason for increasing first crack strength is that before first crack appears on the specimen there are many micro cracks inside the sample, and first cracks appear when these small cracks coalesce. After final failure, the damage of concrete discs for fiber reinforced samples was much more than the damage of plain control samples due to the number of impacts imposed to the samples. Greater damage of the fiber reinforced samples shows that impact forces distribute over the specimen due to bridging effect of the fibers, and the damaged zone didn't appear only in some parts of it. The difference between numbers of first crack and ultimate resistance in HSC is because aggregates can control crack distribution in specimens. Impact resistance associated with the first crack appearance for SFRHSC and PVAFRHSC will increase 220% and 152%, respectively, and final failure resistance of the specimens will increase 499% and 247%, respectively. The difference between number of impacts caused first crack and number of impacts caused final failure shows that PVA fibers have better efficiency in preventing crack growth. First cracks will appear on the surface while many micro cracks are inside the concrete specimens. The difference between impact resistance of PVAFRHSC and SFRHSC is the essence of impact forces which act as high amount of compressive stresses imposed to the specimens in a short time. The weakness of pva fibers in compressive strength in comparison to steel fibers will cause less impact resistance.

CONCLUSION

From the investigation reported in this paper, the following conclusions can be drawn.

1. From the stress strain curves of HSC, SFRHSC and PVAFRHSC, we can see that PVA fibers cannot increase compressive strength, in contrast to steel fibers.
2. After reaching maximum stresses in PVAFRHSC and SFRHSC, the downward slope of the stress strain curve of the PVAFRHSC is less than in SFRHSC, although the maximum compressive strength in SFRHSC specimens is higher. The toughness of the specimens (the area under stress strain curves) is close to each other; so energy absorption by the specimens is almost in the same range, and much more than in plain HSC.
3. In tensile bending tests, PVA fibers show better efficiency in transferring tensile stresses and bridging phenomena will form until final failure of the fibers. In SFRHSC specimens we found slip of the fibers because lack of connection between steel fibers and the concrete and a higher modulus of elasticity due to the presence of steel fibers. In PVA fibers, we had better bonding between cementitious matrix and fibers. Thus, with the growth of cracks, the rate of downward slope after maximum load point in the load-displacement curve will decrease more slowly.

ACKNOWLEGMENT

The authors would like to acknowledge the support of Artman Construction Co. and Khajeh Nasir Toosi University concrete and building materials laboratory.

REFERENCES

H.R.Ahmadian MS.c Theses ‘’Evaluating impact resistance of polyvinyl alcohol fiber reinforced concretes and its comparision with steel fiber reinforced concretes, Tehran central azad university. december 2012.

Y.Sahin, F.Koksal,’’ The influences of matrix and steel fibre tensile strengths on the fracture energy of high-strength concrete’’. Construction and Building Materials, December 2010.

Marar Kh., Eren O., Celik T., “Relationship between impact energy and compression toughness energy of high strength fiber reinforced concrete”, Materials Letters, Vol.47, PP.291-304,2001.

Nataraja M.C., Dhang N., Gupta A.P., “Stress – Strain curves for steel-fiber reinforced concrete under compression” Cement and Concrete Composites. Vol.21, pp. 383-390. 1999

H.Zanganeh MS.c Theses ‘’ Investigation on Impact resistance of RPC concretes an its comparison with plain concrete. July 2006

Neville A.M “Properties of concrete”. 1995.

Jansen, D.C., and Shah, S.P., “Effect of length on compressive strain softening of concrete”, Journal of Engineering Mechanics, Vol. 123, No.1, pp.25-35, 1997.

American Concrete Institute (ACI)-544.2RCommittee report on Fiber Reinforced Concrete, 1999.

State of the Art Report on High Strength Concrete. ACI 363R-92, Reapproved 1997.

Desiccation shrinkage of large structures: is there a size effect?

J. M. Torrenti[1] and F. Benboudjema[2]

[1]Université Paris-Est, IFSTTAR, 14-20 Boulevard Newton, Cité Descartes, Champs sur Marne, F-77447 Marne la Vallée Cedex 2, France; email: jean-michel.torrenti@ifsttar.fr
[2]LMT/ENS Cachan/CNRS UMR 8535/UPMC/PRES UniverSud Paris, 61 Avenue du Président Wilson, F-94235 Cachan, France; email: farid.benboudjema@dgc.ens-cachan.fr

ABSTRACT

When subjected to natural drying, concrete structures are submitted to desiccation shrinkage. This shrinkage has to be taken into account when designing the reinforcement especially in the case of large structures such as the containment vessels of nuclear power plants. In this paper, we discuss the assessment of desiccation shrinkage, focusing on a possible size effect on the final value of the shrinkage. Experimental results are used to investigate the effect of structure size on drying shrinkage. When these tests are analysed with respect to the square root of time to the notional size ratio, in order to get rid of the kinetic of drying which is a diffusive process, indeed a size effect is obtained. Nevertheless, using a coupled model it is not possible to explain this size effect (except of course the size effect due to drying, i.e. the kinetics effect). The physical meaning of this size effect seems to be due to a collateral effect of the different sizes of the samples: for larger samples, the temperature during hydration is higher and there are consequences on the microstructure and then on the delayed behaviour.

INTRODUCTION - EXPERIMENTAL EVIDENCE OF SIZE EFFECT

Drying of cement-based materials induces drying shrinkage, which may cause prestress loss or/and cracking if strains are (self or externally) restrained. Drying shrinkage is difficult to predict, since it depends on the material mix, mechanical and hygral boundary conditions, geometry ... Another difficulty is to take into account a possible size effect on final drying shrinkage. This phenomenon has still not been deeply investigated because to study the size effect of drying shrinkage, samples with very large sizes are needed. And it is obvious that the increase of the structure size slows the drying shrinkage kinetic (since drying is a diffusive process). That is why only two experimental studies (to the author's knowledge for large concrete members sizes) on these subjects are available: Hansen and Mattock (1966) have tested cylindrical samples with a radius between 51 and 303 mm and a slenderness ratio greater than 2 and l'Hermitte et *al.* (1965) have tested prismatic samples with a side between 70 and 1000 mm and a slenderness ratio of 4. If the results of Hansen are

expressed with respect to the square root of time to h_0 (notional size i.e. 2×volume/surface ratio equal to the radius for a cylinder) ratio, in order to get rid of the kinetic size effect, a size effect seems to exist (figure 1). In the European Code model (Eurocode 2, Part 1), a reduction factor is applied to minor final drying shrinkage, which ranges from 1 to 0.7, depending on the notional size of the structural member. In Eurocode 2, the drying shrinkage strains ε_{ds} reads:

$$\varepsilon_{ds}(t) = \beta_{ds}(t, t_s) k_h \varepsilon_{ds,0} \tag{1}$$

where β_{ds} is a term related to the kinetic of drying shrinkage (depending upon size effect), $\varepsilon_{ds,0}$ is the final drying shrinkage value and k_h is a reduction factor which depends upon the notional size of the structure h_0, $k_h = 1$ for $h_0 = 100$ mm and $k_h = 0.7$ for $h_0 > 500$ mm, for instance). If the parameters β_{ds} and $\varepsilon_{ds,0}$ are adjusted to experimental results (by the least squares method), the experimental results of Hansen and l'Hermitte could be compared to the relation proposed by Eurocode 2 – EC2-1 (figure 2): this relation is in good agreement with these results (and was maybe determined using it).

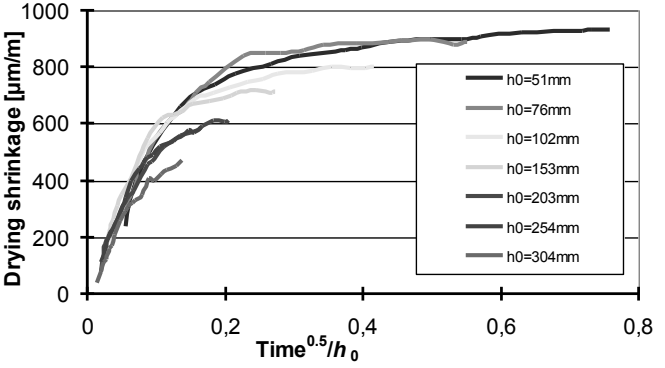

Figure 1. Evolution of drying shrinkage (for different notional size h_0) with respect to the square root of time to h_0 ratio – tests of Hansen (1966)

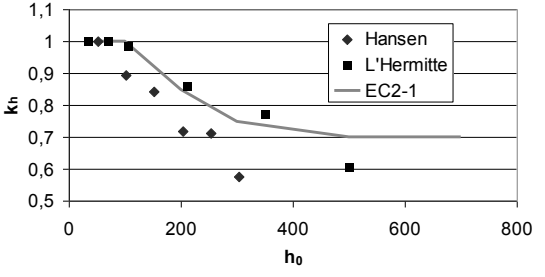

Figure 2. Comparison between size effect proposed by EC2-1 and experimental results tests of Hansen (1966) and l'Hermitte et *al.* (1965)

MODELLING OF DRYING SHRINKAGE

In order to understand the source of this size effect, a complete modelling of the phenomenon was tempted using a model coupling drying and the mechanical behavior (Benboudjema and Torrenti (2013)). In this approach drying is firstly modelled using the mass balance equation of liquid water:

$$\frac{dS_l}{dp_c}\frac{dp_c}{dt} = div\left(k_{rl}(S_l)\frac{K}{\mu_l \phi}\cdot grad(p_c)\right) \tag{2}$$

where S_l, p_c, ϕ, K, k_{rl} and μ_l are, respectively, the saturation degree, the capillary pressure, the porosity, the intrinsic permeability, the relative permeability and the viscosity of the liquid water. The capillary pressure and the relative permeability are related to the degree of saturation through van Genuchten's relation:

$$p_c(S_l) = a\left(S_l^{-b} - 1\right)^{1-1/b} \text{ and } \quad k_{rl}(S_l) = \sqrt{S_l}\left[1-\left(1-S_l^{\,b}\right)^{1/b}\right]^2 \tag{3ab}$$

where a and b are parameters of the material.

On the mechanical point of view, cracking, due to drying, is taken using a damage model. Basic and drying creep are also taken into account assuming drying shrinkage is the consequence of the mechanical deformation due to the effect of the capillary pressure on the solid skeleton. The pressure applied to the solid skeleton p_s at the macroscopic scale is considered to result from a volume average of the capillary pressure:

$$p_s = bS_l\, p_c \tag{4}$$

where b is the Biot coefficient which can be identified from a drying shrinkage test. It is here supposed that the Biot coefficient is not dependent upon cracking. Such a dependency may explain part of drying creep (Sellier *et al.,* 2012), but this is out of the scope of this study. The degree of saturation S_l can be related to the relative humidity by means of the isotherm desorption curve (Eq. 3a).

Using the definition of effective stresses by Gawin et *al.* (2007), the drying shrinkage results from the elastic and the creep response of the solid skeleton under the pore pressure (Eq. 7) (model 1):

$$\varepsilon_{ds}(t) = (1-2\nu)b_{sch}\left(\frac{S_l\, p_c}{E} + \int_{t'=0}^{t'=t} J(t-t',t')\frac{d\left(S_l\, p_c\right)}{dt'}dt'\right) \tag{5}$$

where ν is the Poisson ratio and J is the creep compliance. Using this formulation, it is possible to reproduce irreversible drying shrinkage (after rewetting) and effect of drying rate (Benboudjema *et al.,* 2007). Using an alternative approach and the

definition of stresses by Baroghel-Bouny et *al.* (1999), the drying shrinkage reads (model 2):

$$\varepsilon_{ds}(t) = (1-2\nu) b_{cou} \left[\int_{t'=0}^{t'=t} \left(\frac{S_l \, dp_c}{E} + J(t-t',t') \frac{S_l \, dp_c}{dt'} \right) dt' \right] \quad (6)$$

Using these two models (and also phenomenological ones), Benboudjema and Torrenti (2013) have shown that a size effect on the final amplitude of the drying shrinkage could not be explained (even introducing a size effect on the tensile strength). On the contrary, an increase of drying shrinkage has been found using Eq. (5) and (6) if the structure size increases (in agreement with Delaplace et Noyalet (2013)). This means that another phenomenon should be considered.

INFLUENCE OF HIGH TEMPERATURE AT EARLY AGES ON THE MICROSTRUCTURE AND POSSIBLE CONSEQUENCES ON DRYING SHRINKAGE

When massive concrete structures are built, due to the heat of hydration of cement large increases of temperature are observed. These large temperatures have an effect on the final compressive strength: Chanvillard and D'Aloia (1997) have shown for instance that the final compressive strength of a concrete cured at 40°C is 20% lower than the one of a concrete cured at 20°C. It seems that curing at elevated temperatures has effects on the microstructure: the reaction products are denser, thus there is higher capillarity porosity (Thomas, 2002). This seems to explain the decrease of the compressive strength with a higher curing temperature (van Breugel, 98). This change in the microstructure will also affect the physical properties (desorption curve) and perhaps the mechanical properties (Young modulus, Poisson ratio, creep compliance, Biot coefficient). Because results concerning the effect of curing temperature on these parameters are not available, in the following part of this paper, a parametric study of the influence of these parameters on drying shrinkage will be conducted.

Generation of desorption curves

Following an idea proposed by Georgin *et al.* (2010), for a given pore size distribution, the desorption curve could be estimated assuming a hierarchical organization of the pores and a layer of water absorbed on the surface of the pores (curve t). Using these assumptions a reference desorption curve is obtained (figure 3). Then assuming that the effect of elevated temperatures at early age is a higher capillary porosity, a derived desorption curve is generated (figure 3).

Influence of desorption curve

With the 2 desorption curves generated previously, the prediction of drying shrinkage is performed using models based on capillary pressure mechanisms Eq. (5) or Eq. (6).

Simple phenomenological models relying drying shrinkage strain to either the relative humidity h (Eq. 7) or water content C (Eq. 8) are also used:

$$\dot{\boldsymbol{\varepsilon}}_{ds} = K_{ds}\dot{h}\mathbf{1} \quad \text{and} \quad \dot{\boldsymbol{\varepsilon}}_{ds} = k_{ds}\dot{C}\mathbf{1} \tag{7, 8}$$

The models based on capillary pressure mechanisms need to the characterization of elastic and creep properties and the Biot coefficient. Furthermore, the effect of temperature (which a massive structure may undergo) on these properties needs to be unveiled. First, values obtained by identification using finite element calculations performed in Benboudjema and Torrenti (2013) using experiments on an ordinary concrete are used for the reference (samples of 100 mm size, temperature almost uniform). Secondly, experiments on the elastic properties show that curing at elevated temperatures has a slight impact on the Young modulus (Al-Shama 2012; Chen et *al.*, 2012). To the lack of additional data, it is supposed that all these parameters are not affected by temperature.

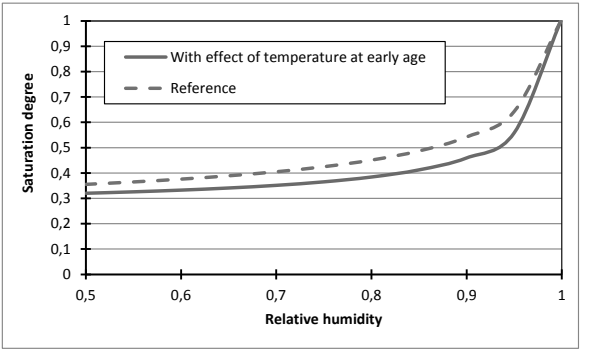

Figure 3. Reference and derived **desorption** isotherms.

A relative humidity history is then imposed started from 100 % HR to 50 % HR (with a square root of time to h_0 ratio going up to 1.5). A notional size of the concrete member of 100 mm is chosen for the reference case, as a notional size of 1 000 mm is chosen for the massive concrete member (which undergoes an increase of temperature an early-age and a modification of the desorption isotherm). In contrary to the previous study (Benboudjema and Torrenti, 2012), calculations at 1 Gauss point are performed in order to understand easily what is the effect of the change in the desorption isotherm.

For the reference state, the evolution of drying shrinkage with the respect to the square root of time to h_0 ratio is plotted in Figure 4. Note that the parameters k_{ds} and K_{ds} have been readjusted. It can be seen that the, expected to model relying the drying shrinkage to the water content, all the drying shrinkage models give almost the same evolution (it was already the case with finite element calculations in Benboudjema

and Torrenti, 2013), if the parameters are readjusted. The difference with the model using the water content is due to the nonlinear relationship between saturation degree and relative humidity.

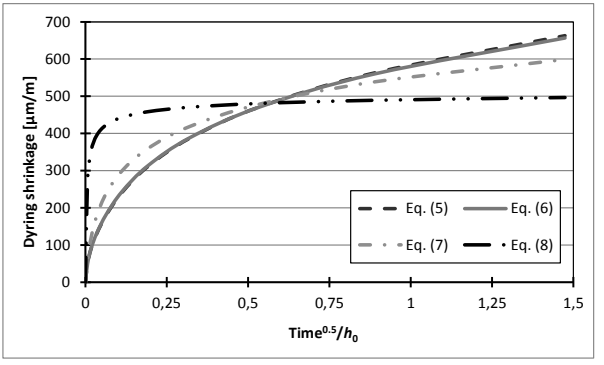

Figure 4. Evolution of drying shrinkage using the different models.

By modifying the desorption isotherm (according to results of Figure 4), the ratio between drying shrinkage using modified desorption isotherm (including effects of temperature at early-age) and the values plotted in Figure 4 is displayed in Figure 5.

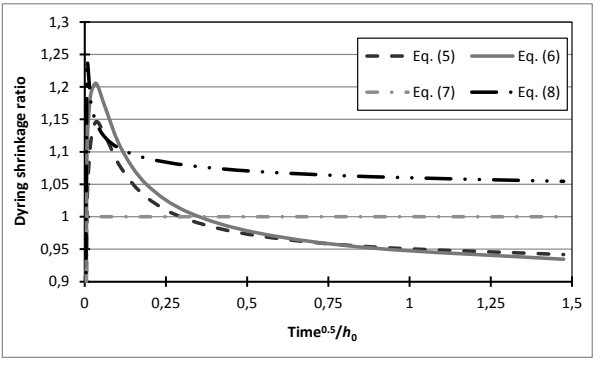

Figure 5. Evolution of the ratio between drying shrinkage using modified desorption isotherm (including effects of temperature at early-age) and the values plotted in Figure 4

The calculations show that:

- The use of Eq. (7) shows no difference, since the same relative humidity history (with the respect of the square root of time to h_0 ratio) is used. Using Eq. (8), a larger drying shrinkage is computed since a larger drop of saturation degree is obtained (see Figure 3),

- Eq. (5) and (6) gives close results. After an increase of computed drying shrinkage, a reduction of drying shrinkage strains is obtained at long term for both models. Nevertheless, the reduction is very low (limited to about 6 %) at the end of the computation.

It should be kept in mind that the models of Eq. (5) and (6), as aforementioned, need the determination of several mechanical parameters. The modification of these parameters and their consequences on the predicted value of drying shrinkage are summarized in Table 1 (as well as the effect of desorption isotherm).

From these results, the expected variations of material parameters have opposite effects on the predicted drying shrinkage strains. At this time, it is difficult to explain the reduction of final value of drying shrinkage as the structure sizes increases!

Table 1. Effect of material parameters on the predicted value of drying shrinkage.

Parameters	Increase (↑) or decrease (↓) of the properties	Effect on drying shrinkage
Desorption isotherm	Saturation degree ↓	6% ↓
Creep compliance[*, ***]	10 % ↑	11.1 % ↑
Poisson ratio[**, ***]	25 % ↑	10 % ↓
Biot coefficient[***]	10 % ↑	10 % ↑

[*] corresponding to a reduction of Young modulus and an increase of specific creep by a factor of 10 % for instance

[**] increase of the Poisson ratio from 0.2 to 0.25 for instance

[***] These tendencies are expected if the temperature rise at early-age is assimilated to an increase of the water to cement ratio, from mechanical numerical simulations on cement paste microstructure (Stefan et *al.*, 2010)

CONCLUSION

While the available experimental results seem to show that a size effect on the amplitude of drying shrinkage exist, with a modeling using a coupled model it is not possible to explain this size effect. Another possibility is the influence of high temperature at early age on the microstructure. Several parameters could be affected and change the final value of drying shrinkage. A change on the desorption isotherm could for instance explain a part of this size effect. But as the changes of the values of the mechanical properties have opposite effects, it is difficult to conclude until complementary experimental results are available.

ACKNOWLEDGEMENTS

The authors would like to thank the French national program CEOS.fr (http://www.ceosfr.org/) for its financial support.

REFERENCES

Al Shamaa M. (2012), Etude du risque de développement d'une réaction sulfatique interne et de ses conséquences dans les bétons de structure des ouvrages nucléaires, PhD thesis, University Paris Est (in french).

Baroghel-Bouny V., Mainguy M., Lassabatere T., Coussy O. (1999), "Characterization and identification of equilibrium and transfer moisture properties for ordinary and high-performance cementitious materials", *Cement and Concrete Research*, 29,1225-1238

Benboudema F., Torrenti, J.M. (2013), "Modelling desiccation shrinkage of large structures", *European Physics Journal*, accepted for publication.

van Breugel K. (1998), "Prediction of temperature development in hardening concrete" in Prevention of thermal cracking in concrete at early ages. Report 15, R. Springenschmid, E & FN SPON.

Chanvillard G., D'Aloia L. (1997), "Concrete strength estimation at early ages: modification of the method of equivalent age", *ACI Mater. J.* 94 (6) 520– 530

Chen W., Darquennes A., Benboudjema F. (2012), "Etude probabiliste du comportement au jeune âge : expérience, modélisation et application à une enceinte de confinement de bâtiments réacteurs nucléaire", MEFISTO ANR Project Report (in french).

Delaplace A., Noyalet H. (2013), "A simple two-stage model for simulating drying shrinkage vs. mass-loss evolution of concrete", 8th International Conference on Fracture Mechanics of Concrete and concrete Structures, Toledo.

Gawin D, Pesavento F, Schrefler BA. (2007) "Modelling creep and shrinkage of concrete by means of effective stresses", *Materials and Structures*, 40: 579–591

Georgin J.F., Le Bihan T., Ambroise J., Pera J. (2010) "Early-age behavior of materials with a cement matrix", *Cement and Concrete Research* 40, 997–1008

Hansen, T.C., Mattock A.H. (1966), "Influence of size and shape of member on the shrinkage and creep of concrete", *ACI J.* 63: 267-290.

L'Hermite, R.G., Mamillan, M. Lefevre, C., (1965) "Nouveaux résultats de recherches sur la déformation et la rupture du béton", *Ann. Inst. Techn. Bâtiment Trav. Publics*, 18(207-208): 323-360 (in french).

Sellier A., Buffo-Lacarrière L., Multon S., Vidal T., Bourbon X. (2012), "Nonlinear basic creep and drying creep modeling", conference Numerical Modeling Strategies for sustainable Concrete Structures, Aix.

Stefan L., Benboudjema F., Torrenti J.-M., Bissonnette B. (2010), "Prediction of elastic properties of cement pastes at early ages", *Computational Materials Science* 47(3): 775-784.

Thomas J., Jennings H. (2002), "Effect of Heat Treatment on the Pore Structure and Drying Shrinkage Behavior of Hydrated Cement Paste", *J. Am. Ceram. Soc.,* 85 [9] 2293–98

Development of Comprehensive Platform for the Estimation of Volume Change and Damage in Cementitious Material

T. Tanabe[1], S.Ono[2] , H. Morimoto[3], H. Nakamura[4] and Y. Ishikawa[5]

[1] CRIIES, Nagoya Wakamizu 2 -3-11,464-0071, PH+81(52)762-7200; FAX+81(52)723-1659; email: tanabe@nagoya-u.jp

[2]C&R Consultant CO.,LTD, Kokubunji Honcho 2-23-3,186-0012, PH+81(42)320-5585;FAX+81(42)320-5506;email: ono@candr.jp

[3]CIAM, Gifu University, Gifu Yanagido 1-1, 501-1193, PH/FAX+81(58) 293-3330; e-mail: morimt@gifu-u.ac.jp

[4]Department of Environmental Science & Engineering, Yamaguchi University, Ube Tokiwadai 2-16-1, 755-8611, PH+81(836)85-9531, FAX+81(836)85-9501 email: nakahide@yamaguchi-u.ac.jp

[5]Department of Civil Engineering, Meijo University, Nagoya Shiogamaguchi 1-501, 468-8502, PH+81(52)838-2343; FAX+81(52)832-1179; e-mail: ishiyasu@meijo-u.ac.jp

ABSTRACT

The paper reports some highlights of the theoretical development included in JCI computer Code for hygro-thermal drying chemo mechanical volume change and damage in cementitious material. Only a few is reported in this paper due to the limited space. The first highlight is the theoretical development of drying shrinkage in the period from fresh concrete to hardened concrete. The second is the method to estimate crack widths and its discrete interval lengths from the smeared crack model. Validity of this theoretical model is shown in comparison with the real size experiment performed at the Metropolitan Highway Corporation.

HYGRO-THERMAL AND HYGRO –THERMAL DRYING ANALYSIS

The JCI Committee is formed 2007 under the auspice of Japan Concrete Institute and the computer code to estimate the volume change of the cementitious material, especially of concrete material and its damages to various concrete structures has been developed and is under the process of further advancement of the

platform. The general figure of the platform can simply seen in Figure1, which shows the platform consists with stress and crack width analysis platform in which hygro-thermal analysis, hygro-thermal-drying analysis, and chemical expansion analysis are embedded. These pillars are connected by common variables and by the chemical energy conservation law which enables to identify the initial strain that varies with the constraint effect.

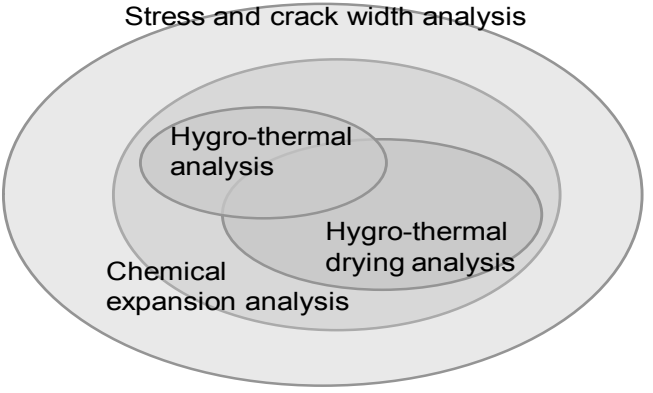

Figure1 Computing Platform to estimate Volume Changes and Damages in early age Concrete

Hygro-thermal drying analysis. Hygro-thermal analysis in the platform is the key pillar but temperature estimation in early age is well established (Tanabe, 2003) except heat evolution amount which is dependent on the cement kinds and heat evolution velocity. These values are revised in the JSCE Standard this spring. Therefore, we start from the hygro-thermal drying analysis. Hygro-thermal drying analysis is not so simple, since initial shrinkage strain is required in the period from fresh concrete to hardened concrete and experimental research on this is few. We do not seek rigorous mathematical model for the hygro-thermal drying shrinkage but seek the model practically usable for the practical purposes. To obtain drying degree, the water migration flux in saturated or unsaturated porous material can be written as

$$\mathbf{J_w} = -C_W \cdot \boldsymbol{\nabla} W - C_H \cdot \boldsymbol{\nabla} T$$

The second term of the right hand side is called Soret effect but neglected in our plat form considering the past research (Bazant,1996).

Rewriting above equation with vapor pressure p, i.e. $\nabla w = (\partial w/\partial p)\nabla p$

$$\mathbf{J_w} = -C_w \frac{\partial w}{\partial p} \cdot \nabla p = -C'_w \cdot \nabla p \qquad \cdots\cdots\cdots (1)$$

Now, divergence of the flux gives the water content rise rewritten with vapor pressure,

$$\left(\frac{\partial w}{\partial p}\right) \dot{p} = -\nabla \cdot \mathbf{J_w} - \dot{w}_d \qquad \cdots\cdots\cdots (2)$$

where w_d is hydrating water rate, which is a part of the solidified material. In this equation, the values of the term $(\partial w/\partial p)$ and C_w are important and they vary with absolute water vapor pressure. What we have done is to use the values experimentally obtained(Nakamura, 2003).

As for boundary condition, Neumann type boundary condition $\mathbf{n} \cdot \mathbf{J_w} = \alpha_w(p - p_0)$ is adopted. The values α_w is also experimentally decided(Nakamura, 2003.). Once, the vapor pressure is given, the corresponding shrinkage strain or force should be given.

We adopted the shrinkage strain for hardened concrete defined in the JCI Code or Euro Code as the final values for the concrete in hardening process. The interpolating function that gives shrinkage strain in hardening process which agrees finally with the values of the Standards may be derived as follows. Shrinkage strain is definitely related with pore distribution of concrete and saturation extent with water. The experimental data are always drying from the fully saturated condition, which means the water vaporizes from the larger pore and the residual water is contained in the smaller diameter pore.

Then, the pore size distribution and its volume will be one representative parameter of shrinkage stress. The equivalent nodal force, F to the distributed pore negative pressure and the stress in solid particles in FEM formulation read assuming evenly distributed pore and solidified particle regardless pore size and particle size,

$$F = \iiint_V B^T \cdot P \cdot dV = \iiint_V B^T \cdot dV \left[\sum \frac{V_i}{V} \cdot p_w^i + \sum \frac{\alpha V_i}{V} \cdot p_s^i\right]$$

$$= \left[\sum \frac{V_i}{V} \cdot p_w^i + \sum \frac{\alpha V_i}{V} \cdot p_s^i\right] \cdot \mathbf{\Gamma} = \omega\left[\sum \frac{r^2{}_i}{V} \cdot r_i \cdot p_w^i + \sum \frac{\alpha r^2{}_i}{V} \cdot r_i \cdot p_s^i\right] \cdot \mathbf{\Gamma},$$

where $\mathbf{\Gamma} = \iiint_V B^T \cdot dV$, p_w^i is the water pore pressure of pore size of i-th grade, $v_{i/v}$ is its volume fraction, while p_s^i is the pressure which work to the solid particle,

of which volume fraction may be expressed some portion, i.e. α of the same pore size volume fraction and ω is the factor to relate the volume to the pore radii. Rewriting pore pressure and particle stress in terms of surface energy, γ_w for water, γ_s for solid particle, and using $p_w^i = \gamma_w/2r_i$ and $p_s^i = \beta\gamma_w/r_i$ (Wittmannn,1983),

$$\mathbf{F} = \omega\left[\sum\frac{r^2{}_i}{4V}\cdot\gamma_w + \sum\frac{\alpha r^2{}_i}{V}\cdot\beta\gamma_s\right]\cdot\boldsymbol{\Gamma} \propto \left[\frac{s_p}{V}\cdot\gamma_w + \frac{\alpha s_p}{V}\cdot\beta\gamma_s\right]\cdot\boldsymbol{\Gamma} = (\gamma_w + \alpha\beta\gamma_s)\frac{S_p}{V}\cdot\boldsymbol{\Gamma}$$

where $s_p = \kappa\sum r^2{}_i$, surface area of hydrated gel particles. Though we do not know exactly the value of α and β, above equation tells the shrinkage inducing stress is directly related to the specific surface area of hygral particles. On the other hand, development of the strength of concrete is also directly related to the specific surface increase. Therefore, shrinkage inducing stress and the concrete strength during the period from early age to haredened concrete, may be written as a monotonically increasing function of the strength development ratio, such as $f(\frac{f_c(t)}{f_{c,28}})$. With these theoretical considerations, we adopted tentatively the initial strain due to hygro-thermal drying initial strain in reference to the hardened concrete shrinkage strain, as

$$\Delta\varepsilon_{sh}(t) = (\frac{f_c(t)}{f_{c,28}})^n \cdot \Delta\varepsilon_{sh,hardened} \ ,$$

where $\varepsilon_{sh,hardened}$ is the shrinkage strain of hardened concrete and its values are found various Standard such as JCI Code, Euro Code once the humidity is obtained through Equation 2 and n=1~3. However, it should be mentioned that this point is still on the development stage.

CRACK WIDTH ESTIMATION

Crack width is the most important factor that affects concrete structures, which lead to various deterioration and should be limited within the range that depends on concrete structural life time expected. The platform provides the estimation of crack widths and its relative distances by smeared crack formulation. It is generally accepted that the smeared formulation is unable to detect discrete crack widths and crack locations. However, we find it is possible with the help of observation of the contour of crack equivalent strain. In the beginnings, the crack equivalent strain is defined as is well established in the past research. Referring to Figure 2 , we consider cracks are regularly existing and its spacing is s. Taking reference point in the zone, of which coordinate is X_0 and X as any point in the

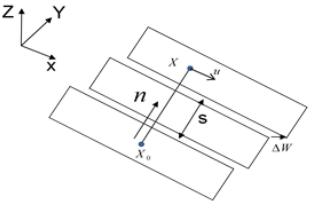

Figure 2 Crack width and spacing

zone, the displacement $\mathbf{u}$ of the point X in reference to X_0 is given as

$$\mathbf{u} = \left[\frac{(\mathbf{X}-\mathbf{X_0})}{\mathbf{s}} \cdot \mathbf{n}\right] \Delta\mathbf{w} = [(\mathbf{X}-\mathbf{X_0}) \cdot \mathbf{n}] \cdot \frac{\Delta \mathbf{w}}{\mathbf{s}} = [(\mathbf{X}-\mathbf{X_0}) \cdot \mathbf{n}] \cdot \Delta \mathbf{w^m}_{\text{crack}}$$

$$\Delta \mathbf{w^m}_{\text{crack}} = \begin{Bmatrix} \Delta \mathbf{w_x}/\mathbf{s} \\ \Delta \mathbf{w_y}/\mathbf{s} \\ \Delta \mathbf{w_z}/\mathbf{s} \end{Bmatrix}$$

which is the mean crack width vector. By definition,

$$\mathbf{u} = [\mathbf{n} \otimes \Delta \mathbf{w^m}_{\text{crack}}](\mathbf{X}-\mathbf{X_0})$$

Crack equivalent strain is defined as the symmetrical part of $\mathbf{n} \otimes \mathbf{w^m}_{\text{crack}}$ and

$$\varepsilon_{\text{crack}} = \frac{1}{2}\left(\mathbf{n} \otimes \Delta \mathbf{w^m}_{\text{crack}} + \Delta \mathbf{w^m}_{\text{crack}} \otimes \mathbf{n}\right)$$

Now diagonal portion of the above tensor, $\varepsilon_{\text{crack}}$ reads, in the case that crack occurs in simple separation mode, that is simple opening mode and have no shear slip between cracks,

$$\varepsilon_{\text{xx,crack}} = \mathbf{n_x n_x}\,\Delta W/s = \cos^2\theta \cdot \varepsilon_{\xi\xi},$$
$$\varepsilon_{\text{yy,crack}} = \mathbf{n_y n_y}\,\Delta W/s = \cos^2\varphi \cdot \varepsilon_{\xi\xi},$$
$$\varepsilon_{\text{zz,crack}} = \mathbf{n_z n_z}\,\Delta W/s = \cos^2\psi \cdot \varepsilon_{\xi\xi}$$

where θ, φ, and ψ are the angles that the normal vector to crack plane make with X,Y and Z axes. Inversely the above equation gives the discrete crack width. The conceptual extension from $\Delta W/s$ to $\varepsilon_{\xi\xi}$ should be noted here. And $\varepsilon_{\xi\xi}$ is variable and we do not assume the crack spacing is regular anymore, that means $\varepsilon_{\xi\xi}$ is given by the smeared model. Then, the situation is that real crack direction and crack equivalent strain along the direction are unknown. However, crack strain along the coordinate axis is known. Recognizing the above situation, the next derivation gives the crack width and its orientation

$$\Delta w_x = \int_{-l/2}^{l/2} \varepsilon_{xx,crack} \cdot dl = \int_{-\frac{l}{2}}^{\frac{l}{2}} \cos^2\theta \cdot \varepsilon_{\xi\xi} \cdot dl = \int_{-s/2}^{s/2} \cos\ \theta \cdot \varepsilon_{\xi\xi} \cdot ds = \cos\theta \cdot \Delta w$$

In analogy, $\Delta w_y = \cos\varphi \cdot \Delta w$ and $\Delta w_z = \cos\psi \cdot \Delta w$

Finally, the crack width can be written as

$$\Delta w = \sqrt{{\Delta w_x}^2 + {\Delta w_y}^2 + {\Delta w_z}^2} \quad \text{and} \quad \mathbf{n} = \begin{Bmatrix} \Delta w_x/\Delta w \\ \Delta w_y/\Delta w \\ \Delta w_z/\Delta w \end{Bmatrix}$$,the normal to crack plane.

In the real practice, the crack equivalent strain curve along the X,Y, Z reference line should be drawn in which the locations of low limit points and high limit points be recognized and the ℓ, the integration length should be taken in such a way that starts from a low limit point and ends at the next low limit point crossing the high limit point. Discrete crack location is considered to be the high limit point.

EXPERIMENTAL VERIFICATION

The Metropolitan Highway Corporation has conducted comprehensive experiment in terms of hygro-thermal stress measurements in concrete and re-bars, crack widths and its locations. Their report is included in JCI Standards for Crack Width Control in Massive Concrete published in 2011. The first series are the four walls which dimension are shown in Figure 3, and specimen number 1-1, 1-3, 1-4 have all same sections. However, the unit cement content is different, i.e. 300kg/m3, 250kg/m3, 380kg/m3 for each. Specimen No. 1-2 has the twice tall height of the wall with the same width, 30cm and unit cement content is same as specimen No1-1. The horizontal reinforcement ratios are all same through the specimens and is 0.25% of the section. All specimen concrete are cast at the same time on the common footing which dimensions are 500cm by 150cm and the 1500cm length. The common use of the footing gave some errors in the hygro-thermal cracking behavior since the thermal deformation of each specimen are different and affect each other through the footing. Therefore, the analysis(Itoh,2010) are carried out as it is, as shown in the Figure 3, casting concrete for all the specimen at the same time. Figure3 shows the common footing on which 4 specimens, 1-1, 1-2, 1-3, 1-4 stand. The left bounding section of the overall figure is the plane of symmetry boundary of total 1500cm length specimens. Material parameters such as adiabatic temperature rise, its velocity, specific density, specific heat, conductivity are shown in Table1 for each specimen. The temperatures by the analysis and experimentally obtained are in good agreement,

of which highest temperature recorded is around 30℃ and then stress and crack width analysis has performed. The calculated crack equivalent strain contours are shown in Figure 4. From the crack equivalent strain, the discrete crack widths are obtained and compared in Figures 5 and 6. Figure 5 shows the crack widths of the 4 specimen at the top surface and the middle height of the wall, though cracks occurring in the same height are summed in this data. Figure 6 shows the maximum crack widths of the specimen including other tested specimens beside the 4 specimens shown in Figure3. The evaluation of the crack width calculation accuracy may be recognized as satisfactory; however, it may be expected further upgrading of its accuracy.

Table 1 Thermal Properties of Specimen Concrete

	footing	No.1-1	No.1-2	No.1-3	No.1-4
Thermal conductivity (W/m・K)	2.7				
Specific heat (KJ/kg・K)	1.1				
Specific density (kg/m³)	2350				
Casting temperature (℃)	15.0 Init. Temp	18.0	18.5	18.0	20.0
Adiabatic temperature rise Q_∞(K)	—	48.7	44.2	42.6	57.0
Temperature rise velocity γ	—	1.00	1.02	0.80	1.02
Unit cement content (kg/m³)	—	300	300	250	380
Cement kind	—	(N)	(N)	(N)	(N)

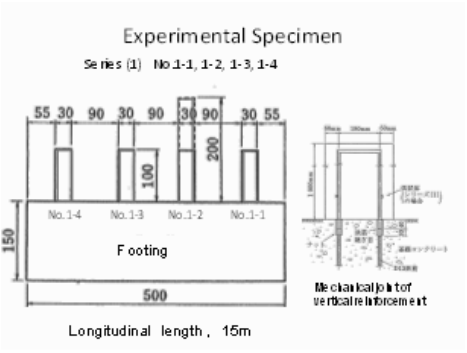

Figure 3. Experimental Specimen.

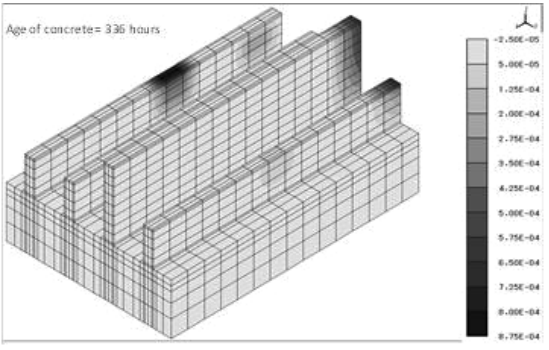

Figure 4. Crack Equivalent Strain Distribution

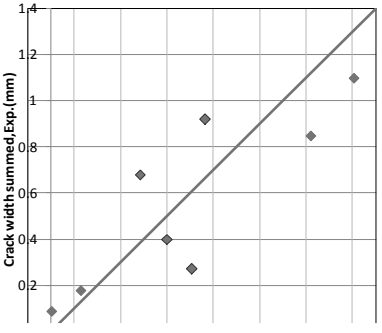

Figure 5 Summed Crack Widths

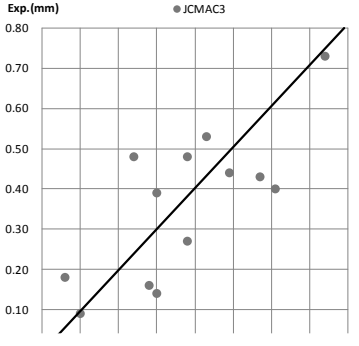

Figure 6 Maximum Crack Width

CONCLUSION

Theoretical development of the drying shrinkage in the period from fresh concrete state to hardened concrete and the crack width estimation through the smeared crack model are reported with the experimental verification. We would like to express our sincere thanks to all the committee members whose names do not appear in the paper and who allowed us to make public some of their contributions.

REFERENCE

Wittmann,F.H.(1983),” Fracture Mechanics of Concrete”, Elsevier.

Bazant, Z. and Kaplan, M.F.(1996),”Concrete at high temperature”, Longman.

Tanabe,T. and et.al.(2003), “Nonlinear Analysis of Concrete with Initial Damages and its Computer Program “, Gihodo.

Nakamura,K.(2003),” Study on Moisture Migration in Concrete”, Thesis presented to Gifu Univ.

Itoh, M.(2010),”JCI Committee Document”.

Simulation of time-dependent tensile behavior of concrete under various loading and drying path

T. Shimomura[1], Y. Aoki[2] and H. Obata[3]

[1]Department of Civil and Environmental Engineering, Nagaoka University of Technology, Nagaoka, Niigata 940-2188, Japan; PH +81 (258) 47-9603; FAX +81 (258) 47-9600; email: takumi@nagaokaut.ac.jp
[2]Department of Civil Engineering, Kisarazu National College of Technology, Kisarazu, Chiba 292-0041, Japan; PH +81 (438) 30-4000; FAX +81 (438) 98-5717; email: aoki@c.kisarazu.ac.jp
[3]Nghi Son Cement Corporation, P801, Sun Red River Building, 23 Phan Chu Trinh Str., Hanoi, Viet Nam; PH +84 (43) 933-0917; FAX +84 (43) 933-0922; email: obata@nghison.com.vn

ABSTRACT

Stress analysis considering spatial distribution of shrinkage and time-dependent deformation characteristic should be carried out in order to predict accurately tensile stress and associated crack in concrete member under restraint drying shrinkage. In particular, a constitutive model for concrete that can adequately express tensile creep under drying is of importance. A new apparatus for sustaining tensile test of concrete was developed in this study to obtain reliable data of tensile creep of concrete which can be a basis to develop an accurate computational model. The testing system, using cylindrical specimen, ensures comparison between experimental and analytical results under ideal condition. Tensile stress and strain of the specimen can be precisely and stably controlled by inducing tensile load into the specimen as a reaction of compressive load in steel rod connected by screw. Consequently, time-dependent tensile behavior i.e., stress, strain and cracking, of concrete can be tested under various loading and drying path programmed. Test results obtained the proposed apparatus are demonstrated. Numerical simulation of tensile behavior of concrete is also conducted in this study. It was verified that reduction of tensile stiffness and cracking stress of concrete under drying can be simulated by strain softening near the surface due to restrained shrinkage.

METHOD OF SUSTAINING TENSILE LOADING TEST

Developed testing apparatus. Figure 1 shows the developed testing apparatus for sustaining tensile loading test of concrete. Tensile behavior of concrete under various loading and deformation path and drying condition can be examined with this apparatus. Figure 2 schematically shows the control system of the testing apparatus.

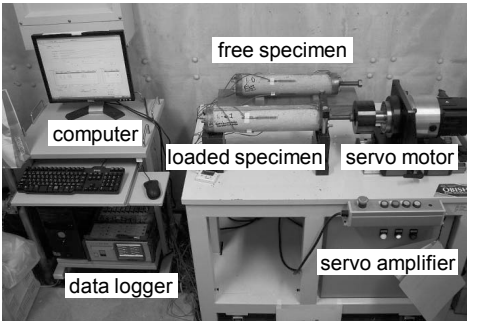

Figure 1. Testing apparatus for sustaining tensile loading test.

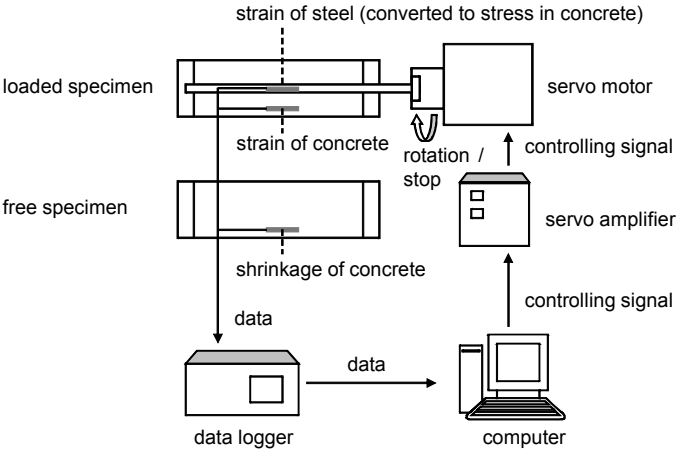

Figure 2. Control system of the testing apparatus.

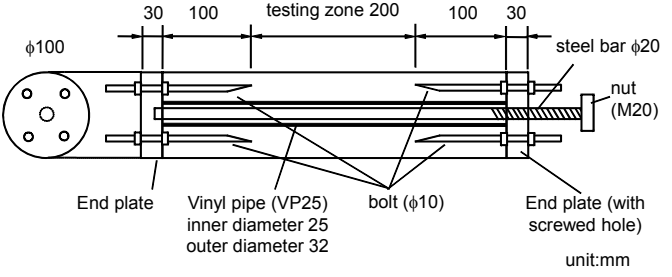

Figure 3. Specimen.

A loaded specimen and a free specimen, which were made with same concrete mix and cured under same condition, are used for one set of loading test. Strain of the loaded and the free specimens and strain of the steel bar in the loaded specimen are measured. Stress of concrete in the loaded specimen can be calculated from strain of the steel bar.

$$\sigma_c = -\frac{A_s}{A_c} \times E_s \varepsilon_s$$

where, σ_c: stress of concrete in the loaded specimen, A_s: cross sectional area of steel bar, A_c: cross sectional area of concrete, E_s: elastic modulus of steel bar and ε_s: strain of steel bar. Effective strain of concrete in the loaded specimen can be calculated as:

$$\varepsilon_e = \varepsilon_c - \varepsilon_{sh}$$

where, ε_e: effective strain of concrete in the loaded specimen, ε_c: strain of concrete in the loaded specimen and ε_{sh}: shrinkage strain of concrete which is measured from the free specimen. As illustrated in Figure 2, ε_c, ε_s and ε_{sh} are monitored at real-time during the test and the steel bar in the loaded specimen is screwed by a servo motor so that σ_c, ε_e or ε_c become the programmed value at the time.

Specimen. Cylindrical concrete specimen with a hole in the centroid shown in Figure 3 is used. Concrete is anchored with two end plates by embedded bolts. One of the end plates has screwed hole in the centroid, in which steel bar is set. Tensile load is induced into concrete as a reaction force of compressive force in the steel bar. Tensile load and strain of concrete in the loaded specimen can be controlled by rotating the steel bar.

The advantage of the developed testing method is that sustaining tensile load can be easily induced into concrete and stably controlled by the screwed steel bar. Spatial distributions of stress, strain, shrinkage and moisture content in concrete are axial symmetry due to the geometry of the specimen, which is suitable to comparison of experimental and analytical results. Various loading and deformation path can be programmed and controlled by a computer. In addition, load induced in specimen can be controlled also by manual operation instead of using servo motor.

SUSTAINING TENSILE LOADING TEST OF CONCRETE

Outline of the experiment. The influence of loading rate and drying condition on tensile behavior of concrete, i.e., stress and effective strain curve and cracking stress and strain, is investigated. Table 1 shows conditions of specimens. Table 2 shows mix proportion of concrete. Concrete was cast in the temperature and humidity controlled room of 20 deg. and 60%RH. Specimens were cured there for 28 days being wrapped with plastic bag to avoid drying. Thereafter, four specimens in the same series were tested simultaneously. Specimen A-1 and B-1 were loaded by servo motor, while A-2, A-3, B-2 and B-3 were loaded by manual operation. Specimens in the series B were kept wrapped with plastic bag during the loading test. Properties of concrete at 28days are shown in Table 3.

Table 1. Test condition of specimens.

Series	Specimen	Drying condition	Tensile loading rate (N/mm^2/day)
A	A-0	unsealed	0 (free shrinkage)
	A-1		0.072
	A-2		0.135
	A-3		0.271
B	B-0	sealed	0 (free shrinkage)
	B-1		0.072
	B-2		0.135
	B-3		0.271

Table 2. Mix proportion of concrete.

W/C	s/a	Air(%)	unit mass (kg/m^3)						
			W	C	S	G	Ad1	Ad2	Ad3
0.5	0.5	5	170	340	891	908	0.51	6.8	0.408
	Ad1: anti segregation agent, Ad2: super plasticizer, Ad3: air reduction agent								
	Gmax: 13mm								

Table 3. Strength properties of concrete.

Series	Age (days)	Compressive strength (N/mm^2)	Elastic modulus ($*10^3$ N/mm^2)	Tensile strength (N/mm^2)
A	28	39.36	32.63	2.66
B	28	44.35	37.39	2.88

Test results and discussion. Figure 4 shows test results of strain of all specimens as a function of time. Shrinkage strain is expressed as positive. Loaded specimens were finally broken with penetrating crack in the testing zone. Observed strain of loaded specimens in series A is in shrinkage side even under tensile load because of drying shrinkage.

Figure 5 shows relationship between tensile stress and effective strain of loaded specimens. A straight line of which slope is static elastic modulus is also indicated for comparison. Table 4 shows experimentally obtained cracking stress, cracking effective strain and average effective elastic modulus of loaded specimens. It is regarded that effective elastic modulus of series A is generally greater than that of series B and smaller than static elastic modulus. Note that effective elastic modulus of specimen B-1 is irregularly great, which might be a mistake of measurement of strain in the experiment.

Since specimen in series B is sealed, the reduction of effective elastic modulus in series B is attributable to basic creep of concrete by sustaining load. In the previous experimental investigation by the authors, it was considered that drying creep is dominant in tensile creep of concrete under restraint shrinkage. However, tensile basic creep is detected in the experimental result this time. One of the reasons is that test result under very slow loading rate is included here.

The reason why effective elastic modulus of series A is smaller that that of series B is explained in terms of drying creep. It is found that the configuration of

stress-effective strain relationship of series A is more curving than that of series B. This is because average tensile stiffness of the specimen gradually decreases with development of spatial gradient of shrinkage from the surface associating with drying.

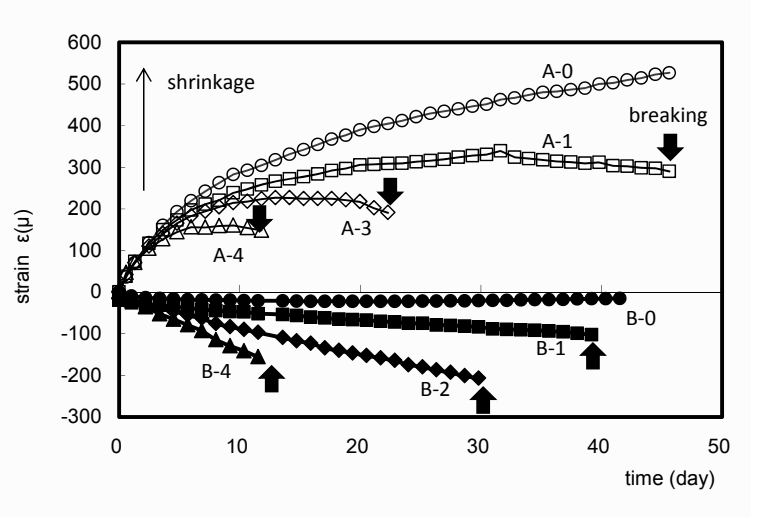

Figure 4. Strain of concrete specimen as a function of time.

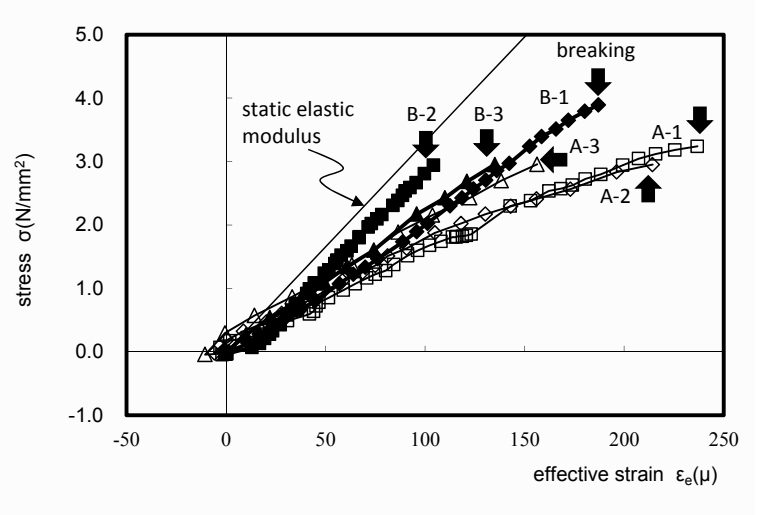

Figure 5. Relationship between stress and effective strain of concrete specimen.

Table 4. Cracking stress and effective elastic modulus of concrete specimen.

Series	Specimen	Cracking (breaking of specimen)		Average effective elastic modulus ($*10^3$ N/mm^2)
		Stress (N/mm^2)	Effective strain (μ)	
A	A-1	3.24	237	13.67
	A-2	2.95	215	13.72
	A-3	3.24	169	19.17
B	B-1	2.97	105	28.29
	B-2	3.88	187	20.75
	B-3	3.24	146	22.19

NUMERICAL SIMULATION

Outline of numerical simulation. Stress and deformation of cylindrical specimen is numerically simulated by moisture transport analysis and stress analysis considering drying shrinkage of concrete. Figure 6 shows outline of the analytical method. Moisture transport in the specimen is regarded as axial symmetry. Stress analysis is carried out considering only longitudinal component of stress and strain. Moisture transport and drying shrinkage in concrete are calculated using computational models developed by the authors, considering pore structures of concrete, transport of water in pores, drying shrinkage of cement paste and mechanical interaction between cement paste and aggregate in concrete.

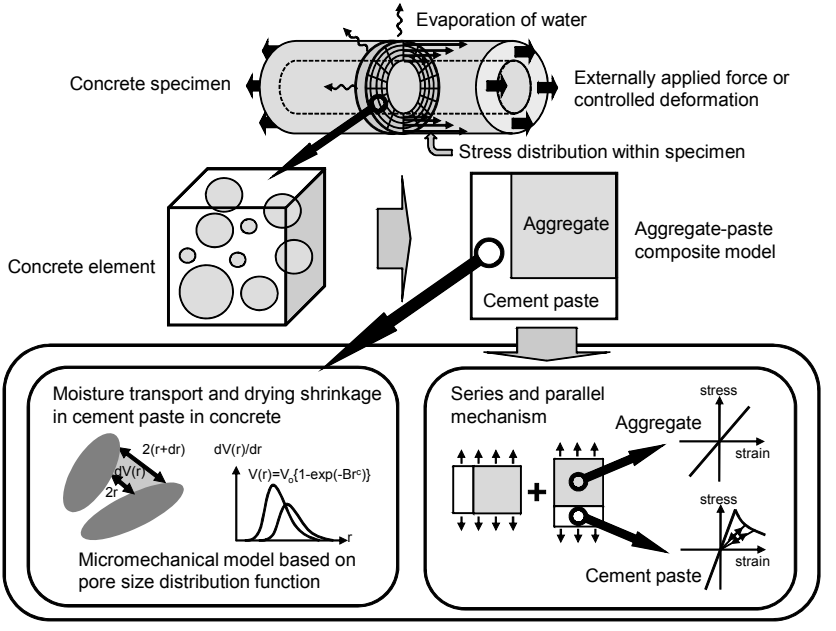

Figure 6. Outline of analytical model for shrinkage and deformation of concrete.

Analytical results and discussion. Analytical results of series A and B are shown in Figure 7 and 8 respectively, in which figure (a) is shrinkage strain of specimen as a function of time and figure (b) is tensile stress as a function of effective tensile strain of specimen. Material parameters in the computational models are determined so that analytical result of time-dependent free shrinkage of specimen A-0 corresponds with experimental result. Same values of material parameters are used for all specimens.

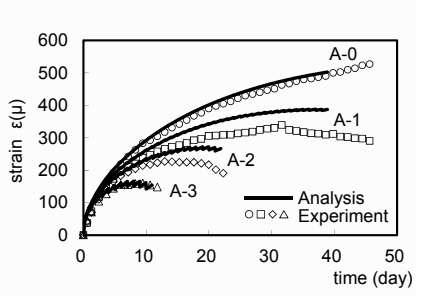

(a) Relationship between time and strain of specimen

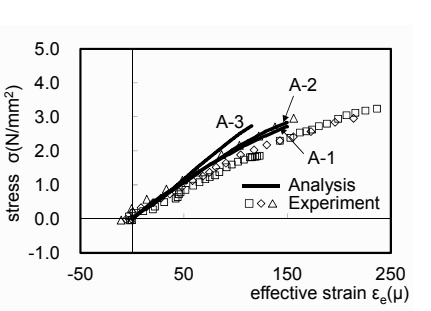

(b) Relationship between stress and effective strain of specimen

Figure 7. Analytical results of series A.

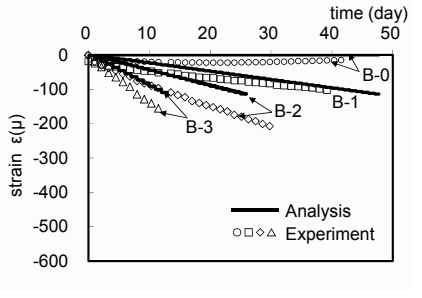

(a) Relationship between time and strain of specimen

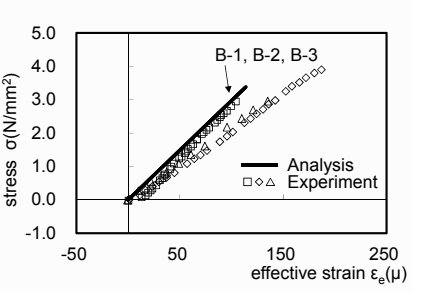

(b) Relationship between stress and effective strain of specimen

Figure 8. Analytical results of series B.

Time-dependent strains of free and loaded specimens in series A in Figure 7 (a) are well simulated by the analysis. Though drying creep as material characteristics of cement paste and aggregate are not taken into account in the computational model, the analytical results in Figure 7 (b) can simulate reduction of effective elastic modulus from static elastic modulus, i.e., apparent drying creep at specimen level. In the analytical model, this phenomenon is expressed as results of restraint of shrinkage

of cement paste by aggregate and strain softening near the surface due to spatial gradient of shrinkage in the specimen. The analytical results imply that this phenomenon also takes place in actual concrete.

Since neither basic creep of cement paste nor aggregate is considered in the model, effective elastic modulus of all specimens in series B correspond with static elastic modulus regardless the loading rate as shown in Figure 8 (b). The fact that analytical effective elastic modulus is greater than experimental ones suggest that tensile basic creep should be taken into account for accurate evaluation of stress induced in concrete member under restraint shrinkage.

CONCLUSION

Following conclusions were obtained through this study.

(1) Using the developed apparatus for sustaining tensile loading test, the influence of loading rate and drying condition on tensile behavior of concrete can be examined.
(2) It was verified that drying creep, i.e., creep associating with drying, is dominant in time-dependent tensile strain of concrete subjected to sustaining load and drying. However, tensile basic creep should be taken into account for accurate evaluation of stress induced in concrete member under restraint shrinkage.
(3) Time-dependent tensile behavior of concrete specimen subjected to drying and externally applied tensile load can be numerically simulated by moisture transport analysis and shrinkage stress analysis by the proposed analytical method.

ACKNOWLEDGEMENTS

The authors would like to express their gratitude to Mr. Saito, Mr. Matsuoka and Mr. Nagoya, who are former graduate students and contributed to this research project.

REFERENCES

Aoki, Y., and Shimomura, T. (2008), "Effects of loading rate and drying condition on uniaxial tensile stress-strain relationship and cracking strength of concrete", *Proceedings of the 8th International Conference on Creep Shrinkage and Durability of Concrete and Concrete Structures* (ConCreep8), 1, 207-214.

Obata, H., and Shimomura, T., (1999), "Time-dependent stress analysis of concrete member by aggregate-paste composite model", *Transactions of the JCI*, 21, 135-142.

Shimomura, T., and Maekawa, K., (1993), "Micromechanical model for drying shrinkage of concrete based on the distribution function of porosity", *Proceedings of the fifth International RILEM Symposium on Creep and Shrinkage of Concrete* (ConCreep5), 133-138.

Matsuoka, Y., Shimomura, T., and Nagoya, T., (2010), "Study on Characteristics in tensile deformation of concrete for prediction of drying shrinkage crack", *Proceedings of the JCI*, 32(1), 389-394. (in Japanese)

The B4 model for multi-decade creep and shrinkage prediction

R. Wendner[1], M. H. Hubler[2], and Z. P. Bažant[3]

[1] University of Natural Resources and Life Sciences Vienna, Department of Civil Engineering and Natural Hazards, Peter-Jordanstr. 82, 1190 Vienna, Austria; email: roman.wendner@boku.ac.at
[2]Northwestern University, Department of Civil and Environmental Engineering, Tech 2145 Sheridan Rd. A236, Evanston, IL 60208-3109; email: m-hubler@u.northwestern.edu
[3]Northwestern University, Department of Civil and Environmental Engineering, Tech 2145 Sheridan Rd. A135, Evanston, IL 60208-3109; PH (847) 491-4025; email: z-bazant@northwestern.edu

ABSTRACT

Presented is a new model, labeled B4, which can overcome some of the shortcomings of the CEB-*fib*, ACI, JSCE and GL prediction models for concrete creep and shrinkage. The B4 model represents an extension and systematic recalibration of the theoretically founded model B3, a 1995 RILEM recommendation. In addition to introducing the so far missing separation of autogenous and drying shrinkage, model B4 takes into account the cement-type and admixture parameters, as well as the effects of various types of aggregate. The new predictors for the creep compliance function more accurately capture the composition information and are recalibrated to match the multi-decade behavior. This behavior has recently been documented by observed deflection records of many bridges, which is evidence that has so far been systematically underestimated. The improved model was calibrated through a joint optimization of a new significantly enlarged database of laboratory creep and shrinkage tests and a new database of bridge deflection records.

INTRODUCTION

The design of new, and assessment of, existing concrete structures requires accurate prediction of the structural response under mechanical and environmental loads during construction as well as operation until the end of the intended service life. Bridges and other important structures are supposed to be designed for a service life of at least 50 years, and large bridges nowadays generally over 100 years. Such design obviously requires realistic multi-decade prediction models.

Recently, it has become clear that the existing prediction models for the time-dependent behavior of concrete are highly inaccurate for the desired multi-decade life spans. This insight was revealed in the deflection analysis of large-span pre-stressed segmental bridges, beginning with the Koror-Babeldaob (KB) Bridge in Palau (Bažant et al., 2010). While most creep prediction equations (ACI 1992, fib 1993, fib

2012, Gardner and Lockman, 2001) approach a finite asymptote, the structural responses and theory reveal a non-zero terminal slope in the logarithmic time scale (Bažant et al., 2011). Another key weakness of the previous prediction equations is a scarcity of laboratory calibration data of the compositions of modern concretes and for the full multi-decade prediction time range.

An extensive database should, in theory, reveal the correct functional form of the creep and shrinkage prediction equation if the appropriate full statistical analysis could be performed for all composition, environmental, and response variables. Unfortunately, such a database does not exist. Most laboratory data usable for model development, calibration, and validation are limited to less than 6 years in duration. The only source of information exceeding the scope of laboratory tests is the structural measurements such as mid-span bridge deflections or column-shortenings of high-rise buildings. These two types of datasets cannot be easily combined. The rapid development of new concretes is reflected only in recent laboratory tests but not in the long monitored structures which consist of old, historically used, concretes. Those concretes, of course, are of less direct significance for the current and future construction industry. Nonetheless, since creep resides only in the calcium silicate hydrates, which are common to both old and new concretes, the creep data for old concretes are still very useful for qualitative information. Therefore, multi-decade structural observations on old structures do provide important insight (Bažant et al., 2011).

The new improved model B4 builds upon the strengths of the B3 model (Bažant, 1995, Bažant and Baweja, 1995, 1996, 2000), which represents a 1995 RILEM recommendation. The theoretical foundation of model B3 are the solidification theory and microprestress theory which provide the correct functional form for multi-decade creep and shrinkage while still allowing for modifications of time dependent effects due to recent cement compositions. To recalibrate the new prediction equations and capture the correct multi-decade trend, a new set of databases, categorized into basic creep, drying creep, total creep, drying shrinkage, autogenous shrinkage and total shrinkage, was compiled at Northwestern University (Hubler et al., 2013). The scope of prediction was expanded to modern concretes with various types of admixtures, which are classified into six different types, some increasing and others decreasing the shrinkage and creep. One major novelty is the separation of drying shrinkage and autogenous shrinkage. Admixtures such as fly ash, silica fume, water reducer, superplasticizer, retarder, accelerator, viscosity agent, and air entraining agent are known to affect creep and shrinkage independently as well as in interaction. These dependencies are captured with optimized parameters, as are the effects of different cement types and aggregate types. Environmental temperature, environmental humidity, and curing time are based on well-established and scientifically sound concepts.

FORMULATION MODEL B4 FOR CREEP AND SHRINKAGE

The B4 prediction model captures the behavior of Portland cement concretes based on model parameters that are derived from the composition of the concrete and the environmental conditions. Since the mathematical form of the short- and long-

term creep behavior is captured in model B3 correctly, the only need is recalibration and extension of the shrinkage part of the model for autogenous shrinkage. Since cracking and other sources of nonlinearity are treated separately, a linear dependence on stress may be assumed as an acceptable approximation for the service stress range (less than $0.4f'_c$ or $0.45f'_c$). This means that, for constant stress σ applied at age t',

$$\epsilon(t) = J(t,t')\sigma + \epsilon_{sh}(t,t_0) + \epsilon_{au}(t,t_0) + \alpha_T \Delta T(t) \tag{1}$$

in which σ is the uniaxial stress. The stress-independent strain is split into the drying shrinkage, $\epsilon_{sh}(t,t')$, autogenous shrinkage, $\epsilon_{au}(t,t_0)$, and thermal expansion; $\Delta T(t)$ is the temperature change, and α_T is the coefficient of thermal expansion. The compliance function, $J(t,t')$, as introduced in equations 4, 8, and 15 of Bažant and Baweja (1995) is adopted without change, including the description of the short-time elastic modulus, E_0, the basic creep compliance, C_0, and the drying creep compliance, C_d;

$$J(t,t') = \tfrac{1}{E_0} + C_0(t,t') + C_d(t,t',t_0) \tag{2}$$

Only the parameters q_1 for the instantaneous compliance, q_2 through q_4 for the basic creep compliance, and q_5 for the drying creep compliance have been adapted and recalibrated. The average shrinkage of a cross-section undergoing drying may be captured with the relation

$$\epsilon_{sh}(t,t_0) = -\epsilon_{sh,\infty}(t_0) k_h S(t,t_0) \tag{3}$$

where $\epsilon_{sh}(t,t_0)$ is the evolution of drying shrinkage strains, $\epsilon_{sh,\infty}(t_0)$ is the final drying shrinkage as function of the curing time t_0, k_h is a factor describing the dependence on environmental humidity as published in (Bažant, 1995), and $S(t,t_0)$ is the well-established time function of drying shrinkage with the correct asymptotic properties (Bažant, 1995);

$$S(t,t_0) = \tanh \sqrt{\tfrac{t-t_0}{\tau_{sh}}} \tag{4}$$

The shrinkage halftime, τ_{sh}, depends on the cement type and admixtures modifying the basic value τ_0 as in B3, which depends on the effective diffusivity and cross section shape through $k_s D$, where k_s is a shape parameter of the cross-section (Bažant, 1995) and D is the effective thickness of cross section. The average composition with an aggregate-cement ratio $a/c = 6$, a water to cement ratio $w/c = 0.38$ and an average cement content c normalized by the concrete mass density ρ, is obtained from the database; in general

$$\tau_{sh} = \tau_0 \left(\tfrac{a/c}{6}\right)^{-p_1} \left(\tfrac{w/c}{0.38}\right)^{-p_2} \left(\tfrac{6.5c}{\rho}\right)^{-p_3} (k_s D)^2 \tag{5}$$

The final shrinkage $\epsilon_{sh,\infty}(t_0)$ is determined accordingly using a cement and admixture dependent basic value ϵ_{sh0}. The influence of ageing and, thus, of the gain in stiffness, is accounted for (as originally proposed in (Bažant, 1995), by the ratio between 607 day modulus and the modulus at the end of curing;

$$\epsilon_{sh,\infty}(t_0) = \epsilon_{sh0} \left(\tfrac{a/c}{6}\right)^{-p_5} \left(\tfrac{w/c}{0.38}\right)^{p_6} \left(\tfrac{6.5c}{\rho}\right)^{p_7} \tfrac{E(607)}{E(t_0+\tau_{sh})} \tag{6}$$

The exponents p_2, p_3, p_6 depend on the cement type while p_1, p_5, p_7 are constants. In model B3, the influence of autogenous shrinkage was considered to be negligible and

thus was lumped into the drying shrinkage. This, however, is not possible for modern high strength concretes, with improved rheology and work-ability such as self-consolidating concretes that heavily rely on admixtures.

The evolution of autogenous shrinkage $\epsilon_{au}(t)$ is, contrary to drying shrinkage, a function of the total time t (*fib* 2012), rather than the drying time, and can be described in logarithmic time by the sigmoid function of the shape

$$\epsilon_{au}(t) = \epsilon_{au0} \left(\frac{a/c}{6}\right)^{-r_5} \left(\frac{w/c}{0.38}\right)^{-r_4} \left[1 + \left(\frac{\tau_{au}}{t}\right)^{\alpha}\right]^{-r_2} \tag{7}$$

with the basic value of the final autogenous shrinkage, ϵ_{au0}, and an empirical correction term for the composition. The speed of the autogenous shrinkage evolution is given by the autogenous shrinkage halftime τ_{au}, the exponent r_2 of the time function and the water-cement ratio dependent exponent $\alpha(w/c)$. Alternative time functions such as the exponential form (RILEM TC 119-TCE 1997, ceb/fip 1999, fib 2012, Lee et al., 2006, Tazawa and Miyazawa, 1995, Yoo et al., 2012), e.g. proposed in the 2010 model code, were not able to represent the time evolution with enough accuracy and flexibility;

$$\alpha = r_7 \left(\frac{w/c}{0.38}\right) \qquad \tau_{au} = \tau_{au0} \left(\frac{w/c}{0.38}\right)^{r_1} \tag{8}$$

Figure 1 shows partial predictions for several sets of shrinkage curves with only two parameters of the drying model (ϵ_{sh0} and τ_0) optimized to the respective concretes. All other parameters and exponents of the model remained unchanged and are based on a full fit of the laboratory data. Dashed lines represent the predicted autogenous shrinkage contribution, solid lines denote total shrinkage predictions, and circles represent experimental measurements. Figure 1a shows two total shrinkage curves as presented by Folliard (Folliard and Berke, 1997) with slightly varying composition. The main difference can be attributed to the addition of silica fume which significantly increases the autogenous shrinkage contribution. Both the final shape and magnitude of the total shrinkage curves can only be obtained by superposition of accurate drying and autogenous shrinkage components. Figure 1b presents the effect of environmental humidity on a set of identical specimens, utilizing data for concrete with rapid hardening cement (Keeton, 1965). Model B4 is able to capture autogenous shrinkage for regular cement (R) and swelling for rapid hardening cement (RS). Figure 1c finally shows the ability of the model the capture the size effect on diffusion and shrinkage on the cross-section level (Shritharan, 1989) for specimens with a volume-to-surface ratio between $V/S = 22$ and $V/S = 78$.

EXTENDED DATABASE

The new formulas are calibrated by unbiased multi-objective optimization of a greatly expanded laboratory database containing over 1,350 creep and 1,800 shrinkage laboratory tests, and by inverse statistical analysis of the terminal deflection trends of 69 bridges. The experimental database (Hubler et al., 2013), fully computerized, is about three-times larger than the previous RILEM database used to calibrate model B3. The creep database encompasses roughly 730 total creep curves and 640 basic creep curves. The shrinkage database encompasses 1220 total, 420 autogenous, and 180 drying shrinkage curves. The majority of data sets concerns

concretes made from the R type cement, followed by RS type and SL type concrete with 15% each.

OPTIMIZATION PROCEDURE

Unfortunately, the practically available data are limited and the required information can be extracted only by suitable statistical techniques. The reasons are as follows: Every investigation found in the literature is biased according to the scope of the study, as is the entirety of the available data due to experimental limitations and to focus of the engineering and scientific community on certain conditions. Furthermore, every test and structural measurement represents only a single realization of the full population which may be polluted by various errors and typically does not conform to the statistical mean.

The obstacle of errors in time or measurement value can be overcome by exploiting well established principles such as the asymptotic shape of drying shrinkage – a square-root time function – for short times after exposure to the environment (Bažant and Baweja, 1995). Consequently, linear extrapolation in the appropriate power scale allows for the extraction of errors in exposure time t_0 of shrinkage tests, and similarly in load application time t' of creep tests.

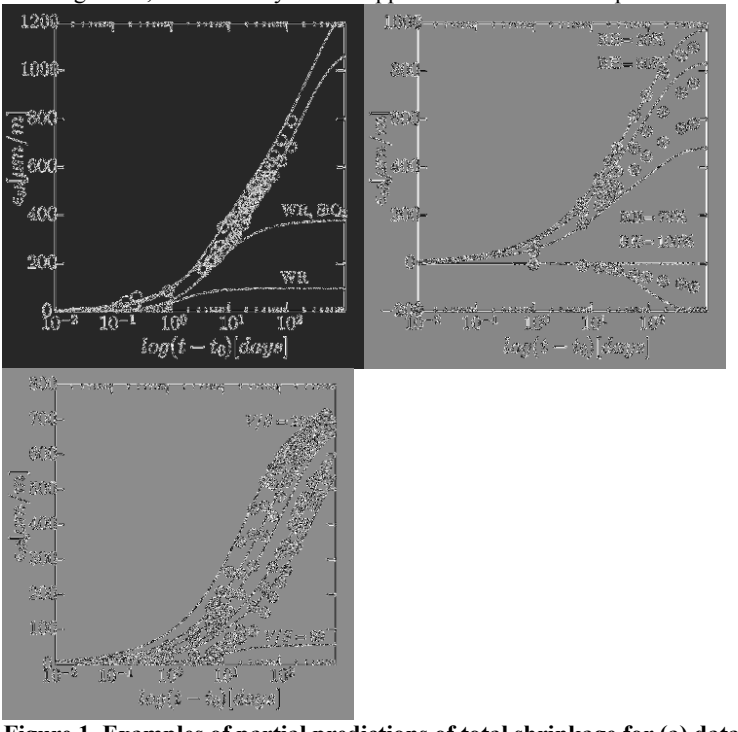

Figure 1. Examples of partial predictions of total shrinkage for (a) data provided by Folliard and Berke (1997), (b) Keeton (1965), and (c) Shritharan (1989).

Alternatively, questionable data may only be used to discern information from the relative shape. In the case of an overall low number of questionable data sets, an iterative optimization procedure is found to lead to good results. This procedure entails alternating optimization of the parameters of the actual prediction equation and shifts of the individual curves, both in time and space. Convergence studies revealed a required minimum of three iterations until satisfactory convergence of more than 95% is reached. All shifts are considered only during the optimization phase to exploit the information that is contained in the relative shape; they do not enter the validation phase that is performed on the reported data.

More challenging than dealing with the unknown measurement errors, is separating out the contributions from different superimposed time functions of similar shape and order of magnitude - two in case of total shrinkage curves, three in case of basic creep compliance, and four in case of total creep data. Especially in combination with an unknown magnitude of measurement errors, the unknown influence of aggregate type, which in many cases is not even reported, cement type and admixture can make the optimization problem quite demanding. Ultimately, an iterative logically deduced strategy was developed and successfully applied to both creep and shrinkage. It entailed a first average fit of the most basic and, thus, independent component such as the autogenous shrinkage, initially neglecting, e.g., the influence of aggregate type and removing all datasets influenced by admixtures. Subsequent iterations slowly enlarged the amount of considered data to a more extensive set by parallel expansion of the model formulation and recalibration of the new parameter set to incorporate additional effects. Correlation coefficients between input parameters and optimization parameters served, together with the elements of the Jacobian matrix $J = \partial F / \partial X_i$, as an indicator for the selection of the most influential parameters, where F = the objective function with regard to the basic variables of the optimization, X_i.

The heteroscedastic nature of the data is a major source of complications for the formulation of statistical indicators. It thus impairs the statistical tests of significance and regression analysis. Suitable weighting strategies based, e.g., on the concept of hyperboxes (Bažant and Li, 2008) can remove the variability of scatter in time as well as the experimental bias with regard to the concrete composition, environmental conditions, test duration and sampling frequency. For optimization and validation two statistical indicators are used simultaneously, the coefficient of determination, $R^2 = 1 - S_{err}/S_{tot}$, which relates the sum of squares of residuals S_{err} to the total sum of squares S_{tot}; R^2 is proportional to the sample variance and can be seen as a measure of how well the trend in the data can be reproduced by the model. The second statistical indicator is the coefficient of variation of the root-mean-square error $CV(RMSE)$ which is defined in analogy to the coefficient of variation. This dimensionless measure quantifies the expected normalized prediction error and is a good measure of accuracy.Prior to this step, systematic errors must be removed based on theoretical considerations. Among others, imprecisely reported concrete ages at time of load application, loading durations and, in particular, measurement errors need to be identified (Hubler et al., 2013). In many cases the elastic deformation in creep tests is not included, the sensor position and gauge length are wrongly reported, or the environmental conditions are unclear.

Two approaches can successfully be applied to the problem of optimizing models for multi-decade creep and shrinkage prediction: A multi-objective optimization of the combined laboratory and structural databases, and a Bayesian updating scheme. In the latter approach (Wendner et al., 2013), the theoretically derived model is first calibrated to the short-term laboratory data utilizing a weighted least-square estimation method and is then updated by Bayesian analysis to obtain an improved multi-decade model.

CONCLUSION

Compared to the existing formulation of Gardner (Gardner and Lockman, 2001), ACI (1992), model code (CEB/fip 1993, 1999, fib 2012) a significantly improved prediction of structural behavior is rendered possible, especially for multi-decade durations. Examples of data fits illustrate the ability of model B4 to capture systematic variations in composition and environmental parameters.

For design applications, model B4 is also presented in a simplified form using solely the compressive strength as the input information, which is needed for preliminary design in which the concrete composition is not yet known. Fortunately, a satisfactory quality of fit can still be achieved. However, it does not reach the level of the full composition-based formulation.

A rate-type variant of model B4 for the point-wise constitutive relation is currently in development. It will allow computationally efficient large-scale structural analyses, in which time-variable environmental conditions, moisture diffusion and various nonlinear effects such as steel relaxation, evolving damage and cracking of concrete can be included.

Acknowledgment: Financial support provided through the Infrastructure Technology Institute at Northwestern University, and the Austrian Science Fund (FWF) in the form of the Erwin-Schrödinger Scholarship J3619-N13 is acknowledged.

REFERENCES

(1992). "Prediction of Creep, Shrinkage, and Temperature Effects in Concrete Structures." *ACI Committee 209*, American Concrete Institute, Farmington Hills, MI, 47.

(1993). "CEB-FIP MODEL CODE 1990." Comitte Euro-International du Béton.

(1997). "Avoidance of thermal cracking in concrete at early age - recommendations, materials and structures." RILEM TC 119-TCE, 451-464.

(1999). *Structural concrete: textbook on behavior, design and performance,*, Sprint-Druck Stuttgart.

(2012). "Model Code 2010 - Final draft, Volume 1." *fib Bulletin 65*, fib, 350.

Bažant, Z. P. (1995). "Creep and shrinkage prediction model for analysis and design of concrete structures - model B3." *Matériaux et constructions*, 28(180), 357-365.

Bažant, Z. P., and Baweja, S. (1995). "Justification and refinements of model B3 for concrete creep and shrinkage 2. Updating and theoretical basis." *Materials and Structures*, 28(8), 488-495.

Bažant, Z. P., and Baweja, S. (1995). "Justification and refinements of model B3 for concrete creep and shrinkage 1. statistics and sensitivity." *Materials and Structures*, 28(7), 415-430.

Bažant, Z. P., and Baweja, S. (1996). "Short form of creep and shrinkage prediction model B3 for structures of medium sensitivity." *Materials and Structures/Matériaux et Constructions*, 29(194), 587-593.

Bažant, Z. P., and Baweja, S. (2000). "Creep and shrinkage prediction model for analysis and design of concrete structures: Model B3." *Adam Neville Symposium: Creep and Shrinkage—Structural Design Effects*, A. Al-Manaseer, ed., ACI, Farmington Hills, Michigan, 1-83.

Bažant, Z. P., Yu, Q., Li, G.-H., Klein, G. J., and Krístek, V. (2010). "Excessive Deflections of Record-Span Prestressed Box Girder - Lessons learned from the collapse of the Koror-Babeldaob Bridge in Palau." *Concrete International*, 32(6), 44-52.

Bažant, Z. P., Hubler, M. H., and Yu, Q. (2011). "Pervasiveness of excessive segmental bridge deflections: Wake-up call for creep." *ACI Structural Journal*, 108(6), 766-774.

Bažant, Z. R., and Li, G.-H. (2008). "Unbiased statistical comparison of creep and shrinkage prediction models." *ACI Materials Journal*, 105(6), 610-621.

Folliard, K. J., and Berke, N. S. (1997). "Properties of High-Performance concrete containing shrinkage-reducing admixture." *Cement and Concrete Research*, 27(9), 1357-1364.

Gardner, N. J., and Lockman, M. J. (2001). "Design Provisions for Drying Shrinkage and Creep of Normal Strength Concrete." *ACI Materials Journal*, 98(2), 159-167.

Hubler, M. H., Wendner, R., and Bazant, Z. P. (2013). "Extensive Concrete Creep and Shrinkage Database - Analysis and Recommendations for Testing and Reporting." *ACI Journal*, (to be submitted).

Keeton, J. R. (1965). "Study of creep in concrete." U.S. Naval civil engineering laboratory, Port Hueneme, California.

Lee, K. M., Lee, H. K., Lee, S. H., and Kim, G. Y. (2006). "Autogenous shrinkage of concrete containing granulated blast-furnace slag." *Cement and Concrete Research*, 36(7), 1279-1285.

Shritharan, S. (1989). "Structural Effects of Creep and Shrinkage on Concrete Structures." M.E. thesis, University Auckland

Tazawa, E.-i., and Miyazawa, S. (1995). "Influence of cement and admixture on autogenous shrinkage of cement paste." *Cement and Concrete Research*, 25(2), 281-287.

Wendner, R., Hubler, M. H., and Bažant, Z. P. (2013). "Recalibration and Uncertainty Quantification of the B3 Creep Model for Long Term Estimates Using Bayesian Methods." *ICOSSAR 2013*New York.

Yoo, S. W., Kwon, S.-J., and Jung, S. H. (2012). "Analysis technique for autogenous shrinkage in high performance concrete with mineral and chemical admixtures." *Construction and Building Materials*, 34(0), 1-10.

Improved Estimation of Long-Term Relaxation Function of Aging Concrete from Its Compliance Function

Z. P. Bažant[1], M. H. Hubler[2], and M. Jirásek[3]

[1]Northwestern University, Department of Civil and Environmental Engineering, Tech 2145 Sheridan Rd. A135, Evanston, IL 60208-3109; PH (847) 491-4025; email: z-bazant@northwestern.edu
[2]Northwestern University, Department of Civil and Environmental Engineering, Tech 2145 Sheridan Rd. A236, Evanston, IL 60208-3109; email: m-hubler@u.northwestern.edu
[3]Czech Technical University in Prague, Thákurova 7, 166 29 Prague, Czech Republic; PH 420-224 354 481; FAX 420-224 310 775; email: Milan.Jirasek@fsv.cvut.cz

ABSTRACT

The age-adjusted effective modulus method (AAEM) is a standard ACI and CEB-*fib* for simplified estimates of the creep response of concrete structures. The AAEM requires the user to supply the relaxation function, $R(t, t')$, of the concrete to be used. This function may be obtained through numerical methods but more easily from a simple closed-form formula. Such a formula was first presented by Bažant and Kim in 1979, but was improved in 2012 by Bažant, Hubler, and Jirásek. This paper summarizes and discusses this recent improvement to the closed-form approximation of $R(t, t')$, which gives a more accurate representation of the multi-decade creep.

INTRODUCTION

The CEB-*fib* Model Code and the standard recommendation of the ACI Committee 209 both list the AAEM method (ACI Committee 209 1982, ACI Committee 209 2008, CEB-FIP 1990, *fib* 1999, *fib* 2010) as the recommended procedure for modeling the response of concrete structures experiencing time-dependent stress redistributions and creep deformation. This method was developed in 1972 at Northwestern University (Bažant 1972b) to approximate the effects of aging creep in structures according to the principle of superposition, neglecting nonlinear and diffusion effects. The user of the AAEM method must compute the relaxation function, $R(t, t')$, which is defined as the uniaxial stress at time t caused by a unit strain sustained since time t'. The numerical method for obtaining a highly accurate $R(t, t')$ function (Bažant 1972a) was greatly simplified by an approximate equation developed by Bažant and Kim in 1979 (Bažant and Kim 1979).

Bažant, Hubler, and Jirásek recently derived improvements that could be made to the simplified approximate equation (Bažant et. al 2013). The original 1979

equation for *R*(*t, t'*) was calibrated to the relaxation function numerically computed from the compliance function specified by the ACI 1971 recommendation (ACI Committee 209 1971). The compliance function used for this calculation contains an upper asymptotic bound instead of the correct unbounded logarithmic shape exhibited by long-term concrete creep (Bažant et. al 2011). Adjusting the approximate equation to capture the correct asymptotic shape was shown to alleviate the considerable error that is found for long times (> 5 years) when compared with accurate linearly viscoelastic calculations for a more realistic compliance function such as that given by model B3. In contrast to the formula developed in 1979 by Bažant and Kim, the new formula ensures non-negativeness of the relaxation function. It is also significantly more accurate for long-time relaxation of concrete loaded at young age.

APPROXIMATION OF THE RELAXATION FUNCTION

The original approximate relaxation function was presented by Bažant and Kim (Bažant and Kim 1979) in the following form:

$$R_{BK}(t,t') = A - B \tag{1}$$

$$A = \frac{1-\Delta_0}{J(t,t')} \quad B = \frac{c_1 \alpha(t,t')}{J(t,t-\eta)} \tag{2}$$

$$\alpha(t,t') = \frac{J(t'+\epsilon,'t)}{J(t,t-\epsilon)} - 1 \tag{3}$$

$$\epsilon = \frac{t-t'}{2}, \eta = 1 \text{ day} \tag{4}$$

where Δ_0 = 0.008 and c_1 = 0.115. This functional form successfully captures the characteristic aging of concrete through the inclusion of the parameter α(t,t'). Because of long-time aging, the compliance depends on both the time lag, *t-t',* as well as the age of loading, *t'* (which means is also depends on the current time, *t*). These additional dependences are what differentiates this formulation from the classical effective modulus approximation for concrete (McMillan 1916) and the relaxation function for non-aging linearly viscoelastic polymers. However, to ensure a thermodynamically admissible approximation, the effect of ageing must not cause the relaxation curves to reach negative values. Since any compliance response may be captured by a Kelvin chain model (Bažant and Huet 1999), a negative relaxation would not be admissible. Consequently, the recently improved formulation (Bažant et. al 2013) ensures a positive value for R by reframing Eq. (1) as follows:

$$\tilde{R}(t,t') = A\left(1 - \frac{B}{qA}\right)^{-q} \tag{5}$$

The empirical constant *q* allows the previous formulation to be recovered as the dominant first term of the binomial expansion while ensuring an asymptotic approach to 0 for large values of *B/A*. The optimal values for empirical constants of the improved formulation were extracted by fitting new formulation to various accurately

integrated compliance rate equations from the B3 model at different loading ages and for different compositions of concrete. The relaxation functions corresponding to each compliance function were calculated by numerical solution of Volterra integral equation (Bažant 1982, RILEM Committee TC 69 1988, Jirásek and Bažant 2002). The resulting parameter values are

$$c_1 = 0.0119 \ln t' + 0.08, \quad q = 10 \tag{6}$$

where *t'* is in the units of days. The complete formulation is:

$$\tilde{R}(t,t') = \frac{1}{J(t,t')} \left(1 + \frac{c_1 \alpha(t,t') J(t,t')}{q J(t,t-\eta)}\right)^{-q} \tag{7}$$

While a number of fitted compositions are presented in Bažant et al. (2013), here we show only the improved approximations for the concrete mixtures listed in Table 1. Figure 1 illustrates the relaxation function development with durations up to a 30-year design life for basic creep of the two selected concrete compositions. For the case of an early loading at 10 days, the improvement in accuracy of the long-term estimate is clearly visible. Similarly, for the product of the ageing coefficient and the creep coefficient the new approximation is much closer to the exact solution obtained by integration in Figure 2. This product represents the dimensionless correction to the effective modulus in the AAEM. This comparison reveals that the new approximation also improves the accuracy of the estimate for short times.

Table 1. Concrete compositions used to illustrate comparisons in Figure 1 and 2.

Concrete type	w/c	a/c	c(lb/ft^3)	f_{28}(psi)
High strength	0.38	3.7	27.7	7700
Nassar 1986	0.60	7.0	13.7	4000

CONCLUSION

1. A new approximate relaxation equation is derived by extending the 1979 Bažant and Kim's formula. This new formula was obtained with the help of the asymptotic condition requiring the relaxation curve to remain positive (and thus thermodynamically admissible) even for very long creep durations and for loading at earlyage.
2. The present more accurate estimate for the relaxation function is of particular interest when a compliance function such as that of the B3 model is used to obtain a creep prediction. Such a compliance function accurately captures the observed asymptotic linear slope in the logarithmic time, for which the old formula would produces a large error when the concrete is loaded at an early age.
3. When using other compliance functions that do not correctly represent multi-decade creep (e.g., those of ACI, *fib*, GL and JSCE), the present more accurate estimate gives only a minor improvement of the relaxation function.

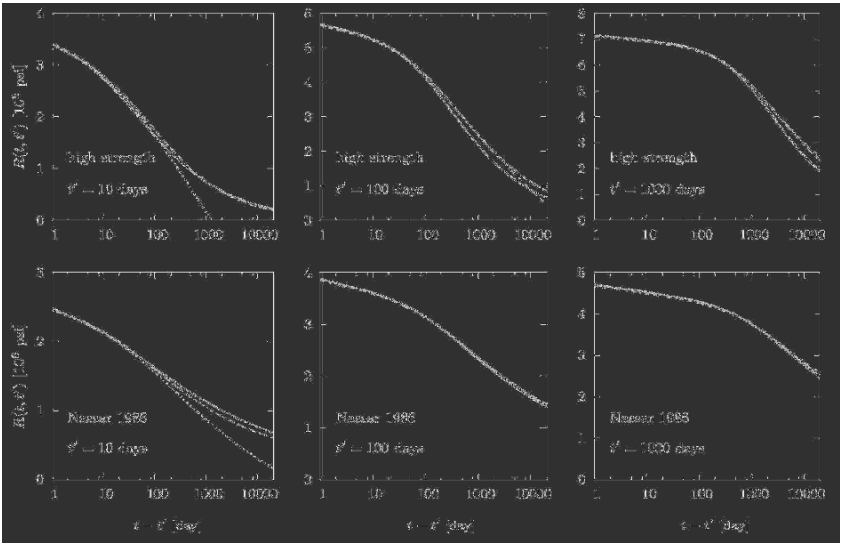

Figure 1. Basic creep: Comparisons of the updated approximate formula for the relaxation function (dashed lines) with the exact solution (solid lines) and the 1979 Bažant-Kim approximate formula (dotted lines.).

4. It must be cautioned, however, that neither the age-adjusted effective modulus method (AAEM), sanctioned by the current standard recommendations of ACI and *fib*, nor accurate solutions of the creep effects according to linear aging viscoelasticity, are sufficiently accurate for predicting the response of structures of high creep sensitivity such as large-span bridges, large-span roofs, nuclear containments and super-tall buildings (a rate-type analysis with a broad retardation spectrum, enhanced for the effects of cracking, variable environment, diffusion and prestressing steel relaxation, is required for that).

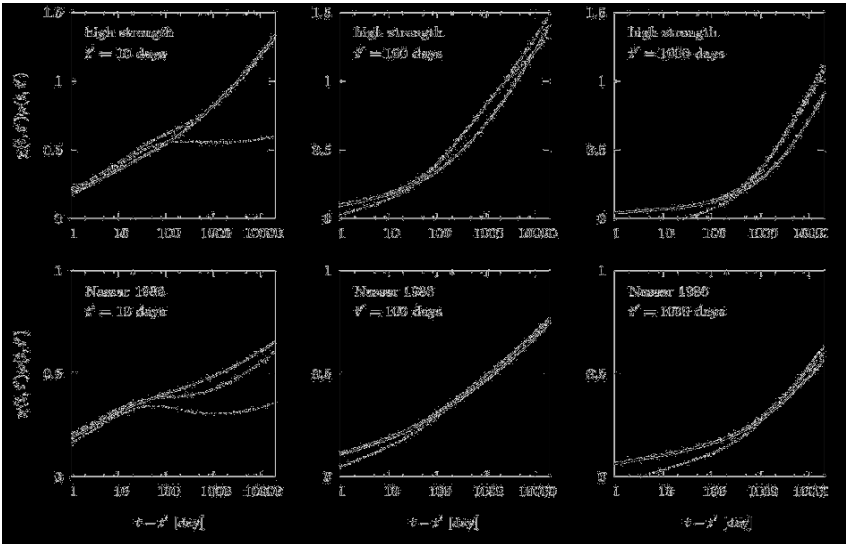

Figure 2. Comparison of the product of the aging coefficient and the creep coefficient based on the improved approximation for the relaxation function (dashed lines), showing the product based on the exact solution (solid lines) and on the previous approximate formula from Bažant and Kim (1979) (dotted lines).

AKNOWLEDGEMENT

Financial support from the U.S. Department of Transportation trough Grant 6002078 from the Infrastructure Technology Institute of Northwestern University is gratefully acknowledged. Additional support was received from the Czech Science Foundation under project No. 105/10/2400.

REFERENCES

ACI (1982). Report of Committee 209 on "Prediction of creep, shrinkage and temperature effects in concrete structures". ACI 209 R-82; also published in ACI SP76, pp. 193-300.

ACI (2008). Report of Committee 209 "Prediction of creep, shrinkage and temperature effects in concrete structures". Am. Concrete Institute, Detroit.

ACI Committee 209 (1971) "Prediction of creep, shrinkage and temperature effects in concrete structures." Designing for Effects of Creep, Shrinkage and Temperature in Concrete Structures, ACI-SP27, Am. Concrete Institute, Detroit, pp. 51-93; reapproved 2008.

Bažant, Z.P. (1972). "Prediction of concrete creep effects using age-adjusted effective modulus method". *ACI Journal* 69, 212-217.

Bažant, Z.P. (1972). ”Numerical determination of long-range stress history from strain history in concrete.” *Materials and Structures* (RILEM) 5, 135-141.

Bažant, Z.P., and Kim, S. S. (1979). “Approximate relaxation function for concrete.” *J. of the Structural Div*., Proc. ASCE, 105, 2695-2705.

Bažant, Z.P. (1982). “Mathematical models for creep and shrinkage of concrete”, Chapter 7 in Creep and Shrinkage in Concrete Structures, Z.P. Bažant and F. H. Wittmann, eds., J. Wiley & Sons, London, 1982, 163-256.

Bažant, Z.P., and Huet, C. (1999). “Thermodynamic functions for ageing viscoelasticity: integral form without internal variables." *Int. J. of Solids and Structures* 36, 3993-4016.

Bažant, Z. P., Hubler, M. H., and Yu, Q. (2011). “Pervasiveness of excessive segmental bridge deflections: Wake-up call for creep.” *ACI Structural Journal*, 108(6).

Bažant, Z. P., Hubler, M. H., and Jirásek, M. (2013). “Improved Estimation of Long-Term Relaxation Function from Compliance Function of Aging Concrete.” *Journal of Engineering Mechanics* ASCE, 139(2), 146-152.

CEB-FIP Model Code 1990. Model Code for Concrete Structures. Thomas Telford Services Ltd., London, Great Britain; also published by Comité euro-international du béton (CEB), Bulletins d'Information No. 213 and 214, Lausanne, Switzerland.

fib (1999). Structural Concrete: Textbook on Behaviour, Design and Performance, Updated Knowledge of the of the CEB/FIP Model Code 1990. Bulletin No. 2, Fédération internationale du béton (*fib*), Lausanne, Vol. 1, pp. 35-52.

fib (2010). Draft of fib Model Code 2010. “Fédération internationale de béton (fib).” Lausanne.

Jirásek, M. and Z. P. Bažant (2002). Inelastic analysis of structures. Chichester, Wiley.

McMillan, F.R. (1916). “Method of designing reinforced concrete slabs—Discussion of A.C. Janni's paper." *Trans ASCE* 80, 1738.

Nassar, K. W., and Al-Manaseer, A. A. (1986). “Creep of concrete containing fly ash and super plasticizer at different stress/strength rations.” *ACI Journal*, Proc., 83(4), 668–673.

RILEM Committee TC 69 (1988). “State of the art in mathematical modeling of creep and shrinkage of concrete”. Mathematical Modeling of Creep and Shrinkage of Concrete, ed. Z.P. Bažant, J. Wiley, Chichester, U.K., and New York, 1988, 57-215.

Overall stiffness reduction of cracked reinforced concrete beams due to long term effects

Arnaud Castel[1], Raymond Ian Gilbert[1], Gianluca Ranzi[2]

[1] Centre for Infrastructure Engineering and Safety, School of Civil and Environmental
Engineering, The University of New South Wales, Sydney, Australia
[2] Centre for Advance Structural Engineering, The University of Sydney, Australia

ABSTRACT

The aim of the research described in this paper is to assess the deformation of cracked reinforced concrete beams under both short and long term service loading. Beams are subjected to short time bending tests including loading cycles with different peak values leading to concrete cracking (pre-cracking tests) and long term tests under sustained loading. Long term deflection appears to be much more important than the deflection due to short term loading and leads to important permanent deformation after unloading. After 6 months under sustained loading, the overall instantaneous stiffness of all beams was substantially reduced.

KEYWORDS: Reinforced concrete, serviceability, long term, deflection, cracking, creep, shrinkage

INTRODUCTION

For reinforced concrete structures, deflection control is an important performance criterion to ensure both serviceability and sustainability. Indeed, excessive concrete cracking resulting from excessive deformation is one of the most common causes of damage and results in huge annual cost to the construction industry. Long-term effects such as time-dependent shrinkage-induced cracking can significantly contribute to excessive cracking which can affect the durability of the structure if not taken into account properly at the design stage (Gilbert 2008; Francois and Castel 2001). For existing structures, including those affected by steel corrosion, structural performance can be assessed by analysing the overall response of the structural members under controlled loading (Zhang et al., 2009a; Zhang et al., 2009b). In a previous paper, a model was proposed allowing predicting the overall stiffness of reinforced concrete under short term loading (Castel et al., 2012). In order to extend this model to longer term performance, this work aims to study both the instantaneous response of an existing concrete structure under live loading taking into account the history of the loading (mechanical or environmental) and the long-term deflection increase under sustained loading resulting from time-dependent effects.

EXPERIMENTS

Experimental program

The aim of the experiments is to assess the deformation of cracked reinforced concrete under both short and long term service loads. A large number of reinforced concrete beams and slabs were cast. The results obtained on five reinforced concrete beams are reported in this paper. The mechanical characteristics of the concrete measured in standard conditions (T^oC = 20^oC and RH% = 100%) are mean compressive strength f_{cm} = 46 MPa, elastic modulus E_c = 33 GPa and mean flexural tensile strength $f'_{ct.f}$ = 3.5MPa. The reinforcement lay-out of the beams is shown in Fig. 1. The main longitudinal steel bars in each specimen are standard Australian deformed bars of 16 mm diameter (N16's). In order to eliminate any influence of stirrups on crack location and spacing, no stirrups were placed in the constant bending moment zone. The characteristic yield stress of the steel bars (the elastic limit) is f_{sy} = 500MPa. After casting and until the load tests commenced at 28 days, some of the beams (labeled: cured beams) were stored in a high moisture environment to reduce the drying shrinkage to as close to zero as possible. The remaining beams were cured for only seven days and then stored in the laboratory where drying commenced 21 days before testing (labeled: uncured beams).

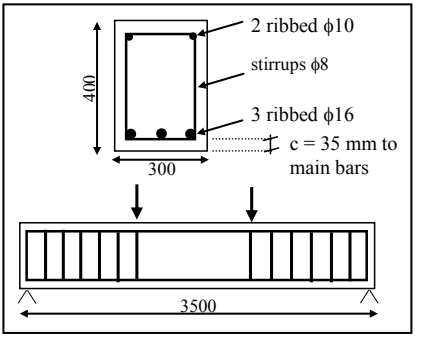

Figure 1. Lay-out of the reinforcement and loading (stirrups spacing: 200 mm)

All beams were tested in 4 point bending (as show in Fig. 1), both for the long term tests and the short term tests. The experiments consisted of:

- Short term tests (pre-cracking tests): All beams were pre-cracked. Two values of maximum loading were defined: namely P_{a1} (= $1.2P_{cr}$) and P_{a2} (= $1.5P_{cr}$), where P_{cr} is the cracking load. At 28 days after casting, the beams were loaded up to either P_{a1} or P_{a2} and then unloaded. This loading cycle was repeated 10 times to assess the global stiffness after cracking and the permanent residual deflection after unloading. Loading and mid-span deflection were measured throughout each loading cycle. Concrete cracking was accurately recorded as well.
- Long term tests: After the specimens were initially cracked under a short-term peak load of either P_{a1} or P_{a2}, they were subjected to a sustained load for a period

of 6 months. An appropriate spring loading device (see Figure 2) was used in order to ensure that the load remained constant for the duration of the tests in spite of creep or the loss of stiffness due to time-dependent cracking. Several values of sustained load were adopted, with the lowest value equal to $0.7P_{cr}$. This sustained load was assumed to represent a typical dead load for a reinforced concrete beam. The highest sustained load was P_{a2} ($=1.5P_{cr}$) and was applied to the beams that were initially pre-cracked using the same load value. One beam was kept unloaded (except for its self-weight) in order to assess the effect of concrete shrinkage with only a minor effect due to loading. The development of cracking and the increase in deflection were monitored over time in order to assess the time-dependent effects of concrete creep and shrinkage. After six months, the beams were unloaded and the permanent residual deflection due to long term effects was measured.

- Failure tests: After the sustained loading period had ended, the specimens were subjected to the same cycles of unloading/reloading up to either P_{a1} or P_{a2} in order to assess the time-dependent change in instantaneous response to live load.
- Finally, all beams were loaded up to failure.

Table 1 shows the identification of each beam, together with the maximum pre-cracking and the sustained loads.

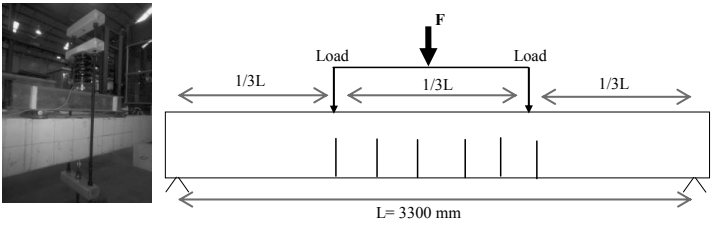

Figure 2. Loading configuration

Table 1. Identification of the beams and values of the loads

Beam	Pre-cracking load	Cured	Sustained load
B1	$1.2P_{cr}$	YES	Self-weight loading
B2	$1.2P_{cr}$	YES	$0.7P_{cr}$
B3	$1.5P_{cr}$	YES	$1.5P_{cr}$
B5	$1.5P_{cr}$	NO	$0.8P_{cr}$
B6	$1.5P_{cr}$	NO	$1.5P_{cr}$

Experimental results

The ultimate capacity and the ductility are not affected by the prior load history (both short and long term). In both the short-term and the long-term tests, the load history was typical of in-service load levels (i.e. less than 50% of the ultimate load).
Figures 3 to 7 show the load-deflection curves for all beams obtained in the short-term (pre-cracking tests) and during the loading cycles applied after six month under sustained load. The overall behaviour during the loading cycles (both pre-cracking or after the long term tests) is linear elastic. The main purpose is to compare the beams stiffness under live loading before and after cracking and before and after the 6 months under sustained loads. In all figures, the straight lines shown through the test data are used to calculate the slope (and hence the stiffness before and after long term tests). Upon unloading, two values of the permanent residual deflections are reported in these figures (after the pre-cracking tests and after the sustained load period). The permanent deflection after pre-cracking is due mainly to flexural cracking and early shrinkage and the long term permanent deflection after the period of sustained loading is due to creep, concrete shrinkage and any time-dependent cracking that may occur at the steel concrete interface due to shrinkage.

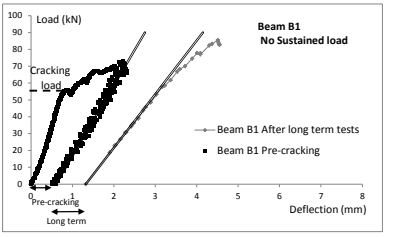

Figure 3. Instantaneous response of beam B1 before (pre-cracking) and after long term tests

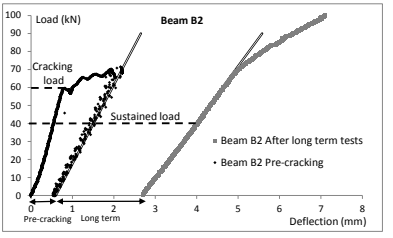

Figure 4. Instantaneous response of beam B2 before (pre-cracking) and after long term tests

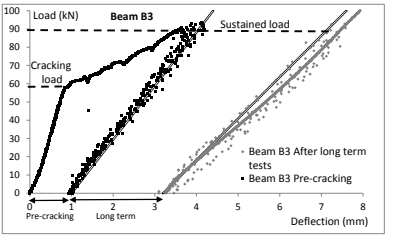

Figure 5. Instantaneous response of beam B3 before (pre-cracking) and after long term tests

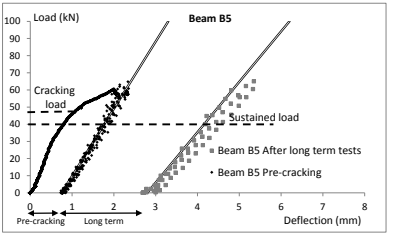

Figure 6. Instantaneous response of beam B5 before (pre-cracking) and after long term tests

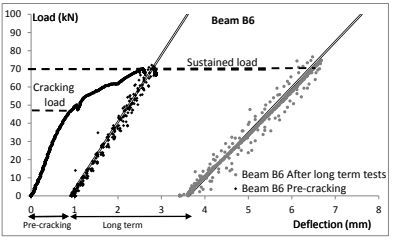

Figure 7. Instantaneous response of beam B6 before (pre-cracking) and after long term tests

Pre-cracking tests: As expected, the cracking load is higher for beams B1, B2 and B3 that were continuously moist cured for the 28 days period before the load tests were performed. The cracking load of these cured beams, ranged between 55 kN and 60 kN, and corresponded to the theoretical value calculated using an extreme fibre tensile stress equal to the concrete tension strength of 3.5 MPa. For the beams B5 and B6, that were moist cured for just 7 days, the cracking load was reduced by approximately 20% as a result of both the modification to the concrete hydration process and the restraint to drying shrinkage that occurred prior to loading. The cracking loads measured experimentally were used to determinate the maximum short-term and long-term loads (eg. $1.2P_{cr}$ or $1.5P_{cr}$) applied to the beams (see Table

1). The permanent deflection (after unloading) ranged between 0.5 and 1 mm depending on the maximum load applied and the irreversible damage caused by cracking. Figure 8 shows the beam overall stiffness versus the peak load applied. As expected, stiffness decreases with increasing peak load after cracking. The stiffness is affected by the number of flexural cracks along the span and eventually by the steel-concrete interface damage associated with increasing applied loading.

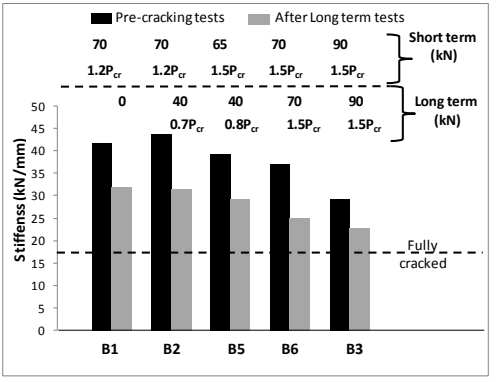

Figure 8. Instantaneous stiffness before and after long term effects

Long term tests: For each beam, after the long-term test, the stiffness was reduced from the value immediately after the pre-cracking tests. Even for beam B1, with only its self-weight acting for 6 months, the stiffness reduced significantly with time. Figure 8 shows the value of the instantaneous stiffness before and after the period of sustained loading for all beams, and compares these values with the calculated stiffness of a fully cracked beam assuming no tension stiffening effect. The stiffness reduction due to long term effects is significant (between 20% and 30%), but the reduction does not appear to be directly related to the magnitude of the sustained load. The maximum reduction was observed in B2 with a sustained loading of $0.7P_{cr}$ (40 kN) and the minimum reduction was in B3 with a sustained load of $1.5P_{cr}$ (90 kN). This indicates that long term concrete creep does not affect significantly the instantaneous beam response to live load. Instantaneous stiffness reduction results from time-dependent shrinkage-induced cracking. To support this statement, Fig. 9 shows that additional cracks resulting from time-dependent effects that occurred along beam B2 during the long term tests.

Deflection increase was monitored during the 6 months period under sustained loading (Fig. 10). By contrast with the instantaneous response, the measured final deflection was clearly dependent on the magnitude of the sustained load, as shown in Fig. 11. Moreover, an increase in the level of sustained loading also caused an increase in the permanent residual deflection (as can be seen in Figs. 3 to 7).

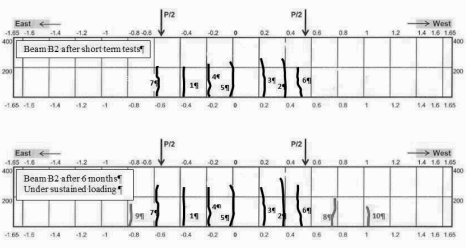

Figure 9. Beam B2 cracking maps after short and long term tests

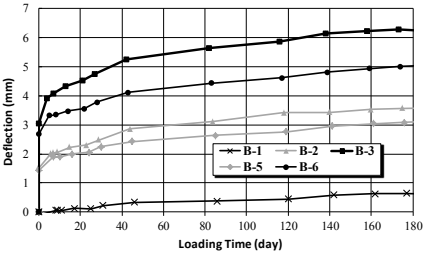

Figure 10. Deflection monitored versus time

In conclusion, an increase in the sustained load causes an increase in the time-dependent deflection resulting in higher permanent residual deflection when unloaded. However, it does not necessarily result in a higher reduction in the instantaneous stiffness. Obviously, the amount of concrete cracking resulting from the pre-cracking test (the prior load history) and the resulting damage at the concrete-steel interface have a great influence on the reduction of long term instantaneous stiffness.

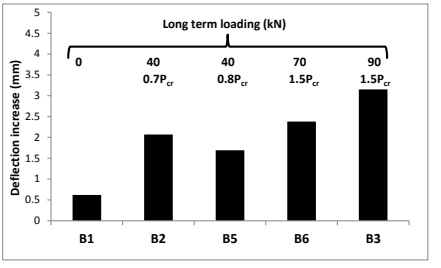

Figure 11. Total deflection increase after 6 months under sustained loading

CONCLUSIONS

The instantaneous and long term response of reinforced concrete beams were analysed experimentally in this paper. Results show that the total deflection of the

beams is the addition of two main components: a permanent and an instantaneous deflection. Both the maximum short term loading and the level of the sustained loading affect the two types of deflection. The permanent component is governed by the amount of irreversible damage is done to the concrete in the tensile zone around the longitudinal tensile reinforcement. This damage is caused by cracking and its extent depends on the peak value of the short term loading and also on the amount of time-dependent shrinkage induced cracking and to some extent creep. Indeed, the permanent residual deflection recorded after the beams had been loaded for 6 months and then unloaded was much higher than the permanent deflection recorded after the short term tests. This permanent deflection is a significant part of the total deflection and it depends mainly on the level of sustained loading.

The instantaneous stiffness of the beams depends on the peak value of the short term loading leading. After 6 months under sustained loading, the overall instantaneous stiffness of all beams was reduced by 20% to 30% from the initial value. However, the reduction in stiffness did not appear to be related to the magnitude of the sustained load. This indicates that long term concrete creep does not affect significantly the instantaneous beam response to load. This reduction in the instantaneous stiffness with time is caused by time-dependent shrinkage-induced cracking.

ACKNOWLEDGEMENT

This research was supported under Australian Research Council's Discovery Projects funding scheme (project number DP110103028). The experimental work was carried in the Structures Laboratory of the School of Civil and Environmental Engineering at the University of New South Wales. The assistance of the laboratory staff is also acknowledged.

REFERENCES

Castel A., Vidal T., François R., (2012) “Finite-element modeling to calculate the overall stiffness of cracked reinforced concrete beams”, *ASCE Journal of Structural Engineering*, Vol. 138, N07, pp. 889-898.

François, R., Castel, A., (2001) Discussion of the paper "Influence of bending cracks and water-cement ratio on chloride-induced corrosion of main reinforcing bars and stirrups" by N. Otsuki, S. Miyazato, N. Diola and H. Suzuki, *ACI Material Journal*, Vol. 98, No3, May-June 2001.

Gilbert, R.I., (2008) “Control of flexural cracking in reinforced concrete”, *ACI Structural Journal*, 105(3), pp.301-307.

Zhang, R., Castel, A., François, R., (2009a) “Serviceability Limit State criteria based on steel-concrete bond loss for corroded reinforced concrete in chloride environment”, *Materials and Structures*, 42 (10), pp. 1407-1421.

Zhang, R., Castel, A., François, R., (2009b) “The corrosion pattern of reinforcement and its influence on serviceability of reinforced concrete members in chloride environment”, *Cement and Concrete Research*, 39, pp. 1077-1086.

An Effective Flexural Stiffness Equation for Long Term Deflection of Prestressed Concrete with and without Cracks

R. Sato[1], K. Nakarai[1], Y. Ogawa[1] and K. Kawai[1]

[1]Graduate School of Engineering, Department of Civil and Environmental Engineering, Hiroshima University, 1-4-1 Kagamiyama, Higashi-Hiroshima, 739-8527, Hiroshima; PH 81(82) 424-7787; FAX 81(82) 424-7787; email: sator@hiroshima-u.ac.jp

ABSTRACT

An effective flexural stiffness equation for long term deflection of prestressed concrete with and without cracks is proposed. The equation is derived by assuming a linear strain distribution through the section as well as considering creep, axial shrinkage and shrinkage gradient of concrete. The effect of creep is considered by applying the effective Young's modulus method, which means that the histories of stress, shrinkage are not considered. The effects of prestressing steel and reinforcement restraining deformation due to creep and shrinkage are also incorporated into the equation. The tension stiffness of concrete with cracks is considered based on Branson's equation.

An existing one span-prestressed concrete cantilever girder bridge with a box type-section is adopted for verifying the validity of the proposed equation by comparing the measured excessive deflection with the calculated values. The verification results showed that the calculated deflection agreed roughly well with the observed values.

INTRODUCTION

Excessive deflections of cantilever - prestressed concrete box girder bridges with a hinge at mid-span have been reported and the causes have also been investigated (Křístek et al. 2006, Bažant et al. 2008). According to these studies, one of the causes of the excessive deflection is a large difference in shrinkage between the top and bottom slabs. On the other hand, Maekawa et al. simulated the long-term deflection based on the multi-scale coupled thermo-hygro and mechanical modeling, which showed that the numerical analysis approximately reproduced the measured excessive deflection of an existing bridge (Maekawa et al. 2011)

Branson proposed a flexural stiffness equation for a cracked RC member (Branson 1963) which has already been recommended in the JSCE Standard (JSCE 1986) in the same way as the ACI Building Code 318. This equation was extended by incorporating creep and shrinkage effects based on the effective Young's modulus

method and using the equation, it was possible to predict the time-dependent mean curvatures of cracked and non-cracked reinforced (RC) and prestressed concrete (PC) members fairly well, in which creep and shrinkage were assumed to be uniform in the whole section (Tsuda et al. 1996). This equation was recommended as a design equation in the JSCE Standard 2002 (JSCE 2002)

This study aims at extending the above equation so as to incorporate the gradient of shrinkage in the whole section and verify the validity of the proposed practical equation through comparing the calculated deflection with the measured values on an existing bridge.

FORMULATION OF AN EFFECTIVE FLEXURAL STIFFNESS EQUATION

Assumptions: The following assumptions are made for formulation of the equation.

(1) Shrinkage distributes uniformly in top and bottom slabs and web, respectively.
(2) Shrinkage distributes linearly through the section based on the above shrinkage.
(3) Plain section remains plain section after bending

Formulation: Formulation is conducted for a cantilever prestressed concrete girder with a box type section shown in Figures 1 and 2. As shown in this figures, prestressing bars are arranged in the top slab and web, and reinforcements are arranged in the top and bottom slabs as well as the web.

(1) Stress-strain relation of concrete and steel

Based on assumption (3) above, concrete strain at the depth of z and steel strain after loading are given by the following equations.

$$\varepsilon_{cz} - \varepsilon_{cg} = \psi\,(z - c_g) \tag{1}$$

$$\varepsilon_{ps} - \varepsilon_{cg} = \psi\,(d_{ps} - c_g) \tag{2}$$

where, as is shown in Figure 2, z: coordinate from the top surface (positive downward), ε_{cz}: strain in concrete at the depth z induced by design load, ε_{cg}: strain of concrete at centroid of transformed section after loading (positive in tension), ψ: curvature after loading, c_g: centroid of transformed section after loading, ε_{ps}: strain of prestressing bar (PC bar) or reinforcement considered after loading (positive in tension), and d_{ps}: distance between top surface and centroid of prestressing steel or reinforcement considered.

As the creep effect of concrete is considered by applying effective Young's modulus method, the stress-strain relation of concrete is given by the following equation.

$$\begin{aligned}\sigma_{cz} &= E_e(\varepsilon_{cz} - \varepsilon_{cs,z}) = E_e\left[\psi\,(z - c_g) + \varepsilon_{cg} - \left\{\psi_{cs}\,(z - c_{cs,g}) + \varepsilon_{cs,g}\right\}\right] \\ &= E_e\left\{(\psi - \psi_{cs})(z - c_g) + (\varepsilon_{cg} - \varepsilon_{cs,g}) - \psi_{cs}(c_g - c_{cs,g})\right\}\end{aligned} \tag{3}$$

where, σ_{cz}: stress in concrete at the depth z induced by design load, c_g, $c_{cs,g}$: centroids of

transformed and pure concrete sections, $\varepsilon_{cs,z}$, $\varepsilon_{cs,g}$: free shrinkage strains at z and $c_{cs,g}$, respectively, ψ_{cs}: free shrinkage curvature, and E_e: effective Young's modulus of concrete defined as Eq.(4).

$$E_e = E_c / (1 + \kappa\varphi) \tag{4}$$

where, E_c: Young's modulus of concrete at the start of measurement of deflection, κ: aging factor, and φ: creep coefficient of concrete in top or bottom slabs or web.

The stress-strain relation of steel is also given by the following equation.

$$\begin{aligned}\sigma_{ps} &= E_s\varepsilon_{ps} = E_s\left\{\psi(d_{ps}-c_g)+\varepsilon_{cg}\right\}\\ &= E_s\left\{(\psi-\psi_{cs})(d_{ps}-c_g)+\varepsilon_{cg}-\varepsilon_{cs,g}+\psi_{cs}(d_{ps}-c_g)+\varepsilon_{cs,g}\right\}\end{aligned} \tag{5}$$

where, σ_{ps}, ε_{ps}: stress and strain of target PC bar or target reinforcement induced by design load (positive in tension), E_s : Young's modulus of PC bar or reinforcement, and d_{ps}: distance between top surface and centroid of PC bar or reinforcement in top or bottom slab or web.

(2) Equilibrium requirement for axial force and bending moment

Equilibrium equations for axial force and bending moment are given by the following equations.

$$P_d = C_c + \Sigma T_{ps} \tag{6}$$

$$M_d = M_c + \Sigma M_{ps} \tag{7}$$

where, P: prestressing force, C_c ($=\int\sigma_c dA_c$): axial force in concrete induced by design load, ΣT_{ps} ($=\Sigma A_{ps}\sigma_{ps}$) : summation of forces in PC bars and reinforcements induced by design load, M_d: bending moment induced by design load including eccentric bending moment of prestressing forces, M_c ($=\int\sigma_c(z-c_g)dA_c$): bending moment of concrete with respect to centroid of effective transformed section, and ΣM_{ps}($=\Sigma A_{ps}\sigma_{ps}(d_{ps}-c_g)$): summation of bending moments of each PC bar and each reinforcement with respect to c_g induced by design load.

(3) Formulation of effective flexural stiffness

From these equations, curvature increased by external load and prestressing forces is given by the following equation.

$$\psi - \psi_{sh} = \frac{M_d - E_s(\psi_{sh}\sum I_{ps} + \varepsilon_{cs,g}\sum G_{ps})}{\sum E_e I_c + E_s\sum I_{ps}} = \frac{M_d - (\Sigma M_{\psi_{cs}} + \Sigma M_{\varepsilon_{cs,g}})}{E_e I_{gcr}} \tag{8}$$

where, G_{ps}: first moment of area of PC bars or reinforcement at a depth, I_c : second moment of area of concrete, I_{ps} : second moment of area of PC bar or reinforcement at a

depth, $\Sigma M_{\psi_{cs}}$, $\Sigma MP_{\varepsilon_{cs,g}}$: apparent bending moments due to restraining free shrinkage, curvature and axial free shrinkage by steels, and E_eI_{gcr}: effective flexural stiffness of transformed section considering creep effect at full or cracked section.

The apparent bending moment due to restraint of each steel are evaluated by rearranging Eq.(6) as follows.

$$\begin{aligned}\Sigma M_{\psi_{cs}} + \Sigma M_{\varepsilon_{cs,g}} &= E_s(\psi_{sh}\sum I_{ps} + \varepsilon_{cs,g}\sum G_{ps}) \\ &= \Sigma M_{cs,ps} = E_s\Sigma(\psi_{cs}I_{ps} + \varepsilon_{cs,g}G_{ps})\end{aligned} \tag{9}$$

where, $\Sigma M_{cs,ps}$: summation of apparent bending moment of each steel due to restraining free axial shrinkage and curvature.

Deflection of the girder is calculated by integrating the following equation under required boundary conditions.

$$\psi = \frac{M_d - (\Sigma M_{\psi_{cs}} + \Sigma M_{\varepsilon_{cs,g}})}{E_eI_{gcr}} + \psi_{sh} \tag{10}$$

Based on Branson's proposal for tension stiffness of cracked concrete, the effective flexural stiffness considering creep effect of cracked girder is obtained by rearranging Eq.(6) as follows.

$$E_eI_e = (\frac{M_{crd}}{M_d})^3 \frac{E_eI_g}{1 - \dfrac{\Delta M_{\psi_{cs}} + \Delta M_{\varepsilon_{cs,g}}}{M_d}} + \left\{1 - (\frac{M_{crd}}{M_d})^3\right\} \frac{E_eI_{cr}}{1 - \dfrac{\Delta M_{\psi_{cs}} + \Delta M_{\varepsilon_{cs,g}}}{M_d}} \tag{11}$$

where, I_g and I_{cr} are transformed second moment of areas of full and cracked section, and I_{cr} is calculated by using the centroid if the neutral axis depth is given.

The above equation corresponds with Branson's equation if creep and shrinkage effects are eliminated and also correspond with JSCE Standard 2002 equation if the shrinkage curvature is eliminated.

(4) Stress loss in PC bar due to creep and shrinkage

Stress losses in PC bars due to creep and shrinkage which are arranged in the top slab and the web are calculated by solving simultaneous equations. Stress relaxations of PC bars are also calculated in accordance with JSCE Standard 2002.

VERIFICATION OF THE PROPOSED EFFECTIVE FLEXURAL STIFFNESS

Target structure. The target bridge is located in Shikoku Island, which was completed in September 1987. This bridge is a one span, box type - prestresed concrete girder bridge with a center span hinge.. The side view and typical cross section are shown in Figures 1 and 2, respectively. The measured deflection at center span was 220mm at 10^4

days after the start of the measurement. The calculation of the deflection was conducted for the girder from section 2 to the center span which is 49,450 mm long. The girder consists of 13 segments and each segment was constructed in 9 days. It took 227 days to complete the construction including the pavement, and the measurement of deflection at the center span was started at the completion day. The PC bar to full section ratios of the "representative sections" in block-4 (Figure 1) and described below, are 0.87%-0.40% in the top slab, 0.42%-0.19% in the web, and the reinforcement ratios are 0.42%-0.19% in the top slab, 0.15%-0.14% in the web and 0.19%-0.09% in the bottom slab, respectively.

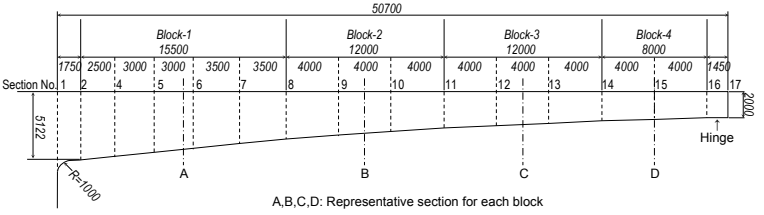

Figure 1 Side view of the girder

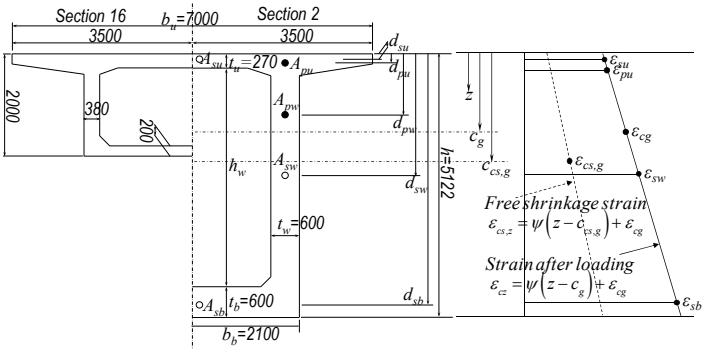

Figure 2 Dimensions and configuration of typical sections and strain distribution of free shrinkage and that after application of design load

Properties of materials. As tabulated in Table 1, the concrete used is 0.38 in water to cement ratio and 40 N/mm^2 in design compressive strength. The compressive strengths and Young's moduli at prestressing and start of deflection measurement are also shown in the same table. Prestressing bars used in longitudinal axis are round ones and 32 mm

in nominal diameter, and the allowable stress just after prestressing was 791 N/mm^2. The pure relaxation rate of PC bar was 3.83 % (JSCE 2012).

Table 1 Properties and design values of concrete

W/C	W	f'ck	Ec,d	f'c,p	Ec,p
	kg/m^3	N/mm^2	kN/mm^2	N/mm^2	kN/mm^2
0.38	170	40	31.0	31.5	28.5
f'ck : Design compressive strength					
Ec,d : Young's modulus used for deflection calculation					
f'c,p : Compressive strength at prestressing in accordance with JSCE Standard used to obtain Ec,p					
Ec,p : Young's modulus at prestressing obtained from f'c,p in accordance with JSCE Standard					

Creep and shrinkage. The creep coefficients as well as the autogenous and drying shrinkage strains were obtained in accordance with equations recommended by JSCE Standard 2012 (JSCE 2012). The creep coefficient depends on the compressive strength at loading age, content of water in the segment, elapsed time and relative humidity. The equations for shrinkage were formulated from computed results based on multi-scale model (Maekawa et al. 2011). The equations are limited to apply to long term deflection of concrete structures. Figure 4 shows the creep coefficients of the top and bottom slabs as well as the web. The relative humidity for the top slab is assumed to be 95 % (JSCE 2012). The relative humidity for the web and the bottom slab is assumed to be a constant value of 67 % (JSCE 2012). According to the figure, the creep coefficient of the top slab concrete is obviously smaller than those of the web and bottom slab concretes, because the creep coefficient depends on the ambient relative humidity. Figures 5 show a typical example of autogenous and drying shrinkage strains of the top and bottom slabs as well as the web of the "representative sections" in block-4. As is shown in the figure, the autogenous shrinkage is dominant compared with the drying shrinkages. Furthermore, the top slab concrete expands and the drying shrinkages of the web and the bottom slab concretes in block-4 are very small, though the thicknesses of both plates are thin (310mm, 200mm). This result is due to the weak effect of the volume to exposure surface ratio (V/S) on the drying shrinkage.

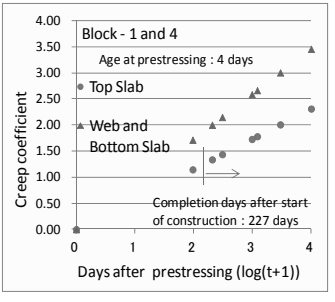

Figure 4 Creep coefficient at the representative sections in block-1 and -4

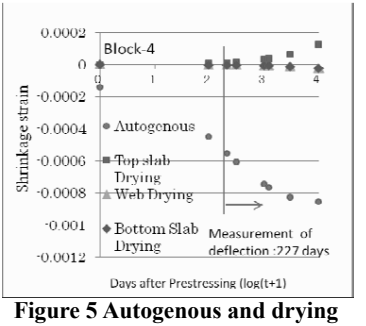

Figure 5 Autogenous and drying shrinkages at the representative sections in block-4

Conditions of calculation. In the calculation, the creep and shrinkage increase after the start of measurement of deflection are used and the aging factor is assumed to be 1. In order to simplify the calculation, as shown in Figure 1, the girder was divided into 4 blocks. Each block consists of 2 to 5 segments. The section representative of each block was set at its center. The dimensions and other factors of the "representative cross section" were determined by averaging the values at both ends of the sections. The age at construction works for each block was determined based on the report related to this bridge (Okada et al. 1986). However, the number of days after placing of concrete until prestressing was conducted was assumed to be 4 days. Furthermore, the effect of sequential construction including the prestressing, the placement of concrete and so on, on the long term deflection was neglected. However, the prestress loss is calculated by considering the age at prestressing, initial development of the autogenous shrinkage and end of curing for each "representative section". The weight of prestressed concrete girder and that of parapet and pavement were set to 202.4 N/mm and 19.2 N/mm (JSCE 2012) in which the density of the girder was 2.45 x 10^{-5} N/mm^3.

Verification. The long term deflection obtained by the present evaluation method is compared with the measured values in Figure 6, together with the deflection due to shrinkage gradient without steel restraint. According to the figure, the present method underestimates the rate of deflection increase and consequently the measured deflection by about 20% at 10,000 days. The reason for this could be explained by the small drying shrinkage of the web and the bottom slab, and elimination of the deflection from the pier center to the section 2 (see Figure 1). The deflection due to the free shrinkage gradient which is almost induced by drying comprises about 30% of the total deflection at 10,000 days.

The deflections induced by creep and shrinkage effects are shown in Figure 7. The shrinkage induced deflection is calculated by setting creep coefficients of concretes

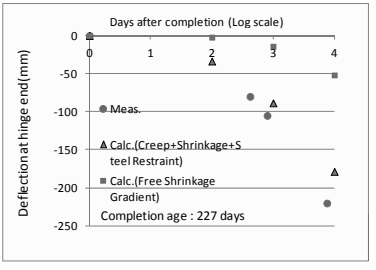

Figure 6 Comparison between calculated and measured deflection, as well as deflection due to shrinkage gradient

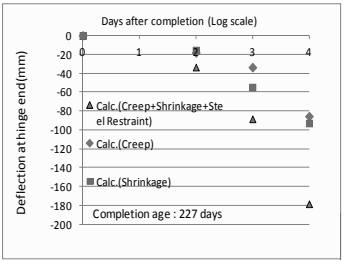

Figure 7 Effects of creep and shrinkage on deflection

in 3 parts to be 0 and the creep induced deflection is obtained by subtracting shrinkage induced deflection from the total deflection. The effect of restraining creep and shrinkage by steels is naturally involved in both deflections. As shown in the same figure, the creep effect is almost equal to the shrinkage effect if no coupling effect of creep and shrinkage exist. The difference in shrinkage related deflection between Figure 6 and Figure 7 is due to the steel restraint which increases deflection by 80% compared with the deflection produced by the free shrinkage gradient.

CONCLUSION AND ACKNOWREDGEMENT

In order to make available for design related to deflection, a practical-effective flexural stiffness equation for cracked and non-cracked prestressed concrete bridge was formulated incorporating the effects of creep, axial shrinkage and shrinkage gradient.

The calculated deflection obtained by the present equation showed a rough agreement with the measured deflection, while an underestimation by 20 % at 10,000 days was observed.

Information related to the present bridge was provided by Prof. Maekawa and his group, which is greatly appreciated.

REFERENCES

Bažant, Z.P., Li, G.-H. and Yu, Q.(2008) "Explanation of excessive long-term deflections of collapsed recorded-span box girder bridge in Palau" Preliminary report presented and distributed at the at the CONCREEP-8, 1, 1-31.

Branson, D.E. (1963). "Instantaneous and Time-Dependent Deflection of Simple and Continuous Reinforced Concrete Beams." *HPR Publication No.7, Part 1*, Alabama Highway Department, Bureau of Public Road, 1-78

Japan Society of Civil Engineers (1986, 2002, 2007, 2012) *Standard Specifications for Concrete Structures-1986, 2002, 2007, 2012*

Křístek, V., Bažant, Z.P., Zich, M. and Kohoutkova, A. (2006). "Box girder bridge deflections: Why is the initial trend deceptive ?", ACI Concrete International, 28(1), 55-63.

Maekawa, K., Chijiwa, N. and Ishida, T. (2011). "Long-term deformational simulation of PC bridges based on the thermo-hygro model of micro-pore in cementitious composites." Cement and Concrete Research, 41(12), 1310-1319

Okada, M., Ueno, I. and Shiba, F. (1986). "Project of Kounaru bridge construction.", Bridge Engineering, 22(12), 20-26 (in Japanese).

Tsuda, M., Sato, R., Wakui, H. and Kakuta, Y. (1996). "A Proposal of effective flexural stiffness of concrete members" *Proc. of the JCI*, JCI, 18(2), 1157-1162 (in Japanese).

Viscoplastic Constitutive Relation for Relaxation of Prestressing Steel at Varying Strain and Temperature

Qiang Yu[1] and Zdeněk P. Bažant[2]

[1]Department of Civil and Environmental Engineering, University of Pittsburgh, Pittsburgh, PA 15261; email: qiy15@pitt.edu
[2]Department of Civil and Environmental Engineering, Northwestern University, Evanston, IL 60208; email: z-bazant@northwestern.edu; corresponding author

ABSTRACT

The stress relaxation of prestressing steel tendons is normally measured at constant strain and constant temperature. The measurement results, embodied in empirical formulas, are then directly used to predict the prestress losses. This classical approach is contingent upon assuming the strain changes during structural lifetime to be negligible compared to the initial strain in steel, and the temperature changes to be unimportant. Recently, however, it transpired that, in creep-sensitive structures such as large-span segmentally erected box girders dominated by their self-weight, the strain changes in concrete are not negligible and the temperature rise in concrete slabs exposed to sun may be important. To take this into account, the existing empirical formulas used in the European (CEB-fib) Model Code and the American practice, which are valid only for constant strain and constant temperature, are now generalized to arbitrarily time-variable strain and variable temperature, heeding obvious asymptotic restrictions and the fact that steel is a viscoplastic material whose constitutive principles are well known. The resulting formula is a memoryless nonlinear equation for the viscoplastic strain rate of steel as a function of the current stress, strain and temperature. Close fits of all the main test data from the literature, including the available data on the effect of strain changes and temperature changes, are achieved. The effect of temperature is found to be important and is formulated on the basis of the activation energy of viscoplastic flow of metals.

INTRODUCTION

Stress relaxation is the gradual stress loss under sustained strain. The classical approach to quantify the relaxation of prestressing tendons is to measure the prestress loss under constant strain and constant temperature. The measurements are then directly used to calibrate a predictive formula for prestress loss calculation. This classical approach, which is enshrined in CEB-fib model (1990) and is followed in the American practice, is generally deemed to be satisfactory. But, as it turns out (Bažant & Yu 2011), this is true only as long as the variations in strain and temperature during the structural lifetime are insignificant.

The importance of strain and temperature changes was brought to light while investigating the ill-fated Koror-Babeldaob (KB) Bridge in Palau, which experienced excessive deflections during its 19-year service and collapsed in 1996, 3 months after a risky retrofit. The stress-relief tests conducted before the retrofit reported a stunning prestress loss (50%), which was more than the double of the standard estimate of 22%, used in design.

A three-dimensional (3D) creep analysis (Bažant et al. 2010), which succeeded in explaining the excessive deflections, highlighted the importance of using a realistic concrete creep model. Subsequent refined analysis (Bažant et al. 2012a,b) further showed that the use of a realistic model of steel relaxation at variable strain and temperature is, in the case of large-span creep-sensitive structures, imperative. Calculations showed that the tendon temperature in the top slab must have reached about 40°C each afternoon and the strain in the top-slab tendons of the KB Bridge must have decreased by about 30% over 18 years. Therefore, if strain and temperature changes are ignored, it will result in substantial error in prestress loss prediction, which is essential for the long-term deflection of large-span bridges, as well as time-dependent moment redistribution.

To overcome these problems, a realistic constitutive law for steel relaxation at variable strain and temperature has been developed at Northwestern and presented in the report of Bažant and Yu (2011). The present paper summarizes, explains and further discusses the development of this law.

STRESS RELAXATION BASED ON VISCOPLASTICITY OF METALS

Stress relaxation in steel is a manifestation of viscoplasticity, which has been systematically studied and is now well understood for metals and alloys at high temperatures (Jirásek and Bažant 2002). The simplest rate-type form to describe it is the Bingham model with no internal friction (Jirásek and Bažant 2002):

$$\dot{\varepsilon} = \dot{\varepsilon}_i + \dot{\varepsilon}_v + \alpha \dot{T}, \quad \dot{\varepsilon}_v = f(\varepsilon, \sigma), \quad \dot{\varepsilon}_i = \dot{\sigma} / E_t \tag{1}$$

where ε, ε_i, and ε_v are total strain, instantaneous (short-time) strain and viscoplastic strain, respectively; the dot denotes a derivative with respect to time t; α = thermal expansion coefficient, and T = temperature; $f(\varepsilon, \sigma)$ is a function to be calibrated by tests; $\sigma = F(\varepsilon)$ is the initial stress-strain diagram; and E_t is the tangential modulus, which is equal to the initial Young's modulus E during reloading and unloading.

For the classical approach, strain ε is a constant, equal to the initial strain ε_0. Obviously, constant strain cannot be assumed if the strain can change very much. To correct it, a hypothesis based on viscoplasticity is made here. For variable strain, the stress relaxation increment $\mathrm{d}\sigma$ occurring at strain ε during time increment $\mathrm{d}t$ may be calculated as if the current strain were maintained constant from the beginning. In other words, the infinitesimal stress-relaxation increments are independent of the previous history and depend only on the current strain and stress. Graphically, this hypothesis means that a small increment of ($\Delta\varepsilon$, $\Delta\sigma$), line 13 in Figs. 1(a,b), may be

decomposed into stress-relaxation increment $\Delta\sigma$ (line 12 in Figs. 1a,b), followed by an instantaneous jump up or down (line 23 in Figs. 1a,b), from the relaxation curve for constant ε (line 12 in Figs. 1a,b) to the relaxation curve for constant $\varepsilon + \Delta\varepsilon$ (line 34 in Figs. 1a,b).

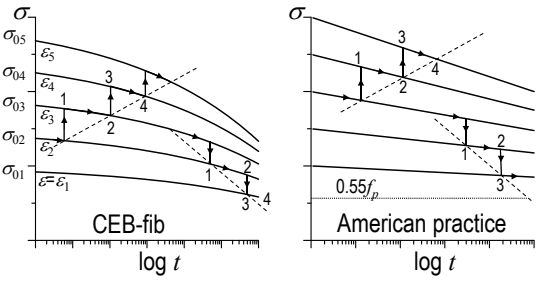

Fig. 1. (a, b) Stress relaxation at various constant levels of strain, with decomposition of stress increment for relaxation during time interval dt at variable strain $\varepsilon(t)$.

RELAXATION FORMULAS FOR VARIABLE STRAIN

Currently, the CEB-fib formula is widely used for prestressed concrete structures. The formula, empirically established based on tests under constant strain and constant temperature, is expressed as

$$[(\sigma_0 - \sigma(t)]/\sigma_0 = \rho_1 (t/\lambda_1)^k \tag{2}$$

where ρ_1 = measured relaxation at 1000 hours (h); λ_1 = 1000 h and k is a constant. For three different classes of prestressing steel, ρ_1 and k are assigned different values.

Differentiating Eq. (2) and replacing σ_0 with $F(\varepsilon_0)$, one gets:

$$d\sigma = -\frac{\rho_1 k}{\lambda_1} F(\varepsilon_0) \left[\frac{\rho_1}{1-\sigma/F(\varepsilon_0)}\right]^{1/k-1} \tag{3}$$

Then based on the hypothesis made, $F(\varepsilon_0)$ is replaced with $F(\varepsilon)$ and the instantaneous stress increment is added. Thus, the general constitutive equation may be written as

$$\dot{\varepsilon} = \dot{\sigma}/E_t - \frac{k\rho_1^{1/k}}{E_t \lambda_1} \frac{F(\varepsilon)}{[1-\sigma/F(\varepsilon)]^{1/k-1}} \tag{4}$$

This constitutive equation can also be written in a form corresponding to a nonlinear Kelvin rheological model with a viscosity parameter that depends on the current stress and strain, but not their history.

The stress-relaxation formula used in American practice can be generalized to a memoryless constitutive equation as follows

$$\dot{\varepsilon} = \dot{\sigma}/E_t - \frac{F(\varepsilon)}{E_t s_y \lambda_0}\langle F(\varepsilon) - s_0\rangle \exp\left[-\frac{s_y}{\langle F(\varepsilon) - s_0\rangle}\left\langle 1 - \frac{\sigma}{F(\varepsilon)}\right\rangle\right] \tag{4}$$

where $\lambda_0 = 1$ h; $s_y = 23\, f_{py}$ (which is the specified yield strength of prestressing steel); $s_0 = 0.55 f_{py}$ is the relaxation threshold. If the stress is less than s_0, no relaxation will happen. One thing needs to be noted is that the formula of American practice is realistic only for medium term relaxation ($t >> l_0$), while its short-term prediction is not. Therefore, the formulation that follows builds on CEB-fib model, with the threshold as the only feature adopted from the formula of American practice.

Since last century, numerous steel relaxation tests were carried out around the world (Kingham et al. 1961, Magura et al. 1964, Glodowski and Lorenzetti 1972, and Buckler and Scribner 1985). Among them, Magura et al.'s (1964) tests at constant strain are most extensive, and Buckler and Scribner's (1985) tests are the only significant tests that include variable strain. In their Test I, the ends of the strands are fixed and the relaxation is measured up to about 1,000 h. In their Test II, a sudden strain (and stress) drop is introduced after measuring relaxation for 24 h, and then further relaxation is measured up to about 1,000 h while both ends of the strands are fixed in their new positions.

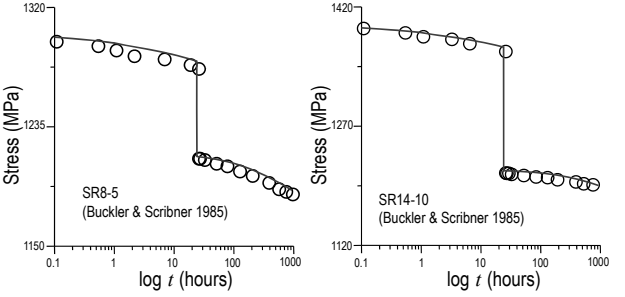

Fig. 2. Simulations based on Eq. (4) are compared with Buckler and Scribner's (1985) tests for 5% load drop (left) and 10% load drop (right) after 24 h.

Fig. 2 shows the comparisons between simulation results based on Eq. (4) and relaxation tests involving a sudden load drop (strain change). The measurements are represented by circles and simulations by solid lines. It can be seen that the memoryless constitutive formula of Eq. (4) predicts the tests very well. One point worth mentioning is that, in the validation of Eq. (4), the values of relaxation parameters ρ_1 and k are not obtained directly by fitting Test II. Instead, they are obtained by optimal fitting of data from Test I, in which the same strands are tested at constant strain for different initial stress levels.

IMPROVED CONSTITUTIVE LAW FOR STEEL RELAXATION

Although Eq. (4) gives good results for the given data range, it has two limitations: 1) a relaxation threshold similar to American practice does not exist in Eq. (4); and 2) for the same steel, the relaxation curves for different constant strains cross each other after a long enough period. To remedy these problems, an improved formula for constant strain is proposed:

$$\sigma = \min(\gamma f_y', \sigma_0) + f_y' \left\langle \sigma_0 / f_y' - \gamma \right\rangle \left[1 + (\rho t^k)/(c\lambda^k)\right]^{-c} \tag{5}$$

Its generalization for variable strain is

$$\dot{\varepsilon} = \dot{\sigma} / E_t + \frac{\left\langle F(\varepsilon) - \gamma f_y' \right\rangle}{E_t} \frac{k\rho^{1/k} c^{1-1/k}}{\lambda \zeta^{1+1/c}} \left(\xi^{1/c} - 1\right)^{1-1/k} \tag{6}$$

where $\xi = [F(\varepsilon) - \gamma f_y']/[\sigma - \gamma f_y']$; $\rho = \rho_0 e^{h\zeta}$; k, c, ρ_1, h = positive constants for a given steel.

The advantages of this proposed formula are four: 1) there is no relaxation if $\sigma_0 \le \gamma f_y'$; 2) the stress approaches $\gamma f_y'$ for $t \to \infty$; 3) for short time duration, Eq. (5) asymptotically approaches CEB-fib formula; and 4) the crossing of relaxation curves for different constant strains will not happen if $c(1-\gamma)h \le 1$. Subsequent studies show that h is very small and can be set equal to 0. Thus, it is ensured that the relaxation curves for different σ_0 would never cross each other.

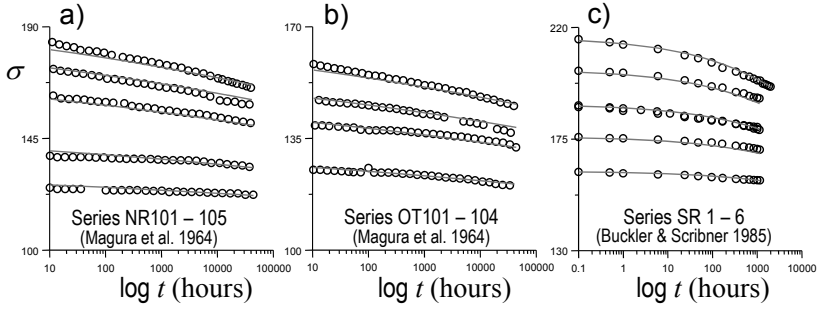

Fig. 3. Simulations based on Eq. (6) are compared with tests under constant strain

The improved formula describes the experiments well. Fig. 3 shows the comparison of the simulation based on Eq. (6) for constant strain with the tests of 1) steel wire (Magura et al. 1964); 2) straight oil-tempered wire (Magura et al. 1964); and 3) stress-relieved strand (Buckler and Scribner 1985). Furthermore, good agreement is also achieved for strain histories with one sudden stress drop of about 5% or 10%, both imposed at t = 24 h (Buckler and Scribner 1985). When plotted out, the curves based on the new proposed formula are almost same as the solid curves that are shown in Fig. 2.

TEMPERATURE EFFECT ON RELEXATION

The importance of temperature level for stress relaxation has long been recognized in the design of prestressed nuclear reactor structures. However, the effect of temperature change is considered neither in CEB-fib model nor in the American practice for prestressed bridges and other creep-sensitive structure. It is well known that a temperature rise will accelerate the flow of metals and thus also the stress-relaxation. The acceleration can be taken into account by replacing the real time with the effective time based on activation-energy theory. The effective time is defined as

$$dt = A_T d\tau \tag{7}$$

where τ is the real time and $A_T = \exp(Q_0 / k_B T_0 - Q_0 / k_B T_0)$ is the Arrhenius factor (Cottrell 1964), which is equal to 1 at room temperature T_0 = 20°C. Here k_B = Boltzmann's constant and Q_0 = activation energy.

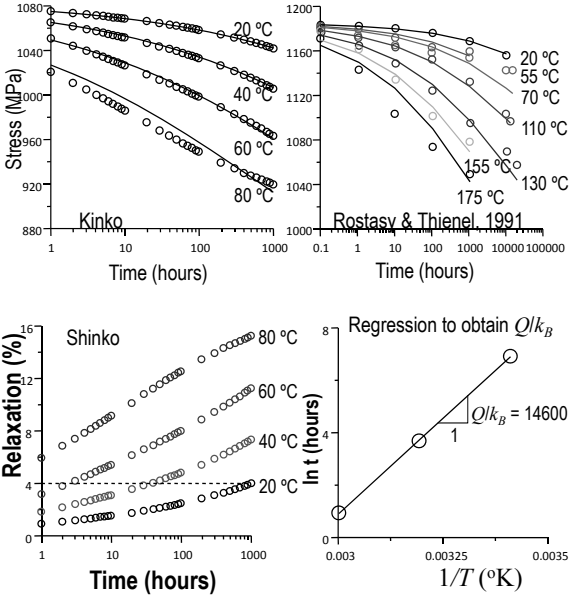

Fig. 4. a) predictions for Shinko tests; b) predictions for Rostásy and Thienel's tests; c) relaxation rates at different temperature; and d) identify Q/k_b based on Kinko tests.

Combined with Eq. (7), the proposed Eq. (6) is able to predict the relaxation for different temperatures. As shown in Fig. 4a, Eq. (6) agrees very well with the data recorded by Shinko. Note that the parameters in Eq. (6) are first obtained by fitting the data for 20°C, and then used to predict relaxation at other temperatures. Similarly, good agreement is also achieved for tests conducted by Rostásy and Thienel (1991); see Fig. 4b. Unlike the data of Shinko, the highest temperature in their tests is 175°C,

and so the effect of temperature on the yield strength and Young's modulus must be taken into account. If the relaxation rate at different temperatures is examined, it can easily be seen that temperature rise from 20°C to 40°C due to sun exposure in hot areas can enormously accelerate the stress relaxation in tendons close to the illuminated surface. A 13% stress loss due to relaxation takes about 100 years if T = 20°C, but only 4 years at temperature 40°C; see Fig. 4c. In all the predictions, parameter Q/k_b can be identified by fitting the times needed to achieve the same amount of stress relaxation at different temperatures, as shown in Fig. 4d.

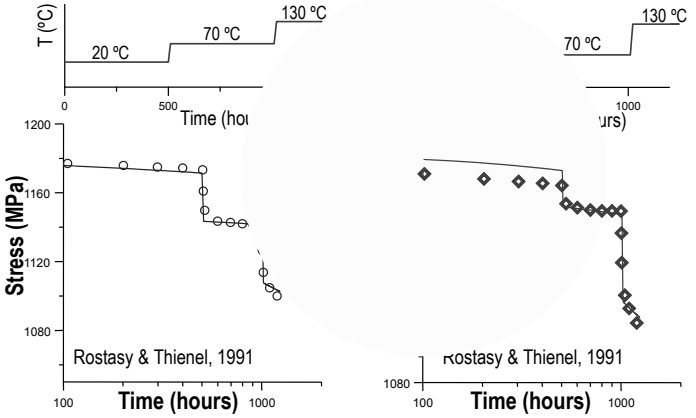

Fig. 5. Prediction based on the proposed formula compared with stepwise heating.

Furthermore, the relaxation formulas proposed here are also compared with the relaxation tests under stepwise heating. The temperature history used in tests is reproduced in Fig. 5. After assuming that, for heating by 1 degree, the average inelastic strain increases by 2.8×10^{-6}, comparison of the prediction with the tests appears to be acceptable; see Fig. 5.

One aspect that needs attention is that, to generalize Eq. (6) to variable temperature, the accumulated thermal strain rate is assumed not to be subtracted from the total strain in function $F(\varepsilon)$. Thus, it is possible that Eq. (6) has $\xi < 1$ during cooling, which makes the power function undefined. Therefore, in programming, ξ must not be allowed to drop below some constant close to 1. To this end, for example, ξ can be replaced by $(\xi^{u+1} + 1.01)/(\xi^u + 1)$, where u is a positive constant. This is, of course, only an ad hoc trick to prevent the program from crashing, but new test data would be needed to validate it experimentally.

CONCLUSION

A general constitutive equation for steel relaxation at variable strain and variable temperature is developed on the basis of metal viscoplasticity and activation-energy theory. Satisfactory agreement has been attained with the main existing test data

including the strain or temperature changes. Calibration of the parameters of the constitutive equation according to the data for the particular prestressing steel used is advisable. Therefore, in addition to relaxation data at room temperature, those at an elevated temperature such as 40°C are also needed. Furthermore, it is important for creep structural analysis to use the present type of general constitutive equation so as to accurately capture the interactions among creep, shrinkage and relaxation, as well as the effect of temperature fluctuation during service lifetime.

REFERENCES

Bažant, Z. P., and Yu, Q. (2011). "Relaxation of Prestressing Steel at Varying Strain and Temperature: Viscoplastic Constitutive Relation." Structural Engineering Report No. 11-3/ITIv, Dept. of Civil & Env. Engrg., Northwestern University; also J. of Engrg. Mechanics ASCE, July 2013, in press.

Bažant, Z.P., Yu, Q., and Li, G.-H. (2012a). "Excessive long-time deflections of prestressed box girders. I: Record-span bridge in Palau and other paradigms." *J. Struct. Eng*., 138(6), 676–686.

Bažant, Z. P., Yu, Q., and Li, G.-H. (2012b). "Excessive long-time deflections of prestressed box girders. II: Numerical analysis and lessons learned." *J. Struct.* Eng., 138(6), 687–696.

Bažant, Z. P., Yu, Q., Li, G.-H., Klein, G. J., and Krístek, V. (2010). "Excessive deflections of record-span prestressed box girder: Lessons learned from the collapse of the Koror-Babeldaob Bridge in Palau." *Concr. Int*., 32(6), 44–52.

Buckler, J. D., and Scribner, C. F. (1985). "Relaxation characteristics of prestressing strand." *Rep. No. UILU-ENG-85-2011*, Univ. of Illinois, Urbana, IL.

Comité Euro-International du Béton (CEB). (1990). "Model code for concrete structures." *Bull. Inform*. *Nos*. 213 and 214, Lausanne, Switzerland.

Cottrell, A. H. (1964). *The mechanical properties of matter*, Wiley, New York.

Jirásek, M., and Bažant, Z. P. (2002). *Inelastic analysis of structures*, Wiley, Hoboken, NJ.

Glodowski, R. J., and Lorenzetti, J. J. (1972). "A method for predicting prestress losses in a prestressed concrete structure." *PCI J*., 17(2), 17–31.

Kingham, R. I., Fisher, J.W., and Viest, I.M. (1961). "Creep and shrinkage of concrete in outdoor exposure and relaxation of prestressing steel." *Special Rep. No. 66*, American Association of State Highway Officials, Ottawa, IL.

Magura, D. D., Sozen, M. A., and Siess, C. P. (1964). "A study of stress relaxation in prestressing reinforcement." *PCI Journal*, 9(2), 13–57.

Rostásy, F. S., and Thienel, K.-Ch. (1991). "On prediction of relaxation of cold drawn prestressing wire under constant and variable elevated temperature." *Nucl. Eng. Des*., 130(2), 221–227.

Material law on the time-dependent stress-strain behavior of young concretes

Isabel Anders[1] and Harald S. Müller[2]

[1] Alumnus of the Institute of Concrete Structures and Building Materials, Karlsruhe Institute of Technology, KIT, Germany, email: isabel.anders@gmx.net
[2] Institute of Concrete Structures and Building Materials, Karlsruhe Institute of Technology, KIT, Germany, email: sekretariat-bt@imb.kit.edu

ABSTRACT

Within the following contribution a material law is presented which allows for the prediction of the basic creep and relaxation behavior of young normal and high-strength concretes. It distinguishes between reversible delayed elastic strains and irreversible flow strains and considers the complex nonlinear creep behavior under constant and variable stresses. The stress-strain behavior corresponds to that of a series connection of different thermodynamically sound rheological elements with aging mechanical parameters. The model was based on a comprehensive experimental program on the creep and relaxation behavior of young concretes.

INTRODUCTION

Adjacent to the instant deformation during loading, concrete shows a distinctive time-dependent stress-strain behavior which has to be considered in construction design. The parameters on long-time creep deformations have been investigated for decades now and the commonly used material laws could be based on a comprehensive experimental data base; see e.g. [ACI 2008, RILEM 1998]. However, as in case of creep in compression mostly higher ages at loading of several days to months were tested, the material laws included in design codes – although commonly valid from ages at loading of one day – do not allow for a reliable prediction of the distinctive creep behavior of very young concretes [Anders 2012].

Furthermore, as most of the design models have been derived from creep experiments under constant stresses, they show several weaknesses concerning the correct prediction of creep under variable stress histories. On one hand this results from the inadequate consideration of the creep nonlinearity and on the other from the chosen mathematical formulation of the time-dependency of creep [CEB 1990].

Particularly suitable for the implementation of the time-stress-strain behavior in FE-programs are models based on rheological elements [Bazant 1989]. However, several models in literature do not satisfy the requirements regarding the thermodynamically sound definition of the mechanical parameters. This however, is a major precondition to avoid the prediction of an unrealistic concrete behavior such as a strain reversal after unloading or the change of sign in stress relaxation.

Against this background a rheological material law was developed which correctly describes the nonlinear creep and relaxation characteristics of young and mature normal strength and high-strength concretes [Anders 2012]. It was based on a comprehensive experimental program on the basic creep and relaxation behavior of young concretes in compression.

EXPERIMENTAL PROGRAM

Within the experimental program one normal strength concrete A and one high-strength concrete B was tested, see Table 1. The given compressive strength f_{cm} was determined at the age of 28 days on cylinder specimens with d/h = 150/300 mm. The solid content of the silica suspension was 10 % of the cement mass. As creep deformations due to diffusion processes are secondary for young concretes all creep specimens (d/h = 150/450 mm) were sealed directly after demolding.

Table 1. Composition and compressive strength of the tested concretes

Composition and compressive strength	Unit	Concrete A (NSC)	Concrete B (HSC)
cement		435	480
water		196	158
silica suspension	kg/m³	-	95
superplasticizer		-	3.4
aggregates		1710	1710
w/c-ratio	-	0.45	0.33
f_{cm}	MPa	55	97

Focus of the creep experiments was set on the investigation of young concretes with ages at loading t_0 between 12 h and 24 h under stress levels $\bar{\sigma}$ between 0.2 and 0.6. The extension of the model's validity to mature concrete required additional creep tests with ages at loading between 3 d and 28 d. Creep recovery was recorded subsequent to selected creep tests and the dependency of creep on the stress history was investigated by several two-step tests starting at young concrete ages between 12 h and 24 h and a subsequent load increase at the age of 4 d and 8 d, respectively.

RHEOLOGICAL MODEL

Within the developed rheological model the instant initial strain during loading of a concrete specimen is described by the deformation behavior of the nonlinear spring element E_1 in Fig. 1. According to a summation approach the subsequent time-dependent creep deformations are separated into reversible delayed elastic strains of an aging Kelvin chain and irreversible flow strains. The delayed elastic strain model is an advancement of the model originally developed by Müller (1986) for normal strength concretes with ages at loading $t_0 \geq 1$ d. Besides the extension on high-strength concrete the adjustment was necessary as for younger ages at loading this previous model violates the requirements regarding a thermodynamically sound

definition of the spring stiffness. This type of model, i.e. a summation approach was chosen as it proved to be superior to comparable approaches, see Anders (2012).

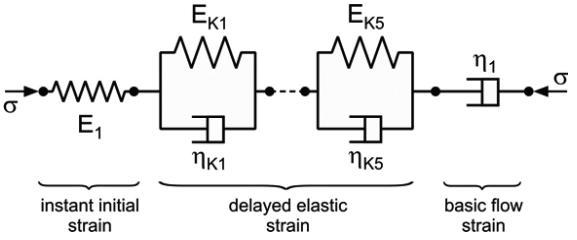

Figure 1. Rheological model [Anders (2012)]

The basic flow corresponds to the deformation behavior of a single dashpot with aging viscosity η_1. Based on the performed experimental program on young concretes with focus on ages at loading $t_0 \leq 1$d in combination with the creep model in the former German design code DIN 1045-1 [DAfStb 2010] for mature concrete a completely new flow model was developed. For ages at loading $t_0 \geq 8$ h and stress levels $\bar{\sigma} \leq 0.7$ all mechanical parameters of the rheological model are defined thermodynamically sound. This means, all spring stiffnesses E and all dashpot viscosities η are always larger than zero and additionally for aging materials such as concrete both parameters age continuously ($\mathrm{d}E/\mathrm{d}t \geq 0$, $\mathrm{d}\eta/\mathrm{d}t \geq 0$), while the deformation kinetics is perfectly predicted.

INSTANT INITIAL STRAIN

In the design of concrete structures the initial strain during load application is usually considered as purely elastic and the irreversible instant plastic strain, especially developing under high stress levels at young concrete ages is added to the creep deformation. In relaxation tests however, the measurement of stress relaxation is not possible until reaching the specified constant initial strain. At that point of time the instant plastic deformation has already developed and does not cause any further stress relaxation. To ensure comparability between the calculated stress relaxation and correspondent relaxation tests, the plastic initial strain is therefore considered within the model of the instant initial strain. Its development bases upon measured stress-strain relations in short-time compression tests for different ages at loading t_0, see Fig. 2 right exemplarily for concrete B.

As shown in Fig. 2 left, the stress-strain relation is purely elastic up to a stress level of 0.2 and the instant elastic strain ε_{ci} may be described by the tangent modulus $E_c(t_0)$. The corresponding relation is subsequently given:

$$\varepsilon_{ci}(t_0) = \frac{\sigma}{E_c(t_0)} \qquad \text{in [m/m]}$$

with $E_c(t_0) = E_{c28} \cdot exp\left(\frac{s_1}{2}\left[1 - \sqrt{\frac{28}{t_0}}\right]\right)$ in [MPa]

Here σ is the applied stress in [MPa] and t_0 the age at loading in [d]. The equation for E_c corresponds to that given in the Model Code 2010, the tangent modulus E_{c28} at the age of 28 d and the parameter s_1 given in Table 2, however, had been adjusted to the experimental data.

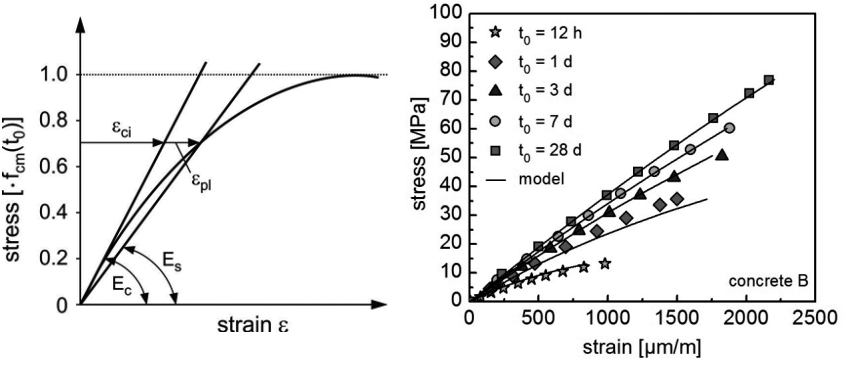

Figure 2. Instant initial strain (left); stress-strain relation measured in short-time compression tests up to a stress level of 0.8 (right), [Anders (2012)]

Under higher stress levels $0.2 < \bar{\sigma} = \sigma / f_{cm}(t_0) \leq 0.8$ the additional plastic strain ε_{pl} in [m/m] may be calculated by

$$\varepsilon_{pl}(t_0) = \frac{k \cdot \sigma}{E_c(t_0) \cdot (1 - k)}$$

with $k = s_2 \left(\frac{\bar{\sigma} - 0.2}{s_3}\right)^{s_4} + s_5(\bar{\sigma} - 0.2) \cdot exp(-s_6 \cdot t_0)$

Table 2. Parameters of the initial strain model

Parameter	E_{c28} [MPa]	s_1	s_2	s_3	s_4	s_5	s_6
				[-]			
Concrete A	33,600	0.20	2.51	2.9	1.7	0.35	0.28
Concrete B	38,000	0.16	0.56	2.7	1.3	0.61	0.88

DELAYED ELASTIC STRAIN

The time-dependent creep deformation measured subsequent to loading does not allow for a direct separation into different creep components. The linear model of the reversible delayed elastic strain ε_v given in the following had therefore been developed from the strain recovery after unloading of selected creep specimens. Information on the used principle of superposition is e.g. published in [Müller 1986]. Due to the thermodynamically sound definition of the rheological model no strain reversal of the creep recovery is predicted.

$$\varepsilon_v(t,t_0) = \sigma \cdot h_1 \cdot g_1(t_0) \cdot f_1(t,t_0) \quad \text{in [m/m]}$$

Multiplied with the applied stress σ in [MPa] the parameter h_1 considers the different delayed elastic creep capability of sealed normal and high-strength concretes.

$h_1 = 1.50 \cdot 10^{-5}$ for concrete A
$h_1 = 0.79 \cdot 10^{-5}$ for concrete B

The aging function g_1 describes the decrease of the delayed elastic strain with increasing age at loading t_0 in [d], see also Fig. 3 right.

$$g_1(t_0) = 0.2 + \frac{45.75}{60 + t_0^{0.68}} + \frac{0.1}{1 + t_0^{0.04}}$$

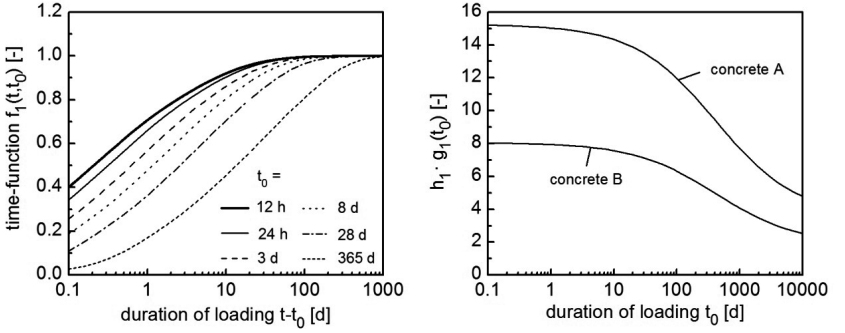

Figure 3. Time-function (left); dependency of the delayed elastic strain on the type of concrete and the age at loading (right), [Anders (2012)]

By introducing the exponent b on both, the time of interest t [d] and the age at loading t_0 [d] the time-function f_1 is dependent on the duration of loading as well as on the age at loading, see Fig. 3 left. The parameters $n_1 \ldots n_5$ define the maximum delayed elastic strains of the individual Kelvin elements and the parameters $a_1 \ldots a_5$ their time-development, see Table. 3. The time-function f_1 is described as follows:

$$f_1(t,t_0) = \sum_{i=1}^{5} n_i \cdot \left[1 - exp\left(-a_i\left(t^b - t_0^b\right)\right)\right]$$

Table 3. Parameters of the delayed elastic strain model

Parameter	Value [-]	Parameter	Value [-]
b	0.35		
a_1	1.0	n_1	0.19
a_2	1.2	n_2	0.22
a_3	7.0	n_3	0.26
a_4	35.2	n_4	0.19
a_5	200	n_5	0.14

FLOW STRAIN

Additionally to the reversible delayed elastic strain ε_v, creep of sealed specimens contains an irreversible flow component ε_f. Considered by the nonlinearity index n, its nonlinearity is not only a function of the stress level $\bar{\sigma} = \sigma / f_{cm}(t_0)$, applied stress σ and compressive strength f_{cm} in [MPa], but also of the duration of loading t-t_0 [d].

$$\varepsilon_f(t, t_0, \sigma) = \sigma \cdot n(t, t_0, \bar{\sigma}) \cdot g_2(t_0) \cdot f_2(t, t_0) \cdot 10^{-6} \qquad \text{in [m/m]}$$

$$n(t, t_0, \bar{\sigma}) = d(\bar{\sigma}) + \frac{\bar{\sigma}^{2.3}}{(t - t_0) + 0.28}$$

$$d(\bar{\sigma}) = \begin{cases} \bar{\sigma} + 0.6 & for\ \bar{\sigma} \geq 0.4 \\ 1.0 & for\ 0 < \bar{\sigma} \leq 0.4 \end{cases}$$

Besides the creep tests under constant stress levels $\bar{\sigma}$ up to 0.6, the nonlinearity index was optimized by means of several tests under variable stress histories. Further information on the used principles of superposition is given in Anders (2012).

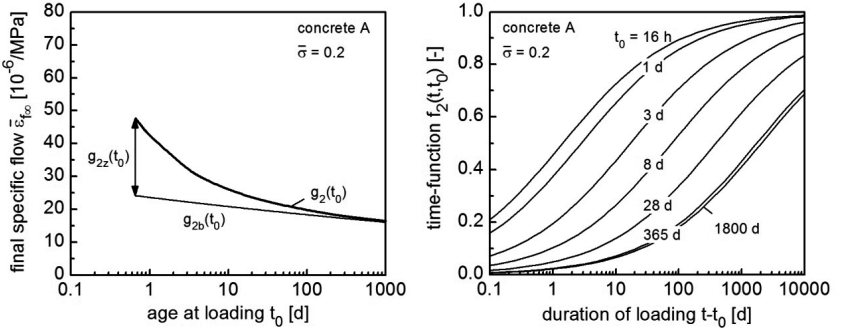

Figure 4. Final specific flow (left); time-function (right), [Anders (2012)]

The high flow capability of young concretes at ages at loading $t_0 \leq 24$ h could only be described by two additive aging functions $g_2 = g_{2b} + g_{2z}$ with t_0 in [d] and the parameters given in Table 4. The final specific flow of concrete A given on the left side of Fig. 4 is calculated by the final flow strain $\varepsilon_{f\infty}$ under a stress level $\bar{\sigma} = 0.2$ related to the creep inducing stress σ in [MPa].

$$g_2(t_0) = g_{2b}(t_0) + g_{2z}(t_0) = \frac{c_1}{0.1 + t_0^{c_2}} + \frac{c_3}{0.07 + t_0^{0.6}}$$

Table 4. Parameters of the aging function g_2

	Concrete	
Parameter [-]	A	B
c_1	26	16
c_2	0.06	0.1
c_3	20	13

Due to the low concrete compressive strength at the beginning of creep tests with young ages at loading, the flow behavior is characterized by a rapid deformation increase whose rate is continuously decreasing with increasing duration of loading. To combine this behavior with the slower time-development of mature concrete the hyperbolic time-function f_2 is dependent on the duration of loading t-t_0 [d] as well as the age at loading t_0 [d], see Fig. 4 right for concrete A.

$$f_2(t,t_0) = \frac{(t-t_0)^{0.5}}{h(t_0)+(t-t_0)^{0.5}}$$

$$h(t_0) = 46.4 \cdot \left(\frac{t_0}{t_0+48.6}\right)^{0.85} \quad \text{for concrete A}$$

$$h(t_0) = 31 \cdot \left(\frac{t_0}{t_0+36.6}\right)^{0.85} \quad \text{for concrete B}$$

TOTAL TIME-DEPENDENT STRESS-STRAIN BEHAVIOR

In Fig. 5 the measured time-dependent creep deformation for different ages at loading t_0 is compared with the prediction of the creep model described above. The given total specific creep $\bar{\varepsilon}_{cc,t}$ corresponds to the sum of delayed elastic strain ε_v and flow strain ε_f related to the creep inducing stress σ. Except from the high creep capability of concrete A for the youngest age at loading, which could not be described even by the additive aging functions defined in the flow model, the creep model allows for a good prediction of the deformation behavior of young and mature normal and high-strength concretes.

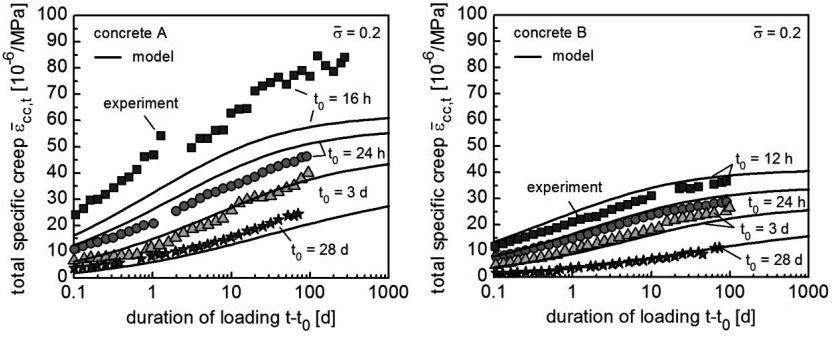

Figure 5. Total time-dependent basic creep deformation, [Anders (2012)]

Besides the numerous creep tests under constant stresses the modeling of the nonlinear dependency of creep on variable stress histories was optimized by several two-step creep tests. As creep and relaxation result from the same micro-structural mechanisms within the cement stone the entire time-dependent stress-strain behavior is described by one material law. In case of relaxation the correspondent integral

equation was solved by a numerical algorithm and the calculated stress development could be compared to that measured in different relaxation tests with ages at loading between 12 h and 3 d. Further information on the entire experimental program as well as the development and evaluation of the material law may be found in [Anders 2012].

CONCLUSION AND OUTLOOK

The developed creep model distinguishes between reversible delayed elastic strains and irreversible flow strains and allows for the correct prediction of the nonlinear deformation behavior under constant and variable stress histories, in particular also for very young concrets. Based on a thermodynamically sound rheological model it does not show weaknesses such as a strain reversal of creep recovery or a change of sign in stress relaxation.

Due to the large differences in the creep behavior of very young normal and high-strength concretes, several parameters had specifically been defined for the tested concretes and not been linked by e.g. the concrete compressive strength or the water-cement ratio. The extension of the model's validity for all concretes would require further comprehensive creep and relaxation tests on different normal and high-strength concretes. Such a data base, complemented by tests with very young ages at loading down to the time of setting, would allow for a reliable determination of the scatter of the used functions. This is a major pre-condition especially for the advancement of the developed aging functions and therefore for a further improvement of the prediction accuracy.

REFERENCES

ACI 209.2R-08 (2008). *Guide for Modeling and Calculating Shrinkage and Creep in Hardened Concrete*. American Concrete Institute, Report of Committee 209

Anders, I. (2012). *Stoffgesetz zur Beschreibung des Kriech- und Relaxationsverhaltens junger normal- und hochfester Betone*, Dissertation at Karlsruhe Institute for Technology, publication in preparation

Bazant, Z.P. (ed., 1989). *Mathematical Modeling of Creep and Shrinkage of Concrete*. John Wiley and Sons

Comité Euro-International du Béton (CEB, 1990). *Evaluation of the Time-Dependent Behavior of Concrete*. CEB Bulletin d'Information, No. 199, Lausanne, Schweiz

Deutscher Ausschuss für Stahlbeton (DAfStb, 2010). *Erläuterungen zu DIN 1045-1*. Heft 525, 2. Auflage

Fédération Internationale du Béton (*fib*, 2012). *Model Code* 2010, Final draft, Vol. 1+2. Bulletins 65+66. Lausanne, Schweiz

Müller, H. S. (1986). *Zur Vorhersage des Kriechens von Konstruktionsbeton*. Dissertation, Universität Karlsruhe, Deutschland

RILEM TC 107 Subcommittee 5 (1998). *Data Base on Creep and Shrinkage*. RILEM Draft Report. Principal authors: Müller, H. S., Bazant, Z. P. und Küttner, C. H., nicht veröffentlichter Arbeitsbericht

Inverse Estimation of Thermal Properties of Concrete During Hydrating Process

Osvaldo D. Quintana[1], Antonio Aquino[1], Rubén López[1], Jean Marie Désir[2], Eduardo M. B. Campello[3]

[1]Computational Mechanics Laboratory, Faculty of Engineering, National University of Asunción, P.O. Box 2160, San Lorenzo, Campus Universitario; PH / FAX (+ 595 21) 585 - 581; email: osvquintana@gmail.com, aaquino@ing.una.py, rlopez@ing.una.py

[2]Civil Engineering Department, Federal University of Rio Grande do Sul, P.O. Box 90035190, Porto Alegre, RS, CEP 90035-190; PH (51) 33083521; FAX (51) 33083449; email: jean.marie@ufrgs.br

[3]Department of Structural and Geotechnical Engineering, Polytechnic School, University of São Paulo, P.O. Box 61548, São Paulo, SP, CEP 05424-970; PH +55 (11) 3091-5489; FAX +55 (11) 3091-5181; email:campello@usp.br

ABSTRACT

At early-ages, thermal stresses that develop as a consequence of cement hydration can cause the evolving concrete tensile strength to be reached, and cracks to appear. A technique to recover the internal heat source and the thermophysical properties (specific heat, thermal conductivity) during hydration process of both normal strength concrete and high performance concrete is presented, in order to solve the direct heat transfer problem of concrete structures. Composite and pozzolanic binder was used. From experimental data an inverse algorithm was implemented to obtain these parameters, the evolution of Young's modulus was obtained through a maturity model and both were combined with the finite element method. The goal is to provide a numerical tool consisting on the use of the inverse method to estimate the thermophysical properties of the material during early stages of hydration. The result provides a good approximation to the experimental data. It is concluded that the proposed method is accurate, stable, and efficient for the analysis of early-ages concrete behavior.

INTRODUCTION

Prediction of temperature evolution is a major concern for massive concrete structures. The hydration of Portland cement in concrete is an exothermic reaction which liberates up to 500 joules of heat per gram of cement (Neville, 1999). Thermal gradients can cause internal stresses which can lead to cracking on a microscopic or macroscopic scale (Metha & Monteiro, 2008). This cracking is also strongly dependent upon the evolutions of Young modulus, tensile strength, creep strains, which are also affected by the evolution of hydration degree and temperature (Briffaut et al., 2011). In addition, new scenarios in the construction industry are

requested, particularly as it refers to the green concrete evolution and those demands lead to the use of new types of concretes with different kinds of components. These facts have clearly generated a great uncertainty in the thermo-mechanical behavior of the concrete and it is necessary to develop new methods to characterize these new cementitious materials. For the above reasons, in this work we develop a methodology based on an experimental program (Lopez et al., 2012) and on a numerical analysis to characterize thermo-mechanically different types of concretes. The main advantage of this methodology consists on simplifying the various parameters that affect thermophysical properties of concrete, such as the amount of cement, the type of cement, the water–cement ratio, some concrete admixtures, etc. and recovering the parameters needed to adequately solve the equation of temperature development in hydrating concrete.

EXPERIMENTAL SETUP

In the experimental program we used thermocouples previously calibrated at eight points inside of cubic samples of concrete of 75 cm of sides under semi-adiabatic boundary conditions, as done by (Lopez et al., 2012) and shown in Fig. 1. They recorded the temperature values generated during the hydration process in a period of twenty-eight days with an interval of one hour between each record.

(a) (b)

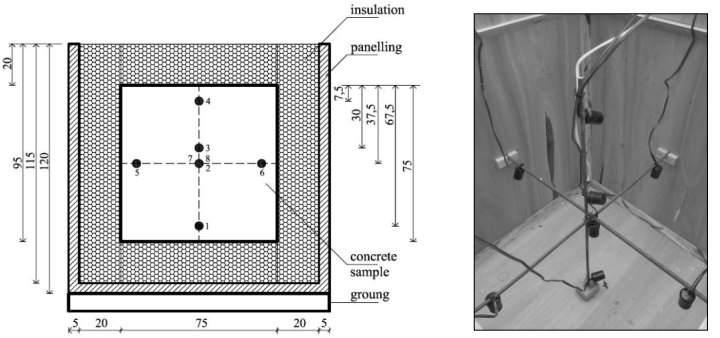

Figure 1. (a) Concrete sample with the side insulation and locations of the thermocouples. (b) Image inside the concrete sample.

NUMERICAL MODEL FOR CONCRETE THERMOMECHANICAL PROPERTIES ESTIMATION

Inverse Heat Transfer Problems (IHTP) use temperature and/or heat flux measurements for the estimation of unknown quantities appearing in the analysis of physical problems in thermal engineering. IHTP are mathematically classified as ill-posed in a general sense, because their solutions may become unstable, as a result of the errors inherent to the measurements used in the analysis (Özisik & Orlande, 2000). However, if properly used they are highly efficient in recovering parameters based on observations or results of a given effect. Among others applications, IHTP also include the estimation of thermophysical properties of materials (Alifanov &

Tryanin, 1985, Artyukhin, 1993, Dantas & Orlande, 1996, Mejias et at., 1999). In this work, in order to obtain the internal heat source and the thermophysical properties of the concrete samples, an inverse algorithm was devised and implemented in Matlab using the technique of the conjugate gradient method (Özisik & Orlande, 2000). To solve the direct heat transfer problem (DHTP), the finite difference method (forward euler) was used, where the stability criterion was based on the Fourier number intended to reproduce the experimental program.

The Direct Problem

The development of temperature in hydrating concrete is usually determined from the transient heat balance, as governed by Fourier's law (Özisik, 1985):

$$\frac{\partial}{\partial X}\left(k_x \frac{\partial T}{\partial X}\right) + \frac{\partial}{\partial Y}\left(k_y \frac{\partial T}{\partial Y}\right) + \frac{\partial}{\partial Z}\left(k_z \frac{\partial T}{\partial Z}\right) + \dot{q} = \rho c \frac{\partial T}{\partial t}, \quad (1)$$

where

k = $k_x = k_y = k_z$ due to the isotropic and homogeneous medium;
ρ = density of the solid;
c = specific heat;
$\dot{q}$ = internal heat source due to hydration.

with boundary and initial conditions.

The initial conditions must be specified as:

$$T(x, y, z, 0) = T_0(x, y, z) \text{ in the domain } \Omega . \quad (2)$$

Values of the heat outflow in the direction n normal to the boundary Γ_q are prescribed as $\bar{q} = (x, y, z, t)$, also called natural boundary condition or Neumann condition:

$$-k \frac{\partial T}{\partial n} = \bar{q} \text{ en } \Gamma_q . \quad (3)$$

Flux across a Γ_q due to convection is given by Newton's law of cooling:

$$\bar{q} = h\left(T_s - T_f\right), \quad (4)$$

where

$\bar{q}$ = convection heat flow; h = film coefficient;
T_s = solid temperature; T_f = fluid temperature.

In the experimental program, surface at a temperature T_1 is completely enclosed by a larger volume at a temperature T_2, the radiation channel is given by:

$$\varepsilon_1 A_1 \sigma (T_1^4 - T_2^4), \quad (5)$$

where ε_1 = is the thermal emissivity of the enclosure surface;
σ = is the Stefan-Boltzmann constant with a value of 5.669 x 10^{-8}W/m^{2}K^4;
A_1 = is the enclosure surface.

Replacing (5) in (3) we have:

$$-k \frac{\partial T}{\partial n} = \varepsilon_1 \sigma (T_1^4 - T_2^4) \quad \text{on } \Gamma_q . \quad (6)$$

Combining (3,4,5,6) we obtain:

$$-k \frac{\partial T}{\partial n} = \bar{q} + h\left(T_s - T_f\right) + \varepsilon_s \sigma \left(T_s^4 - T_f^4\right) \quad \text{on } \Gamma_q, \quad (7)$$

where ε_s = is the emissivity of the solid under consideration, therefore (7) is our boundary condition for this study.

Stability criterion for DHTP

Using a forward Euler integration scheme, time-steps were adjusted according to the Fourier number for a 3-D analysis:

$$\alpha\Delta t\left(\frac{1}{\Delta x^2}+\frac{1}{\Delta y^2}+\frac{1}{\Delta z^2}\right)\leq\frac{1}{6},$$

where

α = thermal diffusivity

$\Delta x=\Delta y=\Delta z\equiv h$ and $\Delta t\equiv k$ of the meshing of the solid in the domain Ω.

Formulation of the IHTP

In the solution of IHTP we describe the internal heat source with a polynomial (Özisik & Orlande, 2000) function given by:

$$\mathrm{g}_P(t)=P_1+P_2\mathrm{t}+\cdots+P_N\mathrm{t}^{N-1}, \tag{8}$$

where

$\mathrm{g}_P(t)$ = is the internal heat source as a function of time;

P = are the coefficients of the polynomial to be determined;

t = is the time instant;

N = is the total number of unknown coefficients.

The estimation of the unknown function $\mathrm{g}_P(t)$ reduces to the obtaining of the N unknown parameters P_j, j = 1,…, N. Such problem is solved here by the minimization of the ordinary least squares norm:

$$S(\boldsymbol{P})=\sum_{i=1}^{I}[Y_i-T_i]^2\,, \tag{9}$$

or in a matrix form

$$S(\boldsymbol{P})=[\boldsymbol{Y}-\boldsymbol{T}(\boldsymbol{P})]^T[\boldsymbol{Y}-\boldsymbol{T}(\boldsymbol{P})]\,, \tag{10}$$

where

S = sum of square-errors or objective function;

$\boldsymbol{P}^T \equiv [P_1, P_2, \ldots, P_N]$ = vector of unknown parameters;

$T_i(\boldsymbol{P}) \equiv T(\boldsymbol{P}, t_i)$ = estimated temperature at a sensor location at time t_i;

$Y_i \equiv \boldsymbol{Y}(t_i)$ = measured temperatures at time t_i as read by the sensors;

I ≡ total number of measurements, where $I \geq N$,

with the superscript "T" denoting the transpose and $[\boldsymbol{Y}-\boldsymbol{T}(\boldsymbol{P})]^T$ being defined as:

$$[\boldsymbol{Y}-\boldsymbol{T}(\boldsymbol{P})]^T \equiv [Y_1-T_1, Y_2-T_2, \ldots, Y_I-T_I]\cdot \tag{11}$$

Computational Algorithm

Our computational algorithm reads as follows:

Step 1 Solve the DHTP (1) by the finite difference method taking as initial condition the initial temperature of the mixing (as measured in the physical experiment) and as boundary condition the one stated in (7), obtaining the vector of estimated temperatures $\boldsymbol{T}_{(P)}$:

$$\boldsymbol{T}_{(P^k)}=[\boldsymbol{T_1}, \boldsymbol{T_2}, \ldots, \boldsymbol{T_I}]\cdot$$

Step 2 Check the stopping criterion. Continue if not satisfied:

$$S(\boldsymbol{P^{k+1}})<\varepsilon \quad \text{for} \quad \varepsilon = 1\times10^{-6}.$$

Step 3 Compute the sensitivity $\boldsymbol{J^k}$:

$$J_{ij}=\frac{T_i(P_1, P_2, \ldots, P_j+\varepsilon, \ldots, P_N)-T_i(P_1, P_2, \ldots, P_j, \ldots, P_N)}{\varepsilon}\cong\frac{\partial T_i}{\partial P_j}\cdot$$

Step 4 Compute the gradient direction: $\nabla S(\boldsymbol{P}^k) = -2(\boldsymbol{J}^k)^T\,[\boldsymbol{Y} - \boldsymbol{T}(P^k)]$.
Compute the conjugation coefficient:

$$\gamma^k = \frac{\sum_j^N [\nabla S(\boldsymbol{P}^k)]_j^2}{\sum_j^N [\nabla S(\boldsymbol{P}^{k+1})]_j^2}, \quad \text{for } k = 1,2,\ldots$$

with $\gamma^0 = 0$ for $k = 0$.

Step 5 Compute the direction of descent: $\boldsymbol{d}^k = \nabla \boldsymbol{S}(P^k) + \gamma^k \boldsymbol{d}^{k-1}$.

Step 6 Compute the search step size:

$$\boldsymbol{\beta}^k = \frac{[\boldsymbol{J}^k \boldsymbol{d}^k]^T [\boldsymbol{T}(P^k) - \boldsymbol{Y}]}{[\boldsymbol{J}^k \boldsymbol{d}^k]^T [\boldsymbol{J}^k \boldsymbol{d}^k]}.$$

Step 7 Compute the new estimate: $\boldsymbol{P}_{k+1} = \boldsymbol{P}^k - \boldsymbol{\beta}^k \boldsymbol{d}^k$.

Step 8 Replace *k* by *k+1* and return to Step 1

Internal heat source

From results obtained by (8), best approximations were observed from an exponential function, therefore the internal heat source was obtained as follows:

$$g(t) = P_1 e^{P_2 \frac{t_k}{t_N}}, \tag{12}$$

where

P_1, P_2 = parameters recovered by the algorithm;
t_k = time in seconds in the current iteration;
t_N = final time at twenty-eight days in seconds.

Thermophysical parameters

To recover the thermophysical parameters for a heat distribution in one dimension and with one heat source, we have the equation (1) reduced to:

$$q_{\vec{x}} + g(t) = C\frac{\partial T}{\partial t}, \qquad \text{if;}$$

$$\frac{\partial T}{\partial t} = cte = D, \qquad \text{then:} \qquad q_{\vec{x}} + g(t) = CD,$$

if $q_{\vec{x}} = a + bx$, as we have obtain from experimental data, then $q_{\vec{x}} = A$ and:

$$g(t) + A = CD, \qquad \text{and then:} \qquad g(t) = CD - A = cte. \tag{13}$$

If the heat flux variation is lineal and the variation of temperature through time is constant, necessarily g(t) will be constant or null, so $CD = K$.

Computation of thermal stresses

Through a maturity model (ASTM C 1074) and the recommendation of the ACI 318 we obtain the evolution of the Young's modulus for the mechanical coupling:

$$E_{c(t)} = \omega_c^{1,5} \times 0{,}043\sqrt{f_c},$$

where E_c = Young's modulus (MPa); f_c = compressive strength (MPa);
ω_c = density of concrete (kg/m^3).

Poisson's ratio was $\upsilon = 0.18$, whereas no consistent relationship between Poisson's ratio and characteristics of concrete as the water / cement ratio, curing time and aggregate size distribution (Metha & Monteiro, 2008). For computation of the resulting thermal stresses derived from the DHTP, standard finite element analysis was performed by the commercial software ANSYS Workbench.

RESULTS AND DISCUSSION

In Table 1, the parameters recovered by the algorithm are presented. Table 2 and Fig. 2a, b, c, d present measured and numerically computed temperatures from the solution of the DHTP based on the parameters presented in Table 1.

Table 1. Parameters recovered by the algorithm.

Concrete (MPa)	Binder	Internal Heat Source		Specific Heat (J/kg °C)	Thermal Conductivity (W/mm °C)
		P_1	P_2		
20	Pozzolanic	0,4722	-38,4612	800	1.00×10^{-03}
20	Composite	0,5055	-40,9155	825	1.12×10^{-03}
60	Composite	0,4149	-4,6830	1017	1.97×10^{-03}
100	Composite	1,1775	-71,5336	1208	2.1×10^{-03}

Table 2. Summary of measured and numerically computed temperatures

Concrete (MPa)	Binder	Experimental (°C)	Numerical (°C)	Time (minutes)
20	Pozzolanic	56,00	55,39	2.118
20	Composite	59,00	58,47	1.836
60	Composite	67,00	66,00	1.567
100	Composite	76,00	75,01	1.093

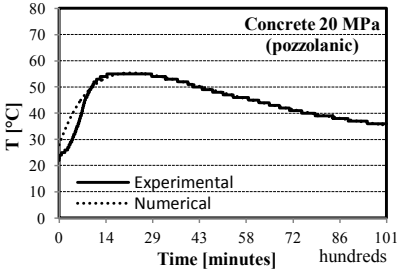

Figure 2. (a)

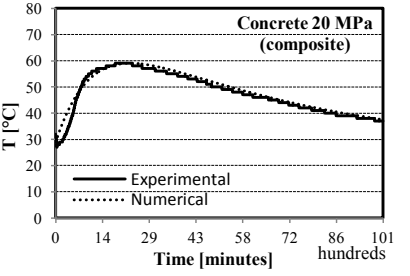

Figure 2. (b)

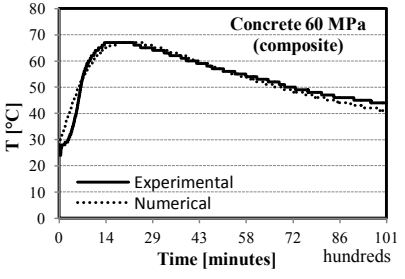

Figure 2. (c)

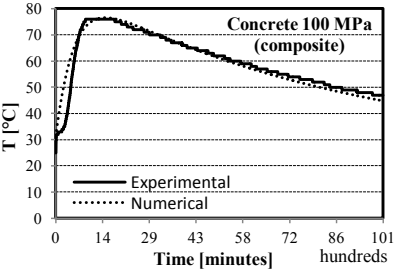

Figure 2. (d)

Figure 2. (a) Temperature history for 20 MPa (pozzolanic). (b) 20 MPa (composite). (c) 60 MPa (composite). (d) 100 MPa (composite).

The following figures illustrate the evolution of thermal stress.

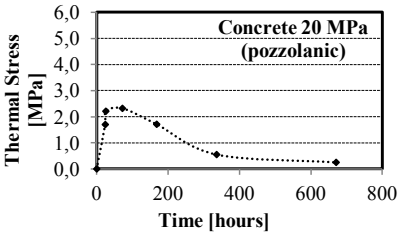

Figure 3. (a)

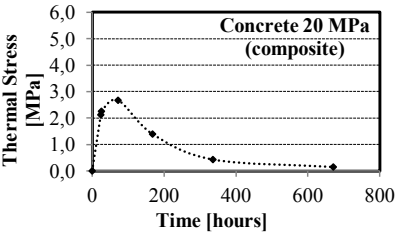

Figure 3. (b)

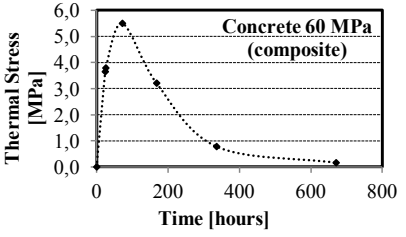

Figure 3. (c)

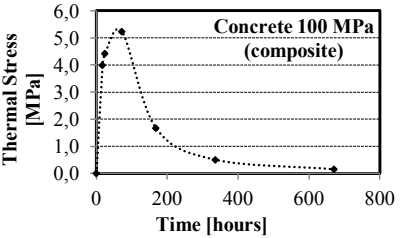

Figure 3. (d)

Figure 3. (a) Thermal stress history for 20 MPa (pozzolanic). (b) 20 MPa (composite). (c) 60 MPa (composite). (d) 100 MPa (composite).

The main objective was to validate the proposed numerical model. Axial symmetry was considered in the numerical analysis. It can be seen from Fig. 2 that the numerically computed temperatures are in very good agreement with the experimentally determined ones. A good match between the simulated and experimental data is due to the boundary conditions (semi-adiabatic) of the simulated samples, when these boundary conditions are modified, we expect some variations in these values. We have seen that the film coefficient is very sensitive and has a strongly nonlinear behavior, affecting the results provided by the simulation. From Fig. 2(d), as expected, the higher cement content results in more intensive hydration process. Furthermore, a rapid dissipation of the heat is observed, the reason for this phenomenon could be that it has a very low porosity and therefore the heat generated is transmitted more quickly to the environment. From Fig. 3, at early hours after casting a low stress development is observed; this effect can be explained by the relaxation of the material due to creep and the boundary conditions. Upper values turn up into the first three days after casting with a nearly linear, steep behavior; this detail is to be taken into account because the tensions are developed very abruptly.

CONCLUSIONS

A numerical method for the prediction of temperature development in early ages of concrete and thermo-mechanical analysis was briefly presented. The inverse algorithm was implemented in Matlab programming environment. The temperature history curves were obtained, based on the parameters (internal heat source, thermal conductivity, specific heat) recovered by the algorithm. For computation of the

resulting thermal stresses, standard finite element analysis was performed. The present methodology enables the determination of the temperature history curve during the hydration process. It was shown that the present model was able to estimate parameters to solve the DHTP for different types of concrete and mixtures with very good accuracy. The approach described in this paper has some features that makes it particularly attractive: (i) the experimental program is easy to implement and does not have to be in a strictly controlled laboratory environment and therefore suitable to use by the concrete companies; (ii) besides recovering the internal heat source, the methodology recovers the thermal conductivity and the specific heat for each type of concrete and mixing designs; (iii) the model can predict the total heat generated in the concrete at any given location and time and this can be useful to decide the timing of operations such as formwork removal and the applications of post-tensioning forces. Finally, we believe this method enables concrete structures designers and contractors to quantify and evaluate the effect of various controllable and uncontrollable parameters on the temperature development in situ.

REFERENCES

ACI Committe 318. (1995). *Building Code Requirements for Structural Concrete and Commentary*, Part 4.

ASTM C1074 – 11. (2011). *Standard Practice for Estimating Concrete Strength by the Maturity Method*, ASTM International.

Alifanov, O.M., Tryanin, A.P. (1985). *Determination of the Coefficient of Internal Heat Exchange and the Effective Thermal Conductivity of a Porous Solid on the Basis of a Nonstationary Experiment*, J. Eng. Phy., 48(3), 356-365.

Artyukhin, E.A. (1993). *Iterative Algorithms for Estimating Temperature Dependent Thermophysical Characteristics*, 1st International Conference on Inverse Problems in Engineering - Proceedings, 101-108, Palm Coast, Florida.

Briffaut, M., Benboudjema F., Torrenti, J., Nahas, G. (2011). *Analysis of semi-adiabiatic tests for the prediction of early-age behavior of massive concrete structures*, Cement & Concrete Composites, 34 (5): 634-641.

Dantas, L., Orlande, H.R.B. (1996). *A Function Estimation Approach for Determining Temperature-Dependent Thermophysical Properties*, Inverse Problems in Engineering, 3, 261-279.

Lopez, R., Aquino, F., Quintana, O.D., Benitez, J., Benitez, M., Martinez, D. (2012). *Study of Thermal Concrete Performance at Early Age in Hot Climate*, Anais do 54° Congresso Brasileiro do Concreto, Ibracon, Maceió, 2012.

Mejias, M.M., Orlande, H.R.B., Özisik, M.N. (1999). *Design of Optimum Experiments for the Estimation of Thermal Conductivity Components of Orthotropics Solids*, Hyb. Meth. Engr., 1, 37-53.

Metha, P. K., Monteiro, P.J.M. (2008). *Concreto, Microestrutura, Propiedades e Materiais*, Ibracon, São Paulo.

Neville, A. M. (1999). *Properties of Concrete*, Pearson Education Limited, London.

Özisik, M.N. (1985). *Heat Transfer, a Basic Approch*, McGraw-Hill Book Co., Singapore.

Özisik, M.N., Orlande, H.R.B. (2000). *Inverse Heat Transfer*, Taylor & Francis, USA.

Effect of Heat Elimination by Pipe Cooling System for Temperature Rise with Heat of Cement Hydration in Beam Using High Strength Engineered Cementitious Composites

T.Mizobuchi[1], T.Kanda[2] and M.Kunieda[3]

[1]Department of Civil and Environmental Engineering, Hosei University, 2-33Tamachi, Ichigaya Shinjuku-ku TOKYO JAPAN; PH +81-3-5228-1450; FAX +81-3-5228-1408; email: mizobuch@hosei.ac.jp
[2]Building Construction and Materials Group, 19-1, Tobitakyu 2-chome, Chofushi, Tokyo 182-0036, Japan; PH+81-42-485-1111; FAX +81-42-485-1111; email: kandat@kajima.com
[3]Department of Civil Engineering Faculty of Engineering, Gifu University, 1-1 Yanagido, Gifu City 501-1193,JAPAN; PH+81-58-293-2410; FAX +81-58-293-2410; email: kunieda@nagoya-u.jp

ABSTRACT

Engineered cementitious composites (ECC) are cementitious materials with high deformability and mixed organic fibers in order to ensure the high toughness. A study with the aim of high strengthening of the boundary beam is carried out. However, in high strengthening, it is reported that temperature in the member exceeds 100^{o}C caused by heat of cement hydration. When temperature in the member exceeds 100 ^{o}C, it is worried that heat of cement hydration affects the performance of organic fibers in the member. Then, in order to control the temperature rise by heat of cement hydration, the analytical study was carried out on effects of control in the countermeasure using pipe cooling system. In this report, the experiments for verifying the effect of pipe cooling in this study will be carried out and the results will be also reported.

INTRODUCTION

ECC is cementitious materials with high deformability and mixed organic fibers in order to ensure the high toughness. In the field of construction, the innovative technique using the boundary beam utilized characteristics of the ECC, which absorbs the energy by concentrating the seismic force in the core wall, is proposed. Moreover, study with the aim of high strengthening of the boundary beam is carried out. However, in high strengthening, it is reported that temperature in the member exceeds 100^{o}C caused by heat of cement hydration. When temperature in the member exceeds 100 ^{o}C, it is worried that heat of cement hydration affects the performance of organic fibers (the high-strength polyethylene fibers) in the member.

Then, in order to control the temperature rise by heat of cement hydration, the analytical study was carried out on effects of control in the countermeasure using pipe cooling system.
Pipe cooling system is generally used in massive concrete structures such as dams or large bridge foundations. In most of the structures where the system has been used until now, the primary objective has been to reduce the temperature of the members to the temperature around the structure. Cases where the primary objective was to aggressively reduce the temperature rise accompanying the heat of hydration are rare. However, if the spacing between pipe installation locations is made small, the rate of flow of water increased and pipe arranged at locations where the temperature in the member becomes a maximum, then a considerably large amount of heat can be removed in a short time. Such a measure can aggressively inhibit thermal stresses caused by heat of cement hydration.

It is necessary to analyze as a coupling problem of the heat balance between the concrete and water which flows in cooling pipe in order to estimate the effect of heat elimination by pipe cooling system. In this study, for this coupling problem, the analysis was carried out using advection and diffusion model according to the equation of heat conduction of the concrete and the equation of governing the temperature of water in the pipe. On the basis of results of temperature measured in the test specimen of the boundary beam using ECC, investigation of the pipe layout in which temperature in the member became less than 90 ^{o}C was carried out, while thermal properties were identified. As the result, if the cooling pipes are appropriately embedded in the member, the simulation results that it was possible to reduce the maximum temperature to about 30 ^{o}C and to control the temperature to be less than 90 ^{o}C in the member were obtained. Moreover, the period in which the pipe cooling has to be implemented was estimated from the relationship between temperature of concrete at the time of placing and properties of adiabatic temperature rise estimated by carrying out identification analyses on the basis of measuring results of concrete temperature carried out in the spring and summer and results of the test of adiabatic temperature rise. As the result, it was anticipated that the execution period of pipe cooling had to be carried out from the beginning of April to the middle of month November. In this report, the experiments for verifying the effect of pipe cooling in this study will be carried out and the results will be also reported.

OUTLINE OF STUDY

In this study, the characteristics of adiabatic temperature rise and heat convection coefficient were identified on the basis of results of measurements of temperature using the actual-sized specimens carried out until now. Next, the analysis on effect of the heat elimination by cooling pipes longitudinally embedded in the boundary beam member was carried out in order to select the number and layout of cooling pipes in which the temperature in the member became 90 ^{o}C or less. However, the layout of cooling pipes would be placed inside reinforcing bars

considering the situation of the re-bar arrangement. The items in this study are shown in the following.

Identification of thermal properties based on the results of temperature measurement. Until now, temperature measurement using the actual-sized specimens was carried out to three times and the test of adiabatic temperature rise was carried out one time. From these measured data, the characteristics of adiabatic temperature rise and heat transfer coefficient were identified. In the measurement of actual-sized specimens, since the measurements were carried out in both of the central and the position of 100mm from concrete surface of the member, the ultimate adiabatic temperature rise, the parameters representing rate of adiabatic temperature rise, age at starting of temperature rise, the interval where temperature rise was suppressed by the effect of chemical admixture agent and the surface transfer coefficient changed so that these two measured values may agree with analytic values.

Analysis of effect of heat elimination by pipe cooling. On the basis of identification analytical results, the thermal analysis on the effect of heat elimination by pipe cooling was carried out. From results of temperature distribution in the center cross section without cooling pipe, the pipe layout in the cases in which the mean temperature in the member did not exceed 90 ^{o}C was selected from analysis cases in which the number of embedded cooling pipes was made to change from one to fifteen.

Verification of effect of heat elimination by pipe cooling. On the basis of the selected layout of the cooling pipes, the experiment was carried out to verify the effect of heat elimination by pipe cooling using the actual-sized specimens. In this experiment, measurement of temperature in the specimens was carried out using both of the actual-sized specimens with cooling pipes and without cooling pipe.

OUTLINE OF BOUNDARY BEAM MEMBER

Figure 1 shows the outline of boundary beam member targeted in this study. The size of member is 913mm in width, 513mm in height and 2,000mm in length. In the member, five re-bars of D29 are used as the main reinforcement bar and twenty re-bars of D13 are used as the shear reinforcement bar. The space inside the arrangement of reinforcement bars consist of 280mm times 650mm. Therefore, the number of cooling pipes is capable to arrange 2 to 3 steps longitudinally and 3 to 5 lines laterally within the section.

ANALYSIS METHOD

Analytical model. In this analysis, thermal analysis was carried out using three-dimensional finite element method. Figure 2 shows the analytical model and the example of the pipe layout in the analysis on the effect of heat elimination by pipe cooling.

Used materials and mix proportion of High Strength ECC. Table 1 shows the materials and mix proportion used the specimen of High Strength ECC.

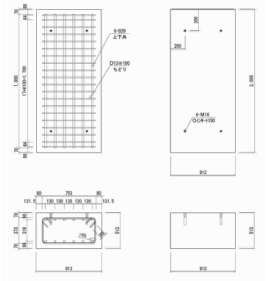

Figure 1 Outline of boundary beam member

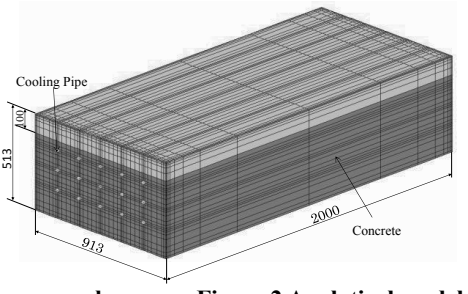

Figure 2 Analytical model

Table 1 Materials and mix proportion used the specimen of High Strength ECC

Items		Materials or Unit Content
Used Materials	Cement	Pre-mixed Silica-fume cement
	Admixture	Expansive Additive
		Limestone Powder
		Silica Sand
	Chemical Admixture	High range water reducing admixtures.
		Antifoaming Agent
	Fiber	High Strength Polyethylene Fiber
Mix Proportion	Water Cement Ratio	28.6%
	Water	320kg/m^3
	Cement	1120kg/m^3

Table 2 Thermal properties of High Strength ECC

Item	Specific heat	Thermal conductivity	Density
High strength	1.28kJ/kg^{o}C	1.4W／m^{o}C	2130kg/m^3

Thermal properties used thermal analysis. The thermal properties of High Strength ECC used thermal analysis were determined on the basis of the results of past researches. Table 2 shows the thermal properties of High Strength ECC.
The equation of adiabatic temperature rise was estimated by carrying out the identification analysis using the results of measurement of the actual-sized specimens. However, in the estimation of the equation of adiabatic temperature rise, as it seems that the delay of heat of hydration caused by influence of superplasticizer is occurred from 8 hours to 10 hours after placement of High Strength ECC, the equation is estimated in dividing into three sections shown in the following.

$$\Delta T = at \qquad (0 \leqq t < t_r) \tag{1}$$

$$\Delta T = bt^c \qquad (\mathrm{tr} \leqq t < t_0) \tag{2}$$

$$Q_{(t)} = Q_\infty \left(1 - e^{-\alpha (t - t_0)^\beta}\right) \qquad (t_0 \leqq t) \tag{3}$$

Where, ΔT= temperature change after placing, a=parameter that presents rate of temperature change with age, t=age (hour), t_r=age of the end between the stage held the heat hydration (hour), Q_∞= ultimate adiabatic temperature rise ($^{\circ}$C), α, β = parameters representing rate of adiabatic temperature rise, t_0= age at starting of temperature rise (day).
As the ambient temperature in the identification analysis of High Strength ECC, temperature around specimen in the measurement of temperature was used.

Equations governing the temperature of water in the pipe. The equation governing the temperature of water in the pipe was derived as below for the case when water flows from direction S_i to direction S_{i+1} at the flow rate u over an infinitesimal distance ds, where S is the distance from the pipe entrance.

$$\rho_w C_w r^2 \pi u \frac{\partial T_w}{\partial S} dS + 2\pi r dS h (T_w - T_c) + \rho_w C_w dS \frac{\partial T_w}{\partial t} = \rho_w C_w u \frac{\partial T_w}{\partial S} + \frac{2h}{r}(T_w - T_c) + \rho_w C_w \frac{\partial T_w}{\partial t} = 0 \tag{4}$$

Here ρ_w :density of water (kg/m^3), C_w: specific heat of water (kJ/kg ºC), and r: radius of the pipe (mm).
The flow rate u in equation (4) was assumed to be uniform within the pipe. Since the range of flow rates during the pipe cooling is generally between 10 *l*/min. to 20 *l*/min., a state of turbulence can be assumed to prevail within the pipe, and heat exchange assumed to be performed adequately.
It was confirmed that the results of analysis using the present procedure agreed well with the results of temperature measurements. Furthermore, the equations have also been used for evaluating primary cooling temperatures of arch dams. Although further studies on the coefficient of heat convection of the pipe wall surface are necessary, the results of analysis using these equations agreed well with the results of measurements near the pipe.

RESULTS OF ANALYSIS

Identification of thermal properties based on the results of temperature measurement. Identification analysis based on the results of measurement of temperature was carried out and thermal properties of the equation of adiabatic temperature rise and surface transfer coefficient were selected. An example of results of identification analysis is shown in Figure 3.

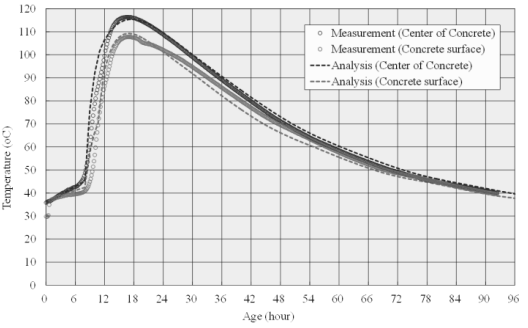

Figure 3 Temperature-age relationship

The relationship between each coefficient and concrete temperature at placing was estimated in order to arbitrarily apply the equation of adiabatic temperature rise in identified range of concrete temperature at placing. It is possible to calculate the relationship between temperature rise and concrete temperature at placing in the stage held the heat hydration in the equation shown in the following.

$$\Delta T=(3.21\times10^{-2}T_a+2.19\times10^{-2})t \qquad (0\leqq t\leqq(2.29\times10^{-2}T_a{}^2+0.825T_a+6.75)) \qquad (5)$$

Where, Ta=concrete temperature at placing (ºC).
Next, it is possible to calculate the relationship between temperature rise and concrete temperature at placing in transition zone to heat of hydration of cement from the stage held the heat hydration using the equation shown in the following.

$$\Delta T=\left(1.12\times10^{-2}T^2\text{-}0.354T+3.76\right)\cdot t^{\left(\frac{T_a}{2.21+0.622T_a}\right)} \qquad (6)$$

On the equation of adiabatic temperature rise, as the test of adiabatic temperature rise has stopped in the temperature rise, the ultimate adiabatic temperature rise was not added.

$$Q_{(t)}=\left(0.292T_a+85.6\right)\left\{1-e^{-\left(0.329T_a-3.36\right)\left(t-\left(2.40\times10^{-2}T_a^2+0.880T_a+8.61\right)\right)^{\left(3.80\times10^{-3}+0.779\right)}}\right\} \qquad (7)$$

Effect of heat elimination by pipe cooling. On the basis of the results of the identification analysis, pipe layout in which the temperature in the member was lower than 90 ºC was selected. Though, the case in which temperature in the member was lower than 100 ºC was made to be the criterion at the beginning, as the case in which 100 ºC was exceeded was anticipated by change of the concrete temperature at placing, the ambient temperature, etc., the temperature in the member should not exceed 90 ºC as the criterion in order to evaluate in the safe side. As the result, it was possible to select the layout in which temperature in the member does not exceed 90

ºC, if the cooling pipes more than 11 are embedded in the cross section. The temperature history of each case is shown in figure 4.

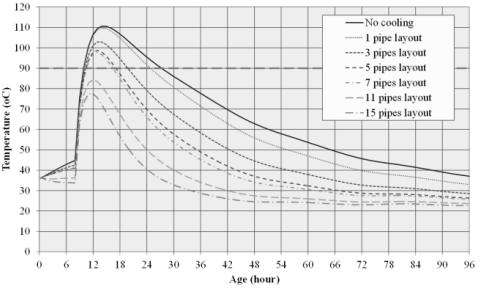

Figure 4 Effect of heat elimination by pipe cooling

Verification of the effect of heat elimination by pipe cooling. From the analytical results on the effect of heat elimination by pipe cooling, if the cooling pipes more than 11 are embedded in the cross section, it is made clear that it is possible that temperature in the member is lower than 90 ºC. In order to verify the analytical result, the specimen without cooling pipe and the specimen that 11 cooling pipes were embedded were simultaneously made and the effect was confirmed by measuring temperature in these members. The results of temperature measurement are shown in Figure 5. In the analysis of the effect of heat elimination by pipe cooling, the analysis was carried out by assuming that flow rate was the 20 *l*/min. However, in this experiment, the flow rate was 35 *l*/min from pump power. Therefore, it was possible to obtain the result of which the effect of decreasing of temperature is higher than the one of assuming at the beginning. As the result of analyzing in this experimental condition, it was confirmed to coincide with measuring results by increasing heat transfer coefficient in the surface of pipe wall at about 3 times. Figure 6 and 7 show the results of thermal analysis considering with the heat elimination by pipe cooling. From these results, it was made to clear that the number of the cooling pipe could be reduced, if the condition of this water conduction is used.

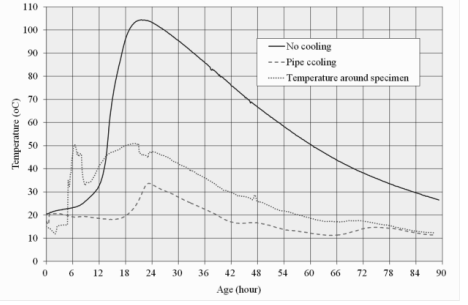

Figure 5 Result of temperature measurement

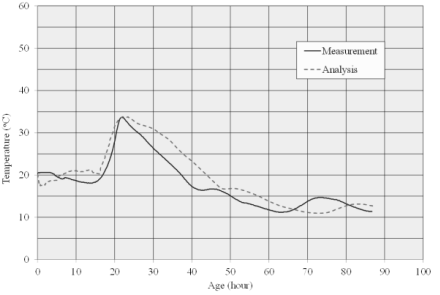

Figure 6 Comparison with measurement and analysis values

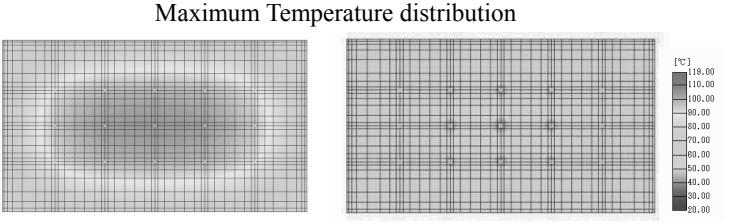

Figure 7 Maximum temperature distributions (effect of pipe cooling)

CONCLUSION

In this study, it was confirmed that it was possible that temperature in the member is reduced below target value by carrying out pipe cooling for the temperature rise by heat of hydration of cement which was a problem with the aim of high strengthening of the boundary beam using the high strength ECC. Hereafter, this study is going to be carried out to examine on the optimum layout of cooling pipes, the optimum number of cooling pipes and the optimum velocity of water conduction.

REFERENCES

Kunimatsu,Y. (1999). Study on the effective range of temperature control using pipe cooling method. *Proceedings of the Japan Concrete Institute* : 1159-1164.

Mizobuchi,T. (1985).”The analysis of the heat elimination by the cooling pipe system of massive concrete”. *Proceedings of the Japan Concrete Institute* .7: 37-40.

Mizobuchi,T. (1997). “An Analytical Study on Thermal Stress Using Pipe Cooling in Arch Dam Concrete.” *Proceedings of the Japan Concrete Institute* .19:1513-1518.

Straus, M. W. (1949). “Cooling of concrete dam.” Denver: U.S.Boulder Canyon Project.

Inoue, I. (2003). “Study on controlling of thermal cracking using pipe cooling method.” *Proceedings of the 58th JSCE Annual Meeting*, Vol.5: 643-644

Development of FEM Thermal Analysis for Concrete Structures with Pipe Cooling System

Yasuaki Ishikawa[1], Toshiaki Mizobuchi[2] and Tada-aki Tanabe[3]

[1]Department of Civil Engineering, Meijo University, Nagoya Shiogamaguchi 1-501, 468-8502, PH +81-52- 838-2343; FAX +81-52-832-1179; email: ishiyasu@meijo-u.ac.jp
[2]Department of Civil and Environmental Engineering, Hosei University, Tokyo Ichigayatamachi 2-33, 162-0843, PH +81-3- 5228-1450; FAX +81-3-5228-1408; email: mizobuch@hosei.ac.jp
[3]CRIIES, Nagoya Wakamizu 2-3-11, 464-0071, PH +81-52-762-7200; FAX +81-52-723-1659; email: tanabe@nagoya-u.jp

ABSTRACT

In this study, a new numerical method of pipe-cooling thermal analysis is presented in order to achieve arbitrary layout of the cooling pipe independent of FEM mesh arrangement. Then, some thermal analyses for concrete structural model with pipe cooling system are executed and validity of the proposed numerical method is discussed. As a result, it is confirmed that the proposed analytical procedure can simulate quite rational temperature histories despite of the cooling pipe layout independent of FEM mesh arrangement.

INTRODUCTION

Recently, heat elimination technology using pipe cooling system has been widely applied to PC bridge structures as well as massive concrete structures and FEM analytical code has been demanded to predict temperature considering pipe cooling under various construction conditions. A theoretical model to express heat elimination effect using pipe cooling system has been firstly developed by Tanabe, Yamakawa and Watanabe (1984). They formulated a governing equation of water temperature in the cooling pipe from equilibrium of heat flux through the pipe surface. Then, coupling the governing equation of water in the cooling pipe and heat transfer condition on the pipe surface with usual heat equation of concrete, the governing equation to predict temperature of both concrete and water in the cooling pipe has

been derived. After that, Mizobuchi et al (2000) completed the governing equation in the discrete form in order to enable numerical calculation numerically for arbitrary concrete structures with pipe cooling system using three dimensional finite element analysis codes. In Japan, most of the conventional FEM thermal analysis codes considering pipe cooling effect have been based on this model. In calculating the heat transfer problem in concrete structures with the pipe cooling system using these codes, concrete region will be usually modeled as a series of solid elements while the cooling pipe region will be modeled as a series of truss elements. However, in the conventional analytical codes, the nodal point as well as the edges composed of truss elements should be coincided with those of solid elements, which will clearly restrict to discuss the cooling pipe layout from various viewpoints.

In this study, a new numerical method of pipe-cooling thermal analysis is presented in order to achieve arbitrary layout of the cooling pipe independent of FEM mesh arrangement. Then, some thermal analyses for concrete structural model with pipe cooling system are executed and validity of the proposed numerical method is discussed.

THEORETICAL MODELING OF HEAT TRANSFER PROBLEM USING THE PIPE COOLING SYSTEM

Tanabe, Yamakawa and Watanabe(1984) firstly formulated heat transfer problem with pipe cooling system. Consider concrete region Ω and boundaries shown in Figure 1. Some cooling pipe elements are embedded in this region. There are two boundaries. One is the boundary S_1 between concrete surface and the atmosphere. The other is the boundary S_2 between the cooling pipe walls and the adjacent concrete surface. Heat equation of the concrete region can be represented as

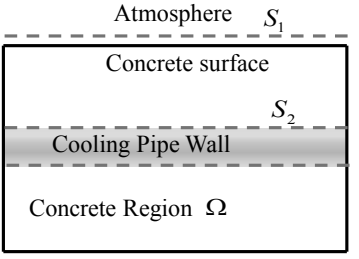

Figure 1 Concrete Region with Pipe System

$$k\left(\frac{\partial^2 T_c}{\partial x^2}+\frac{\partial^2 T_c}{\partial y^2}+\frac{\partial^2 T_c}{\partial z^2}\right)+Q(t)=\rho_c c_c \frac{\partial T_c}{\partial t} \tag{1}$$

in which T_c is temperature in the concrete region. k , ρ_c and c_c are thermal conductivity, density and specific heat of concrete, respectively. $Q(t)$ is calorific value of concrete varying with time t. x, y and z denote global coordinate system.

Heat transfer condition on the boundary between concrete surface and the atmosphere can be given as

$$k\frac{\partial T_c}{\partial x}n_x + k\frac{\partial T_c}{\partial y}n_y + k\frac{\partial T_c}{\partial z}n_z + q_s + \alpha_c\left(T_c - T_a\right) = 0 \tag{2}$$

in which T_a is atmosphere temperature, α_c is heat transfer coefficient between concrete and the atmosphere, q_s is heat flux from the atmosphere. n_x, n_y and n_z denote components of direction cosine. As for boundary between the cooling pipe walls and the adjacent concrete surface, assuming that heat transfer between concrete and water in the cooling pipe is achieved through the cooling pipe walls, heat transfer condition can be analogously given as

$$k\frac{\partial T_c}{\partial x}n_x + k\frac{\partial T_c}{\partial y}n_y + k\frac{\partial T_c}{\partial z}n_z + \alpha_w\left(T_w - T_c\right) = 0 \tag{3}$$

in which T_w is temperature of water in the cooling pipe elements, α_w is heat transfer coefficient between the cooling pipe walls and the adjacent concrete surface.

In general, temperature of water in the cooling pipe will be determined by various factors such as flow velocity, water temperature at entrance of the cooling pipe, radius of the cooling pipe, temperature of the walls and the heat transfer coefficient α_w. Tanabe, Yamakawa and Watanabe(1984) also derived the governing equation of temperature of water in the cooling pipe considering the above factors. Consider an infinitesimal segment of the cooling pipe shown in Figure 2. In the cooling pipe, water flows from left hand to right hand with flow velocity u. Water distribution in the section of the cooling pipe is assumed uniform. From heat equilibrium in the cooling pipe, the governing equation of water temperature can be expressed as

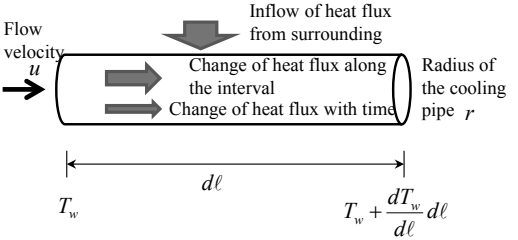

Figure 2 Modeling of Water Flow in the Cooling Pipe

$$\rho_w c_w u\frac{\partial T_w}{\partial \ell} + \frac{2\alpha_w}{r}\left(T_w - T_c\right) + \rho_w c_w\frac{\partial T_w}{\partial t} = 0 \tag{4}$$

in which r is radius of the cooling pipe. ℓ denotes local coordinate system along the cooling pipe.

According to Mizobuchi et al (2000), discretizing from Eq.(1) to Eq.(4) using Galerkin Method, the governing equation in the discrete form can be obtained as

$$\begin{bmatrix} K_c & -K_{cw} \\ -K_{wc} & K_w \end{bmatrix}\begin{Bmatrix} \overline{T}_c \\ \overline{T}_w \end{Bmatrix} + \begin{bmatrix} C & 0 \\ 0 & W \end{bmatrix}\frac{d}{dt}\begin{Bmatrix} \overline{T}_c \\ \overline{T}_w \end{Bmatrix} = \begin{Bmatrix} F_c \\ 0 \end{Bmatrix} \tag{5}$$

in which

$$[K_c] = \int_\Omega [B]^T k [B] d\Omega + \int_{S_1} [N_c]^T \alpha_c [N_c] dS_1 + \int_{S_2} [N_c]^T \alpha_w [N_c] dS_2$$

$$[K_{cw}] = \int_{S_2} [N_c]^T \alpha_w [N_w] dS_2 \,,\ [C] = \int_\Omega [N_c]^T \rho_c c_c [N_c] d\Omega$$

$$\{F_c\} = -\int_{S_1} [N_c]^T q_s dS_1 + \int_{S_1} [N_c]^T \alpha_c T_a dS_1 + \int_\Omega [N_c]^T Q(t) d\Omega$$

$$[K_w] = \left[[N_w]^T \rho_w c_w u [N_w] \right]_{\ell_s}^{\ell_e} - \int_{\ell_s}^{\ell_e} \frac{\partial [N_w]}{\partial \ell} \rho_w c_w u [N_w] d\ell + \int_{\ell_s}^{\ell_e} [N_w]^T \frac{2\alpha_w}{r} [N_w] d\ell$$

$$[K_{wc}] = \int_{\ell_s}^{\ell_e} [N_w]^T \frac{2\alpha_w}{r} [N_c] d\ell \,,\ [W] = \int_{\ell_s}^{\ell_e} [N_w]^T \rho_w c_w [N_w] d\ell$$

Here, $[B]$ is shape function matrix with regard to temperature gradient of concrete, $[N_c]$ and $[N_w]$ are shape function matrices of concrete and water in the cooling pipe, respectively. ℓ_e and ℓ_s are local coordinate of each pipe element.

TECHNICAL ISSUES OF THE CONVENTIONAL NUMERICAL METHOD AND ITS IMPROVEMENT

All temperature histories at all concrete elements and pipe elements can be obtained numerically using finite element method (FEM). A feature of thermal analysis with pipe cooling system is that terms of path integral along pipe element are added in the governing equation. Generally, concrete elements are composed of solid element and cooling pipe elements are composed of truss elements, then, Gauss-

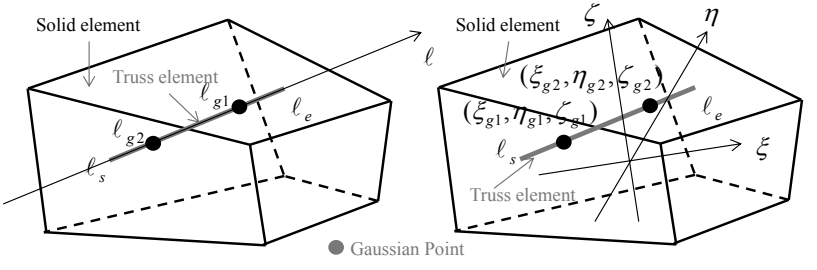

Figure 3 Gauss points for truss and solid elements

Legendre integration will be used in the FEM. If path integration along the pipe element is carried numerically, one must calculate local coordinate values corresponding to gauss points at each pipe element embedded in solid element (Figure 3). For truss element, the local values ℓ_g corresponding to the gauss points can be easily determined. However, for the solid element containing some truss elements, it is quite limited to determine the local values ξ_g , η_g and ζ_g

corresponding to the gauss points. From this reason, in the conventional finite element analysis considering pipe cooling system, all nodal points of the pipe elements must be coincided with nodal points of the concrete elements (Figure 4(a)). Moreover, all pipe elements should be rigorously located along the edge of concrete element. These technical issues have hindered most engineers from discussing the most optimal layout of cooling pipe from various points of view. So, these issues should be improved as shown in Figure 4(b).

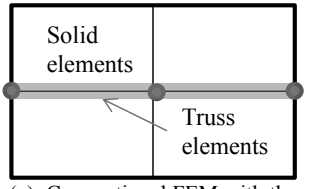

(a) Conventional FEM with the Pipe Cooling System

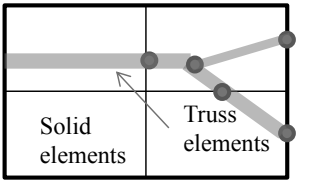

(b) Improved FEM with the Pipe Cooling System

Figure 4 The conventional and improved FEM mesh arrangements

To obtain the local values ξ_g, η_g and ζ_g is equivalent to solve the following equations because global coordinate system may be also functions of the local coordinate system.

$$\begin{aligned} x(\xi_g,\eta_g,\zeta_g) &= x_{pipe} \\ y(\xi_g,\eta_g,\zeta_g) &= y_{pipe} \\ z(\xi_g,\eta_g,\zeta_g) &= z_{pipe} \end{aligned} \tag{6}$$

in which x_{pipe}, y_{pipe} and z_{pipe} are global coordinate value corresponding to gauss points which can be obtained easily. By Taylor series expansion at $\xi_g = \xi_0$, $\eta_g = \eta_0$, $\zeta_g = \zeta_0$ and neglecting all the terms of higher than second order, leftside of equations (6) will be reduced into

$$\begin{aligned} x(\xi_g,\eta_g,\zeta_g) &= x(\xi_0,\eta_0,\zeta_0) + (\xi_g-\xi_0)\frac{\partial x}{\partial \xi} + (\eta_g-\eta_0)\frac{\partial x}{\partial \eta} + (\zeta_g-\zeta_0)\frac{\partial x}{\partial \zeta} \\ y(\xi_g,\eta_g,\zeta_g) &= y(\xi_0,\eta_0,\zeta_0) + (\xi_g-\xi_0)\frac{\partial y}{\partial \xi} + (\eta_g-\eta_0)\frac{\partial y}{\partial \eta} + (\zeta_g-\zeta_0)\frac{\partial y}{\partial \zeta} \\ z(\xi_g,\eta_g,\zeta_g) &= z(\xi_0,\eta_0,\zeta_0) + (\xi_g-\xi_0)\frac{\partial z}{\partial \xi} + (\eta_g-\eta_0)\frac{\partial z}{\partial \eta} + (\zeta_g-\zeta_0)\frac{\partial z}{\partial \zeta} \end{aligned} \tag{7}$$

Substituting equations(7) into equation(6), we finally obtain the following equation in the matrix form

$$\begin{pmatrix} \xi_g \\ \eta_g \\ \zeta_g \end{pmatrix} = [J]^{-1} \begin{pmatrix} x_{pipe} - x(\xi_0,\eta_0,\zeta_0) \\ y_{pipe} - y(\xi_0,\eta_0,\zeta_0) \\ z_{pipe} - z(\xi_0,\eta_0,\zeta_0) \end{pmatrix} + \begin{pmatrix} \xi_0 \\ \eta_0 \\ \zeta_0 \end{pmatrix}, \quad [J] = \begin{pmatrix} \frac{\partial x}{\partial \xi} & \frac{\partial x}{\partial \eta} & \frac{\partial x}{\partial \zeta} \\ \frac{\partial y}{\partial \xi} & \frac{\partial y}{\partial \eta} & \frac{\partial y}{\partial \zeta} \\ \frac{\partial z}{\partial \xi} & \frac{\partial z}{\partial \eta} & \frac{\partial z}{\partial \zeta} \end{pmatrix} \tag{8}$$

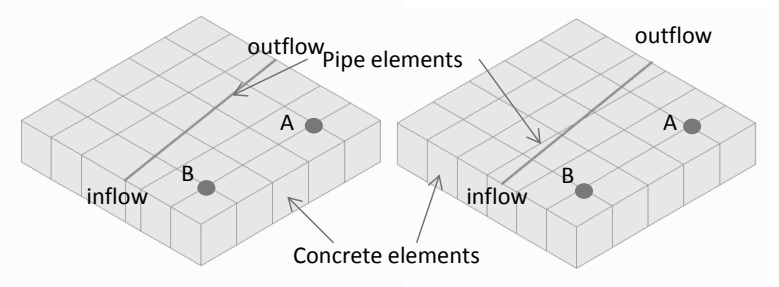

Figure 5 Analytical models (Simple model)

If the trial values ξ_0, η_0 and ζ_0 are given, the local coordinate values ξ_g, η_g and ζ_g on the arbitrary Gaussian point can be calculated numerically from equation (8) using iteration. In other words, thermal analysis can be achieved without any restriction with regard to the pipe layout if the proposed numerical method to calculate the local coordinate value is introduced in conventional FEM program code.

VARIFICATION OF THE PROPOSED NUMERICAL METHOD

By introducing the proposed method into the conventional pipe-cooling thermal analysis program code, validity of the proposed method is numerically discussed. Firstly, comparison between the proposed and conventional numerical method is attempted using some simple models shown in figure 5. The models are cuboid with 1000mm × 1000mm × 200mm composed of concrete material. Pipes are located obliquely across the concrete elements. Difference of the two models is FEM mesh arrangement of concrete model. For one model, FEM mesh division of concrete model is carried so that all pipe elements could lie entirely on the corresponding edge composed of the concrete elements. For the

Table 1 Heat and pipe properties of the analytical models

Thermal conductivity	2.7 W/(m℃)
Specific heat	1.1 kJ/(kg℃)
Density	2300 kg/m^3
Adiabatic temp. rise	46.0(1-exp(-1.104t) ℃
Diameter of pipe	60mm
Amount of flowing	20liter/min.

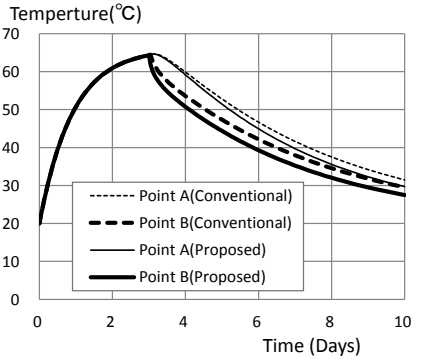

Figure 6 Temperature histories (Simple model)

other model, FEM mesh division of concrete model is carried regardless of the pipe arrangement. Heat and pipe properties are listed in Table 1. The heat transfer coefficient of the cooling pipe walls is estimated using the following relation presented by Mizobuchi et al (2000).

$$\alpha_w = -0.06u^2 + 14.5u - 198 \quad (\text{kcal}/(\text{m}^2\text{hr}^\circ\text{C})) \tag{9}$$

in which the unit of u is cm/sec and applicable range of u in equation (9) is from 20cm/sec to 70cm/sec.

Initial temperatures of both concrete and water is set to 20 ℃ and surrounding condition of concrete is assumed to be adiabatic. It is also assumed that water conduction begins at three days after concrete casting.

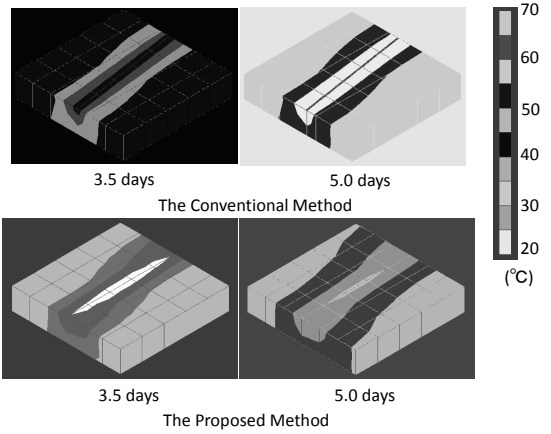

Figure 7 Temperature distributions

Comparison of temperature histories at point A and B with the proposed and the conventional methods are shown in figure 6. The maximum temperature difference between the proposed and conventional methods is almost 2 degrees.

Temperature distributions obtained by the two methods are shown in figure 7. From figures 6 and 7, it is found that the proposed method may give similar solution to the conventional thermal analysis method with the pipe cooling system.

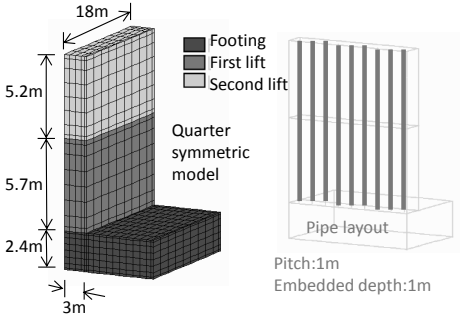

Figure 8 Analytical model (bridge pier)

Next, thermal analyses for another example are carried using the proposed method. Analytical model and pipe layout are shown in figure 8. The analytical model is imagined to be concrete bridge pier. It is assumed that the second lift is casted after

15days at the first lift casting. Atmosphere temperature is assumed to be constant (20 ℃) and the water conduction starts at the bottom side at the same time of the first lift casting. The heat and pipe properties are the same as the aforementioned example. Comparison of temperature histories at the center of all lifts is shown in figure 9. In figure 9, it is discussed whether the pipe cooling system is considered or not. It is found that the proposed model may give rational solution for the effect of pipe cooling system.

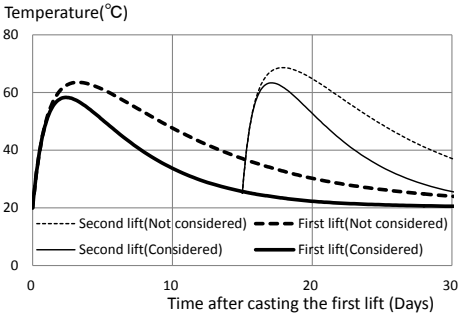

Figure 9 Temperature histories (bridge pier)

CONCLUSION

In this study, it is confirmed that the proposed analytical procedure can simulate quite rational temperature histories despite of the cooling pipe layout independent of FEM mesh arrangement. Extending the proposed method to achieve the bifurcated cooling pipe layout, more comprehensive heat elimination technology using the pipe cooling system will be feasible in the future.

ACNOWLEDGE MENTS

This study was funded in part from the Advanced Research Center for Natural Disaster Risk Reduction, Meijo University, which is supported by the Ministry of Education, Culture, Sports, Science and Technology (MEXT), Japan.

REFERENCES

Tanabe, T., Yamakawa, H and Watanabe, A. (1984). “Determination of Convection Coefficient at Cooling Pipe Surface and Analysis of Cooling Effect.” *Journal of JSCE,* JSCE, No.343, 171-179. (In Japanese)

Mizobuchi, T. et al. (2000). “Effect of Heat Elimination by Pipe-Cooling System in Massive Concrete.” *Journal of JSCE,* JSCE, No.655, 119-132. (In Japanese)